

PROCESSING, CHARACTERIZATION AND MODELLING OF  
BOROSILICATE GLASS MATRIX-PARTICULATE SILICON NITRIDE COMPOSITES,  
CONTAINING CONTROLLED ADDITIONS OF POROSITY, FOR USE IN  
HIGH SPEED ELECTRONIC PACKAGING

By

MICHAEL S. RANDALL

A DISSERTATION PRESENTED TO THE GRADUATE SCHOOL  
OF THE UNIVERSITY OF FLORIDA IN PARTIAL FULFILLMENT  
OF THE REQUIREMENTS FOR THE DEGREE OF  
DOCTOR OF PHILOSOPHY

UNIVERSITY OF FLORIDA

1993

Copyright 1993

by

Michael S. Randall

## ACKNOWLEDGEMENTS

This work would not have been possible without the skilled help of many individuals. First and foremost, I would like to thank my wife, Sara, for her unconditional love, understanding and support. None of this would have been possible without her. I would also like to thank my parents (Randalls and Elders) for their support, understanding and encouragement. I would like to thank my brothers and sisters for their moral support as well.

On the technical side, I would like to sincerely thank Mr. Gary Scheiffele for his vast amounts of training and advice in the area of materials processing. I would like to thank R. Raghunathan and A. Bagwell for their advice and creative discussions as well. Other training and advice, in the area of materials processing, by Dr. M. Amini, Dr. C. Khadilkar, Dr. T.S. Yeh, Dr. S. Vora, Dr. H.W. Lee, Dr. P. Bendale, and Mr. M. Springate, are also greatly appreciated. Furthermore, I would like to gratefully acknowledge the advice of Dr. H.K. Ober, of Cornell University, in the area of dispersion polymerization.

Complex impedance measurements were made possible through the equipment and advice of Dr. L.L. Hench, Dr. J.K. West, and Dr. S. Wallace, at the Advanced Materials Research Center (AMRC). Solution (ICP) and surface (FTIR) analysis was also most graciously provided by Dr. L. Hench and Mr. G. LaTorre. Technical advice and support in the area of electron microscopy (SEM and TEM) from Mr. W. Acree, Mr. R. Crockett, Dr. Y.J. Lin and Dr. S. Bates is also acknowledged gratefully. In addition, I would like to thank Mr. A. Cozzi and Dr. D. Clark for advice and support in doing thermal oxidation experiments. Processing equipment and support was provided by Dr. M.D. Sacks.

I would like to sincerely thank my advisor, Dr. J.H. Simmons, for all of his input and support. I would also like to acknowledge the co-chairman of my committee, Dr. M.D. Sacks for his advice and support. I would like to thank the rest of my committee, Dr. P.H. Holloway, Dr. L.L. Hench, and Dr. D.E. Burke for their assistance as well.

Finally, I would like to thank the Engineering Offices of Gould, Lewis and Proctor, as well as AVX Corporation for providing me employment so that I could pursue my degree during difficult financial times.



## TABLE OF CONTENTS

	<u>Page</u>
ACKNOWLEDGEMENTS .....	iii
ABSTRACT .....	x
CHAPTER ONE: INTRODUCTION .....	1
1.1    The Impact of Electronics on Modern Civilization .....	1
1.1.1    Economic and Political Aspects .....	1
1.1.2    The Future of the Electronics Industry: Impact and Limitations .....	2
1.1.2.1    The Fourth Generation .....	2
1.2    Fundamental Microelectronic Packaging Limitations .....	5
1.2.1    Electron Light Speed Limit .....	9
1.2.2    Conductor Spacing Limit .....	9
1.2.3    Cooling Limitations .....	13
1.3    Electronic Packaging: Overview of the Field .....	18
1.3.1    History .....	18
1.3.2    Importance of the Electronic Package ...	24
1.3.2.1    Economic .....	24
1.3.2.2    Functional .....	24
1.3.3    Properties Desired of Packaging Materials .....	27
1.4    Materials Solutions to Electronic Packaging Problems .....	40
1.4.1    Ceramics versus Polymers .....	40
1.4.2    Methods and Materials .....	43
1.4.2.1    Traditional .....	43
1.4.2.2    Advanced .....	44
1.5    Proposed Packaging Material System: Statement of Thesis .....	51
1.5.1    Choice of Electronic Packaging Material System .....	51
1.5.2    Topics of Investigation .....	53

	<u>Page</u>
CHAPTER TWO: THEORETICAL AND TECHNICAL REVIEW .....	75
2.1 Overview .....	75
2.2 Synthesis and Processing of Uniform Polystyrene Latex Microspheres (UPLMs) .....	75
2.3 Particle Packing .....	85
2.3.1 Monosized Spheres .....	85
2.3.1.1 Ordered Packing .....	85
2.3.1.2 Random Packing .....	85
2.3.2 Packing of Multimodal, Discrete Distributions of Spheres .....	88
2.3.3 Continuous Size Distribution Particles .	105
2.3.3.1 Ideal Packing .....	105
2.3.3.2 Hindered Packing .....	110
2.3.4 Effects of Settling and Segregation ....	110
2.4 Clustering and Percolation Theory .....	112
2.4.1 Clustering .....	115
2.4.2 Percolation .....	116
2.4.3 Application of Percolation to Microstructure .....	123
2.5 Sintering .....	134
2.5.1 General .....	134
2.5.2 Viscous Sintering .....	140
2.5.2.1 Viscous Sintering of Real Systems .....	149
2.5.2.1.1 Effects of Microstructure .....	149
2.5.2.1.2 Viscous Sintering of Glass Matrix Composites Having Nonsintering Inclusions .....	153
2.6 Dielectric Theory .....	158
2.6.1 Dielectric Materials .....	158
2.6.2 Measurement of Dielectric Properties ...	163
2.6.3 Dielectric Properties of Composite Materials .....	170
2.7 Mechanical Properties .....	179
CHAPTER THREE: EXPERIMENTAL PROCEDURE .....	184
3.1 Overview .....	184
3.2 Powder Synthesis and Treatment .....	184
3.2.1 Overview .....	184
3.2.2 Synthesis, Characterization and Preparation of Polystyrene Microspheres	184
3.2.3 Milling and Preparation of Borosilicate Glass Powder .....	199

	<u>Page</u>
3.3 Powder Characterization .....	202
3.3.1 Overview .....	202
3.3.2 Visual .....	203
3.3.3 Density .....	204
3.3.4 Size Characterization of Ceramic Powders .....	206
3.3.5 Surface Area .....	209
3.3.6 Chemical .....	220
3.4 Suspension, Casting and Green Compact Studies .....	224
3.4.1 Overview .....	224
3.4.2 Wet Processing and Characterization ....	225
3.4.2.1 Selection of the Dispersion System .....	225
3.4.2.2 Characterization and Optimization of the Suspension System .....	228
3.4.2.2.1 Overview .....	228
3.4.2.2.2 Rheology of Dispersed Composite Components .	228
3.4.2.2.3 Optimization of the Suspension System ...	230
3.4.2.2.4 Effects of Sonication and Aging Upon Suspension Properties	232
3.4.2.2.5 General Rheology Studies .....	235
3.4.3 Slip Casting of Compact Samples .....	236
3.4.4 Suspension Solids Loading Determination	242
3.4.5 Characterization of Green Compacts .....	243
3.4.5.1 Visual .....	243
3.4.5.2 Hg Porosimetry .....	243
3.5 Thermal Analysis: Oxidation and Pyrolysis Studies .	249
3.5.1 Overview .....	249
3.5.2 Oxidation Studies .....	250
3.5.3 Pyrolysis Studies .....	251
3.6 Thermal Treatments .....	252
3.6.1 Furnace Calibration .....	252
3.6.2 Pyrolysis and Presintering .....	258
3.6.3 Sintering .....	259
3.7 Materials Characterization .....	261
3.7.1 Archimedes Density Characterization ....	261
3.7.2 Dielectric Properties Characterization .	267
3.7.3 Microscopic Investigation of Composites	277
3.7.3.1 Overview .....	277
3.7.3.2 Specimen Preparation .....	277
3.7.3.3 Investigation of Segregation of Included Porosity .....	281
3.7.4 Mechanical Properties Data .....	281

	<u>Page</u>
CHAPTER FOUR: RESULTS AND DISCUSSION .....	286
4.1 Precursor Powders .....	286
4.1.1 Visual .....	286
4.1.2 Powder Density .....	295
4.1.3 Particle Size/Size Distribution .....	298
4.1.3.1 Polystyrene Microspheres ...	298
4.1.3.2 Ceramic Powders .....	315
4.1.4 Powder Surface Area .....	323
4.1.5 Effect of Ball Milling On BS Glass .....	326
4.2 Suspension and Green/Pyrolyzed Structure Characterization .....	337
4.2.1 Suspension Characterization .....	337
4.2.3 Green/Pyrolyzed Structure Characterization .....	349
4.2.3.1 Overview .....	349
4.2.3.2 Structural Characteristics of Polystyrene Latex Compacts .....	349
4.2.3.3 Structural Characteristics of Green and Pyrolyzed Composites .....	360
4.2.3.4 Effects of Aging and Sonication Upon Green Properties .....	382
4.2.3.4.1 Sonication .....	382
4.2.3.4.2 Aging .....	386
4.3 Thermal Processing and Characterization .....	395
4.3.1 Removal of Organics .....	395
4.3.2 Evolution of BS Glass Surface Area .....	399
4.3.3 Oxidation of $\text{Si}_3\text{N}_4$ Powder .....	404
4.3.4 Sintering .....	408
4.4 Characterization and Modelling of Processed Materials .....	450
4.4.1 Characterization of Microstructure .....	450
4.4.2 Modelling of Included Porosity .....	482
4.4.3 Characterization of Dielectric Properties .....	499
4.4.4 Microhardness Characterization .....	534
CHAPTER FIVE: SUMMARY AND CONCLUSIONS .....	542
5.1 Overview .....	542
5.2 Powder Development and Characterization .....	542
5.3 Green Processing and Characterization .....	543
5.4 Thermal Processing and Characterization .....	544
5.5 Characterization and Modelling of Densified Compacts	546

	<u>Page</u>
CHAPTER SIX: SUGGESTIONS FOR FUTURE WORK .....	549
APPENDIX I: MANUFACTURER'S DATA FOR CERAMIC CONSTITUENT POWDERS .....	553
APPENDIX II: PARTICLE SIZE AND SIZE DISTRIBUTION DATA OF UNSETTLED 4.6 $\mu\text{m}$ REGIME (061990 SERIES) UPLM SPHERES .....	564
APPENDIX III: LEAST SQUARES POLYNOMIAL REGRESSION DATA CURVE FITTING PROGRAM (BASIC) .....	576
APPENDIX IV: LIST OF ACRONYMS .....	579
REFERENCES .....	581
BIOGRAPHICAL SKETCH .....	630

Abstract of Dissertation Presented to the Graduate School  
of the University of Florida in Partial Fulfillment of the  
Requirements for the Degree of Doctor of Philosophy

PROCESSING, CHARACTERIZATION AND MODELLING OF  
BOROSILICATE GLASS MATRIX-PARTICULATE SILICON NITRIDE COMPOSITES,  
CONTAINING CONTROLLED ADDITIONS OF POROSITY, FOR USE IN  
HIGH SPEED ELECTRONIC PACKAGING

By

Michael S. Randall

August 1993

Chairman: Dr. Joseph H. Simmons

Major Department: Materials Science and Engineering

Borosilicate glass matrix-particulate silicon nitride composites, with controlled additions of porosity, are produced through suspension processing and slip casting of nonaqueous, codispersed suspensions. Controlled porosity is obtained via the addition and pyrolysis of polystyrene latex microspheres. The effects of latex size and size distribution upon controlled pore structure are investigated. The largest (9.0  $\mu\text{m}$  monosized) latex, at a concentration of 17.6 V%, is found to give the largest amount of closed porosity (15.6 V%).

The borosilicate glass-silicon nitride binary is also investigated in order to determine the effect of nonsintering inclusion concentration upon processing factors as well as upon final composite properties. Composites containing all three constituents (borosilicate glass,  $\text{Si}_3\text{N}_4$ , and polystyrene latex) are also investigated.

Above the percolation threshold of latex addition (i.e. a filled fraction of approximately 16 V% of total space), the pore structure is observed to change rapidly, greatly affecting densification behavior as well as the pore structure. Additions of latex below the percolation

threshold result in hermetic, densified structures subsequent to processing. Silicon nitride additions are found to retard densification kinetics at and above concentrations of 16 volume percent of total space and to arrest sintering at and above  $\text{Si}_3\text{N}_4$  concentrations of 36 volume percent of total space, in accordance with viscous sintering theory.

Hermetic, porous borosilicate glass-particulate silicon nitride composites are produced having maximum closed porosities of approximately 15.6 volume percent (at approximately 16.0 V% total porosity). The densified included pore structure is accurately modelled using a modification of standard series clustering and percolation models.

Corresponding minimum composite dielectric constants of approximately 3.5 are observed. The dielectric constant of the composites are found to be stable over the range of frequencies measured. Dielectric loss values are found to agree well with analogous literature values for the borosilicate matrix glass. Composite dielectric constants are modelled using effective medium theory as well as traditional dielectric mixing rules.

Microhardness evaluations of representative composites are also discussed. The elastic moduli of the composite system are modelled using MacKenzie, linear regression, Voigt and Reuss models. Stoke's settling theory is also extrapolated to explain the lack of segregation observed in this system.



## CHAPTER ONE INTRODUCTION

### 1.1 The Impact of Electronics on Modern Civilization

#### 1.1.1 Economic and Political Aspects

The electronics industry is a \$460 billion industry world wide [88SCH1]. The American electronics industry accounts for 38.1% of this amount, while Japanese and European electronics industries account for 37.7% and 24.2% of the world electronics industry, respectively [88SCH1]. Domestically, the electronics industry accounts for 3.6% of the gross national product (GNP) which amounts to approximately 170 billion dollars [88SCH1, 90WRI]. The electronics industry is currently growing at an annual rate of 13% for Japan, and 11% and 6% for the United States and Europe, respectively [88SCH1].

Demand for improved electronic devices (i.e. higher speed, smaller size, and greater ability, etc.) has provided a driving force for continuous improvements in microelectronic technology. Never have Ralph Waldo Emerson's words, "If a man can write a better book, preach a better sermon, or make a better mouse-trap than his neighbor, though he builds his house in the woods, the world will make a beaten path to his door," been more applicable to an industry [88CAR, p. 84.8].

The electronics industry has generally progressed from analog to digital electronics. The workhorse of digital electronics is the integrated circuit. The IC was simultaneously invented by Jack Kilby of Texas Instruments and by Robert Noyce of Fairchild Industries in 1958 [88MAC]. The field of IC technology has grown through three generations of successively increasing integration (i.e. MSI for medium scale integration, LSI for large scale integration, and VLSI for very large scale integration, respectively), with more generations to come (i.e.



ULSI and WSI, for ultra large scale integration and wafer scale integration, respectively). Furthermore, IC devices are available in many configurations, as required by the exhaustive number of electronic appliance applications. The general trend in these electronic devices is toward maximization of circuit elements per unit volume. Figure 1.1 illustrates the evolution of circuit density for both field effect (FET) and bipolar junction (BJT) transistor IC devices. The relative scale of integration is also indicated in Figure 1.1

### 1.1.2 The Future of the Electronics Industry: Impact and Limitations

#### 1.1.2.1 The Fourth Generation

The major goals influencing the evolution of electronic technology is to increase performance and universality of application. Digital microprocessor-based devices dominate the electronics industry. Therefore, improvements in electronic technology will focus upon advancement of microprocessor technology as well as in advances in microprocessor interlinking and increasing the availability and amount of memory accessible by microprocessors. Other goals include reduction in power consumption, reduction in device size and weight, increased device capability as well as increased device dependability and environmental/thermal stability. Other important requirements are the maximization of device output and quality, at minimized cost.

The methods that will be used in order to achieve the above goals will be quite varied [see 89SER,89TUM3, etc.]. In order to increase computing speed (i.e. electronics performance), non-traditional technologies, which are currently in their infancy, will be applied. Examples of these technologies include optical switching and communication (including holography) [89SER,88YAN,88SRI,87COR1, 87COR2,83BER], electro-optical interfacing [88HUT,87JIN], advanced semiconductor materials, parallel processing [92SKE], artificial intelligence (AI), integrated services digital networking (ISDN)

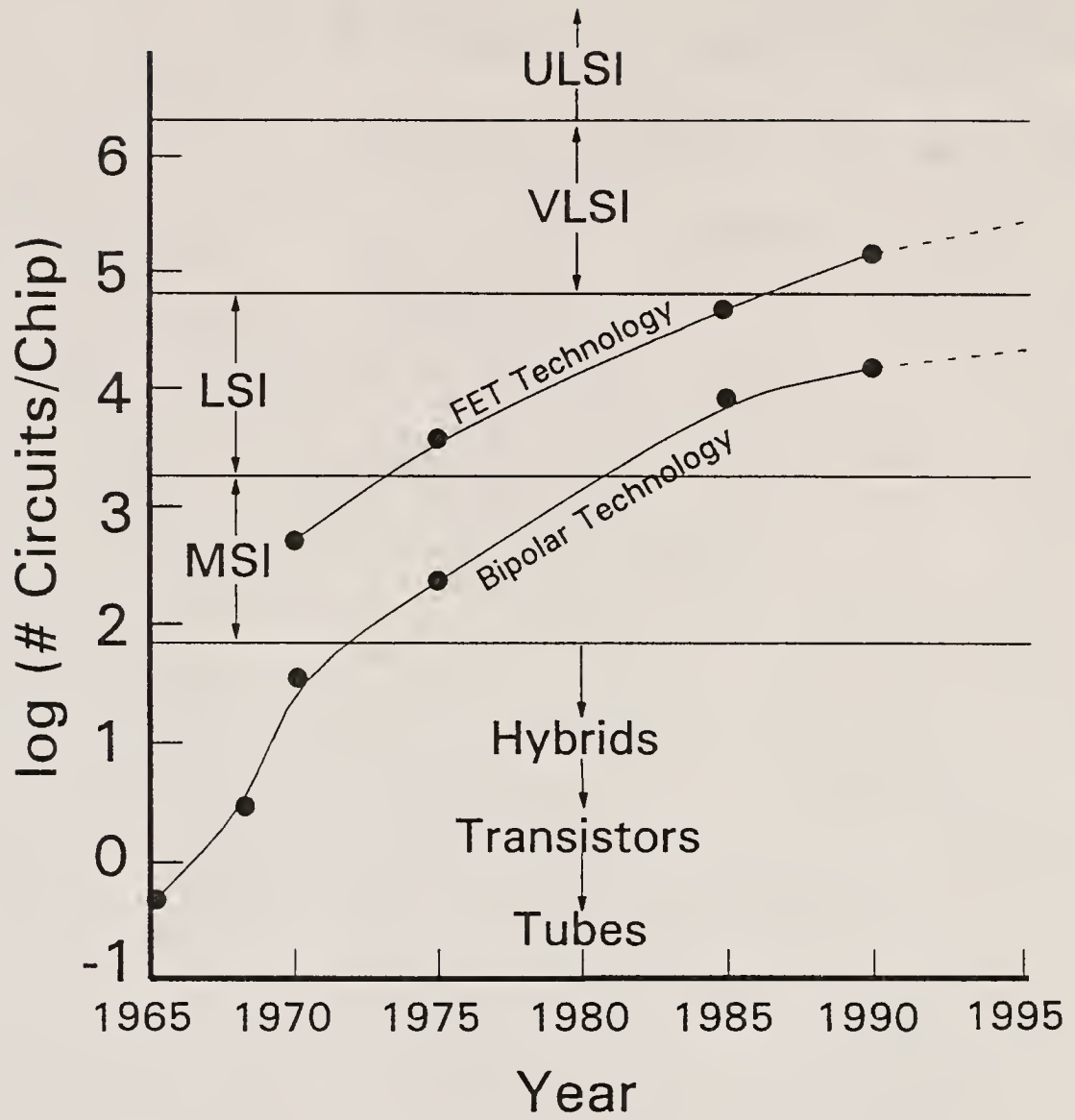


Figure 1.1

Illustration of the increase in electronic circuit density with time [91TUM]

[90OHS], biological systems [89SER], neural networking [89SER], superconductor-based logic and communications [89SER,89TUM3], etc.

Furthermore, electronic performance will be advanced via the continued evolution of traditional technologies, in pursuit of theoretical limitations. One goal is to reduce current packaging hierarchies by at least one level, in order to reduce signal flight distances. This change would result in a reduction in the number of interconnects as well, thereby improving reliability and device longevity, while reducing production costs. The first goal may be achieved by successful implementation of another goal, which is to economically obtain ultra large scale and/or wafer scale integration (ULSI and WSI, respectively). Wafer scale integration results in a dramatic increase in the scaling of microcircuitry, which, in theory, leads to reduced signal flight times due to reduced signal transmission distances. Ironically, however, WSI offsets some of the advantages of removing a packaging level since production costs would definitely increase. Furthermore, it would no longer be possible to replace one individual chip since the smallest field replaceable unit (FRU) would become the integrated wafer itself. As discussed below, there are other drawbacks to WSI as well.

Another goal is to change to higher performance semiconductor materials, having higher electron-hole mobilities, such as GaAs. It is also preferred that the replacement semiconductor material(s) be direct band gap materials, thereby allowing more efficient usage of power as well as less phonon-initiated heat generation.

Finally, a great deal of research effort is currently involved with improving traditional microprocessor and packaging technologies. The focus of such research is to increase the performance of microelectronic systems beyond the state of the art and closer to fundamental theoretic limitations, as discussed in section 1.2 below. Increased clock frequencies; finer scales of microcircuitry; larger

scales of integration; larger, cheaper, and faster memories and microprocessors; use of lower resistivity conductors as well as low dielectric constant, cofirable packaging materials and implementation of increased performance cooling designs and materials are all desired goals of said research. Figure 1.2 illustrates the current and projected trends in the performance of computers based upon traditional silicon IC technology.

Furthermore, environmental concerns are becoming increasingly important. Hazardous materials, involved in the production of electronic appliances, must be properly disposed of or recycled. Also, many of the cleaners and solvents used in IC production and electronic packaging are being replaced by environmentally benign materials and processes [89SER].

In summary, it is quite apparent that the microelectronics industry has a great many opportunities for advancement. However, it is also true that said industry is subject to unparalleled competition as well as a great deal of regulation.

### 1.2 Fundamental Microelectronic Packaging Limitations

The fundamental limitations discussed in this section relate to microelectronic packaging only. Surprisingly, the switching speed of a microelectronic apparatus is as much a function of the packaging configuration and materials as it is a function of the actual switching devices. Figures 1.3 and 1.4 illustrate the theoretical limitations that are involved in digital electronics, in a graphical sense, and are a valuable summary as well as an illustration of the combination of each fundamental limitation. The figures outline the perimeters that provide the limits of maximum performance of a digital electronic system (including switching devices, packaging, interconnection, etc.).

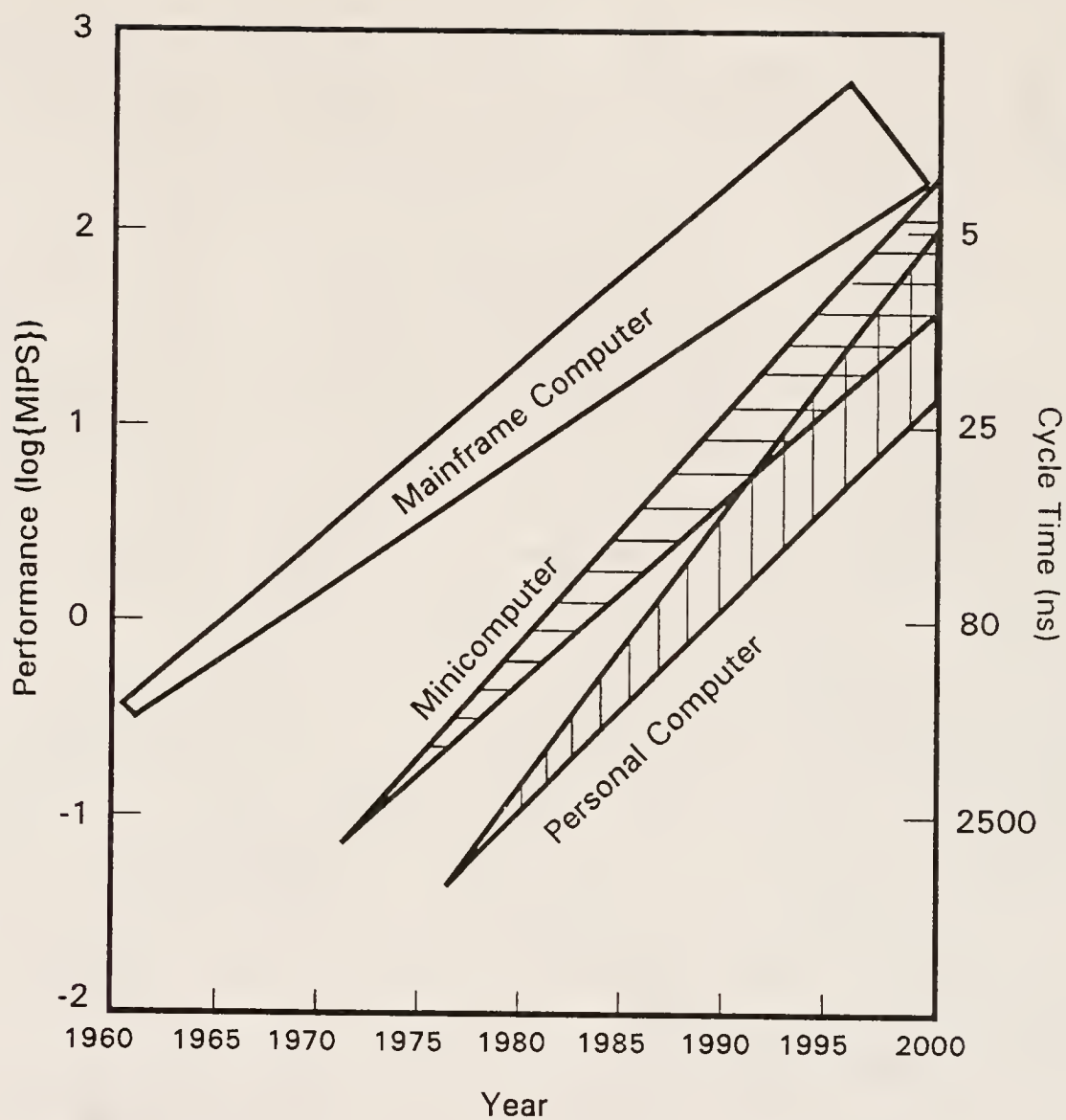


Figure 1.2

Current and projected trends in traditional, silicon-based, computer performance [91TUM]

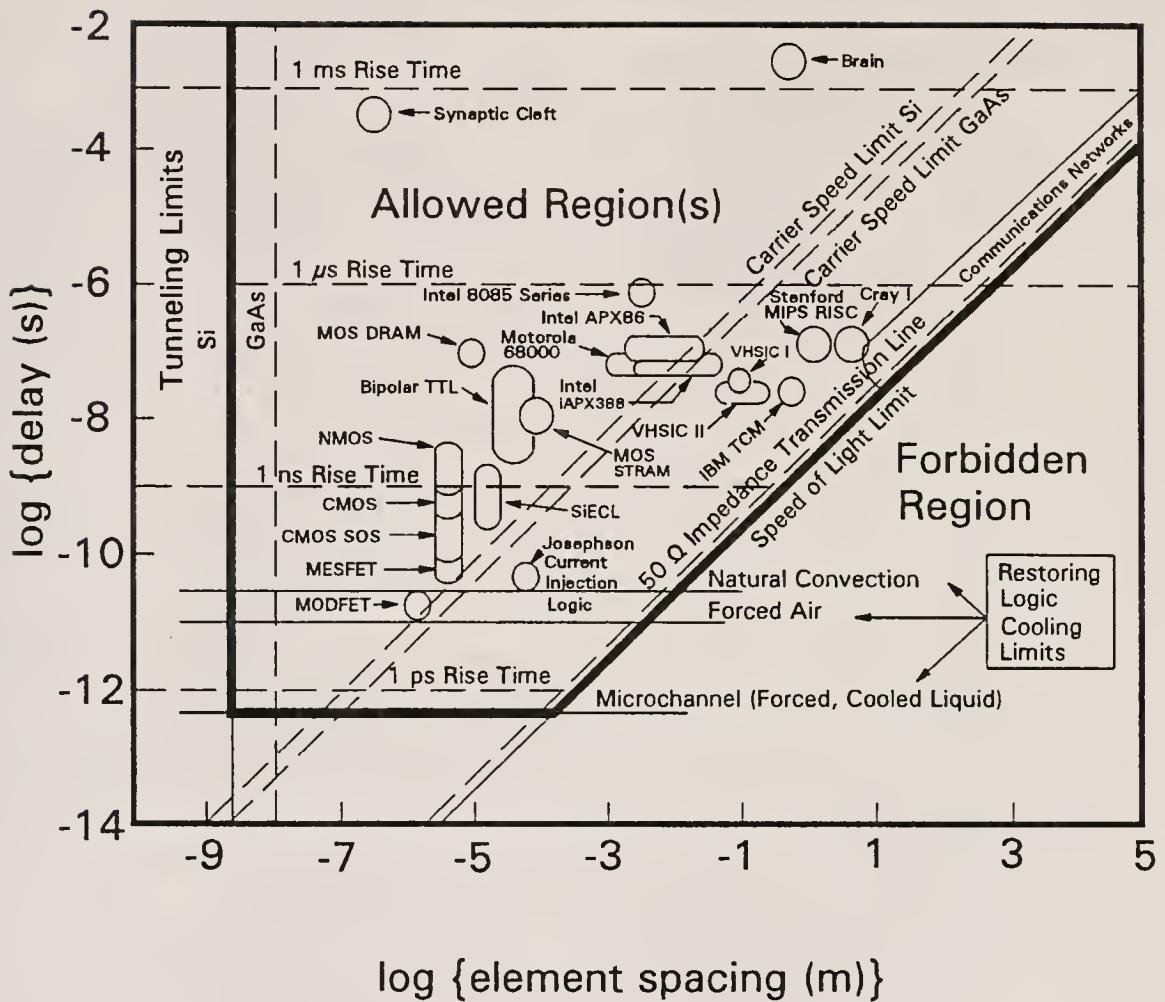


Figure 1.3

Element spacing versus delay time plane of electronic packaging space, illustrating the theoretical limitations in electronic packaging performance with respect to spacing of electronic lines and signal elements [89SER]



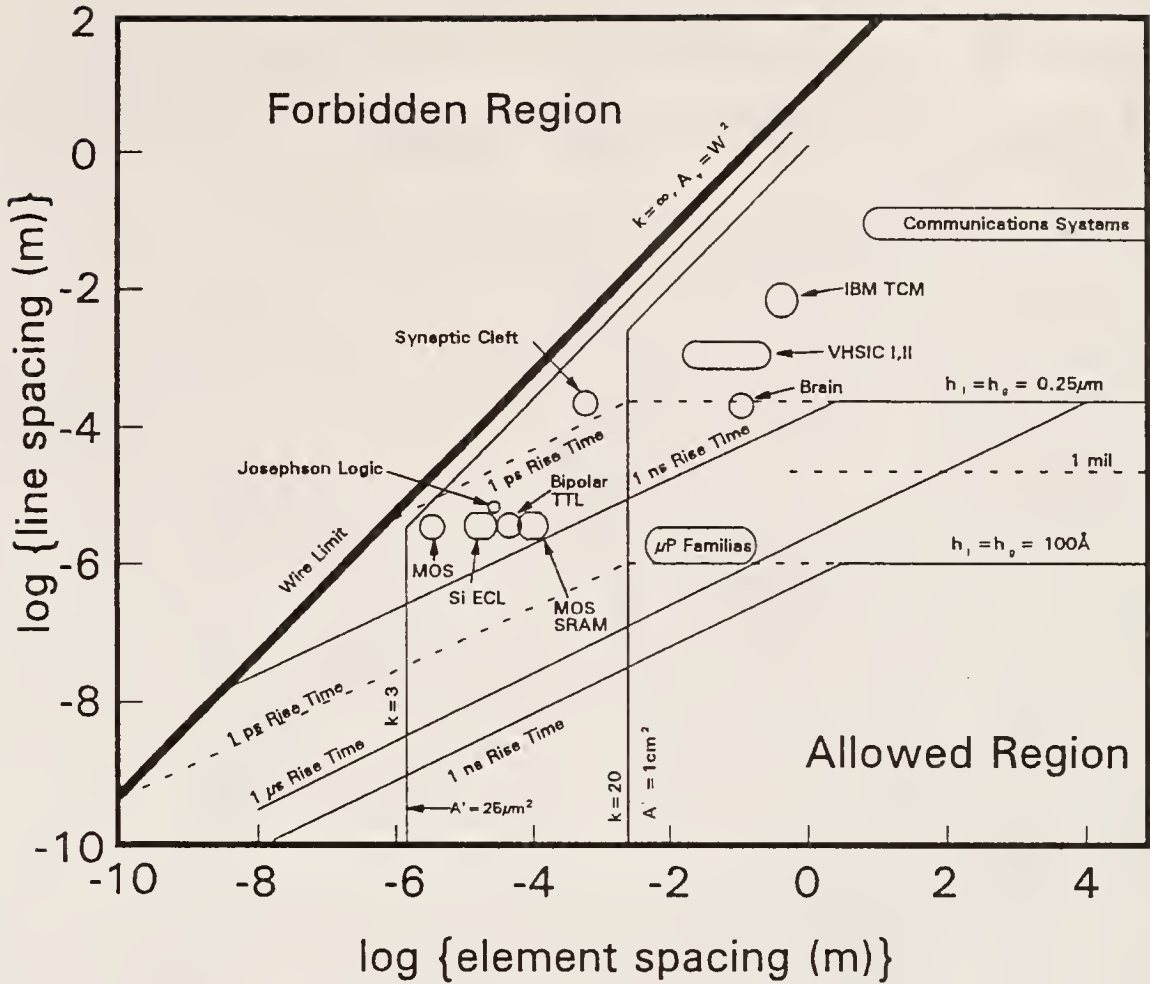


Figure 1.4

Depiction of the theoretical limitations encountered in electronic packaging as defined by the electronic-element-spacing versus signal-line-spacing plane of electronic packaging space [89SER]

### 1.2.1 Electron Light Speed Limit

Electrons can not travel at speeds exceeding the fundamental speed of light in a perfect vacuum (i.e. approximately  $3 \times 10^8$  m/s or 186,000 miles/s), regardless of the medium that they travel through. Electrons travel through perfect (lossless) conductors at the speed of light if said conductor is surrounded by free space. However, if the perfect conductor is surrounded by a dielectric medium other than free space, the speed at which electronic signals will traverse the conductor is expressed through the relation:

$$V = \frac{C}{\sqrt{K}}$$

where K is the dielectric constant of the insulating material surrounding said perfect conductor. From the above discussion, it is evident that use of lossless, low dielectric constant insulating materials, in combination with non-magnetic, nearly perfect conductors, will increase electronic signal speed, and thus, overall performance. Furthermore, it is important to minimize packaging scale (i.e. miniaturization) in order to minimize the signal time of flight (TOF) at the signal speed indicated by the above equation. Therefore, it is important to carefully choose both the electronic packing material and the packaging metallization, as well as to minimize the scale of electronic packaging integration.

### 1.2.2 Conductor Spacing Limit

While the quantum electron tunneling limit is not currently in danger of being approached, using traditional electronic packaging, there are other limitations that do effect conductor spacing in electronic packages. In any electronic package, there is a finite amount of space available for signal transmission lines. It has been shown [89SER,89TUM3,90SHI2,90SHI1,91TUM] that as the number of switching



devices increases, the number of input-output signal lines (I/Os) must also increase according to the relation:

$$I = bC^p$$

where  $I$  is the number of I/Os,  $b$  is the average number of signal connections per circuit, and  $p$  is a positive exponential (research has found that  $p$  is always  $\leq 0.67$  and is usually about 0.5). This relation is commonly known as Rent's rule. In two-dimensional space (i.e. single layer or double sided electronic packaging), this limit has already been approached or exceeded using traditional thick film packaging technology, and, in some cases, using thin film technology [89SER].

The conductor spacing limitation may be circumvented, to a certain extent, by using three dimensional packaging. Multilayer packages, having signal planes interconnected with vias, are an example of three dimensional packaging. However, there are limitations even to multilayer packaging systems. These limitations depend upon the size of the interlayer vias used and the number of layers used [89SER].

The minimum size of signal traces is theoretically limited by quantum effects. Realistically though, the actual size and separation distance of signal traces is most often determined by the ability to produce straight and smooth traces having a uniform cross section.

At high frequencies the skin effect limits electronic current to the outside (skin) of a conductor. At said frequencies the skin depth is on the order of the conductor diameter, thereby decreasing the effective diameter of the conductor. This serves to increase resistive losses. Furthermore, since the current traverses the outside (skin) of the conductor, interruptions in surface smoothness have a much greater effect upon signal integrity. At said frequencies, as the signal changes from one medium to another, any change in conductor cross section will further enhance attenuation and signal reflection.

Thus, it is important not only to match impedances, but also to match signal cross section sizes and geometries in the frequency regime characterized by significant skin effect. Other factors include, switching energy (i.e. maximum current density) and switching frequency as well as dielectric strength and hermeticity of separating insulators. The homogeneity of the conductor material as well as the overall conductor quality (i.e. its resistivity, magnetic susceptibility, and characteristic skin depth as a function of frequency, etc.) is also an important considerations when pursuing minimum conductor spacings.

Conductor spacing limitations are also affected by electronic noise. There are four types of internal electronic noise possible in a packaging system: inductive, capacitive, reflected and power distribution or  $\Delta I$  noise.

Reflected noise is a result of a mismatch in impedance between signal traces and active devices. It is not significant until higher frequencies are reached (i.e. above 10MHz). Reflections may be eliminated by matching the impedance of all elements in the device. In practice, however, this is quite difficult and design goals are toward realistic minimization of reflections.

Power distribution (PDN) or  $\Delta I$  noise results from the switching process itself. As a device switches, it requires a certain amount of power, (typically about 1--10 mW [91TUM]). In a microprocessor, it is possible for many elements to switch simultaneously. Said switching processes are fast, usually occurring in tens of nanoseconds. Therefore, the current demand upon the power supply can be excessive and may cause a drop in the supply voltage. This drop causes a voltage pulse to be sent to the switching devices, due to the parasitic inductance of each microcircuit. The voltage pulses, if significant, cause spurious switching.

Power distribution noise may be reduced through use of high power, self-regulating power supplies, reduction in parasitic inductances

through package design, increased power and ground availability, reducing signal path lengths and placement of signal traces more closely to power and ground traces, etc.

Perhaps the best way to reduce or eliminate  $\Delta I$  noise is to place a small capacitor, having very little parasitic inductance (i.e. a decoupling capacitor), as closely as is feasible to the switching elements themselves. Decoupling capacitors serve as a local current source during periods of transience, reducing  $\Delta I$  noise to acceptable levels.

Both inductive noise and capacitive noise are types of coupling noise. Both are resultant from current changes in adjacent signal traces and may result in the phenomenon commonly known as crosstalk. Inductive noise involves a single voltage pulse, travelling in the opposite direction of the original signal, in signal traces neighboring the element carrying the original pulse. Capacitive coupling noise results in two pulses, travelling in opposite directions from each other, in signal traces neighboring an active trace. The first pulse travels in the direction of the parent pulse and the second in the opposite direction. Both pulses are in phase with the parent. In the reverse direction, capacitive and inductive elements interact. The magnitudes of said pulses depend directly on the distance between the conductive traces and in the dielectric permittivity of the material separating the traces. The ability of these pulses to result in crosstalk depends upon both the voltage and the width of the resultant coupled noise pulses. Both types of pulses can cause erratic switching if the pulse voltage exceeds either the forward or the reverse bias (depending upon the pulse direction), of the switching elements in question, for a duration long enough to switch the elements. Furthermore, reflected coupled pulses may also interact with first order coupled pulses. The entire process is quite complex to model and is handled in several publications [89SER,89TUM3, etc.]. It is sufficient

here to note that reductions in dielectric permittivity of the insulating material will reduce coupled noise in an electronic packaging system. Furthermore, coupled noise may be reduced through utilization of prudent design configurations and criteria [89SER].

### 1.2.3 Cooling Limitations

The issue of electronic device cooling is very involved. As chip integration evolves, switching elements are placed with increasing density. While per device power dissipation has steadily decreased, the rate of decrease of microdevice separation has surpassed this effect (see Figures 1.5, 1.6 and 1.7). As a result advanced ICs have cooling demands that require cooling technology at or beyond the state of the art. Figure 1.7 illustrates the increased trend in cooling requirements for IBM microelectronic packages. The cooling limitation may well be the theoretical limitation that is first reached.

One method to meet cooling needs is to use direct band gap materials or superconducting Josephson logic configurations as switching devices, since they do not dissipate as much switching energy in the form of heat as do indirect bandgap solid state switching materials (see Fig 1.8). However, these switching devices have many drawbacks which limit their successful implementation.

Another method is to use high thermal conductivity packaging materials. Both of the above methods are passive in nature and are somewhat limited, however, because all switching materials dissipate some energy as heat, and because efficient heat sinking as well as heat transfer at interfaces are required, in conjunction with high thermal conductivity materials. These requirements are due to the relatively small difference between heat source and sink temperatures typical in electronic packaging applications.

The most successful cooling methods utilized to date involve active cooling, such as immersion technology [89SER]. A new method, not

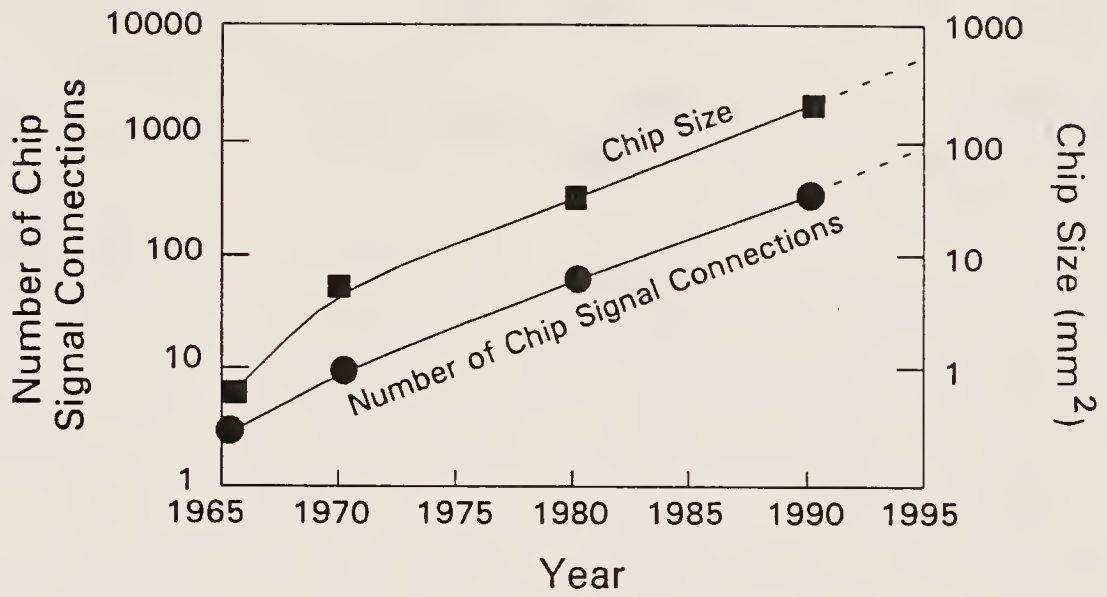


Figure 1.5

Increase in chip signal connections (i.e. device integration) and chip size with respect to time [91TUM]

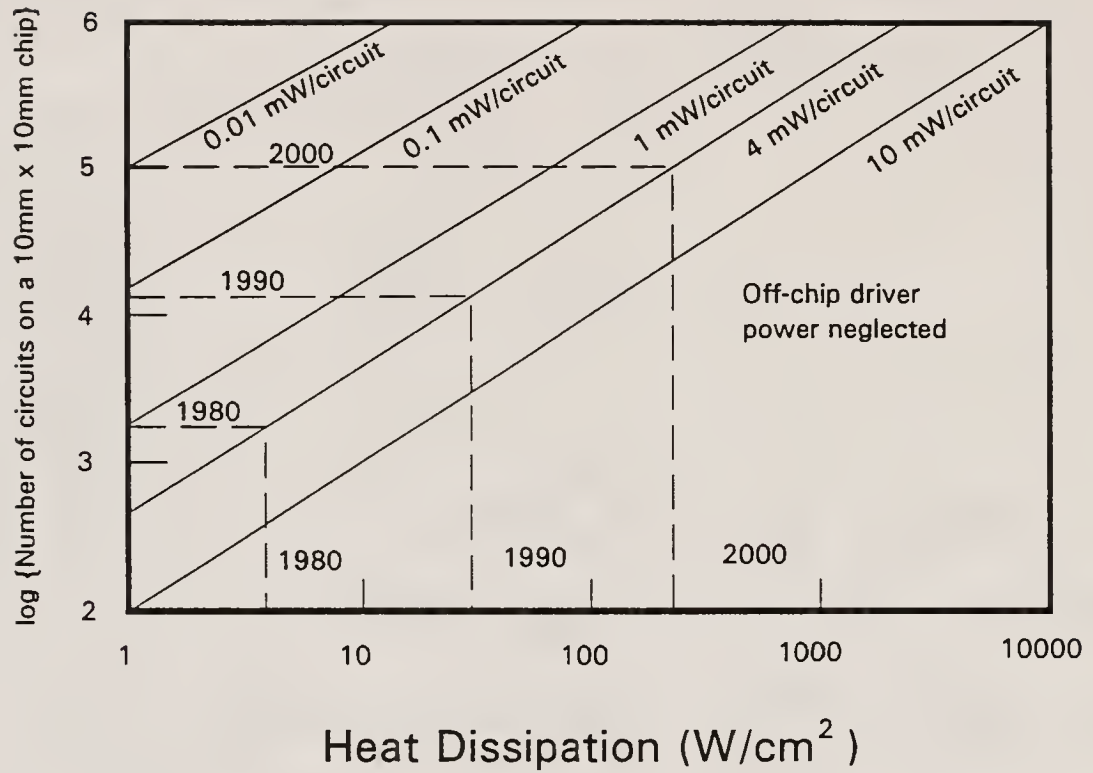


Figure 1.6

Illustration of IC power density as a function of chip integration [91TUM]

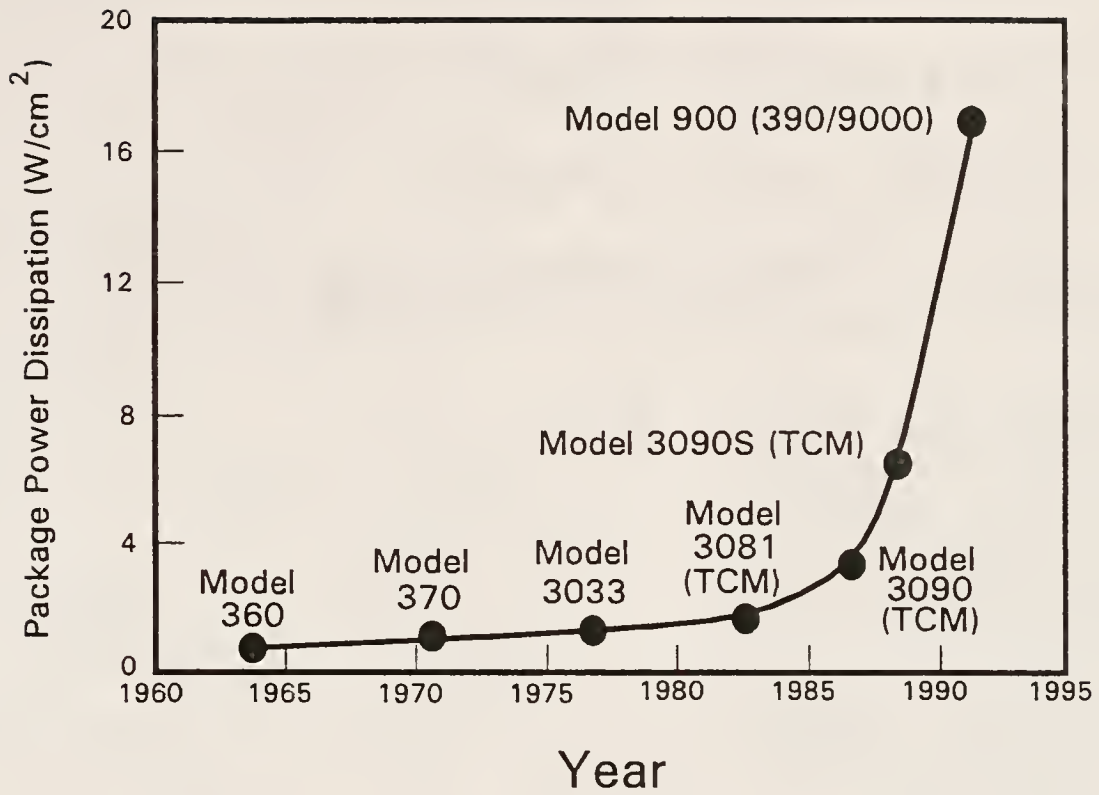


Figure 1.7

Cooling ability (i.e. requirements) of IBM electronic packages as they have evolved with time (i.e. increased packaging integration) [91TUM]



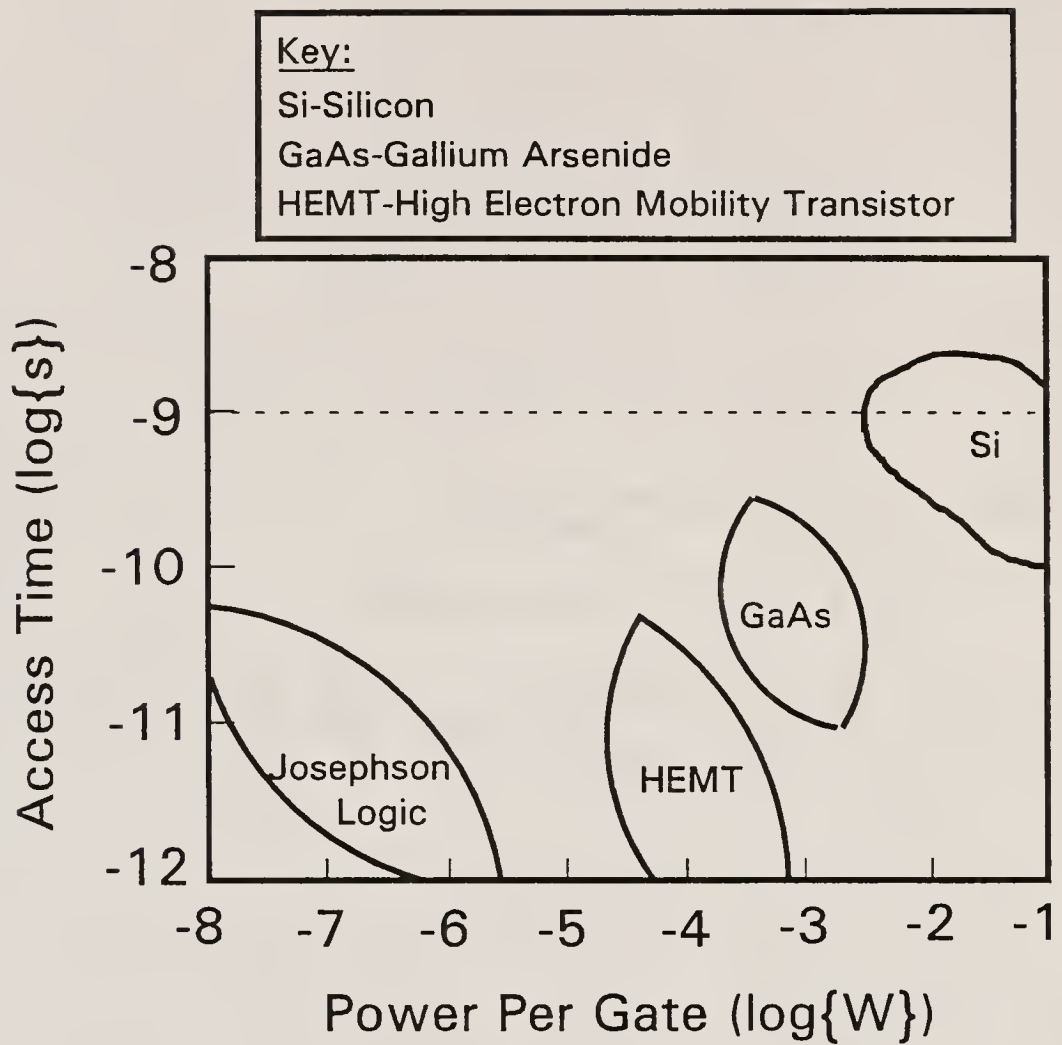


Figure 1.8

Comparison of different switching device technologies with respect to device power dissipation [91TUM]



currently used in production, but showing great promise, is that of microchannel cooling [89SER]. Microchannel cooling involves routing coolant through the back of the IC chip itself. The chip is modified by etching microchannels into its back, using traditional lithography techniques. A plate is then affixed to the chip back, enclosing the channels. Manifolds are then affixed to the chip ends, allowing flow of coolant through the microchannels. This technique allows for a heat dissipation of approximately  $600 \text{ W/cm}^2$  using water, flowing at the rate of  $10 \text{ cm}^3/\text{s}$ , and using a temperature differential of  $60^\circ\text{C}$  and has exhibited a heat exchange as high as  $870 \text{ W/cm}^2$  [89SER]. Using the treatment outlined in [89SER], this cooling technology could allow for a minimum nearest-to-next-nearest propagation delay time of  $5 \times 10^{-13} \text{ s}$  without overheating, using the logic restoration basis theoretical minimum switching energy ( $E_{\text{sw}}$ ) of  $7.7 \times 10^{-15} \text{ J}$ . This could allow for a theoretical maximum switching frequencies in the THz range (if only a few switching elements are involved).

### 1.3 Electronic Packaging: Overview of the Field

#### 1.3.1 History

Electronic packaging was first used, in significant amounts, in Hollerith's card reader [89SER]. The mechanical relays utilized in the machine had slate mounting plates as well as varnish covered solenoid wires. Electronic packaging has advanced a great deal since then. Many packaging changes have been implemented between Hollerith's electromechanical relay-based technology and today's solid state electronics. This section covers packaging methods used only since the introduction of solid state logic.

Until very recently, emphasis for advancement in the field of electronic packaging was limited to the scale of integration of solid state devices. Contemporary chips incorporate up to several million

logic or storage elements, and thus, have eliminated the need for several hierarchies of packaging that were formerly necessary.

Standard modular system (SMS) technology was the first concept introduced for solid state device packaging [89SER]. This technology interconnected singular electronic devices (i.e. transistors, capacitors, etc.) on a printed circuit board. It was developed in 1959 and afforded a far superior alternative to tube technology in speed, size, power consumption and reliability. The circuit boards were connected to a panel and interconnected via wrapped wire and cable connections. Apparatus utilizing this technology were still quite limited, however, and a great deal of effort has since been expended attempting further integration. With the invention of the IC a new implement was provided for use toward this goal.

Solid logic technology (SLT) introduced many of the technological advancements that are used, in modified form, today in ceramic packages. The package was made from 96%  $\text{Al}_2\text{O}_3$ , 4% glass, and used swaged pin technology. The chip was soldered in place, then encapsulated using a metal cap held in place with epoxy. The method of chip attachment utilized was called the controlled collapse chip technology (C4) which involves depositing solder balls on either the IC or the package I/O pads, flipping the chip face down upon the ceramic package carrier, then heating the assembly to let the solder flow and attach the chip to the package. This process is also known as flip-chip technology and is used frequently today [89SER,88TUM,89TUM,91TUM].

Advanced solid logic technology (ASLT) improved upon SLT by screening conductors onto both sides of the substrate. Furthermore, the substrates were made stackable by soldering the pins from the bottom of one package to the top of another. The wiring density was also increased. All these advances yielded significant performance increases [89SER,88TUM,89TUM]. Monolithic systems technology (MST) further

expanded upon this technology. This system basically replicated SLT and ASLT but provided further integration. The MST package provided 18 I/Os.

Vendor transistor logic (VTL) technology helped to introduce the first universal industry standard for ICs [88TUM]. A variation upon vendor transistor logic, card on board (COB) technology, allowed manufacturers the ability to produce electronic appliances using prepurchased ICs. Thus the precedent was established for second party electronics, opening a huge industry and bringing the concept of component interchangeability to integrated logic-based components.

Initially ICs were available with up to fourteen leads. Later, planar or dual in-line packages (DIPs) were developed having as many as 64 leads [88TUM,89TUM]. The DIPs were plugged into cards, which also included other active and passive elements. The cards were plugged into boards and the boards connected to a gate. The gates provided power as well as interconnection [89SER].

Metallized ceramic (MC) technology was the first packaging genre to utilize photolithographic techniques. As circuit integration increased, I/O density requirements mandated that either thin film or multilayer technology be utilized [88TUM,89TUM]. Metallized ceramic technology used the former. The thin films were deposited by either sputtering or thermal evaporation on both sides of an  $\text{Al}_2\text{O}_3$  substrate. The deposition process involved a three-layer deposition of chromium on copper on chromium. The chromium layers were thin and were used to improve adhesion on the inner layer [88TUM,89TUM].

Metallized ceramic polyimide (MCP) technology was the first multilayer thin film technology. A polyimide layer was added to the top of a ceramic substrate, and the polymer surface was deposited with chromium then copper then chromium as above. This process was repeated for several layers, then standard photolithographic techniques were

utilized to etch via spaces between layers. The vias were then back filled with paste, thereby connecting the layers [89SER].

The discussion until now has been centered around the first level of packaging hierarchy. Evolution of chip packages (the zeroeth level), specifically LSI packaging, will now be discussed briefly in order to introduce the next generation of first level packaging. Early large scale integration (ELSI) involved packaging of 100 to 500 circuits, and utilized pluggable module packaging, making it a field replaceable unit (FRU) [89SER]. Large scale integration (LSI) technology was introduced in 1979. The first LSI circuits contained 704 switching elements. The chips had a switching speed as fast as 1 ns. Because the packages had delicate I/O terminations, they were mounted to the first level module utilizing wave soldered through holes. Up to nine LSI chip packages were mounted to a single multilayer ceramic (MLC) module in this manner.

The MLC had been developed in order to accommodate ever increasing chip integration levels. With up to 23 layers, the MLC presented a technologically challenging processing hurdle. Multilayer ceramic packaging technology was borrowed from the field of multilayer capacitors, originated by RCA in the late 1950s [88TUM,89TUM]. Also borrowed from the multilayer capacitor community was the concept of the interlayer connection, or via, as well as tape casting and laminating technologies [88TUM,89TUM]. Variations of MLC technology are still utilized today. The basic process of MLC fabrication is outlined in Figure 1.9 for both the old and new thermal conduction module (TCM) production process. Said technology has been very successful in the area of advanced performance ceramic packaging and is expected to dominate that field, in varied form and in conjunction with thin film multilayer polymer technology, in the future. There are excellent literature sources which describe the process and related fields in detail [82BLO,84BLO,84SCH2,88TUM,89SER,89TUM,91TUM].

	Alumina/Mo Based TCM	Glass-Ceramic/Cu Based TCM
Raw Materials	Alumina + Glass (4-10%)	Glass Powder
↓		
Slurry Preparation	Acid-Base	Acid-Acid
↓		
Casting and Blanking	Continuous Casting	Continuous Casting
↓		
Via Hole Punching	Mechanical	Mechanical
↓		
Metallization (Thick Film)	Mo Paste	Cu Paste
↓		
Stacking/Registering	Automated	Automated
↓		
Lamination	Automated	Automated
↓		
Organics Removal and Sintering	Controlled Hydrogen Atm.	Controlled Steam Atm. Crystallization Step
↓		
Final Ceramic	Alumina + Glass	Glass Ceramic
↓		
Electrical Tests	Automated	Automated
↓		
Attachment of Pins and Flange	Automated Ni and/or Au Plating	Automated
↓		
Substrate Machining and Surface Treatment	Seal Flange	Top and Bottom Surface Finishing and Seal Flange
↓		
Chip Attachment (C-4 Process)	Automated	Automated
↓		
Electrical Testing of Module	Automated	Automated
↓		
Final Module Assembly	Automated	Automated
↓		
Helium Gas Filling of Module	Automated	Automated

Figure 1.9

Flow chart of the MLC production process used in the IBM TCM [82BLO,89TUM,91TUM]



Perhaps the best known example of MLC technology is the IBM TCM series. When introduced in 1981 for the IBM 3081 computer system, the IBM TCM used 96% alumina (4% glass) as the dielectric and either Mo or W metallurgy [89SER,83BLO]. The multilayer module consisted of 33 layers and could accommodate up to 118 IC chips. The layers were configured as either signal (X or Y plane), redistribution, or voltage-reference layers. Said module had up to 320 cm of wiring per cm<sup>3</sup> of package. Furthermore, an ingenious cooling device was utilized on the IBM TCM which used chilled water forced through a hermetically sealed and He backfilled chamber. Said technology was capable of accommodating chip heat dissipations as high as 3 W/cm<sup>2</sup>. Much of the cooling ideologies used in the original TCM (for the 3081) are used in the current TCM.

The state of the art TCM (introduced in 1991 for the IBM 390/9000) seems only subtly different from the original TCM. However, it exhibits markedly improved performance, by utilizing Cu metallurgy as well as low sintering temperature (~1000°C), low K (~5) crystallizable dielectric materials (cordierite with minor clino-enstatite). Furthermore, the 390/9000 TCM can accommodate up to 121 LSI chips, and has 63 wiring layers as well as 9 polyimide signal redistribution layers. All of this was accomplished using special processing to avoid oxidation of the Cu metallurgy during thermal treatment. The CTE of the dielectric used in said package was matched carefully to Si over a broad range of temperatures [91KUM2]. The packaging heat accommodation was increased to ~18 W/cm<sup>2</sup> as well. This TCM represents the current state of the art in high performance electronic packaging, although other corporations have also marketed excellent examples [88BAB,89EMU,89SAW,89SER,89TUM3,91SHE2,etc.].

### 1.3.2 Importance of the Electronic Package

#### 1.3.2.1 Economic

Electronic packaging and interconnects account for a large portion of the advanced ceramics market. The electronic ceramics market is the largest niche within the field of advanced ceramics [91SHE2]. The electronic packaging and interconnects market accounts for approximately 0.05% of the GNP of the United States [90WRI]. This industry involves over \$2.7 billion annually, accounting for approximately 1.5% of the total sales of the entire US electronics industry [88SCH1,91SHE2]. Furthermore, the electronic packaging and interconnects industry currently is experiencing a growth rate of approximately 8.5% per annum [91SHE2], projecting a total market value of approximately \$6.5 billion by the year 2000 [91SHE2].

#### 1.3.2.2 Functional

Upon first inspection, electronic packaging seems deceptively simple. The components of the package are passive and the final packaged structure usually seems like an elementary monolith. Upon further inspection, however, one learns that the electronic package is quite complex. Perhaps no other type of passive device is subject to as many material and environmental constraints.

Electronic packaging is typically divided into as many as six levels. The zeroeth level of packaging involves the IC chip itself (i.e. intra-chip integration), while first level packaging involves the I/Os of the IC chip (i.e. chip level integration). In many instances, the zeroeth order is not considered packaging, since it is inherent in the chip integration itself. First level packaging brings power and signal lines to the IC chip while providing mechanical and hermetic protection.

The second level of the electronic packaging hierarchy involves the interconnection between IC chips as well as other on-card devices

(i.e. card level integration). Second level electronic packaging is task oriented, in that it involves the interconnection of electronic devices that perform a specific task (i.e. video cards, etc.). The second level allows for task diversity (i.e. different cards for different tasks) as well as traditionally offering the smallest scale of easy replaceability (i.e. the field replaceable unit (FRU)). The third level of packaging involves interconnection of cards (i.e. board level integration) and the fourth level in the electronic packaging hierarchy involves the interconnection of boards (i.e. gate level integration). Finally, gates are interconnected to form a main frame in the fifth level of the packaging hierarchy.

As digital systems have evolved, some of these packaging levels have been eliminated. For instance, personal computers (usually denoted card on board (COB) systems) do not have a fourth level of packaging. Use of multichip modules (i.e. chip on board (also COB) systems) also eliminates the second level in the electronic packaging hierarchy. Eventually, the board level may be partially replaced as well if wafer scale integration (WSI) comes to fore.

An electronic package basically provides a fixed structure for active electronic devices. Said structure is subject to many, varied constraints. The structure must be mechanically strong in order to protect the delicate active devices from shock and external forces. The package must also provide shelter from moisture and corrosive environments. Furthermore, the thermal expansion of the electronic packaging material must be similar to that of the active materials that it packages, so that the packaging does not destroy its active occupants when changes in overall temperature, or temperature gradients are experienced.

The electronic package must also provide for one or more means of dissipating heat generated by the active components. Heat dissipation may be either passive or active. For either type of cooling, it is best



(although not mandatory) that the electronic packaging have a high thermal conductivity. A high thermal conductivity is beneficial when it is desirable to avoid thermal shock of the device. Furthermore, by utilizing packaging materials having high thermal conductivities, heat generated via the active devices is spread more quickly and more homogeneously throughout the package, thereby avoiding detrimental hot spots.

The packaging must also provide a satisfactory medium for encapsulating power and signal transmission elements. As a result of the current emphasis upon device miniaturization, this packaging requirement has become quite important. Electrically conductive elements have decreased greatly in height, width and pitch now that high conductivity metals are being utilized, resulting in the need for packaging materials having exceptional surface smoothness, interlayer planarity [90REC] and either minimal or predictable shrinkage and warpage during processing. In ceramic materials, these goals may be attained only with proper processing. It is desirable that the starting ceramic powders be very small in size and that said powders consolidate to a very high green density. Furthermore, the consolidation must not result in particle segregation.

The electronic package must also provide a medium that is suitable for high quality electronic communication, since the electronic devices housed in the package require "clean," constant power and high quality signals. With the current emphasis upon increasing signal speed, this requirement has mandated changes in both materials and design in order to obtain satisfactory packages. As discussed below, this criterion presents perhaps the greatest impediment to advancement in the field of high speed computing.

### 1.3.3 Properties Desired of Packaging Materials

Table 1.1 summarizes both the requirements and the weight of said requirements for electronic packages and packaging materials. Surprisingly, the major barrier to the realization of the next generation of high performance computing lies in limitations in packaging materials and not in switching materials [83VEN,87MOH,87SHI,87YAR]. The unavailability of satisfactory high speed electronic packaging materials results from the fact that successful candidates must satisfy several stringent criteria. First and foremost the candidate must have satisfactory dielectric property requirements. The dielectric constant and loss tangent must be low (3 to 5 or below, and  $\leq 0.005$ , respectively [86CRO,87KEL,87MOH,88GER3,89LEA]), and stable at the frequencies used (MHz to tens of GHz [87YAR]). There are several reasons for the dielectric properties criterion. The time delay ( $T_d$ ) of signal propagation of an electronic pulse through a circuit element is given by the relation:

$$T_d = \frac{L\sqrt{K}}{C}$$

where K is the material dielectric constant, L is the propagation distance, and c is the speed of light [84SCH3,84SCH4]. Thus the signal delay is proportional to the square root of the dielectric constant of the surrounding packaging material. This effect is illustrated for various ceramic materials in Figure 1.10.

The characteristic impedance ( $Z_0$ ) of package signal traces must rest within a narrowly defined field of approximately 40 to 110  $\Omega$  [89TUM3] (the most preferable value is 50  $\Omega$  [88BAL]) due to noise, signal delay and current draw considerations.

Table 1.1

Requirements and Importance of Said Requirements  
for Electronic Packages and Packaging Materials [91TUM]

High Performance Applications		
Property	Importance	Importance Weighting
Dielectric Constant (minimize)	Highest	5
Wiring Density (maximize)	Highest	5
Metallization Conductivity (minimize)	Highest	5
Coefficient of Thermal Expansion (match to IC chip material)	High	4
Dimensional Control (maximize)	High	4
Mechanical Strength (maximize)	Medium-Low	2
Low Performance Applications		
Property	Importance	Importance Weighting
Cost (minimize)	Highest	5
Thermal Conductivity (maximize)	Highest	5
Coefficient of Thermal Expansion (match to IC chip material)	High	4
Wiring Density (maximize)	Medium	3
Mechanical Strength (maximize)	Medium-Low	2

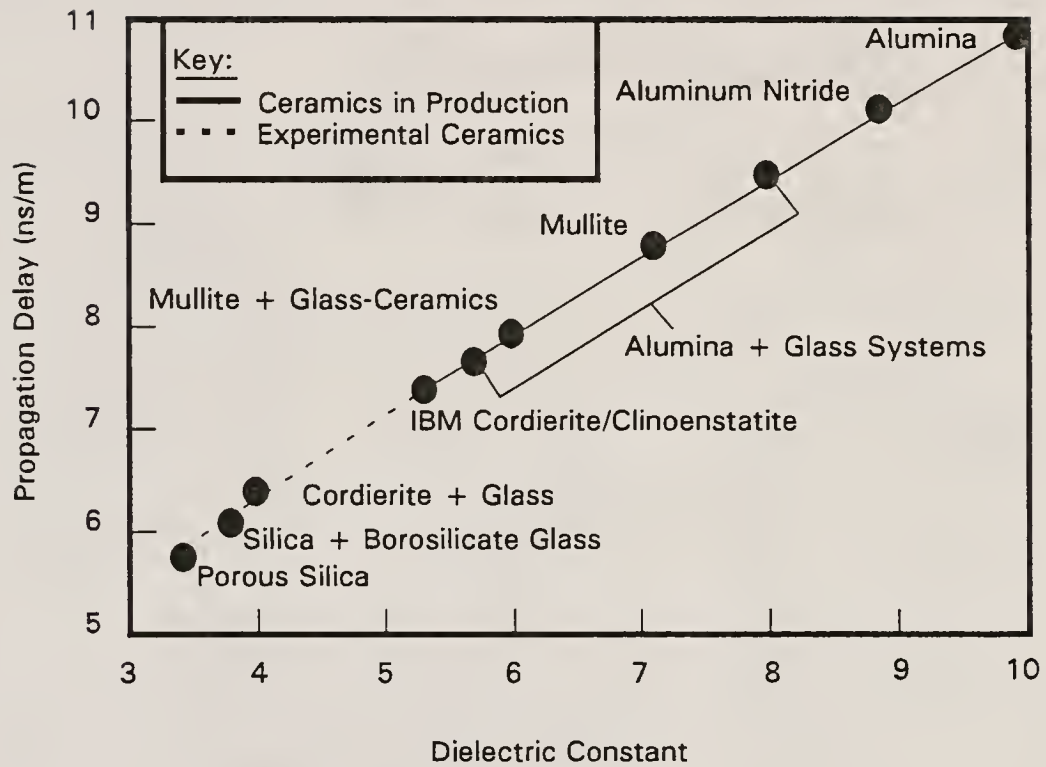


Figure 1.10

Depiction of propagation delay time versus dielectric constant for various ceramic materials [91TUM]

Figure 1.11 graphically illustrates the design criteria for selection of package characteristic impedance.

Furthermore, the minimal thickness of packaging layers between circuit elements required for impedance matching is lowered when a lower dielectric constant material is used, due to the following relation:

$$Z_o = \sqrt{\frac{L}{C}}$$

where  $Z_o$  is the characteristic impedance,  $L$  is the inductance associated with the signal line, and  $C$  is the capacitance associated with the signal line [84SCH3,84SCH4]. By lowering  $K$ ,  $C$  is reduced per unit thickness, thereby increasing  $Z_o$  per unit thickness. Thus a thinner packaging layer may be utilized while maintaining the characteristic impedance, further enhancing miniaturization. Therefore, use of low  $K$  packaging materials allows for increased digital performance in two ways, by increasing signal speed and by helping to decrease signal propagation distance.

The dielectric loss factor must also be low, as illustrated by the relation:

$$P = \pi \epsilon' f V_o^2 \tan(\delta)$$

where  $P$  is the power loss due to dielectric loss,  $f$  is the signal frequency,  $\epsilon'$  is the real portion of the material dielectric permittivity,  $V_o$  is the peak signal voltage and  $\delta$  is the dielectric loss angle ( $\epsilon''/\epsilon'$ ) [76KIN]. From the above relation, it is evident that power dissipation due to dielectric loss may become rampant at high frequencies if insulating materials are not chosen carefully.

Utilization of materials having low  $K$  and  $\tan(\delta)$  values also aids (along with correct design of ground planes) in lessening problems of

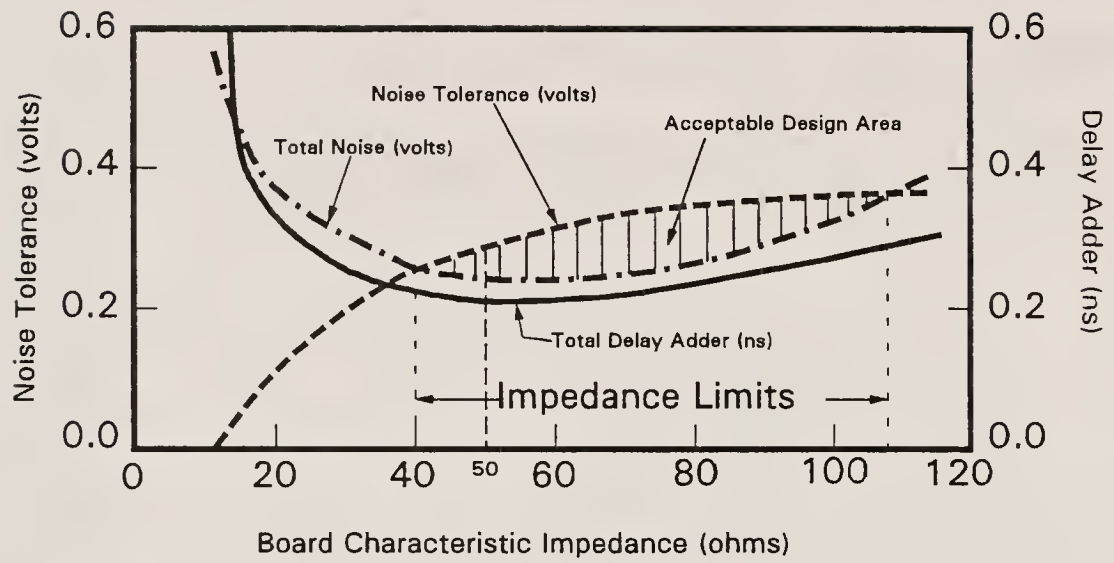


Figure 1.11

Depiction of design considerations for choosing a package characteristic impedance [89TUM3]

crosstalk, signal pulse rounding and other phenomena leading to signal infidelity [87MOH,87YAR,89SER,89TUM,89TUM3,91TUM].

A second goal in the design of electronic packaging is one of expense reduction. In order to reduce production expenses, packaging materials should be developed that are processable at low temperatures. Lower processing temperatures also allow for use of nonrefractory metals (such as silver and copper) as conductive elements. This is advantageous from a performance point of view, since silver and copper have relatively high electrical conductivities ( $6.31 \times 10^7$  and  $5.96 \times 10^7$  (Ohm $^{-1}$ m)<sup>-1</sup> respectively [85CRC]). Therefore, both resistive heating and signal loss would be reduced through the implementation of either conductor material. Thus, cofirability with copper or silver is advantageous from both cost and performance standpoints. Cofirable systems must be totally processable at temperatures significantly below the melting point of the metallic constituents (1083°C and 982°C for copper and silver respectively [85CRC]). Furthermore, cofirable packaging materials must allow for processing treatments which ensure the total pyrolysis of organics, as well as the complete sintering of the metallization, while not adversely affecting the desired properties of the conductor metallurgy.

The coefficient of thermal expansion (CTE) also should be matched closely to that of the semiconductor material utilized. This ensures that the chip bonds will not fail with repeated usage (i.e. when the power is turned on and off). The induced plastic strain ( $\epsilon_p$ ) experienced by the solder connections during thermal cycling of a chip and package assembly is quantified by the relation:

$$\epsilon_p = \frac{\Delta CTE \times \Delta T \times D_{np}}{H}$$

where  $\Delta CTE$  is the difference in the coefficient of thermal expansion



between the IC chip and the packaging material,  $\Delta T$  is the difference between the temperature at which there is no stress and the temperature of interest,  $D_{np}$  is the distance from the neutral point of shear stress on the chip (i.e. the horizontal middle), and  $H$  is the height of the solder pad [84SCH2]. From this relation the number of cycles to failure ( $N_f$ ) may be estimated from the Coffin-Manson equation:

$$N_f = \left( \frac{A}{\epsilon_p} \right)^{\frac{1}{m}}$$

where  $A$  and  $m$  are constants whose values must be empirically determined for the particular system [89TUM3].

From the above relations, it is evident that reducing the difference in CTE between the chip and the package will reduce thermal fatigue. Figure 1.12 illustrates this equation for several materials. Also, plastic shear strain on the solder connections increases toward the outside of the IC chip (i.e. as  $D_{np}$  increases). Therefore thermal cycling fatigue increases in magnitude with the use of larger IC chips (i.e. VLSI). Not as obvious in this discussion is the effect of thermal conductivity of the materials involved. Low thermal conductivities tend to increase stresses within the packaging material but tend to decrease  $\epsilon_p$  by decreasing  $\Delta T$  at the chip-solder-package interface. For this and many other reasons, it is considered most prudent to use cooling methods which extract heat from the back of the chip rather than through the substrate.

Thus it is desirable to have a CTE which is adjustable for different switching materials. Since Si is, by far, the predominant switching material currently in use, the most utilitarian electronic packaging materials will have a CTE that is customized to match that of Si. Furthermore, it is important to match the CTE of Si over all temperatures that the chip-package assembly will experience.



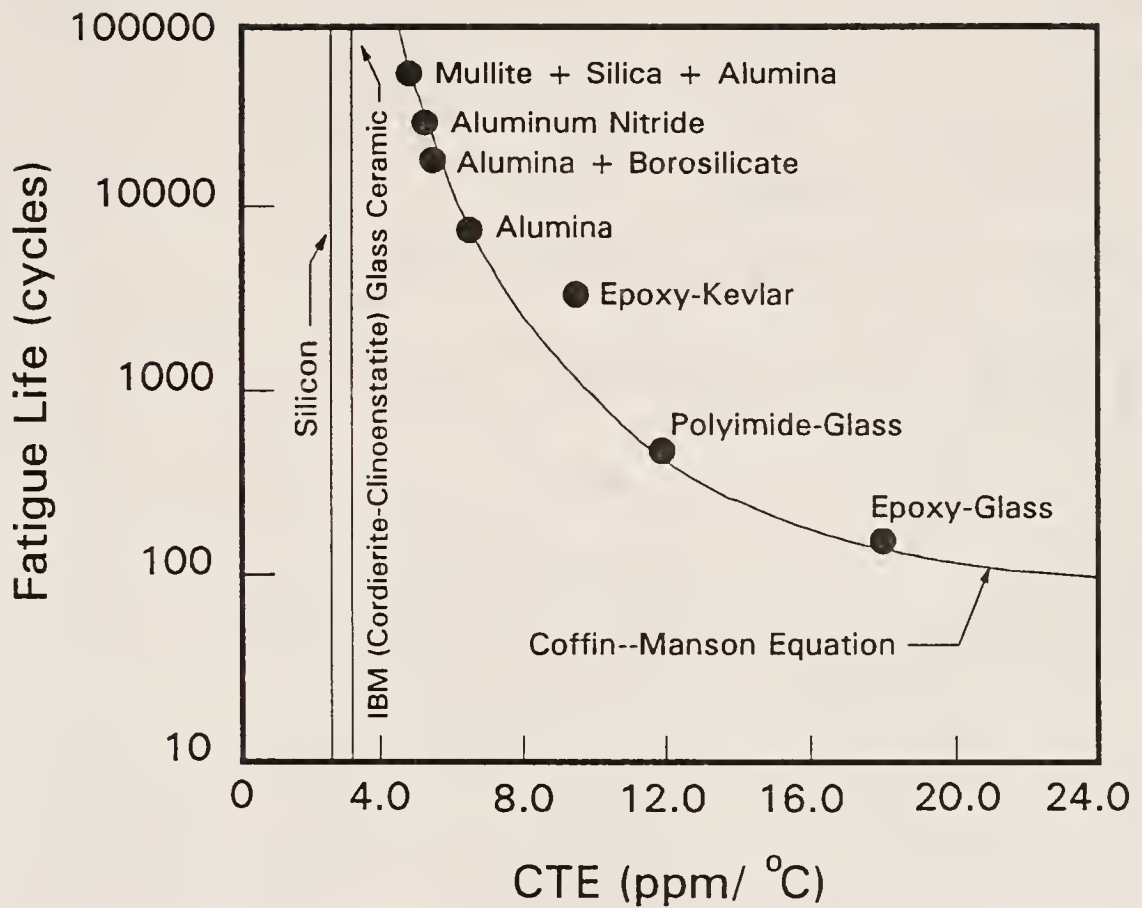


Figure 1.12

Illustration of the Coffin-Manson equation for several materials [91TUM]

Figure 1.13 exhibits the CTE of Si with respect to temperature.

Adjustability of CTE may be provided to varying extent by using ceramic composite systems as packaging materials.

Furthermore, stress resultant from CTE mismatch is reduced between packaging and metallization when lower firing temperatures are used (as in low temperature, cofirable systems) by reducing  $\Delta T$ . Differential stress between metallization and packaging may be further reduced if packaging materials that densify via a viscous sintering mechanism are used, since localized stress may be alleviated if an annealing step is used at temperatures slightly above the glass transition ( $T_g$ ) of the packaging material. Stress on chip pads may be relieved similarly if the chip bonding material requires heat treatment above  $T_g$  of the matrix glass.

The fourth desirable property of an electronic packaging material system is that of high surface smoothness. Surface roughness may cause disabling discontinuities within the package. Acceptable surface flaws are usually no larger than about one tenth the metallization width (typically  $\geq 50 \mu\text{m}$ , [89SER,89TUM3]). As technological advances allow for further miniaturization (i.e. substitution of photolithography for screen printing as the application method for circuit metallizations [90NEB]) this limit will surely decrease markedly.

Hermeticity is also desirable in a satisfactory packaging system. If atmospheric moisture enters the package, dielectric properties will change markedly [89SER,89TUM3,91WAL]. Moisture also contributes to corrosion (and thus embrittlement, due to stress corrosion cracking), exfoliation and delamination of both the packaging and the active electronic elements. Hermeticity of the packaging material may be achieved in several ways such as hermetic coatings, etc. However, it is much simpler and more cost effective if the packaging material is inherently hermetic subsequent to thermal processing.

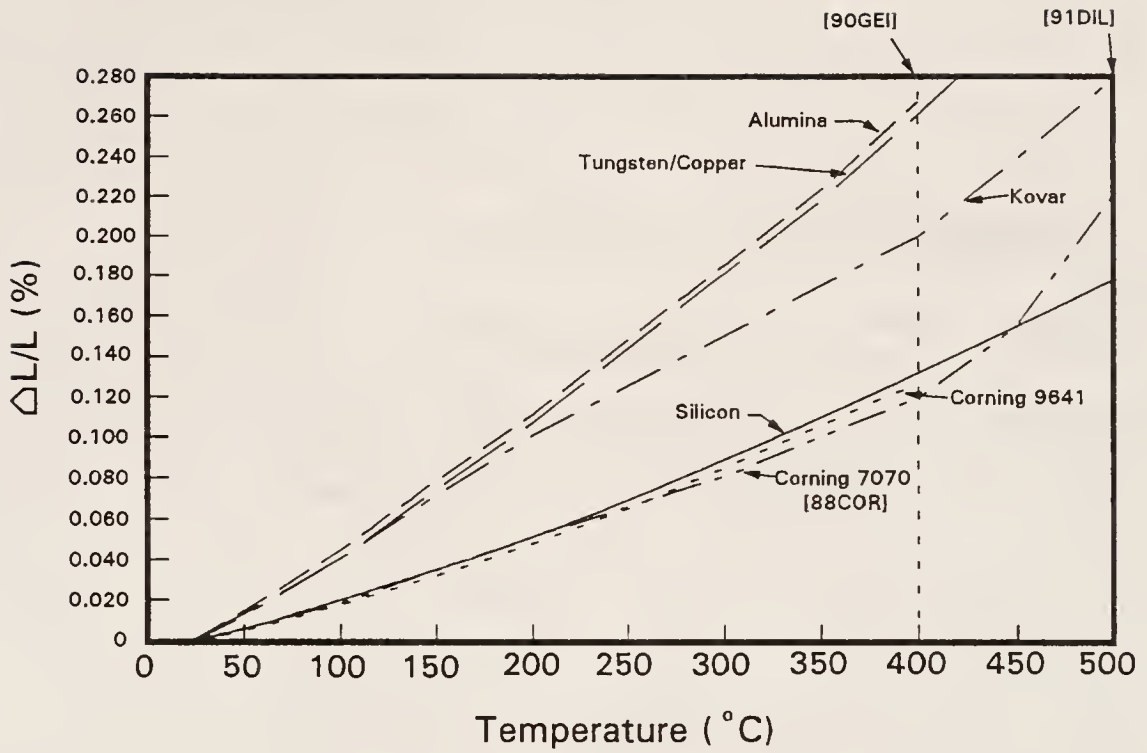


Figure 1.13

Thermal expansion of Si and other selected materials as a function of temperature [88COR, 90GEI, 91DIL]

This is accomplished in most ceramic and glass materials when sintered to more than approximately 95% of theoretical density [76KIN].

Adequate mechanical properties and high thermal conductivity are also desirable in electronic packaging materials. Since mechanical failure is frequently due to CTE mismatch or improper thermal treatment, this problem can be avoided by careful design and processing. Frequently, it is becoming more important that the green package have greater green strength, in order to avoid damage during processing.

Packaging design evolution also has moved away from using the electronic package as a supporting or structural member for the apparatus. Conventional wisdom more frequently dictates that it is better if the package provides support and protection only for the elements that it packages. This further reduces mechanical requirements of the electronic packaging material. However, a minimal mechanical strength is still desirable. The materials utilized in the IBM TCM currently have a bending strength of about three quarters of that of  $\text{Al}_2\text{O}_3$  (i.e. ~210 MPa) [91KUM1,91KUM2,91SHE2,91TUM], while other institutions have decided that lower strengths are permissible [89EMU,89SAW,90RIC,91ALE,etc.].

Indeed, if ceramic materials are to be continued in use as dielectric insulating materials in high performance electronic packages, K will have to decrease, necessitating that composites of ceramic and either polymer materials or porosity be used in the future. This will surely decrease the mechanical strength of said materials [91KUM]. In the future, the consequences of using lower strength packaging materials will be circumvented through proper package design and processing as well as careful materials selection.

High thermal conductivity is no longer as important a material attribute either, since ingenious designs now remove generated heat from the back of the chip instead of through the substrate [82BLO,83BLO,89SER,89TUM3,91TUM].

This method is advantageous in several ways. First, since heat removal through the back of the IC chip is quite amenable to active cooling technologies, a much greater amount of heat may be dispersed through its use. Also, removal of heat through the substrate is generally regarded as an inferior method since it requires that the heat flux traverse the metallizations and chip bonding materials. This increases thermal stresses while reducing electrical conductivity. Also, with continued decreases in conductor scale (i.e. reduction in the size of chip-package interconnections), thermal conductivity would be further retarded. This effect can be offset only through the utilization of thermal vias, which are very costly in terms of IC chip "real estate."

Removal of heat, through the substrate, to a thermal sink rather than to a cold finger on top of the chip, also results in thermal resistances which are significantly greater than in the cold finger method unless ultra high thermal conductivity materials (i.e. diamond, or cubic BN) are used. The Franz-Weideman rule [83POB] indicates that this technique is not useful in high performance packaging applications where a low dielectric constant is also required (with a few notable exceptions such as diamond, cubic BN, or BeO, etc.). The Franz-Weideman principle states that no material may have both an ultra high thermal conductivity as well as a low dielectric constant. The exceptions to this rule are either prohibitively expensive or toxic. Furthermore, there are no exceptions to the Franz-Weideman rule when it is necessary to select materials having a K below 5.5. Since, in high speed electronic applications, satisfactory dielectric properties are most important, the material designer must prioritize on the side of low dielectric constant, low dielectric loss materials.

High thermal conductivity is also important from a thermal shock point of view since a high thermal conductivity promotes heat spreading throughout the package, thus reducing thermal fluctuations within the package. However, as stated in section 1.3.3, use of a high thermal

conductivity material in conjunction with a through-the-substrate cooling mechanism will actually reduce the solder-package interface temperature, thereby increasing the thermally induced shear stresses on the solder pads (relative to use of a lower thermal conductivity material in the same heat removal configuration).

It should be noted that the development of a successful packaging candidate (i.e. one which satisfies the above packaging criteria) requires a two-pronged, holistic approach. Both materials selection and packaging design are extremely important in achieving the criteria discussed above. Furthermore, there is no one package that satisfies all the requirements in all systems. In some cases, mechanical integrity or hermeticity is the most important characteristic, while in others, signal processing is tantamount. Therefore, no one design or material is universally satisfactory to all electronic packaging applications. Furthermore, pursuing more than one of the above packaging criteria, requires skillful design as well as use of engineered (i.e. composite) materials. Therefore, it is of extreme importance to decide what packaging criteria are most important when developing packaging materials or designs for a specific application or family of applications. Table 1.1 can help to serve as a guide in packaging design and materials selection.

This study attempts to present a viable packaging material system that satisfies the materials-based (not design-based) factors of the packaging criteria outlined above. Furthermore, the greatest importance is placed upon a materials solution which emphasizes signal processing speed (i.e. low dielectric loss materials), adjustability for varying application (i.e. composite materials), and cost reduction (i.e. low materials cost, applicability to traditional processing, and thermal processability at reduced temperatures (low temperature cofirability)) while exhibiting environmental stability (i.e. hermeticity and at least a minimum mechanical strength). It is the author's opinion that these



are the most important packaging criteria for the advancement of high speed electronic computing.

#### 1.4 Materials Solutions to Electronic Packaging Problems

##### 1.4.1 Ceramics versus Polymers

Nearly 85% of all electronic packages currently produced are polymer based while ceramic packages comprise approximately two thirds of the monetary value of the electronic packaging market [89TUM3]. So-called plastic packaging systems are based on some type of insulating polymer encapsulant such as epoxy, polyimide, silicone, or, of late, thermoplastics [89TUM3]. They offer several advantages over ceramic systems such as lower cost, lower dielectric constant, and greater ease and adaptability of manufacture as well as greater relative throughput. Seemingly these advantages would mandate that all electronic packages be polymer-based. However, the use of plastic packaging systems has several disadvantages. Table 1.2 shows the advantages and disadvantages of ceramic versus plastic electronic packaging materials.

Currently, no plastic package is truly hermetic although materials are being developed which are less hydrophilic than traditional polymeric packaging materials (i.e. polyquinolines, teflons, and BCBs) [90LEE,90REC,91HEN,91HOR,91ZUS]. Therefore, the packaging thickness must be carefully controlled in order to allow some of the moisture, present within the package, to be evaporatively removed using IC chip heating [89TUM3]. If the electronic device is one that consumes very little power (i.e. dissipates very little heat), such as CMOS devices, special packaging design considerations are mandated. Furthermore, plastic packaging materials have a much greater CTE than the materials which they encapsulate (i.e. Si). Resultant thermal stresses may damage delicate microcircuitry. This requires implementation of careful package design and manufacturing principles.

Table 1.2

Advantages and Disadvantages in the Polymeric  
versus Ceramic Electronic Packaging Materials Debate

Topic	Ceramic	Polymeric	Advantage
Adaptability to Multilayer Packaging	Moderate	Moderate	Depends (Usually Ceramic)
Cost	High	Low	Polymer
Breakdown Voltage	High	High	Depends
Dielectric Constant	Moderate	Low	Polymer
Dielectric Loss	Low	Low	Depends (Usually Polymer)
Ease of Process Automation	Low	High	Polymer
Hermeticity	Hermetic	Non-Hermetic	Ceramic
Inherent $\alpha$ --Radiation	Variable	Variable	Depends (Usually Ceramic)
Process Complexity	High	Low	Polymer
Process Temperature	High	Low	Polymer
Process Throughput	Moderate	High	Polymer
Rigidity	High	Flexible	Ceramic
Strength	High	Flexible	Depends (Usually Ceramic)
Surface Smoothness	Moderate	High	Depends (Usually Polymer)
Tolerance Control and Reproducibility	High	Low	Ceramic
Thermal Conductivity	High	Low	Ceramic
Thermal Expansion	Low (Highly Variable)	High	Ceramic
Volume Resistivity	High	High	Depends

Plastic packaging materials are characterized by poor thermal conductivity as well. Due to the encapsulating nature of most plastic packaging methods used, this factor, when combined with the unfavorably large CTE of polymers, can be quite deleterious. However, the moisture evaporation methods used to compensate for a lack of hermeticity help counteract this problem somewhat (at least in the lower scales of integration), since evaporation is highly endothermic.

Ceramic packages offer the advantages of hermeticity, CTEs comparable to switching materials or metallizations, higher thermal conductivity, and greater integrity. However, ceramics, as a group, have higher dielectric constants and higher dielectric losses, and are more susceptible to stress corrosion cracking [89TUM3]. Furthermore it is difficult and expensive to produce ceramic substrates having relatively high surface smoothness.

Also disadvantageous to both plastic and ceramic packaging is inherent alpha radiation that is emitted from trace impurities within the polymeric and ceramic raw materials. Inherent  $\alpha$ --radiation has been found to cause spurious semiconductor device switching which results in soft errors. For example, concentrations of approximately 1.0 ppm  $U^{238}$  or 0.4 ppm  $Th^{232}$  within a plastic or ceramic package would emit a flux of alpha radiation on the order of  $0.1 \alpha/cm^2/h$ . That level of radiation is one to two orders of magnitude above the acceptable limit established for memory devices [89TUM3].

This radiation problem is currently remedied by adding anti-radiation coatings, as well as through improved raw material processing and careful packaging design. However, these corrections add a great deal to the packaging cost, (which is the main advantage of using plastic packages). Furthermore, as the scale and pitch of integration increase and decrease respectively,  $\alpha$ --radiation switching is expected to become more problematic. Ceramic packaging materials tend to exhibit this problem to a lesser extent than polymeric materials [89TUM3].

However, radiation is a bonafide problem in both, thereby mandating that electronic packaging materials be very highly refined (at least on the first packaging level).

Thus, ceramics are used for high performance applications that are not as cost sensitive as typical consumer electronics while plastic packages are utilized for lower cost electronics. The disadvantages of ceramic-based packaging, in the area of dielectric properties, are currently circumvented through package design (i.e. by using 3--dimensional, multilayer packages, etc.). For the highest electronic performance applications, however, plastic-on-ceramic hybrids are currently used [91KUM1,91KUM2,91SHE2,91TUM]. Porous ceramics and ceramic-plastic composites are also being developed for use in the highest performance applications as well [86CRO,86DAS,87KEL,87MOH,88GER3,88IBR,89JUN,89LEA,89YAM2,90KAT,90STE,91SAC1,91ZUS, etc.].

#### 1.4.2 Methods and Materials

##### 1.4.2.1 Traditional

The history of ceramic electronic packaging is covered in section 1.3.1 above. From the above, it is evident that the evolution of this field has been mainly design (and not materials) oriented. Most ceramic electronic packages and packaging systems were established using alumina-based substrate materials.

However, materials selection has become increasingly important with the advancement of the field. Materials performance limitations are currently thought to be the limiting factor to advancement of the field.

It is of value here to elaborate upon the electronic packaging system that is described in section 1.3.1 above and is generally perceived to be the state-of-the-art in ceramic electronic packaging. This system is IBM's thermal conduction module (TCM). The TCM originally was an alumina-based multilayer package for the IBM 3081

computer system. The original package provided power, cooling and signal integration to more than 100 ICs. The original TCM was a "vertical" design, having 33 ceramic layers interconnected by vias. Due to the relatively high processing temperatures of the original TCM, the conductor metallurgy was based upon "refractory" metal (i.e. tungsten or molybdenum based).

The TCM introduced a very advanced cooling system based upon water-chilled cold fingers, enclosed within a helium-filled chamber, that connected directly to the back of the thermal conductive-paste-covered Si chips. This design made excellent use of C4 or flip chip technology.

The IBM TCM has evolved over its 10+ year life span. The current TCM (produced for use in the IBM system 390/9000), is glass-ceramic-based and has copper metallization. It has 63 dielectric layers and exhibits vastly improved performance. Table 1.3 delineates the differences between one of the alumina-based TCMs (used in the IBM system 3090, ca. 1986) and the latest generation of its evolution.

The process for producing the TCM is outlined in Figure 1.9 above. The basic process has not changed except that the thermal processing treatment now includes a crystallization step.

The thermal conduction module is not the only advanced ceramic electronic packaging system in use today. Some other systems are the liquid-cooled-module (LCM) of NEC, Fujitsu's double-sided board (DSB) system, and Hitachi's card on board (COB) system. These systems, and others, are elaborated upon in various literature sources [89SER, 89TUM3, etc]. These systems all would benefit (or have benefitted) through the use of low dielectric loss, cofirable ceramic packaging materials.

#### 1.4.2.2 Advanced

The subject of advanced electronic packaging is very large and there are several excellent publications which cover the subject

Table 1.3

The IBM Thermal Conduction Module  
Then and Now [91TUM]

Substrate Characteristic	IBM System 3090 Alumina/Molybdenum (ca. 1986)	IBM System 390/ES9000 Glass-Ceramic/Copper (ca. 1991)
Size (mm)	110.5 x 117.7	127.5 x 127.5
Number of Layers	45	63
Number of Vias (Total)	$4.7 \times 10^5$	$2 \times 10^6$
Wiring Density (cm/cm <sup>3</sup> )	450	844
Line Width ( $\mu\text{m}$ )	100	75
Via Diameter ( $\mu\text{m}$ )	125	90 and 100
Dielectric Constant	9.4	5.0
Resistivity ( $\mu\Omega\text{-cm}$ )	11	3.5
CTE (RT to 200°C) (ppm)	60	30
Shrinkage Control (%)	$\pm 0.15$	$\pm 0.1$



[89SER,89TUM3]. Table 1.4 is a comprehensive condensation of recent research performed in the field of advanced ceramic electronic packaging. Data on polymers and metals are also included. Because of the considerable length of Table 1.4, it is placed at the end of Chapter One.

The subject of advanced ceramic packaging may be divided into three general processing categories: thin film, thick film and tape cast processing. Thin films (in this context) may be produced by several means including thermal evaporation, and sputter deposition, etc. Thick films (in this context) are deposited by screen printing and may be used for both insulation and metallization. Tape casting is currently the most used method for producing high performance electronic packaging. Thin film technology offers the advantages of producing comparatively smaller size structures (thinner layers and narrower lines) and thus will become most important in the future. Thin films characteristically have a smoother surface structure than thick films, thereby allowing advanced metallization techniques (i.e. photolithography, e-beam lithography, etc.) to be used. Currently the minimum line width feasible using thin film and optical lithography is approximately  $0.5 \mu\text{m}$  [91CAL].

Thick film materials typically do not display the surface smoothness required for lithography processes and thus minimum line widths are currently limited to approximately 25 to  $50 \mu\text{m}$  [90STE]. However, with the use of smaller particle sizes and improved processing technology, ceramic photolithography has also become the subject of investigation [90NEB]. The thickness (or thinness) of thick film layers is similarly limited. In the future, both types of packages will involve multilayered structures almost exclusively. Furthermore, as mentioned in section 1.4.1 above, polymer-on-ceramic hybrid multilayer structures (similar to those used in the most current IBM TCM) will become very popular.

Metal coated ceramic substrate materials also fit into the category of advanced electronic packaging due to their novelty, toughness, tailorable thermal expansion, high thermal conductivity and low dielectric constant, as a group [81HAN,86SAT,86TEA,87OKA,87SHU]. However, multilayer structures have not yet been produced by this method and, therefore, they are limited to special applications. Generally, ceramic coatings are deposited over metal bases by either electrophoretic or thick film deposition techniques. These composites will see limited future use in such applications as automotive electronics as well as other high temperature, high stress, corrosive environment applications.

From a materials point of view, advanced electronic packaging materials fall into one of two categories: polymer or ceramic. It should be noted that, in this discussion, polymer materials, are carbon-based, organic materials and not ceramic, sol-gel processed materials. The advantages and disadvantages of both types of materials are defined in section 1.4.1.1 above. Generally, polymers are utilized in advanced thin or thick film multilayer structures while ceramics are used to produce advanced thick film or tape cast multilayer packages.

Current polymer materials research for electronic packaging applications is centered mainly in two areas: developing low moisture absorbing polymers, and developing polymeric or polymeric-ceramic materials having thermal expansions matching either Si or GaAs. Thus far, teflons, polyquinolines, and bisbenzocyclobutenes (BCBs) have shown promise as reduced water absorption materials [90REC,91HEN,91ZUS] while composites of epoxy/Kevlar, epoxy/Nextel, polyimide/Kevlar, and polyimide/glass have shown promise as matched thermal expansion materials [88IBR,91ZUS].

Recently, research in the area of advanced ceramic electronic packaging materials has investigated several, varied topics. Low temperature cofirability (allowing the use of low  $\rho$  (resistivity)

metallization) has been a universal trend in almost all of this research. Advanced ceramic electronic packaging materials research may be further divided into the categories of diamond films [91LYN], glass+ceramics, glass-ceramics, and porous ceramics. Table 1.4, placed at the end of this chapter, provides a condensation of materials and processing information for all of these areas, as well as a bibliography for the convenience of the reader. Diamond thin films have not yet been successfully implemented for use in high speed microelectronic packaging, due mainly to the infancy of the field.

Glass+ceramic and glass-ceramic materials are currently the mainstay of the high performance electronic packaging field. However, no ceramic material that is a viable future high speed electronic packaging candidate has a dielectric constant below 3.78 [76KIN]. It has been stated that electronic materials used in future high performance packaging applications will necessarily have dielectric constants below this value [86CRO,87MOH,87YAR,88GIL etc.]. Therefore, the only way to achieve dielectric constant values below 3.78 while using ceramic materials, is to fabricate composites of ceramic materials with non-ceramic, electronically insulating materials, that have lower dielectric constants (i.e. polymers, or air). The decisive majority of this research has been in the area of porous ceramics.

Cofirable, porous ceramic materials may be produced from glass, glass+ceramics or glass-ceramics and are, thus, considered a subset of each group. Porous ceramics may be produced in several ways. Porous ceramic thin films may be produced by partial densification of  $\text{SiO}_2$  sol-gel films [86CRO,87MOH,88MOH], thermal oxidation of sputtered columnar Si [86DAS], and reactive sputtering of  $\text{SiO}_2$  [86DAS], as well as by suspension of latex in silica sol [87MOH]. These methods have not yet been implemented in electronic packaging, however, due to poor film hermeticity as well as inadequate mechanical properties and surface smoothnesses, etc.

Porous thick films have been produced by addition of hollow silica glass microspheres (HGMS) [87KEL,89LEA,89JUN,90KEL], partial sintering of glass frit pastes [90WAH], and controlled gas generation within fully dense glass thick films [90STE,90WAH]. These methods have found greater success. However, problems with surface smoothness necessitate extra thick film applications with sealing pastes. Furthermore, the repetition inherent in thick film processing limits the applicability of the thick film process in general, since only one layer may be produced at one time. Finally, the controlled gas generation method involves a large volume expansion, and thus, dimensional stability becomes a problem in multilayer structures containing porosity produced via controlled gas generation. However, this method has been utilized to produce metallization lines as narrow as 25 to 50  $\mu\text{m}$  in a single layer configuration [90STE].

It is not sufficient simply to add porosity to the insulating material. In order to maintain a hermetic structure, porosity must be non-continuous. Furthermore, the porosity must be small in order to maintain surface smoothness as well as mechanical properties. While surface roughness improves interlayer and metallization adhesion, it is detrimental when the scale of said roughness is within approximately one tenth of the smallest signal line dimension. Roughness on this scale not only increases the possibility of electrical discontinuity of signal traces, but promotes inhomogeneity of the signal trace cross section. This is highly detrimental at high frequencies since it causes inhomogeneities in the characteristic impedance ( $Z_0$ ). Furthermore, variances in cross section force high frequency electronic signals through a relatively tortuous path. This not only increases signal propagation distance, but increases spurious signal reflection [89TYL]. Finally, it is best if included porosity be limited to as small a volume fraction as possible in order to preserve dielectric breakdown strength,

volume resistivity, surface smoothness, sinterability, mechanical properties and thermal conductivity, etc.

Currently, tape casting is the only feasible method by which porous ceramic materials have been produced for electronic packaging. Porosity has been introduced into tape cast ceramics via hollow silica glass microspheres (HGMs) [88LEA1] as well as through the controlled burnout and subsequent differential sintering of organic latex microspheres [89YAM2,90KAT].

The HGM method allows for a greater amount of included porosity to be added to the packaging material than the latex method, since the added porosity, resultant from HGM additions, is non-continuous. Therefore, the HGM method is better in theory and is the only currently viable method for producing tape cast packaging materials having greater than ~13V% non-continuous porosity. However, the only successfully produced and tested ultra low dielectric permittivity, multilayer electronic packages produced, to date, have utilized the latex method [89YAM2,90KAT]. There are several reasons for this. First, HGMs are comparatively quite large (~80  $\mu\text{m}$ ) and thus promote surface roughness. Also, HGMs have very low density (~0.25 g/cm<sup>3</sup> [89LEA]) and thus tend to segregate during suspension processing. Third, HGMs tend to break down during processing (such as pressing, laminating, sonic dismembrating, etc.). Finally, as HGMs become smaller, it will become necessary to add them to the ceramic matrix in larger amounts (compared to latex) due to the wall thickness of HGMs. For example, pores resulting from the burnout of latex and subsequent sintering of the surrounding matrix tend to comprise a volume similar to the volume of the latex spheres which formed them. With HGMs, however, the amount of SiO<sub>2</sub> added to the ceramic matrix per microsphere addition may, in fact, be similar to, or greater than the amount of porosity added. An HGM having a diameter of 5  $\mu\text{m}$  and a wall thickness of 0.5  $\mu\text{m}$  is only 51% porous itself. Said HGM would have a K of ~2.4 (as compared to ~1 for air). In this scenario,



the HGM method would be much less efficient for reduction of K than the latex method. Since it is desirable to add a minimum of either HGM (mainly for sinterability and mechanical integrity reasons) or latex (mainly for hermeticity and mechanical integrity reasons), the latex method is preferable in this sense.

Hermetic ceramic materials having dielectric constants as low as 3.4 have been produced, via tape casting, and utilized in multilayer packages in the laboratory [89YAM2,90KAT]. Commercial introduction of such a product has not yet occurred, however.

Therefore, it is imperative that further research be performed in the area of controlled porosity ceramics for utilization in ultra high speed electronic packaging. Many materials and processing related questions remain in this field. Research in this area should focus upon methods to minimize (and the theories involving minimization of) dielectric constant and dielectric loss while maintaining a hermetic material of dimensional and mechanical adequacy.

## 1.5 Proposed Packaging Material System: Statement of Thesis

### 1.5.1 Choice of Electronic Packaging Material System

The choice of the electronic packaging material system to investigate was based upon creating a relatively low cost, hermetic, ceramic packaging material for use in very high speed electronic packaging applications. From the above criteria, it becomes apparent that no one material is satisfactory for this application. Therefore, it was decided to chose a composite system having carefully selected constituents. This methodology is useful in that the composite may be optimized for different applications. Properties of the materials utilized are outlined in Table 1.4 at the end of this chapter. Cofireability is obtained by using a borosilicate glass as the composite matrix. Surface smoothness is also enhanced when a viscous sintering matrix is used. Low dielectric constant and  $\tan(\delta)$  are achieved by



utilization of materials having low  $K$  and  $\tan(\delta)$  values as well as through the addition of controlled porosity. Furthermore, all materials utilized have dielectric properties which are stable over a broad range of frequencies.

In this study, controlled porosity is achieved via the addition, and subsequent pyrolysis, of uniform polystyrene latex microspheres (UPLMs). The UPLMs are producible in a size range between 3 and 9  $\mu\text{m}$  and are quite monodisperse, thereby allowing a study of the effects of UPLM size and dispersity upon the hermeticity of the sintered material.

The composite system of focus should also be easily adaptable to standard ceramic tape casting processes. Since the maximum diameter of the latex is less than 10  $\mu\text{m}$ , the surface smoothness criterion should also be satisfied for most current thick film signal line widths (if proper dispersion and homogenization are achieved).

There are some problems associated with adding porosity to a brittle material. Porosity in a ceramic material has been shown to reduce the mechanical strength of said material [76KIN]. Furthermore, it is possible to create a non-hermetic material from a formerly hermetic one. Therefore, processing must be optimized to provide hermetic materials having acceptable mechanical properties.

In order to increase the mechanical integrity of the composite system, a hard particulate ceramic is added. Since mechanical strength and toughness must be increased with minimal increase in dielectric properties, the choices for ceramic filler are limited to strong particulate ceramic materials having low  $K$  and  $\tan(\delta)$  (such as diamond, cubic BN or  $\text{Si}_3\text{N}_4$ ). In order to reduce material costs, particulate  $\text{Si}_3\text{N}_4$  was used. Silicon nitride represents the best compromise between desired properties and expense, thereby making this packaging system practical for most electronic packaging applications. Also, since the  $\text{Si}_3\text{N}_4$  was used as a nonreactive addition, all information related to sintering and processed microstructure, gained from this study, should

be generally applicable to similar composites with other, similar, inert additions.

### 1.5.2 Topics of Investigation

This study investigates several factors crucial to the development of the proposed borosilicate glass-particulate  $\text{Si}_3\text{N}_4$ -controlled porosity composite system. This section outlines the topics of research investigated in this study.

The following constituent variables are investigated:

- the effects of ball milling on the properties of the borosilicate glass powder

- the effects of borosilicate glass size and size distribution upon sintering behavior of said glass

- the effects of UPLM volume fraction, size and size distribution upon both green and selected sintered materials properties (see below)

- the effects of  $\text{Si}_3\text{N}_4$  volume fraction and/or included porosity volume fraction upon sintering behavior, and selected sintered materials properties (see below).

The following processing factors are investigated:

- the effects of suspension sonication and aging upon green and non-sintered properties

- the effects of pyrolysis/presintering upon borosilicate glass surface area and surface pore size distribution

- the effect of heat treating  $\text{Si}_3\text{N}_4$  powder in air, at or above composite sintering temperatures, upon the properties of said  $\text{Si}_3\text{N}_4$

- the effect of sintering temperature upon sintering rate.

The following materials parameters are investigated:

- the effect of porosity and  $\text{Si}_3\text{N}_4$  volume fraction upon the dielectric constant of the composite

- the effect of frequency upon dielectric properties

- the effect of atmospheric exposure upon hermetic and non-hermetic materials

- the effect of porosity and  $\text{Si}_3\text{N}_4$  volume fraction upon the hardness of the composites.

Models of composite materials properties, as well as models concerning the effect of pore percolation upon hermeticity, the effect of non-sintering particulate and/or included porosity volume fraction upon sintering behavior and the effect of porosity upon assorted mechanical properties (as described in Chapters Two and Four), are utilized to characterize the composite system. A discussion of the universal applicability of said experimental results to other analogous systems is included as well.

The main emphasis of this study, however, is to investigate and model the phenomena involved in the creation and maximization of closed porosity, produced using the methods described within, in order to reduce the dielectric constant of the composite and while providing a candidate material for MLC applications.

**Table 1.4**  
**Pertinant Materials Properties for Selected Electronic Packaging Materials**

Electronic Properties				Thermal Properties			Physical Properties			
Material	$\epsilon/\epsilon_0$ @1MHz	$\tan \delta$ @1MHz	Volume Res. ( $\Omega$ -cm)	Breakdown Voltage (V/ $\mu$ m)	Thermal Con. (W/m $^2$ °C)	CTE (ppm/°C)	Process Temp. (°C)	$\rho$ (g/cc)	Flexural Strength (MPa)	Ref(s).
Ceramic Materials (Crystalline)										
AlN	8.0-10.0	0.0001-0.0028	$> 10^{14}$	8380	70-320	3.7-4.5	1800-1900* (*CaO add.)	3.20-3.30	280-490	85WEA, 86HAM, 87CHO, 87KUR, 88GER3, 88SEI, 89HIM, 89MAT, 89NIW, 89TAK, 90REC, 91LYN, 91KUM2, 91TUM , 92RIC, 92SHE2
Al <sub>2</sub> O <sub>3</sub>	8.2-10.2	0.0002-0.002	$10^{14}$ - $10^{16}$	9650-15800	19-50	5.6-9.0	1500-1600	3.59-3.97	280-552	84MUS, 85WEA, 86HAM, 87CHO, 88CER, 88GER3, 89KON, 89NIW, 89TAK, 89TAN, 90LEE, 90REC, 91HAN, 91KUM2 , 91SHE2, 91TUM , 91ZUS, 92RIC
Anorthite (CaO-Al <sub>2</sub> O <sub>3</sub> -2SiO <sub>2</sub> )						4.5				91TUM
BeO	5.8-6.9	0.0003-0.001	$10^{15}$ - $10^{16}$	9500-13800	135.5-370	4.2-9.4	1600-2000	1.8-3.01	170-490	85WEA, 87CHO, 87KUR, 88CER, 88GER3, 89MAT, 89TAK, 90LEE, 90REC, 91LYN, 91KUM2, 91SHE2, 91TUM, 92RIC

Table 1.4 Continued

Table 1.4 Continued											
	Electronic Properties					Thermal Properties			Physical Properties		
Material	$\epsilon/\epsilon_0$ @1MHz	$\tan \delta$ @1MHz	Volume Res. ( $\Omega$ -cm)	Breakdown Voltage (V/ $\mu$ m)	Thermal Con. (W/m $^2$ C)	CTE (ppm/ $^{\circ}$ C)	Process Temp. ( $^{\circ}$ C)	$\rho$ (g/cc)	Flexural Strength (MPa)	Ref(s).	
BN ( $\alpha$ -Hex)	4.0-4.4	0.001	$10^{14}$	35000-55000	28-42	3.7-4.3		2.1-2.25	110	85WEA, 87CHO, 88CER, 88GER3, 89MAT, 91CER	
BN (cubic)	5.6-5.8		$> 10^{12}$		760-1300	4	1400 (@6.5 GPa Pressure, with AlN add.)	3.48		87CHO, 88GER3, 89HIR, 89MAT, 91WES	
Celsian (BaO $\cdot$ Al $_2$ O $_3$ $\cdot$ 2SiO $_2$ )						2.7				91TUM	
Ceria (CeO $_2$ )	15.0	0.0007	$10^9$		12.1	10.0		7.0-7.13	110	85WEA, 88CER	
Clinoctatite (MgO $\cdot$ SiO $_2$ )						7.8				91TUM	
Cordierite (2MgO $\cdot$ 2Al $_2$ O $_3$ $\cdot$ 5SiO $_2$ )	4.1-6	0.003-0.007	$10^{16}$	5500-9100	1-4	1-3	925-1050 (IBM, Viscous Sintering, Subsequent Crystallization)	2.0-2.9	70-300	84MUS, 87CHO, 88CER, 88GER3, 89MAT, 89NIW, 89SAW, 91KUM2 , 91TUM	
Diamond (C)	5.5-5.7	0.001	$10^{16}$		650-2000	1.1-3.5		3.5	1400	87CHO, 88GER3, 89MAT, 91LYN, 91WES	
Eucryptite (Li $_2$ O $\cdot$ Al $_2$ O $_3$ $\cdot$ 2SiO $_2$ )	5.3	0.005	$10^{12}$		1.67	-10 to 0.5		2.67	62	66WEB, 88CER, 91TUM	
Forsterite (2MgO $\cdot$ SiO $_2$ )	5.8-6.7	0.0004-0.001	$10^{17}$	7900-11900	1.67-4.18	9.4-10.6		2.8-2.9	140-170	66WEB, 88CER, 89MAT, 89NIW, 91TUM	

Table 1.4 Continued

Table 1.4 Continued										
	Electronic Properties					Thermal Properties			Physical Properties	
Material	$\epsilon/\epsilon_0$ @1MHz	$\tan \delta$ @1MHz	Volume Res. ( $\Omega$ -cm)	Breakdown Voltage (V/ $\mu$ m)	Thermal Con. (W/m <sup>2</sup> C)	CTE (ppm/ <sup>o</sup> C)	Process Temp. ( <sup>o</sup> C)	$\rho$ (g/cc)	Flexural Strength (MPa)	Ref(s).
Gallium Arsenide (GaAs)	12.8				43.0	5.9				90GAG,90REC
Hafnia (HfO <sub>2</sub> )	12.0	0.01	10 <sup>4</sup>		1.67	6.5		9.0-9.68	110	85WEA,88CER
Magnesia (MgO)	8.2-10	0.001	> 10 <sup>14</sup>	8500-11000	39.7-146	8.8-13.5		2.5-3.58	138	85WEA,87CHO, 88CER,90LEE
Micas	5.4-8.7	0.0002	10 <sup>16</sup>	39500-79100	0.33-0.83	7.6-27.0		2.6-3.8		88CER,90LEE
Mullite (3Al <sub>2</sub> O <sub>3</sub> ·2SiO <sub>2</sub> )	6.2-6.8	0.00095-0.005	> 10 <sup>14</sup> -10 <sup>15</sup>	7800	2.51-7.0	4.0-5.5	1400-1600 (CaO, MgO,SiO <sub>2</sub> add.)	2.5-3.1	131-302	(84MUS,87CHO, 88CER,88GER3, 89MAT,89NIW, 89TAN,90KUR, 91KUM2, 91SHE2,91TUM
Silicon (Si)	11.7-12				100-200	2.6-4.0		2.32-2.34		85WEA,87CHO, 87KUR,90GAG, 90LEE,90REC, 90RIC,91LYN
Silicon Carbide (SiC, BeO Doped)	40-45	0.05	> 10 <sup>13</sup>		270-490	3.7-4.3	2000-2100	3.2-3.22	420-450	85WEA,86HAM, 87CHO,87KUR, 88GER3,89MAT, 89TAK,91KUM2 ,91SHE2,91TUM ,92RIC
Si <sub>3</sub> N <sub>4</sub> ( $\alpha$ -Hexagonal)	6.0-7.0	0.0001	10 <sup>14</sup>	15800-19800	12.5-33.5	2.3-3.1	1600-2000	3.1-3.44	350-697	84SCH2,84SCH3 ,85WEA,87CHO, 88CER,88GER3, 88REE,89SAN1, 89SAN2, 91KUM2, 91SHE2,91TUM



Table 1.4 Continued

Electronic Properties					Thermal Properties			Physical Properties		Ref(s).
Material	$\epsilon/\epsilon_0$ @1MHz	$\tan \delta$ @1MHz	Volume Res. ( $\Omega$ -cm)	Breakdown Voltage (V/ $\mu$ m)	Thermal Con. (W/m $^2$ °C)	CTE (ppm/°C)	Process Temp. (°C)	$\rho$ (g/cc)	Flexural Strength (MPa)	
SiO <sub>2</sub> (Quartz)	4.1-4.6				2-40	11.2 (Quartz) 12.5 (Cristoballite) 17.5 (Tridymite)		2.6-2.66	140	85WEA, 87CHO, 88GER3, 89MAT, 90LEE, 91TUM,
Spinel (MgO-Al <sub>2</sub> O <sub>3</sub> )	7.5	0.0004	10 <sup>14</sup>	11900	7.53	6.6		2.8	103	88CER
Spodumene (LiAlSi <sub>3</sub> O <sub>6</sub> )	6.0-6.4	0.004	10 <sup>10</sup>		5.0-5.02	2.0	950	2.4-3.2	250	66WEB, 88CER, 91KUM2
$\beta$ -Spodumene (IBM)	5.3-5.7					0.9-5.5	850-990			89SAW, 91TUM
Steatite (MgO-SiO <sub>2</sub> )	5.7-6.1	0.0008-0.0035	10 <sup>17</sup>	7900-13800	2.5-3.34	7.2-10.4		2.7-2.8	145-170	88CER, 89MAT
Thoria (ThO <sub>2</sub> )	13.5	0.0003	10 <sup>10</sup>	~5300	13.8	5.3-5.9		9.7-9.86	131	85WEA, 88CER
Titania (TiO <sub>2</sub> )	100				7	3.3		3.84-4.26		85WEA, 87CHO
Zirconia (ZrO <sub>2</sub> )	12.0-13.0	0.01	10 <sup>9</sup>	~5000	25.7	3.0-10		5.6-5.89	186-400	85WEA, 88CER, 89NIW
Zircon (ZrSiO <sub>4</sub> )	8-10.5	0.001-0.0014	> 10 <sup>14</sup>	6300-11500	5.02-8.36	3.5-5.5		3.7-4.3	172	88CER
Ceramic Materials (Amorphous)										
Glass (General)	4.3-8.5	0.0005-0.01	10 <sup>12</sup>	7800-13200	0.83-1.67	0.8-1.3		2.0-8.0	110	87CHO, 88CER
Aluminum Silicate	6.3					3.0-4.8	SP=910			89NIW

Table 1.4 Continued

Electronic Properties					Thermal Properties			Physical Properties		
Material	$\epsilon/\epsilon_0$ @1MHz	$\tan \delta$ @1MHz	Volume Res. ( $\Omega$ -cm)	Breakdown Voltage (V/ $\mu$ m)	Thermal Con. (W/m $^2$ °C)	CTE (ppm/°C)	Process Temp. (°C)	$\rho$ (g/cc)	Flexural Strength (MPa)	Ref(s).
Borosilicate Glass	3.7-4.9				1.2-4.0	3.0-4.3	SP=700-850	2.1-2.2	50-70	87CHO, 89MAT, 89NIW, 89SAN1, 89SAN2, 91KUM2, 91SHE2, 91TUM
Barium Borosilicate Glass	5.8					4.6	SP=840			89NIW
Cordierite Composition Glass	6.3					3.7-3.8			100	84MUS
Corning 7052 Borosilicate Glass	4.9	0.013	$10^{17}$		2.09	4.6-5.3	SP=712 WP=1128	2.27		79COR, 84SCH2, 84SCH3, 91WIL1
Corning 7070 (Borosilicate Glass, see Appendix I for Composition)	4.1	0.0006-0.0025	$>10^{17}$			3.2-3.9	Str. Pt.=456 Ann. Pt.= 496 WP=1068	2.13		79COR, 88COR, 89MAT, 91WIL1
Corning 7913 (96% SiO <sub>2</sub> )	3.8	0.0004	$>10^{17}$			0.75	Str. Pt.=890 Ann. Pt.=1020	2.18		79COR
E-Glass	6.4	0.0012				5.2		2.58	5.5	91ART

Table 1.4 Continued

Table 1.4 Continued										
Electronic Properties					Thermal Properties			Physical Properties		
Material	$\epsilon/\epsilon_0$ @1MHz	$\tan \delta$ @1MHz	Volume Res. ( $\Omega$ -cm)	Breakdown Voltage (V/ $\mu$ m)	Thermal Con. (W/m $^2$ °C)	CTE (ppm/°C)	Process Temp. (°C)	$\rho$ (g/cc)	Flexural Strength (MPa)	Ref(s).
Kyocera Matrix Glasses 1) 74W % SiO <sub>2</sub> , 21W % B <sub>2</sub> O <sub>3</sub> , 3W % Al <sub>2</sub> O <sub>3</sub> , 2W % Other 2) 74W % SiO <sub>2</sub> , 17W % B <sub>2</sub> O <sub>3</sub> , 3W % Al <sub>2</sub> O <sub>3</sub> , 1W % CaO, MgO, 5W % Other 3) 80W % SiO <sub>2</sub> , 12W % B <sub>2</sub> O <sub>3</sub> , 2W % Al <sub>2</sub> O <sub>3</sub> , 1W % MgO, CaO, 5W % Other	1) 3.5									89EMU
	2) 3.8									
	3) 4.6									
Lead Aluminosilicate Glass	8.2-15	0.001	10 <sup>15</sup>	8900-16000						88CER
SiO <sub>2</sub> (Amorphous)	3.78-5.4	0.0001-0.0005	10 <sup>12</sup> -10 <sup>18</sup>	9652-25000	1.25-2.1	0.3-1.0		2.2	5.5-50	84SCH2, 84SCH3, 88CER, 88GER3, 89MAT, 89SAN1, 89SAN2, 91ART, 91ZUS
Ceramic Matrix Composite Materials										
96 % Al <sub>2</sub> O <sub>3</sub> , 4 % Glass	8.9-9.6	0.0001-0.0015	> 10 <sup>15</sup> -10 <sup>16</sup>	13970	20-25.1	6.0-7.5	1550-1600	3.73-3.9	317-455	84SCH2, 84SCH3, 85KAW, 87IWA, 87IWA2, 87KUR, 89SAN1, 89SAN2, 90REC, 91DIL, 91KUM2, 92RIC

Table 1.4 Continued

Table 1.4 Continued										
Electronic Properties					Thermal Properties			Physical Properties		
Material	$\epsilon/\epsilon_0$ @1MHz	$\tan \delta$ @1MHz	Volume Res. ( $\Omega$ -cm)	Breakdown Voltage (V/ $\mu$ m)	Thermal Con. (W/m <sup>2</sup> °C)	CTE (ppm/°C)	Process Temp. (°C)	$\rho$ (g/cc)	Flexural Strength (MPa)	Ref(s).
92% Al <sub>2</sub> O <sub>3</sub> , 8% Glass	8.5				16.73	6.5			331	84SCH2, 84SCH3 89SAN1, 89SAN2
Aluminosilicate (Derived from Ion Exchanged Zeolite Precursor)	5.2-6.5	0.0005-0.002	10 <sup>12</sup> -10 <sup>13</sup>			2.4-4.4	950-1050			89SUB
Al <sub>2</sub> O <sub>3</sub> in CaO-Al <sub>2</sub> O <sub>3</sub> - B <sub>2</sub> O <sub>3</sub> -SiO <sub>2</sub> Glass Matrix (60W% Glass/40W% Al <sub>2</sub> O <sub>3</sub> , Crystallizes to Mainly Anorthite, Narumi LFC-I, LFC-II, and LFC-III)	7.7	0.0003	>10 <sup>14</sup>	>6000 V/90 $\mu$ m	2.51	5.5	880-900	2.9	196	86NIS, 89NIS1, 89SAW
Al <sub>2</sub> O <sub>3</sub> in Magnesia-- Calcio--Alumino-- Borosilicate Glass Matrix (Proprietary Composition, Matsushita)	7.1	0.0025					1000			89SAW
Al <sub>2</sub> O <sub>3</sub> + CaZrO <sub>3</sub> in Lead--Alumino-- Borosilicate Glass Matrix (Proprietary Composition, Hitachi)	9-12	0.001-0.003					850			89SAW

Table 1.4 Continued

Table 1.4 Continued										
Electronic Properties					Thermal Properties			Physical Properties		
Material	$\epsilon/\epsilon_0$ @ 1MHz	$\tan \delta$ @ 1MHz	Volume Res. ( $\Omega$ -cm)	Breakdown Voltage (V/ $\mu$ m)	Thermal Con. (W/m $^2$ °C)	CTE (ppm/°C)	Process Temp. (°C)	$\rho$ (g/cc)	Flexural Strength (MPa)	Ref(s).
Al <sub>2</sub> O <sub>3</sub> + Forsterite in Bario-Alumino- Silicate Glass Matrix (Proprietary Composition, Asahi Glass)	5.0-6.5	0.0008-0.002	> 10 <sup>14</sup>		2.93	3.8-6.8	850-900		196	85KAW,89SAW
Boron Doped Colloidal Sol-Gel Silica	2.66-4.53	0.0005-0.005			0.8-1.2	0.4-3.1	1050	2.19 (@ Full Density)	642-663 kg/cm <sup>2</sup>	89SAN1,89SAN2
Borosilicate Glass/Al <sub>2</sub> O <sub>3</sub>	4.9-5.7				2.5-6.0	4.0-4.5	850-1000		200-250	85NIW,89SAW, 91KUM2,91YOK
Lead Borosilicate Glass/Al <sub>2</sub> O <sub>3</sub> (45W %/55W %, NEC)	7.5-7.8	0.002-0.003	> 10 <sup>14</sup>	> 15000	3.6-6.0	4.2-6.1	900-950	3.1-3.15	295-300	84SHI,86UTS, 90LEE,90SHI1, 90SHI2,91BAB, 91KUM2,91SHI2 ,91TUM
CERACOM 001 Epoxy Filled Porous Ceramics with glass cloth outer layer reinforcements (Machinable): 1) Cordierite (30V % Porous)/Epoxy 2) AlN (38V % Por- ous)/Epoxy 3) Al <sub>2</sub> O <sub>3</sub> (33V % Por- ous)/Epoxy 4) SiC (30V % Por- ous)/Epoxy	1) 4.0 2) 4.2 3) 4.0 4) NA	1) 0.0066- 0.0068	1) 2.2x10 <sup>15</sup> - 3.5x10 <sup>15</sup>	1) 22 Kv/mm	1) 0.9 2) 15.2 3) 2.4 4) 2.8	1) 3.8 2) 7.0 3) 10.0 4) 4.7	Partially Sinter Ceramics, Impregnate w/Epoxy	1) 1.8 2) NA 3) 2.9 4) 2.4	1) 177 2) 167 3) 206 4) 345	86IWA,87IWA2





Table 1.4 Continued

Table 1.4 Continued										
	Electronic Properties				Thermal Properties			Physical Properties		
Material	$\epsilon/\epsilon_0$ @1MHz	$\tan \delta$ @1MHz	Volume Res. ( $\Omega$ -cm)	Breakdown Voltage (V/ $\mu$ m)	Thermal Con. (W/m $^2$ °C)	CTE (ppm/°C)	Process Temp. (°C)	$\rho$ (g/cc)	Flexural Strength (MPa)	Ref(s).
DSP Cement + Colloidal Silica	5.1 (Strongly Humidity and Frequency Dependent)	0.006 (Strongly Humidity and Frequency Dependent)								89LEI
DuPont Green Tape™ (Ceramic in Alumino-- Borosilicate Glass Matrix, Proprietary Composition)	7.8-8	0.002-0.003			2.20	7.9	850	3.02	127-206	85STE,86SAW, 87ROM,88BEN, 89SAW,89TYL, 90RIC
Electro-Science REGAL (REinforced Glass ALumina Composite, Proprietary Composition)	~5 @ 1GHz						850			86BLE
Electro-Science (Proprietary Thick Film Compositions) 1) D-111 2) D 4911 3) TF 4000 (Porous)	1) 4.5 2) 4.3 3) 2.5-4.2	1) 0.0009 2) 0.0005 3) 0.0005- 0.0009	1) >10 <sup>12</sup> 2) >10 <sup>12</sup> 3) >10 <sup>12</sup>	1) 1500 V/25 $\mu$ m 2) 1650 V/25 $\mu$ m			2) 850 3) 930-985			90STE,90WAH
Ferro EMD (Crystallizing Glass, Proprietary Composition(s))	4.5-5.8	0.002-0.003	>10 <sup>11</sup> -10 <sup>14</sup>	>1000 V/mil		7.7	850		127	88SHA1,88SHA2 ,91ALE
Glass Ceramics (General)	4.0-8.0	0.002-0.004			1-4	4.5	<1000		100-200	91HAN,91SHII, 91STE,92RIC

Table 1.4 Continued

Table 1.4 Continued											
	Electronic Properties					Thermal Properties			Physical Properties		
Material	$\epsilon/\epsilon_0$ @1MHz	$\tan \delta$ @1MHz	Volume Res. ( $\Omega\text{-cm}$ )	Breakdown Voltage (V/ $\mu\text{m}$ )	Thermal Con. (W/m $^2$ °C)	CTE (ppm/°C)	Process Temp. (°C)	$\rho$ (g/cc)	Flexural Strength (MPa)	Ref(s).	
Kyocera Glass Ceramic Composites (Utilizing Kyocera Matrix Glasses Above, 50/50 Glasses/Ceramic (by Weight))  1. A SiO <sub>2</sub> /Glass 1 B SiO <sub>2</sub> /Glass 2 C SiO <sub>2</sub> /Glass 3  2. A Cordierite/ Glass 1 B Cordierite/ Glass 2 C Cordierite/ Glass 3  3. A Al <sub>2</sub> O <sub>3</sub> /Glass 1 B Al <sub>2</sub> O <sub>3</sub> /Glass 2 C Al <sub>2</sub> O <sub>3</sub> /Glass 3	1A) 4.7					1A) 9.2	1A) 900		1A) 98	89EMU	
	1B) 4.8					1B) 11.5	1B) 925		1B) 118		
	1C) 5.3					1C) 9.0	1C) 950		1C) 128		
	2A) 4.9					2A) 2.2	2A) 950		2A) 128		
	2B) 5.1					2B) 2.4	2B) 950		2B) 137		
	2C) 5.8					2C) 8.0	2C) 975		2C) 167		
	3A) 6.3					3A) 5.5	3A) 950		3A) 177		
	3B) 6.5					3B) 5.6	3B) 950		3B) 196		
	3C) 7.3					3C) 5.7	3C) 975		3C) 245		
	5.2	0.003	$> 10^{14}$	$> 15 \text{ kV/mm}$		3.0	950	2.4	177		
Kyocera LEC Glass Ceramic (50/50 Mixture (by Weight) of Kyocera Compositions 1B and 3B Above)	7.9					7.9	850		150	91SHE2	
Kyocera LTCC (Al <sub>2</sub> O <sub>3</sub> + SiO <sub>2</sub> in Lead Borosilicate Glass, Proprietary Composition)											

Table 1.4 Continued

Material	Electronic Properties				Thermal Properties			Physical Properties		Ref(s).
	$\epsilon/\epsilon_0$ @1MHz	$\tan \delta$ @1MHz	Volume Res. ( $\Omega$ -cm)	Breakdown Voltage (V/ $\mu$ m)	Thermal Con. (W/m $^2$ °C)	CTE (ppm/°C)	Process Temp. (°C)	$\rho$ (g/cc)	Flexural Strength (MPa)	
LaFarge SIFCAR™ 71 (Calcium Aluminate Cement)	10.7-10.9	0.003-0.006	$2.8 \times 10^{15}$				1450	2.66		89SL1
Lead Borosilicate (45W%/Alumina (55 W%))	7.8	0.002-0.003	$> 10^{14}$	$> 15000$	3.6-6.0	4.2-6.1	900-950	3.1	300	91BAB,91KUM2 ,91SH12
Lead Glass + Hollow Glass Microspheres (SiO <sub>2</sub> HGMS, 80 $\mu$ m ave. size, 55-68 V% Porosity)	3.28-3.93	0.004					530-550	1.18-1.70		89LEA
MDF (Macro Defect Free Cements) A. Without Hollow Glass Microspheres (SiO <sub>2</sub> HGMS) B. With SiO <sub>2</sub> HGMS	A. 4-8 B. 4.7	A. 0.02-0.10 B. 0.02								86CRO
Matsushita Glass Ceramic Crystallizes to: Labradorite (0.35NaAlSi <sub>3</sub> O <sub>8</sub> - 0.65CaAl <sub>2</sub> Si <sub>2</sub> O <sub>7</sub> - Major), Albite (NaAlSi <sub>3</sub> O <sub>8</sub> -Minor), and Anorthite (CaAl <sub>2</sub> Si <sub>2</sub> O <sub>7</sub> -Minor) (See Ref. for Precursor Compositions)	7.4	0.002	$> 10^{14}$	$> 15$ KV/mm	2.93	6.12	900	3.07	245	88BAB

Table 1.4 Continued

Electronic Properties						Thermal Properties			Physical Properties		
Material	$\epsilon/\epsilon_0$ @1MHz	$\tan \delta$ @1MHz	Volume Res. ( $\Omega$ -cm)	Breakdown Voltage (V/ $\mu$ m)	Thermal Con. (W/m $^2$ °C)	CTE (ppm/°C)	Process Temp. (°C)	$\rho$ (g/cc)	Flexural Strength (MPa)	Ref(s).	
Mica (Glass Bonded)	6.4-9.2	0.0015-0.003	10 <sup>14</sup>	10600-23700	0.50	10.0-14.5		2.6-3.8	117	88CER	
Mullite/Cordierite/ Glass Composites (See Ref. for Details)	5.1-7.5	0.002			2-4	1.5-4.5	1400-1550	2.5-3.2	150-190	84MUS, 89AND	
Mullite/Glass (72W% Mullite, 28W% Glass, Glass Composition, 90W% SiO <sub>2</sub> , 8W% Al <sub>2</sub> O <sub>3</sub> , 2W% MgO), Hitachi	5.9				3.5	3.5	1600-1650	2.75	215	91FUJ	
Murata Proprietary Composition (contains BaO, SiO <sub>2</sub> , Al <sub>2</sub> O <sub>3</sub> , CaO, and B <sub>2</sub> O <sub>3</sub> )	6.1	0.0007				8	950-1000			89SAW	
NEC Proprietary Compositions (Glass Matrix with either 1) Al <sub>2</sub> O <sub>3</sub> , 2) Cordierite, or 3) SiO <sub>2</sub> (Quartz) Ceramic Filler (see 87SHI)	1) 7.8 2) 5.0 3) 3.9	1) 0.003 2) 0.005 3) 0.003	1) >10 <sup>14</sup> 2) >10 <sup>13</sup> 3) >10 <sup>13</sup>			1) 4.2 2) 7.9 3) 1.9	1) 900 2) 900 3) 900	1) 3.10 2) 2.40 3) 2.15	1) 343 2) 147 3) 137	87SHI, 88SHI, 89SAW	
NGK C-01 or FC-01 Cordierite in Glass Matrix (Crystallizes From Proprietary ZnO-MgO-Al <sub>2</sub> O <sub>3</sub> -SiO <sub>2</sub> Glass)	5.0-5.6	0.0013	5x10 <sup>13</sup>		2.51	2.4-3.0	900-950	2.56	170-200	85KON, 89KON	
Porcelain	5-6.6	0.008-0.02	10 <sup>14</sup>	6100-13000	1.6-2.5	4.4-6.0	1250-1450	2.4	83-90	84SCH2, 84SCH3 , 88CER, 89SAN1, 89SAN2	

Table 1.4 Continued

Electronic Properties										Thermal Properties			Physical Properties		Ref(s).
Material	$\epsilon/\epsilon_0$ @1MHz	$\tan \delta$ @1MHz	Volume Res. ( $\Omega$ -cm)	Breakdown Voltage (V/ $\mu$ m)	Thermal Con. (W/m $^2$ °C)	CTE (ppm/°C)	Process Temp. (°C)	$\rho$ (g/cc)	Flexural Strength (MPa)						
Porous Vycor	2.6-3.5	0.001-0.005						1.45-1.5		79SIM, 86CRO, 87MOH, 89YAM2					
Pyroceram	5.5-6.3	0.0017-0.013	10 <sup>12</sup>	9900-11900	1.67-3.67	0.2-4.0		2.4-2.6	248	88CER					
Quartz + Borosilicate Glass + Cordierite (NEC, Proprietary Compositions):  A. With Porosity: 1) 15W % SiO <sub>2</sub> Glass, 20W % Cordierite Glass, 65W % Borosilicate Glass 2) 35W % SiO <sub>2</sub> Glass, 65W % Borosilicate Glass, 0W % Cordierite Glass  B. Without Porosity	A: 1) 2.9-4.20 2) 3.2-4.1  B. 4.4	A: 1) 0.002 2) 0.002  B. 0.002	A: 1) 10 <sup>10</sup> -10 <sup>14</sup> 2) 10 <sup>10</sup>	A: 1) 65-150 KV/cm		A: 1) 3.2 2) 1.5 B. 3.2	A: 1) 950 2) 950		A: 1) 58.8- 127.5 2) 68.6- 110.8 B. 157.0	89YAM2, 90KAT, 91TUM, 91SHI2					
	Silica, Air (Porosity Range of ~5 V % to ~85 V %)	1.54-4.3	0.008-0.056								87MOH, 87YAR, 88GER3, 89CAO, 89DAS				
Silica (Sol-Gel, Partial-to-full Density)	1.6-7.05	0.0015-0.05	$\geq 10^{15}$	376 V/ $\mu$ m (Film)			500-1200 (Film)	2.20		86CHA, 86CRO, 86DAS, 87MOH, 88MOH, 89CAO, 91SHO					

Table 1.4 Continued

Table 1.4 Continued										
Electronic Properties					Thermal Properties			Physical Properties		
Material	$\epsilon/\epsilon_0$ @1MHz	$\tan \delta$ @1MHz	Volume Res. ( $\Omega$ -cm)	Breakdown Voltage (V/ $\mu$ m)	Thermal Con. (W/m $^2$ °C)	CTE (ppm/°C)	Process Temp. (°C)	$\rho$ (g/cc)	Flexural Strength (MPa)	Ref(s).
Taiyo Yuden Proprietary Composition (Contains Al <sub>2</sub> O <sub>3</sub> , CaO, SiO <sub>2</sub> , MgO, and B <sub>2</sub> O <sub>3</sub> )	6.7	0.001				4.8	900-1000			89SAW
Tektronix Proprietary Glass Ceramic	5.8	0.0016	$\geq 10^{14}$	17780	2.10	4.8	850-900	2.60	214	91DIL
Toshiba Proprietary Composition (Contains BaO, SnO <sub>2</sub> , TiO <sub>2</sub> , B <sub>2</sub> O <sub>3</sub> )	7-13	0.0005-0.0008					850-1050			89SAW
Wollastonite (Derived from 80W% Cement, 20W% SiO <sub>2</sub> , Cement Composition, 48.4W% CaO, 5.8W% MgO, 12.4W% Al <sub>2</sub> O <sub>3</sub> , 30.6W% SiO <sub>2</sub> )	~5					9.4	800-900	1.85-2.70		89PER1, 89PER2,9ITUM
ZnO/Cordierite (Proprietary Composition, NGK)	5.2-5.5	0.001				1.5-3.0	900-1000			89SAW
Ceramic Coated Metal Composites										
CERCIC (Ceramic Coated, Copper Clad Invar™, Texas Instruments)	7-9	0.0003-0.003	10 <sup>19</sup>	500 V/mil			850 (Electro- phoretic Deposition)			87SHU



Table 1.4 Continued

Table 1.4 Continued										
	Electronic Properties				Thermal Properties			Physical Properties		
Material	$\epsilon'/\epsilon''$ @1MHz	$\tan \delta$ @1MHz	Volume Res. ( $\Omega$ -cm)	Breakdown Voltage (V/ $\mu$ m)	Thermal Con. (W/m $^2$ °C)	CTE (ppm/°C)	Process Temp. (°C)	$\rho$ (g/cc)	Flexural Strength (MPa)	Ref(s).
MCS (Metal Core Ceramic Coated Substrate, Sun Wave Industrial)	7.5-8.5	0.005-0.01	$10^{17}$	4000V @190 $\mu$ m	10-120	12.0-14.0	900 (Electro- phoretic Deposition)			86SAT,87OKA
PCS (Porcelain Coated Steel, RCA)	7.5-8.5	0.005-0.01	$10^{17}$	4000V @190 $\mu$ m	1.4 (Porcelain) 70 (Steel)	10.0-14.0	800-900 (Electro- phoretic Deposition)			81HAN
SCCMS (Selective Ceramic Coated Metal Substrate, Allied Signal)	6.5	0.006	$6.3 \times 10^{15}$	400-600 V/mil		6-13	1000-1250 (Thick Film)			86TEA
Polymeric Materials										
BCB (Bisbenzocyclobutene, Polycon)	2.7									90REC
Epoxy	3.4-3.6	0.024-0.032	$10^{14}$ - $10^{15}$							91ZUS
FLARE™ (Fluorinated poly(arylethers))	2.62-2.66					65				91HOR
General Polyimide (* Low CTE Polyimide, Hughes Aircraft)	2.9-4.42	0.002	$> 10^{16}$	$> 5000$ V/mil	0.17-0.47	28-50 3.0*	Tg $> 400$			89BAC,89HIM, 90GAG
Kapton™ (Polyimide)	3-4	0.01	$10^{18}$	177800						91ZUS
Lexan™					0.19	67.5		1.30		90LEE
Mylar					0.14	16.9		1.38		90LEE

Table 1.4 Continued

Table 1.4 Continued									
Material	Electronic Properties				Thermal Properties			Physical Properties	
	$\epsilon/\epsilon_0$ @1MHz	$\tan \delta$ @1MHz	Volume Res. ( $\Omega\text{-cm}$ )	Breakdown Voltage (V/ $\mu\text{m}$ )	Thermal Con. (W/m $^{\circ}\text{C}$ )	CTE (ppm/ $^{\circ}\text{C}$ )	Process Temp. ( $^{\circ}\text{C}$ )	$\rho$ (g/cc)	Ref(s).
Nylon					0.23	90.0		1.13	90LEE
Polyethylene	2.2	0.0003	$10^{16}$	12700					91ZUS
PQ-100 (Polyquinoline)	2.57-3.0								91HEN
Silicone	2.9-3.7	0.003-0.005	$10^{15}\text{-}10^{19}$	7620-17780					91ZUS
Teflon <sup>TM</sup> AF2400 (Poly(tetrafluoroethyl- ene-co-per- fluorodimethyl- dioxole))	1.9	0.00008				80-100			91ZUS
Teflon <sup>TM</sup> ETFE (Poly(ethylene-co- tetrafluoroethylene))	2.6	0.0005				113		1.7	91ZUS
Teflon <sup>TM</sup> FEP (Poly(tetrafluoroethyl- ene-co- hexafluoroisopropylene))	2.1	0.0004				182		2.15	91ZUS
Teflon <sup>TM</sup> PFA (Poly(tetrafluoroethyl- ene-co- perfluoropropylene vinyl ether))	2.05	0.0002				184		2.15	91ZUS
Teflon <sup>TM</sup> PTFE (Polytetra- fluoroethylene)	2.05-2.1	0.00009- 0.0004	$10^{15}$	10922	0.2-0.21	90-156		2.13-2.2	87CHO, 88GER3, 88WAN, 90LEE, 91ART, 91ZUS

Table 1.4 Continued

Table 1.4 Continued										
Electronic Properties					Thermal Properties			Physical Properties		
Material	$\epsilon'/\epsilon_0$ @1MHz	$\tan \delta$ @1MHz	Volume Res. ( $\Omega\text{-cm}$ )	Breakdown Voltage (V/ $\mu\text{m}$ )	Thermal Con. (W/m $^2$ °C)	CTE (ppm/°C)	Process Temp. (°C)	$\rho$ (g/cc)	Flexural Strength (MPa)	Ref(s).
Triazine (Photodefinable Polymer, ATT)	3.6		$> 3.7 \times 10^{12}$	36	0.2		T <sub>g</sub> = 150 (Thermal Stability to 180)			88JAF
Polymeric Matrix Composites										
Epoxy/Glass	4.0-5.8	0.02-0.045	$> 10^{11}$	10160	0.2-0.26	9.9-72		1.8-1.96	441	87TWA2,88IBR, 88WAN,90LEE, 91ZUS
Epoxy/Kevlar						6-7				88IBR
Epoxy/Nextel						7.4				88IBR
Polyimide/Glass	4.2-4.8	0.01	$10^{14}$	17780		11-14				88IBR,91ZUS
Polyimide/Kevlar						3-7				88IBR
Miscellaneous Materials										
Air	1.0	0			0.024-0.025	2000		~0		85WEA,87MOH, 88GER3,89MAT, 90GAG
Helium (He)					0.149					90GAG
Water (H <sub>2</sub> O)	~78						BP = 100	1.0		90REC
Aluminum (Al)					138-250	22.0-23.4		2.71		90LEE,90REC, 91WILL
Beryllium (Be)					163	12.2		1.82		90LEE
Beryllium/Copper (Be/Cu)					106	39.6		8.21		90LEE

Table 1.4 Continued

Material	Electronic Properties				Thermal Properties			Physical Properties		Ref(s).
	$\epsilon/\epsilon_0$ @1MHz	$\tan \delta$ @1MHz	Volume Res. ( $\Omega$ -cm)	Breakdown Voltage (V/ $\mu$ m)	Thermal Con. (W/m <sup>2</sup> C)	CTE (ppm/ <sup>o</sup> C)	Process Temp. (°C)	$\rho$ (g/cc)	Flexural Strength (MPa)	
Cadmium (Cd)					91	13.1		8.62		90LEE
Carbon Steel (1010)					58	11.5		8.02		90LEE
Copper (Cu)			1.72x10 <sup>-6</sup>		368-398	16.7-17.6	< 100, MP = 1084 (Reducing Atmosphere Required)	8.90-8.92		84SCH2,84SCH3, ,85WEA,87CHO, 90GAG,90LEE, 90REC,91KUM2, 91WIL1
Chromium (Cr)			20x10 <sup>-6</sup>		66.9	6.3	MP = 1900			84SCH2,84SCH3
Gold (Au)			2.2-2.35x10 <sup>-6</sup>		297-306	14.0-14.2	< 1000, MP = 1064	18.88- 19.29		84SCH2,84SCH3, ,85WEA,90BUR, 90LEE,91KUM2
Gold/Tin (Au 80%/Sn 20%)					57	15.9				90LEE
Gold/Silicon (Au 97%/Si 3%)					27	12.3				90LEE
Kovar™					16.3-21	13.9-49		8.16-8.84		90LEE,91WIL1
Lead (Pb)			22x10 <sup>-6</sup>				MP = 327	11.34		85WEA,90BUR
Lead/Silicon (Pb 95%/Si 5%)					63	29.0				90LEE
Magnesium (Mg)					86	26.5		1.80		90LEE

Table 1.4 Continued

Electronic Properties					Thermal Properties			Physical Properties		
Material	$\epsilon/\epsilon_0$ @1MHz	$\tan \delta$ @1MHz	Volume Res. ( $\Omega\text{-cm}$ )	Breakdown Voltage (V/ $\mu\text{m}$ )	Thermal Con. (W/m $^2$ °C)	CTE (ppm/°C)	Process Temp. (°C)	$\rho$ (g/cc)	Flexural Strength (MPa)	Ref(s).
Molybdenum (Mo)			$5.2 \times 10^{-6}$		146	5.0-6.0	>1500, MP=2610- 2625 (Reducing Atmosphere Required)	12.2		84SCH2,84SCH3 ,85WEA,90BUR, 91KUM2
Nickle (Ni)			$6.8-7.8 \times 10^{-6}$ (Magnetic, has large skin effect)		75-92	13.1-13.3	MP=1452- 1455	8.84-8.90		84SCH2,84SCH3 ,85WEA,90BUR
Palladium (Pd)			$10.8 \times 10^{-6}$		71.1	11.0	MP=1550- 1554	12.02		84SCH2,84SCH3 ,85WEA,90BUR
Platinum (Pt)			$10.6 \times 10^{-6}$		71.1	9.0	MP=1772- 1774	21.45		84SCH2,84SCH3 ,85WEA,90BUR
Silver (Ag)			$1.59 \times 10^{-6}$		418-420	19.0-19.7	<1000, MP=962	10.5		84SCH2,84SCH3 ,85WEA,90BUR, 90LEE,91KUM2
Silver/Palladium (Ag/Pd)			$> 20 \times 10^{-6}$			>19.0	<1000			85WEA,91KUM2
Stainless Steel					16	16.0		8.02		90LEE
Tungsten (W)			$5.5 \times 10^{-6}$		200.8	4.5	>1500, MP=3410- 3415 (Reducing Atmosphere Required)	19.35		84SCH2,84SCH3 ,85WEA,90BUR, 91KUM2

## CHAPTER TWO THEORETICAL AND TECHNICAL REVIEW

### 2.1 Overview

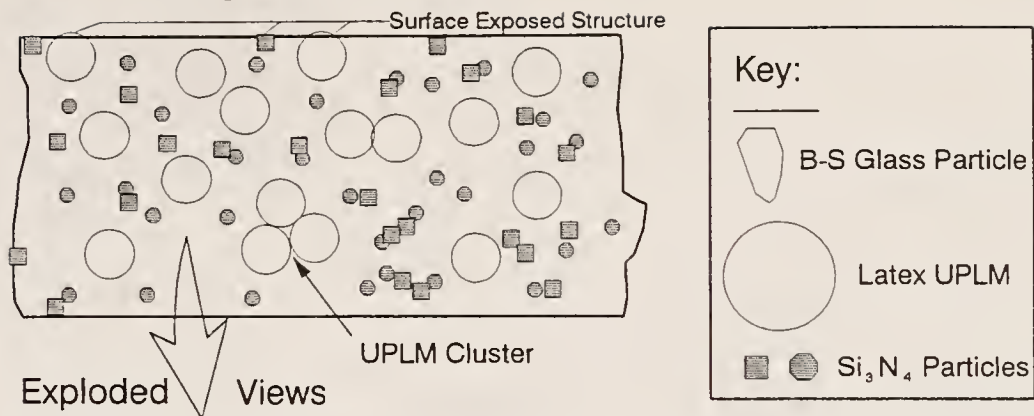
This chapter outlines selected theoretical and technical issues important to this project. The microstructure desired in the porous, glass+ceramic composite system is illustrated in Figure 2.1. Figure 2.2 outlines the process by which said composites are produced. Figure 2.2 also delineates the important factors involved in each processing step. The topics that are discussed in this chapter are depicted in bold faced italic print. The other topics mentioned in Figure 2.2 are not discussed since it is assumed that the reader has sufficient knowledge in said areas. Further information may be obtained from the references accompanying said topics if needed.

### 2.2 Synthesis and Processing of Uniform Polystyrene Latex Microspheres (UPLMs)

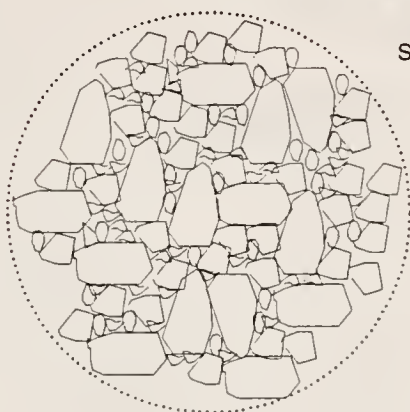
Spherical particles are currently utilized in several applications such as printer inks, and time-released drugs, etc. Hollow spherical particles, as well as organic spherical powders, are also used as composite components in applications requiring low density, rigid materials. There are several review articles in the literature on the subjects of solid spherical fillers [78RYA1] and hollow spherical fillers [78RYA2,86SMI] as well as composites containing them [85VER]. Due to the reasons outlined in Chapter 1, only uniform polymeric microspheres were deemed suitable for this project. Furthermore, other research [89YAM2,90KAT] has revealed that the best uniform polymeric microspheres for this application are those made of polystyrene.



# Microstructure

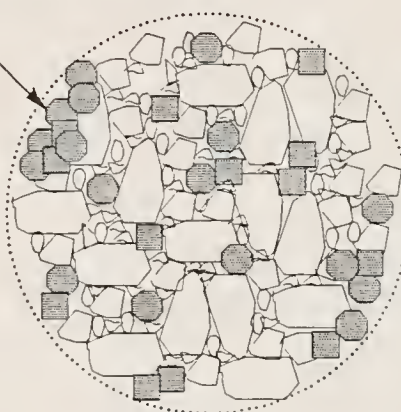


## Green Microstructure (dispersant omitted)

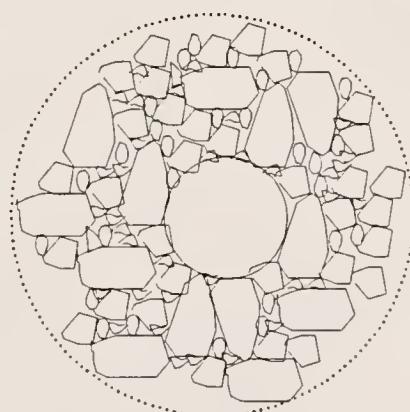


A. Pure B-S Glass

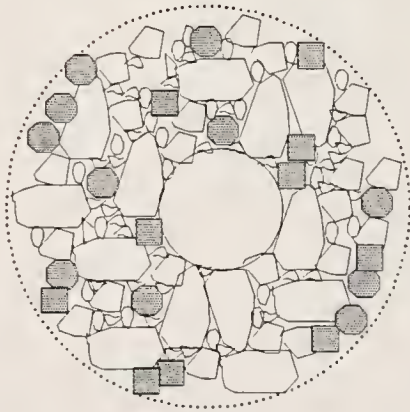
$\text{Si}_3\text{N}_4$  Cluster



C. B-S Glass/ $\text{Si}_3\text{N}_4$



B. B-S Glass/Latex UPLM



D. B-S Glass/ $\text{Si}_3\text{N}_4$ /Latex UPLM

Figure 2.1

Depiction of the glass+ceramic, controlled porosity microstructure desired

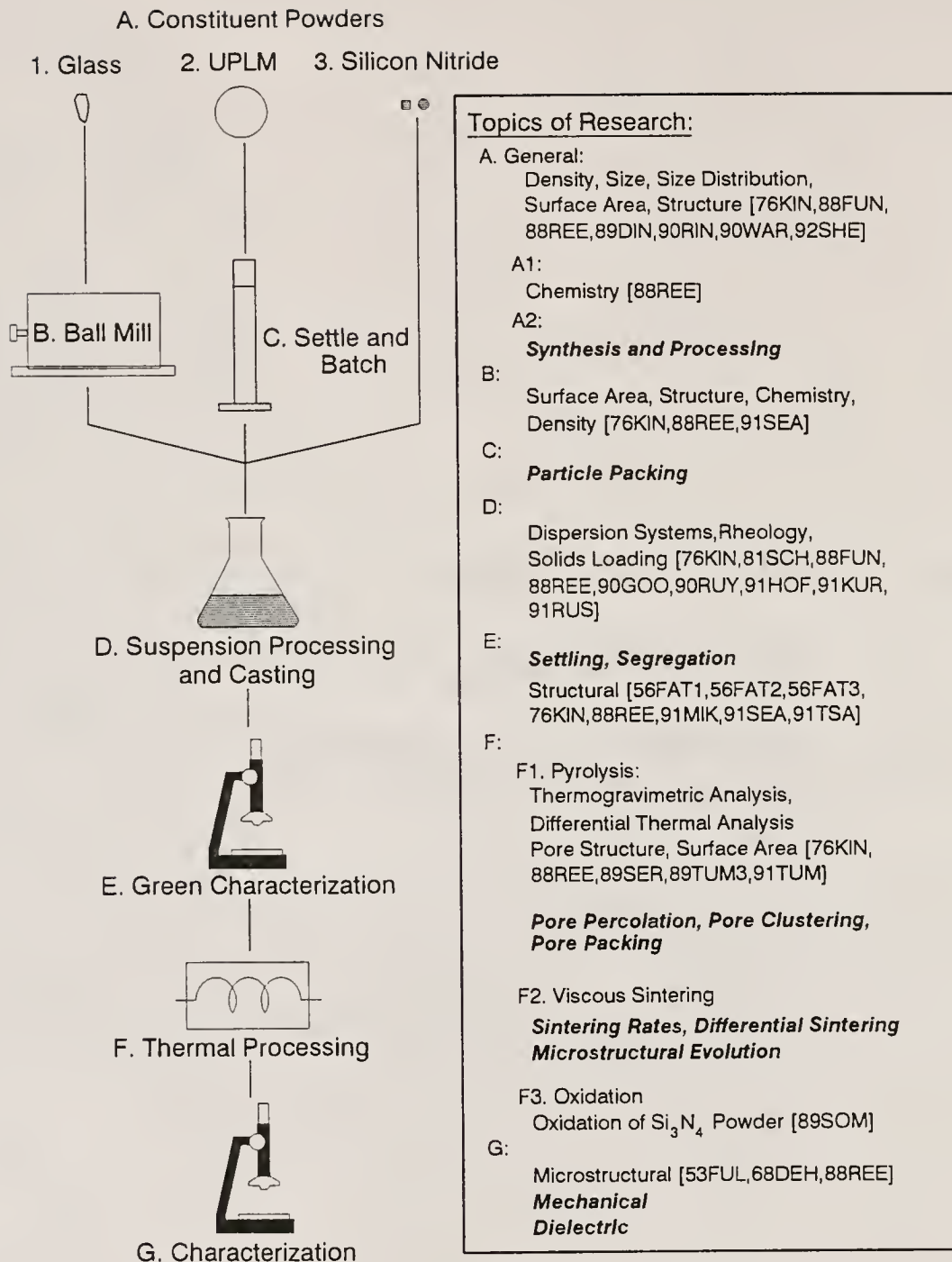


Figure 2.2

Process flow diagram for production of controlled porosity composites, and delineation of important factors for each processing step; topics depicted in boldface italic are discussed in this chapter

There are several methods for synthesizing uniform particles. The literature contains several review articles on the subject [68STO,80UGE,82OVE]. More specifically, there are several methods by which uniform polystyrene latex microspheres (UPLMs) may be produced [85LOK,86TSE,88LU,89FER]. More information about the properties and applications of uniform latex particles is contained within references 87BAN2 and 88MIC as well.

As will be shown in Chapter 4, preliminary research for this project [90RAN] indicated that the UPLM particles should be approximately 4  $\mu\text{m}$  (minimally 2  $\mu\text{m}$ ) in diameter in order to avoid producing obscured porosity. Furthermore, it was decided that the maximum UPLM diameter, used for included porosity, should be less than 10  $\mu\text{m}$  in order to maintain surface smoothness requirements. Therefore, it was necessary to either find or invent a reliable and reproducible method for the synthesis of UPLMs in the size range between 2 and 10  $\mu\text{m}$ . Fortunately, researchers have found synthesis methods which satisfy the above criteria [85LOK,86TSE,88LU]. Said synthesis techniques involve the dispersion polymerization of styrene in EtOH-based solvents. Dispersion polymerization is the only currently known method which may be used to produce UPLMs in the size range of interest via a single set of processing steps [85LOK]. Table 2.1 depicts the differences between dispersion, emulsion and suspension polymerization methods.

The synthesis methods of Lu et al. and Tseng et al. [86TSE,88LU] involve dispersion polymerization via an addition polymerization mechanism in various mixtures of pure EtOH and stabilizer and/or costabilizer while the method of Lok and Ober [85LOK] involves dispersion polymerization of UPLMs via an addition polymerization mechanism in solvent solutions of ethanol and methyl cellosolve mixed with hydroxypropylcellulose (100,000 mw) as a dispersant.

Preliminary research, investigating both of the aforementioned dispersion polymerization methods for synthesis of UPLMS, resulted in

Table 2.1

Comparison of the Different Types  
of Particle Polymerization [85LOK]

	Emulsion	Dispersion	Suspension
Monomer	Droplets Micelles/Particles Little in Medium	Particles Mostly in Medium	Droplets Little in Medium
Initiator	Mostly in Medium	Particles and Medium	Particle/Droplet
Stabilizer	May Be Present	Necessary	Necessary
Surfactant	Present	None	None
Initial Homogeneity	Multiple Phase	Single Phase	Dual Phase

the conclusion that the method of Lok and Ober [85LOK] was far superior for production of UPLMs in the desired size range on the bases of monodispersity, amount of agglomeration and reproducibility of UPLM size and dispersity from batch to batch. Therefore, the method of Lok and Ober was utilized to produce UPLMs of various size for the current study. The synthesis method of Lok and Ober is described in further detail in Chapter 3 as well as in 85LOK.

Figure 2.3 illustrates the dispersion polymerization process. Basically, dispersion polymerization is an addition polymerization which includes nucleation and growth steps. The dispersity of the process depends upon the monomer and initiator concentrations as well as on the dispersive abilities of the dispersant, which is necessarily a graft copolymer. Dispersion polymerization involves the nucleation and growth of polymeric spheres from a single phase solvent via addition reaction. As with other nucleation and growth processes, the size of each polymer nucleus must surpass a critical radius before said nucleus becomes stable. The critical nucleus size depends heavily upon the total system solubility index (including that of the monomer itself) [85LOK]. Furthermore, growth processes apparently occur without further nucleation [85LOK].

The major difference between dispersion polymerization and other polymerization methods is that dispersion polymerization starts as single phase homogeneous system. With dispersion polymerization it is necessary that the monomer be soluble in the solvent while the polymer not be soluble in the solvent. Particle size control with the dispersion polymerization method is dependent mainly upon four factors, monomer versus polymer solubility, reactant composition, temperature, and solvent medium [85LOK].

Said process offers the advantage that it does not require oligomer swelling, etc., in order to obtain the relatively large particles and, therefore, is denoted a single step process.

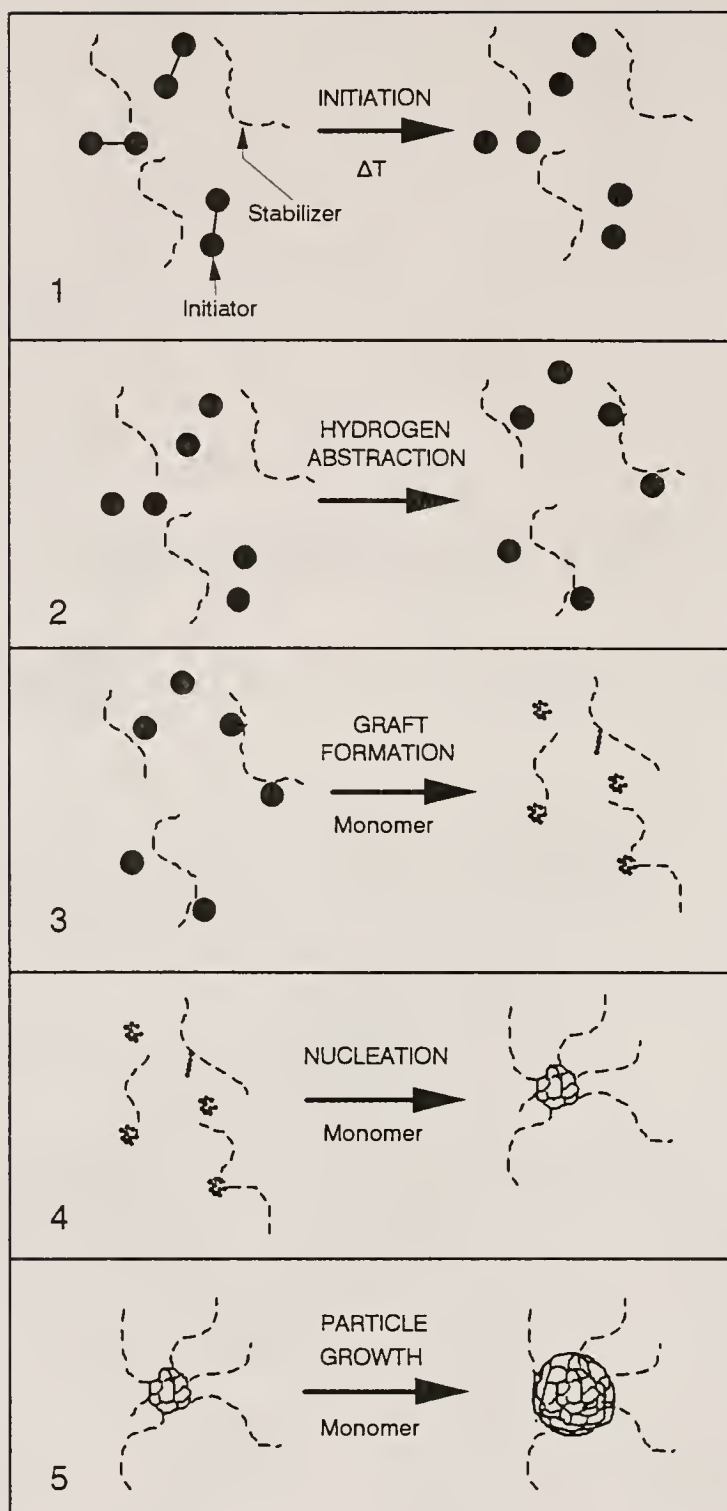


Figure 2.3

Schematic illustration depicting nucleation and growth of a UPLM via dispersion polymerization [85LOK]



The method of Lok and Ober offers a further advantage in that the dispersion mechanism used is steric in nature (ie. non-electrostatic) and, thereby reduces ionic impurities in the resultant UPLMs. Ionic impurities are deleterious because they could leave ionic residues subsequent to pyrolysis. These residual ions would increase K as well as decrease both  $\rho$  and the dielectric breakdown strength.

Lok and Ober were able to produce exceptionally monodisperse polystyrene latex particles of sizes ranging from 3 to 9  $\mu\text{m}$  by varying the solution solubility parameter ( $\delta$ ) from 11.5 to 11.9 [85LOK]. The solubility parameter is resultant from an accumulation of dispersion forces ( $\delta_d$ ), polar forces ( $\delta_p$ ), and hydrogen bonding forces ( $\delta_H$ ) according to the relation:

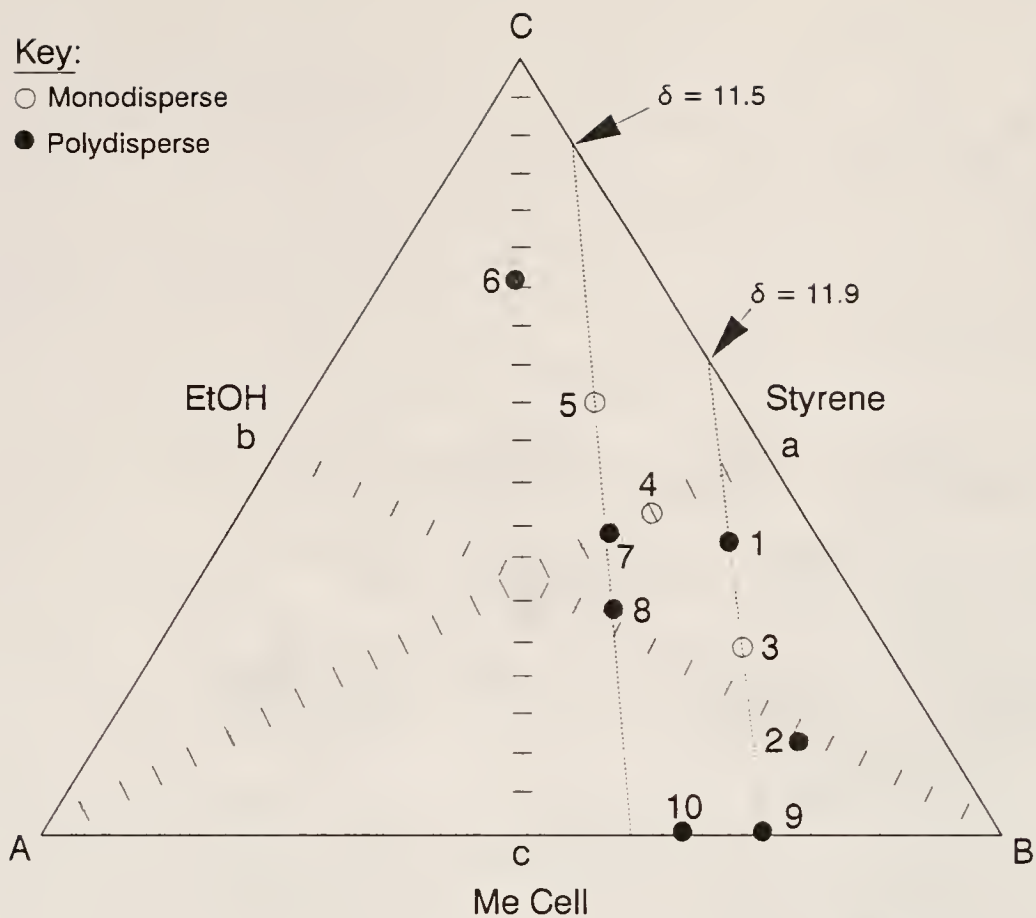
$$\delta^2 = \delta_d^2 + \delta_p^2 + \delta_H^2$$

Table 2.2 lists the solubility parameter as well as other pertinent data of selected dispersant liquids that Lok and Ober used for dispersion polymerization. Figure 2.4 depicts a ternary composition diagram, between EtOH, styrene and McCell (methyl cellosolve), which outlines the compositions at which their latexes were monodisperse as well as the sizes of the respective UPLMs.

It is evident, from the above and from Figure 2.4, that the dispersion polymerization method of Lok and Ober [85LOK] fulfills the criteria necessary for the UPLMs used in this project. Furthermore, through judicious mixing of the UPLMs (as described in the next section), a polydisperse latex could be produced for maximum packing efficiency (PE), thereby allowing an investigation of the effect of included pore size distribution, or possibly pore packing, upon included porosity.

Table 2.2  
Solubility Parameters of Selected Solvents [85LOK]

Solvent	Dielectric Constant (K)	Dipole Moment (D)	$\delta$ (cal/cm <sup>3</sup> ) <sup>1/2</sup>	$\delta_d$	$\delta_p$	$\delta_H$
Dimethoxy- ethane			8.6			
Tetrahy- drofuran	7.32	1.63	9.1	8.2	2.8	3.9
Styrene			9.3	9.1	0.5	2.0
Cellosolve		2.08	10.5	7.8	4.5	7.0
t-Butanol	10.9	1.66	10.6			
Me Cell	16	2.2	11.4	7.9	4.5	8.0
Isopro- panol	18.3	1.66	11.5			
Ethanol	24.3	1.69	12.7	7.7	4.3	9.5
Methanol	32.6	1.70	14.5	7.4	6.0	10.9
Water	78.5	1.84	23.4	6.0	15.3	16.7
Poly- styrene	2.5		8.9			



Sample	Concentrations (V%)			Particle Size ( $\mu\text{m}$ )	Solubility Parameter $\delta_1$ ( $\text{cal}/\text{cm}^3$ ) <sup>1/2</sup>
	Styrene	EtOH	Me Cell		
1	10	51	39	1-3	11.9
2	15	71	14	1-4	12.1
3	15	60	25	3	11.9
4	15	42.5	42.5	7	11.7
5	15	30	55	9	11.5
6	15	14	71	1-50	11.3
7	20	40	40	5-20	11.6
8	26	44	30	5-20	11.5
9	26	74	0	1-5	11.9
10	33	67	0	7-9	11.7

Figure 2.4

Ternary illustration depicting the relative dispersity of UPLMs synthesized via dispersion polymerization in the EtOH-MeCell-styrene system [85LOK]

## 2.3 Particle Packing

### 2.3.1 Monosized Spheres

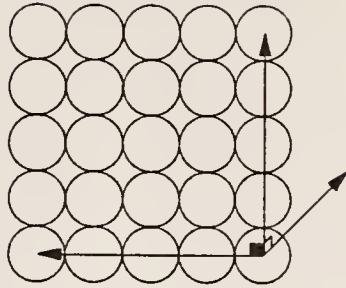
#### 2.3.1.1 Ordered Packing

Ordered packing of hard, uniform spheres may occur in five different configurations: cubic, orthorhombic, tetragonal, pyramidal, and tetrahedral [88REE]. Figure 2.5 illustrates the various configurations and properties of said ordered packing configurations. Table 2.3 depicts some of the characteristics of two types of ordered packing structures: cubic and tetrahedral.

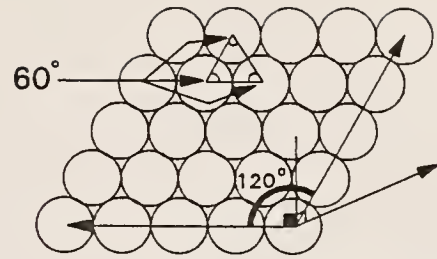
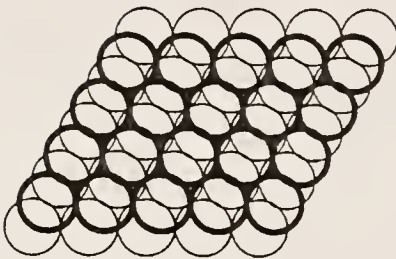
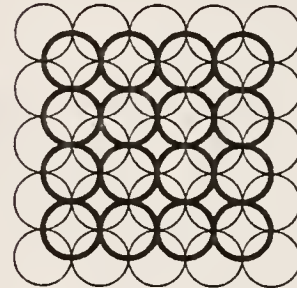
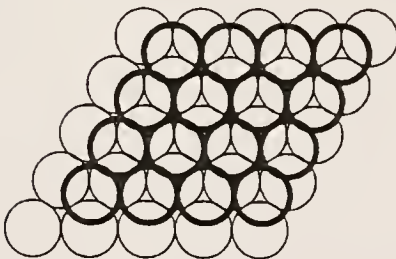
However, hard spheres do not naturally pack in the long range, ordered structures characteristic of crystalline materials. Several researchers have tried to explain the random packing of monosized spheres in terms of mixtures of the above ordered structures [29SMI,61MCG,80PAT], but while three-dimensional, packed beds of monosized spheres may exhibit short range order, or even order throughout a dimension, (depending upon the packing method, or the packing container configuration used, etc.) they are essentially considered to pack in random order over the long range [60BER,62EPS,65LEV].

#### 2.3.1.2 Random Packing

There are two types of random packing for non-interacting, hard spheres, random close packing (RCP) and random loose packing (RLP). Random packing (RP) is defined as packing that has no characteristic ordering. These two types of random packing are considered to be the upper and lower limits to the packing efficiency of randomly packed monosized spheres, and are quite sensitive to both the size and configuration of the bed container as well as the methods used to place the spheres, in said container, in their final state. The generally accepted packing efficiencies for these two types of packing are 64V% and 60V% for RCP and RLP respectively [60SCO,61MCG].



1. Cubic

2. Orthorhombic  
(Single Staggered)3. Tetragonal  
(Double Staggered)4. Pyramidal  
(Cubic Close Packing)5. Tetrahedral  
(Hexagonal Close Packing)

#	Packing Configuration	CN	Packing Density (V%)
1	Cubic	6	52.4
2	Orthorhombic (Single Staggered)	8	60.5
3	Tetragonal (Double Staggered)	10	69.8
4	Pyramidal (Cubic Close Packing)	12	74.0
5	Tetrahedral (Hex- agonal Close Packing)	12	74.0

Figure 2.5

Illustration of the five possible types of ordered packing of monosized hard spheres [80PAT,88REE]

Table 2.3

Some Parameters of Simple Cubic and Tetrahedral Packings of Uniform Spheres [88REE]

Parameter	Cubic	Tetrahedral
Entry Pore Area	$0.21D^2$	$0.04D^2$
$\frac{\text{Entry-Pore-Area}}{\frac{\pi D^2}{4}}$	0.26	0.05
$\frac{\text{Entry-Pore-Diameter}}{D}$	0.51	0.22
$\frac{\text{Entry-Sphere-Diameter}}{D}$	0.42	0.15
Void Fraction	0.48	0.26
$\frac{\text{Volume-Voids}}{\text{Volume-Spheres}}$	0.92	0.34
$\frac{D_{\text{Primary-Sphere}}}{D_{\text{Interstitial-Sphere-Site}}}$	1.37	4.44
D = Sphere Diameter		



The upper limit of random packing (RCP) is never reached in reality, due to packing friction and interaction with the container. The effect of the container interaction may be significantly reduced by using a container having a width dimension that is relatively large compared to the sphere diameter (usually several hundred times larger) as well as through utilization of containers having walls which are either modified with indentations, or that have the ability to conform (i.e. balloons, etc.) [30WES,60SCO,61MCG,69SCO]. Figure 2.6 illustrates the effect of the relative container size on the packing density of RCP beds of monosized spheres. The lower limit to random packing of uniform spheres (RLP) designates the limit below which packed beds cannot support themselves without either cohesion or adhesion [60SCO,80SHA].

In practice, all randomly packed uniform spherical particles will exhibit packing efficiencies (PEs) somewhere between the RCP and RLP limitations. Most research indicates RP packing efficiencies of approximately 61 to 63 V% for beds formed by tamping [30WES,60SCO,61MCG,88REE] and approximately 57 to 59 V% for beds formed by careful pouring [60SCO,62EPS]. This will occur, in packed beds of monosized spheres, regardless of sphere size, unless surface area to volume ratio sensitive factors, such as electrostatic repulsion, etc. become significant (i.e. as in many micron to sub micron particles). In most instances involving packed beds of uniform spheres, the packing is RCP and the generally accepted packing efficiency is 62.5 V% [61MCG,88REE].

### 2.3.2 Packing of Multimodal, Discrete Distributions of Spheres

Furnas is generally believed to have introduced the first packing model (the Furnas model) which predicts the random close packing of multimodal beds of spheres [28FUR,31FUR]. Westman and Hugill also introduced an analogous packing model at about the same time [30WES], and it is believed that the actual mathematical treatment of Westman and Hugill actually preceeded that of Furnas by about one year [79FED].

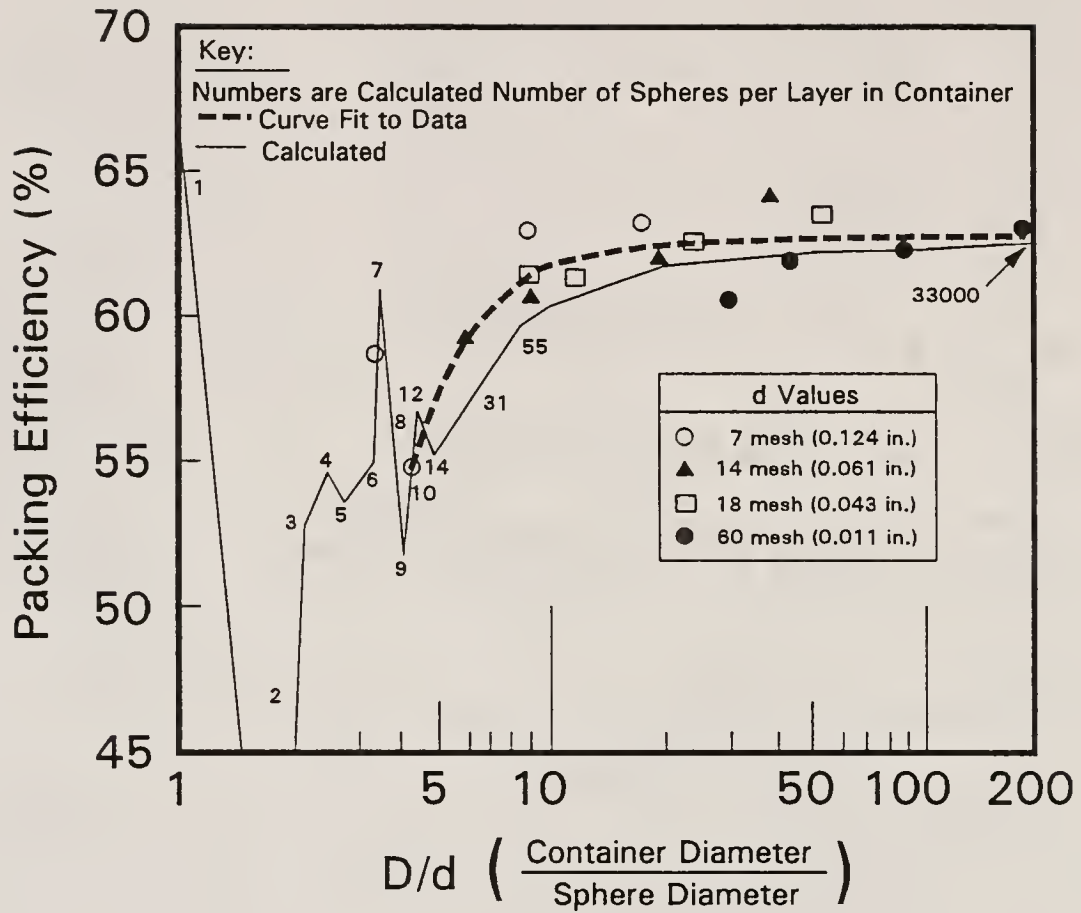


Figure 2.6

Effect of relative container size upon the packing efficiency of random close packed uniform spheres [61MCG]

Both treatments are similar, however. Therefore, they both shall be denoted as the Furnas model, henceforth, in order to follow the more generally accepted convention. The Furnas model involves packing of smaller spheres within interstices produced by larger spheres. A third, smaller size of spheres may also be packed within the interstices between either medium size spheres and large spheres, or between medium size spheres. The common denominator for this type of packing is that the next smallest size of spheres packs "tightly" within the interstices created by larger size spheres. This type of packing shall be denoted type 1 packing. Another type of packing (type 2 packing) occurs when the interstices, created by the large particles, are much larger than the next smallest size of spheres. Figure 2.7 illustrates these two multimode packing relationships. The number of size modes applicable is unlimited as long as the size ratio of each successively smaller size sphere addition is significantly smaller than the next nearest larger size.

The size ratio of the smaller sphere, to the interstice is important in two senses. First, the smaller sphere must be able to fit through the interstice opening, if the smaller sphere is not already there before the interstitial structure formed. Interstitial placement prior to stable bed formation is possible in the case of casting processes, but not when using the methods (i.e. adding smaller particles and vibrating after the large sphere packed bed is formed) used by most researchers in this field [30WES,60BER,60SCO,61MCG,65AYE,66AYE,69SCO,80PAN]. Secondly, packing of the smaller spheres within interstices will be affected by the relative size of the containment volume (i.e. the interstice), just as the PE of monosized spheres is affected by the relative size of the packing container. Thus, PE increases as the relative size of the interstices increase, in a packed bed of spheres. Figure 2.8 illustrates this relationship in terms of relative size. Interestingly, Figure 2.8 is similar to Figure 2.6, without the

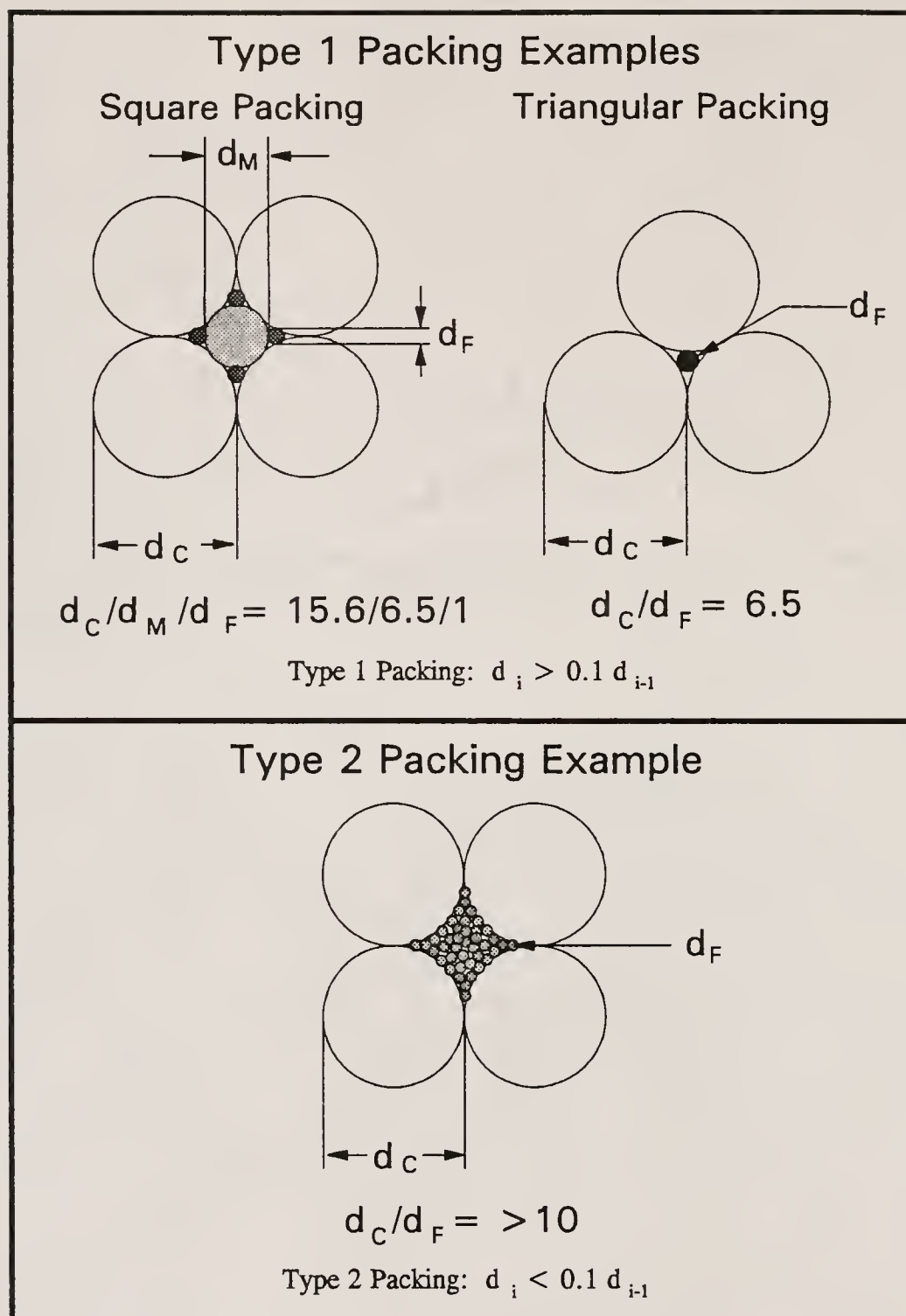


Figure 2.7

Illustration of the two types of multimode packing  
[80PAT,88REE]

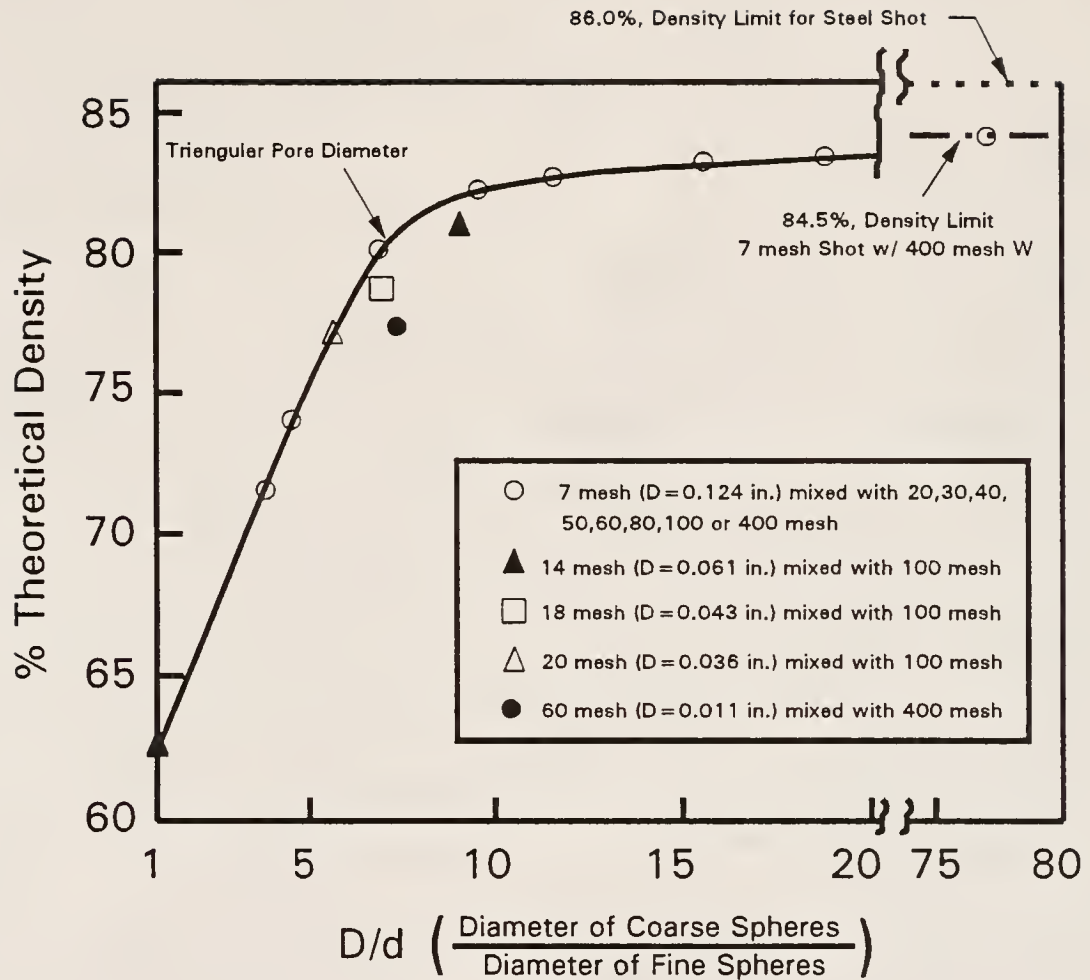


Figure 2.8

Illustration of the effect of relative sphere size upon the maximum packing efficiency of randomly packed beds of bimodal spheres [61MCG]

discontinuities, and that both asymptotically approach a maximum near a value of approximately ten.

Both Furnas [31FUR], and Fedors and Landel [79FED] have developed equations that estimate the packing efficiency of random close packed multimodal beds of spheres as a function relative sphere sizes. The Furnas analog of this relationship, which assumes that all size modes pack with the same efficiency in a monosized sense, and that the volume fractions of each mode are chosen to maximize the packing efficiency, as discussed below, is given by the equation:

$$\frac{(1-PE)^n \ln PE (1-PE)}{(1-PE^{n+1}) [1-(1-PE^n)]} = \frac{(2.62K^{\frac{1}{n}} - 3.24K^{\frac{2}{n}}) \ln K}{(1.0 - 2.62K^{\frac{1}{n}} + 1.62K^{\frac{2}{n}}) n^2}$$

where PE is the packing efficiency, n is one less than the number of size modes and K is the ratio of the smallest to the largest sphere size [79FED]. The numerical values of the above Furnas equation were determined experimentally. The Fedors and Landel relationship, describing the effect of relative sphere size upon the maximum packing efficiency of a random close packed bed of multimodal spheres, is described by the equation:

$$PE_{\max} = PE_1 + (1-a_{1,2}) (1-PE_1) PE_2 + [(1-a_{1,3}) (1-a_{2,3})]^{\frac{1}{2}} \\ \times (1-PE_1) (1-PE_2) PE_3 + \dots + [(1-a_{1,n}) (1-a_{2,n}) \dots (1-a_{n-1,n})]^{\frac{1}{n-1}} \\ \times (1-PE_1) (1-PE_2) \dots (1-PE_{n-1}) PE_n$$

where  $PE_{\max}$  is the maximized packing efficiency,  $PE_i$  is the packing

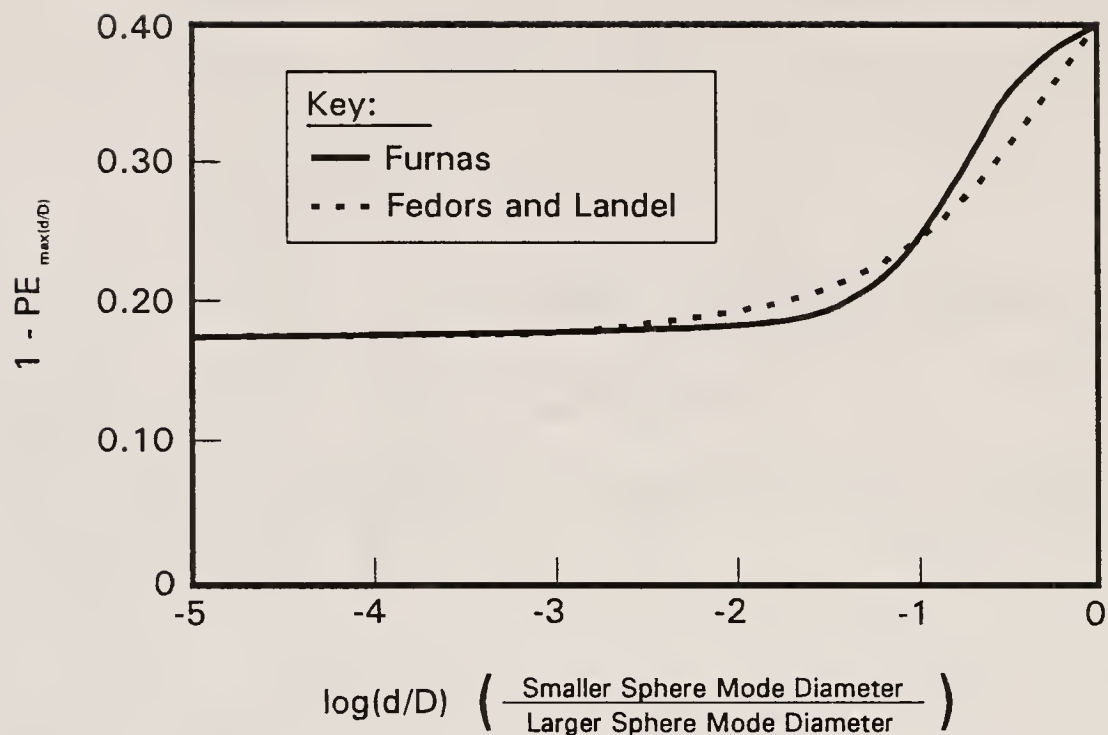


efficiency of sphere size  $i$ , and  $a_{j,i}$  is given by

$$a_{j,i} = \left( \frac{r_j}{r_i} \right)^{\frac{1}{2}}$$

where  $j$  is the respective term in the multiplication series for the respective mode of size,  $i$  is the mode number of the particular series set of interest (i.e. one series set per size mode), and  $r_i$  is the radius of sphere size mode  $i$  [79FED]. A comparison of both models is illustrated in Figure 2.9 for a bimodal distribution of spheres, where  $PE_1$  and  $PE_2$  are set at a value of 0.60. It may be seen that, for a radius ratio ( $r$ ) of less than 0.01, both models agree well, giving a maximum packing efficiency of approximately 82%. This is reinforced by the fact that the model of Fedors and Landel has the same characteristic shape as that exhibited by the relation in Figure 2.8.

The Furnas model, and its numerous variations, may also be utilized to determine the maximum packing efficiency (PE) of random close packed beds of multimodal discrete distributions of spheres, as well as to determine the relative amounts of each mode of sphere necessary to accomplish said goal. The Furnas model utilizes the normalized volumes (the inverse of the respective packing efficiencies) for RCP beds of each discrete mode of spheres. For bimodal mixture of spheres, said normalized volumes are used as the ordinate values of a binary relationship that is analogous to a binary phase diagram. A bisection is placed between the ordinate value for the pure coarser size and the zero value of the normalized volume of the pure finer size. A similar bisection is placed between the unit value of normalized volume of the coarser size of spheres and the ordinate value of normalized volume of the pure finer spheres. The intersection of these bisectors is the indicator of both the minimum normalized volume (i.e. the maximum in packing efficiency ( $PE_{max}$ )) and the relative volume fractions of each mode necessary to achieve  $PE_{max}$ .



Note:  $PE_{\max(d/D)}$  is the Maximum Packing Efficiency at the Diameter Ratio ( $d/D$ )

Figure 2.9

Illustration of both the Furnas, and the Fedors and Landel models of packing efficiency, as a function of relative sphere size, of a bimodal distribution of RCP spheres [79FED]

Figure 2.10 illustrates the Furnas relationship for a two component mixture of uniform spheres.

From Figure 2.10, the first bisector, mentioned above (i.e.  $V_c-F$ ), follows the equation:

$$V_{NM} = V_c X$$

where  $V_{NM}$  is the normalized volume of the mixture,  $V_c$  is the normalized volume of the pure RCP coarse spheres, and  $x$  is the volume fraction of coarse spheres. The second bisector ( $V_f-1$ ) follows the equation:

$$V_{NM} = V_f - V_f X + X$$

where  $V_f$  is the normalized volume of a RCP bed of pure fine spheres. The maximum packing efficiency ( $PE_{max} = V_{NM \min}$ ) is found by setting the two equations equal to each other, and solving for  $x$ , which results in the equation:

$$X_{max} = \frac{V_f}{V_c + V_f - 1}$$

where  $x_{max}$  is the volume fraction of coarse spheres resulting in the minimization of  $V_{NM}$  (or  $PE_{max}$ ).

If the packing efficiencies of both components of the binary system are 0.625 (the generally accepted value for RCP beds of uniform spheres [61MCG,88REE]), the volume fraction of the coarse spheres needed to achieve  $PE_{max}$  is 0.727, and the volume fraction of the fine component of uniform spheres needed to achieve  $PE_{max}$  is 0.272.

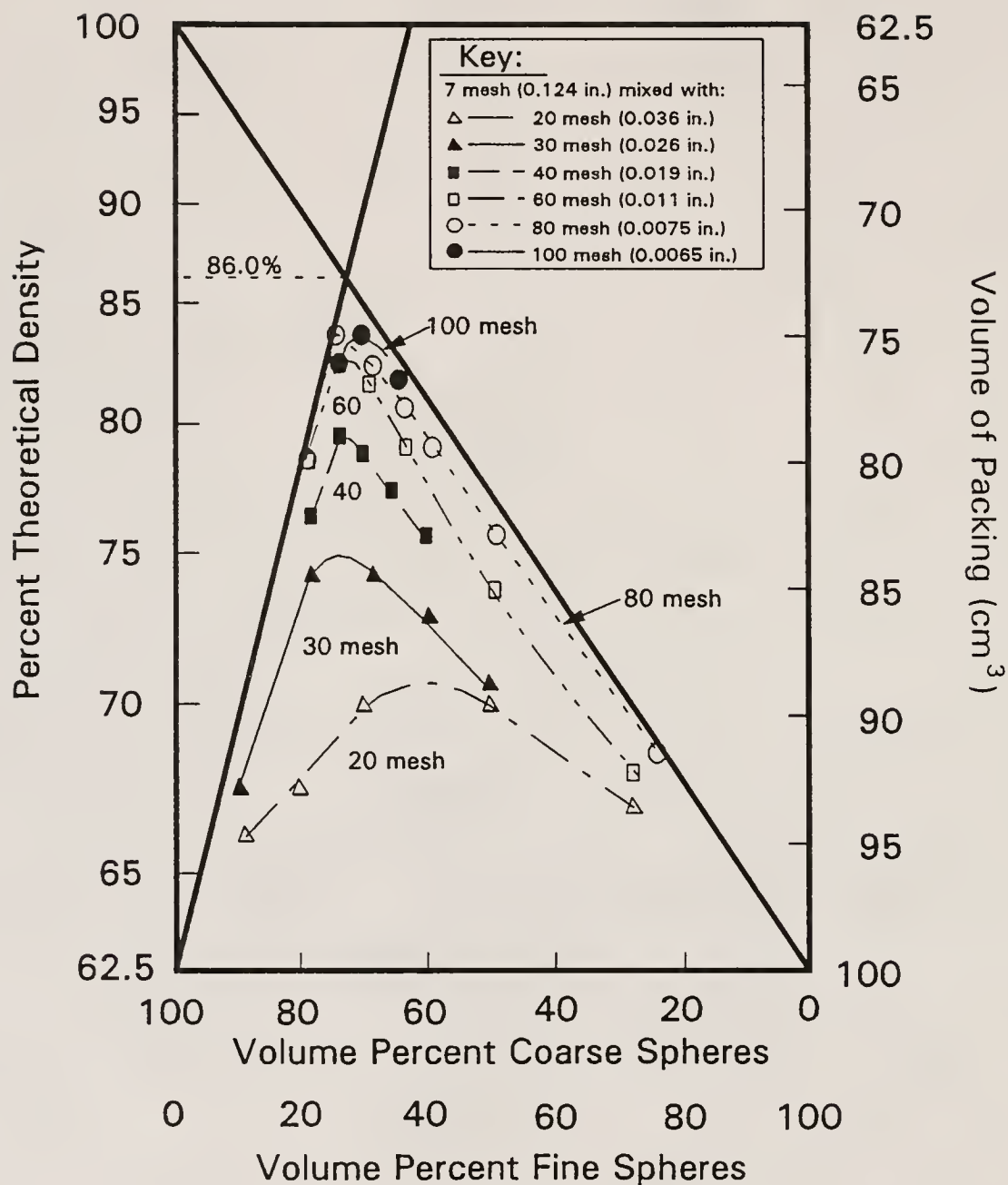


Figure 2.10

Illustration of the Furnas model for bimodal mixtures of uniform spheres [30WES]

The actual value of  $PE_{\max}$  may be found by solving the reciprocal of either of the above bisector equations for said value of  $x$  ( $x_{\max}$ ), or

$$PE_{\max} = \frac{1}{V_c x_{\max}} = \frac{1}{V_f - V_f x_{\max} + x_{\max}} .$$

For the above situation (i.e.  $PE_c$  equal to  $PE_f$  which equals 0.625, or  $V_c$  equal to  $V_f$  which equals 1.60), the value of  $PE_{\max}$  is equal to 0.859 ( $V_{\min}$  equals 1.16). Thus, the highest packing efficiency ( $PE_{\max}$ ) achievable in a mixture of bimodally sized spheres is 0.859. This would occur under conditions of perfect tamping and mixing, using an infinitely large, relatively coarse sphere size. Figure 2.10 illustrates the validity of the Furnas model, compared to the work of various researchers, when used to estimate PE in bimodal mixtures of spheres.

The Furnas model may be applied to mixtures of trimodal and higher-modal, discrete distributions of monosized sphere components as well. For a trimodal mixture of discrete sizes of spheres, the three possible binaries are combined to form a ternary diagram, analogous to a three dimensional ternary phase diagram (Figure 2.11). The ternary surface through each of the ordinates (i.e. Coarse (C) Medium (M) and Fine (F)) is a plane determined by the equation:

$$V = V_c X + V_m Y + V_f Z$$

where  $V$  is the ordinate value of the plane,  $V_i$  is the normalized volume of RCP monosized spheres of size regime  $i$  (i.e. coarse (c), medium (m) or fine (f)). There are also three planes of minimization, necessary to consider in said trimodal system, in order to determine  $PE_{\max}$ .

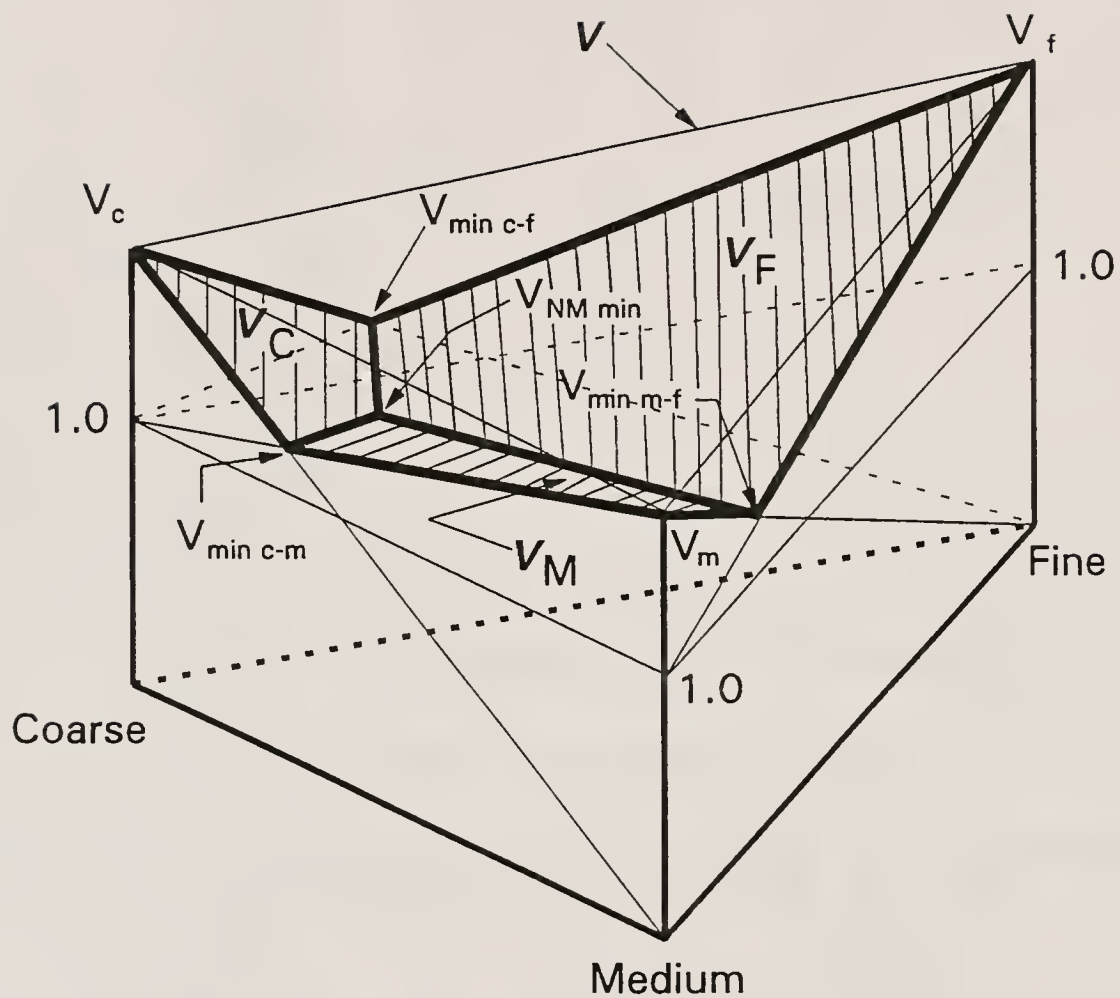


Figure 2.11

Illustration of the Furnas model for trimodal mixtures of random close packed spheres [30WES]



Said planes are denoted by the equations:

$$V_C = V_C X$$

$$V_M = X + V_m Y$$

$$V_F = X + Y + V_f Z$$

for the coarse ( $V_C$ ), medium ( $V_M$ ) and fine ( $V_F$ ) planes of normalized volume minimization, where  $x$ ,  $y$  and  $z$  are the volume fractions of the coarse, medium and fine components respectively. The three planes intercept at the point of minimum normalized volume (or  $PE_{\max}$ ). Said point ( $V_{NM\min}$ ), where  $V_C$  equals  $V_M$  equals  $V_F$ , is determined by the relation:

$$V_{NM\min} = \frac{V_C V_m V_f}{V_C V_m + V_m V_f + V_C V_f - (V_C + V_m + V_f) + 1}.$$

The compositional values leading to  $V_{NM\min}$  ( $PE_{\max}$ ) are determined by the relations:

$$X = \frac{V_{NM\min}}{V_C}$$

$$Y = \frac{V_{NM\min} - \frac{V_{NM\min}}{V_C}}{V_m}$$

$$Z = \frac{V_{NM\min} - \frac{V_{NM\min}}{V_C} - \left( \frac{V_{NM\min} - \frac{V_{NM\min}}{V_C}}{V_m} \right)}{V_f}$$

for the coarse (x), medium (y) and fine (z) volume fractions respectively. If  $V_c$  equals  $V_m$  equals  $V_f$ , the equation for  $V_{NM \min}$  reduces to the equation:

$$V_{NM-\min} = \frac{V_{RCP}^3}{3 V_{RCP} (V_{RCP} - 1) + 1}$$

where  $V_{RCP}$  is the general normalized volume of RCP uniform spheres. By utilizing the simplification used for the bimodal system above (i.e. the assumption that  $V_{RCP}$  is equal to 1.60) the value of  $V_{NM \min}$  becomes 1.06, which corresponds to a  $PE_{\max}$  value of 0.947 for a ideal packing of a trimodal, discrete distribution of uniform spheres. The respective volume fractions of each component of said trimodal mixture of spheres is then 0.660, 0.247 and 0.093 for the coarse medium and fine spheres.

This model may be extended to n-modal systems, where  $PE_{\max}$  is determined from the equation:

$$PE_{\max} = V_1 + (1 - V_1) V_2 + (1 - V_1) (1 - V_2) V_3 + (1 - V_1) (1 - V_2) \dots (1 - V_{n-1}) V_n$$

where n is the number of size modes of the mixture. The corresponding volume fractions of each component may be determined by the relations:

$$VF_1 = \frac{PE_1}{PE_{\max}}$$

$$VF_2 = \frac{(1 - PE_1) PE_2}{PE_{\max}}$$

$$VF_i = \frac{(1 - PE_1) (1 - PE_2) \dots (1 - PE_{n-1}) PE_n}{PE_{\max}}$$

where  $VF_i$  is the volume fraction of size mode  $i$ , and  $PE_i$  is the RCP packing efficiency of mode  $i$ . Table 2.4 delineates the  $PE_{max}$  values and respective compositions, as well as experimental data, for multimodal random close packings of spheres. The data of McGeary [61MCG] seems to agree well with the predictions of the Furnas model. Said data is always slightly lower than the prediction (as would be expected) and always within 6% of the calculated  $PE_{max}$  values (see Table 2.4). Thus, the Furnas model works well for multimodal RCP beds of spheres formed by the method of successive additions with tamping. Furthermore, it is also evident that the Furnas model predicts that component systems, having more than four to five components, result in very little, if any, increase in packing efficiency.

The Furnas model always over-predicts the packing efficiency of a particle system. This is especially true for particle beds which were formed by mixing of the particles prior to bed formation and for systems utilizing non-spherical (mainly angular) particles. Messing and Onoda [78MES1,78MES2] proposed a model to estimate corrections to Furnas-type models necessary to more successfully estimate PE for packed beds of bimodal particles, formed by mixing prior to bed formation [78MES1]. Messing and Onoda hypothesized that the Furnas model was legitimate in localized regions. They hypothesized that the differences between predicted and experimental values are due to compositional fluctuations (i.e. mixing imperfections) in the particle bed [78MES1,78MES2]. By splitting the Furnas bimodal composition diagram (see Figure 2.10) into two regions, one following the PE due to the establishment of a stable coarse particle structure (i.e.  $x$  values below  $V_{NM\ min}$  or Region I) and the other due to a PE determined by the establishment of a stable fine particle structure (i.e.  $x$  values above  $V_{NM\ min}$  or Region II), Messing and Onoda hypothesized that a sampling of any small and discrete volume element of a packed bed of spheres would necessarily fall into one of the above two regimes.

Table 2.4

Packing Efficiencies and Compositions of  
Random Close Packed Beds of Multimodal  
Mixtures of Spheres [61MCG,79FED,88REE]

# Modes	VF <sub>1</sub>	VF <sub>2</sub>	VF <sub>3</sub>	VF <sub>4</sub>	VF <sub>5</sub>	PE <sub>max</sub> (%)	
						Calc.	Exp.
1	1.00					60.5 to 63.0	58.0
2	0.726 to 0.730	0.270 to 0.274				84.8 to 86.0	80.0
3	0.647 to 0.670	0.244 to 0.250	0.090 to 0.109			95.0 to 95.2	89.8
4	0.607 to 0.640	0.230 to 0.240	0.090 to 0.102	0.040 to 0.061		97.5 to 98.0	95.1
5	0.640	0.230	0.080	0.030	0.010	99.0	

- Notes:
1. Experimental Data From [61MCG], Sphere Size Ratio 320/39/7/1
  2. Calculated Data was Provided by [61MCG] and [79FED]

Messing and Onoda used either experimental values for the compositional fluctuation values, or mathematically determined mixture functions to estimate PE as a function of the distribution of particle compositions.

Karlsson proposed a different model to estimate the disparities between the Furnas model and experimental data from beds made from premixed discrete distributions of particles [70KAR]. He hypothesized that the stable structure (i.e.  $x$  values below  $V_{NM\ min}$ ) dilates as a result of adding finer particles. Said dilation reduces  $PE_{max}$ . He further hypothesized this effect is most pronounced in the region immediately encompassing  $V_{NM\ min}$ . Karlsson provided a factor to correct for the "lattice" dilation upon adding fine particles to RCP coarse particles as well as one to correct for the addition of coarse particles to packed beds of fine particles (i.e. the dominant correction factor for Region II above).

Ayer and Soppet later introduced a further correction to the Furnas model, which provided a more correct estimate of the maximum packing efficiency when using angular (as opposed to spherical) particles [66AYE]. The equation, proposed by Ayer and Soppet, for the packing of a discrete bimodal distribution of spheres is

$$PE = 1.270 - 0.216 e^{-0.313 D_{con}/D} - 0.737 e^{-0.201 D/d}$$

where  $D_{con}$  is the container diameter,  $D$  is the diameter of the coarse spheres and  $d$  is the diameter of the fine spheres. The relation, which estimates  $PE_{max}$  for bimodal packings of angular (tetragonal shaped) particles, is

$$PE = 0.812 - \frac{0.017}{D} - 0.037 e^{-0.207 \frac{D_{con}}{D}} - 0.070 e^{-0.098 D/d}.$$

Table 2.5 illustrates  $PE_{max}$  for the Ayer and Soppet models for spherical as well as angular particles, which may be satisfactorily modelled by tetragonal shapes.

### 2.3.3 Continuous Size Distribution Particles

#### 2.3.3.1 Ideal Packing

While it may not be possible to achieve the packing efficiencies detailed above, it is of interest to be able to predict which particle size distributions will pack with the greatest efficiency. This is desirable when it is important to produce near-net-size shapes in the green state. In order to maximize PE in a packed particle system, manipulation of the particle size range as well as the shape of the particle size distribution is necessary [88REE]. Andreasen and Andersen were among the first to introduce an equation to predict the distribution necessary to maximize PE [30AND]. In the Andreasen model, the portion at a particle size is a constant fraction of the proportion of the distribution that is finer than the size of interest. The Andreasen equation is

$$CVFF = \left( \frac{d}{d_{max}} \right)^n$$

where CVFF is the cumulative volume fraction finer,  $d$  is the particle diameter,  $d_{max}$  is the maximum particle diameter of the distribution, and  $n^{-1}$  is the modulus of the particle size distribution [88REE]. The research of Andreasen and Andersen indicated that, for a particular  $d_{max}$ , PE increased as the distribution modulus increased (i.e. porosity decreased as  $n$  decreased). Their research indicated that practical values for  $n$  were between 0.33 and 0.50. Thus, Andreasen and Andersen discovered that wide size distributions of particles packed to greater



Table 2.5

Values of Maximum Packing Efficiency as Estimated  
by the Models of Ayer and Soppet [66AYE]

Number of Components	Maximum Packing Efficiency	
	Spherical Shapes	Angular (Tetragonal) Shapes
1	0.635	0.635
2	0.867	0.812
3	0.951	0.903

efficiency than narrower ones, if both distributions were otherwise identical. Sohn and Moreland later confirmed this conclusion by stating that PE is dependent only upon the size distribution shape and extent within a given system [68SOH]. Their research investigated the effects of log normal and Gaussian size distributions of particles upon PE. Particle shape was also found to be a factor effecting PE of a given particle system. It was found that continuous distributions of angular particles pack less efficiently than analogous, spherical mixtures of particles.

Later, Funk and Dinger proposed a modification to the Andreasen equation. They realized that the Andreasen equation was flawed in the sense that it assumes that all distributions contain infinitely small particles [88FUN]. Said modification included the addition of a minimum particle size term to the Andreasen equation. This equation, frequently termed either the Alfred equation or the Funk and Dinger equation, has the following form:

$$CVFF = \frac{d^n - d_{\min}^n}{d_{\max}^n - d_{\min}^n}$$

where  $d_{\min}$  is the minimum size of the particle size distribution. Funk and Dinger were able to produce a coal slurry particle size distribution (having a  $d_{\min}$  of  $1\mu\text{m}$  and a  $d_{\max}$  of  $200\mu\text{m}$  and an  $n$  of 0.37) which exhibited a PE of 0.90 [90ZHE]. Neither Andreasen and Andersen nor Funk and Dinger, offered a physical explanation of the distribution modulus ( $n^{-1}$ ) or reasons as to why a certain  $n$  value would give a certain PE, however [90ZHE].

Zheng, et. al offered an elegant solution to explain the physical basis of the distribution modulus [90ZHE]. Their model takes particle packing models "full circle" in that it uses the Furnas model to explain the basis of the distribution modulus. Said model further confirms the

empirical conclusions of Funk and Dinger as well (i.e.  $n$  values of 0.37 to 0.40 give the highest PE values for continuous size distributions).

Zheng, et. al envisioned that the continuous particle size distribution, giving the greatest PE, is simply a summation of many discrete Furnas models. Figure 2.12 illustrates this concept. After an exhaustive derivation, Zheng, et. al derived a relation, identical in form to the Alfred equation, that explains the physical meaning of  $n$ , or the distribution modulus.

The Zheng equation states that

$$n = -\frac{\log \phi}{\log R}$$

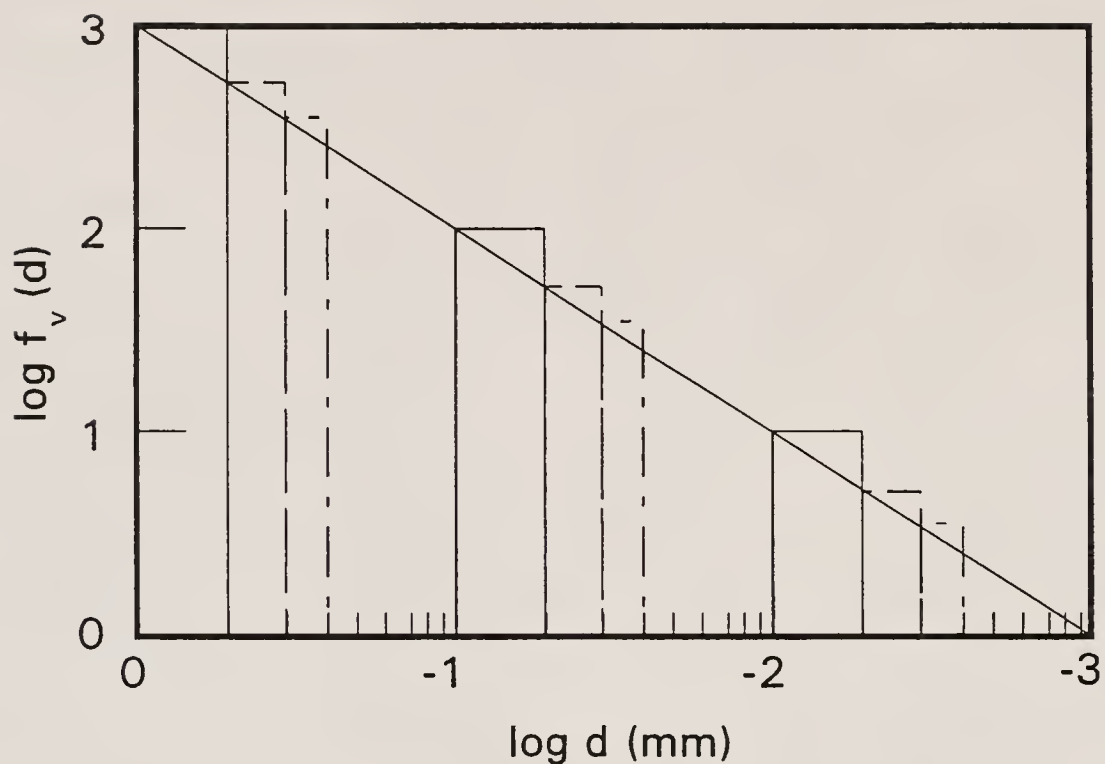
where  $\phi$  is the interstitial pore fraction ( $\phi = 1 - \text{PE}$ ), and  $R$  is the particle size ratio of the particular Furnas model used. This model assumes that  $\phi$  is a constant, regardless of particle attributes. The value of  $\phi$  is estimated from the interstice volume of the largest and smallest particle groups by the relation:

$$-\log \phi = \frac{-\log \phi_{\text{coarse}} - \log \phi_{\text{fine}}}{2}$$

where  $\phi_i$  is the interstice volume of particle size group  $i$  (either coarse or fine). In the case that  $R$  is approximately 10, the above relation for  $n$  reduces to

$$n = -\log \phi.$$

Zheng, et. al found that  $n$  values of approximately 0.40 give maximum packing efficiencies. This is quite similar to the values given by both Andreasen and Andersen, and Funk and Dinger.



Discrete Furnas Groups Fill the Whole Particle Size Range

Figure 2.12

Illustration of the concept of applying discrete Furnas models to a continuous size distribution of particles in order to maximize packing efficiency [90ZHE]

Therefore, as the interstitial volume for the particle bed is reduced, the overall packing efficiency is increased. The effectiveness of  $n$  is regulated by the particle size ratio ( $R$ ) of the Furnas model used to model said system. Both these results are quite logical and totally in agreement with the packing discussions above. Thus, the model of Zheng, et. al provides an interfacing between the theories of Andreasen and Andersen, Funk and Dinger, and Furnas. The model of Zheng, et. al is indirect, however, in that it provides for the effect of particle angularity by allowing modification of the  $\phi$  term only. Thus, further research in the area of particle packing of continuous size distributions of angular particles would be prudent.

#### 2.3.3.2 Hindered Packing

Particle packing may be hindered by several mechanisms, including particle bridging or flocculation, container wall interaction, interparticle friction or adhesion, particle anisometry, binder interaction, and particle segregation. All these factors can only be reduced, and not eliminated, in most real systems. It is sufficient here to state that each factor should be minimized. There are several reviews which cover these factors as they apply to real world situations [76KIN,88REE,89SER,89TUM3].

#### 2.3.4 Effects of Settling and Segregation

Settling, as in slip casting, allows for particle rearrangement prior to the formation of a stable particle structure. In this sense, settling is advantageous. However, formation of particle beds via settling allows segregation to occur in systems having particles of varying size and or density. Settling rates of particles may be estimated by the stokes equation

$$V = \frac{gd^2(\rho_s - \rho_l)}{18\eta_l}$$

where  $g$  is the gravitational constant,  $\rho_i$  is the density of either solid particles (s) or the suspending liquid (l),  $d$  is the particle diameter  $\eta_l$  is the viscosity of the suspending liquid, and  $V$  is the terminal velocity of said particle in said suspending liquid [88REE]. The Stokes relation is valid only for cases of laminar flow at the particle-suspension liquid interface. Laminar flow occurs when the Reynold's number (Re), at the interface, is less than 0.2. The Reynold's number, in this instance is, determined by the equation:

$$Re = \frac{(Vd\rho_l)}{\eta_l}.$$

For ceramic particles, the Reynold's criterion indicates that the upper size boundary is approximately 50  $\mu\text{m}$  [88REE]. Furthermore, the Stokes relation is invalid in instances where there is particle interaction. In ceramic particulate systems, in situations where it is desirable to have conformity to the Stoke's relation (i.e. for particle sizing), the solids loading is kept below approximately 5 V% for this reason.

It is evident from the Stoke's equation that particles of different sizes and or densities will settle at different rates thereby creating a segregated particle bed. Thus, in the settling of wide size distribution particle systems, segregation is an inherent problem. There are various methods by which segregation may be minimized in settled systems of wide size distribution particles, but as mentioned above, it is impossible to completely eliminate segregation in said systems.

Segregation may be reduced by increasing the viscosity of the suspending liquid as well as by reducing the settling distance. Furthermore, in systems having relatively high solids loadings,



segregation may be reduced through particle interaction. A "bridging structure" may occur, trapping the smaller or less dense particles in with the larger or more dense particles.

#### 2.4 Clustering and Percolation Theory

Percolation theories constitute an entire field of scientific literature. Percolation is a universally important concept throughout many scientific fields including, composite design, sol to gel transformations, alloy and microstructure modelling, and mass transport, etc. [83ZAL2,91SAV]. Initial percolation theories were all based upon some type of n-dimensional lattice. Furthermore, these discrete percolation models were based upon the filling of either allowed sites or bonds between allowed sites. Figure 2.13 illustrates each type of discrete percolation. The bond model is a special case of the site model, and any site model may be modified into a bond model with the proper choice of covering lattice [64SYK].

Percolation theory has further evolved to include entities that are not constrained to a defined or discrete lattice [88SEV,90BLE,91SAV]. Said continuum or random percolation models involve the interaction of entities which are randomly placed in n-dimensional space. Continuum percolation may be subdivided as well, into theories involving either randomly centered particles or particles placed randomly within concentric shells [85CHI,89WU]. Finally, both continuum percolation models may be further subdivided into mechanisms involving totally hard particles (impenetrable), or penetrable particles, or any variance in between [85CHI,85RIC,88LEE,89WU]. Figure 2.14 illustrates each of the continuum models of percolation theory.

All percolation theories have a common theme. A function is utilized to determine the mean cluster size, as a function of entity concentration. The percolation threshold ( $p_c$ ) is defined as the entity concentration at which the mean cluster size becomes infinitely large.

## Plumbing Analogy for the Distinction Between Site and Bond Percolation

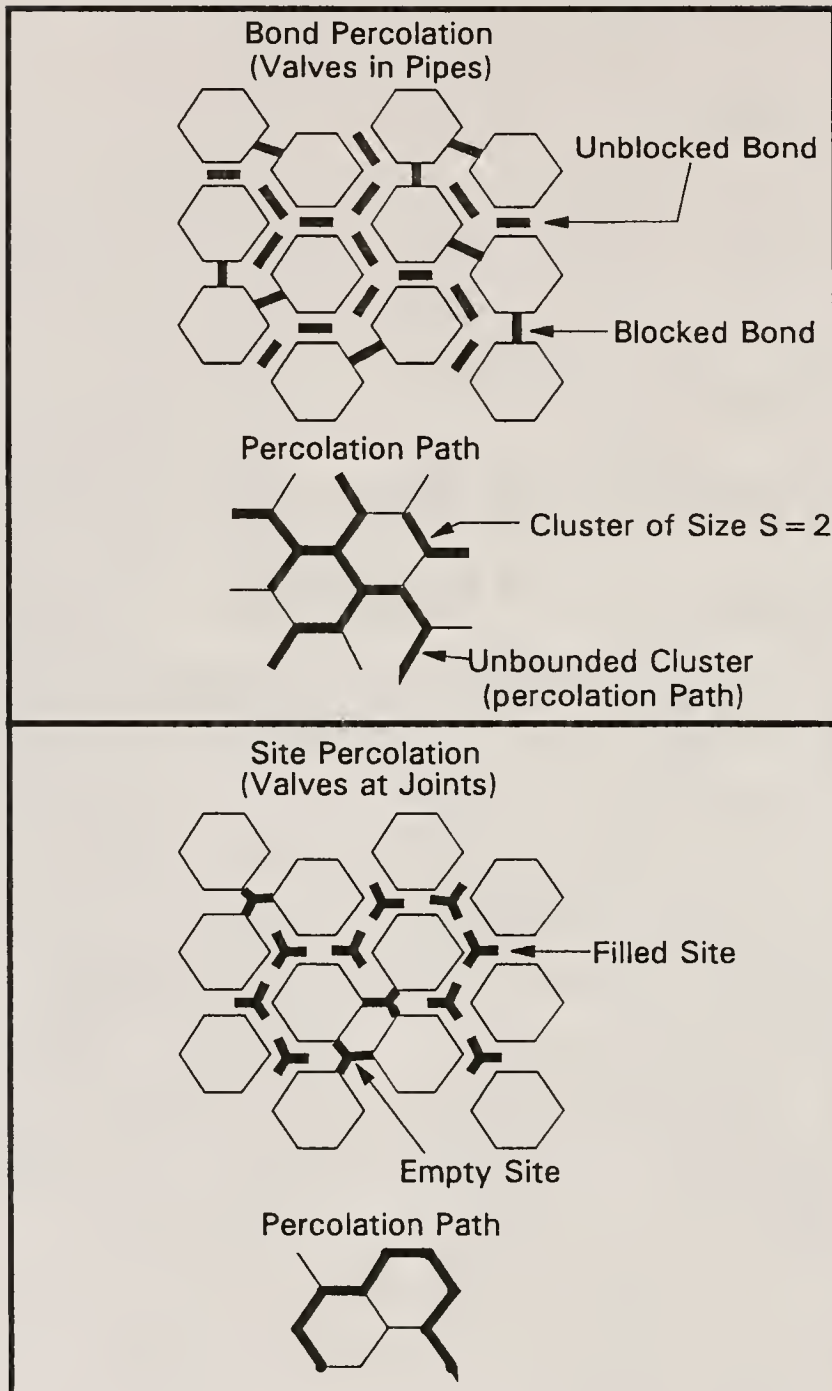


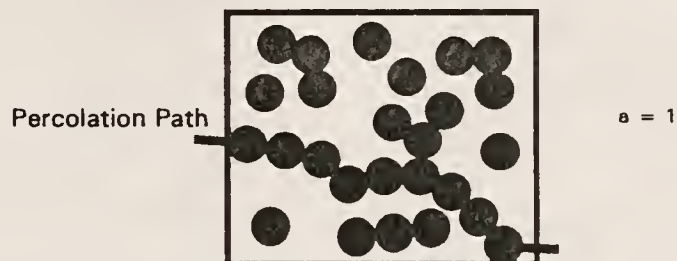
Figure 2.13

Illustration of discrete site and bond mechanisms of percolation [83ZAL2]

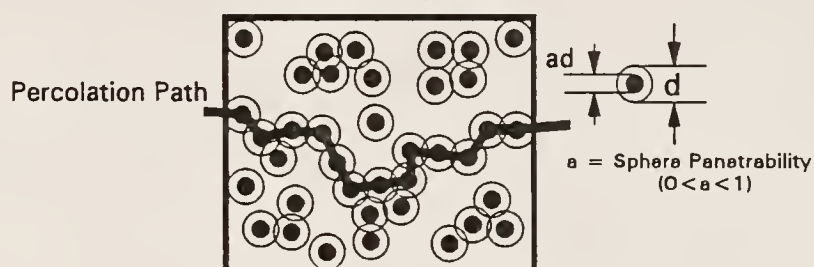
## Continuum Percolation

### 1. Randomly Centered

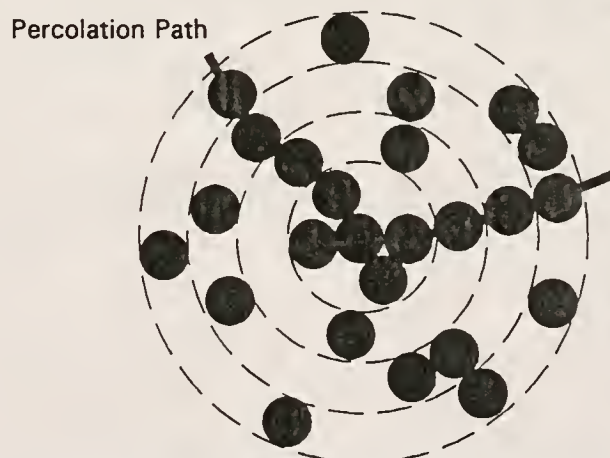
#### A. Impenetrable Spheres



#### B. Penetrable Spheres



### 2. Concentric Shells



Note: Concentric Shell Models May Also Use Penetrable Spheres

Figure 2.14

Illustration of continuum percolation models  
[85BUG,88LEE,89WU]

This phenomenon is physically correlatable to a cluster structure which spans the  $n$ -dimensional space, thereby percolating said space. The various methods utilized, by each model, to produce the mean cluster size function vary significantly with each model, and are not covered in this paper. However, the literature is filled with excellent overviews of each of the areas of percolation theory [59DOM,61FIS1,61FIS2,63FRI,83ZAL2,85CHI,85STA,88LEE,88SAV,89CHI,89WU,90BLE,91SAV].

Furthermore, the above percolation studies may be categorized as either classical or mechanistic. Classical percolation models involve theoretic ideologies combined with mathematical simplifications, in order to solve the percolation problem. Mechanistic models involve computer generation and monitoring of clusters of randomly placed entities according to a set of specifically defined criteria. Mechanistic models usually are Monte Carlo simulation based and are very computationally intensive, while theoretic models are mathematically complicated, but not as computationally intensive. The common goal of each of these methods is to obtain results that agree with each other as well as with available experimental data.

#### 2.4.1 Clustering

Clustering theory involves the interaction of units, with one another, in  $n$ -dimensional space, as the volume fraction of said units is increased [83ZAL2]. As described above, there are two types of clustering, site and bond. The site model involves the occupation of either lattice or random sites, while the bond model involves the interconnection of units placed previously at said sites.

While there are many ways to predict cluster size as a function of either site or bond occupied volume fraction, the simplest and most straight forward method is that involving exact series expansions [61DOM,64SYK]. The series method is valuable in that it provides a simple, physical-based, model which provides estimations for both the

average cluster size as a function of volume fraction of occupied sites (or bonds) as well as a method of accurately estimating the percolation threshold ( $p_c$ ) for a diverse range of site (or bond) lattices for any dimensionality (as long as the number of combinations necessary to form a cluster, for each incremental cluster size, is definable).

The method of exact series expansions for determining cluster size as well as percolation statistics was introduced by Domb and Sykes [61DOM], and was later refined by Sykes and Essam [64SYK]. The mean cluster size, as a function of basic unit concentration ( $S(p)$ ), is described by the series expansion

$$S(p) = 1 + \sum_n a_n p^n$$

where  $n$  is the number of unit members in the cluster,  $a_n$  is the number of possible configurations for cluster size  $n$ , and  $p$  is the fraction of lattice bonds or sites occupied. Table 2.6 depicts the  $a_n$  coefficients for several, three dimensional site and bond configurations. In its present state, this method is valid only for discrete percolation. As shall be outlined in Chapter 4 below, this method may be extended to RCP structures as well.

Until now, the discussion has covered the clustering of monosized spherical entities only. Clustering and percolation of  $n$ -modal size distributions of spheres, as well as nonspherical particles, is touched upon in section 2.4.2, below.

#### 2.4.2 Percolation

As mentioned above, all percolation models involve defining where the mean cluster size ( $S(p)$ ) becomes infinity. Figure 2.15 illustrates the generic evolution of mean cluster size, and of a conductive-type percolation property, as a function of filled site or bond fraction. At  $p_c$  the site or bond interconnection length as well as the mean cluster

Table 2.6

The Number of Possible Configurations ( $a_n$ )  
for a Cluster Size of  $n+1$  (Three Dimensional  
Bond and Site Configurations) [64SYK]

$a_n$ for Various Lattice Configurations				
n	Site Mechanism			
	Face Centered Cubic (PE=0.74)	Body Centered Cubic (PE=0.68)	Simple Cubic (PE=0.52)	Diamond Cubic (PE=0.34)
1	1	1	1	1
2	12	8	6	4
3	84	56	30	12
4	504	248	114	36
5	3012	1232	438	108
6	17142	5690	1542	264
7		26636	5754	708
8		113552	19574	1668
9			71958	4536
10				10926
11				28416
Bond Mechanism				
1	1	1	1	1
2	22	14	10	6
3	234	98	50	18
4	2348	650	238	54
5	22726	4202	1114	162
6	214642	26162	4998	456
7	1993002	163154	22562	1302
8		984104	98174	3630
9		6015512	434894	10158
10			1855346	27648
11				77022
12				206508



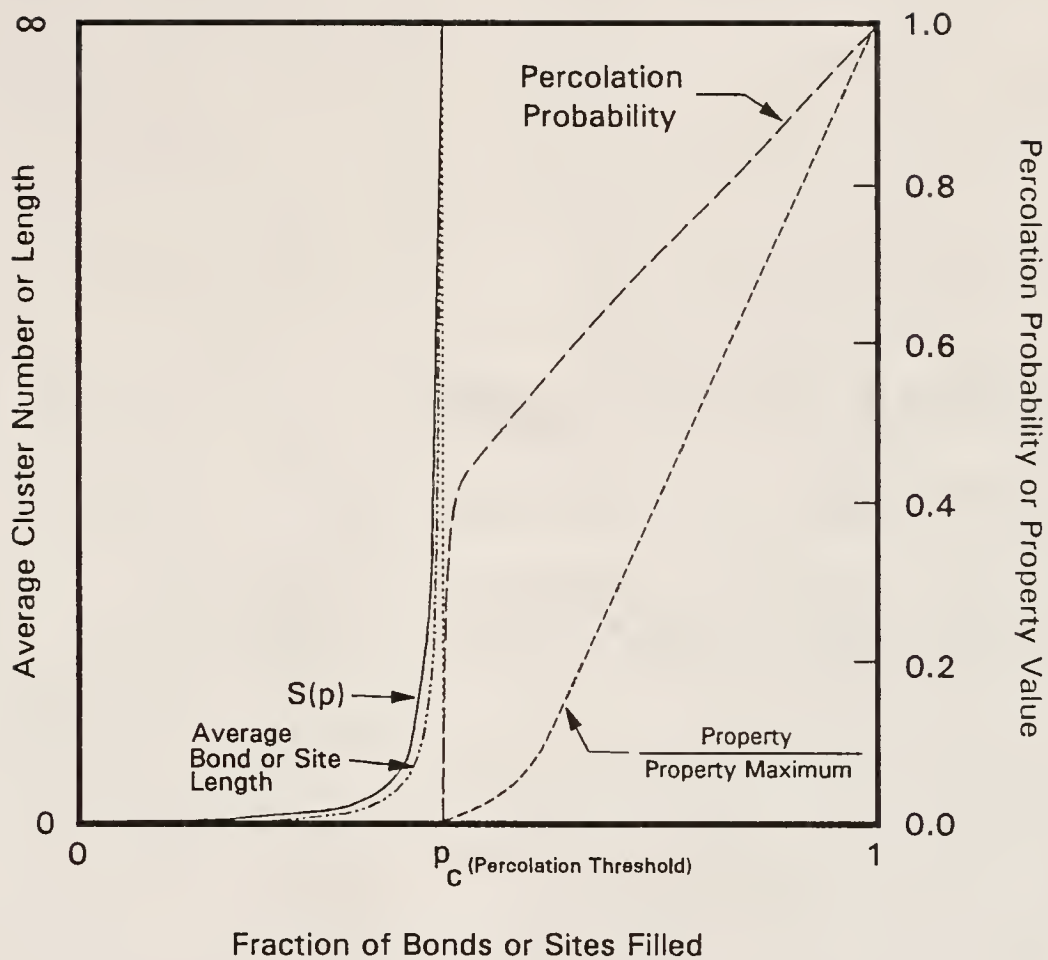


Figure 2.15

Evolution of mean cluster size and percolation properties as a function of filled fraction of sites or bonds [83ZAL2]

size goes to infinity. At this point, the conductive-type material property becomes finite, increasing gradually, then linearly to its maximum at a site or bond fraction of unity. The percolation probability initially increases rapidly, then gradually increases to one at a filled bond or site fraction of unity.

It should be noted that the actual value of  $p_c$  depends upon the packing arrangement of either the entities or the bonds between said entities. The percolation threshold also is heavily dependent upon the dimensionality of the filled space. Various pertinent percolation data for both discrete and continuum (i.e. RCP) percolation is shown in Table 2.7. It should be noted that there is debate as to whether random close packing is truly a purely continuum case or if it is a combination of separate discrete lattices, or a combination of discrete and continuum models [29SMI,61MCG,83ZAL2,90ZHE]. There is also debate as to whether a discrete system may be universally modified for use in continuum-type systems [90BLE].

Perhaps the most interesting result of discrete percolation theory is that there is a dimensional universality of the volume fraction at percolation (i.e.  $PEp_c^{\text{Site}}$ ) [83ZAL2]. Table 2.7 illustrates this effect for two and three dimensional spaces. For the three dimensional case, said universal volume fraction at percolation has been found to be approximately 0.157. Analogously, there is a dimensional universality of total bond fraction at percolation (i.e.  $Zp_c^{\text{Bond}}$ ). Said value was found to be approximately 1.45. Thus, the total volume fraction of entities at  $p_c$  is a universal constant, regardless of the lattice used. Zallen also applied said universality to a random close packed structure with success, thereby heavily implying that said dimensional universality may be extrapolated to the appropriate continuum models (i.e. randomly placed or bonded, hard, impenetrable particles) [83ZAL2]. Zallen termed this dimensional universality as the critical volume fraction for the site percolation case and as the critical bond fraction

Table 2.7

Pertinant Factors for Site and Bond Percolation  
on a Variety of Lattices [83ZAL2]

Dimensionality (d)	Lattice or Structure	$P_c$ Bond	$P_c$ Site	Coordination Number (Z)	Packing Efficiency (PE)	$Zp_c^{\text{Bond}}$	$PEp_c^{\text{Site}}$
1	Chain	1	1	2	1	2	1
2	Triangular	0.3473	0.5000	6	0.9069	2.08	0.45
2	Square	0.5000	0.593	4	0.7854	2.00	0.47
2	Kagum'e	0.45	0.6527	4	0.6802	1.80	0.44
2	Honey comb	0.6527	0.698	3	0.6046	1.96	0.42
Dimensional Average						$2.0 \pm 0.2$	$0.45 \pm 0.03$
3	FCC	0.119	0.198	12	0.7405	1.43	0.147
3	BCC	0.179	0.245	8	0.6802	1.43	0.167
3	SC	0.247	0.311	6	0.5236	1.48	0.163
3	Diamond	0.388	0.428	4	0.3401	1.55	0.146
3	RCP		0.27*		$0.637$ $0.6^*$		0.16*
Dimensional Average						$1.5 \pm 0.1$	$0.16 \pm 0.02$
4	SC	0.160	0.197	8	0.3084	1.3	0.061
4	FCC		0.098	24	0.6169		0.060
5	SC	0.118	0.141	10	0.1645	1.2	0.023
5	FCC		0.054	40	0.4653		0.025
6	SC	0.094	0.107	12	0.0807	1.1	0.009

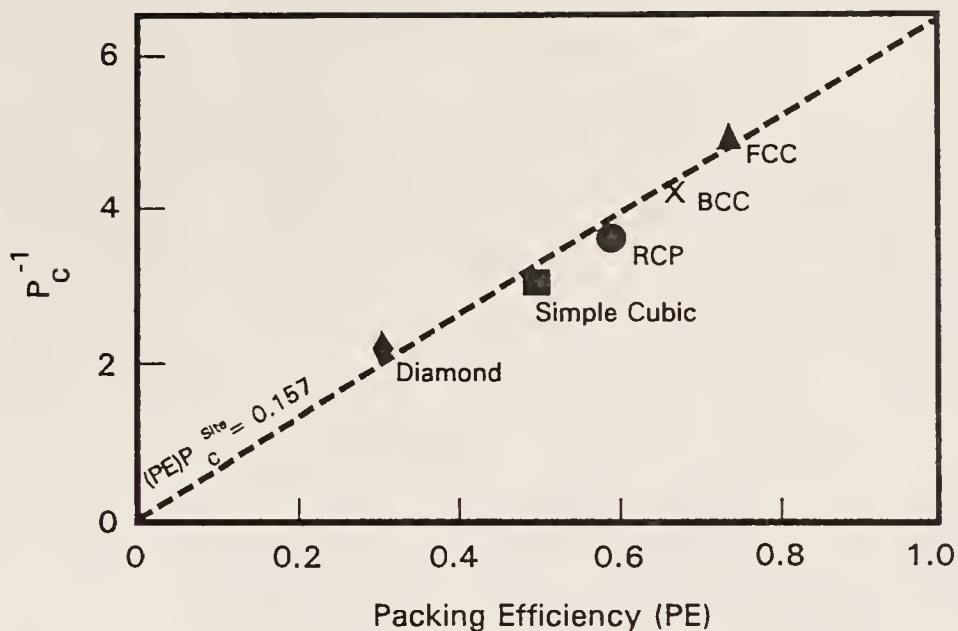
Notes: \*Experimentally Derived Values

for the bond case [83ZAL2]. These phenomena are illustrated in Figure 2.16, where the inverse of the percolation threshold ( $p_c^{-1}$ ) is plotted as function of either the packing efficiency (PE) or the coordination number ( $Z$ ) for site and bond models respectively. This is perhaps the most important revelation of percolation theory.

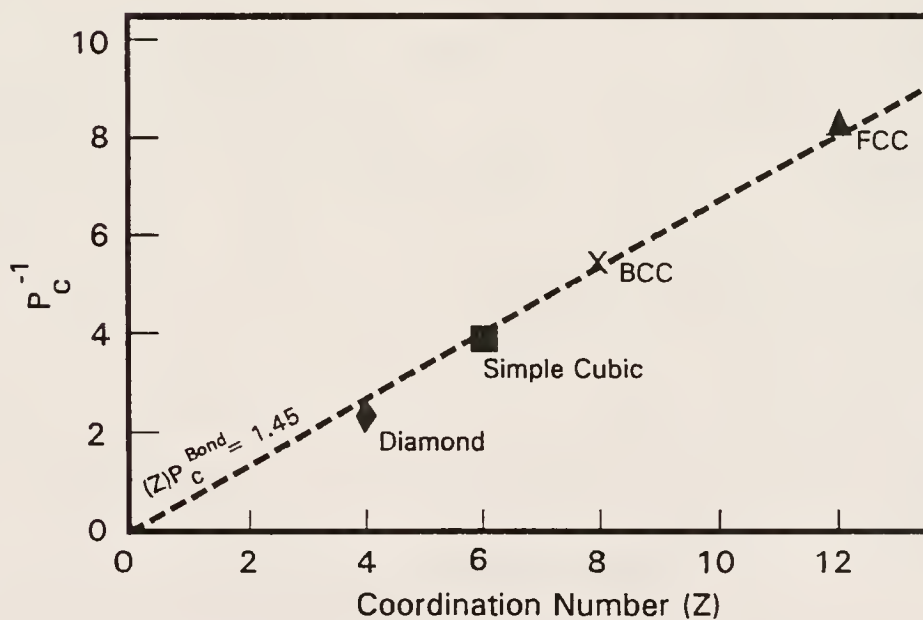
The material property resultant from percolation, and possibly the percolation threshold, may have a dependence upon particle size. This was experienced by Ruschau, et. al and by Newnham, et. al in their investigations of volume resistivity as a function of conductor particle size and volume fraction [78NEW,90RUS]. They experienced a shift in  $p_c$  to higher values with smaller particle size. They attributed this to more contacts in systems using smaller particles, since the contact resistance would be decisively larger for systems utilizing smaller conductive particles. This would effectively increase the minimum resistivity as well as possibly push  $p_c$  to higher fractions. Thus, in percolation experimentation, it is important to realize that the physical size of the volume investigated must be several orders of magnitude larger than the entity size as well as that other factors (such as contact resistance, etc.) must be considered.

Percolation theories involving bimodal distributions of spherical particles or monosized, nonspherical particles are still in a stage of relative infancy. Chiew, et. al and Wu and Chiew modelled the effect of bimodality of entity size on the percolation threshold for various continuum systems (i.e. randomly centered impenetrable and penetrable systems) [85CHI,89WU].

Using Ornstein-Zernike forms of cluster integral equations, in combination with the Percus-Yevik approximation for pair connectedness and, ultimately, for mean cluster size, Chiew, et. al found that a multicomponent mixture of randomly centered, impenetrable spheres percolates at a constant value, regardless of concentration and size distribution [85CHI]. They extended this conclusion to multimodal and



A. Site Percolation



B. Bond Percolation

Figure 2.16

Illustration of the critical volume and bond fractions at percolation in three dimensional space [83ZAL2]

continuous distributions as well. They calculated that said continuum percolation occurs at an inclusion volume fraction of 0.393. This is a somewhat different value than that cited in Table 2.7 above. The value of Chiew, et. al has been the subject of correction, however, and the accuracy of said value is still somewhat debatable [89CHI]. Thus, it may be assumed that the philosophy of Chiew, et. al is correct while the actual percolation value may not be.

#### 2.4.3 Application of Percolation to Microstructure

Percolation theory may be utilized to describe many phenomena, such as composite properties, catalytic reactions, ferroelectricity, etc. The expansion of percolation theory in this section is limited to porous structures and the characterization of porous structures using penetration-extrusion and sorption techniques, however.

Percolation theory has been utilized to model both real and ideal, pore structures. Modelling of real systems requires experimental data, which are generally obtained by either microscopic, porosimetric, or sorption techniques. Yanuka, et. al proposed a percolation model which utilized intersecting ellipsoids to estimate pore structure as determined via microscopic techniques [86YAN]. Said investigations are tedious when many samples need to be investigated, however, and are frequently subject to error due to the relatively traumatic sample preparation techniques involved.

Porosimetry and nitrogen ( $N_2$ ) sorption techniques are more convenient techniques of characterizing pore structure. Both characterization methods also have associated problems. It is difficult to discern pore shape of the material structure using either technique. Indeed, the Washburn equation, which is the generic equation utilized in the characterization of porosity via mercury (Hg) porosimetry, assumes that all pores are cylindrical in geometry [86LAN]. Other problems with porosimetry techniques are the hysteresis exhibited



by intrusion-extrusion curves, which has been (until recently) insufficiently attributed to contact angle hysteresis as well as to the stranding of Hg as modelled by the classical "ink bottle" pore model [86LAN,91ZGR]. Furthermore, there is a definite breakthrough intrusion pressure, commonly observed when using Hg porosimetry, which is frequently obscured by surface effects [86YAN,91SHI3].

Porosimetry and sorption techniques have other inherent errors as well. Intrusion porosimetry overestimates the volume fraction of small pores, since intrusion will only occur when the system pressure is sufficient to overcome the surface tension that results from constricting the Hg through the smallest area indigenous to the pore channel [86LAN]. Due to mass balance, the volume fraction of large pores indicated by intrusion porosimetry is underestimated as well. Extrusion porosimetry has inherent errors as well. In order to extrude to the surface of the sample, a continuous Hg path must be present. As the system pressure is reduced, the Hg extrudes from throats in pore channels due to surface tension. Thus, menisci are formed in the pore channels. Said formation initially occurs only at the smallest restrictions in each pore channel, effectively blocking extrusion from other parts of the pore structure. Therefore, extrusion porosimetry underestimates the volume fraction of small pores [86LAN]. A second phenomenon associable to extrusion porosimetry is the underestimation of the volume fraction of larger pores due to mercuric stranding. This results from the same factor that causes shadowing. As Hg extrudes from the pore structure, menisci form at pore channel constrictions (throats) first, thereby creating a discontinuous (i.e. impossible) path for Hg extrusion. As extrusion continues, this effect becomes increasingly significant until the largest Hg-filled pores become stranded [86LAN]. Thus, extrusion porosimetry underestimates the volume fractions of both the smallest and the largest members of a porous structure. Furthermore, since some of the Hg is stranded within the pore structure,

mass balance is no longer satisfied. In the event that stranding is relatively small, however, a mass balance is still an appropriate approximation and, thus, the volume fraction of intermediate sized pores is necessarily overestimated [86LAN].

Sorption techniques have analogous errors that are inherent in the technique as well. In the case of  $N_2$  gas adsorption-desorption analysis, hysteretic relations similar to those characteristic of porosimetry, are exhibited. Said hysteretic behavior is not dependent upon pore restriction properties in the same sense as in porosimetry, however. In the sorption case, the displayed hysteresis is resultant from pore channel blockage. Upon adsorption, the gas is free to adsorb on any surface having the proper surface curvature [87ZHD]. The areas of greatest curvature will adsorb first. As the relative pressure of  $N_2$  is increased, smoother surfaces (i.e. larger pores) will adsorb the gas as well. As the nitrogen partial pressure ( $P_{N_2}$ ) is further increased capillary condensation occurs in pore channel throats, thereby blocking access of nitrogen (or other adsorbate gas) to the larger pores. Conversely, as  $P_{N_2}$  is decreased (i.e. gas evaporation and desorption), evaporation and desorption can only occur from surface accessible pores. Thus, gas adsorption in porous materials is not a cooperative phenomenon, while gas desorption is. This is different from the situation characteristic of Hg porosimetry, in that porosimetric intrusion and extrusion are both cooperative. However, both hysteretic phenomena are quite similar (i.e. adsorption "leads" desorption and intrusion "leads" extrusion) [91ZGR].

There is a great deal of debate about which values (i.e. adsorption versus desorption, or intrusion versus extrusion) should be utilized to define the pore size distribution of a porous material [91MAS2,91NEI,91ZGR]. It seems that an average of both curves, that is weighted according to the various phenomena involved, should be utilized in the case of porosimetry, while adsorption data (if and only if

condensation is prevented) should be used in the case of nitrogen gas sorption characterization. This is usually not the case however. Generally, intrusion data is quoted in porosimetry studies, while desorption data is cited in studies involving gas sorption [88REE].

Fortunately, both curves of each type of hysteresis contain valuable information. Many percolation models have recently been developed which attempt to correlate hysteresis structure with pore structure data [85RIC,86LAN,86YAN,87ZHD,91MAR,91MAS2,91NEI,91SHI3,91ZGR]. This area of research is not mature as of yet, and more research in this field is warranted. Percolation theory was first applied to porous systems by Fatt [56FAT1,56FAT2,56FAT3]. The field has developed greatly since then. The most successful percolation models of this type involve site and bond percolation models which are utilized in conjunction [86LAN,87ZHD,91ZGR]. In said models sites are used as pore bodies (i.e. the physical pores) and bonds are used for pore channels or channel restrictions. The coordination number ( $Z$ ) is defined as the number of bonds per site. Thus far, these models involve  $Z$  only as a constant and not a distribution function. Furthermore, these models typically do not correlate bond size with site size (i.e. they are totally random), which is usually not the case in real systems [91ZGR]. However, as presented, these models are all highly intuitive, and thus, are useful for investigating pore structure.

Zgrablich, et. al introduced a site-bond, continuum percolation model which utilizes size distribution functions for both the sites and the bonds of a porous material [91ZGR]. For materials having a large difference between bond and site distributions (i.e. pores and throats formed by RCP beds of monosized spheres), both size distributions are discrete. For lamellar or platey structures, having similar pore and pore channel structure sizes, the relative size distributions of bonds

and sites, overlap. Figure 2.17 illustrates both the bond-site structure model as well as the bond and site distributions and overlaps that are associable to selected microstructures.

Zgrablich, et. al then calculated bond and site percolation probabilities ( $P^S$  and  $P^B$  respectively) using the bond and site size distributions for various microstructures. They used a correlated Bethe lattice model (although other models may be used as well). The percolation probabilities were then used to determine the sorption and porosimetry hystereses for each of the selected microstructures. The models used were solely bond sensitive in the sorption case, and bond sensitive and site sensitive in the cases of intrusion and extrusion porosimetry respectively, due to the reasons of relative cooperativity, espoused above. The relationship utilized to determine the selected adsorption-desorption hystereses is

$$1-V_{des}(r_k) = (1-V_{ads}(r_k)) P^B(r_k)$$

where  $1-V_{des}(r_k)$  is the fraction of emptied pores as a result of desorption,  $1-V_{ads}(r_k)$  is the total volume that could be desorbed, independent of pore structure considerations, and  $P^B(r_k)$  is the bond percolation probability (note that all are functions of the Kelvin radius,  $r_k$ ). The relationships used for the various porosimetry hystereses are

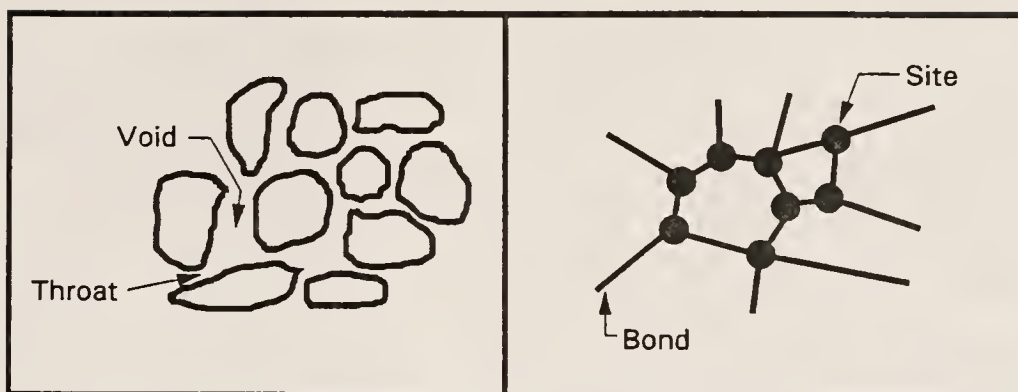
$$\Phi = P^B(r_L) [1-B(r_L)] V^+(r_L)$$

and

$$1-\Phi = P^S(r_L) [S(r_L)] V^-(r_L)$$

for intrusion and extrusion porosimetry respectively. In these equations,  $\Phi$  is the fraction of available porous volume filled,  $P^S(r_L)$

## Site-Bond Analogy to Porous Structure



Site and Bond Size Distributions for Selected Pore Structures

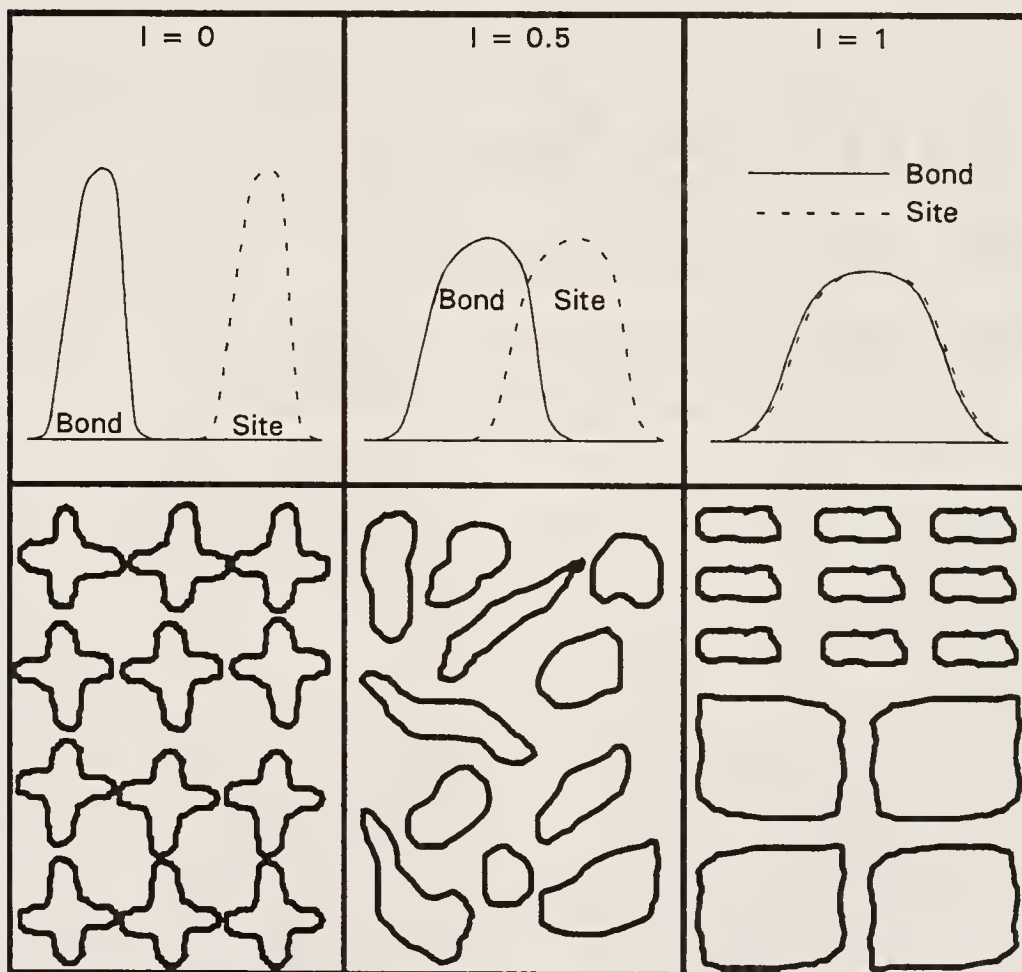
 $I$  = Size Distribution Overlap

Figure 2.17

Illustration of the bond-site model of continuum percolation, and the bond and site size distributions and overlap related to selected microstructures [91ZGR]



and  $P^B(r_L)$  are the site and bond percolation probabilities respectively,  $V^+$  is the fraction of volume corresponding to sites that are larger than the Laplace radius ( $r_L$ ),  $V$  is the fraction of volume corresponding to sites that are smaller than  $r_L$ , and  $B(r_L)$  and  $S(r_L)$  are the bond and site distribution functions respectively (note that they are both functions of the Laplace radius,  $r_L$ ), and  $r_L$  is the Laplace radius.

Figures 2.18 and 2.19 illustrate the sorption and porosimetry hystereses, calculated by the appropriate equations above, for theoretically packed beds of spheres rods needles and plates. The site and bond distributions for said model porous structures are included as well.

Finally, the model was subjected empirically to available experimental data [91ZGR]. Data were obtained from porosimetry hystereses of real porous materials of the categories mentioned above. The ratio of intrusion pressure to extrusion pressure ( $P_i/P_e$ ) was plotted as a function of volume fraction filled ( $\Phi$ ). The results are illustrated in Figure 2.20. It is evident, from Figure 2.20, that both sphere and rod structures should yield hystereses having relatively constant  $P_i/P_e$  values. This would result in both the intrusion and extrusion curves being very similarly shaped. Conversely, structures having a site-bond size distribution overlap (i.e. changing  $P_i/P_e$ ) would be expected to have dissimilarities in shape between the respective intrusion and extrusion curves. Furthermore, the negative slopes in  $P_i/P_e$  of the plate and needle pore structures would lead to relatively narrow shoulders in the respective hystereses.

Lane, et. al also accounted for the expected correlation between relative site and bond sizes (i.e. nonrandom, correlated bond distributions). Figure 2.21 illustrates the general effect of correlated bonds on a hypothetical intrusion curve. Other models are valuable for determination of the relative amount of stranded Hg as a function of pore structure (i.e. "ink bottles" having a near-infinite



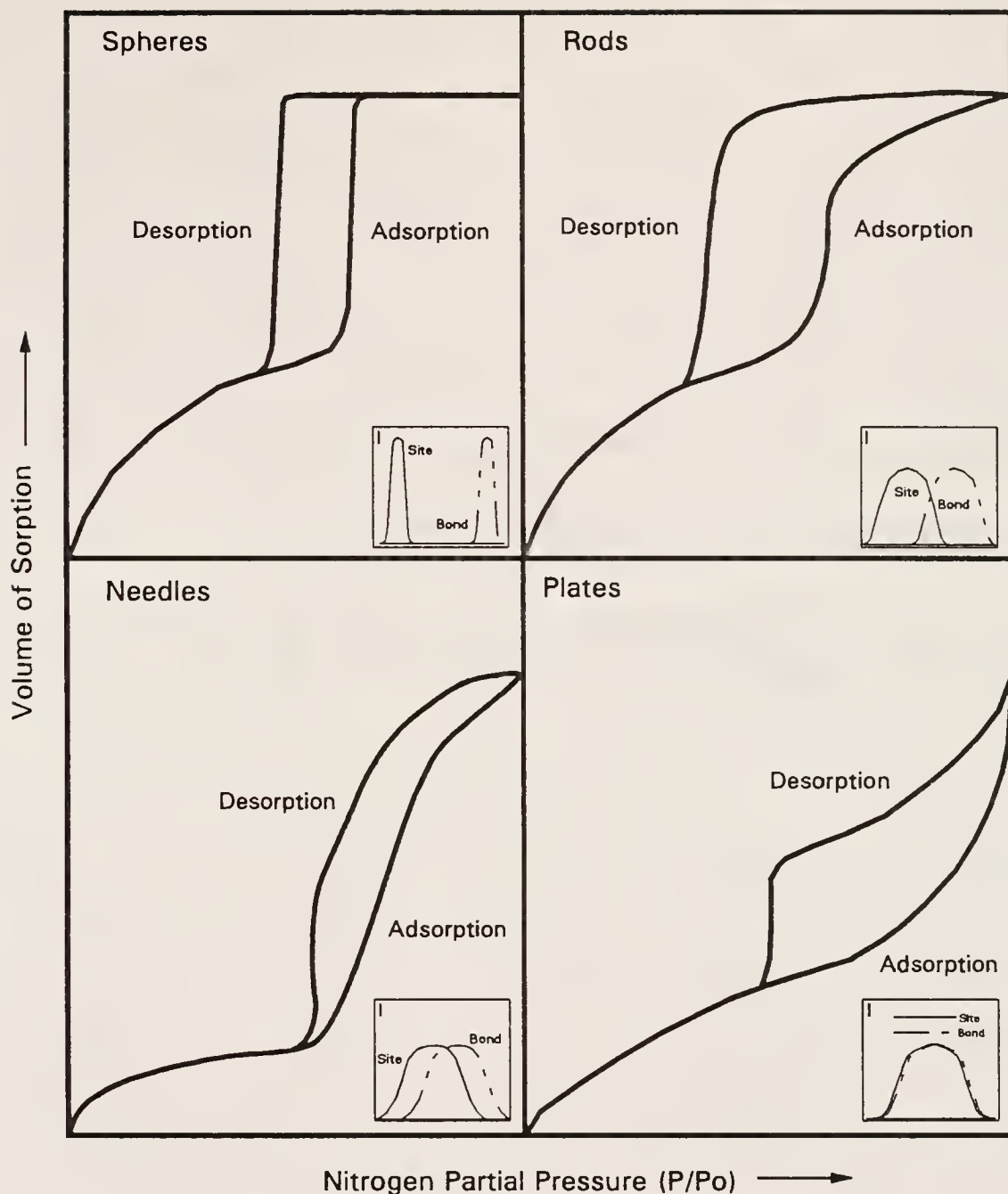
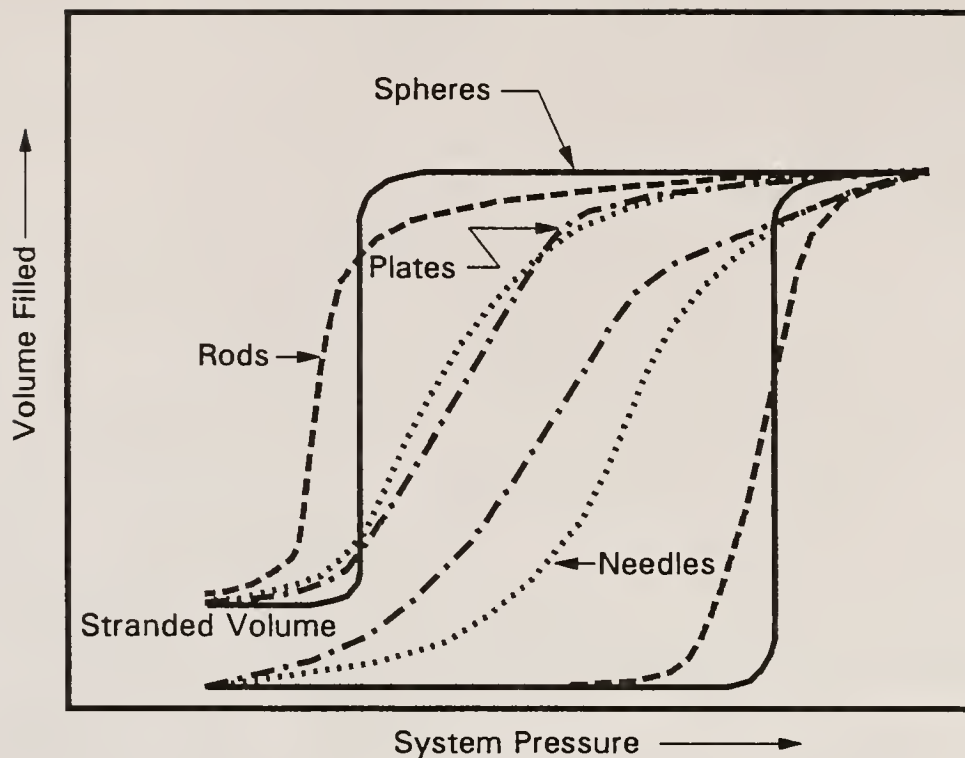


Figure 2.18

Generic sorption hystereses, calculated using a bond-site continuum percolation model, and the corresponding site and bond size distributions for each respective pore structure [91ZGR]



Size Distribution Overlap (I)

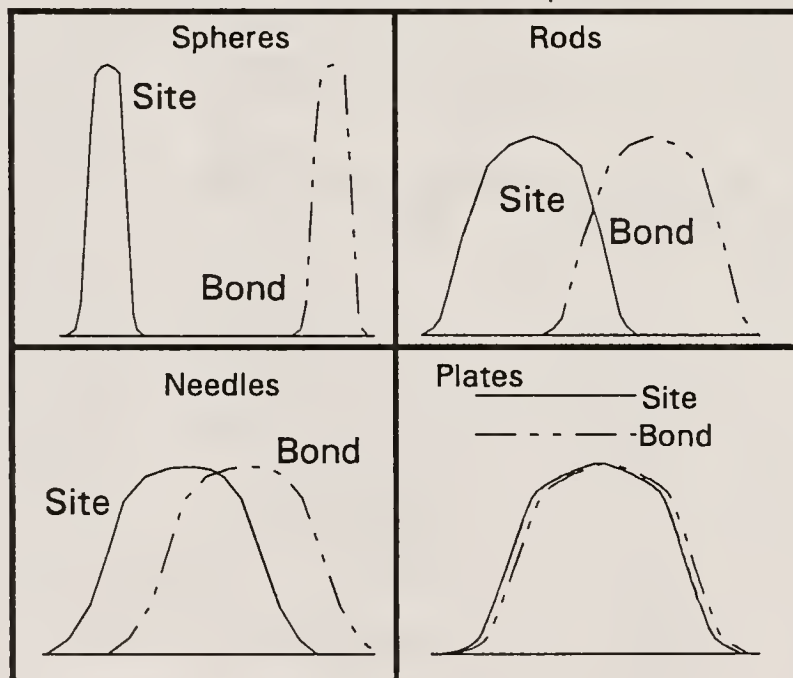


Figure 2.19

Generic porosimetry hystereses, calculated using a site-bond continuum percolation model, and the site and bond size distributions corresponding to the respective pore structures [91ZGR]

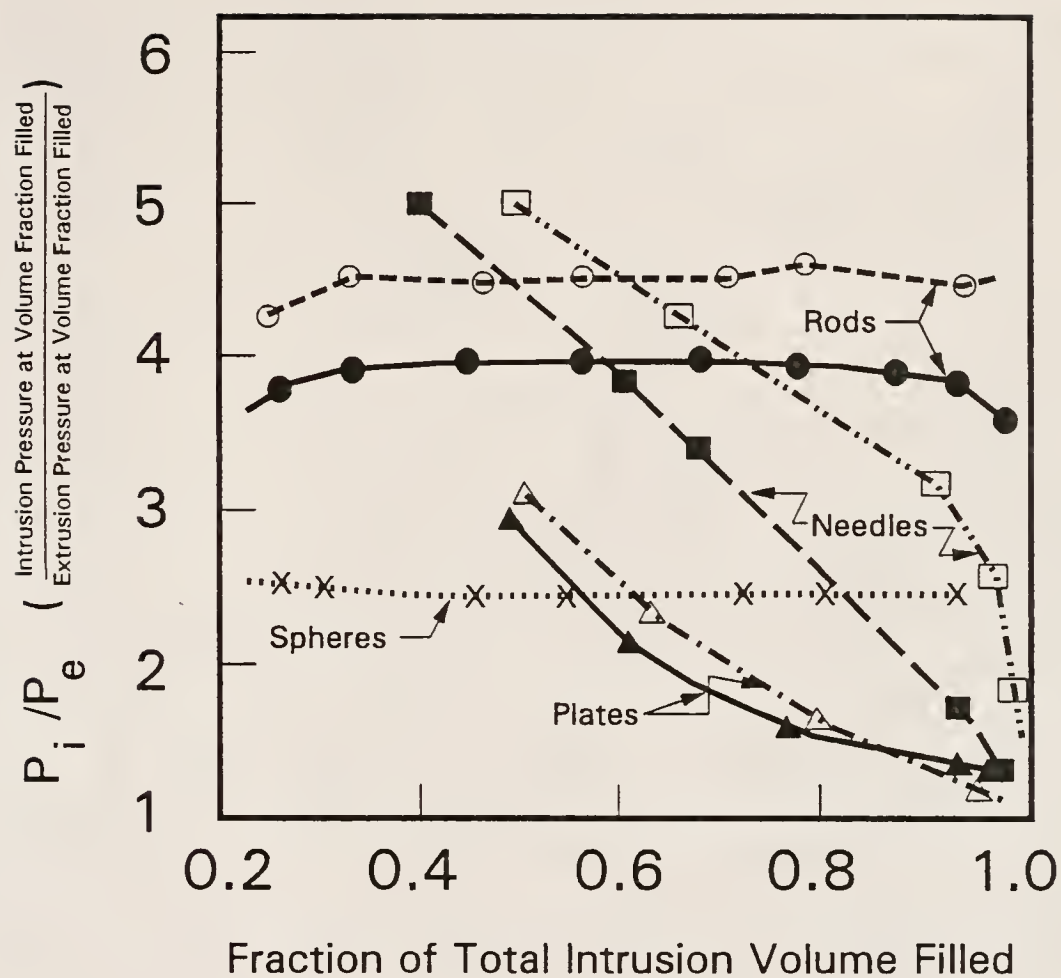


Figure 2.20

Relationship of the ratio of the pressure of intrusion to the pressure of extrusion, at a specific filled volume fraction ( $\phi$ ), as a function of filled volume fraction ( $\phi$ ) [91ZGR]

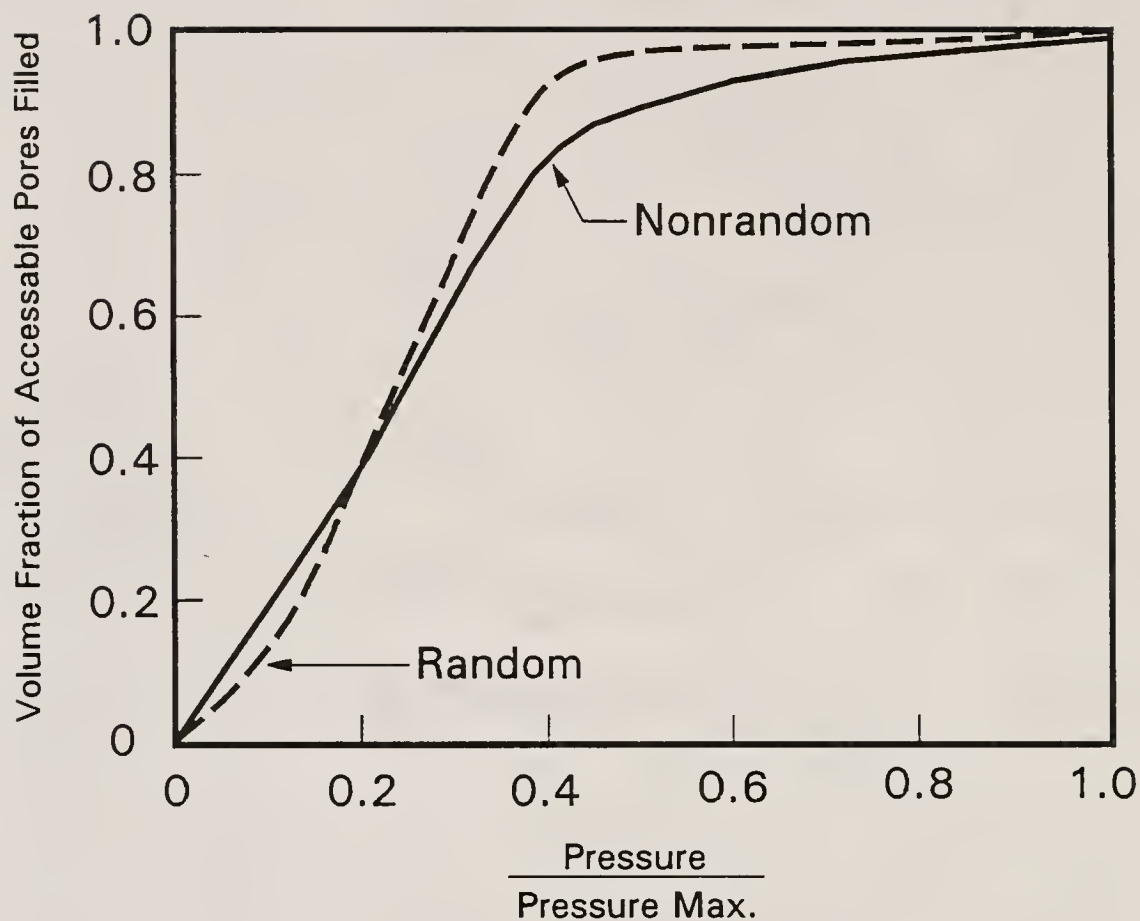


Figure 2.21

Illustration of the difference between intrusion porosimetry curves, calculated for totally random and for correlated site-bond structures [86LAN]

relative diameter ratio, leave maximal amounts of stranded Hg) as well as the dimensionality of the corresponding pore structure [86LAN,91SHI3].

## 2.5 Sintering

### 2.5.1 General

Sintering may be defined as the consolidation and densification of particulate materials below the melting point (or range) of said materials. Other definitions have also been proposed. In fact the very definition of the term sintering is the subject of a great deal of debate, due to the complexity of the process [79HAU,85KUC]. Sintering theory is generally delineated into two categories, solid state sintering and viscous sintering. Solid state sintering occurs in crystalline materials, while viscous sintering occurs in amorphous solids. Solid state sintering is usually considered to occur via either various diffusional mechanisms or by an evaporation-condensation mechanism, while viscous sintering is generally agreed to be a flow process. Table 2.8 outlines the various diffusion and flow mechanisms involved in both types of sintering. Densification of a packed bed of particles will normally start when the heat treatment temperature is approximately 40 to 50% of the melting point (or range) of said material, while consolidation, or interparticulate bonding may initiate well below this temperature [79HAU].

Sintering of particles is an exothermic reaction [FRE45]. The driving force for all types of sintering (as with all thermodynamic reactions) is the ultimate reduction of the total free energy of the system. Specifically, the factors involved, are delineated by the following relation:

$$\Delta G_T = \Delta G_v + \Delta G_b + \Delta G_s$$

Table 2.8

Mass Transport Mechanisms Involved in Sintering [88REE]

Mechanism	Densification?
Surface Diffusion	No
Evaporation-Condensation	No
Boundary Diffusion	Yes
Lattice Diffusion	Yes
Viscous Flow	Yes
Plastic Flow	Yes

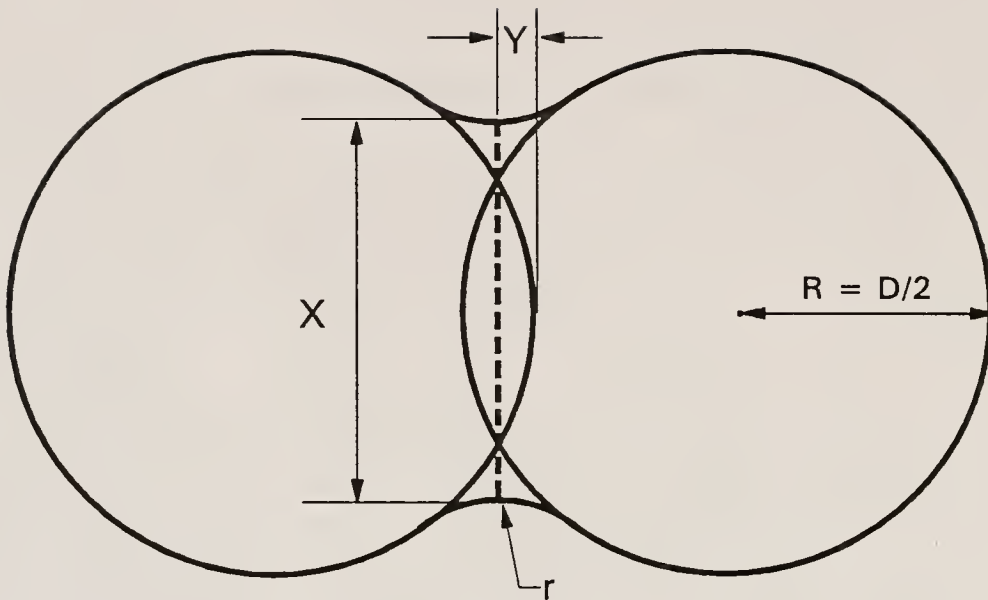


where  $\Delta G_T$  is the system total free energy,  $\Delta G_v$  is the change in volume free energy,  $\Delta G_b$  is the change in boundary free energy, and  $\Delta G_s$  is the change in surface free energy, with respect to the sintering reaction [88REE].

Sintering is frequently modelled using spherical particles. Figure 2.22 illustrates a sintering model that involves two spheres in contact. The diameter of the contact area of the two spheres ( $X$ ) increases with time when appropriately heat treated. Table 2.9 denotes the rate of change of contact area diameter ( $X$ ), with respect to sintering mechanism, for isothermally treated systems. Figure 2.22 also shows that material transport depends upon the relative surface curvature involved. Basically, material flows from convex surfaces to concave ones, via one of the previously mentioned mass transport mechanisms. As a result, the centers of the spheres gradually approach each other, thereby resulting in densification.

It is generally agreed that sintering from green compact to fully dense material involves three distinct stages. In the first stage of sintering, particle rounding and interparticle bonding dominates. The total volume change during the initial stage of sintering is usually less than 12% [88REE]. The second stage of sintering involves the movement of particle centers toward each other as the result of mass transport. This intermediate stage results in the greatest amount of densification. During the intermediate stage, the pores remain connected. The final stage of sintering is the slowest, involving the lowest driving force. Final stage sintering initiates at approximately 92% of theoretical density [88REE]. During this stage, all porosity becomes discrete and will either shrink or expand depending upon the size of the pore, and the amount and solubility of the gas entrapped by the pore. The three stages of sintering are illustrated in Figure 2.23.

There have been other sintering models proposed as well. In fact, the initial viscous sintering model was a two stage model [45FRE].



$X$  = Sphere Contact Area Diameter

$Y$  = Amount of Movement of Sphere Centers  
Toward One Another (per Sphere)

$R = D/2$  = Sphere Radius

$r$  = Radius of Curvature of Throat Interconnection

Figure 2.22

Illustration of a classical sintering model,  
consisting of two spheres interacting at a contact  
surface (the diameter of which is denoted as  $X$ )  
[88REE]

Table 2.9

The Rate of Change of Contact Area Diameter  
with Respect to Sintering Mechanism for Isothermally  
Treated Monosized Spheres [49KUC]

Sintering Mechanism	Time Dependence of Contact Area
Viscous Flow	$X^2 \propto t$
Evaporation-Condensation	$X^3 \propto t$
Volume (Lattice) Diffusion	$X^5 \propto t$
Surface Diffusion	$X^7 \propto t$

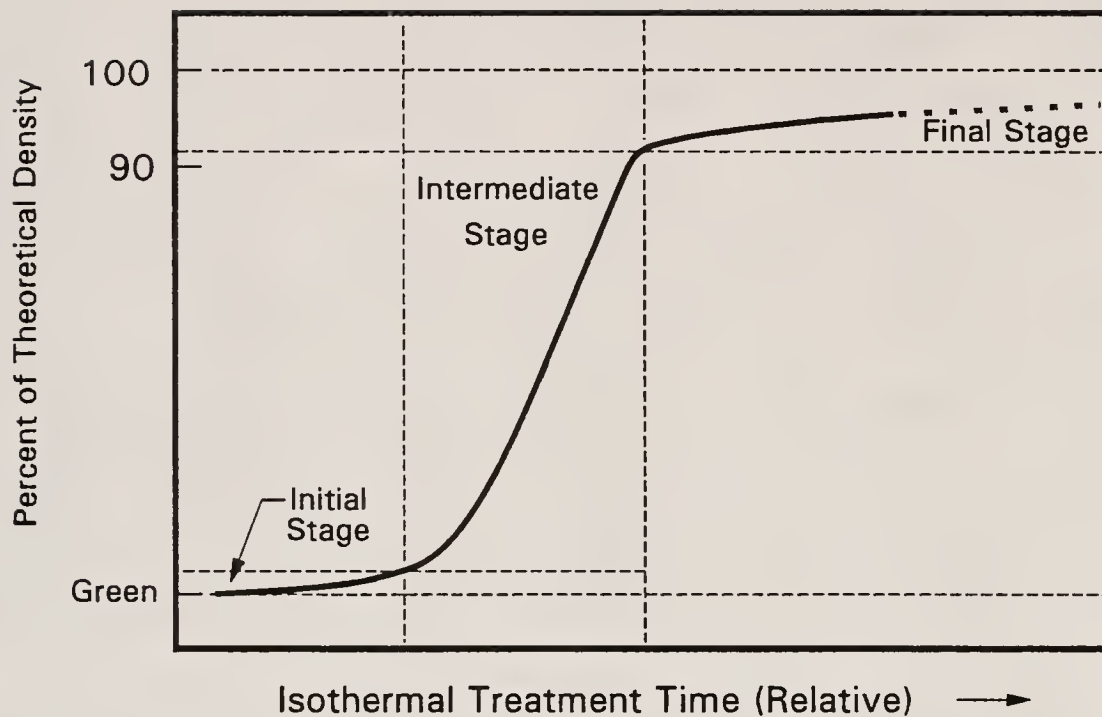


Figure 2.23

Illustration of the three stages of sintering [88REE]

Others have added a fourth stage (or second part of the third or final stage) in order to explain pore bloating and/or grain growth [88REE].

### 2.5.2 Viscous Sintering

Among the first sintering models, was that of Frenkel [45FRE]. Kuczynski was the first to confirm Frenkel's theory that glasses sinter via a viscous flow mechanism [49KUC]. It is generally agreed upon that the Frenkel model, while not adequate for solid state sintering, is a satisfactory basis for viscous sintering theory [49KUC,55KIN,88REE,90EWS]. Unlike the classical, three-stages-of-sintering model, the Frenkel model divides the sintering process into two stages which are governed by the following relations,

$$\frac{\Delta L}{L_o} = \left(\frac{1}{3}\right) \left(\frac{\Delta V}{V_o}\right) = \left(\frac{X}{2D_o}\right)^2 = \frac{3\gamma_s t}{2\eta D_o}$$

(which was later corrected to reflect another factor of two in the denominator of the last term [75EXN,84SCH1]) for the initial stage of sintering and,

$$\tau = \frac{4}{3} \frac{\eta D_o}{\gamma_s}$$

for the second and final stage. In the above equations,  $\Delta L/L_o$  is the initial rate of shrinkage,  $\Delta V/V_o$  is the volume shrinkage,  $X$  is the sphere contact area diameter,  $\tau$  is the time required to close off discrete porosity,  $D_o$  is the initial particle diameter (assuming a uniform spherical approximation),  $t$  is the isothermal sintering time,  $\eta$  is the viscosity of the sintering material, and  $\gamma_s$  is the surface tension of the glass powder [45FRE,88REE]. In the Frenkel model the first stage involves volume shrinkage of packed particles, as well as increasing interparticle contact. The first stage ends with the

formation of enclosed, residual pores. The second stage begins with a matrix of enclosed pores, and predicts sintering behavior until maximum density is achieved [45FRE]. The mathematical assumption, used by Frenkel, in the first stage equation has since been shown to be incorrect for volume shrinkages of greater than 10% [84SCH1]. However, said relation has been found to model the viscous sintering process well beyond 10V% densification. This is probably the result of unknown factors which tend to offset Frenkel's error [84SCH1].

Later, Mackenzie and Shuttleworth contributed to viscous sintering theory by modelling the final stage of sintering using a pressure balance relation [49MAC]. The Mackenzie-Shuttleworth (MS) model considers the effect of gas entrapment, in closed porosity, upon the rate of densification in the final stage of viscous sintering. The MS model predicts that the sintering rate of an amorphous bed of particles, depends upon the net summation of pressure differences resultant from the combination of the negative pressure, exerted by trapped gas, and the hydrostatic sintering pressure, resultant from surface curvature. According to the MS theory, the rate of densification of an amorphous matrix of monosized, discrete pores may be determined by the relation,

$$\frac{d\rho}{dt} = \frac{3}{2} \left( \frac{4\pi}{3} \right)^{\frac{1}{3}} \frac{\gamma_s n^{\frac{1}{3}}}{\eta} (1-\rho)^{\frac{2}{3}} \rho^{\frac{1}{3}}$$

where  $\rho$  is the density of the compact relative to the theoretical density of the material,  $\gamma_s$  is the surface tension of the material,  $\eta$  is the viscosity of the material, and  $n$  is the number pore density [49MAC]. With manipulation of this relation (i.e. integration from green density to theoretical density to determine isothermal sintering time, then inversion to solve for  $\rho$  as a function of reduced time), the compact relative density may be plotted as a function of reduced time, where



reduced time is given by the relation,

$$K=Reduced-Time=\frac{\gamma_s n^{\frac{1}{3}}}{\eta} (t-t_o) .$$

Figure 2.24 illustrates the rate of sintering predicted by the MS model. The MS model is applicable to viscous sintering materials, having microstructures which contain discrete, spherical pores, providing that the fields of flow, surrounding each of the pores, do not interact significantly with one another (i.e. usually at or above 90% of theoretical density) [84SCH1].

The MS model was the first to introduce a theory which, when modified, can account for pore expansion or bloating. Bloating of closed pore materials may occur via either gas dissolution-evolution processes or by Ostwald ripening.

The glass matrix will dissolve gases present in the sintering atmosphere and may later evolve said gases, depending upon the gas solubility equilibrium (which changes with temperature, etc.). Gas dissolution-evolution is a kinetic phenomenon as well. Therefore, the actual conditions that result in bloating, via this mechanism, are complex. Kiparisov and Levinskij have modelled gas dissolution-evolution bloating using a model which considers the dynamic balance between the gas existing in a pore and that dissolved in the glass matrix [79KIP]. Generally, less soluble sintering atmospheres (i.e. N<sub>2</sub>, air, SO<sub>2</sub>, Cl<sub>2</sub>, etc.) will increase the amount of bloating observed, while more soluble gases (i.e. H<sub>2</sub>, O<sub>2</sub>, etc.) will allow the elimination of porosity, because the pore gases dissolve into the glass matrix. Subsequently, bloating is reduced [88REE].

Ostwald ripening theory states that pores, below a critical size, will shrink, while pores above a critical size will expand (i.e. the larger pores grow at the expense of the smaller ones) [73KUC]. In the case of closed pore expansion, this effect is further augmented, since

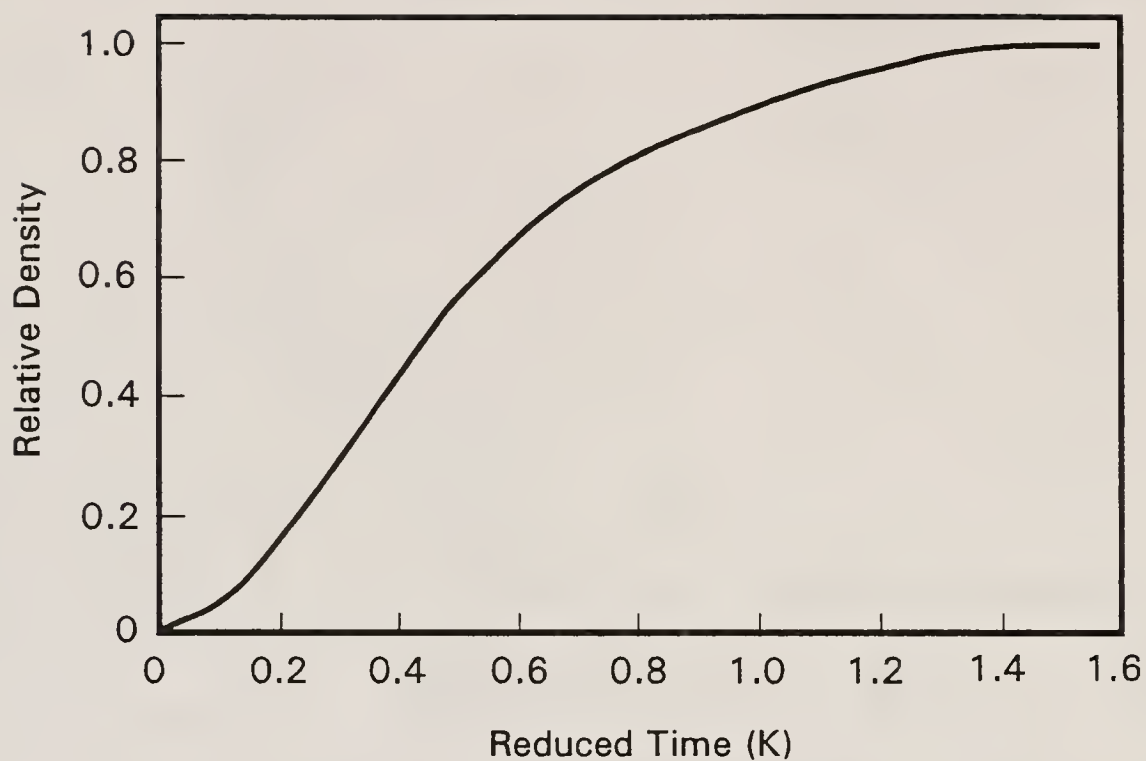


Figure 2.24

Densification of a viscous material, with respect to reduced time, as predicted by the Mackenzie-Shuttleworth sintering model [49MAC]

the sintering (or pore closure) potential is reduced as surface curvature is reduced. A constant volume of entrapped gas will have a constant outward pressure. Thus, pores having low surface area to volume ratios (i.e. relatively low sintering potentials) will tend to expand.

Scherer later proposed a more advanced model of viscous sintering [77SCH1]. Realizing that the MS model was not accurate during the initial stages (i.e. before pore closure) of sintering, Scherer devised a model based upon a novel microstructure of intersecting cylinders, of length  $L$  and diameter  $A$ , interconnected upon a cubic lattice (see Figure 2.25). Said structure is totally open, and thus, appropriate for the initial stages of sintering, even though it bears little resemblance to typical packed powder structures. If one imagines spheres placed at the interconnections of the cylinders, the structure resembles that of simple cubic packing, however. The model was found to be applicable for continuous, interconnected pore structures (that are throatless), in sintering situations prior to pore closure [77SCH2,85RAB]. Scherer determined that the limit of this structure (i.e. the onset of pore closure) occurs at a value of  $A/L$  of 0.5. This was found to occur at a corresponding relative density of 94.2% [77SCH1,85RAB]. Scherer then combined the cubic array of cylinders model with the MS model (at theoretical densities above 94.2%) using the assumption that

$$n = \left( \frac{L_o^3 \rho_o}{\rho_T} \right)^{-1}$$

where  $n$  is the pore number density,  $L_o$  is the unit cylinder cell length,  $\rho_o$  is the initial (green) density, and  $\rho_T$  is the theoretical density of the material. Using mathematical manipulation similar to that involved in the MS model, Scherer's model may be directly compared with the MS model. However, the reduced time, as used in the Scherer model of viscous sintering, is different from that used in the MS model, and is

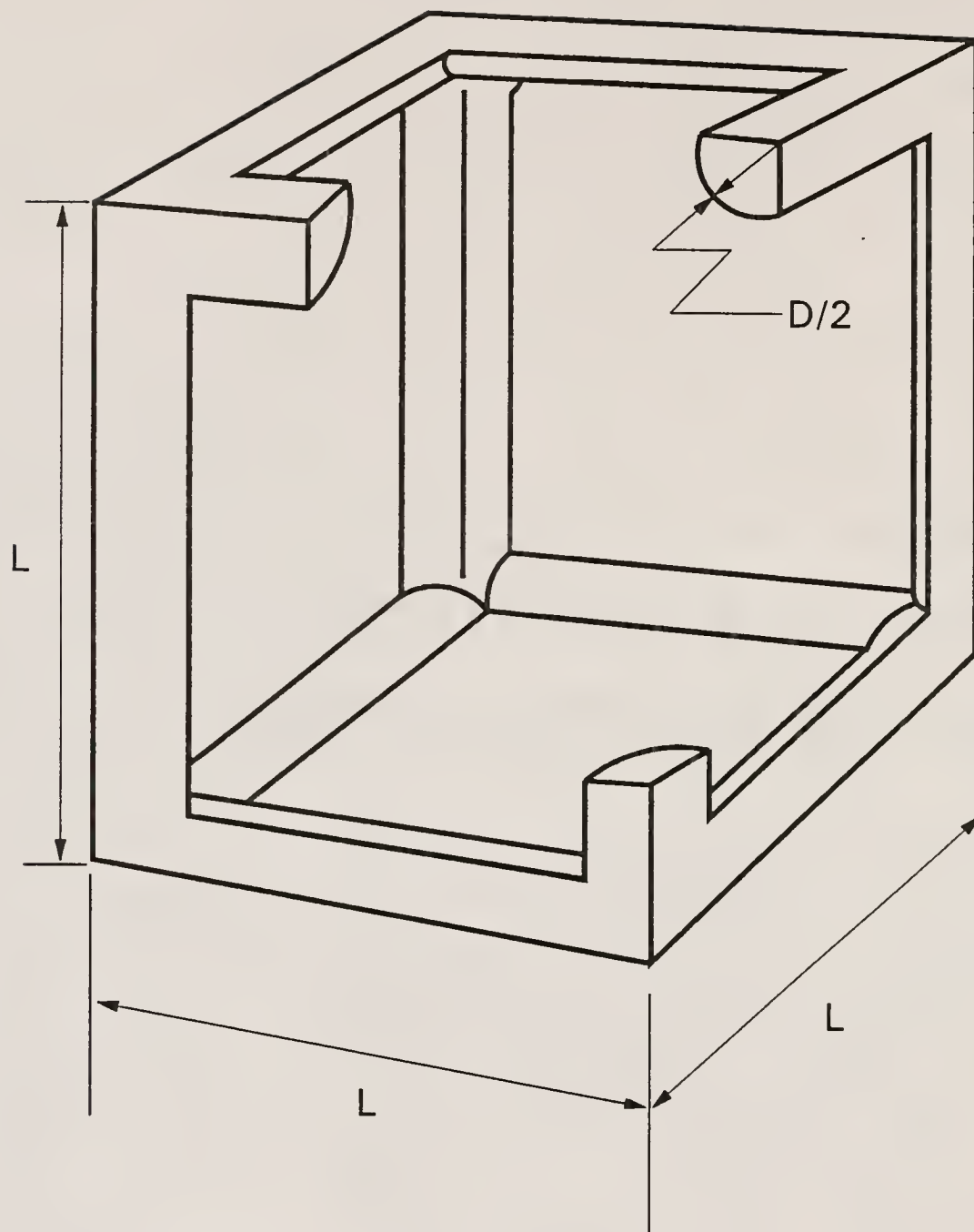


Figure 2.25

Basic cell model, of cylinders of length  $L$  and diameter  $D$ , and interconnected in a cubic arrangement, used in the Scherer viscous sintering model [77SCH1] (later, other cell configurations were introduced [91SCH3])

described by the relation,

$$K=Reduced-Time=(\frac{\gamma_s}{\eta L_o})(\frac{\rho_s}{\rho_o})^{\frac{1}{3}}(t-t_o)$$

where  $\rho_s$  is the theoretical density of the material,  $\rho_o$  is the initial density,  $\eta$  is viscosity,  $\gamma_s$  is the surface tension,  $L_o$  is the initial cell length of the cylinders,  $t$  is the time, and  $t_o$  is time at the beginning of the experiment.

Figure 2.26 compares the MS and Scherer models. In order to superimpose the two relations, it was necessary to derive a corrected reduced time. The corrected reduced time is determined by the relation,

$$Corrected-Reduced-Time=(\frac{\gamma_s n^{\frac{1}{3}}}{\eta})(t-t_f)$$

where  $t_f$  is the time at which the material densifies to theoretical density [84SCH1]. It is evident from Figure 2.26 that the Scherer model has a low density "tail" that is not given by the MS model and is thus more realistic. Both models are valuable to experimentalists in that the actual sintering time may be compared to the reduced time at a specified relative density. A plot of reduced time as a function of relative density, as a function of isothermal sintering time as a function of relative density, should yield a linear relation, having a slope equal to the reduced time constant (K) [77SCH1,84SAC2,85RAB,90VOR]. From the slope value, either the material surface tension, or the material viscosity may be determined, if either is known. It is also necessary to know one microstructural parameter of the green material. In the case of the Scherer model, it is necessary to determine  $L_o$ , and in the MS model,  $n$  must be known.  $L_o$  may be determined via Hg porosimetry, with the caveats mentioned in section 2.4.3 above.

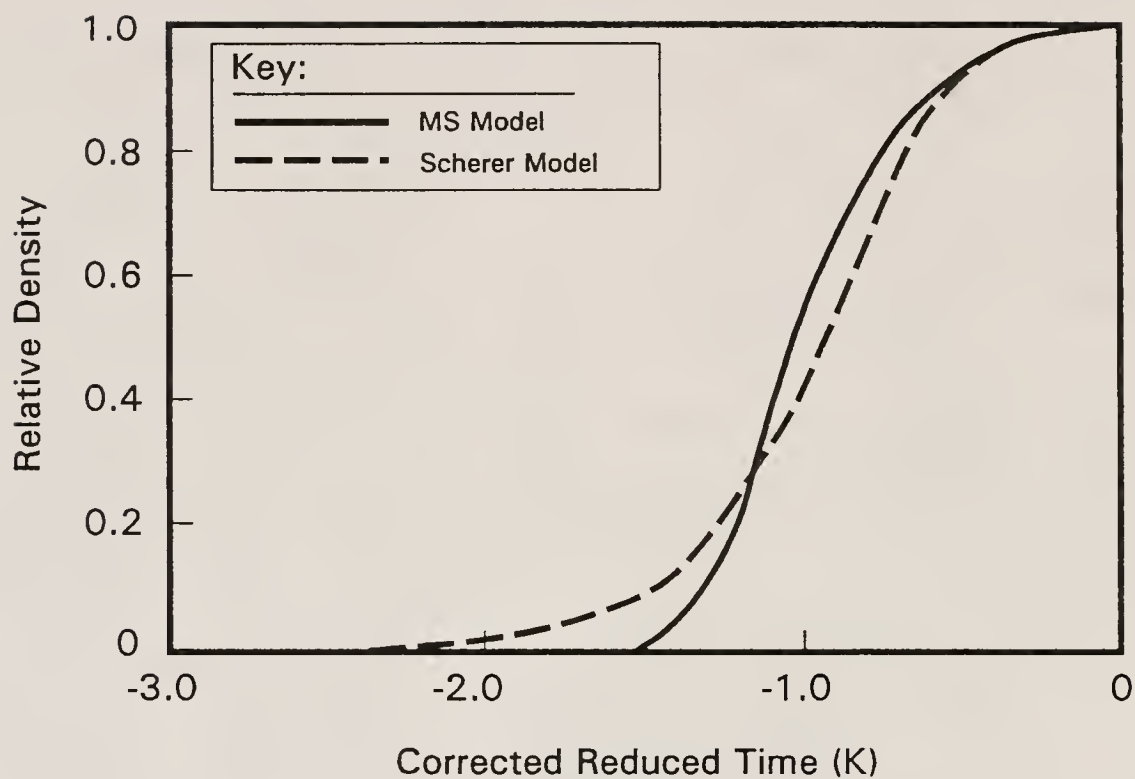


Figure 2.26

Comparison of the MS and the Scherer viscous sintering models (relative density is plotted as a function of corrected reduced time, K) [77SCH1]



To a first approximation,  $L_0$  may be (and has been) equated with the median pore channel diameter [77SCH2,84SAC2,90VOR]. In order to determine the number density of porosity ( $n$ ), which is necessary to determine either  $\gamma$ , or  $\eta$ , from  $K$ , when the MS model is utilized.

The Scherer model (and in several cases, the MS model) has been applied to silica, in the forms of flame-hydrolysis preforms, and gel monoliths, as well as to a phase separated and differentially etched, high silica glass (Corning Code 7930 Porous Vycor<sup>R</sup>) [77SCH2].

Said model has also been somewhat successfully expanded to the characterization of the sintering of packed spherical powders [84SAC2,90VOR].

The Scherer model has also been modified for different situations, including various pore structures and configurations [91SCH3,91SCH4], various pore size distributions [77SCH3,84SCH2], uniaxial load [86SCH], and sintering on a rigid substrate [85SCH2]. Bordia and Scherer have also introduced models that attempt to predict sintering behavior in materials that are constrained (either internally, or externally), through the utilization of self consistent models, based upon the constitutive equations [87SCH3,88BOR,88BOR2,88BOR3,88SCH2,91SCH2,91SCH3,91SCH4], some of which will be discussed, where appropriate, below.

Many other sintering models exist as well. Most are based upon some variation of the above models however. In fact, Scherer proved that the Frenkel, MS, and cylinder models predict viscous densification kinetics that are similar to the extent of being experimentally indistinguishable from one another [84SCH1]. Experimental research in the area of sintering is usually quite difficult, due to the various competing transport phenomena, etc., involved. Indeed, there is a great deal of debate as to which experimental methodology(ies) is(are) best for investigating sintering kinetics [73JOH]. Some researchers have investigated near-ideal systems [84SAC1,84SAC2,87CLA,90VOR,etc.], while

others have proposed increasingly complex models or modifications of basic models.

#### 2.5.2.1 Viscous Sintering of Real Systems

Real systems of particles may deviate greatly from the above viscous sintering models. Sintering may be expedited or retarded if the viscosity of the glass changes during heat treatment. Water vapor in the sintering atmosphere, will tend to enhance densification initially due to a reduction in the viscosity of the glass [64HET,82BAR,85SCH,88REE]. Inherent water in an amorphous material will also enhance viscous sintering. Specifically, this has been observed in sol-gel derived  $\text{SiO}_2$  powders, where it has been found that the removal of inherent hydroxyls increases viscosity during sintering, thus resulting in an initial enhancement in sintering kinetics, that fades with heat treatment time [90VOR]. When significant crystallization occurs during viscous sintering, the sintering process may be severely retarded. This is generally regarded as a hinderance, since it is usually desirable that the fired material be fully dense. Residual hydroxyls, as well as alkali and other impurities, may also enhance crystallization kinetics during viscous sintering [59BRO,66WAG,85RAB]. When the sintering heat treatment is nonisothermal, the effect of heating rate upon crystallization is also of concern [89PAN]. In short, there are many factors which effect viscous sintering and sintering kinetics. The effects of initial microstructure are discussed below.

##### 2.5.2.1.1 Effects of Microstructure

The ideal microstructure for sintered powder compacts is that of uniform sized spheres, close packed in an ordered fashion (i.e. all pore channels are identical, or simple cubic packing). There are several reasons why most sintering models use this microstructure. In a uniform packing having universally identical pore channels, all spheres (except

for those at the compact surface) have the same number of contacts per sphere. Furthermore, in a close packed arrangement, no particle rearrangement occurs during sintering, since the force distribution around each sphere in the interior of the compact, is homogeneous. Finally, the spherical shape of powders guarantees that the surface energy distribution is homogeneous throughout the ideally packed powder. In the above situation the pore size distribution is very sharp and decreases continuously throughout the sintering process. This has been experimentally confirmed in compacts of uniform spherical powders, having random close packing [90VOR].

Most powder compacts are far from the above ideal, however. In most situations, it is desirable to start with a green compact having greater density than that typical of the above situation (i.e. a PE greater than 0.524). In fact, it is usually not possible to arrange monosized, microscopic, spherical particles in a simple cubic arrangement, due to nesting, etc. The compaction method used also introduces packing heterogeneities which significantly affect sintering [88REE,88ROO]. Furthermore, most powders have constituent particles which are neither spherical nor monosized. Frequently, said constituent powders have a significant amount of agglomerates that further affect sintering. Thus, it is important to be able to model and predict sintering of nonideal powder compacts.

The particles in an amorphous powder, formed by traditional techniques (i.e. crushing, grinding, and milling, etc.), are usually conchoidal in nature and, thus, deviate from sphericity. The nonuniformity of this structure produces heterogeneities in surface curvature that cause differential sintering potentials. The nonuniform shape of the powders also affects the number of interparticle contacts, as well as the packing efficiency of the powder compact. Sintering of conchoidal amorphous powders tends to be accelerated, in the initial stages of sintering, due to interparticle contacts at sharp regions of

the particles, and to the greater net surface curvature (i.e. higher surface area to volume ratio) of the nonspherical powders. Cutler and Henrichsen investigated the effect of particle geometry upon the sintering kinetics of amorphous powders [68CUT]. They found that the sintering rate could be accelerated as much as five fold by using crushed and sieved glass powders.

Using crushed glass powders is not a panacea, however. As mentioned above, both packing efficiency (PE) and packing uniformity are adversely affected when nonspherical particles are used. Therefore, the later stages of sintering should be retarded when using traditional powders. Powder agglomerates also retard later stage sintering. Furthermore, in nonideal packing situations, particles will rearrange during sintering in order to minimize localized stresses [73EXN,75EXN,89SCH3]. The above factors may result in localized sintering without overall densification [73EXN].

Traditional glass powders typically have a particle size distribution as well. This increases packing efficiency, but produces compacts having comparatively wide pore size distributions [85PAT]. Said pore size distributions affect the evolution of pore structure during sintering. Small pores tend to shrink and disappear while large pores either shrink more slowly or not at all. In the final stage of sintering, larger pores may even grow, as discussed above.

Evolution of the mean pore size will reflect this relationship. If the mean pore size constantly increases during sintering, the smaller pores are reduced at a much greater rate than the larger pores. This behavior is characteristic of a bimodal pore size distribution, and will be discussed below. If the mean pore size constantly decreases, the difference in pore reduction rate is relatively insignificant and the sintering may be characterized by a single pore size, instead of a pore size distribution [77SCH3]. In the sintering of traditional powders,

the mean pore size usually will either initially decrease, then increase, or will constantly increase [79WHI,88REE].

Kingery and Francois introduced the concept of a critical pore size in relation to sintering kinetics of crystalline materials [76KIN2]. They stated that there is a critical pore size to mean particle size ratio, above which, pore size reduction is retarded.

Zheng and Reed later expanded upon this work and postulated that pores could be categorized into one of two classes, pores smaller than a critical size and pores larger than a critical size [89ZHE]. This quasi-bimodal model states that the subcritical sized pores affect the ultimate sintering shrinkage while the supercritical porosity controls the ultimate density of the sintered material.

Zheng and Reed further proposed that the critical pore size to mean particle size ratio is approximately 0.5 [89ZHE].

Zhao and Harmer also expanded upon the theories of Kingery and Francois [88ZHA]. In their experimentation they added large size, included porosity to alumina compacts, through controlled pyrolysis of monosized spherical latex. The latex was added to the compacts during green processing in order to create packed beds of particles having a bimodal pore size distribution. They produced sintering maps for this situation and, using thermodynamic criteria, they concluded that supercritical pores would be eliminated as a result of increasing grain size. Therefore, the critical pore size will continuously increase as a result of grain growth. However, they further concluded that it is not beneficial to augment grain growth for kinetic reasons. It is interesting to note that Zhao and Harmer observed no effect of sintering atmosphere (either soluble  $H_2$  or insoluble  $N_2$ ) upon the removal of supercritical pores [88ZHA].

The above models were all proposed for solid state sintering, and, although the concept of pore size to mean particle size ratio is applicable to viscous sintering, that of grain growth is not.



Scherer expanded his model of cylinders to predict the sintering of glass powders that have a bimodal pore size distribution [84SCH1]. He used the phenomena of localized stresses, due to particle packing and pore size heterogeneities [82EVA,86HSU2], to predict the effect of a bimodal pore size distribution on the sintering behavior of amorphous materials. Scherer stated that the small pores would be subjected to tensile forces, while the large pores would be subjected to compressive forces during sintering. The net result of these forces is to impede sintering of the small pores while enhancing the shrinkage of large porosity in the initial stages of sintering. Figure 2.27 shows the local stresses on each the two size regimes throughout sintering. This effect was determined to be substantial for a large to small pore size ratio of 4. The effect was predicted to increase with increasing large to small pore size ratio.

The sintering of amorphous powders, having bimodal pore size distributions, was also found to be influenced by the relative volume fractions of each of the porosity sizes. Furthermore, it was found that the small pores controlled the sintering rate in the initial stages of sintering, while the large pores dominated the final stages of sintering. Figure 2.28 illustrates the predicted sintering curves for various relative pore volume fractions.

#### 2.5.2.1.2 Viscous Sintering of Glass Matrix Composites Having Nonsintering Inclusions

The viscous sintering of amorphous particulate compacts, having bimodal porosity distributions, is similar to the sintering of amorphous powder compacts that contain nonsintering inclusions, in that both examples are subtopics of the field of constrained sintering. The densification rate of compacts, containing rigid inclusions, is retarded in comparison to that of the pure glass. This is a result of the hydrostatic tensile forces that the inclusions place upon the glass matrix during the sintering process. Said forces are quite analogous to



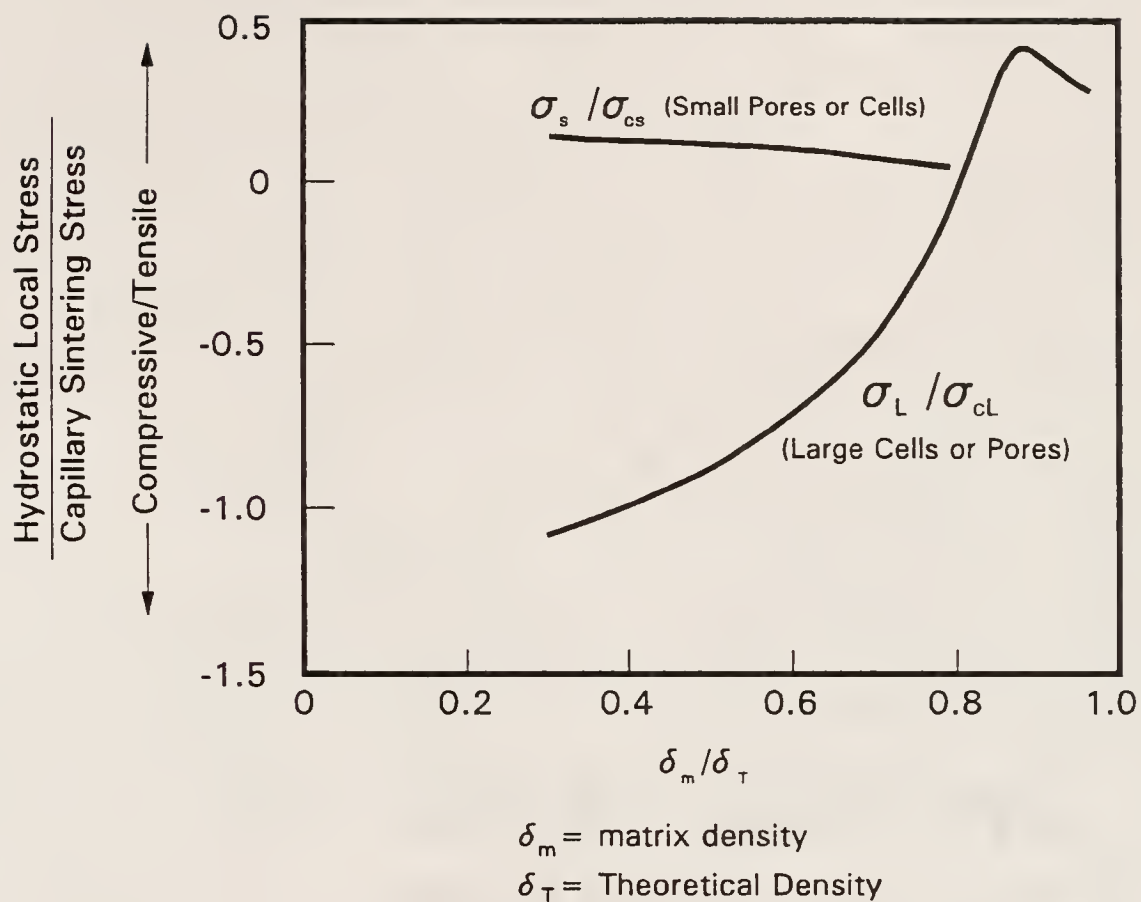
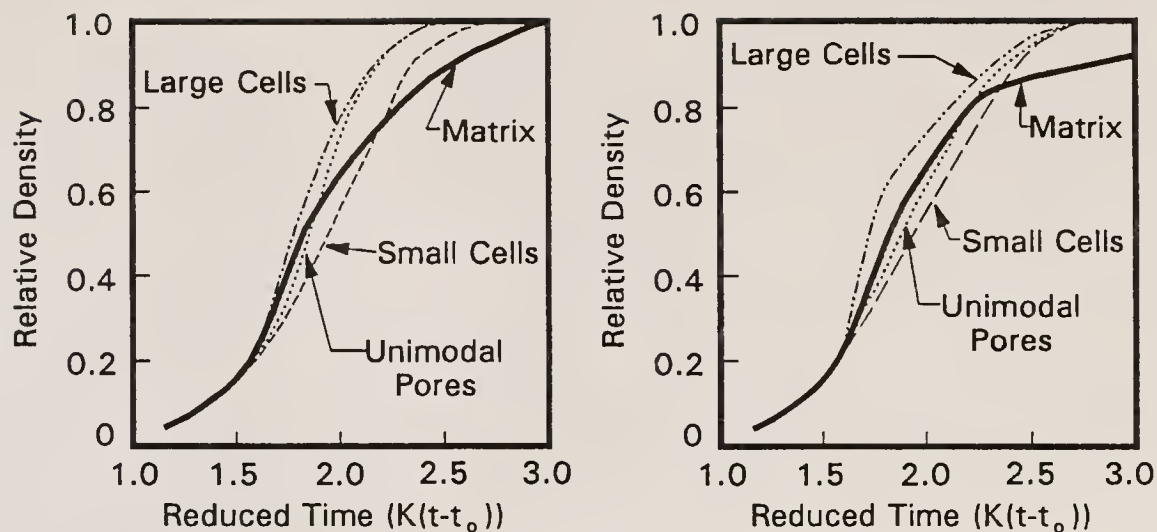


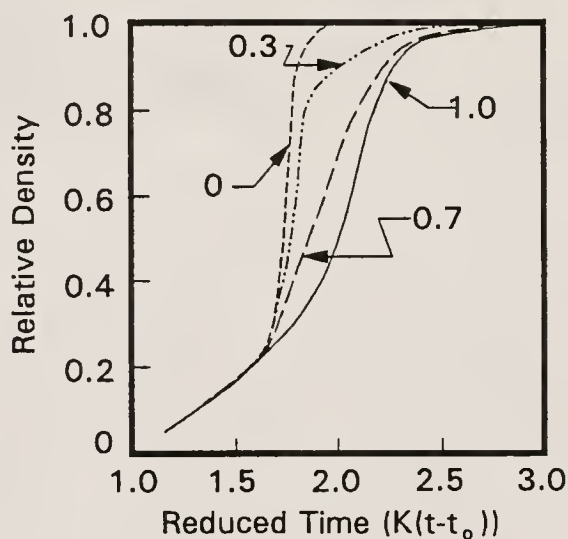
Figure 2.27

Stresses imposed upon large and small pores during viscous sintering ( $\sigma_L$  and  $\sigma_s$  are imposed stresses,  $\sigma_{cL}$  and  $\sigma_{cs}$  are capillary stresses) [84SCH1]



A. Initial Relative Volume  
Fraction of Small Pores = 0.3

B. Initial Relative Volume  
Fraction of Small Pores = 0.7



C. Initial Relative Large Pore  
Volume Fraction Varied From 0 to 1

Figure 2.28

Illustration of sintering curves modelling viscous sintering of bimodal pore size distribution compacts, having various relative volume fractions of pore sizes [84SCH1]

those in large pores in amorphous powder compacts, containing bimodally sized pores, mentioned above. There are two exceptions, however. First, the nonsintering inclusions are hard and, thus, are not influenced by hydrostatic compressive forces. This is in contrast to the behavior of pores subjected to hydrostatic stresses. Second, when nonsintering inclusions interact, they can form rigid, contiguous structures (at volume fractions above the percolation threshold) that drastically hinder, or even halt, the sintering process. When pores interact, they combine with one another, and no such rigid, contiguous network can form at any pore volume fraction.

When nonsintering rigid inclusions (NSRIs) interact with one another, they may stick to each other or slide over each other, depending upon whether or not the glass matrix material wets the NSRI surfaces. If the NSRI particles stick to each other (either because of surface roughness, or due to interparticle reaction) local hydrostatic stresses will be enhanced due to viscous drag, thereby, greatly retarding the sintering process. If the volume fraction of NSRIs is significantly above the percolation threshold, a rigid network will form and sintering will cease.

Conversely, if the NSRI particles are wetted by the glass matrix, interacting NSRIs will not form a rigid network until well above the percolation threshold (i.e. 30 to 50 V%) [91SCH2]. This limit has been approached or exceeded in the case of carefully prepared, glass coated NSRIs. Sacks, et. al have produced fully dense glass-Si<sub>3</sub>N<sub>4</sub> (NSRI) composites, containing 40V% or greater ceramic filler [91SAC1].

Scherer has also extended his viscous sintering models (both the cylinder and the self consistent models, as well as a spherical composite model) for the situation of sintering of amorphous glass powders, containing NSRIs [87RAH1,87SCH3,88BOR3,88SCH2,91SCH2,91SCH3,91SCH4]. The extension of said models, however, has been limited to the case of NSRIs that bond together when they contact. In real systems,

this is frequently not the case. Usually NSRIs are wetted (at least somewhat) by the matrix glass. Therefore, said sintering models, are accurate only below the percolation threshold [87RAH1,91SCH2,91SCH3,91SCH4]. For comparison, the rule of mixtures also gives acceptable results at volume fractions of NSRIs below approximately 10V% [87RAH1,91SCH2,91SCH3,91SCH4]. Investigation of the situation of sintering under conditions of NSRI wetting is currently underway, however [91SCH3].

Ewsuk has recently proposed another model to predict the sintering behavior of glass powders that contain NSRIs [90EWS,91EWS]. Ewsuk investigated ceramic filled glass (CFG) composites that densify via nonreactive liquid phase sintering (NLPS). Ewsuk stated that NLPS is a three stage process that describes the densification of CFG composites by a combination of glass particle redistribution, NSRI grain rearrangement, and viscous flow. He postulated that the NLPS rate is a function of pore size, filler particle size, filler concentration, and a combination of glass properties, including glass viscosity, wetting angle, and surface tension. Ewsuk's model predicts densification rates for the final stage of sintering, where densification is controlled by the remnant pores, as well as the surface tension of the glass and the viscosity of the CFG composite material. He utilized Eiler's relative viscosity model for concentrated suspensions to estimate the CFG composite viscosity. Ewsuk then constructed sintering maps that predict critical filler concentrations, below which dense composites may be produced (for a specific composite viscosity, and a predetermined sintering time period).

Ewsuk successfully modelled final stage sintering of an alumina-filled borosilicate glass composite system, using the above model. Said model predicts that fully dense composites could be produced having NSRI concentrations as high as 51 V% [90EWS,91EWS].

## 2.6 Dielectric Theory

Dielectric theory is the investigation of the polarization characteristics of insulating materials. The field may be divided into two regimes, linear and nonlinear dielectric materials. This section discusses linear dielectrics. The different polarization mechanisms, and their frequency dependence, are discussed. A description of dielectric loss and loss tangent is included. Various models, used to predict the dielectric constant of composite materials as a function of porosity and/or composite composition are discussed. Methods of measuring dielectric constant are also discussed.

### 2.6.1 Dielectrics Materials

Dielectric materials respond to an applied electric field by exhibiting a short range motion of internal charge carriers (i.e. internal polarization) [90HEN]. The absence of long range electrical conduction necessitates that dielectric materials be electrical insulators. Linear dielectric materials exhibit a linear polarization response to applied electrical fields, while nonlinear dielectric materials do not. Some materials may exhibit both linear and nonlinear dielectric behavior, depending upon crystal structure, etc. [90HEN].

Dielectric materials may be characterized by several factors, such as dielectric constant and dielectric loss (and the effect of electrical field frequency upon both), as well as dielectric conductivity and dielectric breakdown strength. The selection of dielectric material for an application, is usually based upon the above materials values. As mentioned in Chapter 1, favorable candidates for electronic packaging materials should have a minimized dielectric constant and dielectric loss (that are stable over all frequencies of use) as well as dielectric conductivity, while exhibiting maximized dielectric breakdown strength.

There are four mechanisms which give rise to polarization (i.e. short range motion or alignment of internal charge carriers), electronic polarization, atomic or ionic polarization, dipole or orientational

polarization, and interfacial or space charge polarization. Figure 2.29 provides an illustration of each type of polarization mechanism. These polarization mechanisms vary greatly in magnitude. Similarly, the electrical field frequency ranges, in which each of the polarization mechanisms is operational, also vary.

Interfacial polarization is a relatively low frequency phenomenon (i.e. below 1000 Hz), which may have a relatively large magnitude. It is the result of charge carriers amassing at either blocking electrodes or grain boundaries, etc. Interfacial polarization has the longest range of the polarization mechanisms, and is thus the slowest or lowest frequency phenomenon involved in ceramic dielectric materials.

Dipole polarization results from the perturbation and subsequent rearrangement of either ionic or molecular dipoles, in an electric field, and against thermal randomization forces. This polarization mechanism may be separated into two categories, Stevels deformation polarization and spontaneous dipole polarization [90HEN].

Stevels deformation polarization involves the oscillation of molecular bonds about an equilibrium position when subjected to an oscillatory, or alternating current (AC), electric field. Stevels deformation polarization is important in silicate glasses, since the Si-O-Si bond exhibits an asymmetry, which results in a molecular dipole moment, when subject to AC fields [90HEN]. Oscillation of hydroxyls in Si-OH bonds in silicate glasses may also result in a Stevels deformation dipole polarization [90HEN]. Both mechanisms are operant to relatively high frequencies (i.e.  $10^{11}$  to  $10^{12}$  Hz).

Spontaneous polarization involves the spontaneous arrangement of dipoles into one of two equilibrium positions. This polarization mechanism is responsible for the nonlinear dielectric behavior exhibited in ferroelectric materials, where the effect is coherent over large domains and has a potentially large magnitude (i.e. leading to dielectric constant values as great as  $10^4$  or more [90HEN]).



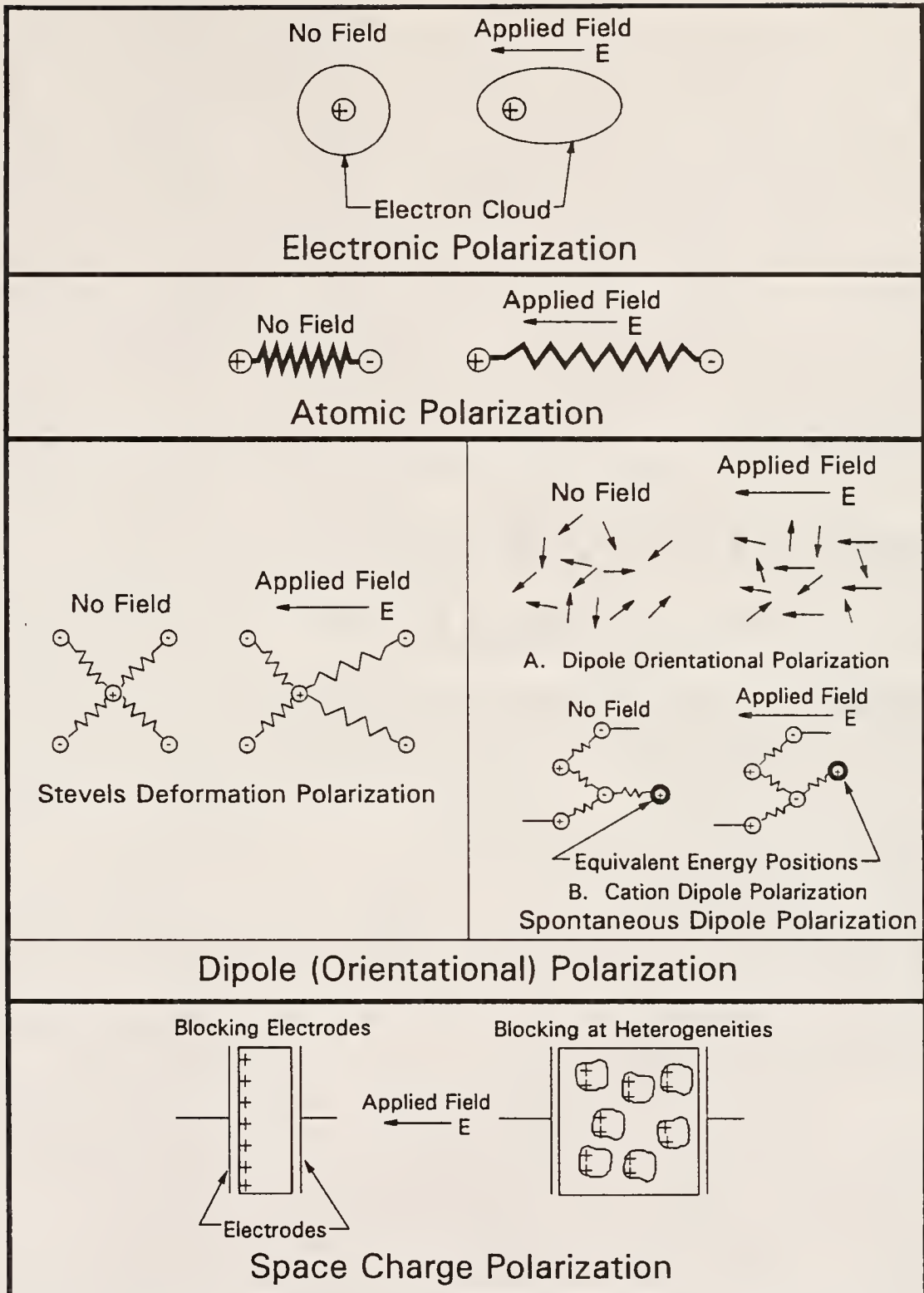


Figure 2.29

Illustration of polarization mechanisms operant in dielectric materials [76KIN1,90HEN]

In linear dielectric materials spontaneous dipole polarization results from the motion of ions between equivalent positions within the atomic structure. Said ionic motion occurs continuously, as well as randomly, in the material at appreciable temperatures (i.e. around room temperature). When an electric field is applied, the random nature of this process is statistically skewed in the direction of the electric field, thereby causing a net polarization of the material. An appreciable distance is involved in these ionic jumps. Thus, spontaneous dipole polarization is a relatively low frequency phenomenon, occurring at frequencies below  $10^6$  Hz at room temperature).

Atomic or ionic polarization involves the displacement of ions in a molecule, with respect to one another, under an applied electric field. This is a high frequency phenomenon, operating up to frequencies of  $10^{13}$  Hz [76KIN1,90HEN]. At the resonant frequency of the bonds, the polarizability increases greatly, causing a dispersion in polarization behavior. The frequency at which said polarization increase occurs depends upon the masses of the ions involved, the bond strengths between the ions and the configuration of the atomic or ionic molecule of interest. Furthermore, the frequency broadness of the resonant polarization will increase as the complexity and number of both the atomic constituents and the interatomic bonds increases.

Electronic polarization is the highest frequency mechanism of polarization. It involves the deformation of the electron clouds, that surround each atom, in the atomic structure of a material. This polarization mechanism is responsible for the index of refraction at visible frequencies. Electronic polarization can operate up to frequencies of  $10^{15}$  Hz [76KIN1,90HEN].

Figure 2.30 illustrates the generic frequency dependence of each polarization mechanism at room temperature. It should be noted that each of the lower frequency polarization mechanisms will shift to higher frequencies as the temperature of the materials is increased.

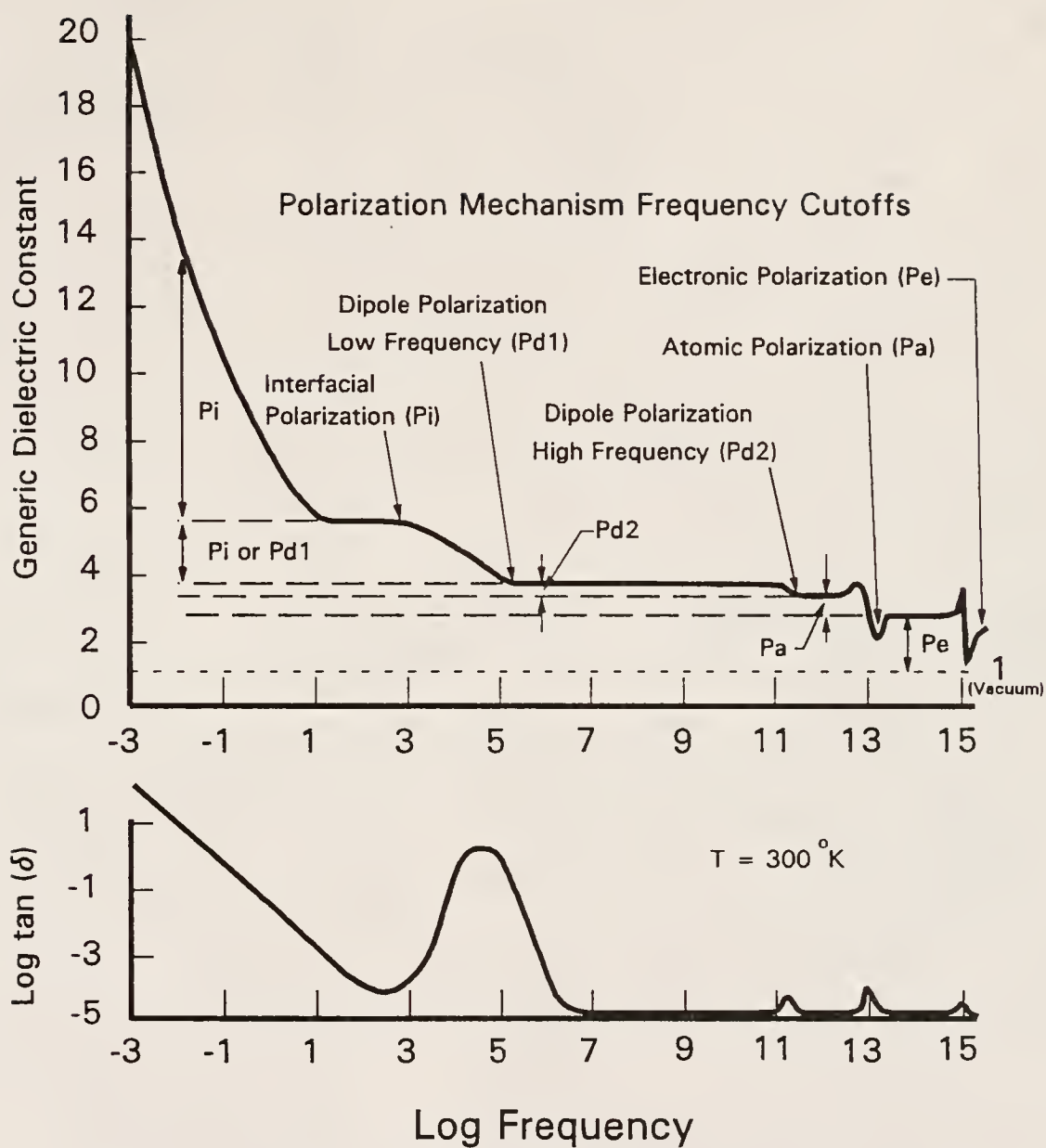


Figure 2.30

Illustration of the contribution of polarization mechanisms to the generic dielectric constant and loss tangent as a function of AC electric field frequency [90HEN]

Temperature affects dielectric loss and conductivity of ceramic materials (especially glasses) similarly. Excellent and exhaustive discussions of dielectric properties of materials may be found in available literature [76KIN1,90HEN].

### 2.6.2 Measurement of Dielectric Properties

The dielectric constant of a material ( $K$  or  $K^*$ ) is a measure of the electrical polarizability of said material. Dielectric constant is related to polarizability through the Clausius-Mosotti relation:

$$\frac{K^*-1}{K^*+2} = \frac{1}{3\epsilon_0} [N_e\alpha_e + N_a\alpha_a + N_d\alpha_d + N_i\alpha_i]$$

where  $K^*$  is the complex dielectric constant,  $\epsilon_0$  is the dielectric permittivity of free space ( $8.854 \times 10^{-12}$  F/m),  $N_i$  is the number of dipoles per unit volume of type  $i$  ( $i = e, a, d$ , and  $i$ , for electronic, atomic, dipole, and interfacial polarization mechanisms respectively), and  $\alpha_i$  is the polarizability of the  $i$ th polarization mechanism operant in the material of interest (where  $i$  is explained above). Therefore, the total polarizability of a material may be determined directly from the dielectric constant, where the total polarizability is defined as the summation of the numbers and polarizabilities of each polarization mechanism, for the material of interest.

There are many ways to measure the dielectric constant of a material. Exhaustive discussions of said methods may be found in the literature [54VON,88STOL,88SAE,88SLI,89HEW1,89HEW2,89RIA,89TED,90ANG,90CAN,91SU1,91SU2]. Relative capacitance techniques are most generally used, but are limited to lower frequencies (i.e.  $\leq 20$  MHz) than other, more recently investigated techniques, due to stray capacitances, signal reflectance and device impedance matching problems. For higher frequencies (i.e. into the GHz regime), resonant cavity or time domain

reflectometry (TDR) techniques are usually used [88SAE,89RIA,90ANG,91SU1,91SU2]. For dielectric characterization in the far infra-red (FIR) frequency regime, Kramers-Kronig analysis of reflectance spectroscopy has been utilized [88SLI]. Indeed, at optical frequencies, the dielectric constant is simply the square of the index of refraction, since electronic polarization is the only polarization mechanism operant [76KIN1].

For this study, dielectric properties investigations were limited to relative capacitance techniques due to limited equipment availability. However, since most K values are reported at 1 MHz, and since K generally either remains constant or decreases between 1 MHz and the highest frequencies that high performance electronic packaging is subjected to, this is not considered a significant limitation.

Generally, relative capacitance techniques measure dielectric constant by comparing the capacitance of a set electrode geometry, with the dielectric material of interest in place (C) and comparing this capacitance value to that obtained with the dielectric material removed (C<sub>o</sub>). The dielectric constant is found by the relationship,

$$K = \frac{C}{C_o}.$$

There are many variations of relative capacitance techniques and the subject is covered in several publications [54VON,88STO1, etc.].

The best relative capacitance techniques are those that provide a guard electrode to minimize fringing of electrical fields. Methods that utilize fixed (and not applied) electrodes are also better, since they eliminate errors associable with electrode application, electrode area measurement, electrode geometry assumptions, and sample thickness measurement, as well as being more reproducible and easier to use [54VON,88STO1,89HEW1,89HEW2]. Therefore, fixed electrode testing

devices generally provide more data (that is more accurate and reproducible) in less time.

The air gap or non-contacting electrode method fulfills the above criteria [89HEW1,89HEW2]. Figure 2.31 illustrates the air gap method of measuring dielectric constant. Using the air gap technique, the dielectric constant of a material under test (MUT) is determined through the relation,

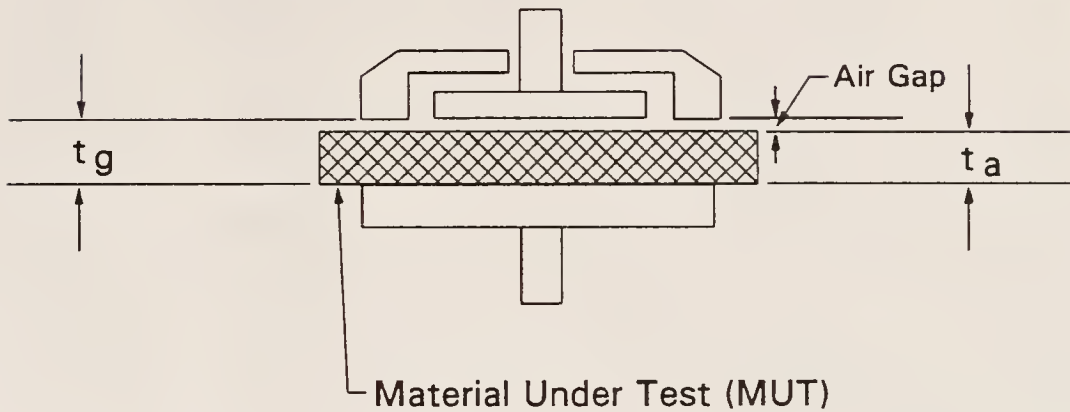
$$K = \frac{1}{1 - \left(1 - \frac{C_o}{C}\right) \times \frac{t_g}{t_{ave}}}$$

where  $C_o$  is the measured capacitance of the device under test (DUT) with the sample removed,  $C$  is the measured capacitance of the DUT with the sample inserted,  $t_g$  is the distance between the fixed electrodes, and  $t_s$  is the average measured thickness of the sample. This technique is quite accurate if the distance of the air gap (i.e.  $t_g - t_s$ ) is held within 10% of the value of  $t_s$  and if the electrodes, as well as circular surfaces of the sample, are made parallel. In this method, the cross-sectional shape of the sample is irrelevant (as long as it is larger than the electrodes) since the electrodes are of fixed size. Using the non-contacting electrode technique, dielectric constants may be measured with accuracy as high as  $\pm 1\%$  while the dissipation factor ( $\tan(\delta)$ ) may be measured with accuracies as high as  $\pm 5\%$  [89HEW1].

It is also desirable to use instrumentation that measures complex impedance, of variable AC electric fields, when measuring dielectric properties so that dielectric loss may also be determined from the shift in phase angle, as described below. Use of said instrumentation also makes it possible to measure dielectric properties as function of applied voltage and frequency.



### 1. Measure Capacitance with Sample Inserted ( $C$ )



### 2. Measure Capacitance with Sample Removed ( $C_o$ )

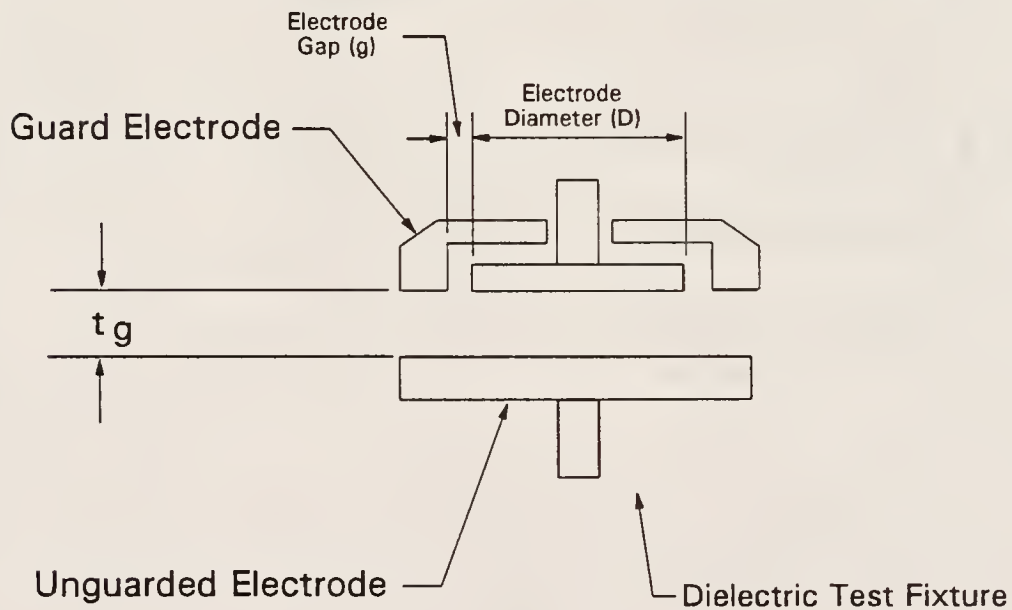


Figure 2.31

Illustration of the air gap or non-contacting electrode technique used to measure material dielectric constant [89HEW1,89HEW2]

The dielectric loss tangent ( $\tan(\delta)$ ) may also be obtained from complex impedance analysis. In a perfectly capacitive material, subjected to an AC electrical field, the voltage-current characteristics are such that the charging current leads the applied voltage by a phase angle ( $\Theta$ ) of exactly  $90^\circ$  [76KIN1]. In a real capacitive dielectric material, this is not exactly the case.

The charging current leads the applied AC voltage by an angle that is less than  $90^\circ$ . The deviation of the voltage-current characteristics of a real material from an ideal capacitive material is given by the loss or phase defect angle ( $\delta$ ), where

$$\delta + \Theta = 90^\circ.$$

Figure 2.32 illustrates the concept of phase defect angle for a real dielectric material when modelled as either a series or a parallel resistance-capacitance (RC) circuit. The tangent of the loss angle is termed the dissipation factor (D) or loss tangent. It can be shown that

$$D = \tan(\delta) = \frac{K''}{K'}$$

where  $K''$  is the imaginary portion of the dielectric constant and  $K'$  is the real portion of the dielectric constant [88ST01]. The complex dielectric constant ( $K$  or  $K^*$ ) may be found via the relation

$$K = K^* = K' - iK''$$

where  $i$  is the square root of  $-1$ . In near perfect dielectric materials,  $\delta$  is very small, and thus,  $K$  is approximately equal to  $K'$ . Furthermore, it may be shown that the dissipation factor may also be determined from the

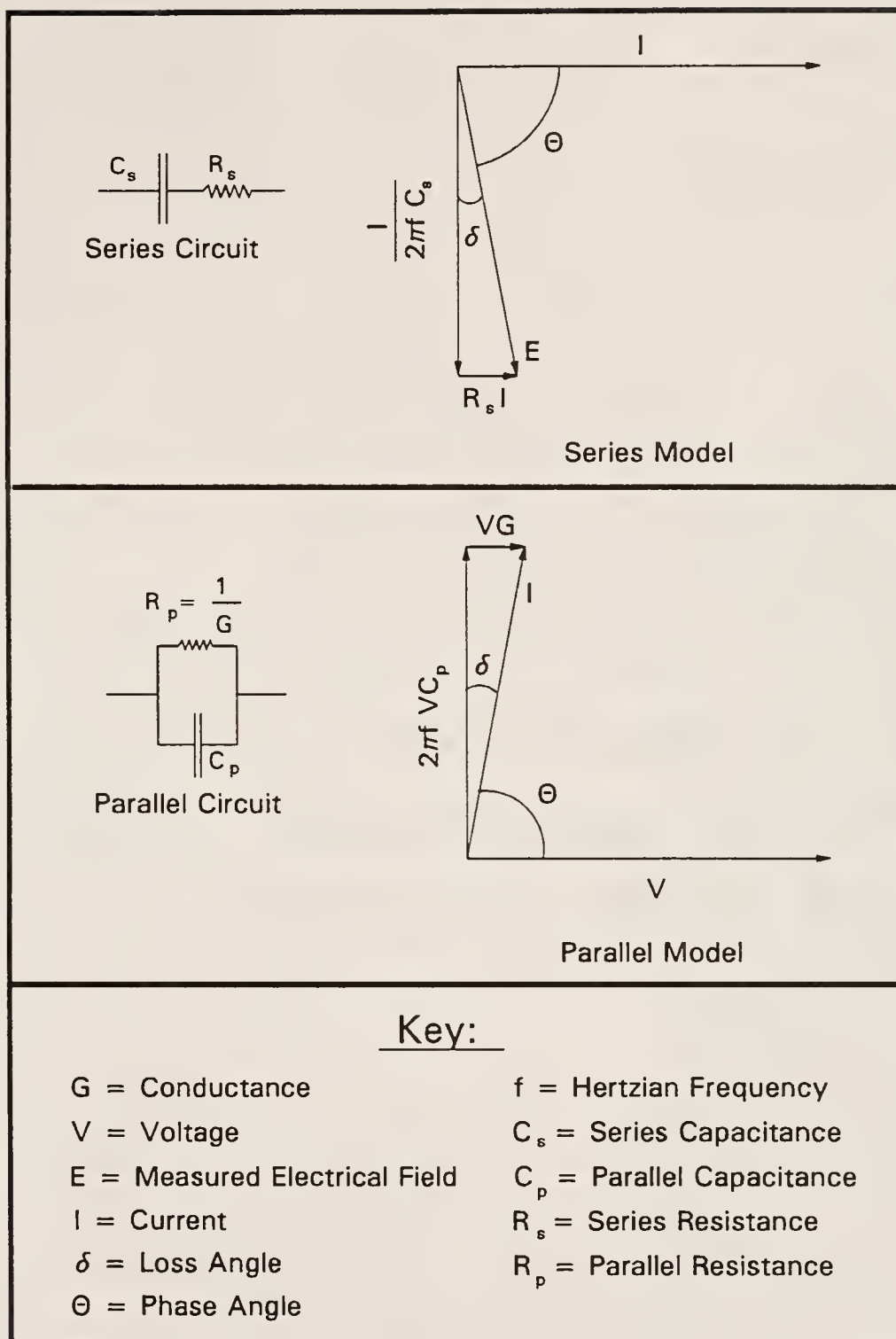


Figure 2.32

Illustration of phase defect angle ( $\delta$ ) in a real dielectric material, using series and parallel RC circuit vector modelling [88AST1]

following relation

$$D = \tan(\delta) = \cot(\Theta) = \frac{X_p}{R_p} = \frac{G}{\omega C_p} = \frac{1}{\omega C_p R_p} = \omega R_s C_s = \frac{1}{Q}$$

where  $X_p$  is the equivalent parallel reactance,  $R_p$  is the equivalent parallel resistance,  $G$  is the AC conductance,  $C_p$  is the equivalent parallel capacitance,  $C_s$  is the equivalent series capacitance,  $R_s$  is the equivalent series resistance,  $Q$  is the quality or storage factor, and  $\omega$  is the angular frequency of the AC field ( $\omega = 2\pi f$ , in a sinusoidal field wave, where  $f$  is Hertzian frequency). As mentioned above, real dielectric materials may be represented by equivalent parallel or series RC circuits. Usually, it is preferable to use the parallel RC circuit model, but the series model may be used in certain situations. The relationships between equivalent series and parallel RC circuit models are

$$C_p = \frac{C_s}{(1+D^2)}$$

for capacitance conversion, and

$$\frac{R_p}{R_s} = \frac{(1+D^2)}{D^2} = 1 + \left(\frac{1}{D^2}\right) = 1 + Q^2$$

for the relationship between equivalent series and parallel resistances [88ST01]. In some cases, more complex circuit models may be used. However, in the situation of near perfect, high  $Q$  materials (i.e.  $\delta \leq 7^\circ$  or 0.1 radians), dielectric properties may be satisfactorily approximated by an ideal capacitor, and a small angle approximation (i.e.  $\delta \approx \tan(\delta)$ ) is valid.

Once  $K'$  and  $\tan(\delta)$  are measured, the loss index or loss factor ( $K''$ ) may be determined from the product of  $K'$  and  $\tan(\delta)$ . The power dissipation factor (PF) may also be determined from the relation,

$$PF = \frac{D}{\sqrt{1+D^2}}.$$

When the dissipation factor ( $D$  or  $\tan(\delta)$ ) is less than 0.1, the PF differs from  $D$  by less than 0.5% [88ST01].

Thus, the dielectric material may be evaluated as an electronic packaging material candidate using the above technique. Dielectric properties should be evaluated either at the temperatures, atmospheres and frequencies of usage, or over as broad a range of these factors as is feasible.

### 2.6.3 Dielectric Properties of Composite Materials

The area of study of dielectric properties of composite materials is very large. A comprehensive overview of the dielectric behavior of heterogeneous systems has been provided by van Beek [67VAN]. Other models (i.e. the Banno and percolation models) are covered elsewhere [83ZAL2,85HSU,87BAN1]. Discussion in this section is limited to composites having constituents that are near perfect insulators, as well as having low  $K$  and  $D$  values. The majority of the available literature involving the modelling of the dielectric constant of porous materials mentions four basic models that may be used to predict  $K$  as a function of pore concentration [86CRO,88GER3,89CAO,89LEA]. In all of these models the size of the constituent components is irrelevant as long as they are small with respect to the sample size.

Said models are the parallel slabs model, the perpendicular slabs model, the Maxwell spherical inclusions model, and the Lichteneker logarithmic model. Figure 2.33 shows the equations involved as well as the microstructures that they model. In theory, these models predict  $K$

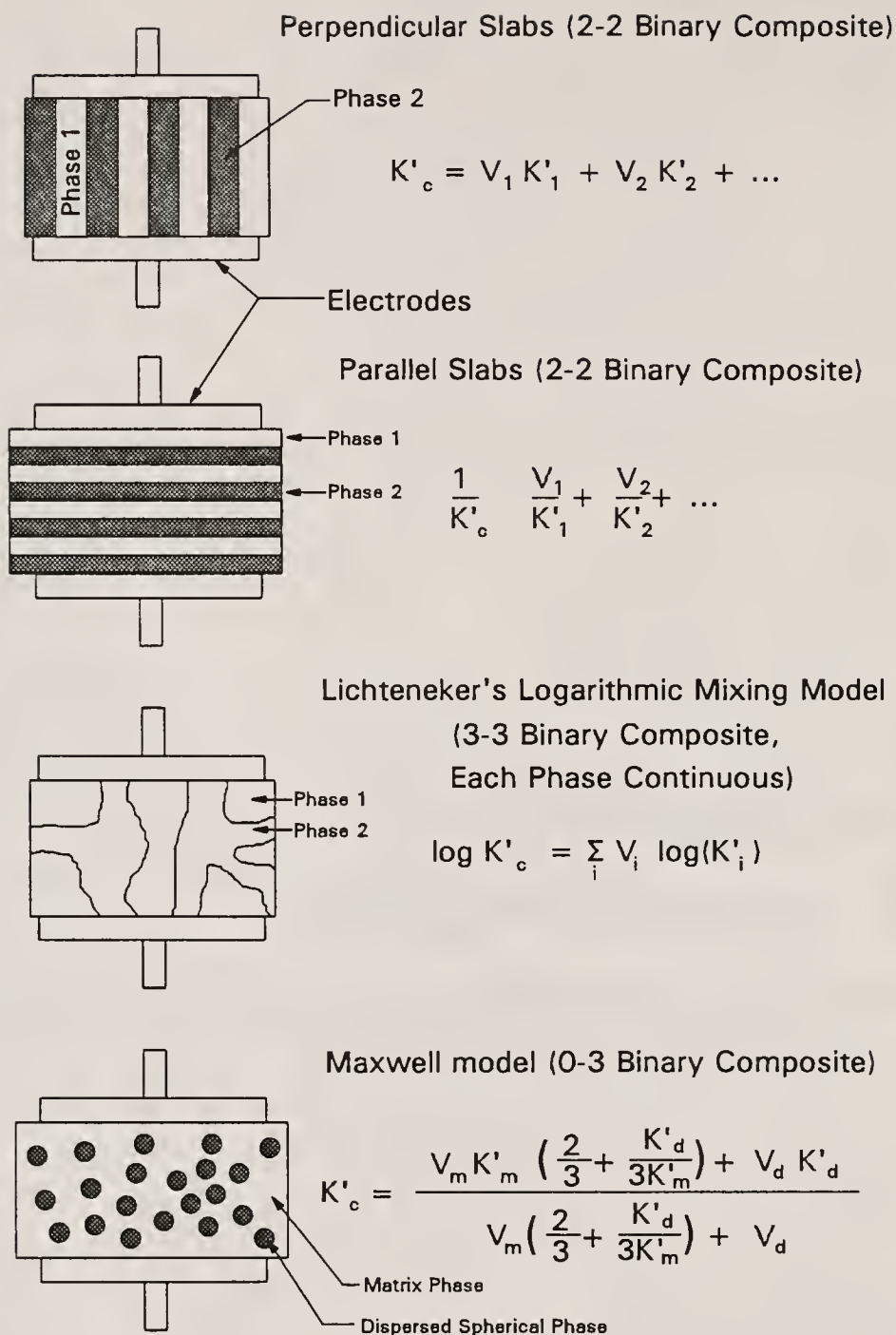


Figure 2.33

Equations and microstructures associated with the parallel slabs, perpendicular slabs, logarithmic and Maxwell models for predicting the dielectric constant of composite materials



for different pore structures (or composite microstructures), and thus provide a means by which composite microstructure may be predicted.

The parallel slabs model predicts the dielectric behavior of composites that have the slabs oriented parallel to the capacitor electrodes (in a parallel plate capacitor configuration), while the perpendicular slabs model predicts the behavior of composites having slabs oriented perpendicular to the capacitor electrodes. Both models are special cases of the general empirical relationship,

$$K'_c = \sum_i V_i K_i'^n$$

where  $K'_c$  is the composite dielectric constant,  $V_i$  is the volume fraction of the  $i$ th constituent,  $K'_i$  is the dielectric constant of the  $i$ th component, and  $n$  is a structural configuration parameter. The value of  $n$  for the parallel and perpendicular slabs models is  $-1$  and  $1$  respectively [76KIN1]. Figure 2.34 illustrates the additivity rule for these models (as well as the Maxwell and Lichteneker models) for a binary composite system, having one component with  $K = 1$  and the other with  $K = 10$ . The perpendicular slabs model gives linear (i.e. standard rule of mixtures) results, while the parallel slabs model gives maximum deviation from linearity.

Similarly, Lichteneker's logarithmic dielectric mixing rule is another special case of said empirical relationship where  $n$  is set to  $0$  [76KIN1]. Logically, the logarithmic mixture rule gives values intermediate between the parallel and perpendicular slabs models, which are extrema of the, above mentioned, empirical relationship. The logarithmic mixing model predicts values of  $K$  for composites in which all constituents are continuous and interconnected.

The Maxwell model predicts  $K$  for binary composites having spherical inclusions (i.e. 0-3 composites). From Figure 2.34 it is evident that the Maxwell model predicts  $K$  values that are quite close to

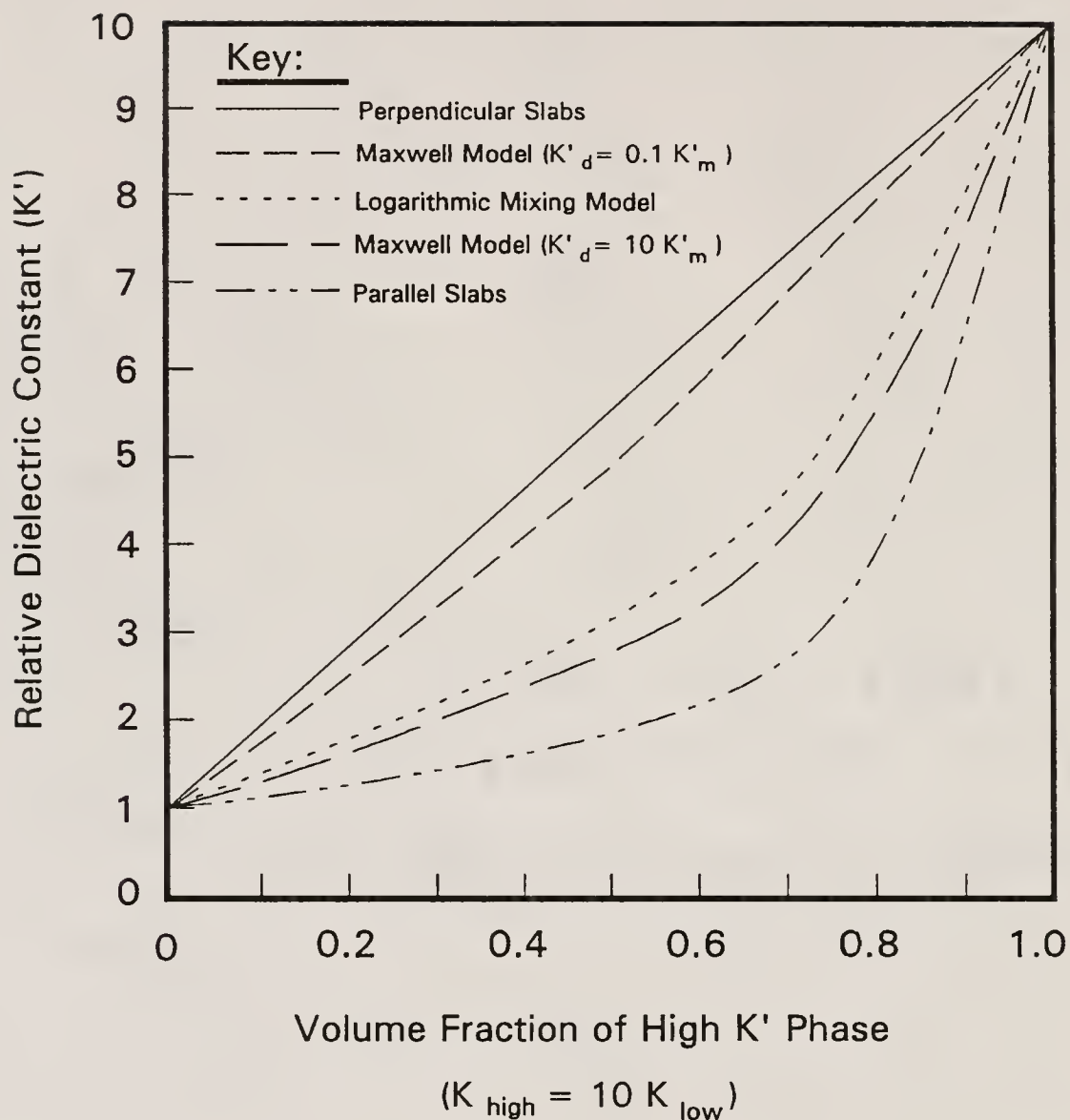


Figure 2.34

Illustration of the parallel slabs, perpendicular slabs, Lichteneker's logarithmic mixing and Maxwell models for a binary composite having  $K_1$  of 1 and  $K_2$  of 10 [76KIN1]

(but are slightly less than) those predicted by the logarithmic mixing model, when the dielectric constant of the dispersed phase is significantly larger than the matrix phase. It is also evident that the Maxwell model more closely resembles the perpendicular slabs model, when the dielectric constant of the dispersed phase is significantly less than that of the matrix phase.

An advantage of all of the empirically based models is that composites having more than one component may be modelled relatively easily. This is not the case for the Maxwell model. Dielectric values of binary composites may be predicted accurately for structures, that are different than those covered by either of the empirical-based models, or the Maxwell model, by using general effective medium (GEM) theory [83HSU,85HSU]. The GEM model is similar to the above mentioned empirical models, with the exception that the structural parameter value it gives (which is analogous to  $n$  used in empirical models), has significance for non-integer values as well as for integer values.

Effective medium theories replace the composite matrix, surrounding a discrete inclusion, with a homogeneous field value. The effective medium model, of Hsu et. al, is generally applicable to many materials properties, including elastic modulus, conductivity, dielectric constant, etc., as long as the material property of interest, of each of the components of the binary composite follow the relation,

$$10^{-2} \leq \frac{X_1}{X_2} \leq 10^2$$

where  $X_i$  is the material property of interest (i.e. dielectric constant) of composite component  $i$  [83HSU,85HSU].

In this model, the composite contains spheroidal inclusions which may be stretched into fibrils or lamellae. This is accomplished by assigning an eccentricity value ( $e$ ) to the spheroids characteristic of the internal composite structure of interest.

The eccentricity is defined by the relation,

$$e = (1 - (\frac{C}{A})^2)^{\frac{1}{2}}$$

where  $C/A$  is the aspect ratio of the semi-principal axes of the spheroids (in all cases, two of the three semi-principal axes are set equal to each other). When the aspect ratio is 1, all the axis of the spheroid are equal, and the eccentricity value is 0, relating to the case of perfect spheres. Figure 2.35 illustrates the geometry of the spheroids used in the model of Hsu, et. al.

In the case of prolate spheroids, the  $A$  axis is larger than the two equal minor axes (i.e.  $A \geq B = C$ ). When  $A$  is much greater than  $C$ , the model predicts  $K$  values for fibrillar microstructures having the fibers oriented perpendicular to the electrodes (parallel to the electric field). This is analogous to the perpendicular slabs model mentioned above. For oblate spheroids, the two major axes are set equal to each other (i.e.  $A = B \geq C$ ) which, in the extreme case, this represents a lamellar structure having the planes of the lamellae oriented parallel to the electrodes (perpendicular to the electrical field). This is analogous to the parallel slabs model.

For a binary composite system, the effective medium equation derived by Hsu et al. is

$$[1 - F(e)] K_c^2 + (K'_1 [F(e) - V_1] + K'_2 [F(e) - V_2]) K'_c - K'_1 K'_2 F(e) = 0$$

where  $F(e)$  is a function of spheroid eccentricity and is

$$F(e) = \frac{1 - e^2}{2e^3} [\ln(\frac{1+e}{1-e}) - 2e]$$

for prolate spheroids, and

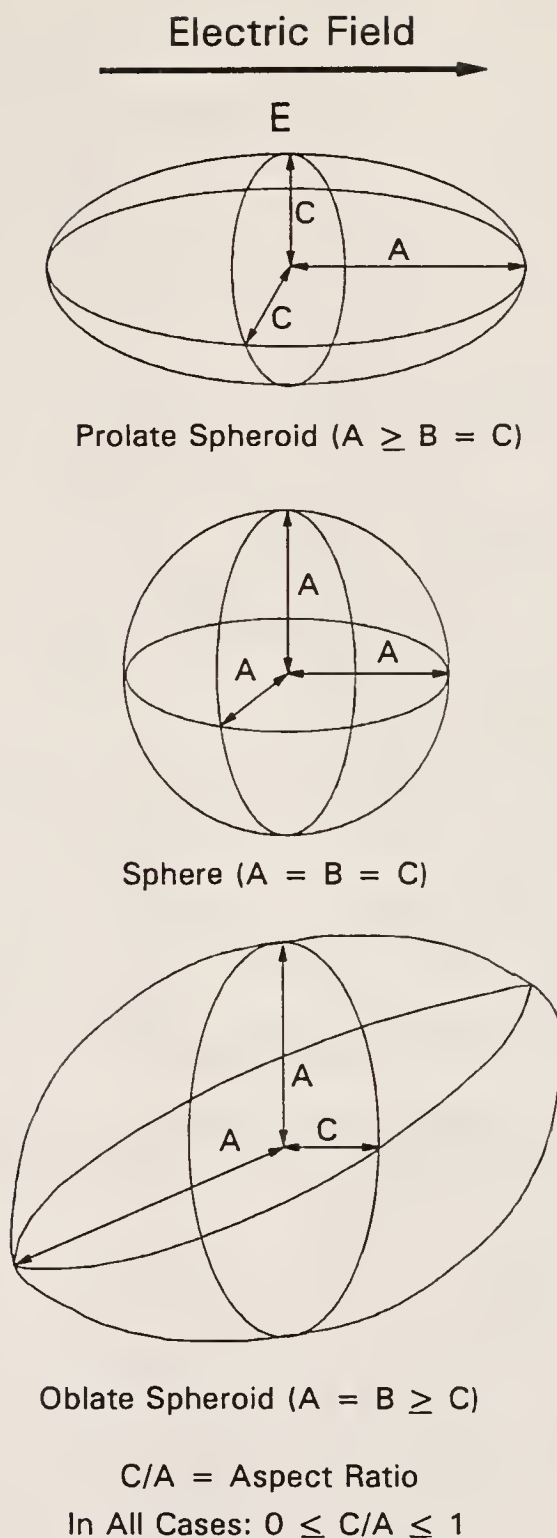


Figure 2.35

Geometry and orientation of prolate, oblate and perfect spheroids, used in the effective medium model of Hsu, et. al [85HSU]

$$F(e) = \frac{1}{e^2} \left[ 1 - \frac{\sqrt{(1-e^2)}}{e} \tan^{-1} \left( \frac{e}{\sqrt{1-e^2}} \right) \right]$$

for the oblate spheroids,  $K'_c$  is the composite dielectric constant,  $K'_i$  is the dielectric constant of the  $i$ th component (either 1 or 2), and  $V_i$  is the volume fraction of component  $i$ . The  $F(e)$  values for both prolate and oblate spheroids are plotted as a function of spheroid eccentricity ( $e$ ) in Figure 2.36.

The effective medium equation may be solved for  $K'_c$  using the quadratic equation,

$$K'_c = \frac{-B \pm \sqrt{B^2 - 4AC}}{2A}$$

where,

$$A = [1 - F(e)],$$

$$B = K'_1 [F(e) - V_1] + K'_2 [F(e) - V_2],$$

and

$$C = -K'_1 K'_2 F(e).$$

It can be shown that for  $F(e) = 0$  (i.e. maximum prolation), the effective medium theory (EMT) model reduces to the perpendicular slabs equation and that for  $F(e) = 1$  (i.e. maximal oblation), the EMT model reduces to the parallel slabs equation [83HSU,85HSU]. Similarly, the EMT model has been shown to be nearly analogous to models predicting properties of 0--3 composites when  $F(e) = 1/3$  (i.e. perfect sphericity) [83HSU,85HSU]. Thus, the EMT model may be used to predict  $K'_c$  for binary composites having structures intermediate of those discussed above. The EMT model may be used to estimate  $K'_c$  for composites having



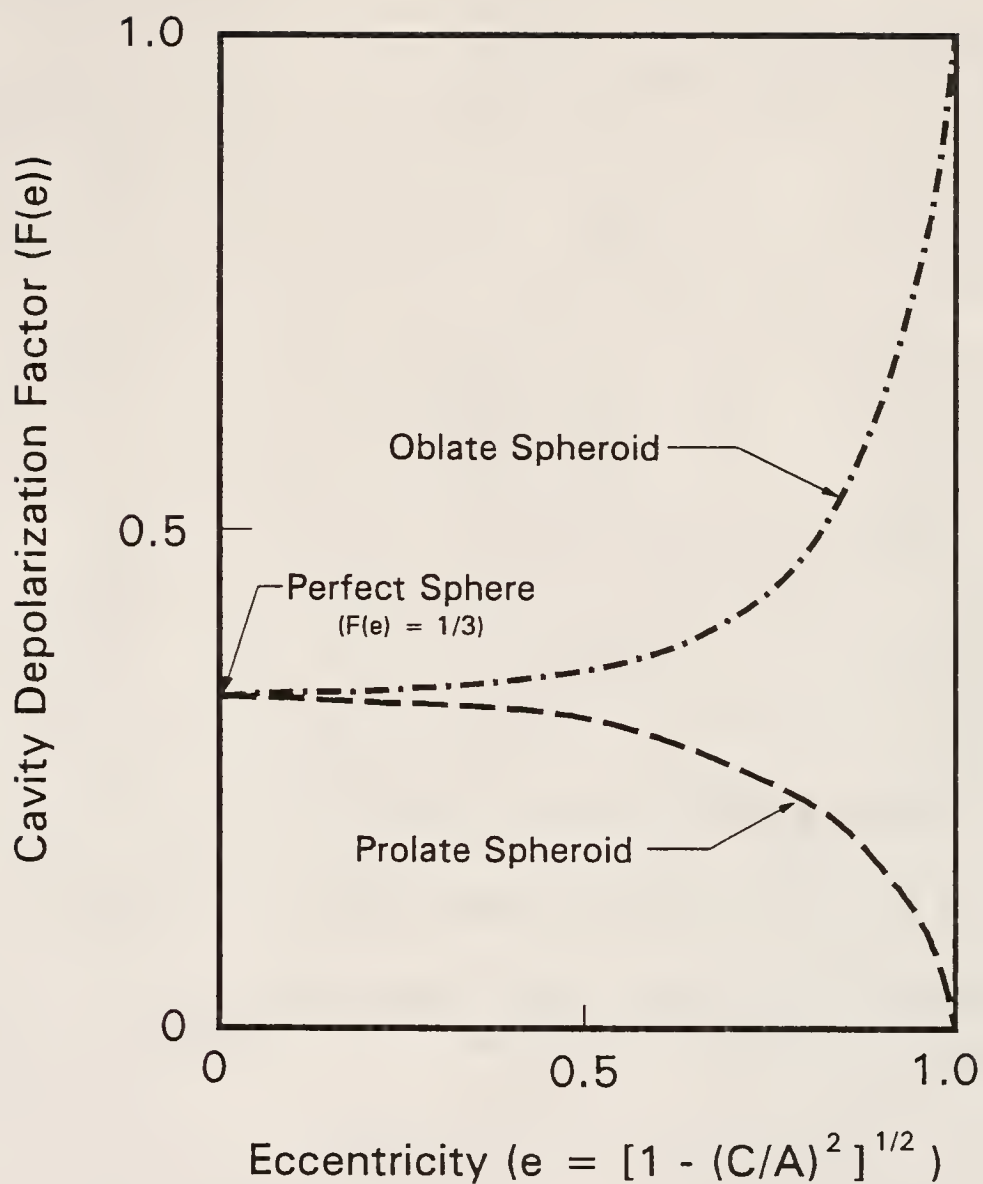


Figure 2.36

Cavity depolarization factor ( $F(e)$  for dielectric EMT) as a function of spheroid eccentricity, for prolate and oblate spheroids [85HSU]

more than two constituents, if an iterative process (i.e. combining two phases into one for each iteration) is used.

## 2.7 Mechanical Properties

Inclusions (either soft or hard), within glass matrix composites, greatly affect the mechanical properties of the material. Porosity (i.e. very soft inclusions) tends to decrease the mechanical strength and elastic modulus of a material, while hard inclusions usually increase the fracture toughness and strength of a material, if the additions of said inclusions do not result in a large concentration of flaws or stress concentrators [76KIN1]. Soft inclusions do not alter the crack path, but do alter crack velocity, while hard inclusions alter the crack path [81BIS]. Both these mechanisms may serve to increase fracture toughness [81BIS].

Inclusions may act as flaws within a material, thereby decreasing mechanical strength and fracture toughness [84RIC]. Both fracture toughness and mechanical strength are inversely proportional to inclusion, or flaw size [76KIN1,81BIS]. In amorphous materials the stress field about inclusions may be modified to either increase or decrease fracture toughness, by either deflecting or attracting cracks [81KRS,89JES]. This is a function of both differential thermal expansion of the composite constituents and of heat treatment near the glass transition temperature [81KRS,89JES].

In glasses, pores tend to act as blunt cracks, with pore clusters increasing the effective flaw size [84RIC]. Smoother pores (i.e. pores without sharp discontinuities) act as blunter cracks. The strength and elastic modulus of porous materials are also predicted to decrease rapidly at and above the porosity percolation threshold [85SIE].

This section discusses the elastic modulus as a function of inclusion concentration. It is important to look at various models, considering the maximum and minimum values predicted. Models covering

both types of inclusions (hard and soft) are discussed, since the composite system studied involves both hard and soft inclusions.

The effect of porosity concentration upon elastic modulus ( $E_p$ ) is modelled by the MacKenzie equation,

$$E_p = E_o (1 - 1.9 V_p + 0.9 V_p^2)$$

where  $E_o$  is the elastic modulus of the fully dense material, and  $V_p$  is the volume fraction of porosity [76KIN1]. This is an empirical model, that has been shown to fit experimental data well [76KIN1]. Dean and Lopez fitted experimental elastic modulus data to four other empirical models, including the linear model, the two-thirds power law model, an exponential model, and the Hasselman or nonlinear model [83DEA]. Table 2.10 lists the empirical elastic modulus versus porosity relations they studied. They found that, on the whole, the linear law gives a superior fit to experimental data, using the criteria of fit to data, extrapolation to  $E_o$ , and the consistency of correctly predicting

Poisson's ratio and bulk modulus from said extrapolation to full density.

Ramakrishnan and Arunachalam modelled the effect of porosity upon elastic modulus using quantum mechanical principles [90RAM]. They found this model fit experimental data well when a variable Poisson's ratio factor was used. Said factor is not calculable from experimental data, and it was necessary to use finite element analysis to model the effective Poisson's ratio.

Elastic modulus, as a function of inclusion (hard or soft) concentration, is found to be intermediate between the Voigt and Reuss models, which predict the extrema for said relationship [76KIN1]. The Voigt model uses the assumption that strain is homogenous throughout the composite. It predicts the upper limit of  $E$  as a function of

inclusion volume fraction. The Voigt equation is

$$E_{cU} = V_1 E_1 + V_2 E_2 + \dots$$

where  $E_{cU}$  is the upper limit composite elastic modulus prediction, and  $E_i$  and  $V_i$  are the elastic modulus and the volume fraction of the  $i$ th component respectively. It is evident that the Voigt model is similar to the perpendicular slab model, mentioned above, in that they both use a simple rule of mixtures to predict composite properties. Thus, both models predict the upper limit of the respective effects.

The Reuss model assumes that the stress is homogeneous throughout the composite, and predicts the lower limit of elastic modulus as a function of inclusion concentration. It is defined by the relation,

$$\frac{1}{E_{cL}} = \frac{V_1}{E_1} + \frac{V_2}{E_2} + \dots$$

where  $E_{cL}$  is the lower limit of the composite elastic modulus. The Reuss model is similar to the parallel slab model, for predicting composite dielectric constant, in that both predict lower limits to composite properties.

Intermediate values of the  $E_c$ , as a function of inclusion concentration, are predicted by the Hashin-Shtrickman relations [76KIN1]. The Hashin-Shtrickman model predicts upper and lower bounds that are considerably narrower than those set by the Voigt and Reuss models. The model also does not include any assumptions about relative phase geometries. The upper and lower bounds to the Hashin-Shtrickman relation are simply the same equation, with the modulus values interchanged (i.e.  $E_1$  and  $E_2$  are switched).

The Hashin-Shtrickman model is not easily applicable to experimental data, however. Also, it is difficult to expand it to composite systems having more than two components. Furthermore, the Hashin-Shtrickman model requires both bulk modulus and shear modulus

Table 2.10

Empirical Elastic Modulus versus Porosity  
Models Investigated by Dean and Lopez [83DEA]

Model Type	Model Equation
Linear	$E_p = E_o (1 - bV_p)$
Exponential	$E_p = E_o \exp(-bV_p)$
Hasselman (Non-Linear)	$E_p = E_o \left( \frac{1 - V_p}{1 + bV_p} \right)$
Two-Thirds Power	$E_p = E_o (1 - bV_p^{\frac{2}{3}})$

Note:  $b$  is an empirical constant that is sensitive to pore structure, as well as to the particular material, in each of the above models.

data of both components, as well as statistical details of the phase distributions, and thus, has found limited application [76KIN1].

However, when it has been applied to experimental data, it has predicted the elastic modulus, as a function of inclusion concentration, more accurately than the Voigt-Reuss extrema [76KIN1].

The elastic modulus of a material (E) may be measured, using microhardness indentation techniques (combined Knoop and Vickers), using the following equation:

$$E = \frac{0.45 (H)}{\left( \frac{b}{a} - \frac{b'}{a'} \right)}$$

where H is the measured Vicker's hardness, b/a is the dimension ratio of the indenter (b/a = 1/7 for the Knoop anvil) and b' and a' are one half the length values of the minor and major dimensions of the Knoop indentation, respectively. The fracture toughness ( $K_{Ic}$ ) of a material may also be calculated using microhardness indentation, using the equation:

$$K_{Ic} = H\sqrt{A} \left( \frac{E}{H} \right)^{\frac{2}{5}} \left[ 0.057 \left( \frac{C}{A} \right)^{-\frac{3}{2}} \right]$$

where A is one half the dimension of the Vicker's indentation, and C is one half the imposed crack length. This is only valid if C is greater than 2A, since the crack must exceed the field of complex localized stress, caused by the indentation [81ANS,81CHA]. Furthermore, said technique is valid only if radial cracks are formed, since circumferential cracks might interact with the radial cracks, absorbing energy [81ANS,81CHA]. Also, this technique is only valid when the microstructure is significantly smaller than the indenter. Finally, when investigating porous materials, or when circumferential cracking is significant, crushing may occur. Thus, the microhardness indentation technique is only valid under certain, limiting circumstances.



## CHAPTER THREE EXPERIMENTAL PROCEDURE

### 3.1 Overview

This chapter describes the actual experimental procedures used. The sequence of experimental investigation is outlined in Figure 3.1, which is a flow diagram denoting both the succession of experiments and the feedback optimization mechanisms utilized. Figure 3.1 also aids in the clarification of where each experimental procedure is utilized and the importance of each procedure to the overall research project.

### 3.2 Powder Synthesis and Treatment

#### 3.2.1 Overview

Of the materials chosen for the investigation, only one was used as-received, the  $\text{Si}_3\text{N}_4$ . The polystyrene latex used for creating controlled porosity was produced and classified as described in section 3.2.2. The borosilicate glass powder was milled and prepared as described in section 3.2.3.

#### 3.2.2 Synthesis, Characterization and Preparation of Polystyrene Microspheres

Production of the uniform polystyrene latex microspheres (UPLMs or latex) was based largely upon work performed by Lok and Ober [85LOK] involving dispersion polymerization of polystyrene latex. A block diagram outlining the procedure used to the produce UPLMs is illustrated in Figure 3.2. A schematic representation of the apparatus utilized for UPLM production is illustrated in Figure 3.3.

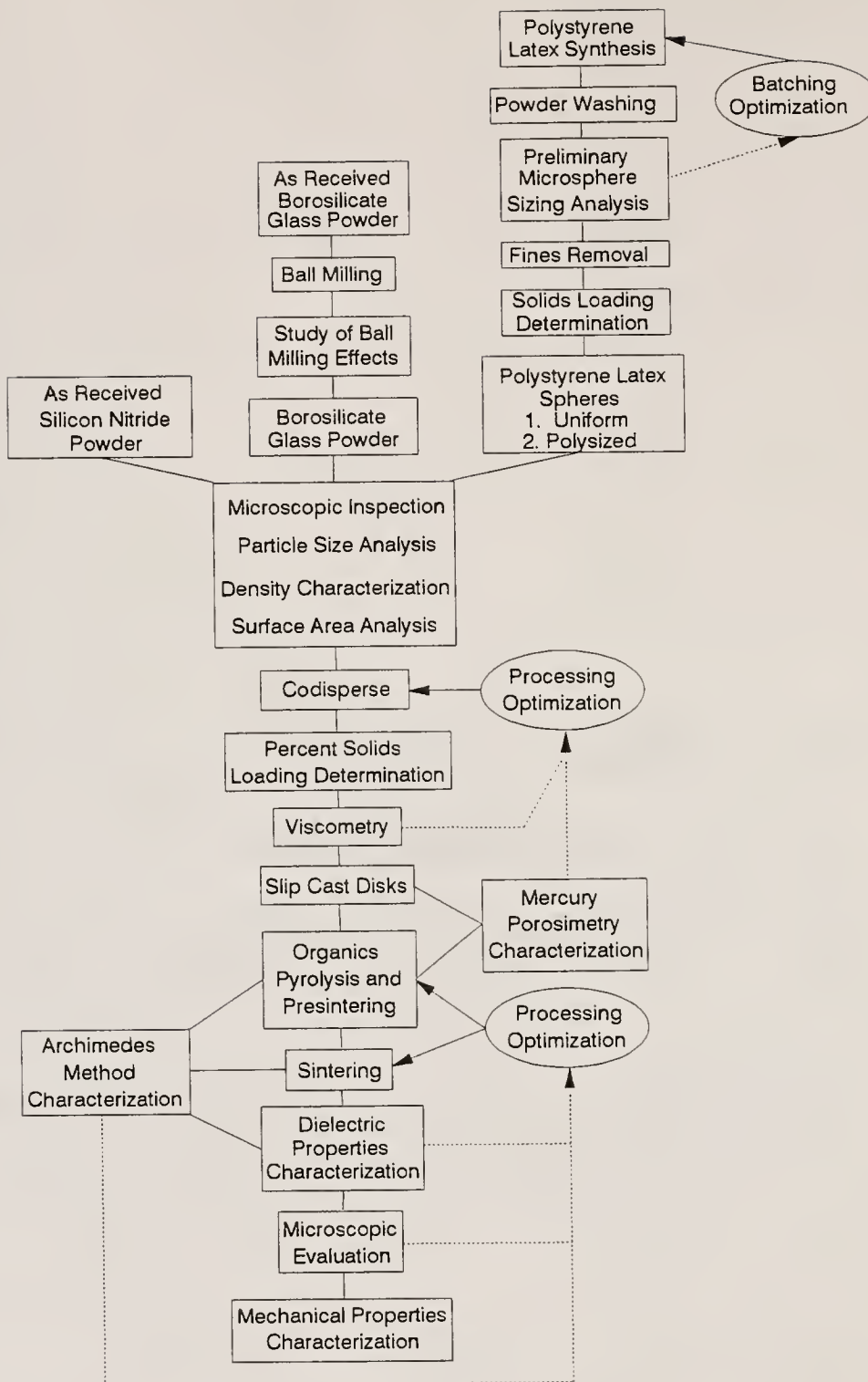


Figure 3.1

Block Diagram depicting the experimental flow of the research project as well as the feedback optimization mechanisms used

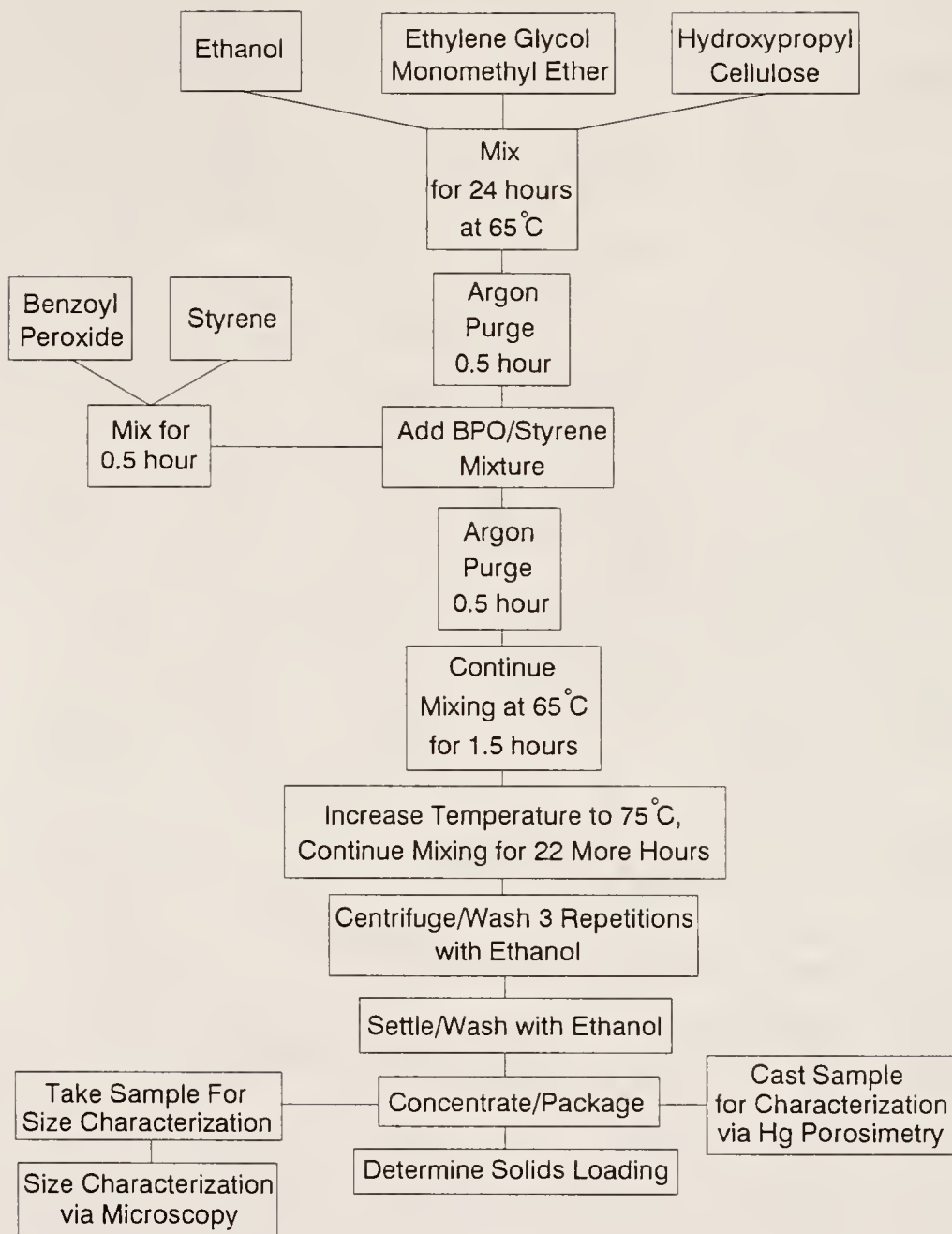


Figure 3.2

Block diagram outlining the procedure used for production of dispersion polymerized latex



Into a 500 ml round bottom flask,<sup>1</sup> in which a magnetic stir bar<sup>2</sup> had been placed, predetermined amounts of EtOH,<sup>3</sup> methylcellosolve (MeCell, also known as ethylene glycol monomethyl ether),<sup>4</sup> and hydroxypropyl cellulose 100,000 molecular weight,<sup>5</sup> (HPC 100,000 MW) were mixed until the HPC had completely dissolved (approximately 12 h). During the mixing process, the flask was sealed using a glass stopper<sup>6</sup> sleeved in teflon<sup>7</sup> and clamped with a plastic joint clamp.<sup>8</sup> During said mixing process, the flask was also isothermally maintained at 65°C. This was accomplished by way of the hot oil bath/mixer depicted in Figure 3.3. The hot oil bath/mixer temperature was controlled via a digital setpoint controller<sup>9</sup> which had been previously calibrated to agree with the 0.1°C resolution thermometer<sup>10</sup> also depicted in Figure 3.3. In order to achieve temperature homogeneity, a second magnetic

---

<sup>1</sup> Catalog Number: 10-067G, Fisher Scientific, 1600 Parkway View Drive, Pittsburgh, PA 15205

<sup>2</sup> Catalog Number: 14-511-58B, Fisher Scientific, 1600 Parkway View Drive, Pittsburgh, PA 15205

<sup>3</sup> Reagent Grade Ethanol, Florida Distillers Company, Lake Alfred, FL 33850.

<sup>4</sup> Catalog Number: E-182, Fisher Scientific, 1600 Parkway View Drive, Pittsburgh, PA 15205

<sup>5</sup> Catalog Number: 19188-4, Aldrich Chemical Company, Inc., Milwaukee, WI, 53233.

<sup>6</sup> Catalog Number: 14-640J, Fisher Scientific, 1600 Parkway View Drive, Pittsburgh, PA 15205

<sup>7</sup> Catalog Number: 6194, Nalge Company, Rochester, NY, 14602

<sup>8</sup> Catalog Number: 05-880E, Fisher Scientific, 1600 Parkway View Drive, Pittsburgh, PA 15205

<sup>9</sup> Model Number: 49 (type K thermocouple), Love Controls Corp., 1714 S. Wolf Rd., Wheeling, IL 60090

<sup>10</sup> Model Number: 15168B, Fisher Scientific, 1600 Parkway View Drive, Pittsburgh, PA 15205

stirrer<sup>11</sup> was used in the controlled temperature oil bath. The mixing rate used was controlled via a variable AC transformer<sup>12</sup> and was adjusted to the maximum rate achievable before the onset of stirrer instability.

After the above mixing step, predetermined amounts of styrene<sup>13</sup> and benzoyl peroxide (BPO),<sup>14</sup> both previously refrigerated, were added to a 50 ml graduated cylinder.<sup>15</sup> Next the cylinder was double sealed with laboratory film,<sup>16</sup> then capped with a rubber septum.<sup>17</sup> The styrene and BPO were then vigorously mixed by inverting the sealed graduate for approximately 50 repetitions.

During this time, the flask containing the EtOH-MeCell-HPC solution was purged for 30 min. with Ar<sup>18</sup> introduced via a metal lance<sup>19</sup> puncturing a rubber sealing septum<sup>17</sup> which covered the opening of the flask. Exhaust of purging gases was provided via a hypodermic needle,<sup>20</sup> also penetrating the sealing septum.

---

<sup>11</sup> Catalog Number: 14-511-93, Fisher Scientific, 1600 Parkway View Drive, Pittsburgh, PA 15205

<sup>12</sup> Model Number: 3PN1510 Variac, Staco Energy Products Co., Dayton, OH

<sup>13</sup> Catalog Number: O4507, Fisher Scientific, 1600 Parkway View Drive, Pittsburgh, PA 15205

<sup>14</sup> Catalog Number: 17998, Aldrich Chemical Company, Inc., Milwaukee, WI 53233

<sup>15</sup> Catalog Number: 08-552D, Fisher Scientific, 1600 Parkway View Drive, Pittsburgh, PA, 15205

<sup>16</sup> Parafilm M, American National Can, Greenwich CT, 06836

<sup>17</sup> Catalog Number: Z10,145-1, Aldrich Chemical Company, Inc., Milwaukee, WI 53201

<sup>18</sup> Catalog Number: UN1006, Jacksonville Compressed Gases Corp., Jacksonville, FL 32204

<sup>19</sup> Catalog Number: 14-819-169, Fisher Scientific, 1600 Parkway View Drive, Pittsburgh, PA 15205

<sup>20</sup> Catalog Number: 14-826-5B, Fisher Scientific, 1600 Parkway View Drive, Pittsburgh, PA 15205



The Ar flow rate was adjusted to a level high enough to visibly expand the septum thus ensuring the purged system was under a slight positive pressure. During the purging operation, the previously mentioned mixing and temperature conditions were maintained.

After Ar purging for 30 min., the styrene-BPO solution was added to the EtOH-MeCell-HPC solution in the flask, the flask opening recovered, and the above-mentioned purging continued for another 30 min. After this purging step was completed, the teflon sheathed<sup>7</sup> glass stopper<sup>6</sup> was quickly clamped in the flask opening, thereby sealing the system.

Two hours after the styrene-BPO addition, the oil bath temperature was raised to 75°C. This treatment was maintained for 22 more hours. After a total of 24 h, the sealed flask was removed from the stirred oil bath and stirred at room temperature on a different stir plate<sup>21</sup> while cooling. When the flask reached a comfortably handleable temperature (approximately 50°C), it was washed on the outside with tap water in order to cool the UPLM suspension more quickly. The resulting UPLM suspension was quite viscous, having a consistency similar to glycerin at room temperature. After cooling, the flask was opened and the UPLM suspension decanted into a 1 pint (473 ml) clear glass bottle and capped.

Later the suspension was centrifuged<sup>22</sup> in 50 ml polyallomer centrifuge tubes.<sup>23</sup> An initial centrifugation time and speed of about 4,000 rpm for 30 min. worked well for all UPLM sizes produced. This centrifuge treatment separated the latex from the relatively viscous

---

<sup>21</sup> Catalog Number: 14-493-120M, Fisher Scientific, 1600 Parkway View Drive, Pittsburgh, PA 15205

<sup>22</sup> Model Number: J2-21, Beckman Corp., Palo Alto, Ca, 94303-0803

<sup>23</sup> Catalog Number: 05-563-10G, Fisher Scientific, 1500 Parkway View Drive, Pittsburgh, PA 15205

supernatant effectively, yet still allowed for easy redispersion of the latex.

The supernatant was then replaced with denatured EtOH,<sup>24</sup> and the centrifugation process was repeated for 2 more repetitions, further washing the UPLMs. For the second and third washing repetitions, the centrifuge speed was adjusted for the UPLM size being washed. A speed of 3,000 rpm for approximately 20 min. was sufficient to separate the smallest spheres while 1,500 rpm for 20 min. was found satisfactory for the largest spheres.

As will be discussed later, the target diameter for the UPLMs used in most experiments was approximately 5  $\mu$ m. Thus, the batch recipe was modified to target this sphere diameter using an interpolation of data reported by Lok and Ober [85LOK].

After the centrifugation/washing process, a sample was taken for preliminary size/size distribution characterization via scanning electron microscopy (SEM).<sup>25</sup> Approximately one drop of the UPLM suspension was decanted into a 20 ml polystyrene sample vial<sup>26</sup> using a 5 ml capacity (24 to 26 drops per ml) PE disposable transfer pipette.<sup>27</sup> Denatured EtOH was then added to the vial to dilute the UPLM suspension until turbidity was barely apparent via visual inspection. The vial was then capped and the diluted suspension was subjected to 15 min. of sonic

---

<sup>24</sup> Catalog Number: A407, Fisher Scientific, vacuum filtered through numbers 4 and 1 Whatman qualitative filter paper, Whatman International, Ltd., Maidstone, England, using Catalog Number: 10-437-23A, Fisher Scientific suction funnel

<sup>25</sup> Model Number: JSM-35CF, JEOL Ltd., Tokyo, Japan

<sup>26</sup> Catalog Number: 03-341-13, Fisher Scientific, 1600 Parkway View Drive, Pittsburgh, PA 15205

<sup>27</sup> Catalog Number: 13-711-5A, Fisher Scientific, 1600 Parkway View Drive, Pittsburgh, PA 15205

exposure, in a sonic dismembrator,<sup>28</sup> in order to break apart any agglomerates in the suspension. After sonication, the suspension was vigorously hand shaken for approximately one minute, the vial uncapped, and approximately 3 drops decanted from another disposable transfer pipette<sup>27</sup> onto a precleaned glass substrate<sup>29</sup> affixed to a 1" (2.54 cm) diameter aluminum SEM specimen stub<sup>30</sup> via double stick tape.<sup>31</sup> The specimen was then placed into a covered petri dish<sup>32</sup> and allowed to dry. The dried specimen was then examined with an optical microscope,<sup>33</sup> in reflection mode, in order to determine if it was satisfactory. Satisfactory samples were then Au-Pd DC sputter coated<sup>34</sup> and packaged for future SEM analysis.

Preliminary SEM sphere size analysis involved imaging the spheres at a magnification of 1000X, then measuring and recording the diameter of 125 spheres. The diameter measurements were taken on the viewing CRT using a pair of vernier calipers.<sup>35</sup>

---

<sup>28</sup> Either Model Number: LW-375, Heat Systems Ultrasonics, Inc., Plainview, NY 11803, or Model Number: VC-600, Sonics and Materials, Inc., Danbury, CT, the sample container was clamped over the sonic transducer, immersed within a chilled circulating water bath

<sup>29</sup> Catalog Number: 12-568-15, Fisher Scientific, 1600 Parkway View Drive, Pittsburgh, PA 15205, the suspension was deposited upon nonfrosted areas, the glass was made the appropriate size (approximately 20 x 20 mm) by scribing to size, wetting the scribe mark, then snapping the glass to size using a Model Number: 08-675, Fisher Scientific diamond scribe

<sup>30</sup> Fabricated from 1" (2.54 cm) diameter aluminum rod stock at the Department of Materials Science and Engineering Machine Shop, University of Florida, Gainesville, FL 32611

<sup>31</sup> Model Number: 665, Scotch Double-Coated Tape, Commercial Office Supply Division of 3M, St. Paul, MN 55144-1000

<sup>32</sup> Catalog Number: 08-757-100B, Fisher Scientific, 1600 Parkway View Drive, Pittsburgh, PA 15205

<sup>33</sup> Nikon Optiphot Model, Nikon Instruments, Japan

<sup>34</sup> Model: Desk II Sputter Coater, Denton Vacuum, Inc., Cherry Hill, NJ

<sup>35</sup> Catalog Number: 12-122, Fisher Scientific, 1600 Parkway View Drive Pittsburgh, PA 15205

The size reference bar was also measured and recorded periodically in order to provide a conversion factor. The raw data were then encoded into a computer spreadsheet program<sup>36</sup> which converted the measured diameters into actual diameters. From the spreadsheet, mean size, largest size, smallest size, standard deviation and variance were obtained. The spreadsheet was also used to sort the diameter data from largest to smallest size. The sorted diameter data was then used to create a size histogram. The histogram system utilized diameter increments of 0.1  $\mu\text{m}$  and the number of spheres at the diameter of interest were encoded manually on a data sheet. These data were then encoded into another computer spreadsheet program<sup>36</sup> which converted the data into number, volume and estimated surface area data. This spreadsheet was also utilized in plotting various characteristics dependent upon sphere diameter. Table 3.1 outlines the equations used to perform all size, size distribution, surface area and geometric standard deviation calculations to characterize all powders sized.

This method of measurement was used for preliminary (presettled) diameter characterization. Subsequent to the settling process (described below) diametric measurements were also provided by taking micrographs of 1000 spheres at a magnification of 1000X. The UPLM diameters were then measured directly from the micrographs utilizing a 6X optical comparator<sup>37</sup>. All other methods used in sphere diameter measurement (i.e. specimen preparation and data manipulation, etc.) were the same for both sets of UPLM diameter measurement.

The latter method was used to characterize the settled UPLMs because it removes an element of possible data biasing since almost all spheres photographed are measured.

---

<sup>36</sup> A product of LOTUS Development Corporation, Cambridge, MA

<sup>37</sup> Catalog Number: 12-056, Fisher Scientific, 1600 Parkway View Drive, Pittsburgh, PA 15205

Table 3.1

Equations Used Determine UPLM Size, Size  
Distribution, Geometric Standard Deviation  
and Surface Area Data of the Latexes Produced

1. Sphere Diameter,  $X$  ( $\mu\text{m}$ ):

$$X = \frac{A}{D} \times 10$$

where:  $A$  is length of measured magnified diameter (mm)  
 $D$  is length of measured magnified 10  $\mu\text{m}$   
reference marker (mm)

2. Mean Sphere Diameter,  $X_{ave}$  ( $\mu\text{m}$ ):

$$X_{ave} = \frac{\sum_i n_i X_i}{\sum_i n_i}$$

where:  $n_i$  is the number of measured spheres at size  
increment  $i$   
 $X_i$  is the diameter of the spheres at increment  $i$   
( $\mu\text{m}$ )

3. Number Fraction at Size,  $N_f$ :

$$N_f = \frac{n_i}{\sum_i n_i}$$

4. Volume Fraction at Size,  $V_f$ :

$$V_f = \frac{\left(\frac{X_i}{2}\right)^3 n_i}{\sum_i \left(\frac{X_i}{2}\right)^3 n_i}$$

5. Powder Surface Area,  $S_A$  ( $\text{m}^2/\text{g}$ ):

$$S_A = \frac{6}{\rho} \sum_i X_i^{-1} n_i$$

where:  $\rho$  is the powder density ( $\text{g}/\text{cm}^3$ )

6. Cumulative Number Percent Larger Than, CNPL (%):

$$CNPL_{\text{size}} = \frac{\sum_{i=X_{\text{size}}}^{i=X_{\text{max}}} n_i}{\sum_i n_i} \times 100$$

Table 3.1 (continued)

7. Cumulative Number Percent Finer Than, CNPF (%):

$$CNPF_{\phi size} = \frac{\sum_{i_{\phi min}}^{i_{\phi size}} n_i}{\sum_i n_i} \times 100$$

8. Cumulative Volume Percent Larger Than, CVPL (%):

$$CVPL_{\phi size} = \frac{\sum_{i_{\phi size}}^{i_{\phi max}} \left(\frac{X_i}{2}\right)^3 n_i}{\sum_i \left(\frac{X_i}{2}\right)^3 n_i} \times 100$$

9. Cumulative Volume Percent Finer Than, CNPL (%):

$$CVPF_{\phi size} = \frac{\sum_{i_{\phi min}}^{i_{\phi size}} \left(\frac{X_i}{2}\right)^3 n_i}{\sum_i \left(\frac{X_i}{2}\right)^3 n_i} \times 100$$

where:            CNPL + CNPF = 100  
                      CVPL + CVPF = 100

10. Geometric Standard Deviation, GSD (for log normal distributions):

A. Traditional:

$$GSD_m = \frac{X_{\phi CPF_m = 84.13\%}}{X_{median_m}}$$

where:            CPF is cumulative percent finer than  
                      m is mode (either number or volume basis)

B. Inverse:

$$GSD_m^{-1} = \frac{X_{\phi CPL_m = 84.13\%}}{X_{median_m}}$$

where:            All types of geometric standard deviation  
                      are 1 for a perfectly monodisperse system



It also is more accurate due to the measurement technique used. However, this method is less precise since the comparator scale limit is 0.125  $\mu\text{m}$  on 1000X micrographs.

From presettled diametric characterization, the initial batch was deemed satisfactory, uniform in size and having a mean sphere diameter of 4.6  $\mu\text{m}$ . As a result, nine more batches of the same recipe were produced. Ten batches, of approximately 50 g UPLM each, were produced in order to provide an amount sufficient for planned experimentation, as well as for settling losses and for exclusion of up to two batches, in order to keep the size distribution as tight as possible. Appendix II depicts sizing data of the batches before classification via settling (obtained using the first measurement technique described). From additive analysis of the initial sizing results for each batch, it was deemed that batches 03199001-08 and 03199001-10 would widen the size distribution the greatest amount. Therefore, these batches were not used in the mixed batch. The remaining 8 batches were then mixed together and settled. Subsequent to said characterization, the eight batch amalgam was diluted to approximately 5 V% solids in denatured EtOH, then settled in two 4,000 ml polymethylpentene (PMP) graduated cylinders<sup>38</sup> to eliminate the fines. The supernatant (which included the fines) was then pumped off using a peristaltic pump<sup>39</sup> with flexible plastic tubing.<sup>40</sup> The liquid pickup utilized was a glass tube having a hooked end,<sup>41</sup> which allowed a maximum pumping rate with minimal loss of settled latex.

---

<sup>38</sup> Catalog Number: 08-572-5J, Fisher Scientific, 1600 Parkway View Drive, Pittsburgh, PA 15205

<sup>39</sup> Model Number: 7520-25, Cole Parmer Instrument Company, Chicago, IL, 60648

<sup>40</sup> Model Number: R-1000, Tygon plastic tubing, Norton Performance Products, Akron, OH, 44309-3660

<sup>41</sup> Catalog Number: 11-365A, Fisher Scientific, 1600 Parkway View Drive, Pittsburgh, PA 15205, the hook was made on one end using an oxy-hydrogen torch

After supernatant removal, the settled material was then redispersed in fresh denatured EtOH. This process was repeated until the supernatant was visibly clear. At this point, the settled powder was redispersed in a minimal amount of denatured EtOH and the resulting dispersion was moved to a 2,500 ml clear glass jug. After settling within the jug, more supernatant was pumped off, thereby maximizing the solids loading of the UPLM dispersion. The solids loading of the batch was determined after this point, as described below, and the packaged UPLMs were then stored for future use.

In order to allow investigation of the effects of size of included porosity upon properties of the materials containing included porosity, single batches of UPLMs were made of 6 other sizes. The fabrication method of these UPLMs was as described above.

Basically, the EtOH to MeCELL ratio (and thus, the solution solubility parameter) was manipulated using interpolations of both the data of Lok and Ober [85LOK] and from sizing data of the batches produced for this study, as the data became available. Modifications were made in said ratio as deemed necessary to pursue a specific uniform sphere diameter. Table 3.2 outlines the batches produced as well as other pertinent characteristics of said batches.

In order to investigate the effect of size distribution of included porosity upon the composite microstructure, a suspension of latex was produced by mixing controlled portions of the largest, median and smallest latex batches (07249001, 06199001-07+09 and 07269001 respectively) together. The amount of each batch used was determined following a maximization of packing factor criterion. Since the smallest batch was found to be bimodal in size distribution, the required portions of each batch were determined by interpolating between 3 and 4 component sphere models for packing maximization, introduced by Westman and Hugill [30WES] and later elaborated further upon by McGeary [61MCG].

Table 3.2

Batch Compositions and Target Sizes For Dispersion  
Polymerized Uniform Polystyrene Latex Microspheres

Batch ID Number	Component Concentration <sup>1</sup>					Solu- bility Para- meter (cal/cm <sup>3</sup> ) <sup>1/2</sup>	Target Mean Sphere Diam. ( $\mu$ m)
	EtOH (V%)	MeCell (V%)	HPC (g)	Sty- rene (V%)	BPO (g)		
07269001	70	15	5.00	15	2.00	12.1	3.0 <sup>2</sup>
07309001	65	20	5.00	15	2.00	12.0	3.0 <sup>2</sup>
07199001	60	25	5.00	15	2.00	11.9	3.0 <sup>2</sup>
06199001 -10	51.25	33.75	5.00	15	2.00	11.8	5.0
07219001	42.5	42.5	5.00	15	2.00	11.7	7.0 <sup>3</sup>
08029001	36.25	48.75	5.00	15	2.00	11.6	7.0 <sup>3</sup>
07249001	30	55	5.00	15	2.00	11.5	10.0

- Notes:
- 1 Volume fraction calculations assume no volume additions from dissolved powders (i.e. HPC and BPO)
  - 2 Each successively dated batch was calculated pursuing a 3.0  $\mu$ m target diameter from the most current data available at the time (i.e. using feedback optimization)
  - 3 Each successively dated batch was calculated pursuing a 7.0  $\mu$ m target diameter from the most current data available at the time (i.e. using feedback optimization)

Table 3.3 indicates the amounts of each batch used to produce the wide size distribution (quadramodal) latex batch with the goal of achieving a maximized packing factor. Microscopic analysis was also used to determine the size and surface area characteristics of the wide size distribution latex batch through the use of the previously mentioned spreadsheet programs.

### 3.2.3 Ball Milling and Preparation of Borosilicate Glass Powder

The as-received, borosilicate (BS) glass powder<sup>42</sup> size was <325 mesh and was used, during experimentation, either as-received or after ball milling, in methanol, for 20 hours. The ball milling procedure follows.

To a large, precleaned, ceramic milling vessel,<sup>43</sup> 5000 g of  $\text{Al}_2\text{O}_3$  milling media<sup>44</sup> was added. Next, 780 g of the glass powder was added to the milling vessel. Subsequent to the glass powder addition, 700 ml of methanol<sup>45</sup> was added. The container was then carefully sealed, and placed upon a rolling mill<sup>46</sup> for 20 h, after which the vessel was removed. The milling jar was then unsealed and the milled glass/MeOH slurry was decanted into an evaporation dish<sup>47</sup> through a 14 mesh sieve<sup>48</sup>

---

<sup>42</sup> Glass Number: 7070, Materials Business, Corning Glass Works, Corning, NY 14831

<sup>43</sup> Origin unknown: Similar to Catalog Number: 08-382D, Fisher Scientific, 1600 Parkway View Drive, Pittsburgh, PA 15205

<sup>44</sup> Origin unknown: Similar to Catalog Number: 08-412-15A, Fisher Scientific, 1600 Parkway View Drive, Pittsburgh, PA 15205

<sup>45</sup> Catalog Number: A411-20, Fisher Scientific, 1600 Parkway View Drive, Pittsburgh, PA 15205

<sup>46</sup> Model Number: CF-81106, Norton Chemical Process Products Division, Akron OH, 44309

<sup>47</sup> Catalog Number: 08-741H, Fisher Scientific, 1600 Parkway View Drive, Pittsburgh, PA 15205

<sup>48</sup> The W.S. Tyler Company, Cleveland, OH

Table 3.3  
Composition of Polysized (Quadramodal) Latex Batch

1. Maximization of Packing Factor:

A. 3 Uniform Components [30WES]:

Component Size	Component Volume Fraction
A	66.0
B	25.0
C	9.0

B. 4 Uniform Components [61MCG]:

Component Size	Component Volume Fraction
A	60.7
B	23.0
C	10.2
D	6.1

C. Hybrid System Produced (interpolation of the above models):

Component Size	Volume Fraction (4 Component Eq.)	Volume Fraction (3 Component Eq.)
A	62.8	62.8
B	23.8	23.8
C	10.4	13.4
D	3.0	

Notes:

1.  $A > B > C > D$
2. Each Component is Perfectly Uniform
3. The Size Ratio Between Two Consecutive Components is Recommended to Be (At Least) 7:1 [61MCG]

in order to separate the slurry from the milling media. A magnetic stir bar<sup>49</sup> was then placed in the decanted slurry. The container was then placed on a stirrer/hot plate,<sup>50</sup> and covered loosely with aluminum foil.<sup>51</sup> The heat was set to a low level (3) and the stirring to a moderate speed (6). The latter was chosen to promote vigorous stirring without causing splashing of the slurry. The entire apparatus was enclosed within a fume hood<sup>52</sup> to vent the MeOH fumes. The slurry was heated and stirred in this manner until it became a solid cake. At this point the evaporating dish was removed from the stirrer/hot plate and the cake was broken up into small chunks using both a metal spatula<sup>53</sup> and a pestle.<sup>54</sup> The evaporating dish, containing the glass powder, was then placed in a vacuum oven<sup>55</sup> and heated to approximately 175°C in a vacuum of >30" Hg (gauge) until dry (usually overnight).

The criterion for powder dryness was that the vacuum gauge indicate a maximum vacuum reading (>30" Hg (gauge)), and remain stable over a period of at least, 30 min. without vacuum pumping. Pumping was limited to periods of no longer than 15 min. in order to prevent contamination of the milled glass powder with backstreamed vacuum pump oil. A total of 10 batches were milled in this manner. After drying, each powder batch was mixed with the others in one of two 1 gallon (3.79

---

<sup>49</sup> Catalog Number: 14-511-93, Fisher Scientific, 1600 Parkway View Drive, Pittsburgh, PA 15205

<sup>50</sup> Model Number: PC-520, Corning Inc., Corning, NY 14831

<sup>51</sup> Heavy Duty Reynold's Wrap, Reynold Metals Company, Richmond, VA, 23261

<sup>52</sup> 8' laboratory fume hood, Kewaunee Scientific Corp., Statesville, NC 28677

<sup>53</sup> Catalog Number: 14-373-25A, Fisher Scientific, 1600 Parkway View Drive, Pittsburgh, PA 15205

<sup>54</sup> Catalog Number: 12-961-5D, Fisher Scientific, 1600 Parkway View Drive, Pittsburgh, PA 15205

<sup>55</sup> Model Number: 5831, National Appliance Company, Portland, OR



1) polyethylene (PE) jars<sup>56</sup> by inverting the powder-filled container for approximately 250 repetitions after each batch addition. After all the batches were mixed together in this manner, portions of the powder in each of the two PE jars were removed and mixed together in the opposite jar, using the above method, in order to further pursue powder homogeneity. This removal/mixing process was repeated 5 times. The powder was then stored in the two PE jars and sealed for future experimentation.

### 3.3 Powder Characterization

#### 3.3.1 Overview

Powder characterization was performed in order to gain a knowledge of the composite precursor powders and to investigate the effect that ball milling, in MeOH, has upon the BS glass. It is necessary to know the powder density when designing and batching composites. Furthermore, a knowledge of the powder size and size distribution, as well as the powder surface area and appearance is helpful in optimizing processing parameters and material properties.

Composition data is necessary in order to ensure that the powder precursors are what they are supposed to be. This is very valuable when comparing experimental results to data reported in the literature. Since the  $\text{Si}_3\text{N}_4$  was used as-received (and came with a guaranteed analysis), composition investigation was not necessary. Chemical composition analysis of the latexes investigated was also deemed unnecessary, since the UPLMs were produced from pure styrene, and since the latexes were only used as a filler and were removed completely during pyrolysis and sintering procedures (as indicated by dielectric data). However, it was deemed necessary that a study be performed investigating the effects of ball milling, in MeOH, on the composition of the BS glass powder since

---

<sup>56</sup> Catalog Number: 11-815-11B, Fisher Scientific, 1600 Parkway View Drive, Pittsburgh, PA 15205

milled powder compositions are frequently different from their precursors, due to dissolution of either the powder or the milling media.

Finally, a knowledge of how the powder surface evolves with heat treatment is also helpful when optimizing thermal treatment schedules. Since crystalline silicon nitride is stable with regard to sintering and viscous flow at the temperatures investigated, no such study was performed upon the  $\text{Si}_3\text{N}_4$  powder used in this study. Since the polystyrene latexes were removed via pyrolysis, no studies of surface area, as a function of thermal treatment, were performed upon them either. However, investigation of the evolution of powder surface area with thermal treatment was performed upon the ball milled BS glass powder since it was the sintering matrix in the materials investigated.

### 3.3.2 Visual

Visual inspection of the precursor powders was provided via SEM.<sup>25</sup> The powder specimens were prepared as via a method similar to that described in section 3.2.2 above, with the exception that the dispersion system used was aqueous (pH ~9.5). As will be discussed below, it was desirable to investigate the surface smoothness of the borosilicate glass powder both prior and subsequent to milling in order to investigate dissolution effects of milling upon the glass. Since said porosity was expected to be smaller than the minimum resolution of the SEM, transmission electron microscopy (TEM)<sup>57</sup> was used.

Specimens were prepared by dispersing approximately 20 mg of the respective powder in denatured  $\text{EtOH}^{24}$  in a polystyrene sample vial,<sup>26</sup> capping the vial, and subjecting the dispersion to approximately 15 min. of sonic treatment in order to assure destruction of soft agglomerates.

---

<sup>57</sup> Model Number: 200CX, JEOL Ltd, Tokyo, Japan

Approximately 1 drop of said suspension was then gently decanted onto a holey-carbon-substrate-covered TEM specimen grid<sup>58</sup> using a 20  $\mu$ l capillary pipette.<sup>59</sup> The specimen grid was placed on top of 0.22  $\mu$ m pore size, nylon filter paper,<sup>60</sup> which had been previously placed upon absorbent tissue,<sup>61</sup> in order to provide a driving force for dispersion flow through the holes in the carbon substrate. A glass specimen cover<sup>62</sup> was then placed over the specimen, during drying, in order to prevent contamination. Specimens were viewed uncoated in a TEM<sup>57</sup> utilizing 200 KeV electron accelerating potential at magnifications of up to 300,000X.

### 3.3.3 Density

Powder density was determined using He gas pycnometry,<sup>63</sup> as recommended,<sup>64</sup> using the large sample cell. A representative powder sample was taken from the powder container and placed in a preweighed large sample cup. The sample with cup weight was then measured and recorded. The cup and powder were then dried in a vacuum oven<sup>55</sup> at >30" Hg (gauge). The drying temperature used was approximately 60 and 175°C for polymeric and ceramic materials respectively. A vacuum was pulled on the chamber periodically for durations not exceeding 15 min. in order

---

<sup>58</sup> Prepared by C. E. Randall, NYSCC at Alfred University, Alfred, NY

<sup>59</sup> Catalog Number: 5878 Unopette pipette, Becton Dickinson Vacutainer Systems, Rutherford, NJ 07070

<sup>60</sup> Catalog Number: NO2-SP142-25, Fisher Scientific, 1600 Parkway View Drive, Pittsburgh, PA 15205

<sup>61</sup> Catalog Number: 06-666-11, Fisher Scientific, 1600 Parkway View Drive, Pittsburgh, PA 15205

<sup>62</sup> Catalog Number: 08-749, Fisher Scientific, 1600 Parkway View Drive, Pittsburgh, PA 15205

<sup>63</sup> Model Number: MVP-1 Multipycnometer, Quantachrome Corporation, Syosset, NY, 11791

<sup>64</sup> See pages 7-14 of Operating Manual for footnote 66.

to reduce backstreaming of vacuum pump oil onto the powder samples. The samples were dried in this manner for approximately 12 h. The sample was allowed to cool, in the vacuum oven, to ambient temperature.

UPLM powder samples were obtained by filtering from suspension using a vacuum filtering apparatus.<sup>65</sup> The filter cake was then dried at approximately 60°C at ambient pressure. The dry cake was then broken up, placed in a clean 125 ml PE bottle.<sup>66</sup> The bottle was then tightly capped and shaken vigorously by hand for approximately 3 min. in order to further break up agglomerates. The resulting powder was then subjected to the drying treatment outlined above for polymers, and was then ready for density characterization.

After powder sample drying, the cup was removed from the vacuum oven and quickly placed inside the pycnometer sample chamber. The sample was then subjected to a He<sup>67</sup> gas flow for no less than 15 minutes. Subsequent to said gas purging the experiment was performed.

All external gas valves were closed and the chamber/reservoir valve was closed. The external He valve was then opened allowing the pycnometer reservoir to fill with gas. This valve was then closed as the pressure gauge reading approached 15 psi (0.103 MPa) and said reading was recorded. Next the chamber/reservoir valve was opened, allowing the pycnometer sample chamber to fill with the He previously in the pycnometer reservoir. After pressure equilibration of the two chambers was achieved (as determined by a stable pressure gauge reading) the pressure was again recorded. The He external exhaust valve was then opened and the reservoir and sample chamber allowed to come to ambient

---

<sup>65</sup> Filtered through number 1 Whatman qualitative filter paper, Whatman International, Ltd., Maidstone, England, using Catalog Number: 10-437-23A, Fisher Scientific suction funnel

<sup>66</sup> Catalog Number: 02-893-5C, Fisher Scientific, 1600 Parkway View Drive, Pittsburgh, PA 15205

<sup>67</sup> Catalog Number: UN1046, Liquid Air Corp., Walnut Creek, CA 94596

pressure as indicated by a null reading of the pycnometer pressure gauge. The gauge was then rezeroed and the process repeated.

After no less than 4 repetitions of this procedure, the sample container and sample were removed from the sample chamber and reweighed. The powder density was then determined. The equations used to calculate powder density by way of gas pycnometry are outlined in Table 3.4. The powders were then returned to their original container for further use.

No less than two independent runs were performed upon each powder in order to provide a measurement of precision for said experimentation. The pycnometer was also calibrated prior to testing following the recommended procedure.<sup>64</sup>

#### 3.3.4 Size Characterization of Ceramic Powders

The particle sizes and size distributions of the ceramic powders were determined using both gravitational and centrifugal sedimentation techniques. Latex powder sizes and size distributions were determined as described above in section 3.2.2. Gravitational sedimentation characterization utilized an x-ray attenuation technique.<sup>68</sup> A variety of dispersion mediums were used on each ceramic powder, including aqueous (approximately pH 9.5 via concentrated  $\text{NH}_4\text{OH}$ <sup>69</sup> addition),  $\text{MeOH}$ <sup>45</sup> and denatured  $\text{EtOH}$ .<sup>24</sup> The powder volume fraction used in all cases was between 2 and 3 V%.

Centrifugal sedimentation characterization was provided via a horizontal platen centrifuge, light attenuation technique.<sup>70</sup> The dispersion medium utilized for this technique was approximately pH 9.5

---

<sup>68</sup> Model Number: 5000 Sedigraph, Micromeritics, Corp., One Micromeritics Drive, Norcross, GA 30093

<sup>69</sup> Catalog Number: A669-500, Fisher Scientific, 1600 Parkway View Drive, Pittsburgh, PA 15205

<sup>70</sup> Model Number: CAPA 700, Horiba Ltd., Kyoto, Japan

Table 3.4

Equations Used to Determine Powder Density  
Using He Gas Pycnometry

1. Powder Density,  $\rho$  (g/cm<sup>3</sup>):

$$\rho = \frac{W_p}{V_p}$$

where:  $W_p$  is powder weight (g)  
 $V_p$  is powder volume (cm<sup>3</sup>)

2. Powder Volume,  $V_p$  (cm<sup>3</sup>):

$$V_p = V_c - V_r \left[ \left( \frac{P_1}{P_2} \right) - 1 \right]$$

where:  $V_c$  is sample cell volume (cm<sup>3</sup>)  
 $V_r$  is reference volume (cm<sup>3</sup>)  
 $P_1$  is pressure reading after pressurizing  
the reference cell (psi)  
 $P_2$  is pressure reading after including the  
sample cell in the pressurized circuit  
(psi)

- Notes:
1. Powder weights obtained to nearest tenth of milligram using a model number: XD 100A, Fisher Scientific precision scale
  2.  $V_c$  used for the large cell was 149.064 cm<sup>3</sup>
  3.  $V_r$  used for the large cell was 66.820 cm<sup>3</sup>



aqueous (pH adjusted using concentrated  $\text{NH}_4\text{OH}$ <sup>69</sup>). A much lower (approximately 0.1 V%) powder volume fraction was used in making suspensions for this technique. The suspension solids loading was adjusted until a maximum light attenuation of greater than 90% of full scale was achieved. For both particle sizing techniques, the suspensions were sonicated for approximately 15 min., prior to testing, in order to break up agglomerates.

The x-ray sedimentation-derived ceramic particle sizing data for each ceramic powder characterized was obtained by averaging the data of no less than three separate settling repetitions at cumulative volume percent less than (CVPF) intervals of 5 V%. It was necessary to average the data in this manner since the instrument<sup>68</sup> provided output in a log-linear fashion. This methodology was used in order to avoid errors of estimation associated with reading constant intervals on a log axis.

The averaged data was then fitted utilizing the least squares polynomial regression computer program illustrated in Appendix III. The order of the polynomials used for curve fittings was determined from the same program and was chosen to minimize the standard error of estimate. The averaged data was then manually encoded into a computer spreadsheet<sup>36</sup> program, and the experimental data and the corresponding polynomial fit were compared.

Typically, polynomial regression becomes inaccurate at range extrema. In cases where this occurred, linear and linear spline fits were utilized to make the least squares regression polynomials fit the data better at the range extrema. The spreadsheet utilized converts the input CVPF data to cumulative volume percent larger than (CVPL), cumulative number percent finer than (CNPF), cumulative number percent larger than (CNPL) and estimated powder surface area ( $S_A$ ) data. All particle sizing calculations are based upon spherical particle geometries. The spreadsheet also provides output in histogram form, as well as a medium for calculating geometric standard deviation (GSD).

The equations used by the spreadsheet to perform said calculations are outlined in Table 3.5 (part A). Centrifugal particle sizing data was taken from an average of at least three experimental repetitions as well. In this case however, the averaging involved the volume fraction between two contiguous sizes on a linear axis, and thus, no polynomial fitting was required. The averaged data were then encoded manually into a computer spreadsheet, as above, to obtain similar outputs. The equations utilized for centrifugal particle size analysis are outlined in Table 3.5 (part B) as well.

### 3.3.5 Surface Area

Surface areas of the respective powders were measured using gas adsorption/desorption methods. Surface area and, when deemed necessary, the powder surface pore size distribution was determined for each powder used in the investigation. Data were obtained utilizing either a manual<sup>71</sup> or an automated<sup>72</sup> surface area analysis unit.

When performing manual surface area analysis, the sample holder tube was precleaned, dried and weighed. An amount of powder (previously dried as described in section 3.3.3 above) was added to the sample holder and any powder sticking to the inside of the vertical extensions of the sample holder was brushed into the bottom using a pipe cleaner.<sup>73</sup> A sealing apparatus was then connected to the sample holder and the assembly was affixed to the outgas section of the manual surface area analysis unit where it was purged with N<sub>2</sub> gas<sup>74</sup> for not less than 2 h at approximately 150°C.

---

<sup>71</sup> Model Number: OS-7 BET unit with Model Number: LMFC-4 gas mixing unit, Quantachrome Corp., 69 Glen Cove Rd, Greenvale, NY 11548

<sup>72</sup> Model Number ASAP 2000, Micromeritics Corp., One Micromeritics Drive, Norcross, GA 30093

<sup>73</sup> Catalog Number: 03-642B, Fisher Scientific, 1600 Parkway View Drive, Pittsburgh, PA 15205

<sup>74</sup> Catalog Number: 1066, Liquid Air Corp., Walnut Creek, CA 94596

Table 3.5.

Equations Used to Calculate Size, Size Distribution, Estimated Surface Area and Geometric Standard Deviation of Sizing Data (Based on Spherical Powders) Obtained for the Ceramic Powders Investigated Using X-Ray Sedimentation and Centrifugal Particle Size Analysis Techniques

1. Size:

Size is determined by averaging the cumulative percent finer than size data at 5 V% intervals for no less than three experimental repetitions. The size distribution data is plotted as equivalent spherical diameter (abscissa) versus cumulative volume percent finer than (ordinate). The median particle size is determined by said average at 50 V% CVPF. After polynomial fitting, cumulative surface area and cumulative number percents are calculated.

2. Spherical Surface Area at Size, SSAAS, (Sedigraph Only, Automatically Calculated with CPSA)  $\text{m}^2/\text{g}$ :

$$SSAAS = \frac{6 \times \frac{\Delta M\%}{100}}{\rho \frac{(D_{\text{Larger}} - D_{\text{smaller}})}{2}}$$

where:  $D_{\text{Larger}}$  is the largest equivalent spherical diameter of the size region of interest ( $\mu\text{m}$ )

$D_{\text{smaller}}$  is the smallest equivalent spherical diameter of the size region of interest ( $\mu\text{m}$ )

$\Delta M\%$  is the change in mass percent between  $D_{\text{Larger}}$  and  $D_{\text{smaller}}$

$\rho$  is the theoretical density of the powder  $\text{g}/\text{cm}^3$

3. Cumulative Spherical Surface Area, CSSA,  $\text{m}^2/\text{g}$ :

$$CSSA = \sum_{i=\text{size1}}^{i=\text{size2}} SSAAS_i$$

where:  $i_{\text{size1}}$  and  $i_{\text{size2}}$  are set to the maximum and minimum particle sizes of the powder for Total Specific Surface Area

Table 3.5 (continued)

4. Polynomial Curve Fit for Mass Percent at Size,  $M\%_{@size}$ :

$$M\%_{@size} = \sum_{i=0}^{i=n} C_i \times D^i$$

where: D is the equivalent spherical diameter ( $\mu\text{m}$ )

$C_i$  is the  $i^{\text{th}}$  polynomial coefficient

n is the order of the polynomial

## Relevant Data and Coefficients Utilized

## A. Sedigraph:

Corning 7070 As-Received Borosilicate Glass Powder			
Coefficient	Value		
0	2.562431	Order	5 <sup>th</sup>
1	13.333852	Correlation	0.9979
2	-0.9415702	Standard Error of Estimate	2.309 $M\%_{@size}$
3	0.03502355	Linear Extrapolation	
4	$-6.219517 \times 10^{-4}$	High End	Yes, Above 57.0 $\mu\text{m}$
5	$4.107572 \times 10^{-6}$	Low End	No

Corning 7070 Ball Milled Borosilicate Glass Powder			
Coefficient	Value		
0	0.191787	Order	6 <sup>th</sup>
1	12.78353	Correlation	0.9999
2	18.60418	Standard Error of Estimate	0.2795 $M\%_{@size}$
3	-7.567243	Linear Extrapolation	
4	1.184119	High End	Yes, Above 7.5 $\mu\text{m}$
5	-0.08355908	Low End	No
6	$2.169674 \times 10^{-3}$		



Table 3.5 (continued)

Ube SNE03 As-Received Silicon Nitride Powder			
Coefficient	Value		
0	131.1378	Order	11 <sup>th</sup>
1	-497.6126	Correlation	0.9991
2	547.9822	Standard Error of Estimate	2.014 M% <sub>@size</sub>
3	-136.0857	Linear Extrapolation	
4	-31.98561	High End	Yes, Above 4.8 $\mu\text{m}$
5	7.148575	Low End	No
6	2.59008		
7	-0.3918017		
8	0.4788766		
9	0.01901949		
10	$5.456677 \times 10^{-4}$		
11	$-1.595376 \times 10^{-3}$		

## B. Centrifugal Particle Size Analysis:

Corning 7070 As-Received Borosilicate Glass Powder			
Coefficient	Value		
0	-1.825504	Order	9 <sup>th</sup>
1	13.59646	Correlation	0.9995
2	-0.9358228	Standard Error of Estimate	1.252 M% <sub>@size</sub>
3	0.0254202	Linear Extrapolation	
4	$-5.821581 \times 10^{-5}$	High End	Yes Above 28.0 $\mu\text{m}$
5	$-2.938714 \times 10^{-6}$	Low End	Yes, Below 0.7 $\mu\text{m}$
6	$-9.496944 \times 10^{-9}$		
7	$-7.946381 \times 10^{-9}$		
8	$2.832732 \times 10^{-10}$		
9	$-2.477481 \times 10^{-12}$		

Table 3.5 (continued)

Corning 7070 Ball Milled Borosilicate Glass			
Coefficient	Value		
0	0.110559	Order	8 <sup>th</sup>
1	-2.9455459	Correlation	0.9997
2	25.04777	Standard Error of Estimate	0.3146 M% <sub>@size</sub>
3	-5.796151	Linear Extrapolation	
4	-0.3954611	High End	Yes, Above 6.3 $\mu\text{m}$
5	0.2121908	Low End	Yes, Below 0.2 $\mu\text{m}$
6	$3.228821 \times 10^{-4}$		
7	$-4.345972 \times 10^{-3}$		
8	$3.132128 \times 10^{-4}$		

Ube SNEO3 As-Received Silicon Nitride Powder			
Coefficient	Value		
0	8.467468	Order	8 <sup>th</sup>
1	-167.6861	Correlation	0.9995
2	331.6824	Standard Error of Estimate	1.240 M% <sub>@size</sub>
3	-127.6637	Linear Extrapolation	
4	-4.449819	High End	Yes, Above 1.5 $\mu\text{m}$
5	1.441593	Low End	Yes, Below 0.7 $\mu\text{m}$
6	2.07041		
7	0.3125768		
8	-0.1546427		

Note: For the specifics of the polynomial regression algorithm used, see APPENDIX III

5. Polynomial Derived Values:

- a. Mass Percent at Size, M%<sub>@size</sub>: (see 4 above)
- b. Equivalent Spherical Surface Area at Size, SSAAS, (see 2 above)



Table 3.5 (continued)

- c. Cumulative Spherical Surface Area, CSSA: (see 3 above)
- d. Relative Number of Equivalent Spherical Particles at Size, RNSPAS:

$$RNSPAS = \frac{\left( \frac{M_{\text{size}}}{100} \right)}{\frac{4\pi}{3} \left( \frac{D_{\text{Larger}} + D_{\text{smaller}}}{4} \right)^3}$$

where:  $D_{\text{Larger}}$  is the largest equivalent spherical diameter of the size region of interest ( $\mu\text{m}$ )

$D_{\text{smaller}}$  is the smallest equivalent spherical diameter of the size region of interest ( $\mu\text{m}$ )

- e. Total Relative Number of Spherical Equivalent Particles, TRNP:

$$TRNP = \sum_{\text{smallest}}^{\text{Largest}} RNSPAS$$

- f. Number Percent at Size,  $N_{\text{size}}$ :

$$N_{\text{size}} = \frac{RNSPAS}{TRNS} \times 100$$

- g. Cumulative Number Percent Finer, CNPF:

$$CNPF = \sum_{\text{smallest}}^{\text{size of interest}} N_{\text{size}}$$

- h. Cumulative Number Percent Larger, CNPL:

$$CNPL = \sum_{\text{size of interest}}^{\text{Largest}} N_{\text{size}}$$

Note: g and h have exact analogs for Cumulative Mass Percent Finer (CMPF), and Cumulative Mass Percent Larger (CMPL).

After outgassing was completed, the sample fixture was removed from the outgassing unit and mounted to the adsorption unit of the manual surface area analysis unit. The  $N_2/He$  ratio was then set to 6.0/14.0 and the apparatus was switched to absorption mode. The mixed gas signal meter as well as the digital gas counter was then zeroed. At this point the sample was immersed in a liquid  $N_2$ <sup>75</sup> ( $LN_2$ ) bath. After the digital counter ceased counting, the mode switch was changed to desorption and the previously mentioned zeroing procedure was performed again. The  $LN_2$  immersion bath was then removed and the sample was allowed to warm-up to ambient temperature. After a short period, this procedure was aided by immersing the sample in an ambient temperature water bath. After the digital gas counter stopped increasing, its reading was recorded.

Next, a gas volume standardization was performed. The meters were zeroed as previously mentioned and a known amount of gas was extracted from the gas outlet port using a calibrated syringe,<sup>76</sup> then reinjected into the gas inlet port. After the digital counter ceased counting, the reading was again noted. This was repeated until a reading was achieved that was within 5% of the desorption reading. At this point, both the volume of gas injected and the counter reading were recorded. The  $N_2/He$  ratio was then changed to the next lowest of the  $N_2$  concentration investigated.

This process was performed at  $N_2/He$  ratios of 6.0/14.0, 4.0/16.0, 3.0/17.0 and 2.0/18.0. The sample cell was then removed, the outside thoroughly wiped off and quickly weighed. A computer spreadsheet<sup>36</sup> was then utilized to determine the specific surface area, the correlation of data point linearity with  $N_2$  concentration coefficient and the mean particle size using a spherical approximation.

---

<sup>75</sup> Burmac Enterprises, Orlando, FL 32808

<sup>76</sup> Model Number: 1010, Hamilton Corporation, Reno, Nevada

Table 3.6 illustrates the equations utilized to perform the manual surface area analysis calculations. The entire process was repeated for each sample tested in order to ensure data reproducibility.

Automated surface area analysis was performed when multipoint surface area analysis was desired. Into a precleaned, dried and weighed sample holder, an amount of powder was placed. Any powder sticking to the cell walls was removed with a bottle brush.<sup>77</sup> The sample cell was then sealed and outgassed at 200°C (60°C for latex) in a vacuum for no less than three h. The sample cell was then removed, allowed to cool and reweighed. The sample cell was then placed in the BET unit, the pressure gauges zeroed and the run initialized. The rest of the run was automatically performed by the microprocessor controlled apparatus. At the end of the run, the sample was removed and again weighed in order to monitor any weight change during the analysis.

The data output of said instrument covers a myriad of various factors. Most important to this study are the adsorption and the desorption surface areas as a function of calculated pore size. Also important were the specific surface area and the mean pore size during desorption.

Surface area analysis was also utilized to investigate the effect of MeOH exposure on the as-received BS glass powder. This investigation was necessary in order to help determine the effects of ball milling, in MeOH, on the BS glass powder. Two different routes were pursued.

The first involved mechanical stirring of a 10 V% solids BS glass in MeOH<sup>45</sup> suspension in an aluminum foil<sup>51</sup> covered 250 ml beaker<sup>78</sup> at ambient temperature.

---

<sup>77</sup> Catalog Number: 03-637, Fisher Scientific, 1600 Parkway View, Pittsburgh, PA 15205

<sup>78</sup> Catalog Number: 02-540K, Fisher Scientific, 1600 Parkway View Drive, Pittsburgh, PA 15205

Table 3.6

Calculations Utilized to Perform Manual  
Surface Area Analysis

1. Adsorption Calibration,  $X_{cal}$  is performed for each  $P/P_0$  (point) characterized:

$$X_{cal} = \frac{P_{amb} \times MW_{N_2} \times V_{cal}}{62350 \times T_{Abs}}$$

where:

- $P_{amb}$  is ambient pressure in mm Hg
- $MW_{N_2}$  is the molecular weight of  $N_2$  in g/mol
- $V_{cal}$  is calibration volume of  $N_2$  in ml
- $T_{Abs}$  is temperature ( $^{\circ}K$ )
- $P$  is the  $N_2$  partial pressure of the adsorption gas mixture
- $P_0$  is the total pressure of the adsorption gas mixture

2. The Adsorption Value,  $X$  is the determined for each point:

$$X = X_{cal} \times \frac{D}{D_{cal}}$$

where:

- $D$  is the desorption count number
- $D_{cal}$  is the calibration count

3. The Normalized Adsorption Values ( $Y$ ) are then plotted as a function of  $P/P_0$ :

$$Y = \frac{1}{X \left( \frac{P_0}{P} - 1 \right)}$$

and a linear least squares regression performed.

Table 3.6 (continued)

4. The Total Surface Area,  $SA_{Tot}$  ( $m^2$ ), is then calculated:

$$SA_{Tot} = \frac{\left(\frac{1}{m+D}\right) N_{Av} X_{ads}}{MW_{N_2}}$$

where:  $X_{ads}$  is the adsorption crosssection of an  $N_2$  molecule ( $1.62 \times 10^{-19} m^2$ )  
 $N_{Av}$  is Avogadro's number ( $6.023 \times 10^{23}$  molecules/mol)  
 $m$  is the slope of the linear regression  
 $b$  is the intercept of the linear regression

5. The Specific Surface Area,  $SA$  ( $m^2/g$ ), is then calculated:

$$SA = \frac{SA_{Tot}}{W}$$

where:  $W$  is the sample weight (g)

6. Also, the Equivalent Spherical Diameter,  $D_{eq}$  ( $\mu m$ ), is calculated:

$$D_{eq} = \frac{6}{SA \times \rho}$$

where:  $\rho$  is the powder density ( $g/cm^3$ )

Stirring was achieved through the use of a 1" (2.54 cm) polytetrafluoroethylene (PTFE) covered magnetic stir bar<sup>79</sup> powered by a magnetic stirplate.<sup>21</sup> Stirring durations of 1, 3, 5 and 10 days were investigated. After stirring, the suspensions were uncovered and allowed to dry without stirring, at ambient temperature. The resulting powder was then dried as described in section 3.3.3 above. After drying, manual surface area analysis was performed upon the respective powders as outlined above. It was realized, however, that this methodology may be flawed since mechanical stirring might result in powder milling, which would also increase powder surface area.

Thus, a second experiment was performed in which no milling was involved. The as-received BS glass powder was dispersed in MeOH<sup>45</sup> at the same concentration as that prepared during ball milling. Approximately 50 ml of said suspension was mixed in a 125 ml PE bottle.<sup>80</sup> The bottle was sealed and placed within a heated shaker<sup>81</sup> bath for 20 h (the duration used for ball milling). The temperature was set at 40°C (an estimate of the temperature achieved during milling processes). The bottle was then removed, uncapped and dried in a vacuum of >30" Hg (gauge) at ambient temperature. The dry powder was then further dried at approximately 180°C overnight in a similar vacuum. Automated surface area and pore size analysis was then performed on said powder as described above.

Automated surface area analysis was also utilized in order to investigate changes in both surface area and surface pore size distribution of both ball milled BS glass powder and slip cast compacts of ball milled BS glass powder (produced by the method described below)

---

<sup>79</sup> Catalog Number: 14-511-60B, Fisher Scientific, 1600 Parkway View Drive, Pittsburgh, PA 15205

<sup>80</sup> Catalog Number: 02-923-C, Fisher Scientific, 1600 Parkway View Drive, Pittsburgh, PA 15205

<sup>81</sup> Model Number: 129 Shaking Heated Water Bath, Fisher Scientific, 1600 Parkway View Drive, Pittsburgh, PA 15205



as a result of thermal treatment. The thermal treatments emulated the time-temperature schedule used for both organics pyrolysis and sintering with the exception of ultimate temperature. Samples were heat treated to ultimate temperatures of 250, 350, 450, 500, 550, and 600°C then furnace cooled.

Figure 3.4 illustrates the heat treatments used for said experiments. The procedure used for the heat treatments is described below in the pyrolysis/presintering section.

### 3.3.6 Chemical

In order to further investigate changes in the BS glass powders, both prior and subsequent to ball milling and dissolution, inductively coupled plasma (ICP)<sup>82</sup> solution analysis was performed on the glass powder. Table 3.7 outlines the various BS glass powders analyzed via ICP spectroscopy.

From 0.05 to 0.15 g of finely ground BS glass powder was weighed into a pre-tared teflon digestion bomb.<sup>83</sup> The digestion bomb was then placed within a fume hood and 15 ml of concentrated (49%) HF<sup>84</sup> was added dropwise to the powder, using a class B polypropylene pipette,<sup>85</sup> taking care to avoid possible violent reaction(s). The digestion bomb was then carefully and securely assembled.

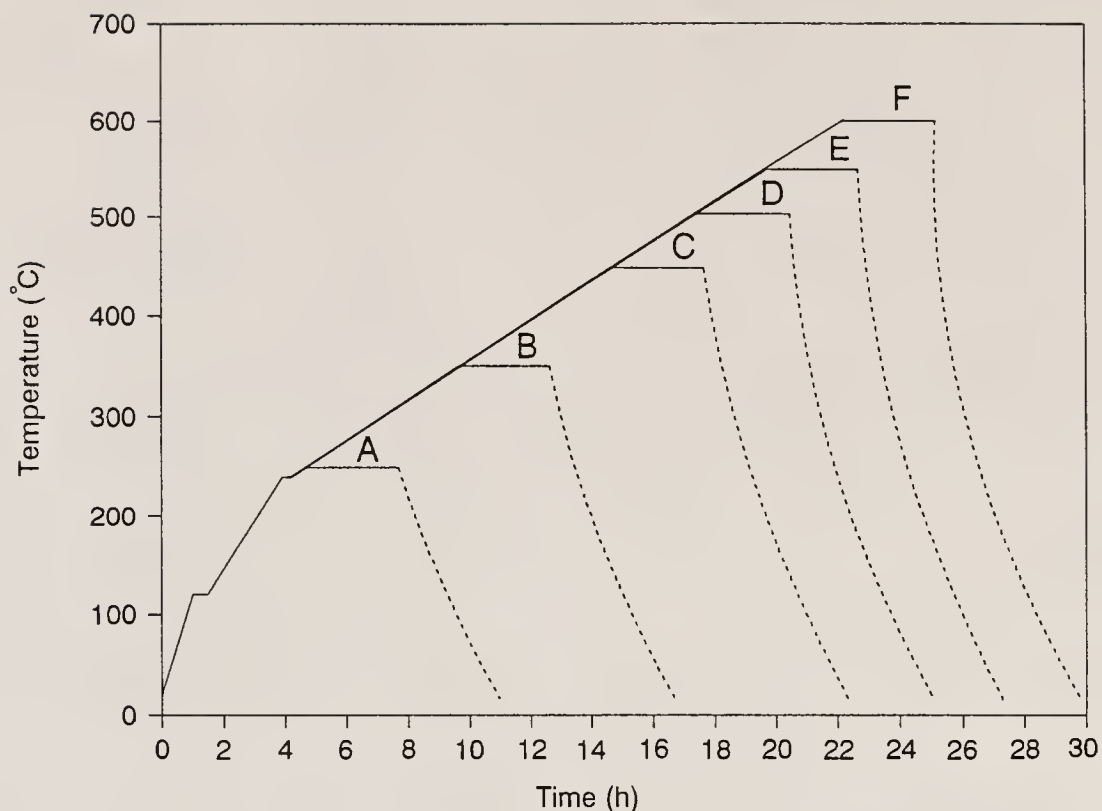
---

<sup>82</sup> Model Number: PLASMA 200 Inductively Coupled Plasma Spectrometer, Instrumentation Laboratory Inc., Lexington, MA 02173

<sup>83</sup> Catalog Number: 01-023, Fisher Scientific, 1600 Parkway View Drive, Pittsburgh, PA 15205

<sup>84</sup> Catalog Number: A147-1LB, Fisher Scientific, 1600 Parkway View Drive, Pittsburgh, PA 15205

<sup>85</sup> Catalog Number: 13-662-10, Fisher Scientific, 1600 Parkway View Drive, Pittsburgh, PA 15205



Curve	Set Point (°C)	Rate to Set Point (°C/h)	Time at Set Point (h)
All	20	0	0.0167 (1 minute)
All	120	100	0.5
All	240	50	0.25
A	250	20	3.0
B	350	20	3.0
C	450	20	3.0
D	500	20	3.0
E	550	20	3.0
F	600	20	3.0
All	RT	Furnace Cool	End

Note: RT designates Room Temperature (usually 20 to 25 °C)

Atmosphere: Compressed Air

Flow Rate: Approximately 240 cm<sup>3</sup>/m

Figure 3.4

Thermal treatment schedules used in the investigation of the effect of thermal treatment upon the surface areas of ball milled BS glass powder and of slip cast BS glass compacts

Table 3.7

Description of BS Glass Powders  
Investigated Chemically Using ICP and FTIR

I.D. #	Designation	Description
1	7070 INGOT	Ground BS Glass Ingot Received From Corning Glass
2	7070 AR	<325 Mesh BS Glass Powder As Received From Corning Glass
3	7070 MEOH	7070 AR Powder Stirred in MeOH at 40°C for 20 h (see section 3.3.5)
4	7070 BM	7070 AR Powder, Ball Milled in MeOH For 20 h (see section 3.3.3)

The bomb was then removed from within the fume hood and placed inside an oven<sup>86</sup> for 12 h at a temperature of 80°C. During this time, a 100 ml capacity polypropylene volumetric flask<sup>87</sup> was filled with approximately 75 ml of deionized (DI)H<sub>2</sub>O.<sup>88</sup> After said heat treatment, the digestion bomb was removed from the oven, placed again in the fume hood and allowed to cool to ~60°C. The digestion bomb was then opened, being careful not to spill the contents (the acid bomb must be opened while still fairly hot in order to avoid vacuum sealing of the digestion bomb). The dissolved BS glass-HF solution was then transferred to the volumetric flask. Any remaining solution was carefully rinsed from the digestion bomb with approximately 5 ml of DI H<sub>2</sub>O.<sup>88</sup> The polypropylene volumetric flask was then filled to its calibration mark with DI H<sub>2</sub>O, then allowed to cool to room temperature (RT).

Reference standards for ICP analysis were produced by dilution of commercially available reference standards,<sup>89</sup> in the above volumetric flask, using the same HF/H<sub>2</sub>O concentration as the samples had. Standards were made for Si, B, Al, Na and Li in the above manner (K was not analyzed, due to the lack of a proper PM (photomultiplier) detector). The quantitative chemical analysis data were then examined for variance both from the literature data<sup>90</sup> and between each type of treatment the powders received.

---

<sup>86</sup> Catalog Number: 13-258-10B, Fisher Scientific, 1600 Parkway View Drive, Pittsburgh, PA 15205

<sup>87</sup> Catalog Number: 10-198-50B, Fisher Scientific, 1600 Parkway View Drive, Pittsburgh, PA 15205

<sup>88</sup> Continental Deionized Water Service, 2300 N.W. 71<sup>st</sup> Pl., Gainesville, FL 32606

<sup>89</sup> Catalog Numbers: SS465-500, SB155-500, SA442-500, SS139-500, and SL45-500 for Si, B, Al, Na and Li Reference Standards respectively, Fisher Scientific, 1600 Parkway View Drive, Pittsburgh, PA 15205

<sup>90</sup> Corning Glass Product Data Literature

Fourier transform infrared (FTIR) spectroscopy<sup>91</sup> was also performed, upon the BS glass powders in Table 3.7 in order to characterize possible differences in surface chemistry between the different powders. The powders were first dried at 120°C for approximately 48 h. A representative sample of the dried powder was then placed in a DRIFT<sup>92</sup> cell and the apparatus placed within the spectrometer. Analysis was then performed in the diffuse reflection mode (which measures both the diffuse and specular components of the reflected infrared radiation) over wave numbers ranging from 4000 to 400 cm<sup>-1</sup>. A nitrogen<sup>74</sup> purge was used during the analysis. All spectra recorded were normalized to a background standard in order to provide a background correction.

### 3.4 Suspension, Casting and Green Compact Studies

#### 3.4.1 Overview

This section discusses the batching, wet processing and characterization, and green characterization of the BS glass, Si<sub>3</sub>N<sub>4</sub>, latex composites produced for this study. Details of processing and characterization methods used to investigate suspensions of each pure component are also described. These studies were necessary in order to pursue ideal green microstructures, so that the controlled microstructures could be characterized and manipulated most predictably and reproducibly over a wide range of composite compositions.

---

<sup>91</sup> Model Number: 20FXB, Nicolet Instrument Corporation, 5225 Verona Rd, Madison, WI 53711

<sup>92</sup> Spectratech Corporation, 200 Harry S. Truman Parkway, Annapolis, MD 21401

### 3.4.2 Wet Processing and Characterization

#### 3.4.2.1 Selection of the Dispersion System

In the system studied, all materials seemed to disperse well in aqueous suspensions at high pH (approximately pH 9.5). However, in order to avoid powder dissolution and/or powder surface modification during dispersion of the BS glass powder, a satisfactory non aqueous suspension system was pursued. The BS glass used (Corning 7070) is a Class I glass in regard to corrosion resistance in aqueous media (see Figure 3.5). Although the dissolution rates at the pHs of interest are not yet devastating, they could be somewhat significant for a fine powder of comparatively high surface area.

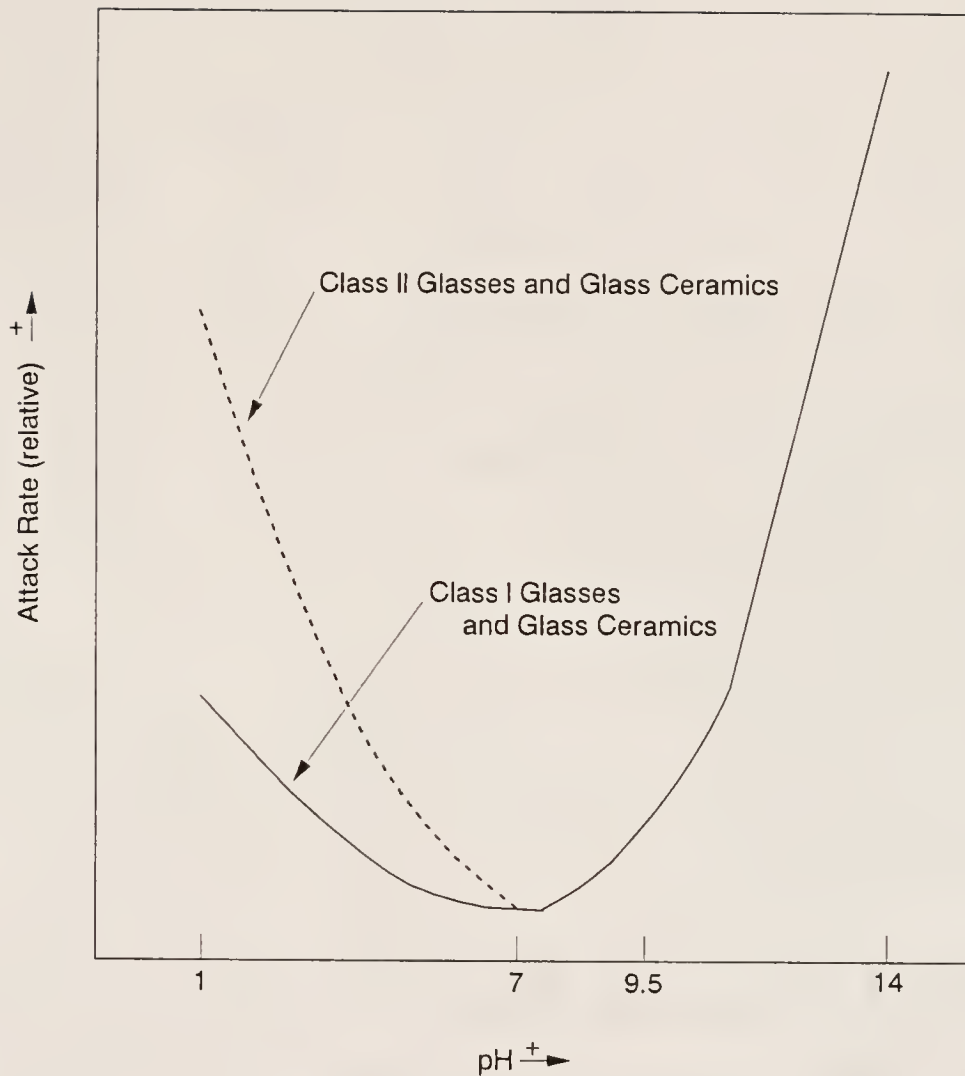
Also, an aqueous system at pH 9.5 would have a significant concentration of hydroxyls that could adversely effect dielectric properties if not totally removed during the pyrolysis/presintering, sintering or dielectric specimen preparation processes. Therefore it was decided to investigate nonaqueous dispersion systems. Initially, methyl isobutyl ketone (MIBK)<sup>93</sup> and either MeOH<sup>45</sup> or EtOH,<sup>24</sup> in the volume ratio of 3 to 1, were used as the dispersion solvent. The dispersant utilized for this system was polyvinyl butyral (PVB).<sup>94</sup> This system was found satisfactory for making quality dispersions of BS glass and Si<sub>3</sub>N<sub>4</sub>. However, it was soon found that MIBK dissolves the polystyrene latex used. Furthermore, both MIBK and MeOH are toxic. Therefore a different dispersion system was investigated. Since the latex is synthesized via dispersion polymerization in MeCell and EtOH, the next dispersion systems investigated used EtOH<sup>24</sup> as the dispersion solvent. The dispersants investigated for the EtOH based dispersion system were SMA

---

<sup>93</sup> Catalog Number: M-213, Fisher Scientific, 1600 Parkway View Drive, Pittsburgh, PA 15205

<sup>94</sup> Butvar B-98, Monsanto Company, St. Louis, MO 63166





General Effect of pH in Aqueous Solutions

Source: Corning Glass Works, Properties of Corning's Glass and Glass Ceramic Families: Materials for the Design Engineer, p. 5, (1979).

Figure 3.5

Dissolution characteristics of Corning Glasses in aqueous media (source: [COR79])

1440A,<sup>95</sup> Klucel E,<sup>96</sup> and PVP K-30.<sup>97</sup> Preliminary investigation indicated that Klucel was not a satisfactory candidate due to its limited solubility in EtOH. Further investigation indicated that both PVP K-30 and SMA 1440 performed quite similarly as dispersants in this system, with PVP K-30 giving a slightly increased casting density. Therefore, PVP K-30 was used, as received, in making all suspensions.

Since the main impetus of this study was to produce a cofirable material, having controlled porosity (i.e decreased dielectric loss), no other materials were used in the dispersion system that could make the microstructure less ideal. Therefore, no plasticizers, defoaming agents, etcetera, were used in this study. Only powders, dispersion solvent and dispersant (in a minimal amount) were used.

Preliminary investigations indicated that green density increased about 1 to 2% of theoretical density as the PVP K-30 concentration was increased from 0.5 to 1.0 wt% of the total solids in the suspension in pure, ball milled BS glass suspensions. Said characterization indicated that the green density increased less than 0.5% of theoretical density as the PVP K-30 concentration was further increased from 1.0 to 2.0 wt% of the total solids in similar suspensions. Therefore, in order to pursue maximization of green density while using a minimal amount of dispersant, the concentration of the PVP K-30 dispersant used was 1.0 wt% of the total solids in the suspension for all suspensions produced for this study.

---

<sup>95</sup> ARCO Chemical Company, 1500-T Market Street, Philadelphia, PA 19101

<sup>96</sup> Hercules Incorporated, Wilmington, DE 19894

<sup>97</sup> Polyvinyl Pyrrolidone, Catalog Number: PVP K-30 (molecular weight ~ 30,000), GAF Chemicals Corporation, 1361 Alps Road, Wayne, NJ 07470

### 3.4.2.2 Characterization and Optimization of Suspension System

#### 3.4.2.2.1 Overview

When investigating composite systems, it is necessary to maximize component homogenization. Component mixing is augmented in suspensions having relatively low viscosities, while segregation during casting processes is minimized in suspensions having relatively high viscosities. Thus, a compromise must be reached in suspension viscosity that allows for adequate mixing, in reasonable time frames, while minimizing segregation during casting. Furthermore, it is necessary to choose a suspension viscosity that is low enough to allow one to handle, dispense and cast the suspension.

Finally, in order to compare different composite compositions, processing factors should remain reasonably constant. Therefore, where possible, constant solids loadings were pursued when preparing all composite suspensions investigated. This methodology was utilized so that changes in suspension parameters and green characteristics, as a function of composite composition, could be investigated.

#### 3.4.2.2.2 Rheology of Dispersed Composite Components

In order to investigate how well each of the composite components disperses in the EtOH/PVP system described above, suspensions of 20, 30 and near maximum solids loading (as described in section 3.4.2.2.3 below) were produced using the standard dispersion method described in section 3.4.3 below. Table 3.8 describes the suspensions produced for this study. A precision viscometer,<sup>98</sup> maintained isothermally at 25°C, was utilized to perform viscometry measurements.

---

<sup>98</sup> Model Number: CV100 Precision Viscometer, utilizing Model Numbers: RV20 and RC20 Control Units; the sensor system used was Number: ZA-15 Cup and Spindle, Haake, Mess-Technik GmbH. Co., Dieselstr. 4, 7500 Karlsruhe 41, West Germany

Table 3.8

Specifications for Single Composite Component  
Batches Used for Rheological Characterization

Designation	Composite Component	Vol. % Solids Loading
7070-01	Ball Milled BS Glass Powder	20
7070-02	Ball Milled BS Glass Powder	30
03209001	Ball Milled BS Glass Powder	52
SNE03-01	As-Received $\text{Si}_3\text{N}_4$ Powder	20
SNE03-02	As-Received $\text{Si}_3\text{N}_4$ Powder	30
01319101	As-Received $\text{Si}_3\text{N}_4$ Powder	46
LATEX-01	Monodisperse Polystyrene Latex Powder	20
LATEX-02	Monodisperse Polystyrene Latex Powder	30
02159103	Monodisperse Polystyrene Latex Powder	52

- Notes:
1. All suspensions dispersed in denatured  $\text{EtOH}^{24}$  using the methods described in section 3.4.3 below
  2. All suspensions had PVP K-30 concentrations of 1 wt% of the total solids in said suspension

The system was first set to recommended calibration presettings as outlined.<sup>99</sup> The system was then allowed to equilibrate for approximately 30 min. before the measurements were taken. During this warm-up period, several blank runs were performed with tap water. After this period, the sample cup and spindle were thoroughly cleaned and dried.

The dry spindle was carefully replaced and the sample cup was filled with approximately 1.5 ml of suspension, decanted from a disposable pipette.<sup>100</sup> The sample cup was then quickly placed within its holder, and an evaporation shield was placed over the sample cup holder assembly. The measurement was then initiated. The shear rate was increased from 0 to 300  $\text{s}^{-1}$  in a period of 2 min., then decreased to a shear rate of 0  $\text{s}^{-1}$  in a period of another 2 min. The sample was then removed and the sample cup and spindle thoroughly cleaned and dried. This process was repeated until two runs, having excellent agreement, were obtained.

#### 3.4.2.2.3 Optimization of Suspension System

As mentioned above, it was necessary to find a solids loading that would give a corresponding viscosity that would allow for a balance between maximization of mixing and minimization of composite component segregation during casting. Therefore, studies were performed to determine both the maximum possible solids loading (i.e. the point at which the suspension appears "doughy" or non-liquid), and the maximum process solids loading (i.e. the solids loading giving the maximum viscosity allowable for the processing methods utilized, henceforth denoted as the optimum solids loading).

---

<sup>99</sup> See the Operations Manual of Footnote 96

<sup>100</sup> Catalog Number: 13-711-5A, Fisher Scientific, 1600 Parkway View Drive, Pittsburgh, PA 15205, modified by cutting approximately 0.5 inches (1.27 cm) from the bottom of the pipette to allow transfer in the case of relatively viscous suspensions

A suspension of pure ball milled BS glass was prepared, having an initial solids loading of 45 V%, using the standard method outlined below in section 3.4.3. In this case however, a slight excess of PVP K-30 was added to allow for additional powder charging of the suspension. Powder additions of a few grams were made and recorded, and the suspension was again shaken and sonicated as in the standard dispersion method. This process was repeated until the suspension became overloaded. Suspension overloading was evident when the suspension would no longer flow and obtained a "doughy" rather than a liquid appearance.

The suspension solids loading was then calculated by summing the total powder additions, converting this value to a volume using the powder density, and dividing the obtained value by the summation of the solvent volume plus itself. The entire process was then repeated in order to insure a measure of reproducibility. The maximum solids loading obtainable by this method was approximately 54 V% solids loading.

The optimum solids loading was then determined by diluting the overloaded suspension with a relatively small amount of denatured EtOH,<sup>24</sup> to the suspension, then reshaking. This process was repeated until the suspension became liquid-like again. The amount of EtOH used for each dilution was 1 g per each dilution, to an approximately 80 cm<sup>3</sup> suspension. The optimum solids loading was determined by adding the number of additional grams of EtOH necessary for dilution to the amount in the original suspension, converting it to a volume of EtOH, then performing the solids loading calculation described above using the total amount of BS glass powder used. This process was also repeated to determine reproducibility and yielded an optimum solids loading of approximately 52 V%. This number was utilized in all the batches produced for this study.



While both these investigations were crude and by no means exacting, they did provide valuable insight that allowed for the production of homogeneous composite samples.

#### 3.4.2.2.4 Effects of Sonication and Aging Upon Suspension Properties

It was decided that a sonication experiment should be carried out in order to determine the amount of sonication necessary to insure a homogeneous suspension. This experiment involved making an 80 ml suspension (initially calculated to have 52V% total solids loading) of a 60/40 mixture of ball milled BS glass and  $\text{Si}_3\text{N}_4$  powders, in EtOH with 1 wt% PVP K-30 as a dispersant. This particular mixture was used since it had the highest viscosity and lowest green density and therefore was most difficult of the composite compositions to disperse via sonication. The batch was made in the normal manner (outlined in section 3.4.3 below), with the exception that no sonication was used during batching.

It should be noted that 52V% solids loading could not be achieved, in this manner, without overloading the suspension. Therefore, the entire batching materials were added, then a small amount of EtOH was added in order convert the overloaded paste back into a liquid-like slurry.

After significant mixing, via shaking on a paint shaker,<sup>101</sup> the slurry was rheologically characterized using the method described in section 3.4.2.2.2 above, with the exception that the M-Head<sup>102</sup> sensing system, with sensor SVII, was utilized instead of the CV100 sensing unit. This was necessary because, at this point, the suspension was too viscous to characterize via the standard sensor system.

---

<sup>101</sup> Model Number: 5400-02 Paint Conditioner, Red Devil Co., Union NJ 07083

<sup>102</sup> Part Number: M-HEAD, utilizing sensor SVII, Haake, Mess-Technik GmbH. Co., Dieselstr. 4, 7500 Karlsruhe 41, West Germany

Even using the above sensor system, the shear stress overloaded the system at approximately  $400 \text{ s}^{-1}$ . Therefore, no decreasing shear rate data was obtained for the totally unsonicated suspension.

At this point, percent solids loading analysis (as outlined in section 3.4.4 below) was performed, in order to determine the solids loading of the suspension. Also, a sample was slip cast (as outlined in section 3.4.3 below) for characterization by Hg porosimetry (as described in section 3.4.5.2 below) and by SEM (as described in section 3.4.5.1 below).

The remainder of the suspension was again paint shaken for 5 more minutes and sonicated for 15 min. After sonication, the suspension was shaken by hand for about 2 min., and another sample was taken for viscosity measurement. This time the ZA--15 sensor system was utilized in the RV--100 system (the standard protocol).

Again the upper limit of shear stress was reached before the decreasing shear rate portion of the cycle was reached, and thus, no decreasing shear rate data is available for this particular sample set either. At this point, samples were again cast for characterization via Hg porosimetry and SEM.

This procedure was repeated for sonication times of 30, 45, 60, 90, 120, and 180 min. of total sonication time. Solids loading of the suspension was measured again after 120 and 180 min. of sonication in order to monitor solvent evaporation.

After drying, the cast specimens were removed and Hg porosimetry was performed upon them. Since it was assumed that some of the samples might contain large voids, low pressure porosimetry was also performed upon the 0, 15 and 30 min. sonicated samples. Since no intrusion (within the sensitivity limits of the porosimeter) was observed, only high pressure porosimetry was deemed necessary for the characterization of the green microstructures. Mercury porosimetry experimentation was performed by the standard method, outlined below in section 3.4.5.2.

There are two problems observable from this study. First, since additional EtOH had to be added to the suspension in order to convert the overloaded suspension to a liquid-like suspension, the solids loading of the suspension (ranging from 50.0 to 50.9) is less than that of the standard suspensions used. Secondly, since samples were continuously removed from the suspension, the total amount of the suspension was constantly reduced. The final amount of suspension was approximately 35 cm<sup>3</sup>. Thus total sonication times used were greater than those deemed necessary by this study. Therefore, it was decided that total sonication times should be no less than 120 min. for a standard batch. This sonication duration proved satisfactory and was used as a minimum total sonication time when producing batches for this study.

A final flaw in this study is that suspension aged approximately 5 h from the initial sonication treatment to the final sonication treatment. Since aging also has an effect upon rheological properties, this factor can not be discounted. However, there is no way to perform said experimentation without limited aging due to the time required for shaking and sonication.

In order to determine the effect of aging upon rheological properties, an aging study was also performed. A 180 ml suspension of 64 V% ball milled BS glass, 16 V% Si<sub>3</sub>N<sub>4</sub> powder and 20 V% 4.6 μm UPLM powder was produced by the standard method outlined in section 3.4.3 below, with the exception that the suspension was not aged prior to the investigation (other than the time required for batching and sonication). This composition was chosen since it also should be relatively viscous compared to the rest of the batches produced. Suspension solids loading was determined as outlined in section 3.4.4 below after 38 and 70 h of aging. Rheometry characterization was performed, as described in section 3.4.2.2.2 above, at aging durations of 0, 12, 24, 48 and 72 h. Samples were also cast at the above aging

times for green characterization via Hg porosimetry, as outlined in section 3.4.5.2 below as well as compact top surface visual inspection via SEM as outlined in section 3.4.5.1 below.

This experimentation provided valuable insight into the effect of aging on the suspension and green properties of codispersed composites within this system. From the results of the study, it was decided that the standard batch aging time should be 48 h.

#### 3.4.2.2.5 General Rheology Studies

A description of the method used for rheological characterization of the slurries produced is outlined in section 3.4.2.2.2 above. The general rheology studies were performed to investigate various rheological trends of the slip systems used in this study. Each batch was characterized after an aging time of approximately 48 h. The ZA--15 sensor was utilized for all viscosity characterization of suspensions in this section. All characterization was performed for shear rates ranging from 0 to 300  $\text{s}^{-1}$ . The shear rate was increased from 0 to 300  $\text{s}^{-1}$  in 2 min., then decreased to 0  $\text{s}^{-1}$  in another 2 min. time.

All the suspensions characterized in this study had a total solids loading of approximately 52 V% with the exception of the samples having a  $\text{Si}_3\text{N}_4$  concentration greater than 50 V% (total solids basis) which were characterized at a total solids loading of 46 V%. This was necessary because suspensions containing  $\text{Si}_3\text{N}_4$  concentrations greater than 50 V% became overloaded as solids loadings neared 52 V%. The single value of 46 V% was chosen for these three suspensions in order to afford a comparison between the rheological properties of the three. Generally, the viscosity of these batches was greater than all of the others.

### 3.4.3 Slip Casting of Compact Samples

The samples were produced via slip casting of codispersed slurries as described below. Figure 3.6 illustrates a flow diagram of the procedure utilized for the convenience of the reader.

In a clean polyethylene (PE) bottle,<sup>103</sup> to which a (2.54 cm) polytetrafluoroethylene (PTFE) stir bar<sup>79</sup> had been added in order to facilitate mixing, the appropriate amount of latex/EtOH dispersion was added. This amount was determined from both the solids loading of the latex/EtOH mixture (determined twice, as outlined in section 3.4.4 below) and the required amount of latex and EtOH determined from batch calculations. The additional EtOH,<sup>24</sup> required to round out the batch calculations, was then added. After this addition, 1 wt% (of the total solids weight) PVP K-30 was added to the suspension. The suspension was then shaken for approximately 5 min., while the PVP K-30 dissolved. Next the total required batch amount of  $\text{Si}_3\text{N}_4$  was added to the suspension. The suspension was then shaken for another 5 min. and sonicated for 15 min. The shaking and sonication was again repeated, without further addition, for another repetition. At this point, approximately one half of the total batch amount of the BS glass powder was added. The resultant slurry was shaken again for 5 min. and sonicated for 15 more min. Approximately one half of the remaining glass was then added and the shaking and sonication step repeated. The final amount of glass powder was then added and further shaking and sonication were performed upon the slurry (again 5 and 15 min. respectively). After these treatments, the slurry was subjected immediately to two more repetitions of shaking/sonication (5 and 15 min. again).

---

<sup>103</sup> Catalog Number: 02-893-5C, Fisher Scientific, 1600 Parkway View Drive, Pittsburgh, PA 15205

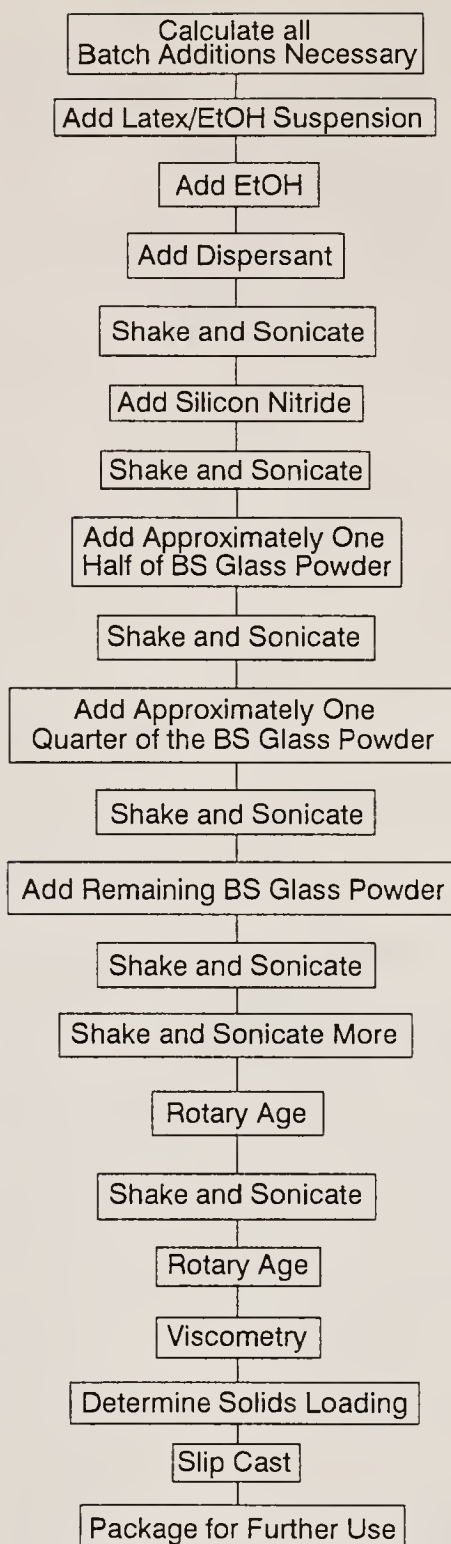


Figure 3.6

Flow diagram illustrating the procedure utilized to produce, via slip casting of codispersed suspensions, the samples used in this study



The suspension was then subjected to rotary mixing (aging), upon a rotary conditioner,<sup>104</sup> for approximately 48 h. Some time during the aging process, the suspension was subjected to the shaking/sonication process, mentioned above, for two repetitions of 5 min. of shaking and 30 min. of sonication. After these treatments, the suspension was replaced on the rotary mixing apparatus for the remainder of the aging time.

Just before the casting process, rheology measurements were performed, upon the suspension, as described in sections 3.4.2.2.2 and 3.4.2.2.5 above. Suspension solids loading measurements were performed, as outlined in section 3.4.4 below at this point as well.

The suspension was then slip cast onto 0.22  $\mu\text{m}$  nylon filter paper,<sup>105</sup> setting on plaster<sup>106</sup> ingots, that had been presaturated with EtOH<sup>24</sup> prior to casting. Phenolic casting rings<sup>107</sup> (29 mm diameter), which had been polished on one end to a 600 grit surface finish, and to which a very light coating of vacuum grease<sup>108</sup> had been applied as a mold release agent, were used as the suspension container during the casting process.

---

<sup>104</sup> Bodine Electric Company, Chicago, IL

<sup>105</sup> Catalog Number: N02-Spl42-25, Fisher Scientific, 1600 Parkway View Drive, Pittsburgh, Pa 15205

<sup>106</sup> Item Number: 53005, Bondex International Inc., 3616 Scarlet Oak BLVD, St. Louis, MO 63122

<sup>107</sup> Item Number: 20-8152-010, Buehler Ltd., 41 Waukegan Rd., Lake Bluff, IL 60044

<sup>108</sup> High Vacuum Grease, Dow Corning Corp., Midland, MI 48640

Approximately 6 ml of suspension was then quickly dispensed into the casting rings, using a disposable glass pipette<sup>109</sup> attached to a pipette pump.<sup>110</sup> After approximately three samples were cast, the remaining uncast suspension was recapped and reshaken, and the pipette was replaced with a fresh one. The suspension-filled casting rings were then covered with glass slip covers<sup>111</sup> in order to prevent solvent evaporation from the top of the compact, which would cause surface drying and cracking. Said drying and cracking not only increases the size of the meniscus on the cast sample, but also causes casting flaws in the compact which make the compacts very fragile.

Before the compacts were completely dry, they were gently removed from the filter paper and then very carefully removed from the casting rings. The first and last cast samples were then stored separately for Hg porosimetry characterization, as outlined in section 3.4.5.2 below. The remaining samples were then stored for further processing and characterization, as outlined in Figure 3.1. Table 3.9 depicts each batch produced and the pertinent characteristics of each. It should be noted that the pure latex batches were not aged and were sonicated for only approximately 30 min. Also, the solids loadings were not adjusted to 52 V% prior to casting.

---

<sup>109</sup> Catalog Number: 13-668-80, Fisher Scientific, 1600 Parkway View Drive, Pittsburgh, PA 15205

<sup>110</sup> Catalog Number: 13-683D, Fisher Scientific, 1600 Parkway View Drive, Pittsburgh, PA 15205

<sup>111</sup> Catalog Number: 12-550C, Fisher Scientific, Glass Microscope Slides, cut to size by scribing and snapping. The scribes were produced using a Catalog Number: 08-675, Fisher Scientific Diamond Marking Pencil

Table 3.9

Specifications of Each Codispersed and Slip Cast  
Sample Batch Produced for This Study

Designation	Glass Type	Borosilicate Glass-Si <sub>3</sub> N <sub>4</sub> Ratio	Composition BS Glass/Si <sub>3</sub> N <sub>4</sub> /Latex Ratio	Volume Percent Latex	Latex Mean Diameter (μm)	Latex Dispersion
12119001	As Rec.	100/0	100/0/0	0	NA	NA
03209001	Ball Milled	100/0	100/0/0	0	NA	NA
05109102	Ball Milled	100/0	95/0/5	5	4.6	Uniform
01039101	Ball Milled	100/0	90/0/10	10	4.6	Uniform
05179101	Ball Milled	100/0	85/0/15	15	4.0	Quadramodal
05179102	Ball Milled	100/0	85/0/15	15	2.4	Bimodal
05069101	Ball Milled	100/0	85/0/15	15	4.6	Uniform
05099101	Ball Milled	100/0	85/0/15	15	9.0	Uniform
05069102	Ball Milled	100/0	82.4/0/17.6	17.6	9.0	Uniform
12109001	Ball Milled	100/0	80/0/20	20	4.6	Uniform
02069101	Ball Milled	100/0	80/0/20	20	4.6	Uniform
05109101	Ball Milled	100/0	75/0/25	25	4.6	Uniform
06019101	Ball Milled	100/0	72.5/0/27.5	27.5	4.6	Uniform
05079101	Ball Milled	100/0	70/0/30	30	4.6	Uniform
05079102	Ball Milled	100/0	60/0/40	40	4.6	Uniform
01049101	Ball Milled	90/10	81/9/10	10	4.6	Uniform
05119101	Ball Milled	85/15	72.25/12.75/15	15	4.6	Uniform

Table 3.9 (continued)

Designation	Glass Type	Borosilicate Glass-Si <sub>3</sub> N <sub>4</sub> Ratio	Composition BS Glass/Si <sub>3</sub> N <sub>4</sub> /Latex Ratio	Volume Percent Latex	Latex Mean Diameter (um)	Latex Dispersity
03219001	Ball Milled	80/20	80/20/0	0	NA	NA
01249101	Ball Milled	80/20	72/18/10	10	4.6	Uniform
01069101	Ball Milled	80/20	64/16/20	20	4.6	Uniform
03199001	Ball Milled	60/40	60/40/0	0	NA	NA
01279101	Ball Milled	60/40	54/36/10	10	4.6	Uniform
10109001	Ball Milled	60/40	48/32/20	20	4.6	Uniform
08159001	Ball Milled	50/50	40/40/20	20	4.6	Uniform
02149101	Ball Milled	40/60	40/60/0	0	NA	NA
02149102	Ball Milled	20/80	20/80/0	0	NA	NA
01319101	NA	0/100	0/100/0	0	NA	NA
05169101	NA	NA	0/0/100	100	4.0	Quadramodal
07269001	NA	NA	0/0/100	100	2.4	Bimodal
07309001	NA	NA	0/0/100	100	3.1	Bimodal
07199001	NA	NA	0/0/100	100	3.6	Bimodal
06199001-07+09	NA	NA	0/0/100	100	4.6	Uniform
07219001	NA	NA	0/0/100	100	6.1	Uniform
08029001	NA	NA	0/0/100	100	6.8	Uniform
07249001	NA	NA	0/0/100	100	9.0	Uniform

#### 3.4.4 Suspension Solids Loading Determination

Knowledge of suspension solids loading is valuable in several ways. In order to determine the correct amount of latex suspension to use in sample production, it was necessary to know the solids loading of said dispersion. This was also true when making the wide size distribution latex dispersion. Knowledge of the suspension solids loading is also valuable when comparing viscosity data of different batch compositions. Finally, by monitoring the total solids loading of each dispersion produced, as described in section 3.4.3 above, a measure of quality control is assured. If the solids loading varies significantly from that calculated, the researcher is informed immediately that there maybe a batching problem. The procedure used to determine solids loading follows.

An aluminum sample pan<sup>112</sup> was weighed and recorded. Next, a well shaken and dispersed sample was quickly removed from the suspension and decanted into the sample pan, which was already placed on the balance,<sup>113</sup> utilizing a disposable dropper.<sup>27</sup> The combined weight of the sample pan and wet suspension was then measured and recorded. The suspension-filled sample pan was then transferred to a drying oven<sup>55</sup> using nylon-reinforced, fiberglass tweezers<sup>114</sup> to prevent adding additional weight to the pan by touching. The pan was placed upon a precleaned setter inside the oven. The sample was then dried at approximately 60°C for no less than 3 h. After drying, the sample pan was removed from the drying oven and reweighed. This amount was recorded as the dry weight.

---

<sup>112</sup> Catalog Number: 08-732, Fisher Scientific, 1600 Parkway View Drive, Pittsburgh, PA 15205

<sup>113</sup> Model Number: XD 100A, Fisher Scientific, 1600 Parkway View Drive, Pittsburgh, PA 15205

<sup>114</sup> Catalog Number: 02-354, Fisher Scientific, 1600 Parkway View Drive, Pittsburgh, PA 15205

These values were then utilized to calculate the total volume percent solids loading utilizing the methods and equations outlined in Table 3.10. Two repetitions of the above procedure were performed upon each batch in order to insure reproducibility. The solids loadings values from each repetition were then averaged. All solids loadings values were found to agree within approximately 0.5 V% between the two repetitions.

### 3.4.5 Characterization of Green Compacts

#### 3.4.5.1 Visual

Visual analysis of representative green compacts was provided via SEM.<sup>25</sup> A compact was gently broken into smaller pieces in order to allow the sample to fit upon the sample stub.<sup>30</sup> Care was taken not to damage or disrupt the sample surface. The green compact piece was then affixed to the sample holder with double stick tape.<sup>31</sup> The compacts were then Au/Pd DC sputter coated.<sup>34</sup> A conductive path was then put between the sample and the sample holder with carbon paint.<sup>115</sup> The samples were then viewed using the SEM. During viewing, an accelerating potential of 20 KV was used and the working distance was approximately 30 mm. The samples were generally not tilted, unless necessary, and the condenser lens setting used was between 2 and 4.

#### 3.4.5.2 Hg Porosimetry

Mercury porosimetry was utilized to investigate the green microstructures of the samples made for this study. Porosimetry data was obtained from at least four samples, for each batch produced. The first and last cast sample from each batch was further divided into as cast and presintered categories.

---

<sup>115</sup> Conductive Carbon Paint, SPI Supplies, a Division of Structure Probe Inc., P.O. Box 656, West Chester, PA 19381



Table 3.10

Method and Equations Used to Calculate  
Suspension Total Solids Loading

1. Determine the Dry Solids Weight,  $D$  (g):

$$D = D_p - p$$

where:  $D_p$  is the dried sample pan with suspension weight (g)

$p$  is the pan weight (g)

2. Determine the Liquids Weight,  $L$  (g):

$$L = W_p - D_p$$

where:  $L_p$  is the sample pan with wet suspension weight (g)

3. Determine the Density of Composite Solids,  $\rho_s$  (g/cm<sup>3</sup>):

$$\rho_s = V_{f_1}^{\text{dry}} \rho_1 + V_{f_2}^{\text{dry}} \rho_2 + \dots$$

where:  $V_i^{\text{dry}}$  is the dry basis volume fraction of the  $i^{\text{th}}$  component

$\rho_i$  is the density of solid component  $i$  (g/cm<sup>3</sup>)

4. Calculate the Volume of Solids in the Suspension,  $V_s$  (cm<sup>3</sup>):

$$V_s = \frac{D}{\rho_s}$$

Table 3.10 (continued)

5. Calculate the Volume of the Liquids in the Suspension,  $V_l$  ( $\text{cm}^3$ ):

$$V_l = \frac{L}{\rho_l}$$

where:  $\rho_l$  is the density of the liquid in the suspension ( $\text{g}/\text{cm}^3$ )

6. Calculate Volume Percent Solids Loading,  $V\%$  (%):

$$V\% = \frac{V_s}{V_s + V_l} \times 100$$

- Notes:
1. In systems using non reactive multicomponent liquids, the liquid density may be calculated using a weighted average similar to step 3 above.
  2. The effect of dispersant volume (PVP K-30) is not included.

The as-cast samples were characterized without further treatment, while the presintered samples were subjected to pyrolysis and presintering treatments, as described in section 3.5.2 below. This experimental methodology allowed for differentiation of green properties between as cast and presintered samples of the same batch. The methodology also was useful as a quality control measure, since the first and last cast samples were both characterized. Differences in microstructural properties between the first and last cast samples would indicate segregation, flocculation or mixing problems.

The Hg porosimetry unit<sup>116</sup> and sample cells used were calibrated using the recommended procedure,<sup>117</sup> prior to experimentation. All experimental calculations were performed using the constants outlined in Table 3.11.

In order to determine whether relatively large (i.e. greater than approximately 5  $\mu\text{m}$  pore channel radius) porous microstructures exist within the green and presintered samples, low pressure porosimetry was performed, as outlined,<sup>117</sup> upon selected samples. The samples chosen for low pressure porosimetry were from batches suspected to have the largest pore structures of the materials studied (i.e. presintered samples of batches containing relatively high amounts of latex, large latex, etc.).

None of the samples tested (including an as cast sample of pure latex, from the largest size of latex) intruded a detectable amount in the low pressure regime. Therefore, only high pressure porosimetry was used to investigate the porous green and presintered structures of the materials made for this study.

---

<sup>116</sup> Model Numbers: FA-1 and SP-20LV Computer Interfaced Autoscan Mercury Porosimeter Apparatus using 2  $\text{cm}^3$  sample volume sample cells, each separately calibrated, Quantachrome Corporation, Syossett, NY 11791

<sup>117</sup> See the Operations Manuals for Footnote 116

Table 3.11

Experimental Values and Parameters Utilized During  
Experimentation and/or in the Computation of Hg Porosimetry Data

Experimental Parameter	Value
Mercury Density	13.534 g/cm <sup>3</sup>
Mercury Contact Angle ( $\theta$ )	140°
Mercury Surface Tension ( $\gamma_{LV}$ )	480 ergs/cm <sup>2</sup>
Scan Rate	5.5
Moving Point Average	9
Cell Sample Chamber Volume	2 cm <sup>3</sup>
Cell Stem Volume	0.5 cm <sup>3</sup>
Evacuation Pressure	< 50 $\mu$ m Hg
Modes for Taking Data	Intrusion/Extrusion
Mode for Calculations	Intrusion
High Pressure Range ( $P_H$ )	Ambient to 60 Kpsi
Pressurizing Fluid	Hydraulic Oil
Low Pressure Range ( $P_L$ )	< 50 $\mu$ m Hg to 25 psi
Pressurizing Fluid	N <sub>2</sub> gas <sup>74</sup>

- Notes:
1. Data is obtained by monitoring the volume intruded (calculated from changes in capacitance measured) as a function of pressure. The pressure is then converted to a pore channel radius using the equation in Note 2. This gives a plot of V (volume intruded) versus R.
  2. The equation used to convert pressure to a pore channel radius (the Washburn Equation [88REE]), R ( $\mu$ m):

$$R = \frac{-2\gamma_{LV}\cos\theta}{P} \times 10^6$$

where:

- $\gamma_{LV}$  is Hg liquid-vapor surface tension (N/m)
- $\theta$  is the Hg-sample contact angle (°)
- P is the intrusion pressure (Pa)
- 1 erg/cm<sup>2</sup> = 10<sup>-3</sup> N/m
- 1 Pa = 1.451 x 10<sup>-2</sup> psi

Table 3.11 (continued)

3. The fractional pore size distribution is given by:

$$f(R) = \frac{dV}{dR}$$

4. The median pore channel radius occurs at the maximum of the relationship depicted in Note 3.

High pressure porosimetry was performed upon four samples from each batch as described above. The general parameters used for this study are outlined in Table 3.11 as well as a brief explanation of how porosimetry calculations are performed.

High pressure Hg porosimetry was also used to investigate the packing efficiency of slip cast pure latex compacts with respect to size and size dispersity.

### 3.5 Thermal Analysis: Oxidation and Pyrolysis Studies

#### 3.5.1 Overview

Thermal analysis studies were performed upon the components of this system and upon a slipcast compact in order to characterize the materials in the system with respect to several factors. Oxidation studies were performed upon the  $\text{Si}_3\text{N}_4$  powder in order to determine if the  $\text{Si}_3\text{N}_4$  utilized in this study was truly inert with respect to oxidation when subjected to the thermal processing conditions of this study. Any oxidation of the  $\text{Si}_3\text{N}_4$  could provide experimental error since the composite density would change. Also the event of a substantially large siliceous layer, forming on the  $\text{Si}_3\text{N}_4$  could change the sintering characteristics of the composites in the system.

The second part of the thermal analysis studies were used in two ways. Preliminary thermal analysis studies were used in conjunction with empirical experimentation to determine the best pyrolysis and presintering schedule to use for the green compacts in this study. After a pyrolysis/presintering schedule was established, a second set of thermal analysis experiments were performed in order to confirm that said pyrolysis/presintering schedule was satisfactory. Preliminary dielectric properties data were also examined in order to determine whether or not significant carbon remained subsequent to pyrolysis/presintering heat treatment.



### 3.5.2 Oxidation Studies

Thermal analysis studies were performed upon the  $\text{Si}_3\text{N}_4$  powder using a computerized TGA/DTA apparatus.<sup>118</sup> The first set of experiments involved heating approximately 0.2 g of powder at a rate of  $10^\circ\text{C}/\text{min}$  from 100 to  $1500^\circ\text{C}$ , in air<sup>119</sup> flowing at a rate of approximately  $2 \text{ ft}^3/\text{h}$  ( $47 \text{ cm}^3/\text{min.}$ ). This experimentation was performed in order to determine the onset temperature regime of oxidation of the  $\text{Si}_3\text{N}_4$  powder. The reference powder used in each instance was alumina<sup>120</sup> (which is inert over the conditions experienced during the thermal analysis experimentation). Two repetitions of this experiment were performed, one with the  $\text{Si}_3\text{N}_4$  powder as the sample powder and one with  $\text{Al}_2\text{O}_3$ <sup>120</sup> powder as the sample powder. The  $\text{Al}_2\text{O}_3$  sample powder run was performed in order to provide a baseline standardization. The data for each run were stored and developed via a computer spreadsheet program<sup>36</sup> which also provided graphical output.

The above-mentioned TGA data provided the non-isothermal onset temperature of oxidation of the  $\text{Si}_3\text{N}_4$  powder. In order to simulate conditions similar to those of the sintering treatments, a second set of oxidation studies were performed. In the second oxidation study, the temperature was held isothermally at  $820^\circ\text{C}$  (the highest sintering temperature used in this study), under the air flow conditions of the above thermal analysis experiment. The sample was heated to a temperature of  $820^\circ\text{C}$  at a rate of  $45^\circ\text{C}/\text{min}$ . The sample was then isothermally treated for 12 h. Since the computer software did not allow for said characterization, the sample weight was manually recorded

---

<sup>118</sup> Model Number: ST-736, Harrop Industries, Inc., 3470 E. 5<sup>th</sup> Ave., Columbus, OH 43219-1797

<sup>119</sup> Grade E Compressed Air, Liquid Air Corp., 2121 North California BLVD, Walnut Creek, CA 94596

<sup>120</sup> Catalog Number: A-591, Fisher Scientific, 1600 Parkway View Drive, Pittsburgh, PA 15205

periodically over the 12 h period. Due to the above-mentioned software limitations, however, differential thermal analysis was not possible.

Again, two repetitions of the above experiment were performed, one with  $\text{Si}_3\text{N}_4$  powder and one with  $\text{Al}_2\text{O}_3$  powder to provide a baseline standardization. The sample weight used was approximately 0.2 g in each case also. Alumina powder was also used as the reference powder.

### 3.5.3 Pyrolysis Studies

A second TGA/DTA apparatus<sup>121</sup> was utilized for pyrolysis studies. The materials analyzed had been stored and not predried in order to determine the amount of adsorbed moisture within the materials. This was relatable to the actual materials used in this study. Experimental runs were performed upon latex powder, PVP K-30 powder (the dispersant) in both air<sup>117</sup> and  $\text{N}_2$ ,<sup>74</sup> and upon a green slip cast sample of a compact representative of this study (i.e. 80 V% BS glass powder, 20 V% latex, prepared as outlined in section 3.4.3 above) in air.

Preliminary experiments were performed upon the latex only. The latex powdered samples were heated at a rate of 10°C/min from ambient to 1000°C in air only. From this data and from preliminary pyrolysis experiments, within the pyrolyzation furnace, the pyrolysis/presintering schedule was established (see section 3.4.2 below).

Later, thermal analysis characterization was performed upon both the polymer powders utilized in this study (i.e. the latex and the dispersant). Sample weights of approximately 50 and 100 mg were used for air<sup>117</sup> and  $\text{N}_2$ <sup>74</sup> atmosphere experiments respectively. The gas flow rate used was approximately 60 ml/min.

---

<sup>121</sup> Model Number: SAT409, Netzsch, Inc., Exton, PA, data acquisition through Model Numbers: HP 3421A data acquisition/control unit and Model Number: HP86B computer, Hewlett Packard Co., P.O. Box 3640, Sunnyvale, CA 94088

The reference powder used in all experiments was 100 mg of  $\text{Al}_2\text{O}_3$ ,<sup>122</sup> and buoyancy correction was utilized in each experimental repetition. During organic powder thermal analysis, the measuring head utilized was one designed for TGA/DTA measurements.

In the case of the green slip cast compact, a different measurement head, designed for TGA, was utilized. Therefore, no DTA data was obtained for this experimentation. The sample weight used in this case was approximately 525 mg. The thermal schedule utilized in this instance mimicked that depicted in Figure 3.10. The gas flow rate used in this experiment was also approximately 60 ml/min. Only air<sup>117</sup> was used as the atmosphere in this experimentation. Due to the relatively high sample weight, no buoyancy correction was used in this case.

### 3.6 Thermal Treatments

#### 3.6.1 Furnace Calibration

Figure 3.7 illustrates the apparatus used for pyrolysis/presintering operations as well as for sintering studies discussed below. The digital controller<sup>123</sup> utilizes a PLII type control thermocouple placed centrally within in the furnace<sup>124</sup> and slightly outside the pyrolysis tube apparatus.<sup>125</sup> Prior to experimentation, the controller was calibrated following a standard calibration procedure.<sup>126</sup>

---

<sup>122</sup> Powder Number: C75RG, Alcan Aluminum Corp., 100 Erieview Plaza, Cleveland, OH 44114, previously calcined to 1000 °C

<sup>123</sup> Model Number: 58114-P programmable control console, Lindberg Corp., A Unit of General Signal, 304 Hart Street, Watertown, WI 53094

<sup>124</sup> Model Number: 58114-P Lindberg Corp., A Unit of General Signal, 304 Hart Street, Watertown, WI 53094

<sup>125</sup> 2" O.D. fused quartz tube modified for use at the Department of Chemistry Glass Shop, University of Florida, Gainesville, FL 32611

<sup>126</sup> As outlined in Chapter 7 of DOC. 818/EN-1, Eurotherm Corporation, 11485 Sunset Hills Road, Reston, VA 22090-5286

## Key:

- A. 1200 °C Clamshell Type Tube Furnace
- B. Digital Furnace Controller
- C. 0.001 mV Resolution Voltmeter
- D. Type PLII Control Thermocouple
- E. Type PLII Reference Thermocouple
- F. Controllable Flow Meter
- G. Exhaust Gas Bubbler
- H. 220 V AC Power Source
- I. 120 V AC Power Source

- J. Furnace Tube Assembly
- K. Furnace Tube
- L. Sample Setter
- M. Sample
- N. Tube End Sealing Elements
- O. Controlled Atmosphere Inlet
- P. Tube Gas Exhaust
- Q. 0.1 °C Resolution Cold Junction Compensation Thermometer

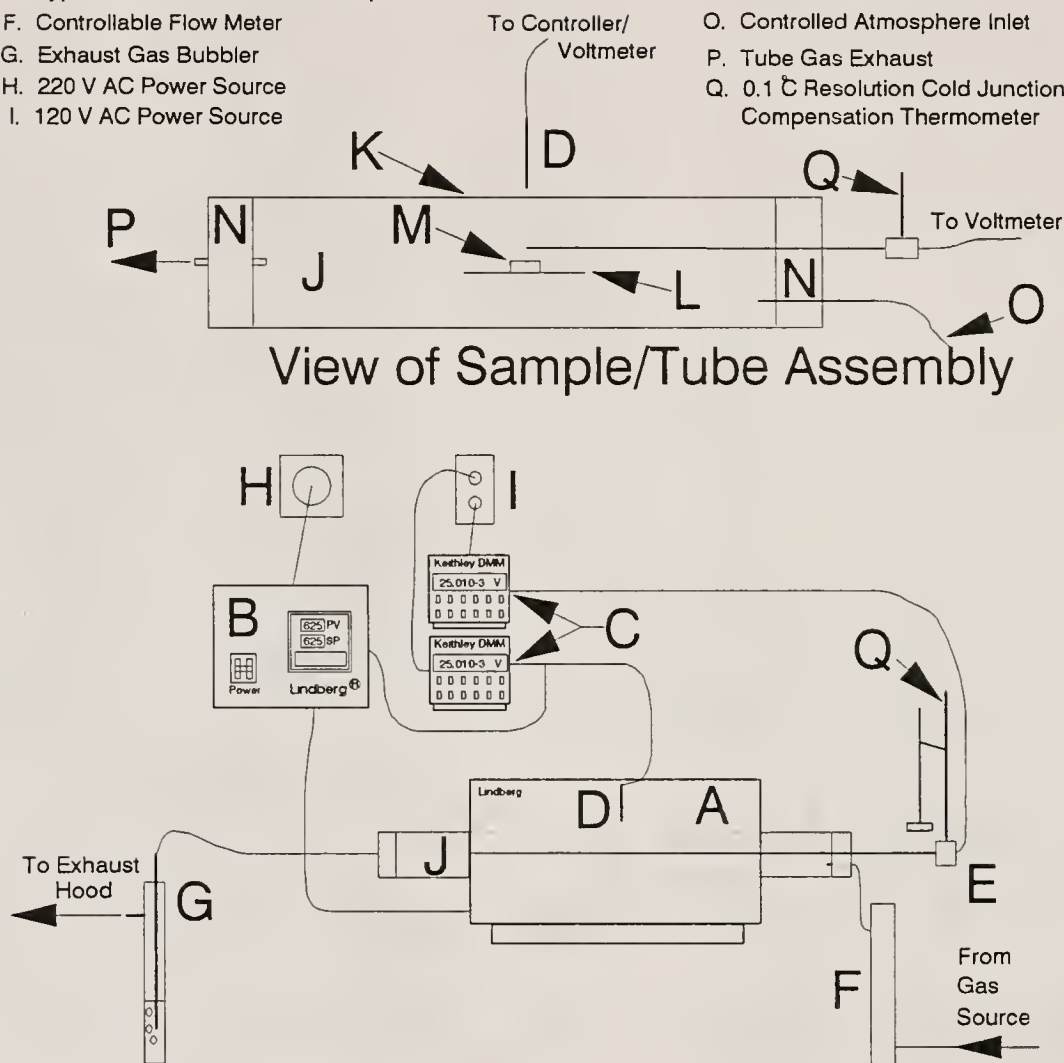


Figure 3.7

Schematic representation of the tube furnace apparatus used in this study

The microvoltage source used for calibration was provided via a standard 1.5 V alkaline battery<sup>127</sup> connected to the furnace controller in series with a 500 ohm, 5% tolerance resistor<sup>128</sup> and a 10,000 part adjustable resistance apparatus.<sup>129</sup> Also connected in parallel at the controller input nodes were two high impedance ( $>1$  G-ohm), 100 nV resolution digital multimeters<sup>130</sup> which were utilized to monitor the input signal to the controller. Two meters were used in order to insure both accuracy and reproducibility of the input signal. Each had been recently calibrated by two independent sources.<sup>131</sup>

Temperature monitoring was provided during pyrolysis/presintering treatments via a second type PLII thermocouple<sup>132</sup> located centrally inside the pyrolysis tube (next to the sample compacts). Said reference thermocouple output was direct to a 100 nV resolution digital multimeter.<sup>123</sup> At this point, a cold junction compensation was manually added to the voltage reading and the temperature found from a reference table.<sup>133</sup> A 0.1°C resolution thermometer, manually fixed to the reference thermocouple cold junction housing, was utilized to obtain said cold junction compensation values.

---

<sup>127</sup> Model MN1500, 1.5 V AA Duracell Battery, Duracell, Inc., Bethel, CT 06801

<sup>128</sup> Two 5% tolerance, 1000 ohm resistors connected in parallel, Model Number: 271-023, Radio Shack, A Division of Tandy Corp., Fort Worth, TX 76102

<sup>129</sup> Kelvin-Varley Type 10,000 part voltage divider, Manufactured by C.E. Randall, Arkport, NY 14807

<sup>130</sup> Model Number 195 Digital Multimeter, Keithley Instruments, Inc., 28775 Aurora Road, Cleveland, OH, 44139

<sup>131</sup> A. Digital Design Facility, University of Florida, Gainesville, Fl 32611 B. Keithley Instruments, Inc. 28775 Aurora Road, Cleveland, OH 44139

<sup>132</sup> Model P/N PII-E-B/28-0-TP/96 thermocouple modified with P2X-20-TEF extension wire, Engelhard Corporation, Engineered Materials Division, Industrial Products, 70 Wood Ave. South, CN770, Iselin, NJ 08830

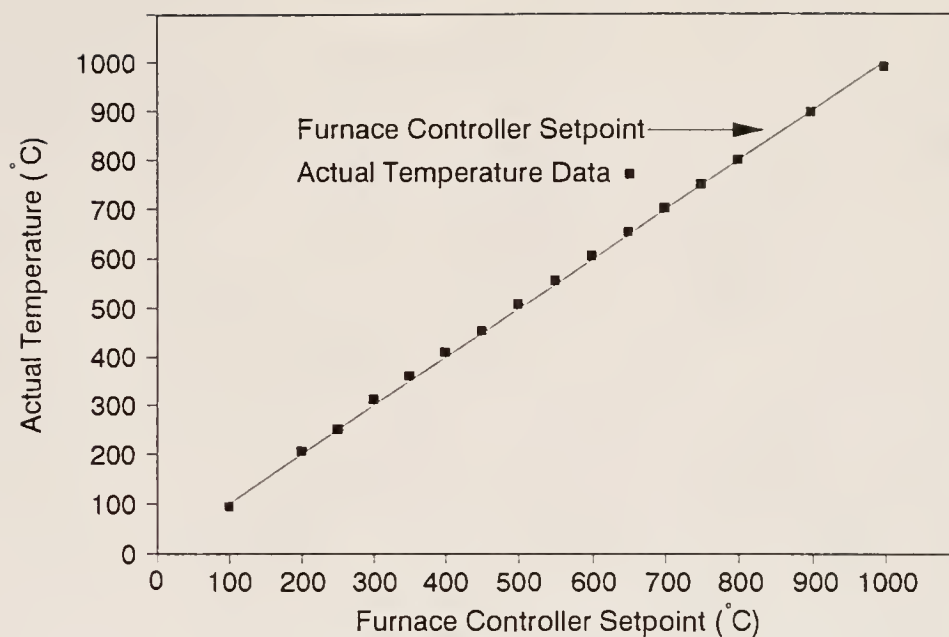
<sup>133</sup> Source: Lindberg Corp., 304 Hart Street, Watertown, WI 53094



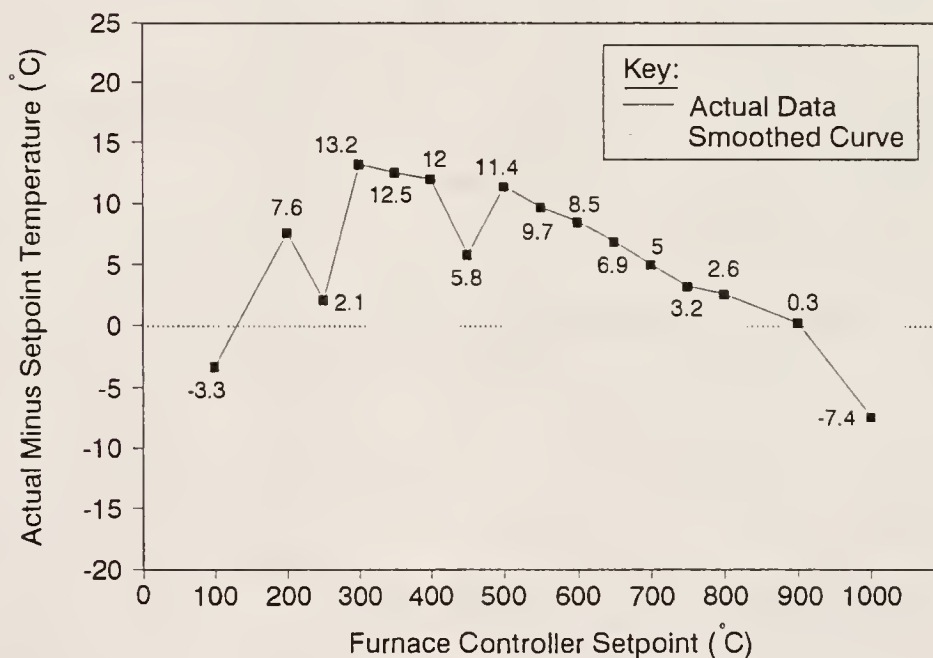
An experiment was performed in order to characterize the relationship between setpoint and actual reference temperature. With the reference thermocouple centered within the furnace tube, the controller setpoint was established and allowed to equilibrate for a duration not less than 30 min. The reference thermocouple output was then obtained, cold junction compensated, then transformed to a temperature. A new, higher setpoint was then established and the process repeated. Said experiment was performed on 16 different setpoints, ranging from 100°C to 1000°C. The resulting furnace temperature as a function of set point relationships are illustrated in Figure 3.8. These data indicate that the reference temperature is never more than 14°C different from the setpoint and that the actual temperature is generally slightly greater than the indicated setpoint for the temperatures of interest in this study.

Similarly, an experiment was performed in order to determine the fluctuation of actual temperature within the pyrolysis tube with respect to the longitudinal distance from the point of maximum temperature of the furnace since the furnace utilized for pyrolysis/presintering was a single heating zone type. The reference thermocouple was centered radially within the furnace tube at a longitudinal distance of 10 cm from the physical center of the furnace toward the exhaust end of the furnace tube. The furnace controller setpoint was then adjusted to 750°C and allowed to equilibrate for no less than 1 h. After equilibration, the temperature was corrected, as described above, and recorded. The reference thermocouple was then repositioned 0.5 cm displaced toward the physical center of the furnace, equilibrated again and a temperature again measured. The above process was repeated until a range of 17.0 cm, equally distributed about the physical center of the furnace, had been characterized. The data are illustrated in Figure 3.9. Figure 3.9 shows that the point of maximum temperature is displaced slightly from the physical center of the furnace. The point





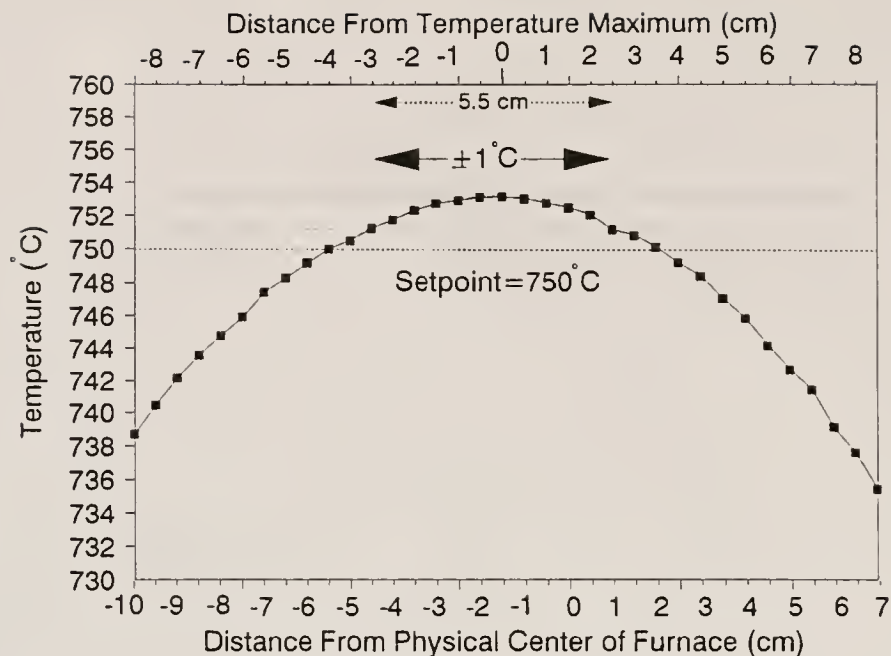
A. Actual Temperature Versus Furnace Controller Setpoint



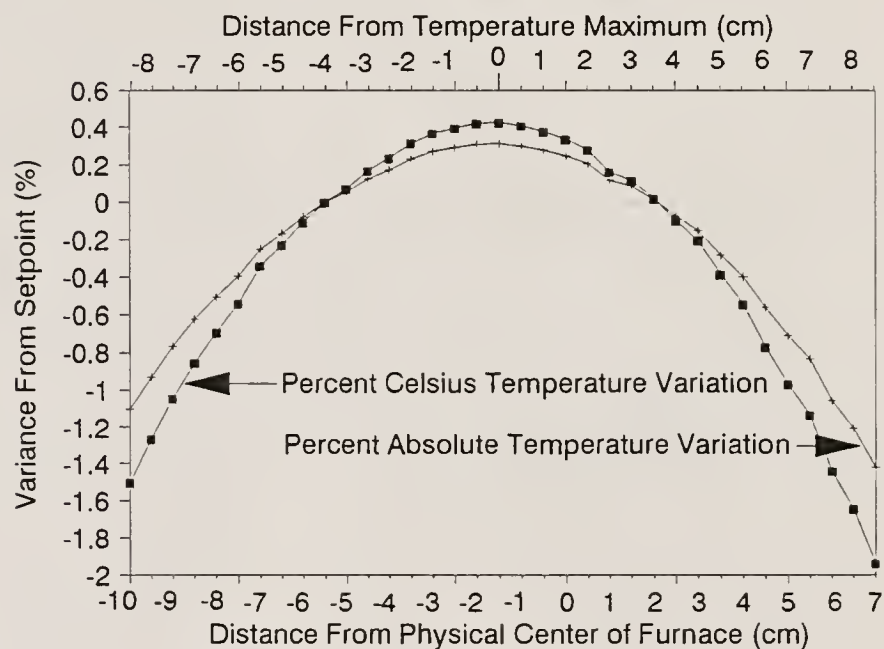
B. Actual Minus Furnace Controller Setpoint Versus Furnace Controller Setpoint

Figure 3.8

Actual centerpoint temperature versus setpoint for the furnace used in pyrolysis/presintering and in sintering; A. Actual Temperature, B. Temperature Variance



A. Temperature versus Distance



B. Percent Temperature Variance From Setpoint versus Distance

Figure 3.9

Measured temperature versus lateral placement in the furnace tube center

of maximum temperature was then marked on the furnace and the reference thermocouple was always adjusted to said mark using a plastic drafting triangle<sup>134</sup> prior to either pyrolysis/presintering or sintering treatments.

It was assumed that temperature variation radially within the tube is minor, due to excellent insulation as well as the radial symmetry of the tube furnace. Also, due to the tube configuration, only a small radial displacement of either the thermocouple or the sample is possible. Therefore, no experimentation, attempting to characterize radial temperature variation within the furnace tube assembly, was performed.

### 3.6.2 Pyrolysis and Presintering

The dry, slip cast disks were pyrolyzed and presintered. Typically from 3 to 7 compacts were arranged upon an  $\text{Al}_2\text{O}_3$ <sup>135</sup> setter then placed within a tube apparatus<sup>125</sup> inside the furnace.<sup>124</sup> An end cap<sup>136</sup> was then clamped<sup>137</sup> in place on the tube and compressed air,<sup>117</sup> at the rate of approximately 240 cm<sup>3</sup>/min, was flowed through the pyrolysis tube. A slight positive pressure of air in the pyrolysis tube was assured by flowing the tube exhaust through a bubbler unit.<sup>138</sup>

---

<sup>134</sup> Model Number: 12014-12, Dietzgen Corp., 250 Willie Rd., Des Plaines, IL 60018

<sup>135</sup> Ceramics Process Systems, 840 Memorial Dr., Cambridge, MA 02139

<sup>136</sup> Catalog Number: 7655-72 pyrex socket member enclosed at the end via Catalog Number: 8847-04 pyrex end plug, Ace Glass Inc., 639 South Hanock St., Louisville, KY 40201. Glasswork performed by Department of Chemistry Glass Shop, University of Florida, Gainesville, FL 32611

<sup>137</sup> Catalog Number: 7670, Ace Glass Inc., 639 South Hanock St., Louisville, KY 40201

<sup>138</sup> Catalog Number: 11-184-1C, Fisher Scientific, 1600 Parkway View Drive, Pittsburgh, PA 15205

The exhaust gas was then vented to a fume hood<sup>139</sup> via plastic tubing.<sup>140</sup> The pyrolysis run was then initialized. The time-temperature schedule was controlled and monitored through the digital furnace programmer.<sup>116</sup> At the end of each pyrolysis/presintering run, the specimens were removed and packaged for future treatment or characterization.

The appropriate pyrolysis/presintering schedule was determined with the aid of TGA/DTA data, obtained as described in section 3.5.2 above, as well as with empirical experimentation. It was necessary to pyrolyze both the polystyrene latex and the dispersant as much as possible before the onset of sintering of the BS glass matrix phase. Since the BS glass sinters at relatively low temperatures, the pyrolysis time-temperature schedule had to be chosen carefully. The standard pyrolysis/presintering treatment chosen is illustrated in Fig. 3.10. The presintered samples appeared very white (for pure BS glass and BS glass-UPLM samples; however, the  $\text{Si}_3\text{N}_4$  powder used has a greyish appearance, and thus, imparts that hue to compacts containing the  $\text{Si}_3\text{N}_4$ ), indicating a successful pyrolysis of included organics.

The pyrolysis condensate at the exhaust end of the pyrolysis tube was a brownish-black substance with the consistency of a thick tar. It dissolves completely in EtOH.<sup>24</sup> Thus, EtOH was utilized to thoroughly clean the tube apparatus prior to sintering treatments.

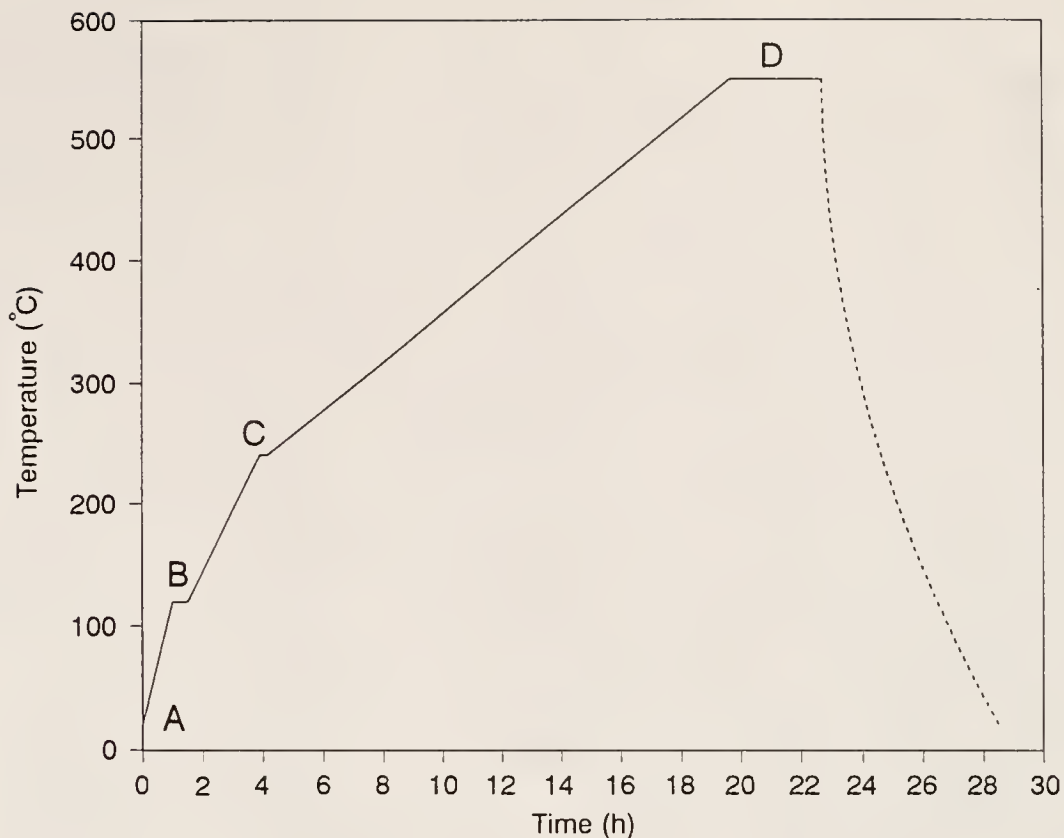
### 3.6.3 Sintering

As previously mentioned, sintering treatments were performed in the same apparatus as the pyrolysis/presintering treatments, after thorough cleaning. The furnace was allowed to equilibrate at the predetermined setpoint (618 and 644°C for sintering temperatures of 625 and 650°C respectively).

---

<sup>139</sup> Kemmetal 4' model, Kewaunee MFG. Co. Adrian, MI

<sup>140</sup> Catalog Number: 14-169-1M, Fisher Scientific, 1600 Parkway View Drive, Pittsburgh, PA 15205



Point	Set Point (°C)	Rate to Set Point (°C/h)	Time at Set Point (h)
A	20	0	0.0167 (1 minute)
B	120	100	0.5
C	240	50	0.25
D	550	20	3.0
All	RT	Furnace Cool	End

Note: RT designates Room Temperature (usually 20 to 25 °C)

Atmosphere: Compressed Air

Flow Rate: Approximately 240 cm<sup>3</sup>/m

Figure 3.10

The pyrolysis-presintering thermal treatment schedule utilized in this study

The specimen to be sintered was placed upon an  $\text{Al}_2\text{O}_3$  setter,<sup>128</sup> then placed in the uncapped end of the furnace tube. A hooked rod<sup>141</sup> was then used to move the specimen/setter to directly beneath the reference thermocouple join. At this point, the furnace end was recapped and the setpoint increased  $3^\circ\text{C}$  until the actual temperature reached the desired value. The setpoint was then reduced gradually to the appropriate setpoint. This temperature equilibration was observed to take approximately 5 min., and thus, said amount was added to each isothermal sintering duration. A count down timer<sup>142</sup> was utilized to ensure accuracy and the actual temperature monitored periodically throughout the process. Compressed air at a rate of  $240\text{ cm}^3/\text{min.}$  was flowed through the tube during the entire process. When the sintering duration had expired, the sample/setter was gradually removed from the tube using the hooked rod and a pair of forceps.<sup>143</sup> Removal time was approximately 3 to 5 min. in order to avoid thermally shocking the sintered specimen. The specimen was then packaged, labelled and stored for future archimedes density characterization.

### 3.7 Materials Characterization

#### 3.7.1 Archimedes Density Characterization

Material bulk properties were determined using ASTM standard C 373-72 [88ST01] as a guideline. The general method and apparatus utilized is illustrated in Figure 3.11.

---

<sup>141</sup> Catalog Number: 11-365B, Fisher Scientific, 1600 Parkway View Drive, Pittsburgh, PA 15205. The hook (a  $90^\circ$  bend) was made on one end using an oxy-hydrogen torch.

<sup>142</sup> Catalog Number: 06-662-7, Fisher Scientific, 1600 Parkway View Drive, Pittsburgh, PA 15205

<sup>143</sup> Catalog Number: 15-200, Fisher Scientific, 1600 Parkway View Drive, Pittsburgh, PA 15205



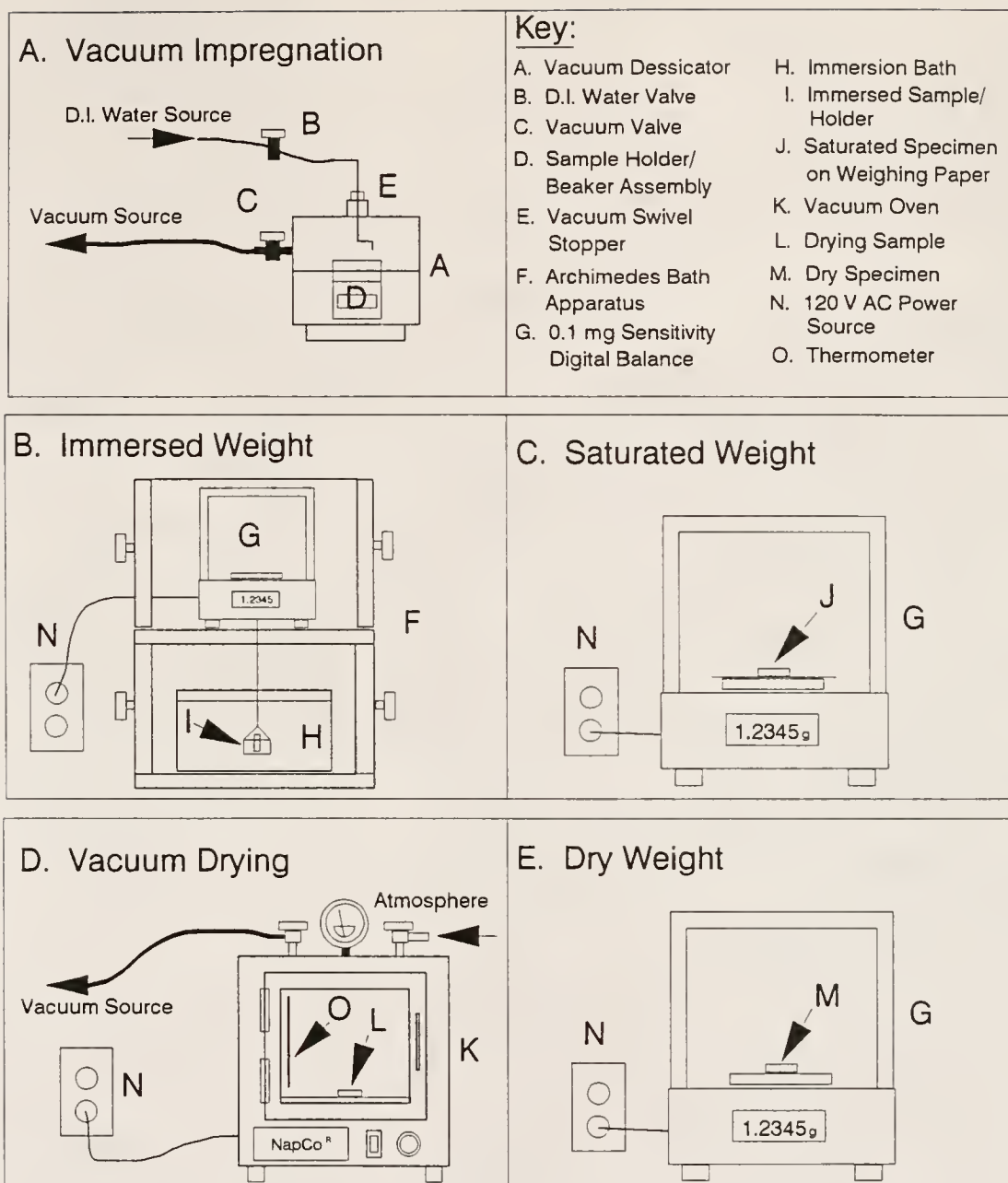


Figure 3.11

Schematic representation of the methods and apparatus used in the Archimedes Method density characterizations performed for this study

The samples were placed in a supported basket inside a beaker.<sup>144</sup> The beaker was then placed within a vacuum desiccator<sup>145</sup> which had been modified as shown in Figure 3.11. A vacuum of >32" Hg (gauge) was then pulled on the desiccator for no less than 15 min. in order to remove residual gases within the pores of each specimen. At this point, deionized (DI) water<sup>88</sup> was introduced to the samples (see Figure 3.11) and a similar vacuum was pulled on the desiccator for no less than 2 h more. The side of the desiccator was periodically tapped during this stage in order to help remove bubbles sticking to specimens. When few or no bubbles were released during the tapping process (after the prestatd 2 h period), the samples were subjected to atmospheric pressure. This further aided in total impregnation of the specimens with water.

The beaker of impregnated specimens was then removed from the sample desiccator and placed next to the archimedes water bath overnight in order to allow temperature equilibration.

The immersed weight of each specimen was obtained by first zeroing the 0.1 mg sensitivity balance,<sup>111</sup> then placing the specimen into the nylon mesh basket and recording the balance reading. This procedure was repeated until two recorded balance readings agreed to within 0.0002 g. The two values were then averaged and used as the specimen immersed weight.

The specimen saturated weight was obtained by first patting the specimen off on a tissue<sup>61</sup> to remove water from the surface, placing the saturated specimen on a pretared balance pan, then recording the balance readout. The saturated specimen was then placed in its open packaging

---

<sup>144</sup> Catalog Number: 02-540P, Fisher Scientific, 1600 Parkway View Drive, Pittsburgh, PA 15205

<sup>145</sup> Catalog Number: 08-594-15C, Fisher Scientific, 1600 Parkway View Drive, Pittsburgh, PA 15205

container which was then placed within a vacuum oven<sup>55</sup> at approximately 100°C for no less than 4 h.

Next a >30" Hg (gauge) vacuum was pulled on the vacuum oven and the vacuum pump<sup>146</sup> then shutoff. The gauge of the vacuum oven was then monitored over a period of approximately 10 min. in order to determine if the drying process was complete. The dry specimen weight was then obtained from the previously zeroed balance. This measurement was performed quickly in order to minimize readsorption of atmospheric water by the specimen.

The bulk density, percent of theoretical density, apparent density, open porosity, total porosity and closed porosity were then calculated via a computer spreadsheet program.<sup>36</sup> The calculated bulk density data were stored in said spreadsheet for future use. Table 3.12 denotes the various equations used for bulk density characterization.

The above archimedes density characterization process was repeated until the following two criteria were satisfied:

1. values of bulk and apparent density, from two separate repetitions, agreed within 0.01 g/cm<sup>3</sup>
2. values of % of theoretical density, % total, % open, and % closed porosity respectively, from the same two runs, agreed within 0.5 %

The respective values from the two archimedes method characterization repetitions were then averaged. Said average was used for all sintering characterizations.

It should be noted at this point that, generally, samples that were sintered to approximately 5 % closed porosity required several repetitions to complete this process. The general behavior of said specimens was to increase in apparent density and open porosity until an equilibrium was achieved.

---

<sup>146</sup> Model Number: 1405-6 Duo Seal vacuum pump, W.M. Welch Manufacturing Co., Chicago, IL

Table 3.12

## Equations Utilized in Bulk Density Characterization

1. Bulk Density,  $\rho_{Bulk}$  (g/cm<sup>3</sup>):

$$\rho_{bulk} = \frac{M_{Dry}\rho_{Liq}}{(M_{Sat} - M_{Imm})}$$

where:  $M_{Dry}$  is sample dry mass (g)  
 $M_{Sat}$  is sample saturated weight (g)  
 $M_{Imm}$  is sample immersed weight (g)  
 $\rho_{Liq}$  is immersion liquid density (g/cm<sup>3</sup>)

2. Percent Theoretical Density, %ThD (%):

$$\%ThD = \frac{\rho_{Bulk}}{\rho_{Theo.}} \times 100$$

where:  $\rho_{Theo.}$  is the theoretical density of the material (g/cm<sup>3</sup>)

3. Apparent Specific Gravity, ASG (g/cm<sup>3</sup>):

$$ASG = \frac{M_{Dry}\rho_{Liq}}{M_{Dry} - M_{Imm}}$$

4. Percent Total Porosity, %TP (%):

$$\%TP = 100 - \%ThD$$

5. Percent Open Porosity, %OP (%):

$$\%OP = \frac{M_{Sat} - M_{Dry}}{M_{Sat} - M_{Imm}} \times 100$$

Table 3.12 (continued)

6. Percent Closed Porosity, %CP (%):

$$\%CP = \%TP - \%OP$$

7. Composite Theoretical Density,  $\rho_{\text{Theo. Composite}}$  (g/cm<sup>3</sup>):

$$\rho_{\text{Theo. Composite}} = \sum_i V_i \rho_{\text{Theo. } i}$$

where:  $V_i$  is the volume fraction of component  $i$   
 $\rho_{\text{Theo. } i}$  is the theoretical density of  
 component  $i$  (g/cm<sup>3</sup>)

This behavior was most pronounced in specimens containing controlled porosity and will be discussed further in Chapter 4 below.

Archimedes density measurements were repeated, on each specimen, after dielectric properties characterization (described in section 3.7.2 below). This was done in order to determine if any of the density-related values changed as a result of preparation for dielectric properties measurements. If the above values agreed within the prestated criteria, the values used for sintering characterizations were also used in dielectric properties characterizations. If the new data did not satisfy the above criteria, the process was repeated until the above criteria were satisfied and these new data were used in all dielectric properties characterizations.

### 3.7.2 Dielectric Properties Characterization

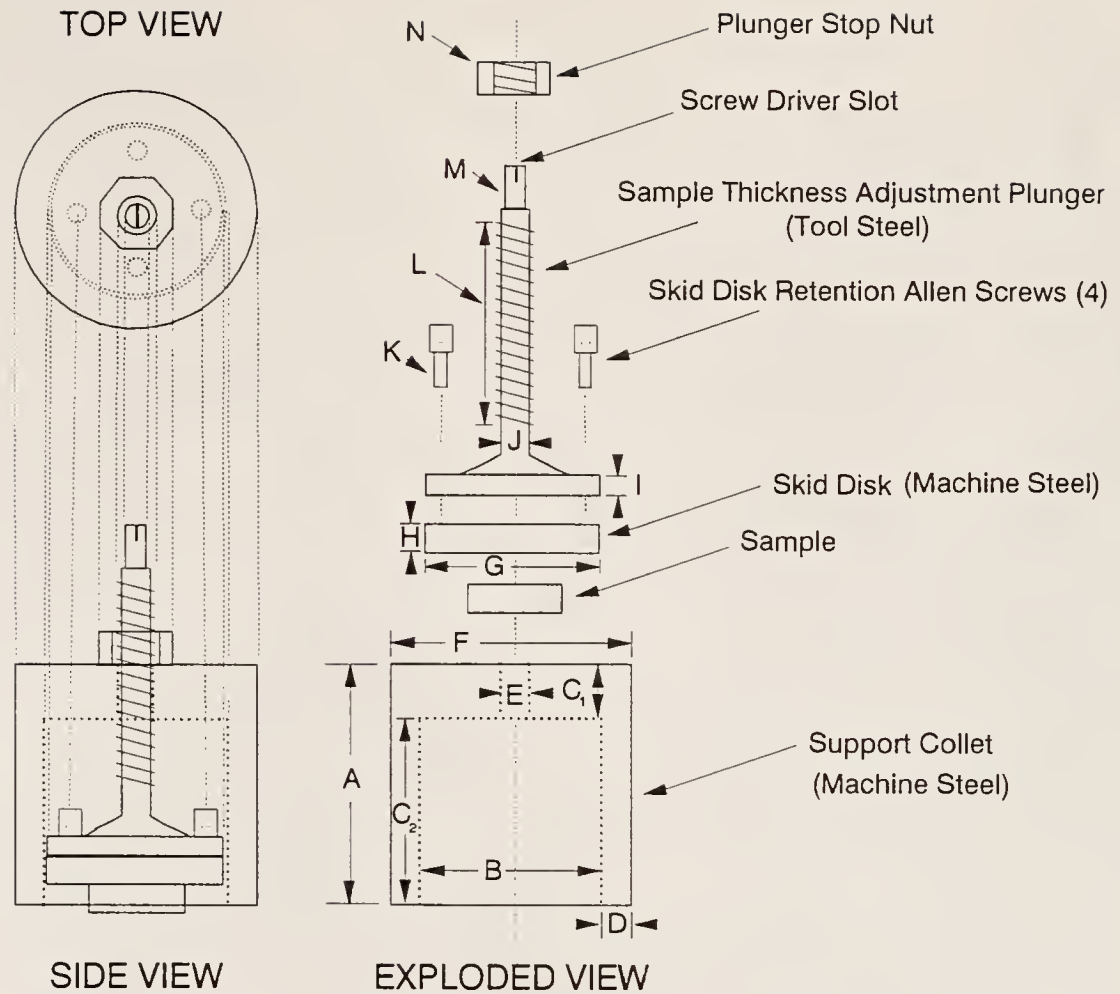
Sintered/presintered specimens that were large enough were then prepared for dielectric properties measurement. This involved grinding the disks to a thickness of approximately 1 to 5 mm to a surface smoothness of 600 grit. The thickness criterion above was chosen with consideration of the dielectric standards data depicted below. It was also paramount that both surfaces of circular cross section be parallel. The following procedure helped achieve these goals.

A specimen for grinding was mounted to the grinding fixture illustrated in Figure 3.12 using Canadian balsam.<sup>147</sup> The removable inner portion of the grinding fixture was placed in boiling water to heat it to the melting temperature of the balsam. It was then removed and dried. The balsam was applied at this point and the flattest portion of the sample (the bottom) was affixed to the grinding fixture. The affixed pair were then placed in water at ambient temperature to cool the balsam below its hardening point. After cooling, the affixed

---

<sup>147</sup> Catalog Number: 40-8110-004 BALSAM, Buehler Ltd., 41 Waukegan Rd., Lake Bluff, IL 60044





### Dimensions:

- |   |                                    |
|---|------------------------------------|
| A. 42.5 mm  | H. 4.5 mm                          |
| B. 50.8 mm  | I. 2.3 mm                          |
| C. C <sub>1</sub> 13.0 mm, C <sub>2</sub> 29.5 mm | J. 9.5 mm, Threaded 0.945 turns/mm |
| D. 4.6 mm   | K. Number 4/40 Allen Screws (4)    |
| E. 9.5 mm, Threaded 0.945 turns/mm                | L. 32.0mm of Threaded Length       |
| F. 60.0 mm  | M. 6.2 mm                          |
| G. 50.6 mm  | N. 9.5 mm, Threaded 0.945 turns/mm |

Figure 3.12

Schematic illustration of the plane-parallel, dielectric specimen grinding fixture utilized

pair were reinstalled within the rest of the grinding fixture, and the decking height was adjusted using vernier calipers.<sup>148</sup> A locking nut was then tightened to ensure that the decking height did not change.

The specimen was then ground to the decking height using SiC powders<sup>149</sup> dispersed in DI water on glass plates.<sup>150</sup> A circular grinding motion was used and the entire apparatus was thoroughly rinsed with tap water between each grinding or polishing stage. The grinding/polishing stages were 120, 240, 320, 400 and 600 grit.

After the last polishing stage, the apparatus was disassembled and washed. The removable portion (with the specimen) was again immersed in boiling water and the specimen was removed after heating. The empty grinding fixture was then reimmersed in ambient temperature water to again cool the remaining balsam. The remaining hard balsam was then removed by scraping the flat surface with a flat spatula.<sup>151</sup> The clean grinding fixture was then reheated in the boiling water and the opposite side (i.e. the side that had just been ground and polished) was affixed to the grinding fixture. The entire process was then repeated in order to insure that the previously mentioned conditions for satisfactory specimens were met.

The collet of the grinding fixture was cleaned between grinding and polishing each side and the inner surface was coated with a thin layer of silicone grease.<sup>106</sup> The fixture was stored greased and dry in order to prevent corrosion.

---

<sup>148</sup> Catalog Number: 12-122, Fisher Scientific, 1600 Parkway View Drive, Pittsburgh, PA 15205

<sup>149</sup> Catalog Number: 40-6905-XXX-080, where XXX denotes SiC powder grit size, Buehler Ltd., 41 Waukegan Rd., Lake Bluff, IL 60044

<sup>150</sup> E Float Glass, Ace Hardware

<sup>151</sup> Catalog Number: 14-373, Fisher Scientific, 1600 Parkway View Drive, Pittsburgh, PA 15205

The parallel ground and polished specimens were washed in 3 separate acetone<sup>152</sup> baths. The first was used to remove bulk balsam remaining on the specimens. The second two washes in acetone were performed in a sonication bath in order to remove all soluble impurities.

The washed specimens were then placed within their respective, open packaging containers and dried within a vacuum oven at approximately 70°C overnight at ambient pressure. After drying the specimens were repackaged and stored for future dielectric properties measurements.

Immediately prior to dielectric characterization the samples were placed in their respective open containers and dried at 180°C for no less than 2 h in a microprocessor controlled<sup>153</sup> drying oven<sup>154</sup> in order to remove any bound water which would result in erroneous dielectric data. Dielectric measurements were performed using the air gap method<sup>155</sup> in a guarded electrode dielectric test fixture,<sup>156</sup> using electrode B (5 mm solid electrode) connected to a low frequency impedance analyzer.<sup>157</sup>

The test fixture was connected to the impedance analyzer which was allowed to warm up for approximately 30 min. At this point the proper frequency and circuit mode were set and the device subjected to a zero-

---

<sup>152</sup> Catalog Number: A18-20 ,Fisher Scientific, 1600 Parkway View Drive, Pittsburgh, PA 15205

<sup>153</sup> Model Number: 828D Micristar, Research Inc., Box 24064, Minneapolis, MN 55424

<sup>154</sup> Model Number: LEB-1-27, Despatch Corp., 619 SE 8<sup>th</sup> St., P.O. Box 1320, Minneapolis, MN 55440

<sup>155</sup> See Operations Manual for Footnote 156

<sup>156</sup> Model Number: HP 16451B, Yokogawa-Hewlett-Packard, LTD., 9-1, Takakura-cho, Hachioji-shi, Tokyo, Japan

<sup>157</sup> Model Number: 4912A, Hewlett Packard, Yokogawa-Hewlett-Packard, Ltd., 9-1, Takakura-cho, Hachioji-shi, Tokyo, Japan

short/open calibration correction.<sup>158</sup> The test fixture electrodes were then adjusted as recommended.<sup>155</sup> After electrode adjustment, a second zero-short/open correction was performed. Since no load feature is available on the dielectric test apparatus, a  $\tan(\delta)$  compensation correction factor was determined for each frequency of interest.

After the previously mentioned calibrations and adjustments were performed, the electrodes were moved together with no sample between them until a  $\tan(\delta)$  value was indicated by the impedance analyzer. This value was monitored over time and is indicated in Table 3.13 for the various frequencies. These values were observed to oscillate approximately  $\pm 0.0005$  with time and thus should be considered accurate only within that range. In order to check the accuracy of said  $\tan(\delta)$  compensation, several standards of known  $\tan(\delta)$  were tested at 1 MHz. These data are also in Table 3.13 in order to provide a basis for the accuracy of  $\tan(\delta)$  data.

In order to investigate the relative accuracy of the dielectric measurement apparatus, discoidal quartz<sup>159</sup> and pyrex<sup>160</sup> standards of various diameters and thicknesses were obtained and measured via the method above (without the 180°C heat treatment) at 1 MHz. Table 3.13 depicts this data as well as pertinent literature data, thereby allowing the reader an estimate of the relative accuracy of said apparatus. From this data, it was decided that it would be best to try to keep sample thickness between approximately 2 and 4 mm. Also from these data, it was decided to keep the sample diameter between 0.75 (1.91 cm) and 1.5" (3.81 cm).

---

<sup>158</sup> See Operations Manual for Footnote 157 above

<sup>159</sup> GM Associates, 9803 Kitty Lane, Oakland, CA 94603

<sup>160</sup> Ace Glass Inc., 639 S. Hancock St., Louisville, KY 40201

Table 3.13

Measured Dielectric and Physical Data  
of the Dielectric Standards Used

Description	Bulk Properties				Dielectric Properties	
	Dia- meter (mm)	Thick- ness (mm)	Bulk Density (g/cm <sup>3</sup> )	%Th D	$\epsilon$	$\tan(\delta)$
7070 INGOT (SQUARE AS RECEIVED)	NA	3.37	2.13	100	4.06	0.0006
FUSED SiO <sub>2</sub> 1.5" (A)	37.90	9.56	2.20	100	4.14	<0.0001
FUSED SiO <sub>2</sub> 1.5" (B)	38.40	6.22	2.20	100	3.95	<0.0001
FUSED SiO <sub>2</sub> 1.5" (C)	38.05	3.20	2.16	98.0	3.80	<0.0001
FUSED SiO <sub>2</sub> 1.5" (D)	38.15	1.60	2.10	95.6	3.71	<0.0001
FUSED SiO <sub>2</sub> 1.0" (E)	25.45	9.50	2.19	99.5	3.95	<0.0001
FUSED SiO <sub>2</sub> 1.0" (F)	25.41	6.63	2.20	100	3.92	<0.0001
FUSED SiO <sub>2</sub> 1.0" (G)	25.05	3.26	2.20	100	3.82	<0.0001
FUSED SiO <sub>2</sub> 1.0" (H)	25.32	1.65	2.20	100	3.73	<0.0001
FUSED SiO <sub>2</sub> 0.5" (I)	12.75	9.56	2.20	100	3.68	<0.0001
FUSED SiO <sub>2</sub> 0.5" (J)	12.50	6.41	2.22	101	3.69	<0.0001
FUSED SiO <sub>2</sub> 0.5" (K)	12.60	3.17	2.19	99.5	3.64	<0.0001
FUSED SiO <sub>2</sub> 0.5" (L)	12.85	1.54	2.21	100	3.66	<0.0001

Table 3.13 (continued)

Description	Bulk Properties				Dielectric Properties	
	Dia- meter (mm)	Thick- ness (mm)	Bulk Density (g/cm <sup>3</sup> )	%Th D	$\epsilon$	$\tan(\delta)$
7740 PYREX 0.75" (M)	18.85	10.00	2.23	100	4.66	0.0048
7740 PYREX 0.75" (N)	18.80	6.49	2.23	100	4.63	0.0044
7740 PYREX 0.75" (O)	19.05	3.29	2.23	100	4.61	0.0043
7740 PYREX 0.75" (P)	19.05	1.74	2.23	100	4.56	0.0045

- Notes:
1. The bulk density of all samples other than the 7070 sample was determined by measuring the sample diameter, calculating the volume using a discoidal approximation, and dividing the measured sample weight by said volume. The bulk density of the 7070 sample was measured using the Archimedes method.
  2. The literature value theoretical densities used were, 2.20 g/cm<sup>3</sup> for fused SiO<sub>2</sub> [79COR], 2.13 g/cm<sup>3</sup> for 7070 [79COR, 88COR] and 2.23 g/cm<sup>3</sup> for 7740 Pyrex [79COR, 88COR].
  3. Literature value dielectric constants ( $\epsilon$ ) are 3.78 for fused SiO<sub>2</sub> [76KIN], 4.1 for 7070 [79COR, 88COR] and 4.6 for 7740 Pyrex [79COR, 88COR].
  4. Literature value loss tangents ( $\tan(\delta)$ ) are 0.0001 for fused SiO<sub>2</sub> [76KIN], 0.0006 for 7070 [79COR, 88COR] and either 0.0057 [79COR] or 0.004 [88COR] for 7740 Pyrex.



Therefore, the casting tubes used during slip casting (as described in section 3.4.3 above) were chosen to have an inner diameter of approximately 1.125" (2.86 cm). Thus, the sample diameters remained between the diameter limits, established using the data in Table 3.13, after densification.

The specimen to be measured was quickly removed from the drying oven using tweezers<sup>161</sup> and placed between the electrodes of the dielectric test fixture. The electrode distance was then quickly reduced (using the clutch drive to avoid damage) until the electrode touched the sample. The sample thickness was then measured using the 10  $\mu\text{m}$  resolution micrometer on the dielectric test fixture. The electrode distance was then increased to an amount between 100 and 110% of the measured sample thickness. This reading was also recorded with said micrometer. After equilibration of values (i.e. the capacitance and  $\tan(\delta)$  of the specimen decreases until cooling to near ambient temperatures), the capacitance and  $\tan(\delta)$  were recorded. The specimen was then removed and the process repeated for other specimens. Once dielectric characterization was completed on the specimen, the sample thickness was remeasured, using a precision micrometer.<sup>161</sup> This thickness measurement was recorded and used in all calculations requiring the sample thickness. The specimen was then repackaged and stored for the second set of archimedes density characterizations. Table 3.14 depicts the calculations used for dielectric properties calculations.

The effect of atmospheric moisture adsorption was also investigated. Seven samples, representative of the composite matrix produced, were heated in the previously mentioned drying oven at 180°C for no less than 2 h.

---

<sup>161</sup> Catalog Number: 12-125, Fisher Scientific, 1600 Parkway View Drive, Pittsburgh, PA 15205

Table 3.14

## Equations Used in Calculating Dielectric Properties

1. Dielectric Constant,  $\epsilon$ :

$$\epsilon = \frac{1}{1 - \left(1 - \frac{C_{sg}}{C_{si}}\right) \times \frac{t_g}{t_a}}$$

where:  $t_g$  is the air gap width (i.e. the distance between the sample top and the electrode surface (mm))

$t_a$  is the thickness of the specimen under test (mm)

$C_{sg}$  is the series analog capacitance measured with the material under test (MUT) removed (pF)

$C_{si}$  is the series analog capacitance measured with the MUT inserted (pF)

2. Dissipation Factor,  $\tan(\delta)$ :

$$\tan\delta = D + CF$$

where:  $D$  is the measured dissipation factor of the MUT

$CF$  is the estimated correction factor for the DUT

Notes: 1. Standard measurements taken at a frequency of 1 MHz

2.  $CF$  is frequency dependent:

Correction Factor ( $CF$ ) as a Function of Frequency

Frequency (Hz)	Correction Factor
$10^6$	0.0012
$10^7$	0.0040
$1.3 \times 10^7$	0.0083

These specimens were also of two different groups, one having less than 1% open porosity, one having almost totally open porosity. Furthermore, the highly sintered samples would have very low specific surface areas, whereas the specific surface areas of the open porosity samples were greater as outlined above and further explained below. Each specimen was then removed and the dielectric properties were quickly measured. The sample weight was also recorded using a 0.1 mg resolution balance at that time.<sup>162</sup> This was established as a zero point of time and a timer<sup>142</sup> was started. This procedure was performed at 0, 1, 2, 5, 10, 30, 60, 120, 180, 240 and 1440 min. for each sample. In order to avoid time discrepancies, the procedure was performed up to the 10 min. repetition on each consecutive sample before starting the next. Specimens were characterized in sets of three samples in this manner (since the timer had three separate timing circuits).

Finally, the effect of frequency upon dielectric properties was investigated. Dielectric properties measurements were performed on 4 representative hermetic samples at frequencies of 1 kHz, 10 kHz, 100 kHz, 1 MHz, 10 MHz and 13 MHz. At each frequency, an zero-short/open calibration<sup>158</sup> was performed prior to measurement. It should be noted that at lower frequencies, the dielectric test apparatus loses accuracy in capacitance measurements and therefore, relationships concerning capacitance related dielectric properties with respect to frequency are plotted with dashed lines below frequencies of 10 kHz. It is assumed however, that changes in capacitance related dielectric properties with decreasing frequency are directly a result of this inaccuracy, since the data of others indicates that the dielectric constant of these materials is very stable with respect to frequency (as will be discussed in Chapter 4 below), at low frequencies.

---

<sup>162</sup> Model Number: AE 100, Mettler Instrument Corp., Hightstown, NJ

Furthermore,  $\tan(\delta)$  was not measurable below 1 MHz due to the previously mentioned limitations of the test apparatus.

### 3.7.3 Microscopic Investigation of Composites

#### 3.7.3.1 Overview

This section describes the experimental procedures utilized to microscopically investigate sintered composites. The experimental details of microscopic investigations of the latex powders used in this study are described in section 3.2.2 above. The procedures used to microscopically characterize the ceramic powders are outlined in section 3.3.2 above. Microscopic investigation of green compacts is detailed in section 3.4.5 as well.

Microscopic investigation of sintered compacts was used mainly to investigate the appearance of included porosity (i.e pore size, smoothness, cluster size, dispersedness, and possible segregation). Microscopy was also utilized to examine  $\text{Si}_3\text{N}_4$ -BS glass interfaces in order to determine if the  $\text{Si}_3\text{N}_4$  powder reacted noticeably with the BS glass matrix. A rough, qualitative measure of surface smoothness was also obtained by examining the top surface of representative sintered compacts.

Where possible, polished specimens were examined. However, as is common in porous composite systems, it was not always possible to do so. In these situations, fracture surfaces were examined.

#### 3.7.3.2 Specimen Preparation

Polished specimens were produced by mounting the specimen in polymethyl methacrylate (PMMA) prior to polishing. The specimen of interest was placed inside a glass vial.<sup>163</sup> The specimen was held

---

<sup>163</sup> Catalog Number: 03-337-5, Fisher Scientific, 1600 Parkway View Drive, Pittsburgh, PA 15205

vertically within the vial with a mounting clip<sup>164</sup> and approximately 3 ml of 2,2'-Azobis [2-methyl-propionitrile] (AIBN)<sup>165</sup>/MMA (methyl methacrylate)<sup>166</sup> solution was decanted inside the glass vial using a disposable pipette.<sup>167</sup> The AIBN/MMA concentration used was 9 mg to 5 ml (AIBN to MMA). The AIBN acted as the initiator of the addition polymerization reaction that forms PMMA. This process was carried out beneath a fume hood<sup>52</sup> in order to avoid exposure to hazardous MMA fumes. The glass vial was then sealed tightly and placed within an oven<sup>168</sup> to promote polymerization of the MMA. The oven was isothermally maintained at approximately 63°C as indicated by an 0.1°C resolution thermometer.<sup>10</sup> The thermometer bulb was placed next to the MMA in the glass vial in order to assure accurate temperature measurement.

After the MMA polymerized, the vial was removed from the oven and allowed to cool to ambient temperature. The vial was then decapped and wrapped in a tissue.<sup>61</sup> A hard object was then used to break the vial and the PMMA mounted sample was removed.

The sample was then ground flat on a polishing wheel<sup>169</sup> using a 120 grit SiC abrasive paper.<sup>170</sup> Each sample was similarly ground and polished to 600 grit using successively smaller SiC papers (i.e. 120,

---

<sup>164</sup> Catalog Number: MK-C-101, Fisher Scientific, 1600 Parkway View Drive, Pittsburgh, PA 15205

<sup>165</sup> Catalog Number: 118-4746, Eastman Kodak Company, Rochester, NY 14650

<sup>166</sup> Catalog Number: 03629-4, Fisher Scientific, 1600 Parkway View Drive, Pittsburgh, PA 15205

<sup>167</sup> Catalog Number: 13-711-5A, Fisher Scientific, 1600 Parkway View Drive, Pittsburgh, PA 15205

<sup>168</sup> Model Number: 126G ISOTEMP OVEN, 100 Series, Fisher Scientific, 1600 Parkway View Drive, Pittsburgh, PA 15205

<sup>169</sup> Model Number: ECOMET III, Buehler Ltd., 41 Waukegan Rd, Lake Bluff, IL 60044

<sup>170</sup> Catalog Number: 30-5108-XXX-100, where XXX is grit size, Buehler Ltd., 41 Waukegan Rd., Lake Bluff, IL 60044



180, 240, 320, 400 and 600 grits). Tap water was used as the lubricant during these polishing and grinding steps. The sample was rinsed thoroughly in tap water after each step.

Each sample was then polished using 1000 grit SiC powder<sup>171</sup> on a glass plate.<sup>150</sup> The grinding lubricant used in this instance was DI H<sub>2</sub>O.<sup>88</sup> Each sample was then rinsed and sonically cleaned for several minutes then rinsed again in DI H<sub>2</sub>O. Each sample was then dried with a tissue.<sup>61</sup>

The dry samples were then polished with diamond<sup>172</sup> either by hand or on a vibrating polisher.<sup>173</sup> Lapping oil<sup>174</sup> was utilized for the lubricant during diamond polishing. Hand polishing was performed on a raised nap cloth,<sup>175</sup> while cloths having no nap<sup>176</sup> were used for vibratory polishing. The samples were polished using 6, 1 and 0.25  $\mu\text{m}$  size diamond paste. The samples were sonically cleaned between each diamond size, then dried with a tissue.

After polishing, the PMMA was removed from each specimen by a two step process. Each mounted specimen was first put in an oven<sup>177</sup> at approximately 300°C for about 10 min. in order to soften the PMMA. After removal from the oven each polished specimen was quickly removed

---

<sup>171</sup> Catalog Number: 40-8418-000-016, 1000 grit SiC Powder, Buehler Ltd., 41 Waukegan Rd, Lake Bluff, IL 60044

<sup>172</sup> Designation Series: METADI II, Buehler Ltd., 41 Waukegan Rd, Lake Bluff, IL 60044

<sup>173</sup> Model Numbers: VIBRAMET I and VIBRAMET 2, Buehler, Ltd., 41 Waukegan Rd, Lake Bluff, IL 60044

<sup>174</sup> Catalog Number: 60-3250-128, Buehler Ltd., 41 Waukegan Rd, Lake Bluff, IL 60044

<sup>175</sup> Catalog Number: 40-7218 MICROCLOTH, Buehler Ltd., 41 Waukegan Rd, Lake Bluff, IL 60044

<sup>176</sup> Catalog Number: 40-7070 NYLON, Buehler, Ltd., 41 Waukegan Rd, Lake Bluff, IL 60044

<sup>177</sup> Catalog Number: 10-553, Fisher Scientific, 1600 Parkway View Drive, Pittsburgh, PA 15205



from the PMMA using two pairs of tweezers.<sup>178</sup> The polished specimen was then heat treated in an oven at approximately 600°C for approximately 4 h in order to remove any remnant PMMA.

After cooling, the each  $\text{Si}_3\text{N}_4$ -containing specimen was etched in HF. Preliminary studies indicated that an HF etch of approximately 60 seconds, in 2% HF, was the best and samples produced subsequent to said studies were etched at that exposure. Each etched sample was next thoroughly rinsed in tap water, then sonically cleaned.

Each polished specimen was mounted on a 1" (2.54 cm) aluminum SEM specimen stub<sup>30</sup> with silicone sealant.<sup>179</sup> After the silicone dried, a conductive path was painted from the specimen to the specimen stub with carbon paint.<sup>115</sup> The sample was then sputter coated with a film of Au/Pd and was ready for viewing via SEM.

The above method worked well for samples containing mainly open porosity. In the later stages of sintering however, this is not the case. Polished specimens of samples containing mainly closed porosity were characterized by pullout around said porosity. Furthermore, samples containing  $\text{Si}_3\text{N}_4$  also exhibited substantial pullout when polished. Also it was possible to view only relatively small areas of each etched surface of  $\text{Si}_3\text{N}_4$ -containing specimens. Therefore, no segregation studies of  $\text{Si}_3\text{N}_4$  in this system were possible. Thus, samples containing an appreciable amount of closed porosity and/or  $\text{Si}_3\text{N}_4$  were prepared from fracture surfaces.

Specimen fracture surfaces were obtained by fracturing sintered samples with a hard object. Contaminants were blown off from fracture

---

<sup>178</sup> Catalog Numbers: 08-953D and 08-887, Fisher Scientific, 1600 Parkway View Drive, Pittsburgh, PA 15205

<sup>179</sup> Catalog Number: 04-769-5, Fisher Scientific, 1600 Parkway View Drive, Pittsburgh, PA 15205

surfaces using compressed gas.<sup>180</sup> The specimens were then mounted and coated utilizing the procedures described above for polished specimens. Specimens of sintered compact surfaces were prepared in a manner identical to the method used to prepare specimens of fracture surfaces.

#### 3.7.3.3 Investigation of Segregation of Included Porosity

In order to determine if segregation of included porosity occurred within the composite system, several micrographs of the top, middle and bottom of a sintered specimen containing approximately 14 V% closed porosity were obtained. The volume fractions of included porosity at the top middle and bottom of the specimen were determined by a manual point count method [68DEH]. The manual count was continued in each of the above-mentioned areas until one hundred pore points had been obtained. The volume fraction of included porosity was then obtained by dividing the number of pore points observed by the total number of points observed.

#### 3.7.4 Mechanical Properties Data

Limited mechanical properties data were obtained using microhardness indentation techniques. Figure 3.13 illustrates the pertinent relationships utilized in said characterization. Representative samples were mounted in epoxy<sup>181</sup> and were then ground to a 1000 grit surface finish with SiC as described in section 3.6.3 above. A final polish was obtained, manually, with CeO<sub>2</sub> dispersed in H<sub>2</sub>O on a napped cloth.<sup>175</sup> The polished specimens were then cleaned sonically, swabbed with a clean tissue,<sup>61</sup> and dried at ambient temperature overnight. Samples to be characterized were chosen on the basis of

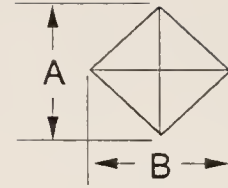
---

<sup>180</sup> Catalog Number: 15-232-20, Fisher Scientific, 1600 Parkway View Drive, Pittsburgh, PA 15205

<sup>181</sup> Catalog Number: 12-253-50A, Fisher Scientific, 1600 Parkway View Drive, Pittsburgh, PA 15205

1. Vickers Hardness, (H):

Average of A and B  
(calculated by the microhardness tester)

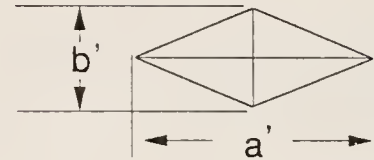


2. Knoop Hardness, (K):

(hardness calculated by  
microhardness tester)

Knoop Indenter Ratio:  $b/a = 1/7$

Knoop Indentation Dimensions ( $a'$ ,  $b'$ )



3. Elastic Modulus, (E):

$$E = \frac{0.45(H)}{\left(\frac{b}{a} - \frac{b'}{a'}\right)}$$

Figure 3.13

Microhardness indentation techniques and relationships used in this study

maximum variability in both closed porosity and silicon nitride content. Table 3.15 illustrates the samples chosen for characterization via microhardness indentation. A specimen from an as-received Corning 7070 BS glass ingot was also produced for this study. Since it is an optically clear sample having no visible seeds, it was assumed that porosity of the sample is near zero. Said assumption was used when performing data characterization.

The samples were then characterized using microhardness indentation. Each sample was evaluated using both Vickers and Knoop indenters. First, each specimen was subjected to successively increasing loads (25, 50, 100, 200, 500, 1000, 2000 g) until cracking (either lateral or radial) was observed. This load was noted. After determining the lowest values at which cracking occurs, for all samples, the indent loads to be used on all samples were determined. These loads were determined to be 25 and 50 g for Vickers indentation and 100, 200 and 300 g for Knoop indentation. On two samples, said Vickers loads were determined to be too low and higher loads were used (100 and 200 g respectively).

Vickers microhardness determination consisted of measuring and averaging both the indentation dimensions. The microhardness was then calculated by the microhardness tester<sup>182</sup> and the output was recorded in units of  $\text{kg/mm}^2$ . Similarly, both Knoop indentation dimensions were measured and the Knoop hardness was recorded in the same units as above. Both dimensions of the Knoop indentation were documented, since both are required in order to determine the elastic modulus of a material. A total of 25 data points were taken for each sample. The raw data was then encoded into a computer spreadsheet<sup>36</sup> which gave output for elastic modulus as well as standard deviation data of the above values.

---

<sup>182</sup> Model Number: MICROMET 3, Buehler Ltd., 41 Waukegan Rd, Lake Bluff, IL 60044

Table 3.15

## Samples Investigated by Microhardness Indentation

Designation	Composition			Lat. Dia. ( $\mu\text{m}$ )	Thermal Treatment		Bulk $\rho$ %ThD
	BS Glass	$\text{Si}_3\text{N}_4$	Latex		( $^{\circ}\text{C}$ )	(h)	
7070 INGOT	100	0	0	NA	NA	NA	100
03209001E	100	0	0	NA	650	6	97.0
05109102F	95	0	5	4.6	625	12	92.2
01039101B	90	0	10	4.6	625	18	90.2
05069101A	85	0	15	4.6	625	18	86.2
05179102A	85	0	15	2.4	625	24	89.7
05099101G	85	0	15	9.0	625	15	85.9
05179101B	85	0	15	POLY	625	18	86.7
03219001F	80	20	0	NA	650	24	96.9
01249101G	72	18	10	4.6	650	24	91.4
01069101F	64	16	20	4.6	625	144	89.0
03199001F	60	40	0	NA	650	72	89.6
01049101B	81	9	10	4.6	625	18	88.7
05119101C	72.25	12.75	15	4.6	625	48	87.7

- Notes:
1. Lat. Dia. is the number basis mean UPLM diameter (POLY means polydisperse latex).
  2. NA means Not Applicable.

It was not possible to determine the fracture toughness of samples within the composite system of this study because the type of cracking that occurred within the pure BS glass samples (both with and without added porosity) was always lateral. No radial cracks were evident in these samples at any loadings. In samples containing  $\text{Si}_3\text{N}_4$  however, some radial cracking was vaguely evident. Therefore, samples containing  $\text{Si}_3\text{N}_4$  were Au/Pd sputter coated for 40 s at 45 mA and at a pressure of 50 mTorr, in order to increase the reflectivity of the samples so that microcracking would be more evident.

Vickers indentation was again performed on the samples in order to attempt to determine the fracture toughness of the material. In order for this method to be valid, however, the radial crack length initiated via the indentation must be at least twice that of the dimension of the indentation itself. All radial cracks were smaller than this value at all loads at which radial cracking was observed. Therefore, this method is not a viable technique for determining fracture toughness of compositions in this composite system.



## CHAPTER FOUR RESULTS AND DISCUSSION

### 4.1 Precursor Powders

#### 4.1.1 Visual

Figures 4.1 and 4.2 illustrates the BS glass powders used in this study. Figure 4.1 depicts the as-received powder while Figure 4.2 illustrates the powder after ball milling, as described in Chapter Three. Both glasses appear to have a conchoidal nature and a wide distribution in particle size. It is evident from these that figures the ball milled BS glass powder also has a smaller mean size.

Figure 4.3 depicts the  $\text{Si}_3\text{N}_4$  powder used. The  $\text{Si}_3\text{N}_4$  powder was used as-received. The  $\text{Si}_3\text{N}_4$  powder has a characteristic shape of either cubes or hexagonal cross-section cylinders. The powder appears to have a narrower size distribution than the BS glass powder as well. It should be noted that the as-received  $\text{Si}_3\text{N}_4$  powder has a significant amount of agglomerates, which remained even after aggressive sonic dismembration.

Figures 4.4 through 4.6 illustrate the range of polystyrene latex powders (largest, medium and smallest sizes respectively) utilized in this study. Figure 4.7 portrays the quadramodal ("wide") size distribution latex powder used. Figure 4.8 depicts a representative latex powder (medium sized), before settling, to provide a comparison between settled (i.e. compare Figs. 4.5 and 4.8) and non-settled uniform polystyrene latex microspheres (UPLMs). It can be seen that the latex particles are quite spherical and that the UPLMs are predominantly monomodal. It may also be observed that UPLM powders may be produced with different sizes and size distributions.

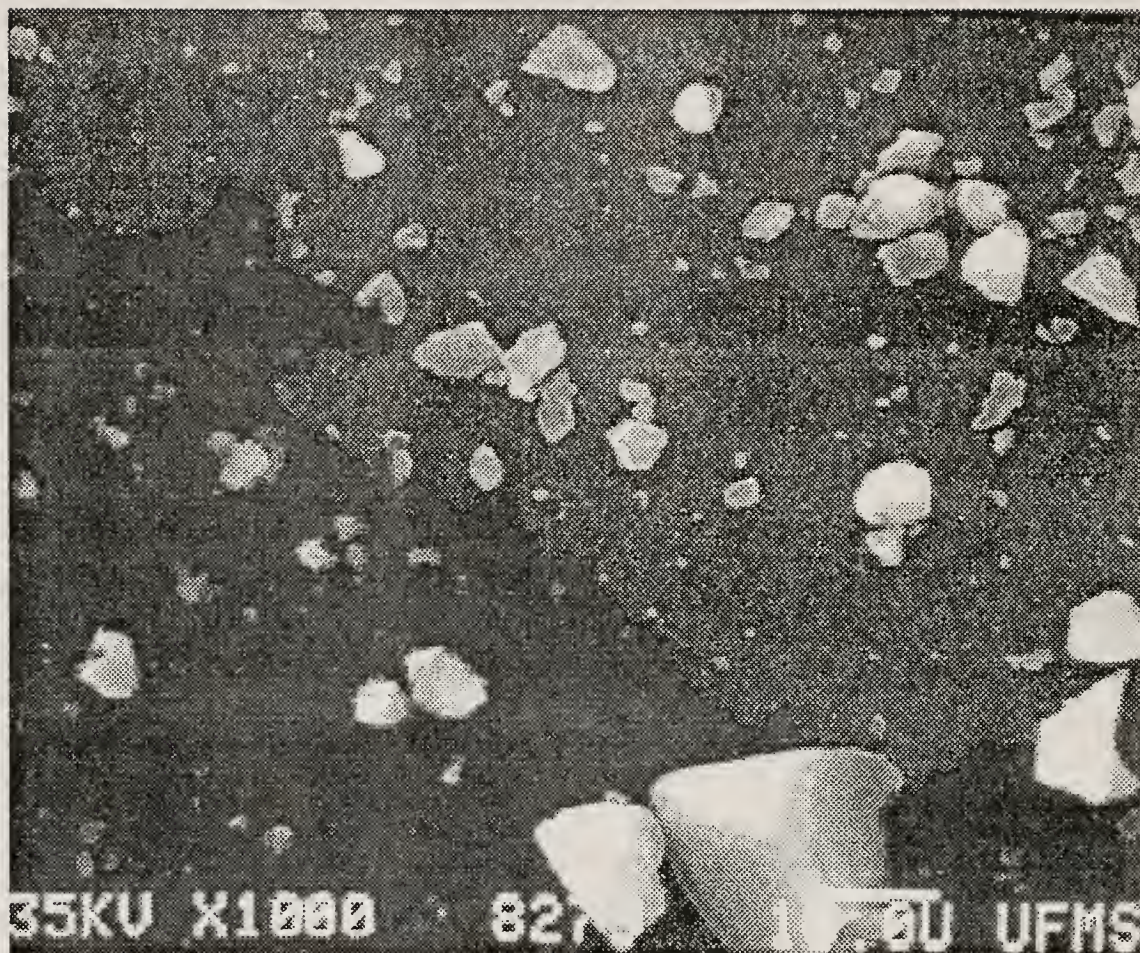


Figure 4.1

Scanning electron micrograph of the, as-received, borosilicate glass powder used in this study (Bar = 10  $\mu\text{m}$ )



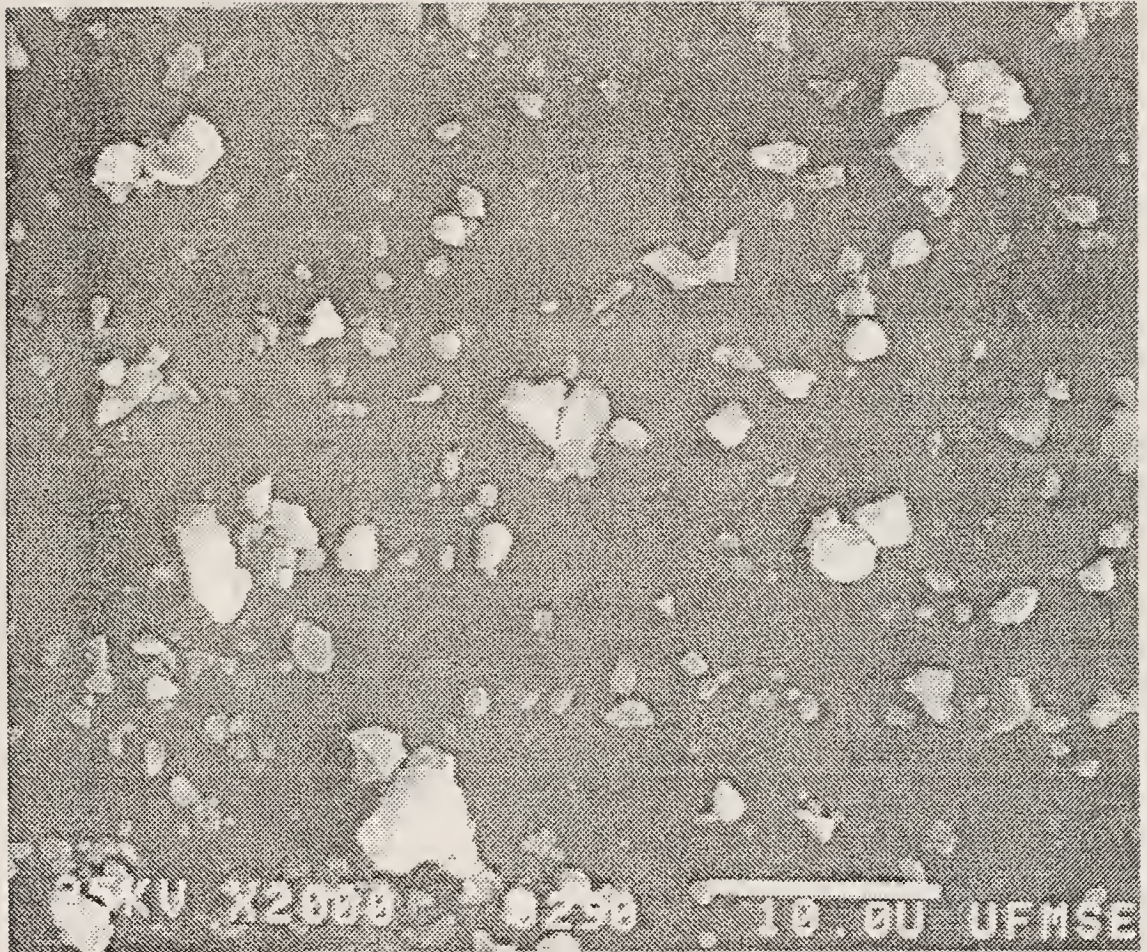


Figure 4.2      Scanning electron micrograph of ball milled borosilicate glass powder (Bar = 10  $\mu\text{m}$ )



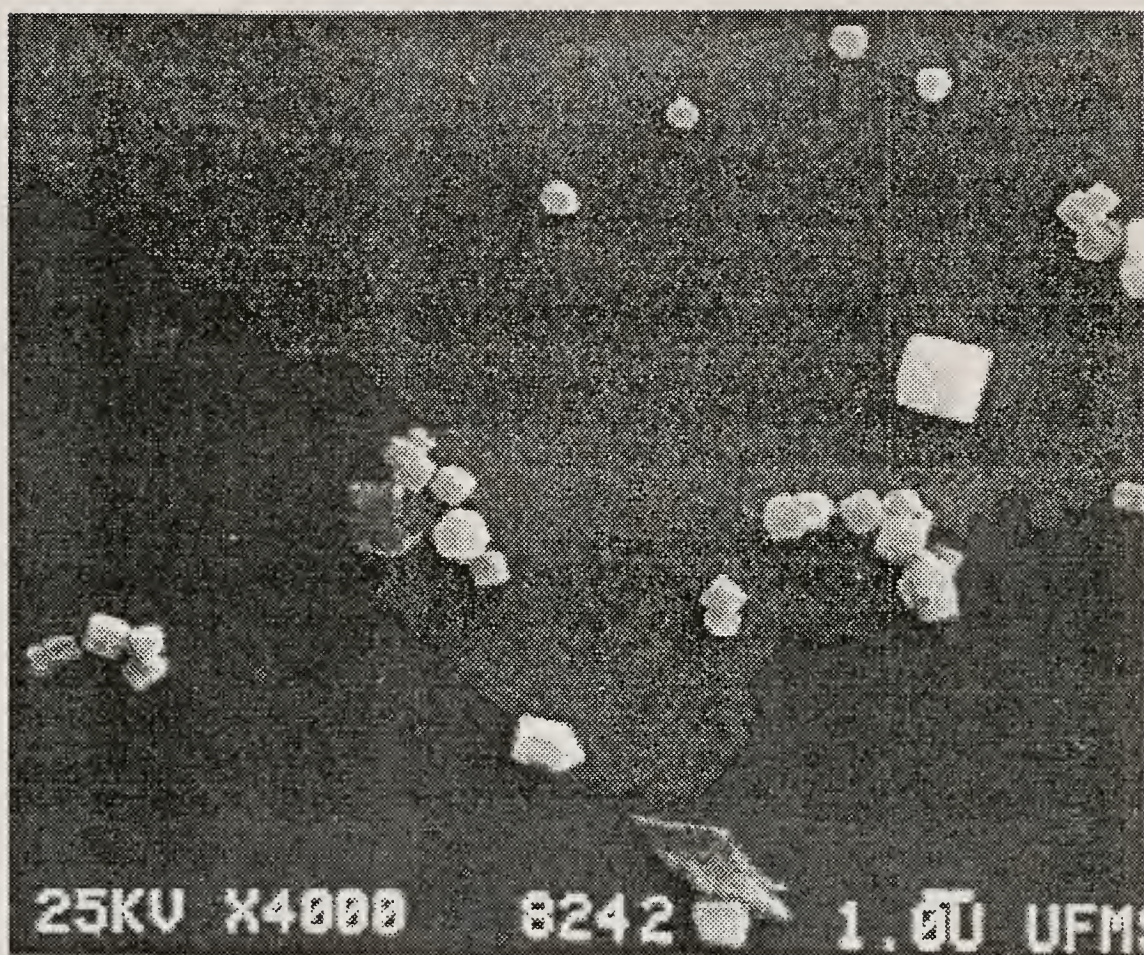


Figure 4.3

Scanning electron micrograph of the  $\text{Si}_3\text{N}_4$  powder used  
(Bar = 1  $\mu\text{m}$ )



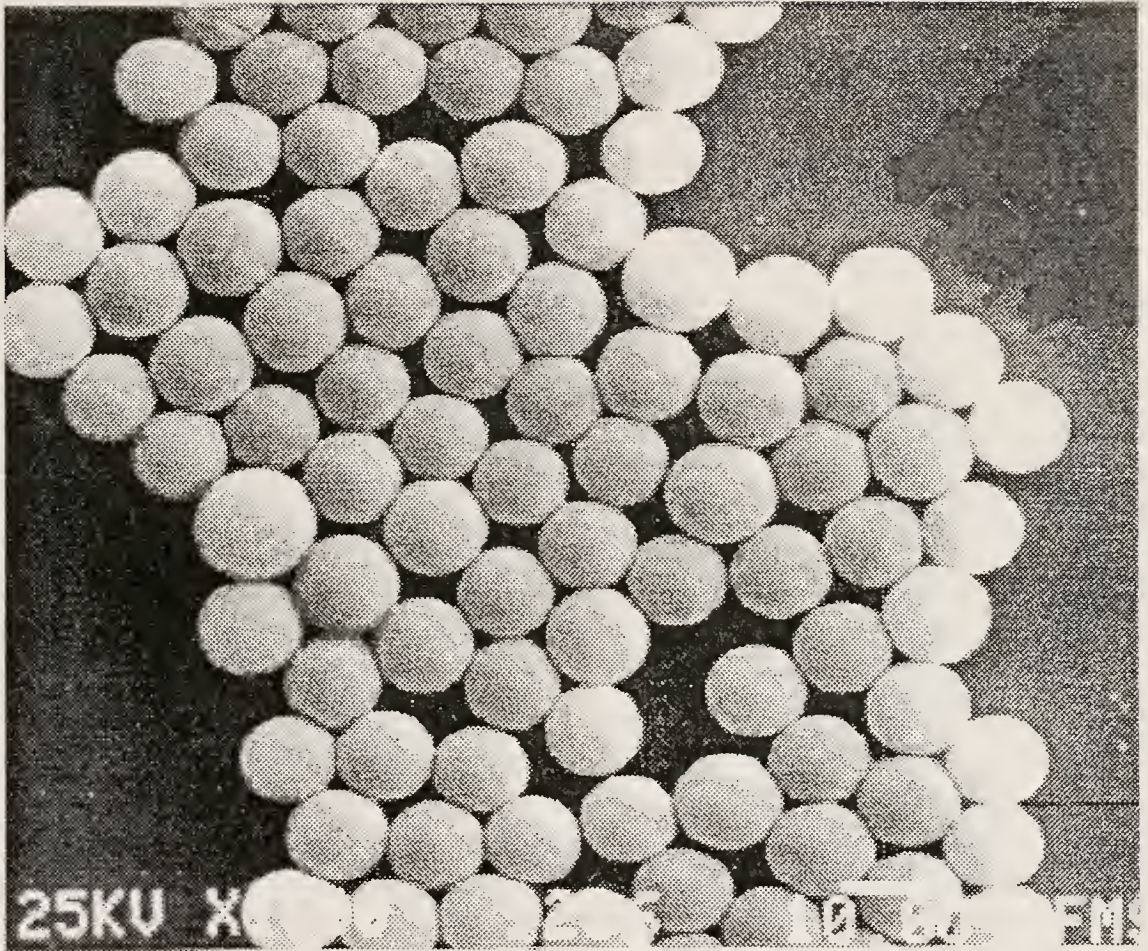


Figure 4.4

Scanning electron micrograph of settled, large size UPLM powder (Bar = 10  $\mu\text{m}$ )



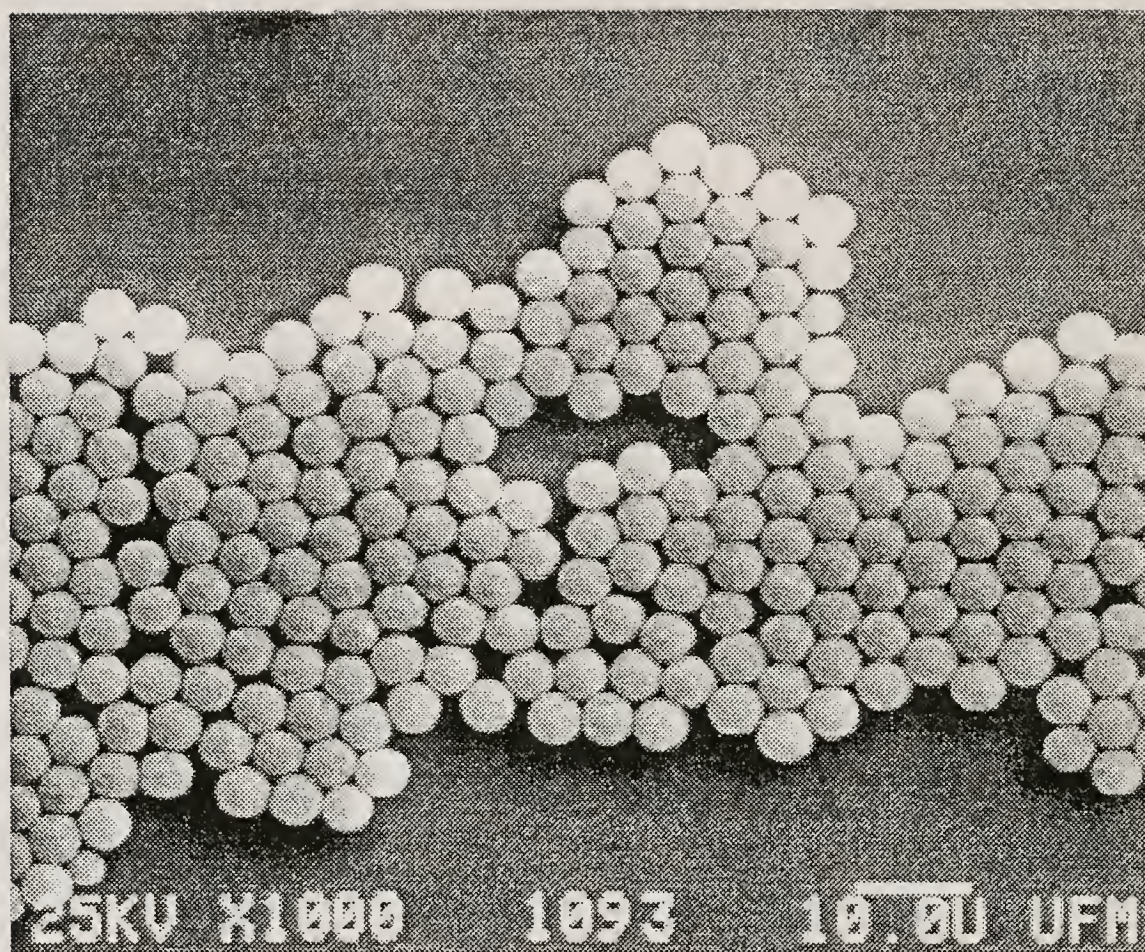


Figure 4.5

Scanning electron micrograph depicting the settled, medium sized, UPLM powder utilized in the study (Bar = 10  $\mu\text{m}$ )



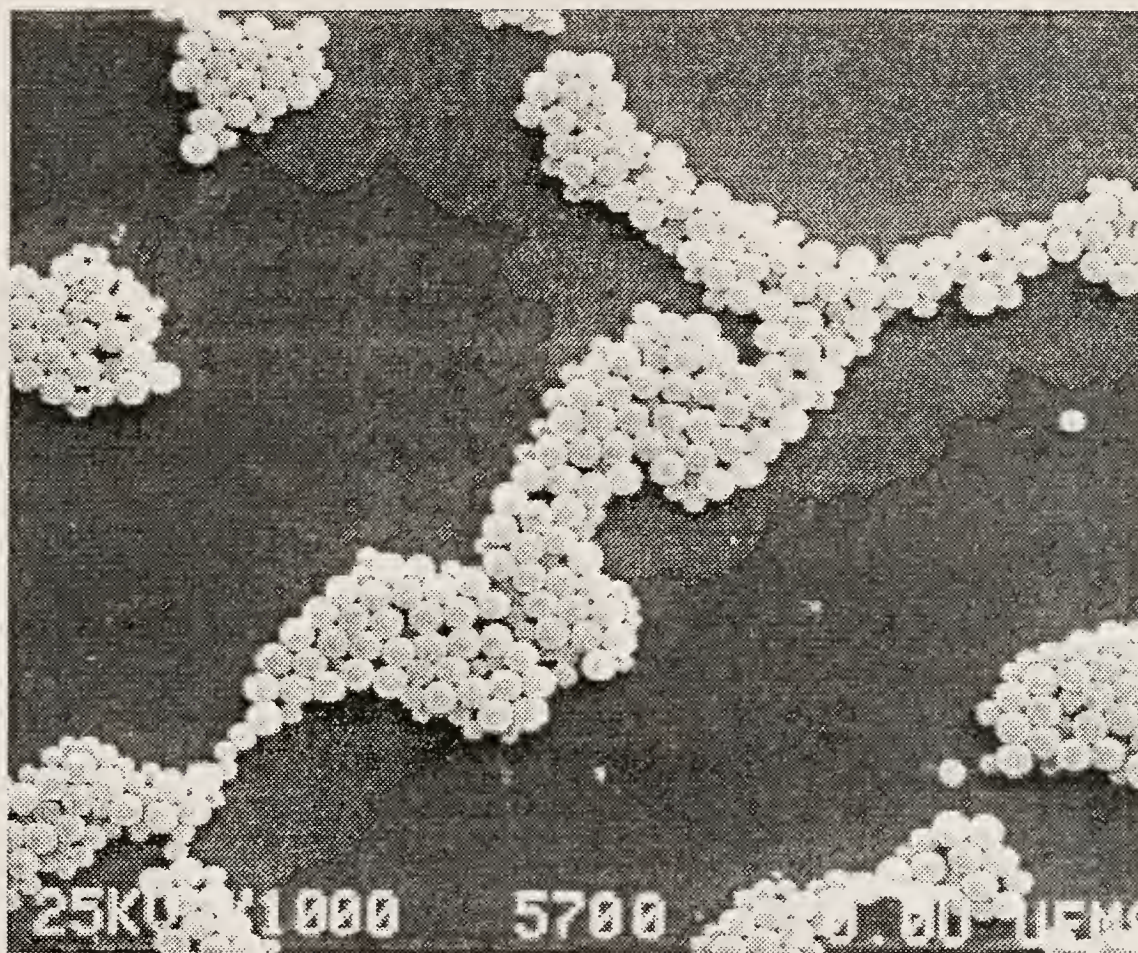


Figure 4.6

Scanning electron micrograph depicting the settled, smallest size, latex powder used (Bar = 10  $\mu\text{m}$ )



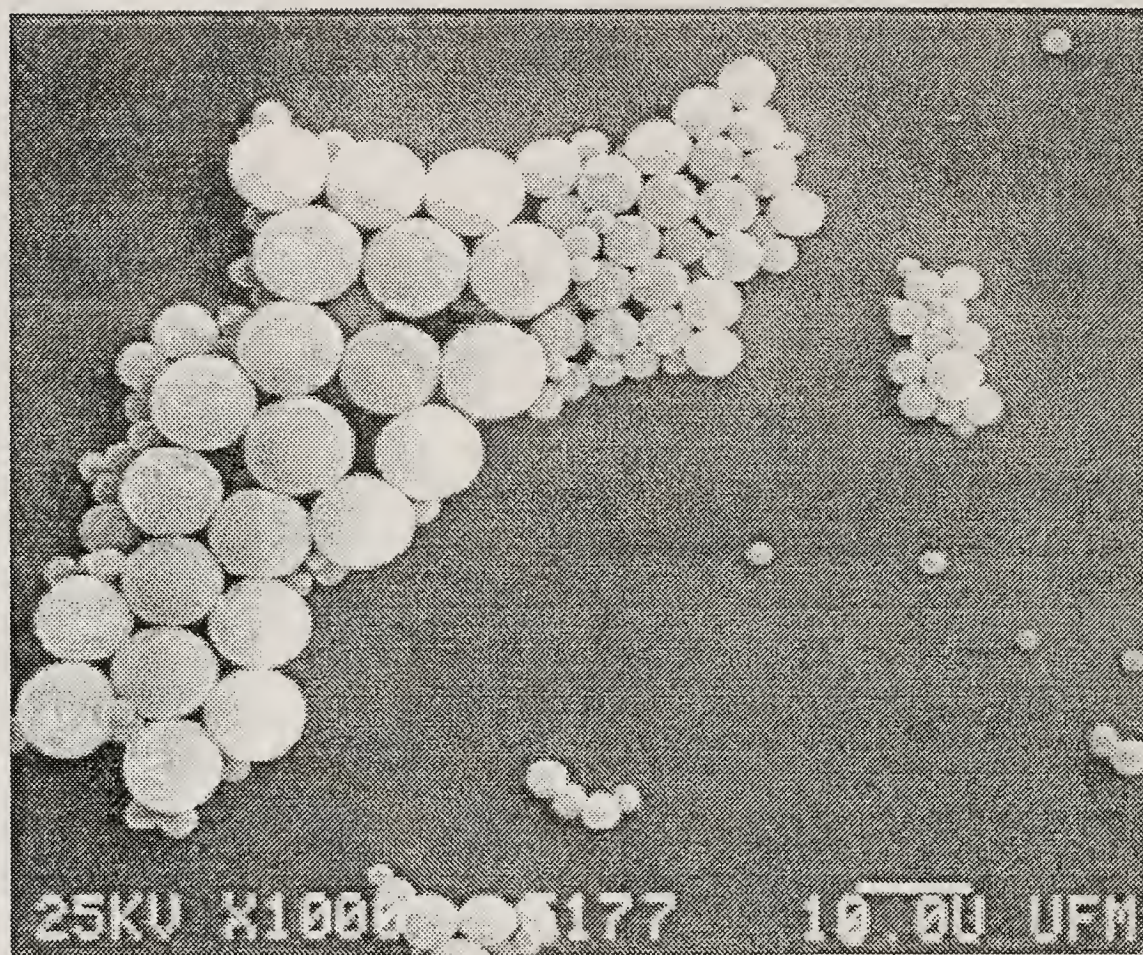


Figure 4.7

Scanning electron micrograph of the wide (quadramodal) size distribution latex powder used in this study (Bar = 10  $\mu\text{m}$ )



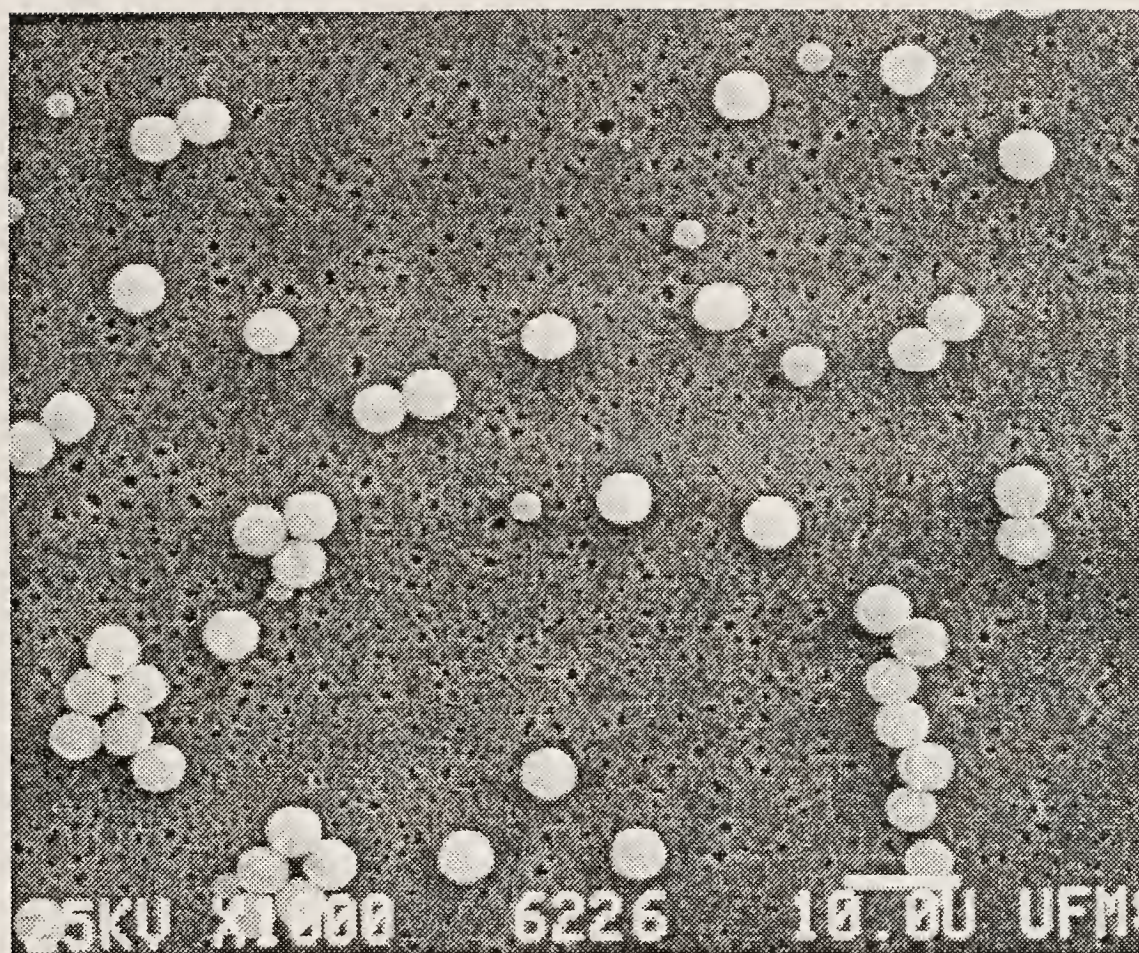


Figure 4.8

Scanning electron micrograph depicting a representative sample of the medium size latex powder before classification via settling (Bar = 10  $\mu\text{m}$ )

#### 4.1.2 Powder Density

Powder densities were determined using helium gas pycnometry, as described in Chapter 3. Table 4.1 indicates the results of said analyses for the BS glass powder (as-received as well as ball milled), the  $\text{Si}_3\text{N}_4$  powder, and the polystyrene latex UPLMs. Table 4.1 also provides manufacturers or literature data in order to provide a basis for comparison to the measured powder density values.

Table 4.1 indicates that the density values for both the  $\text{Si}_3\text{N}_4$  powder and the polystyrene latex powders agree very well with either the manufacturer's values or available literature values. Table 4.1 also indicates that the density values of both the BS glass powders is higher than the manufacturer's value for the bulk glass. It may be further noted that the ball milled BS glass powder has a greater density than the as-received glass powder.

Since smaller powder particles have a greater surface area to volume ratio, the relative concentration of surface-connected porosity is increased as well. The result of this effect is to increase the measured powder density through the decrease of the relative amount of closed porosity [88REE]. Thus, it is logical that the as-received (i.e.  $\leq 325$  mesh) BS glass powder would have a greater density than the manufacturer's value for the bulk glass. Furthermore, it is logical that the ball milled BS glass powder would have the highest measured density of the three, since the size of the ball milled powder is smaller than that of the as-received BS glass powder (as will be discussed in section 4.1.4 below).

The effect of aggregate and particle size upon density has been documented, and Figure 4.9 illustrates this relationship for tabular  $\text{Al}_2\text{O}_3$  particles [88REE]. From Figure 4.9 it may be ascertained that apparent density may increase more than 8% from a reduction in particle size from the bulk value. Thus, it is reasonable that the increase in measured density be due solely to a reduction in particle size.



Table 4.1  
Measured Powder Densities and Relevant Data

Powder	Experimental Values					Literature Value (g/cm <sup>3</sup> )	%Δ
	Density (g/cm <sup>3</sup> )	Standard Deviation (± g/cm <sup>3</sup> )		# of Independent Samples	Total # of Repetitions		
		Pop.	Sample				
BS Glass, (As-Received)	2.176	0.0104	0.0112	2	8	2.13	2.2
BS Glass (Ball Milled)	2.197	0.0040	0.0041	4	17	2.13	3.1
Si <sub>3</sub> N <sub>4</sub> Powder	3.175	0.0113	0.0116	3	20	3.10-3.44 (3.18)	0.2
Poly-styrene Latex	1.055	0.0030	0.0031	3	12	1.05	0.5

Notes: 1. Literature values cited for the BS glass are manufacturer's data (for Corning 7070 bulk borosilicate glass) [79COR,88COR]. The Si<sub>3</sub>N<sub>4</sub> values were obtained from Table 1.IV.B.2.1, and the manufacturer's data, in parentheses, for UBE SN--W (Si<sub>3</sub>N<sub>4</sub> whiskers [89SOM]). The density value for UBE SNE03, Si<sub>3</sub>N<sub>4</sub> powder was not available. The %Δ, for the Si<sub>3</sub>N<sub>4</sub> powder, is calculated using the manufacturer's data as described. The literature value for the polystyrene latex is that cited for polystyrene [87BAN2,88MIC].

2. The relationship utilized to calculate %Δ is

$$\% \Delta = \frac{|\rho_{\text{exp}} - \rho_{\text{lit/man}}|}{\rho_{\text{lit/man}}} \times 100$$

where:  $\rho_{\text{exp}}$  is the experimentally measured mean density value

$\rho_{\text{lit/man}}$  is either the literature or manufacturer's density value

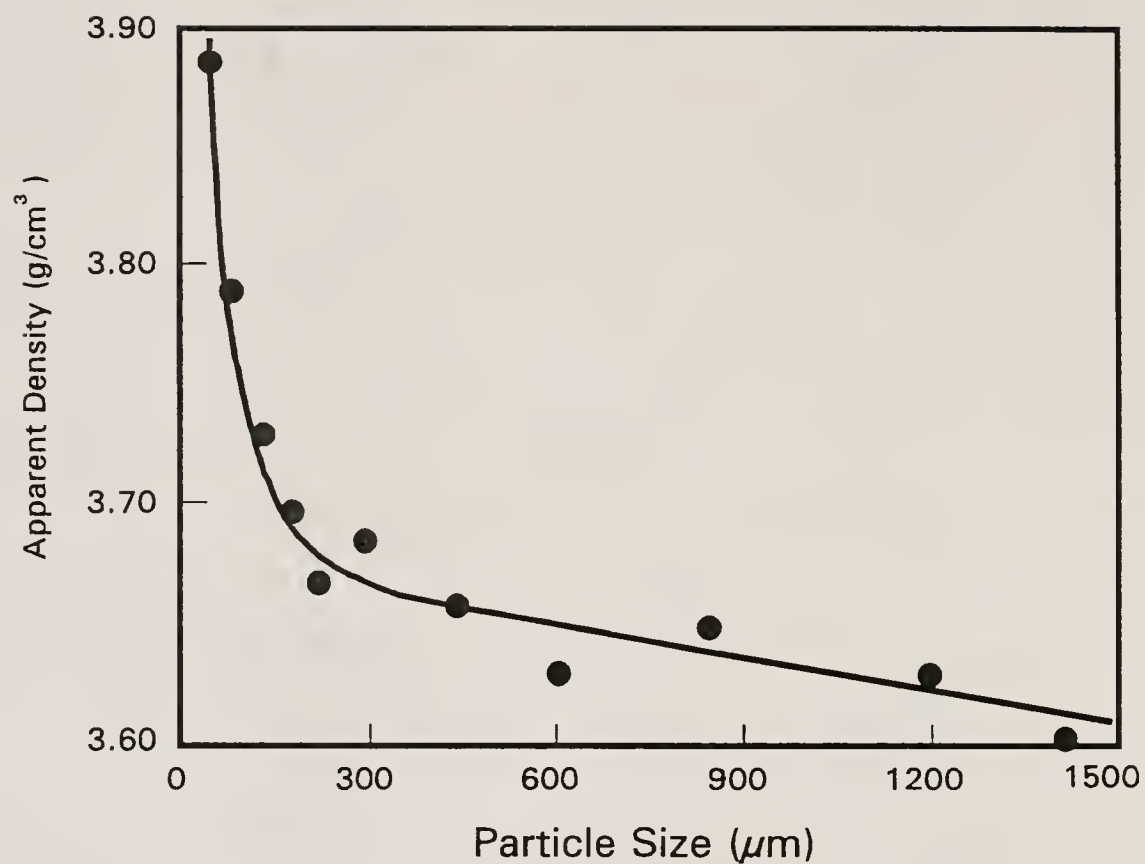


Figure 4.9 Relationship between particle size and apparent density for tabular alumina particles [88REE]



However, there are other phenomena that occur during ball milling that may also influence the measured density of a powder. Said phenomena shall be discussed in section 4.1.5 below.

#### 4.1.3 Particle Size/Size Distribution

##### 4.1.3.1 Polystyrene Microspheres

Particle size and size distribution data for the polystyrene microspheres produced for this study are illustrated in Figures 4.10 through 4.16. Said data are presented using a number basis, and the tabulated data gives two significant digits plus an extra digit, in order to give significance to the geometric standard deviation (GSD) values. In these figures, the GSD values were calculated using the diameter at 84.13% finer than values divided by the respective 50.00% finer than values. It should be noted that, since these distributions are not log normal, the meaning of the GSD values is somewhat negated. However, these values still have meaning among similar particle size distribution sets. The median value corresponds to the diameter at which the cumulative number percent finer (CNPF) value is 50.00%, while the standard deviation values correlate to the arithmetic mean values.

It should be noted that the smallest three batches actually exhibited bimodal size distributions, even though they had been classified by settling numerous times. The GSD values only reflect this bimodality in the smallest size batch of spheres, however. Again, this is a flaw inherent in using GSD values to characterize the width of non-log-normal size distributions.

The polystyrene microsphere batches having a mean diameter of greater than 4  $\mu\text{m}$  were highly monodisperse however. They are designated uniform polystyrene latex microspheres (UPLMs). The advantage of classification via settling may be noted by comparing Figure 4.13 to Figure AII.11. Settling effectively removed the small particle portion (the tail) from the size distribution. It is interesting to note that,

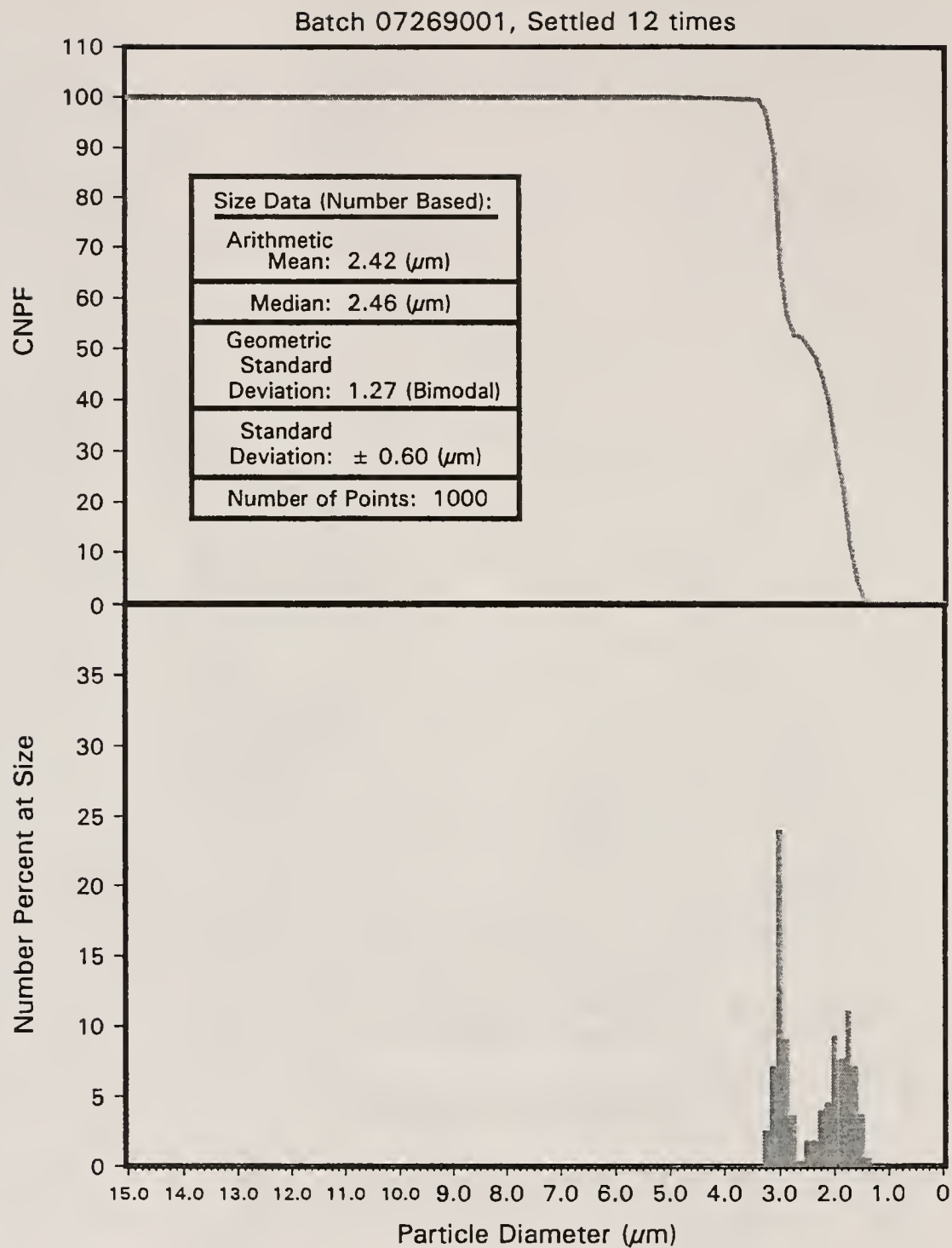


Figure 4.10

Number basis particle size and size distribution data for polystyrene microsphere batch 07269001, classified by settling

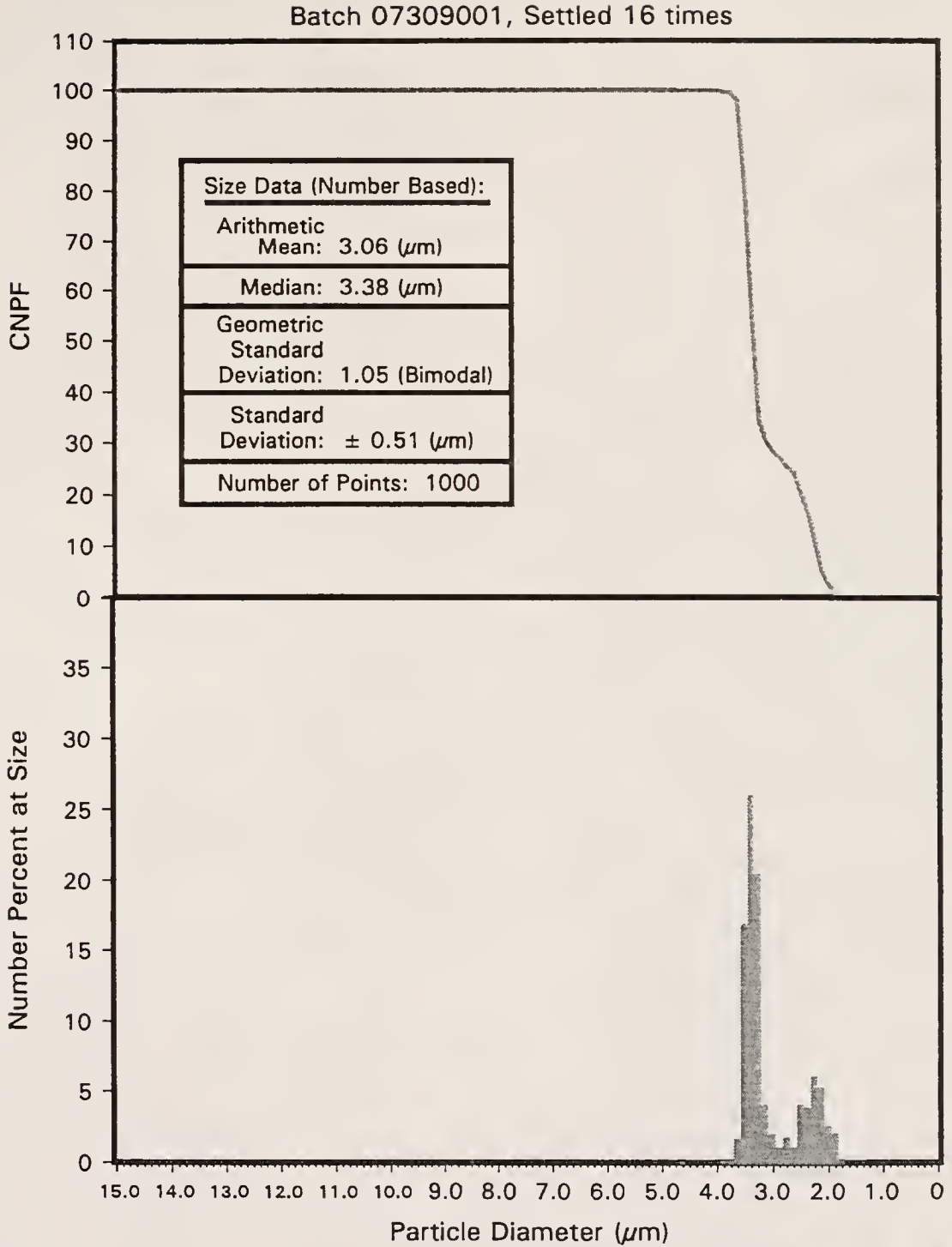


Figure 4.11

Number basis particle size and size distribution data for polystyrene microsphere batch 07309001, classified by settling

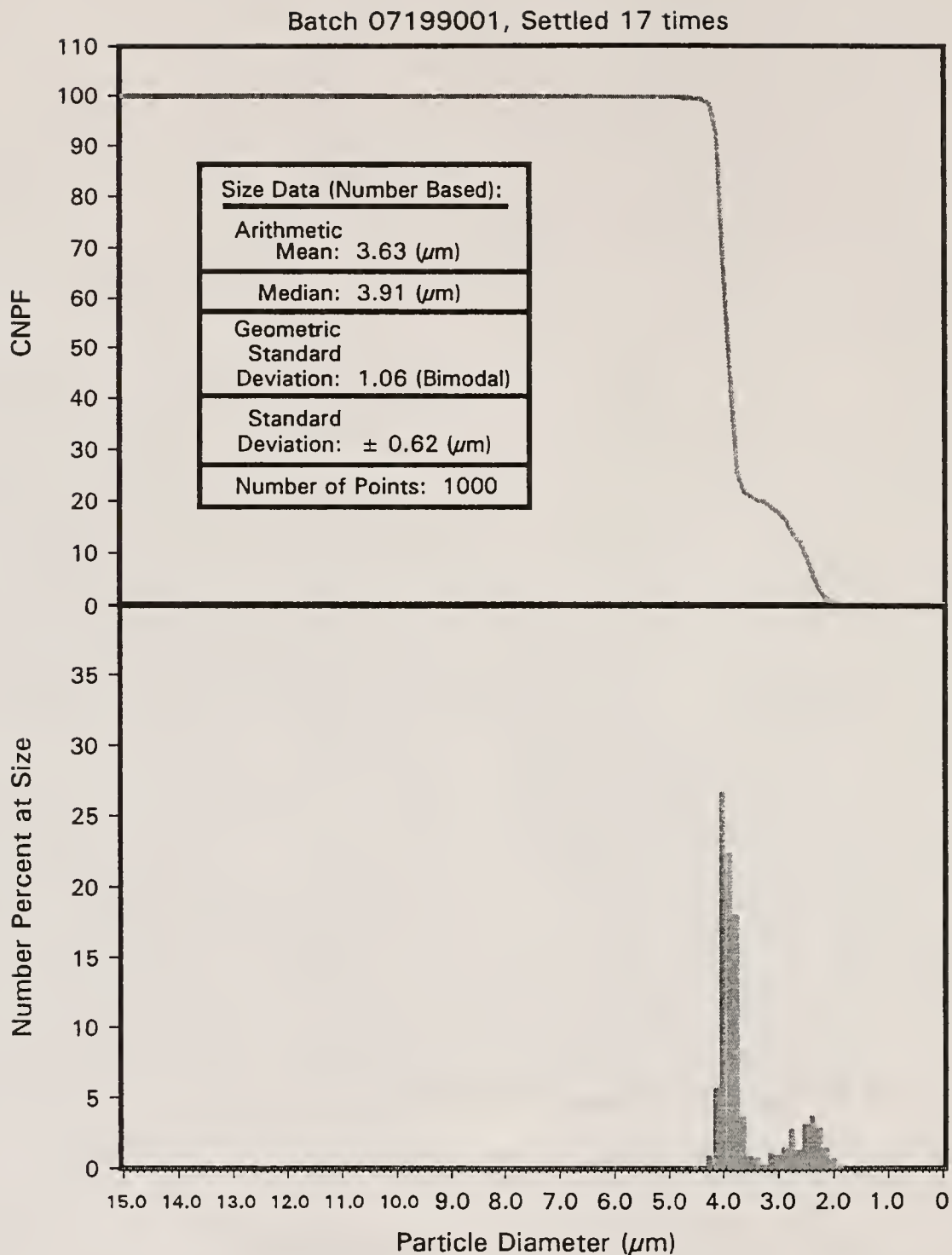


Figure 4.12

Number basis particle size and size distribution data for polystyrene microsphere batch 07199001, classified by settling

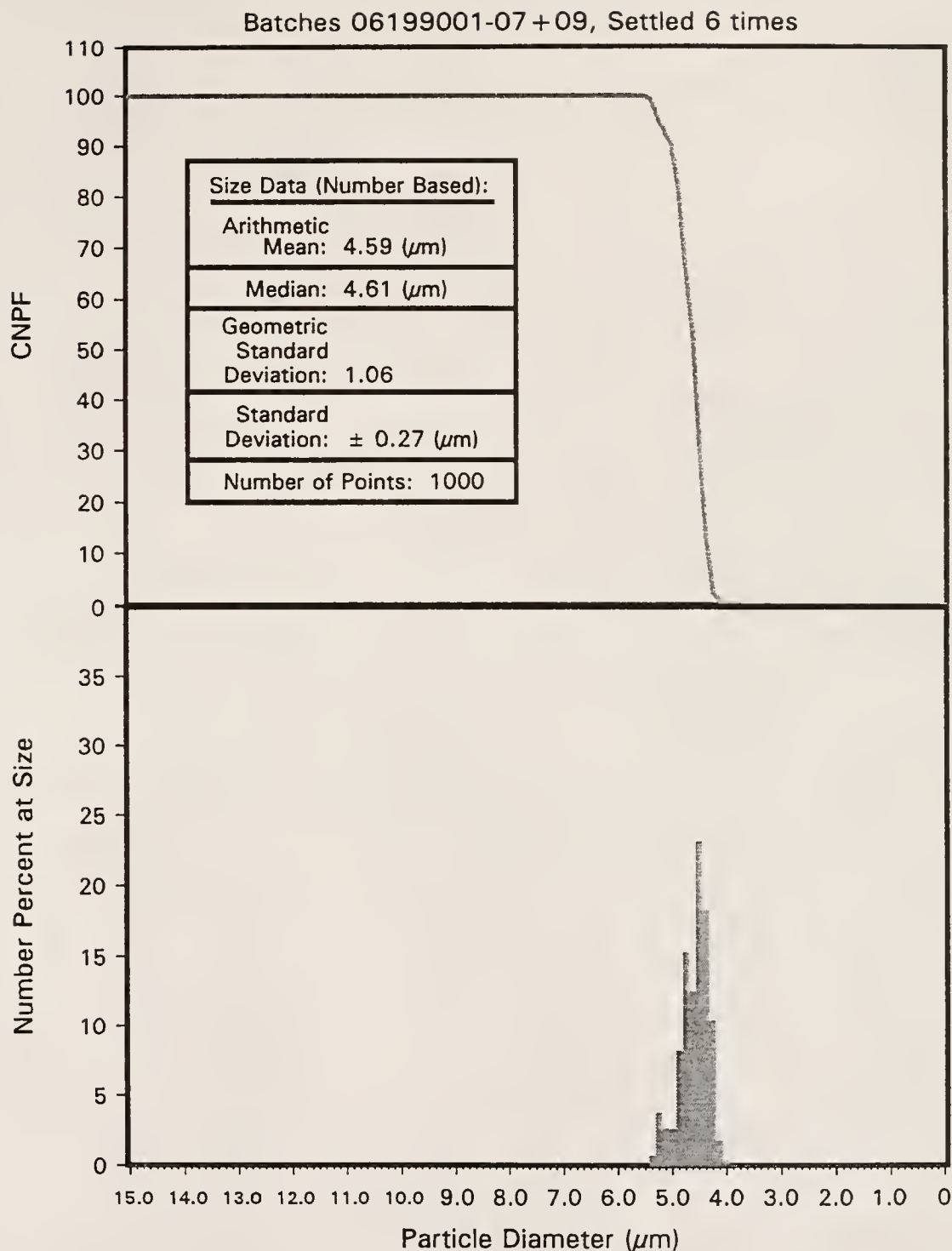


Figure 4.13

Number basis particle size and size distribution data for polystyrene microsphere batch 06199001-07+09, classified by settling

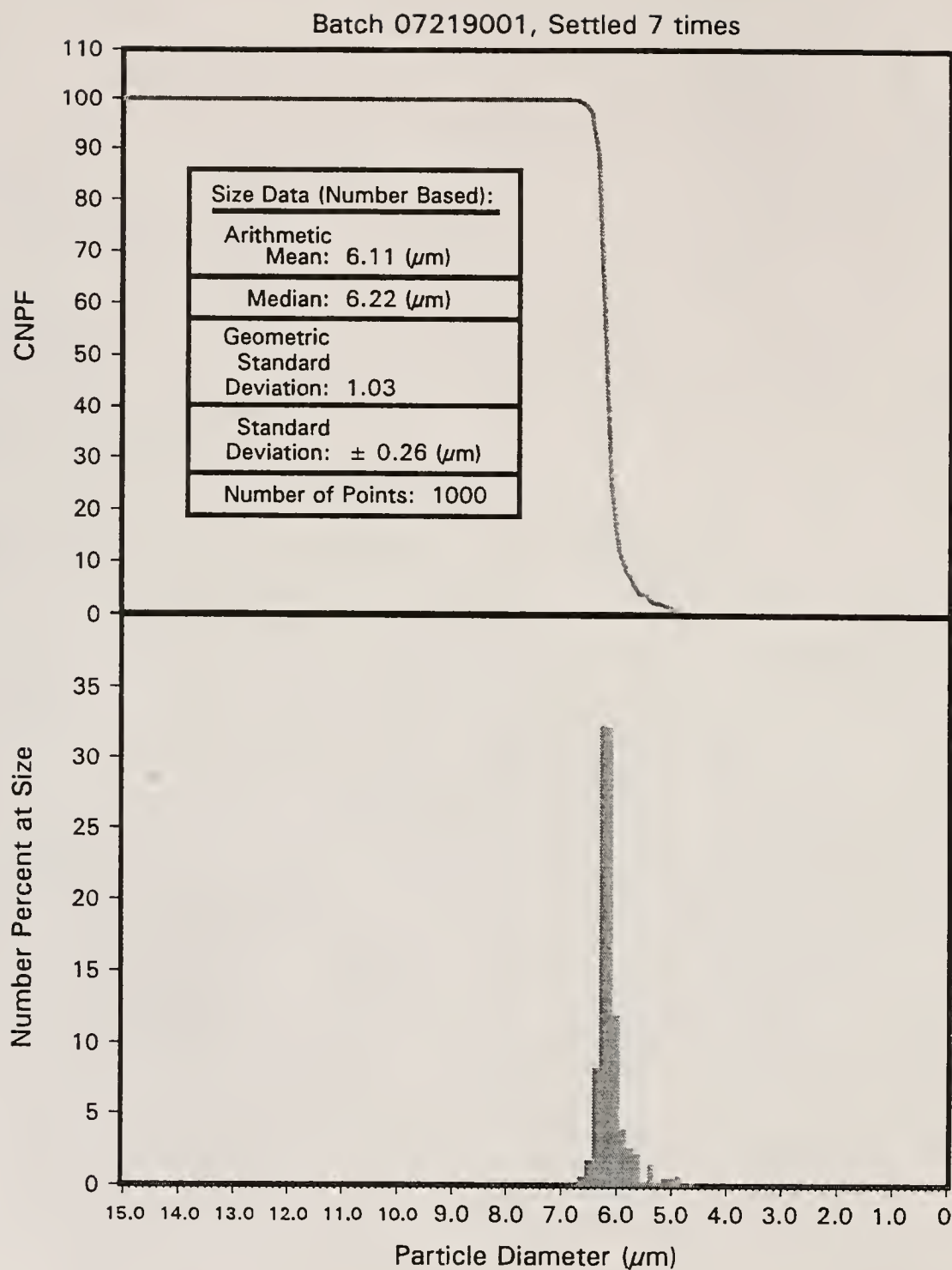


Figure 4.14

Number basis particle size and size distribution data for polystyrene microsphere batch 07219001, classified by settling



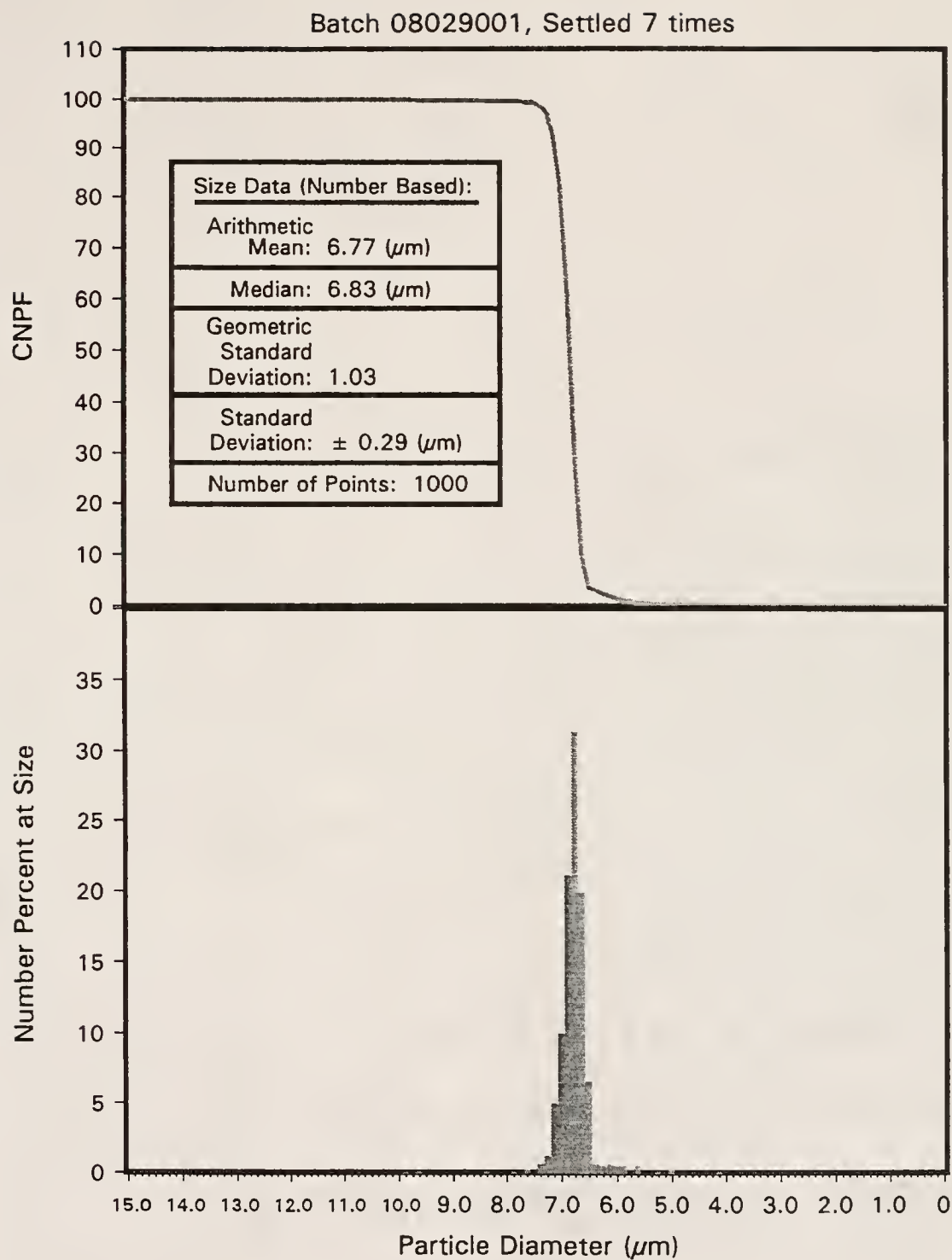


Figure 4.15

Number basis particle size and size distribution data for polystyrene microsphere batch 08029001, classified by settling

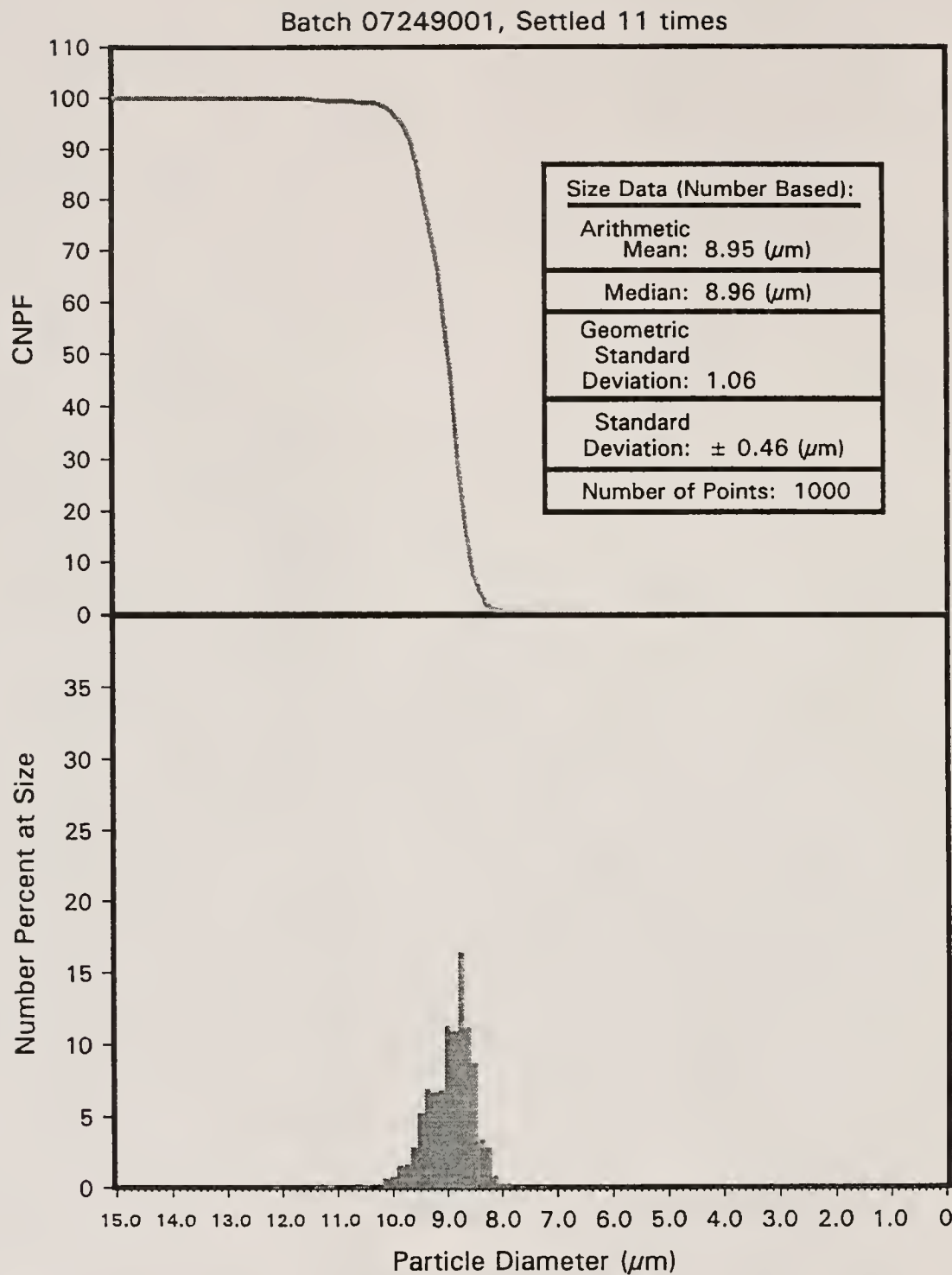


Figure 4.16

Number basis particle size and size distribution data for polystyrene microsphere batch 07249001, classified by settling

even though the settled spheres (i.e. settled batch 06199001-07+09) clearly are closer to a monodisperse distribution than the unsettled spheres (i.e. unsettled batch 06199001-07+09), the GSD values for both size distributions are the same. Thus, it may be concluded that GSD values should not be used alone to compare particle size distributions. This is logical, since GSD values only involve 34.13% of the total size distribution.

Figure 4.17 illustrates the experimental data of this study, compared to the data of Lok and Ober [85LOK]. The data of the current study agrees quite well with that of Lok and Ober, with the possible exception that the range of monodispersity is slightly narrower (i.e. it was not possible to produce 3  $\mu\text{m}$  UPLMs in this study, although it was attempted three times). Furthermore, the size distribution of the largest size UPLM batch was the broadest of the monodisperse batches produced for this study, possibly indicating the beginning of an upper limit to the monodisperse region of the phase composition relationship. Generally, the mean size data matched that of Lok and Ober quite well.

Figure 4.18 illustrates the particle size and size distribution data for the polysized batch of polystyrene microspheres produced for maximum packing efficiency (PE) using the methods of Westman and Hugill [30WES] and McGeary [61MCG], as described in Chapter 3. It should be noted that the size distribution data for the middle two nodes of the quadramodal size distribution are based at slightly greater particle diameter values than the same nodes illustrated in Figures 4.10 and 4.13. This effect may be due to the smaller spheres being hidden among the largest spheres, although the particle size measurements were carefully taken in order to minimize this effect. This explanation also does not explain the near exact match of the smallest node to that illustrated in Figure 4.10. It is also possible that the measurements taken to minimize the effects of small sphere hiding, slightly biased the measured distribution or that this is an effect of sampling

**Key:****Data of Lok and Ober:**

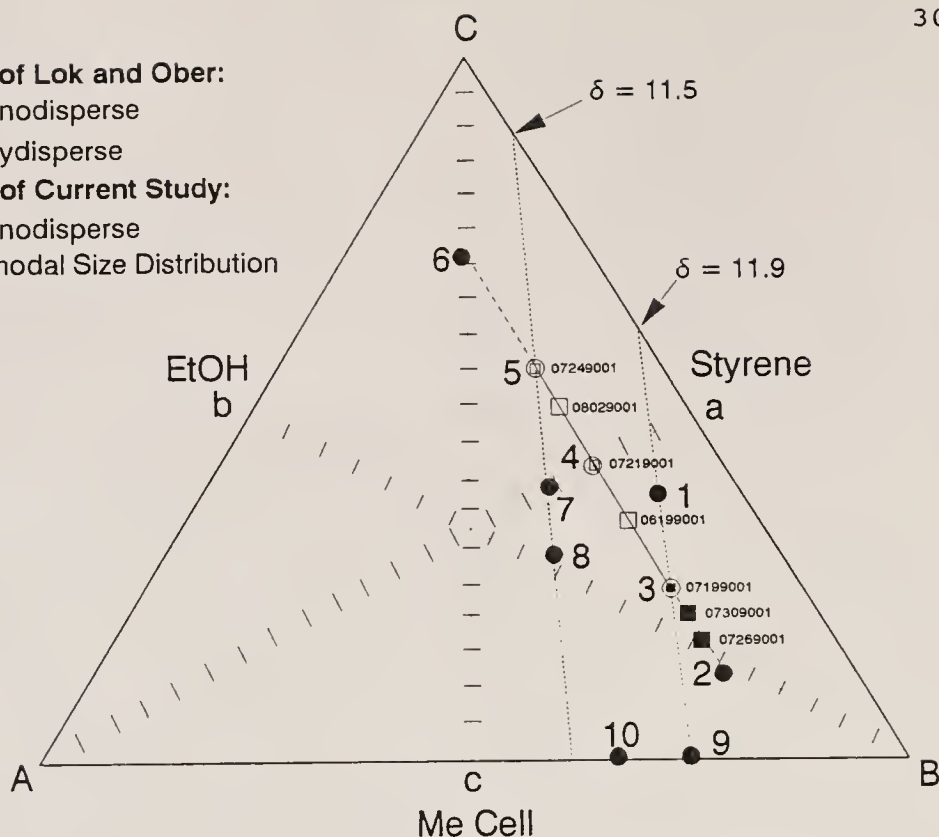
○ Monodisperse

● Polydisperse

**Data of Current Study:**

□ Monodisperse

■ Bimodal Size Distribution



Sample	Concentrations (V%)			Particle Size ( $\mu\text{m}$ )	Solubility Parameter $\delta_i$ ( $\text{cal}/\text{cm}^3$ ) <sup>1/2</sup>
	Styrene	EtOH	Me Cell		
1	10	51	39	1-3	11.9
2	15	71	14	1-4	12.1
07269001	15	70	15	2.4	12.1
07309001	15	65	20	3.1	12.0
3	15	60	25	3	11.9
07199001	15	60	25	3.6	11.9
06199001	15	51.25	33.75	4.6	11.8
07219001	15	42.5	42.5	6.1	11.7
4	15	42.5	42.5	7	11.7
08029001	15	36.25	48.75	6.8	11.6
07249001	15	30	55	9.0	11.5
5	15	30	55	9	11.5
6	15	14	71	1-50	11.3
7	20	40	40	5-20	11.6
8	26	44	30	5-20	11.5
9	26	74	0	1-5	11.9
10	33	67	0	7-9	11.7

Figure 4.17

Comparison of the size and composition data for polystyrene microspheres produced for this study versus that of Lok and Ober

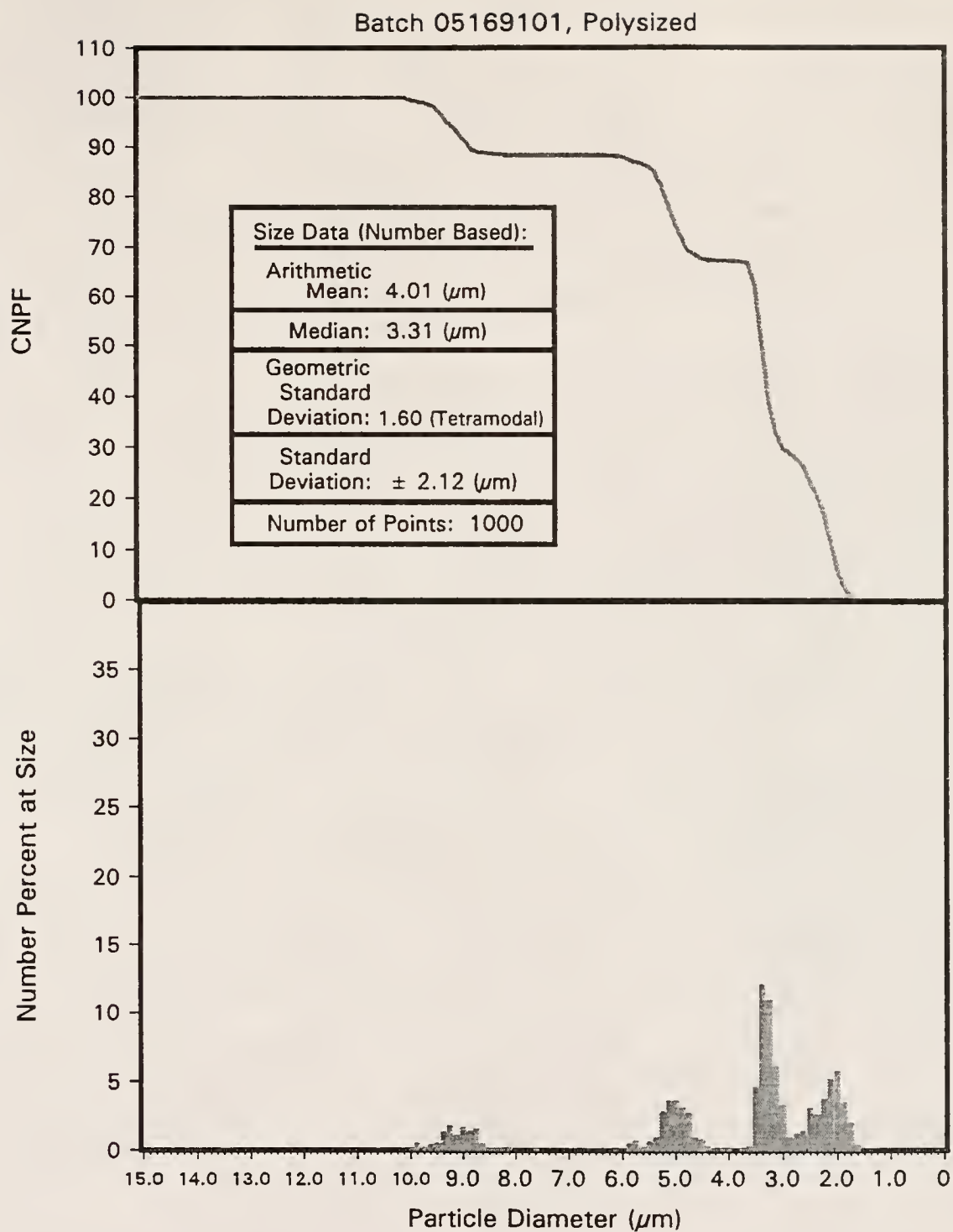


Figure 4.18

Number basis particle size and size distribution data for the quadramodal polystyrene microsphere batch, prepared as outlined in Chapter 3

statistics. In any event, the measured size distribution data for the quadramodal assemblage of polystyrene microspheres is acceptably close to that expected in comparison with Figures 4.10, 4.13 and 4.16, for the purposes of this study.

It is also important to note that a particle size distribution may change a great deal, depending upon the basis of the particle sizing data. For example when a mass or volume basis is used the particle size distribution will be shifted toward larger sizes with respect to the same particle sizing data presented using a number basis (assuming that the distribution is not perfectly monosized). This effect is largest in wide particle size distribution powders, decreasing as the size distribution tightens. For a perfectly monomodal size distribution powder, there is no difference between mass or volume, and number-based particle size data.

For this study, mass and volume bases are used interchangeably. This is true only for powders that do not change density with particle size [88REE]. In most cases, this is not strictly true (i.e. see Figure 4.9), but the error of said approximation is usually relatively small. Consequently, mass and volume basis are generally used interchangeably when discussing particle sizing data [88REE].

Since particle sizing data depends upon the basis used, it is important to present said data using the same basis for all the powders investigated. The polystyrene latex particle size data were presented using a number basis, while the techniques utilized to characterize the ceramic powders use a mass basis. In order to provide a legitimate comparison between the two classes of powders, the particle sizing data of the latexes used to produce controlled porosity in this study are illustrated in Figures 4.19 to 4.22 below. The top portion of each of these graphs illustrates the effect of mass versus number basis, and, for increased clarity, the bottom portion of each figure represents the mass basis particle size distribution of each of the respective latexes.



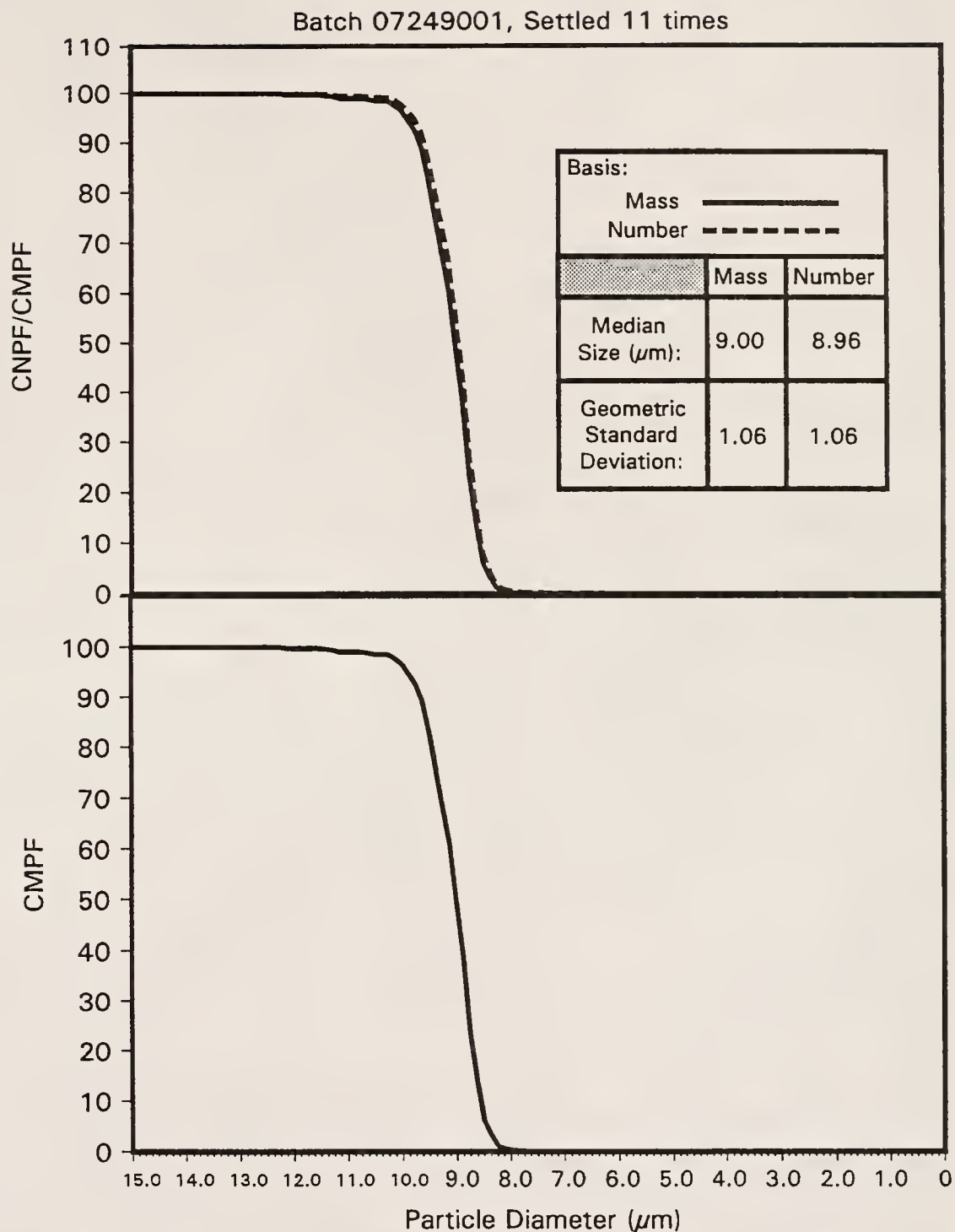


Figure 4.19

Illustration of the contrast and similarity between mass and number-based particle size distributions for the largest monosized latex (07249001) used in this study

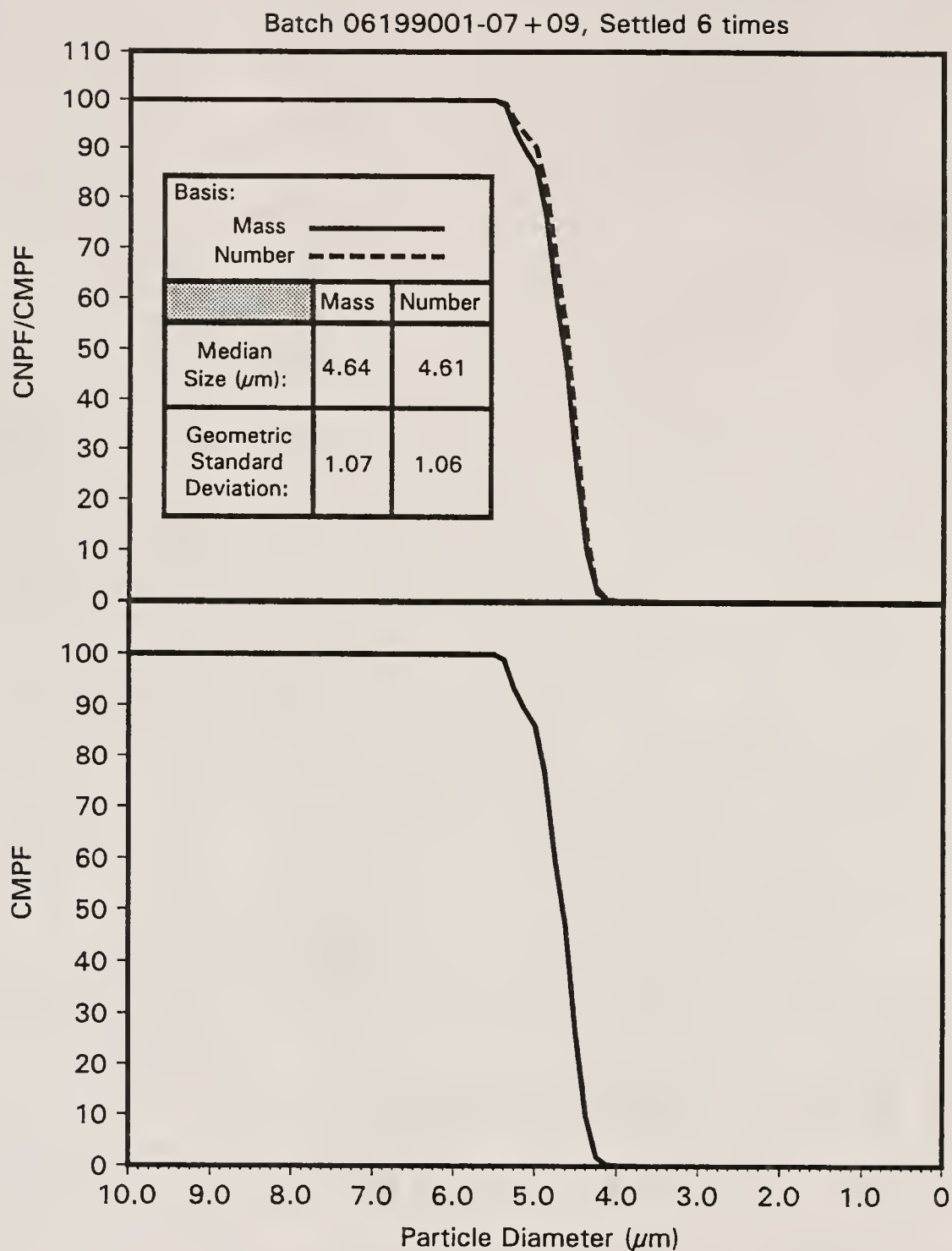


Figure 4.20

Illustration of the similarity and contrast of mass versus number-based particle size distribution data for the medium sized latex spheres (06199001-07+09) used in this study

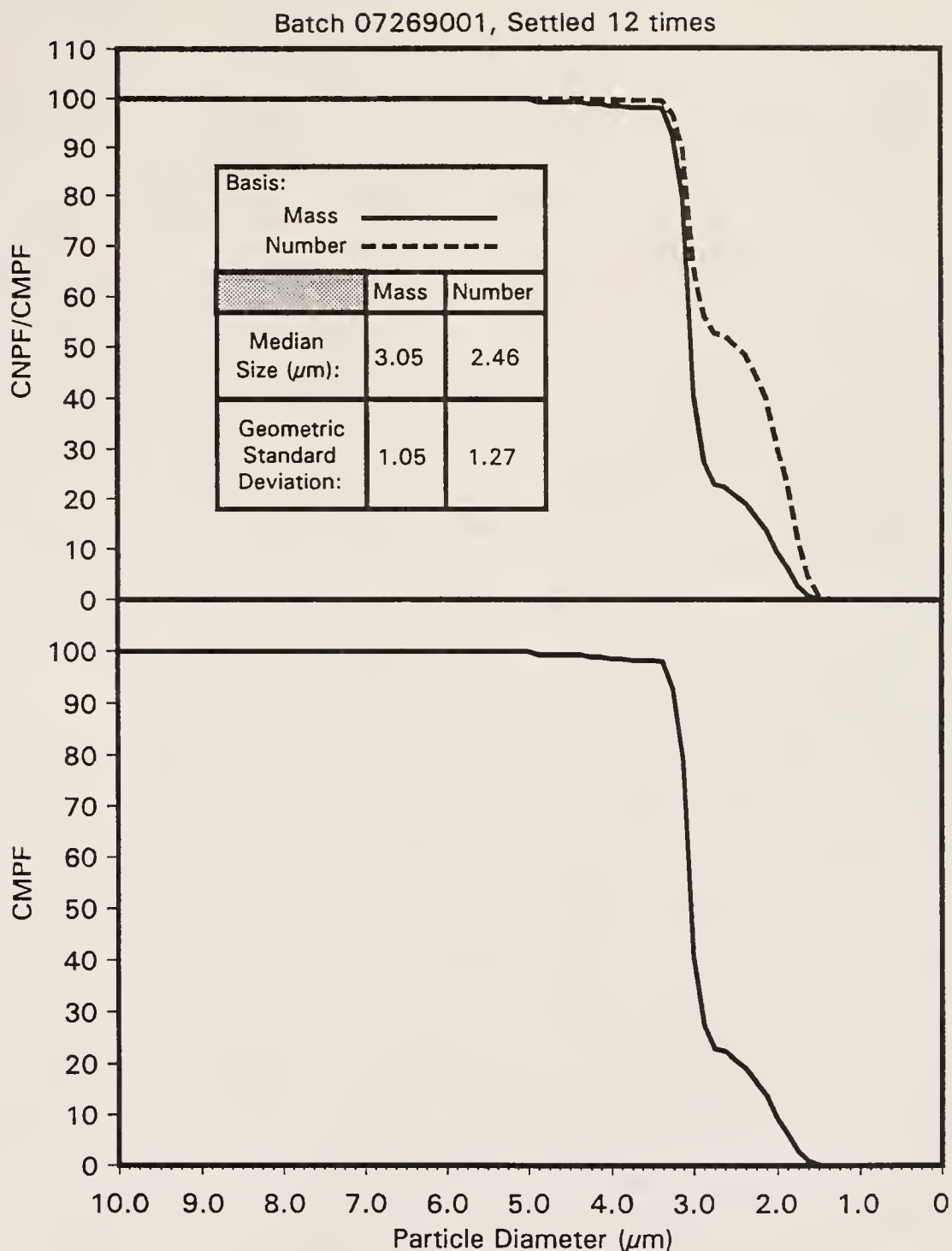


Figure 4.21

Illustration of the similarity and contrast between mass and number-based particle size distributions of the smallest sized latex powder (07269001) used in this study

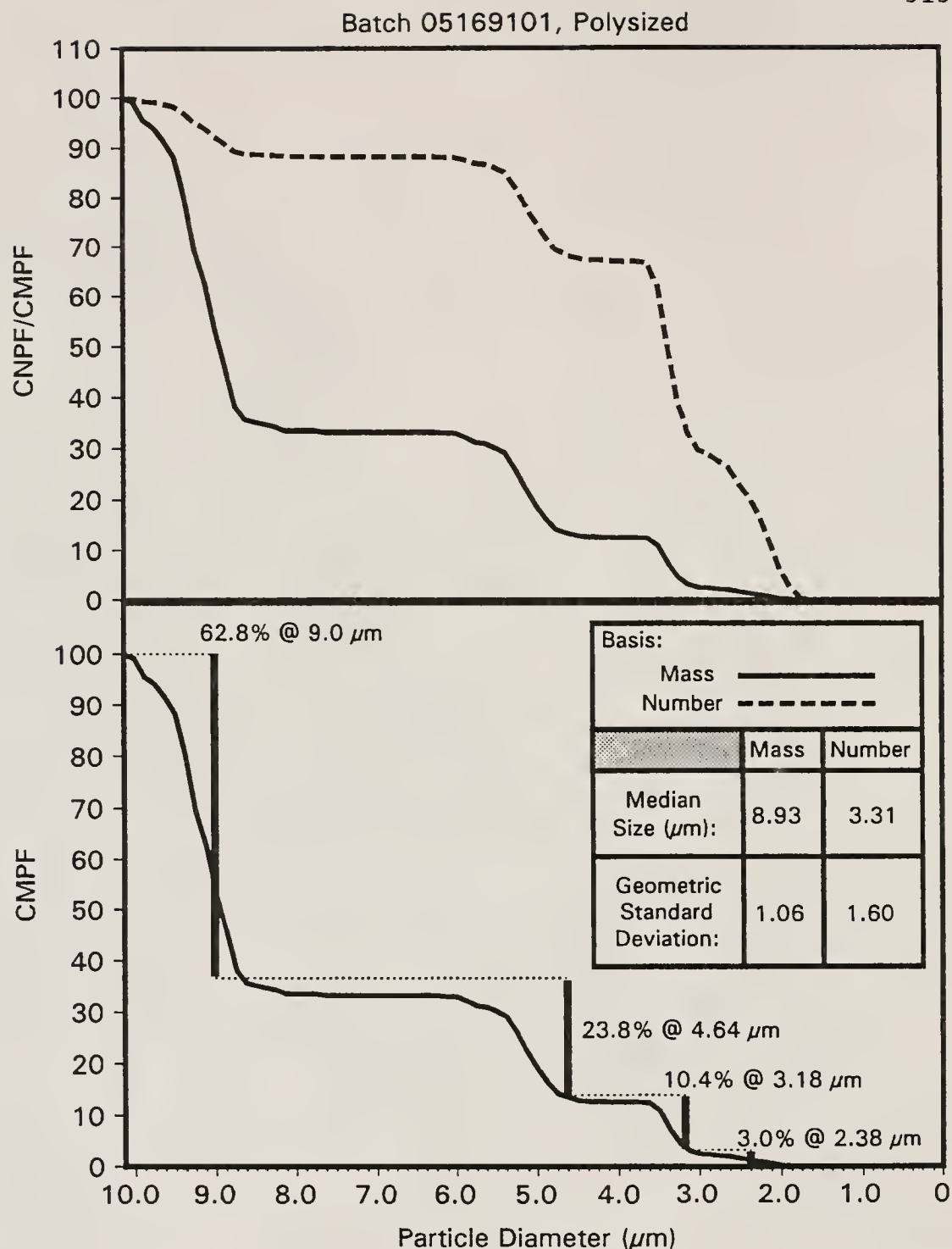


Figure 4.22

The contrast between mass and number-based particle size data for the quadramodal latex (05169101) used, vertical bars illustrate target composition for maximization of PE (as outlined in Chapter 3)

Figure 4.19 illustrates this affect for the largest monosized batch, while Figure 4.20 shows this affect for the midsized latex powder. Figure 4.21 illustrates the number versus mass-based size distributions for the smallest (bimodal) sized latex powder, and Figure 4.22 shows this effect for the quadramodal latex powder. Figure 4.22 also shows the target amounts of each size mode of the quadramodal latex powder, as calculated to maximize packing efficiency (PE), as outlined in Table 3.3, (shown as vertical lines, in the bottom portion of the figure).

It is interesting to note that the shift in particle size depends upon the size distribution. In the extreme case (i.e. the quadramodal latex distribution), the median size increases almost three-fold when the sizing basis is changed from number-based to mass-based. Conversely, the two distributions most closely modelling true monodispersity (Figures 4.19 to 4.20) change very little with a change in sizing basis.

The vertical bars in Figure 4.22 may be used to compare the measured particle size distribution with the target size distribution predicted for maximal PE. The mass (or volume) percentage of each mode quite closely matches the target amounts calculated in Chapter 3. However, as mentioned above, the median sizes of the two intermediate modes do not closely match the measured median size of the latexes that were used to make the quadramodal mixture. Thus, the technique used to measure the particle size distribution of the quadramodal powder was not biased as far as the relative portions of each size mode, but was biased with respect to measured size. This is quite enigmatic, and the above explanation for the difference between the measured versus predicted size distribution (i.e. hidden spheres) does not sufficiently explain this occurrence. Thus, there must have been biasing in the sizing technique that did not affect relative fractions of each size, but did affect the median size of each of the intermediate modes.

#### 4.1.3.2 Ceramic Powders

The particle size distributions of the three ceramic powders used in this study (i.e. the as-received BS glass, the BS glass, ball milled in MeOH, and the as-received  $\text{Si}_3\text{N}_4$  powder) were measured using two separate techniques, x-ray sedigraph and centrifugal particle size analysis (CPSA), as described in section 3.3.4. The sedigraph technique gives data on a mass-basis, while the data obtained using the CPSA technique are area-based.

Figure 4.23 illustrates the particle sizing data for the as-received BS glass, while Figure 4.24 illustrates the sizing data for the ball milled BS glass powder. Similarly, Figure 4.25 illustrates the particle sizing data for the as-received  $\text{Si}_3\text{N}_4$  powder.

As shown in Figures 4.23 to 4.25, the sedigraph and CPSA data are in good agreement. However, it is interesting to note that, in both of the BS glasses, the CPSA data are skewed toward slightly larger sizes, while the CPSA data for the as-received  $\text{Si}_3\text{N}_4$  powder are skewed (after a crossover) to slightly smaller particle sizes. It is not known whether this is an effect traceable to the difference in the methods used, or the actual apparatus used, or to the relative dispersedness of the powders in the dispersion medium. It is also possible that this is due to the slight increase in density with respect to reduction in particle size discussed in section 4.1.2 above.

However, it is also possible that  $\text{Si}_3\text{N}_4$  agglomeration, or poor dispersion of the  $\text{Si}_3\text{N}_4$  powder, or both are influential in this effect as well, since the dispersions used in CPSA were more dilute than those used in sedigraph, thus improving the dispersion condition (all other things being equal). Furthermore, both the BS glass powders behaved similarly. Finally, it may be that this effect is just a result of the different bases used to measure the particle size distribution. However, the latter hypothesis does not explain why the BS glass powders did not exhibit this effect while the  $\text{Si}_3\text{N}_4$  powders did.



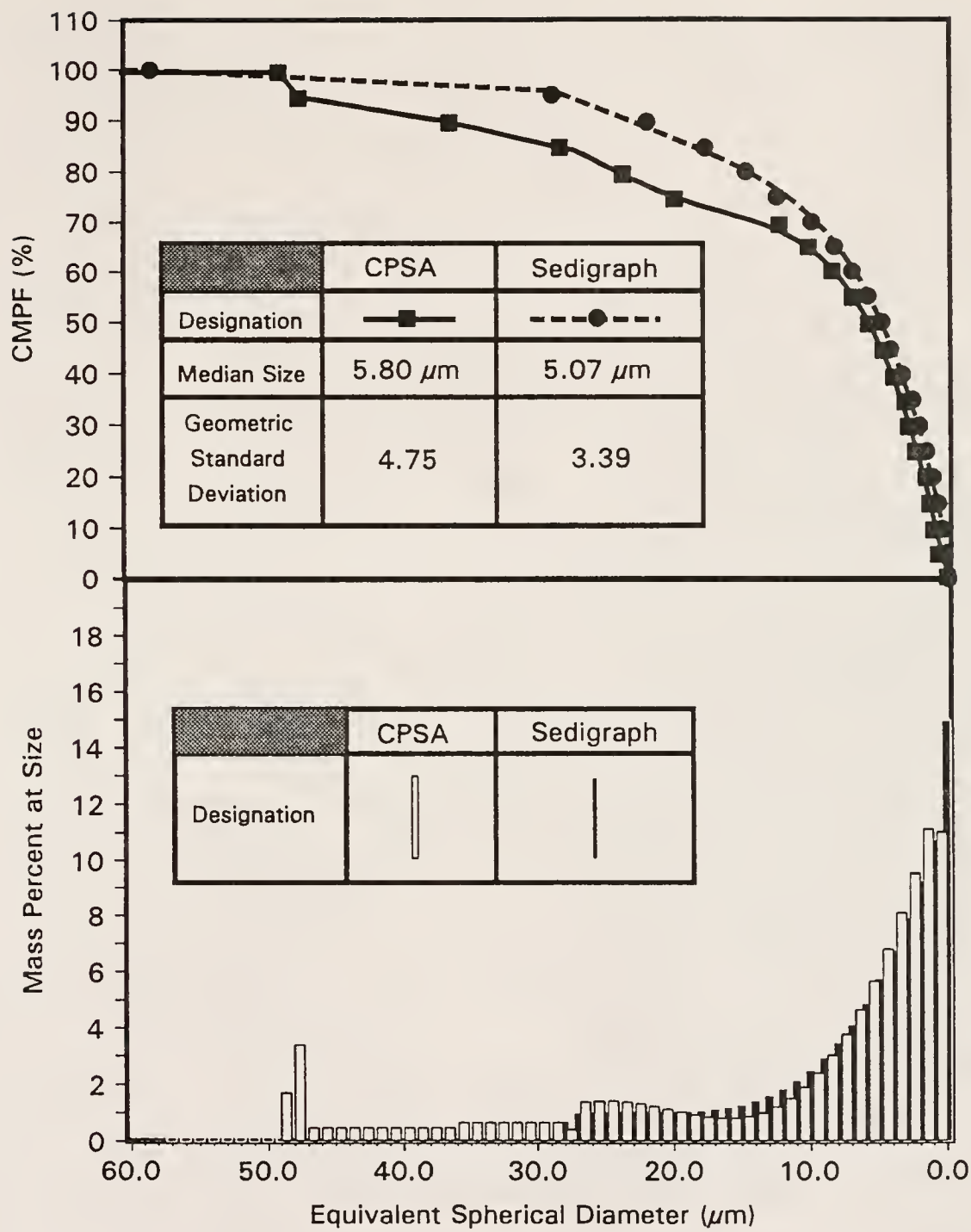


Figure 4.23 Illustration of the particle sizing data (both sedigraph and CPSA) for the as-received BS glass powder

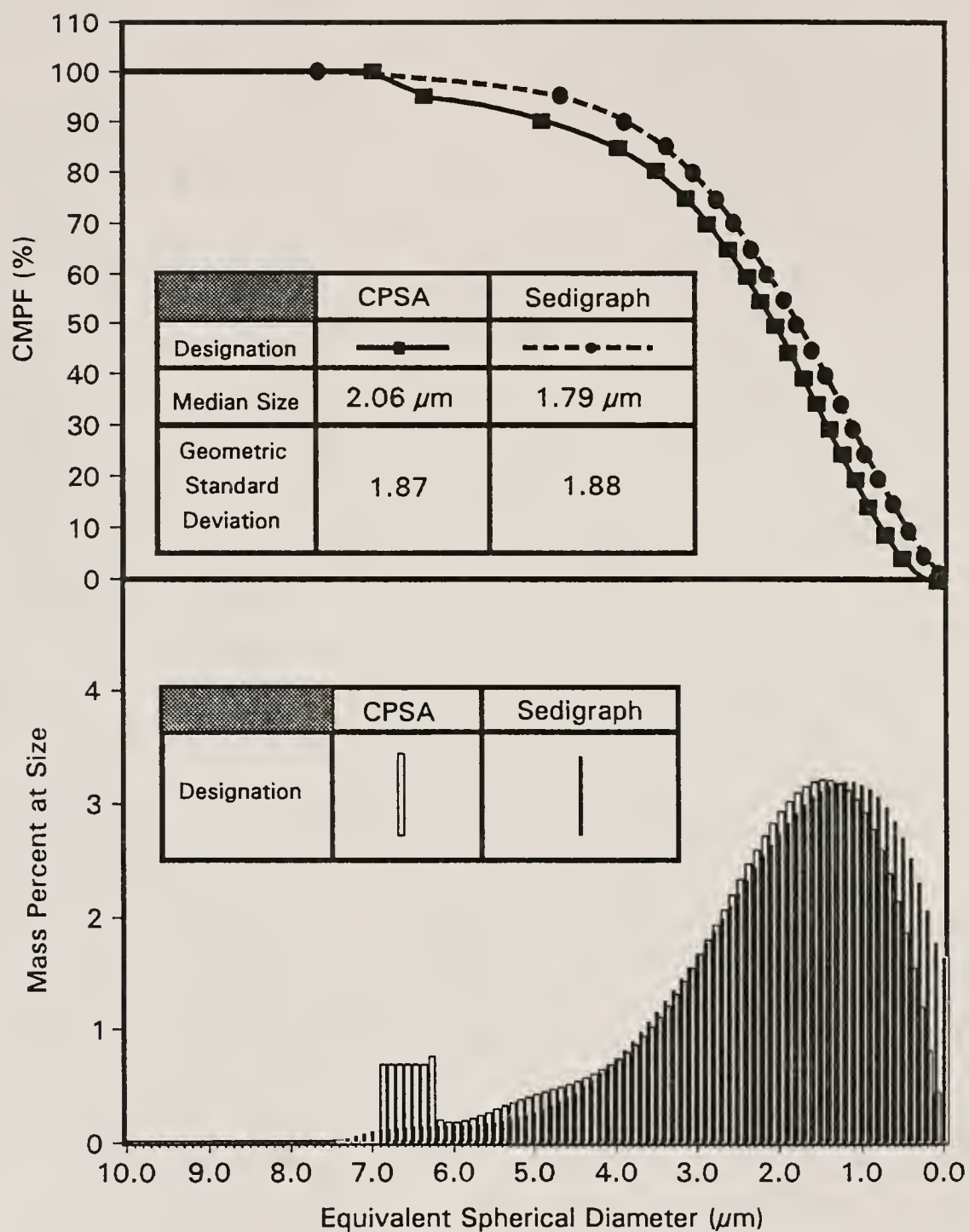


Figure 4.24

Illustration of the particle sizing data (both sedigraph and CPSA) for the ball milled BS glass powder used in this study

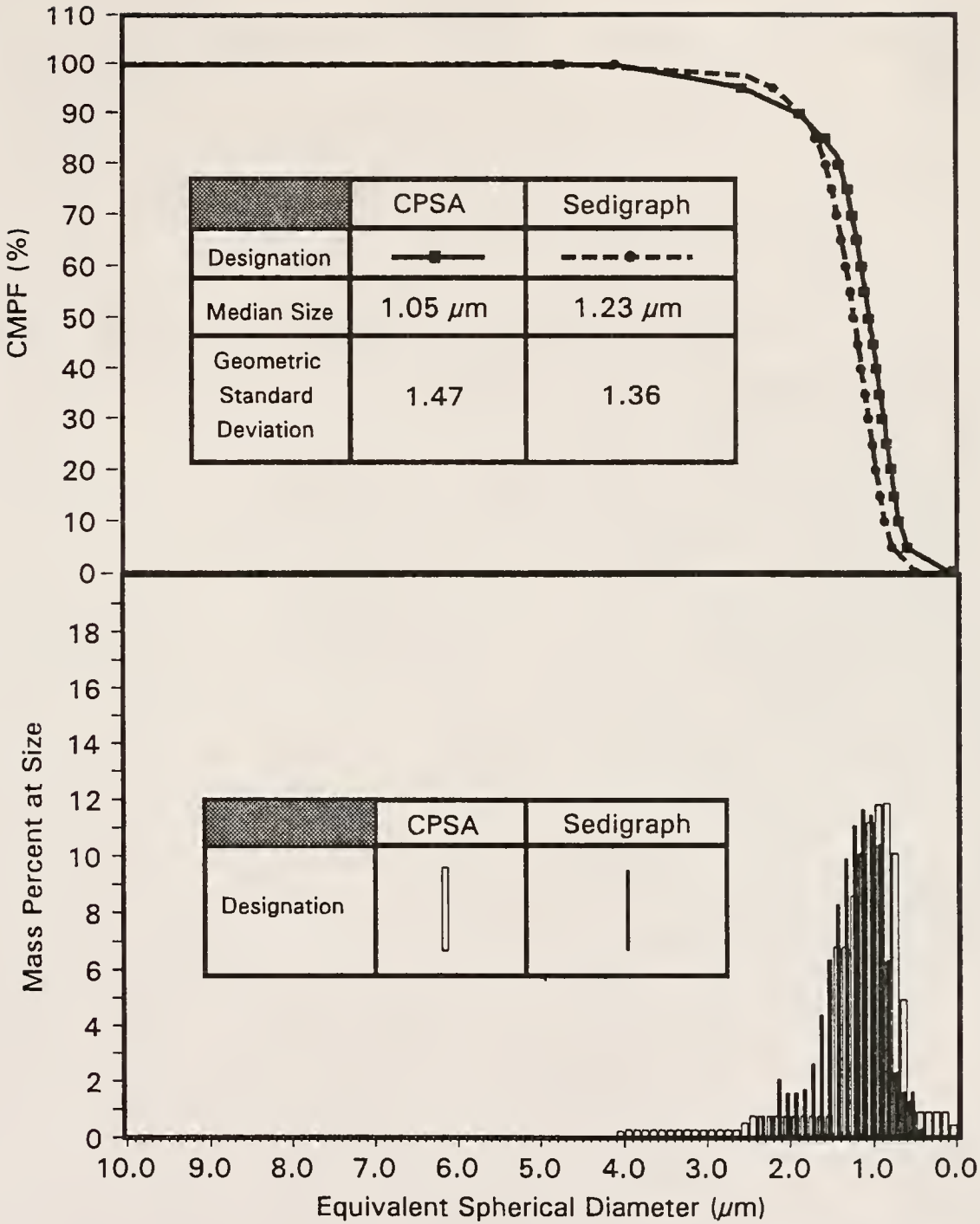


Figure 4.25 Illustration of the particle sizing data (both sedigraph and CPSA) for the as-received  $\text{Si}_3\text{N}_4$  powder used in this study

A measure of maximal packing efficiency for a continuous size distribution powder may be made through an extension of discrete sphere packing, as outlined in section 2.3. The Andreasen model was the first to predict powder size distributions that would result in maximal PE [30AND,88REE]. Later, Funk and Dinger extended the Andreasen model [88FUN], and recently Zheng, et al. proposed the most evolved extrapolation of the model [90ZHE], which showed that the Andreasen and Funk and Dinger models are simplified extrapolations of the Furnas model to continuous particle size distributions.

A conclusion, common to all of these models is that a log normal, or nearly log normal (in the Funk and Dinger and Zheng, et al. models) particle size distribution, having a slope between 0.33 and 0.5, gives the greatest packing efficiency [30AND,88REE,90ZHE]. The Andreasen equation indicates that optimal particle size distributions (from a particle packing viewpoint) will be linear, having a slope between 0.33 and 0.5, when plotted in a log-log manner. Consequently, it is important to determine the slope of the log-log particle size distribution in order to compare it to the ideals set by the above-mentioned models (i.e. slopes between 0.33 and 0.5).

Figures 4.26 to 4.28 illustrate the log-log distributions of the as-received BS glass, the ball milled BS glass, and the as-received  $\text{Si}_3\text{N}_4$  powder respectively. Each figure also illustrates the Andreasen distributions (with slopes of 0.33 and 0.5), based upon the maximum and minimum measured particle sizes of the respective powders.

While none of the powders are linear when plotted in a log-log manner, there is a definite trend in their respective log-log particle size distributions. The as-received BS glass powder is the most linear, while the ball milled BS glass is the next closest to linear. The as-received  $\text{Si}_3\text{N}_4$  powder is the least linear of the powders characterized in this manner. Furthermore, the as-received BS glass most closely fits the Andreasen targets (i.e. log normal, with a slope of between 0.33 and

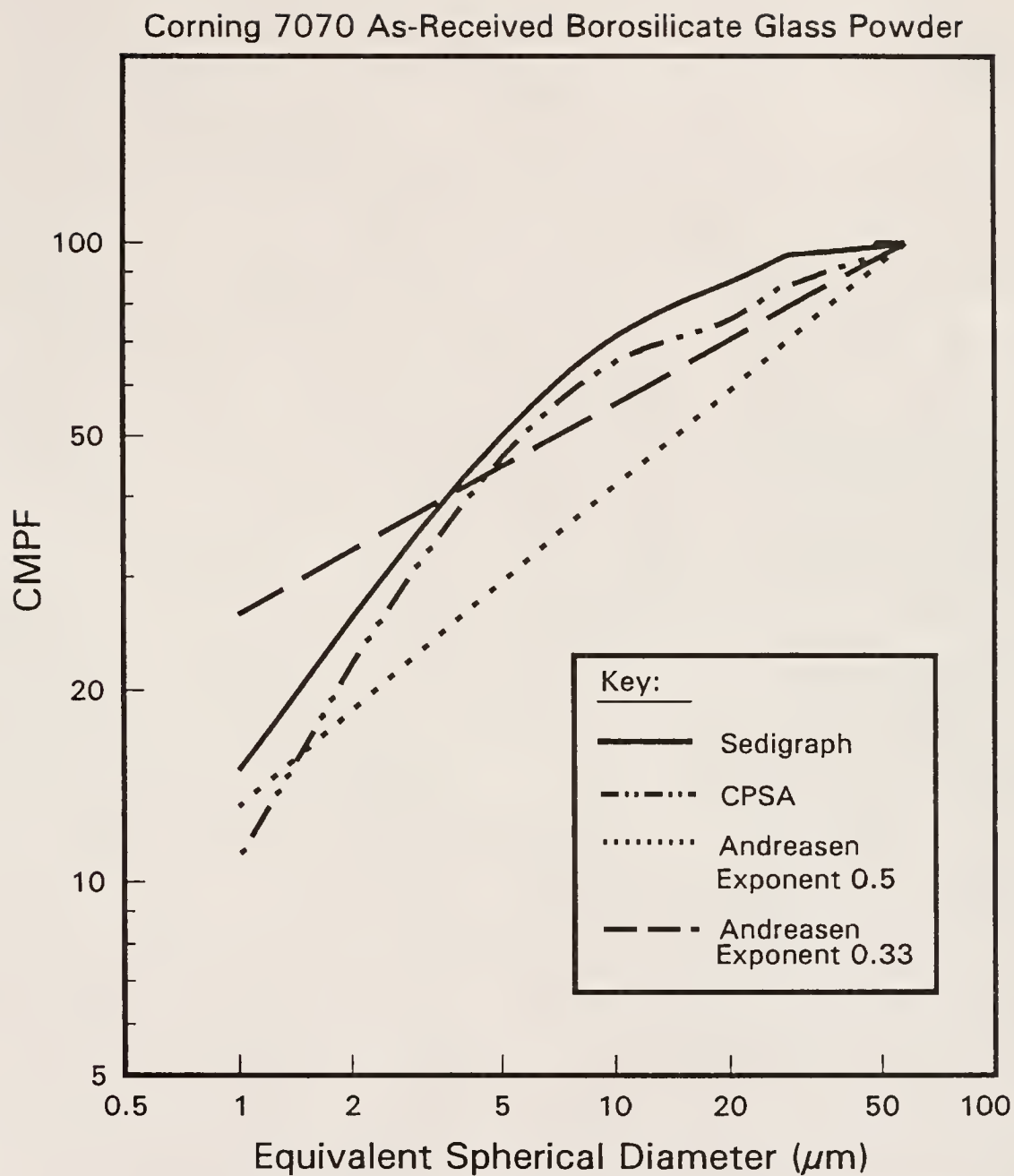


Figure 4.26

Log-log plot of the as-received BS glass particle sizing data, also showing respective Andreasen distributions, having slopes of 0.33 and 0.50

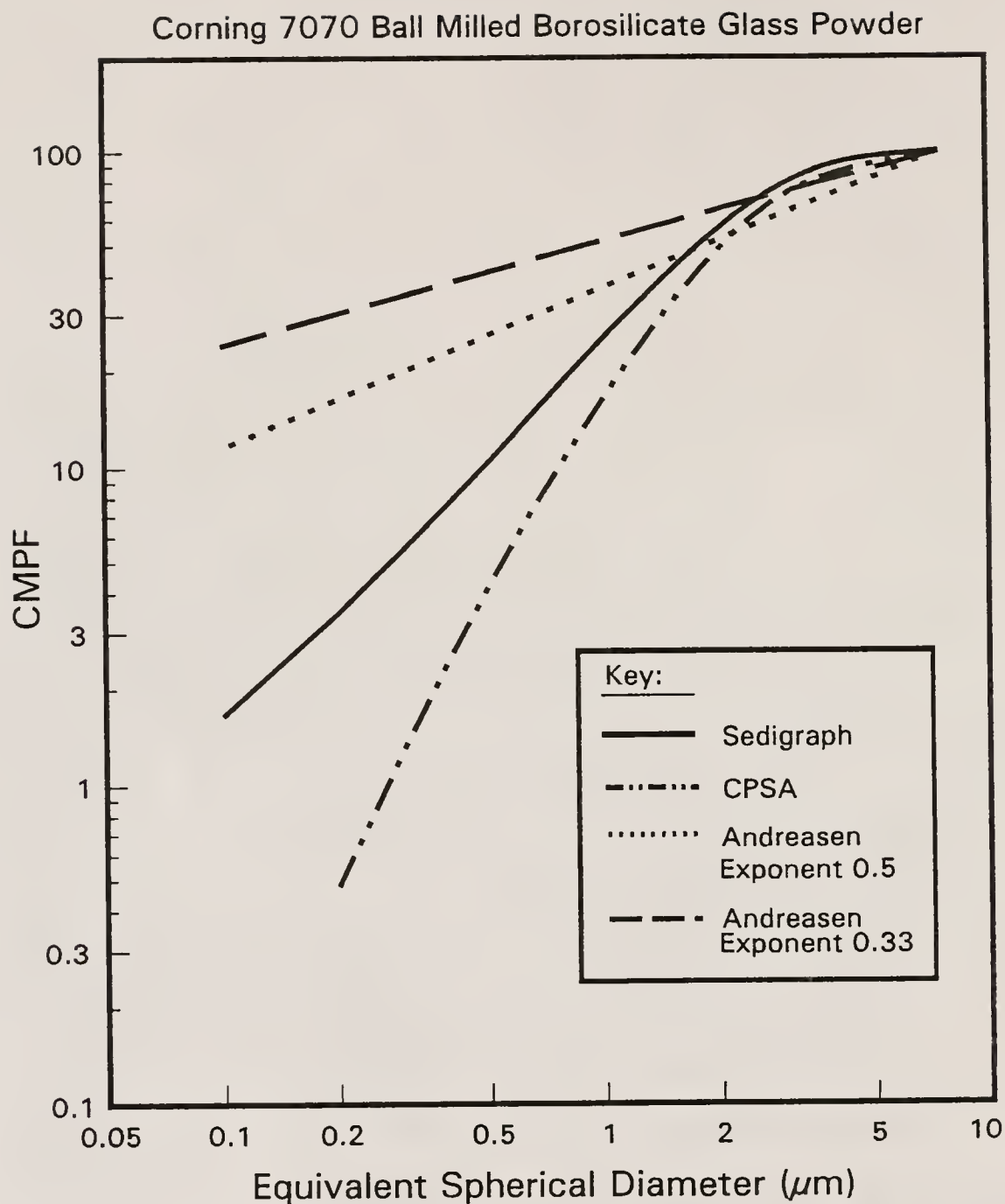


Figure 4.27

Log-log illustration of the ball milled BS glass powder sizing data, including the respective Andreasen plots having slopes of 0.33 and 0.50



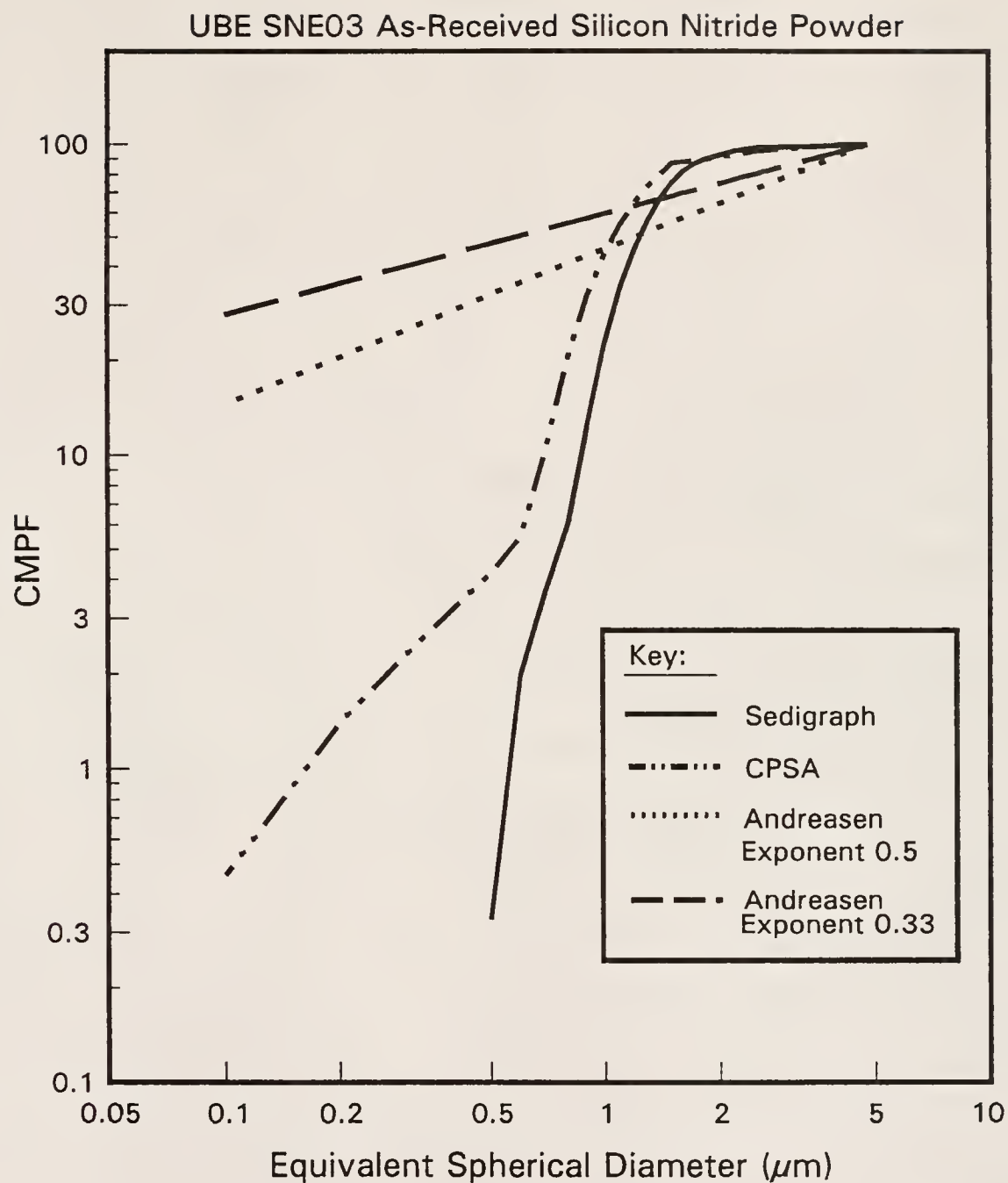


Figure 4.28

Log-log illustration of the as-received  $\text{Si}_3\text{N}_4$  powder size distribution, including respective Andreasen distributions of slope 0.33 and 0.50

0.5), while the ball milled BS glass is second closest, and the  $\text{Si}_3\text{N}_4$  is third. Thus, the as-received BS glass powder should exhibit the highest PE, while the ball milled BS glass should give an intermediate PE, and the lowest PE should be exhibited by the as-received  $\text{Si}_3\text{N}_4$  powder (all other things being equal).

It should be noted that all of these powders should pack more efficiently than perfectly monodisperse, irregularly shaped powders, if they are well dispersed during packing.

#### 4.1.4 Powder Surface Area

Specific surface area of both the BS glass powders, the  $\text{Si}_3\text{N}_4$  powder and the 4.6  $\mu\text{m}$  UPLM powder was measured, as outlined in section 3.3.5, using either an automated or a manual technique (or both). The results of said measurements are illustrated in Table 4.2. Table 4.2 also includes estimated surface areas calculated from the various particle size measurement techniques (i.e. CPSA, Sedigraph and manual SEM) utilized in this study. Where applicable (i.e. for the two BS glass powders), the automated and manual surface area analysis techniques agree with each other within experimental variation.

The calculated value for the specific surface area of the 4.6  $\mu\text{m}$  UPLM powder is in reasonable agreement with its respective measured surface area. It is logical that the calculated surface area of the 4.6  $\mu\text{m}$  UPLM powder is closest to the respective measured value, of the powders investigated, since the UPLM powder is almost perfectly monosized and spherical. Also, the SEM pictures showed the UPLM surfaces to be smooth. Therefore, the surface area of said powder should be estimated most accurately (and most simply) of the powders studied. Furthermore, the agreement of the measured and calculated surface areas further proves that the latex powders are high surface smoothness materials.

Table 4.2

Measured and Calculated Specific Surface Areas  
of the Powders Used in This Study

Powder	Specific Surface Area (m <sup>2</sup> /g)						
	Measured				Calculated		
	Manual	# Reps	Automated	# Reps	CPSA	Sedi- graph	SEM
BS Glass (As- Rec.)	3.39±0.04	2	3.36±0.04	2	0.97	1.55	
BS Glass (Ball Milled)	13.05±0.41	3	12.69±0.52	2	1.87	3.44	
Si <sub>3</sub> N <sub>4</sub> Powder (As- Rec.)			2.82±0.06	3	1.96	1.58	
4.6 μm UPLM			1.05±0.04	3			1.23

Note: # Reps is the number of experimental repetitions used to  
obtain the measured specific surface area value

The estimated surface areas of the three ceramic powders, calculated by both CPSA and Sedigraph, do not agree well with the measured surface areas of said powders. Furthermore, the two calculated surface areas of each respective ceramic powder do not agree well with each other. The specific surface areas estimated by CPSA show an increase in calculated surface area with decreasing median particle size. The Sedigraph estimates also predict that the surface area will increase with decreasing median particle size, for the BS glass powders. However, the Sedigraph calculated specific surface area estimate of the  $\text{Si}_3\text{N}_4$  powder is less than that estimated for the larger median particle size ball milled BS glass. In fact, the specific surface areas of the as-received BS glass powder and the as-received  $\text{Si}_3\text{N}_4$  powder, as calculated by Sedigraph, are quite similar. The only possible explanation for this phenomenon is that the as-received BS glass powder has a much broader particle size distribution than the  $\text{Si}_3\text{N}_4$  powder. Since small particles contribute to surface area to a much greater degree than large particles, it is logical that a broad size distribution powder could have a surface area comparable to, or larger than, a relatively narrow size distribution powder having a smaller median size. It is interesting to note that this phenomenon is evident when comparing the measured surface areas of the two as-received ceramic powders. The respective measured surface areas of the two powders are quite similar. Thus, the trend in the Sedigraph calculated values is not unrealistic. However, the Sedigraph estimated surface area values for the two as-received ceramic powders are off by approximately a factor of two.

The calculated surface areas for the ball milled BS glass powder disagree with the respective measured values by a factor of between 4 and 7, depending upon the surface area estimation technique of comparison. A possible reason for the relatively large difference between estimated and measured specific surface area is that the BS

glass may experience significant surface dissolution or reaction during ball milling in MeOH (e.g. micropore formation at the powder surface), or that some glass may dissolve during milling, and later may reattach to the powder surface, as high surface area precipitates, during the drying step subsequent to ball milling. The effect of ball milling on the BS glass is discussed in the next section.

#### 4.1.5 The Effect of Ball Milling on BS Glass

As mentioned in section 4.1.4, the measured surface area of the BS glass powder increased by a factor of approximately 3.8 as a result of ball milling in MeOH, while the increase in calculated surface area was only approximately a factor of 2.1. It was also noted that this difference may be a result of an increasing portion of ultrafine powder resulting from milling. This is not obvious when comparing Figures 4.1 and 4.2, however. Furthermore, there are other possibilities that can explain the unexpectedly large increase in surface area subsequent to ball milling, such as surface corrosion (MeOH has a strong tendency to dissolve  $B_2O_3$ ), differential dissolution, or dissolution and precipitation, etc. Therefore, further investigation of the ball milling process was warranted.

Selected area diffraction (SAD), during transmission electron microscopy (TEM) investigation, indicated that there were no precipitated crystallites on any of the powder particles viewed (i.e. all SAD patterns were diffuse, indicating the powders to have an amorphous atomic structure). Thus, dissolution and precipitation of high surface area crystalline compounds as a source for the extra increase in surface area is not likely. Furthermore, the powder surfaces, as viewed during TEM investigation, appeared to be free of precipitates.

However, the surfaces of the ball milled BS glass powder particles appeared to be somewhat rougher than the those of the as-received BS

glass powder particles. Representative TEM micrographs of the particle surfaces of an as-received BS glass powder and of a ball milled BS glass powder are illustrated in Figure 4.29 and 4.30 respectively. The surface of the ball milled glass powders appears to have a structure on the order of about 4 to 14 nm (i.e. 2.5 to 10  $\mu\text{m}$  on Figure 4.30), that is not as apparent when viewing the as-received powder. This "pitting" may be resultant from  $\text{B}_2\text{O}_3$  corrosion.

Inductively coupled plasma photospectroscopy (ICP) analysis indicated that the relative concentration of  $\text{SiO}_2$  increases with milling (and/or MeOH exposure), as compared to the  $\text{B}_2\text{O}_3$  concentration of the BS glass. This effect is shown in Table 4.3. The table also indicates that there is a gradual decrease in both [Li] and [Na] during milling and/or MeOH exposure. As discussed in chapter 3, it was not possible to measure [K].

Table 4.3 also indicates that there is little difference between the composition of the MeOH treated and the ball milled BS glass, with the exception that the ball milled BS glass is significantly increased in Al concentration. Said increase in Al is a result of using alumina-rich milling media. Thus, it may be concluded that most of the change in concentration of the BS glass, during milling (except for the increase in [Al]), is due to MeOH interaction, and that mechanical milling does not significantly increase this effect, other than to create new surfaces for MeOH interaction (assuming that the temperature during milling was the same as during the MeOH treatment (i.e.  $40^\circ\text{C}$ )).

It is also interesting to note that the composition of the BS glass changed from the bulk glass to the as-received <325 mesh powder. It is not known how the manufacturer milled the BS glass from the bulk to the powdered form. Furthermore, it is interesting that the measured composition of the bulk glass was not necessarily any closer to the manufacturer's data than the measured compositions of the powdered glasses. The as-received glass powder was closest to the Air Force





Figure 4.29

TEM micrograph illustrating a representative surface of a particle of as-received BS glass (Scale: 1 mm = 1.4 nm)



Figure 4.30

TEM micrograph illustrating the surface of a representative particle of ball milled BS glass (Scale: 1 mm = 1.4 nm)

Table 4.3

## ICP Measured Composition of BS Glasses Investigated

## 1. Bulk Borosilicate Glass

Constituent		Measured ICP Composition		Composition (Oxide)	
Element	Oxide	PPM ( $\mu\text{g/ml}$ )	St. Dev. <sup>1</sup> ( $\pm\mu\text{g/ml}$ )	Measured <sup>2</sup> (Wt%)	Literature <sup>3</sup> (Wt%)
Si	SiO <sub>2</sub>	414.70	3.78	68.5 $\pm$ 0.6	72.0 (70.0)
B	B <sub>2</sub> O <sub>3</sub>	116.70	0.82	29.0 $\pm$ 0.2	25.0 (28.0)
Al	Al <sub>2</sub> O <sub>3</sub>	2.42	0.04	0.4 $\pm$ 0.0	1.0 (1.1)
Li	Li <sub>2</sub> O	6.03	0.22	1.0 $\pm$ 0.0	0.5 (1.2)
Na	Na <sub>2</sub> O	1.42	0.12	0.2 $\pm$ 0.0	0.5 (0.0)
K	K <sub>2</sub> O	N/A	N/A	N/A	1.0 (0.5)

## 2. As-Received Borosilicate Glass Powder

Constituent		Measured ICP Composition		Composition (Oxide)	
Element	Oxide	PPM ( $\mu\text{g/ml}$ )	St. Dev. <sup>1</sup> ( $\pm\mu\text{g/ml}$ )	Measured <sup>2</sup> (Wt%)	Literature <sup>3</sup> (Wt%)
Si	SiO <sub>2</sub>	467.20	8.50	70.6 $\pm$ 1.3	72.0 (70.0)
B	B <sub>2</sub> O <sub>3</sub>	119.00	1.55	27.1 $\pm$ 0.4	25.0 (28.0)
Al	Al <sub>2</sub> O <sub>3</sub>	2.90	0.00	0.4 $\pm$ 0.0	1.0 (1.1)
Li	Li <sub>2</sub> O	5.10	0.30	0.8 $\pm$ 0.1	0.5 (1.2)
Na	Na <sub>2</sub> O	1.93	0.18	0.2 $\pm$ 0.0	0.5 (0.0)
K	K <sub>2</sub> O	N/A	N/A	N/A	1.0 (0.5)

Table 4.3 (continued)

## 3. MeOH Treated Borosilicate Glass

Constituent		Measured ICP Composition		Composition (Oxide)	
Element	Oxide	PPM ( $\mu\text{g/ml}$ )	St. Dev. <sup>1</sup> ( $\pm\mu\text{g/ml}$ )	Measured <sup>2</sup> (Wt%)	Literature <sup>3</sup> (Wt%)
Si	SiO <sub>2</sub>	575.20	9.75	73.8 $\pm$ 1.2	72.0 (70.0)
B	B <sub>2</sub> O <sub>3</sub>	125.30	1.37	24.2 $\pm$ 0.3	25.0 (28.0)
Al	Al <sub>2</sub> O <sub>3</sub>	2.77	0.05	0.3 $\pm$ 0.0	1.0 (1.1)
Li	Li <sub>2</sub> O	4.95	0.21	0.6 $\pm$ 0.0	0.5 (1.2)
Na	Na <sub>2</sub> O	1.28	0.38	0.1 $\pm$ 0.0	0.5 (0.0)
K	K <sub>2</sub> O	N/A	N/A	N/A	1.0 (0.5)

## 4. MeOH Ball Milled Borosilicate Glass

Constituent		Measured ICP Composition		Composition (Oxide)	
Element	Oxide	PPM ( $\mu\text{g/ml}$ )	St. Dev. <sup>1</sup> ( $\pm\mu\text{g/ml}$ )	Measured <sup>2</sup> (Wt%)	Literature <sup>3</sup> (Wt%)
Si	SiO <sub>2</sub>	611.80	7.31	73.7 $\pm$ 0.9	72.0 (70.0)
B	B <sub>2</sub> O <sub>3</sub>	129.70	1.37	23.5 $\pm$ 0.3	25.0 (28.0)
Al	Al <sub>2</sub> O <sub>3</sub>	10.47	0.05	1.1 $\pm$ 0.0	1.0 (1.1)
Li	Li <sub>2</sub> O	5.28	0.26	0.7 $\pm$ 0.0	0.5 (1.2)
Na	Na <sub>2</sub> O	1.32	0.57	0.1 $\pm$ 0.1	0.5 (0.0)
K	K <sub>2</sub> O	N/A	N/A	N/A	1.0 (0.5)

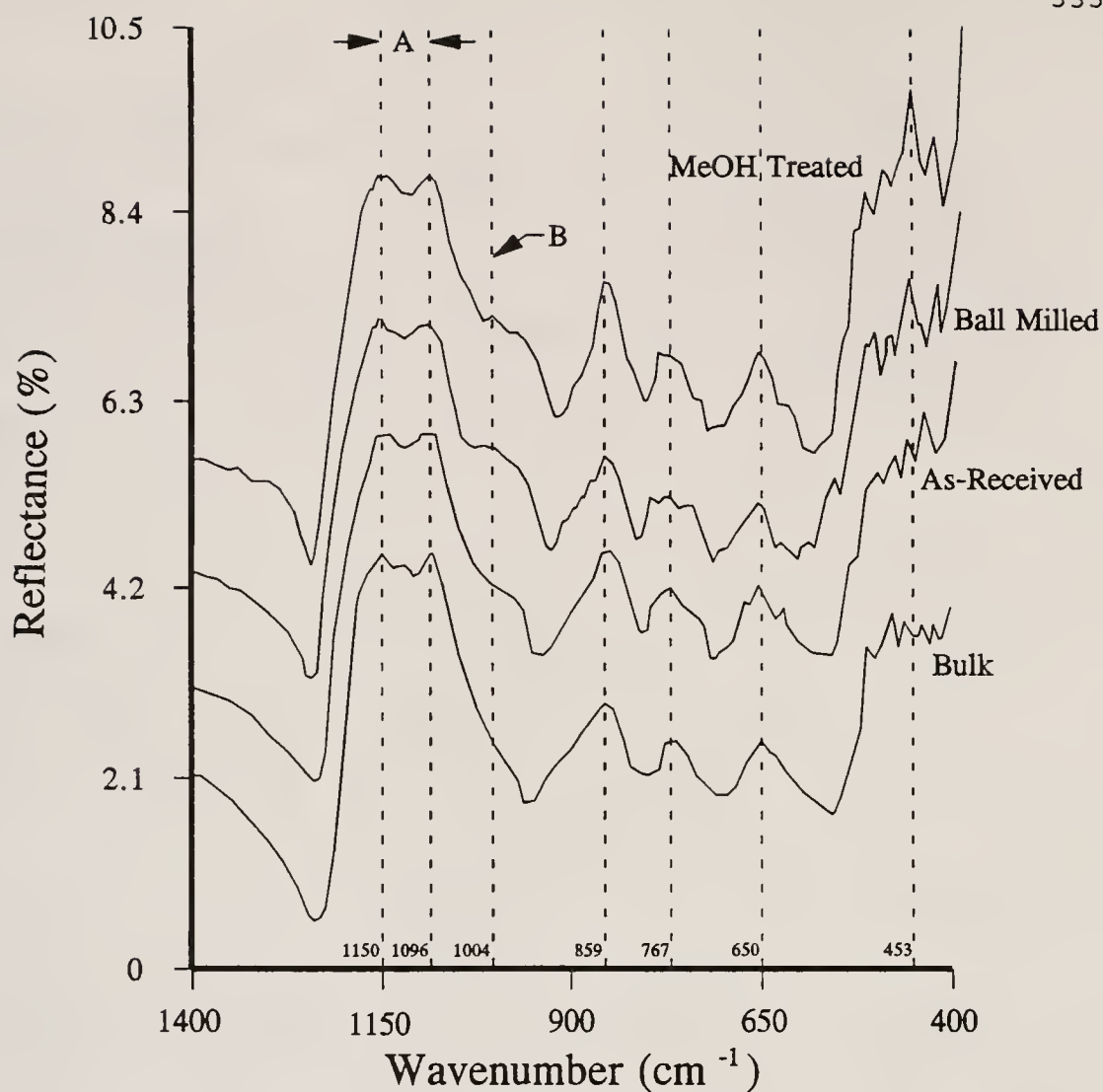
- Notes:
1. The standard deviation of each ICP PPM value is based upon 6 measurements.
  2. Measured oxide composition includes a correction for K<sub>2</sub>O,  $\pm$  values indicate plus or minus one standard deviation.
  3. Literature values outside of parentheses are those from Corning Incorporated [79COR, 88COR], while those in parentheses are those provided by the Air Force Materials Laboratories (prepared by the Electronic Properties Information Center, Hughes Aircraft Company, Culver City, CA). Note that the parenthetical values sum to 100.8 wt%.



Materials Laboratory compositional data, while the two MeOH exposed glasses were closest to the manufacturer's data.

Reflection mode Fourier transform infrared spectroscopy (FTIR) was also used to investigate the powder surface of the various BS glasses, as outlined in section 3.3.6. The respective FTIR reflection spectra of each of the BS glasses are illustrated in Figure 4.31. The spectral peaks at 1150 and 1096  $\text{cm}^{-1}$  are resultant from Si-O-B and Si-O-Si stretching peaks (they are actually one peak, but due to the Reststrahlen effect, they are recorded as a doublet) on the surface or near-surface of the glass powder. The shoulders centered about 1004  $\text{cm}^{-1}$  are a result of silicon-non-bridging oxygens. The spectral peaks at 859  $\text{cm}^{-1}$  are a due to the Si--O--Si bending mode, the peaks at 767  $\text{cm}^{-1}$  are resultant from an Si--O--Si tetrahedron response, the peaks at 650  $\text{cm}^{-1}$  are also due to a vibration of  $\text{SiO}_2$ , and the spectral peaks at 453  $\text{cm}^{-1}$  result from rocking of Si--O--Si bonds [85LEE1].

Normally (in bulk material analysis) the stretching peak shifts to lower wavenumber [79HEN]. However, since the IR radiation penetrates approximately 0.5  $\mu\text{m}$  into the sample [79HEN], it is expected that the IR radiation would penetrate into the "bulk" of the powder particles. Thus, in the BS glass powder, it would be expected that the stretching peak would remain stationary (possibly shrinking in intensity somewhat) while the non-bridging oxygen peak would develop. Therefore, the relative ratio of the non-bridging to the stretching peak should be a measure of corrosion on the powder particle surfaces. Figure 4.31 illustrates the ratio of the 1004 peak height divided by the 1160/1096 peak height for each of the respective BS glasses. It is evident from Figure 4.31 that, while there is little difference between the spectra of any of the glasses, there is a definite increase in the number of non-bridging oxygens as a result of MeOH interaction and/or mechanical milling. The peaks occurring at 1004  $\text{cm}^{-1}$  increase steadily from bulk to as-received powder, to the MeOH interacted powders.



Powder	Peak Height Ratio
MeOH Treated	0.631
Ball Milled	0.670
As-Received	0.554
Bulk	0.468

Note: Ordinate values do not reflect spectra offsets.  
 Peak height ratio =  $B/A$  (corrected for offset).

Figure 4.31

FTIR reflection spectra of the BS glasses investigated in the ball milling study



Furthermore, the difference between the non-bridging oxygen peaks of the two MeOH interacted powders is substantial, (i.e. the B/A ratio of the ball milled glass is significantly greater than that of the MeOH treated glass) indicating that non-bridging oxygens occur as a result of both mechanical milling and of MeOH interaction.

This hypothesis is also supported by BET surface area analysis data. Figure 4.32 shows the relatively dramatic increase in surface area during milling. Figure 4.32 also indicates that the surface area approximately doubles after 10 days of stirring in MeOH at room temperature (as outlined in section 3.3.6). Furthermore, the figure also illustrates the effect of shaking in MeOH for 20 h, at 40°C. The surface area of the BS glass, treated in this manner, also approximately doubles, in spite of the significantly shorter stirring time, as well as using a non-interactive shaking mechanism. Thus, it may be concluded that the temperature at which the MeOH exposure occurs is quite a significant factor.

Figure 4.33 illustrates the multipoint isothermal gas desorption relationships for the as-received BS glass powder, the MeOH-treated powder and the ball milled BS glass powder. From Figure 4.33 it is evident that both the MeOH-treated and the MeOH ball milled BS glasses exhibit a significant desorption peak at a pore diameter of approximately 4 nm, while the as-received BS glass powder did not. This behavior was exhibited only during desorption and not during adsorption. Furthermore, the peak is significantly larger in the ball milled BS glass powder, indicating that the exposure of fresh surfaces augments the MeOH-BS glass interaction. It is interesting to note that the pore size of the desorption peaks is on the order of the surface roughness of the ball milled BS glass, as viewed by TEM (see Figure 4.30).

Thus, it may be concluded that milling in MeOH did affect both the surface area and the composition of the BS glass used. However, this effect did not significantly alter the properties of the BS glass (i.e.

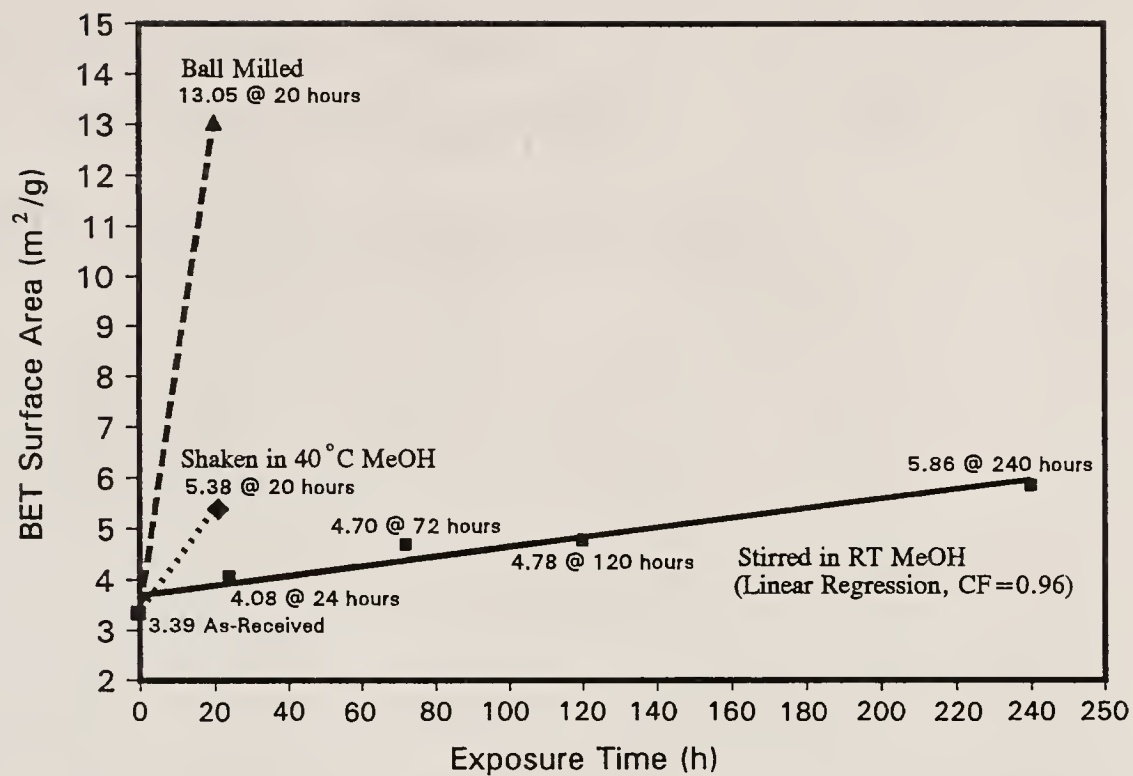


Figure 4.32

Illustration of the effect of MeOH exposure on BS glass surface area

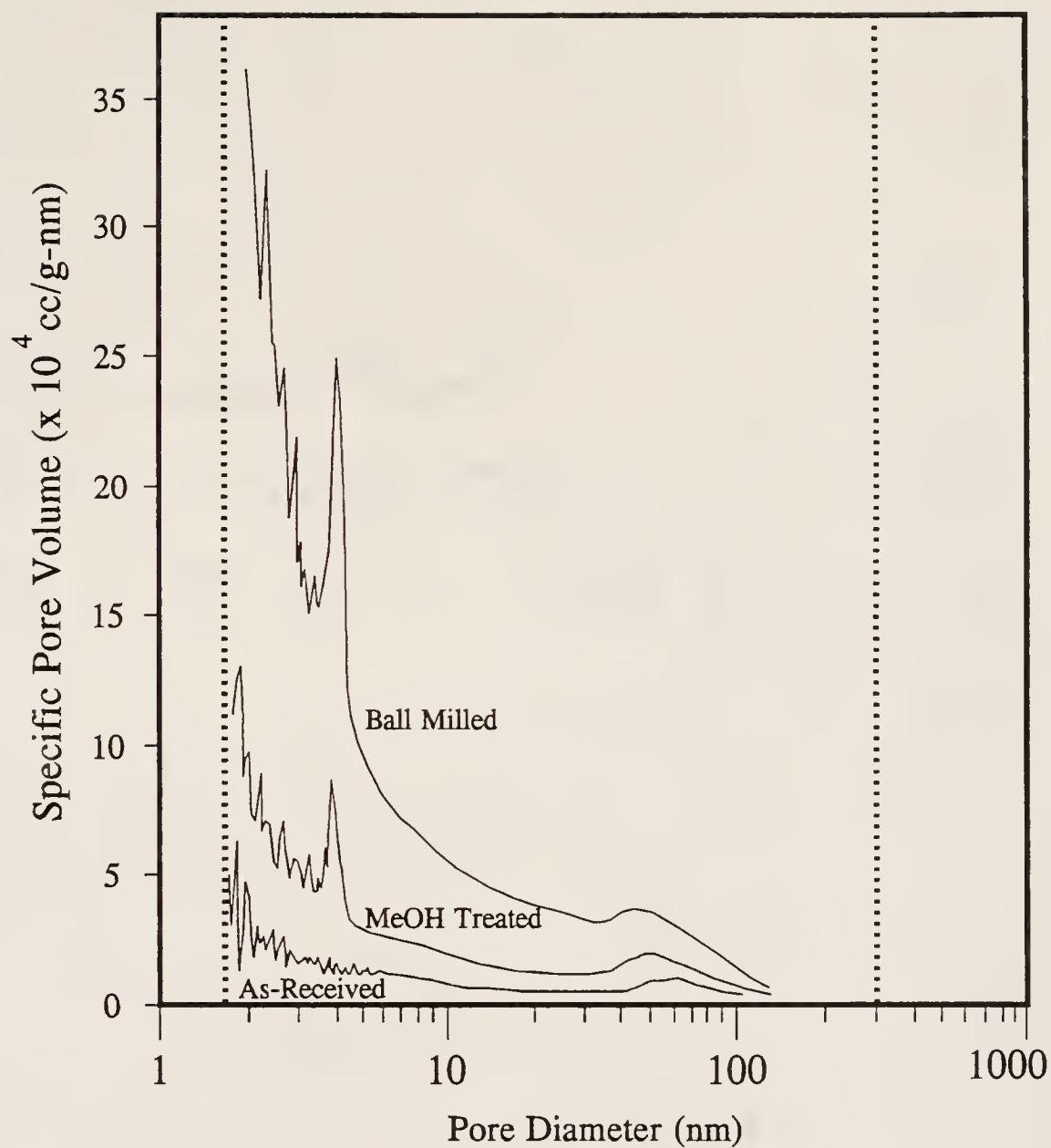


Figure 4.33

Multipoint desorption isotherm of the as-received BS glass powder, the MeOH treated BS glass powder, and the ball milled BS glass powder

dielectric constant and loss, etc.) for the purposes of this study, as will be seen in subsequent sections. It is assumed, however, that the exposure to MeOH during ball milling effectively increased the surface area of the BS glass powder by a factor of approximately 2. It is not known whether the change in measured density subsequent to ball milling is a result of compositional change during MeOH exposure, or to the effect of decreased particle size as indicated in section 4.1.2, since this increase in density is quite small and could be accounted for by either or both effects. It should be noted that centrifugal particle size analysis (CPSA) indicated no discernable change in particle size between the as-received BS glass powder and the powder shaken in MeOH for 20 h at 40°C. Therefore, the size of the powder is not significantly effected by the above-described corrosion process. However, the surfaces of the powder particles are affected measurably.

## 4.2 Suspension and Green/Pyrolyzed Structure Characterization

### 4.2.1 Suspension Characterization

Rheometry was utilized to characterize the shear stress versus shear flow rate behavior as well as the viscosity of suspensions utilized in this study, as described in section 3.4.2.2.2. All data illustrated in the following figures were taken during increasing shear rate. Rheometry was utilized to investigate the effect of solids loading upon the rheological properties of said suspensions.

Unfortunately, it was not possible to obtain shear stress data at shear rates near zero, due to the noise of the data. Therefore, it is not possible to comment of the yield behavior of these suspensions.

The effects of increased solids loading upon the viscosity and the shear stress of pure suspensions of ball milled BS glass powder,  $\text{Si}_3\text{N}_4$  powder, and UPLM powder in EtOH are illustrated in Figures 4.34 through 4.36 respectively.

As shown in Figure 4.34 the ball milled BS glass is nearly Newtonian at solids loadings of 20 and 30 V%, while it is slightly shear

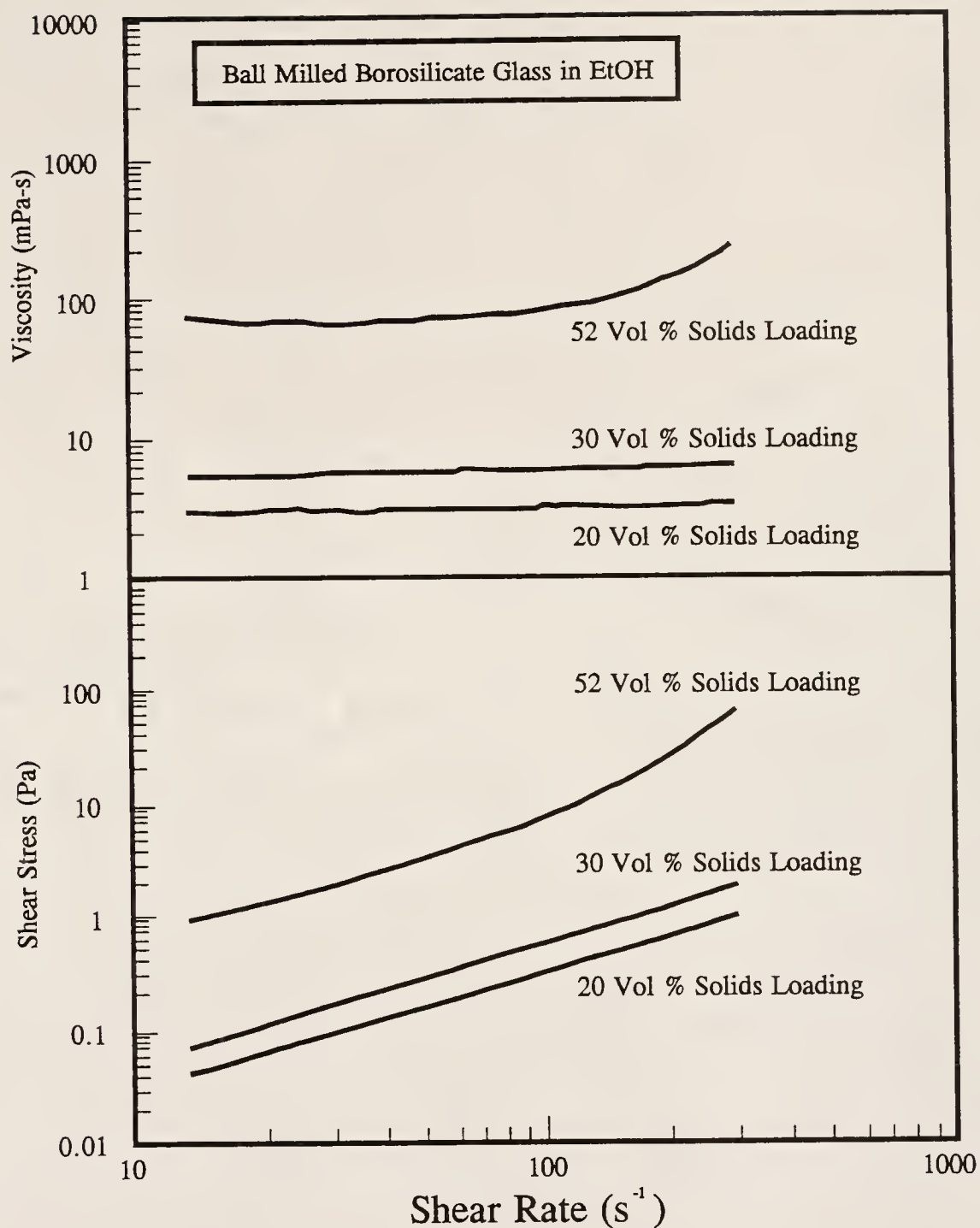


Figure 4.34

Viscosity and shear stress as functions of shear rate and solids loading of suspensions of pure ball milled BS glass powder in EtOH

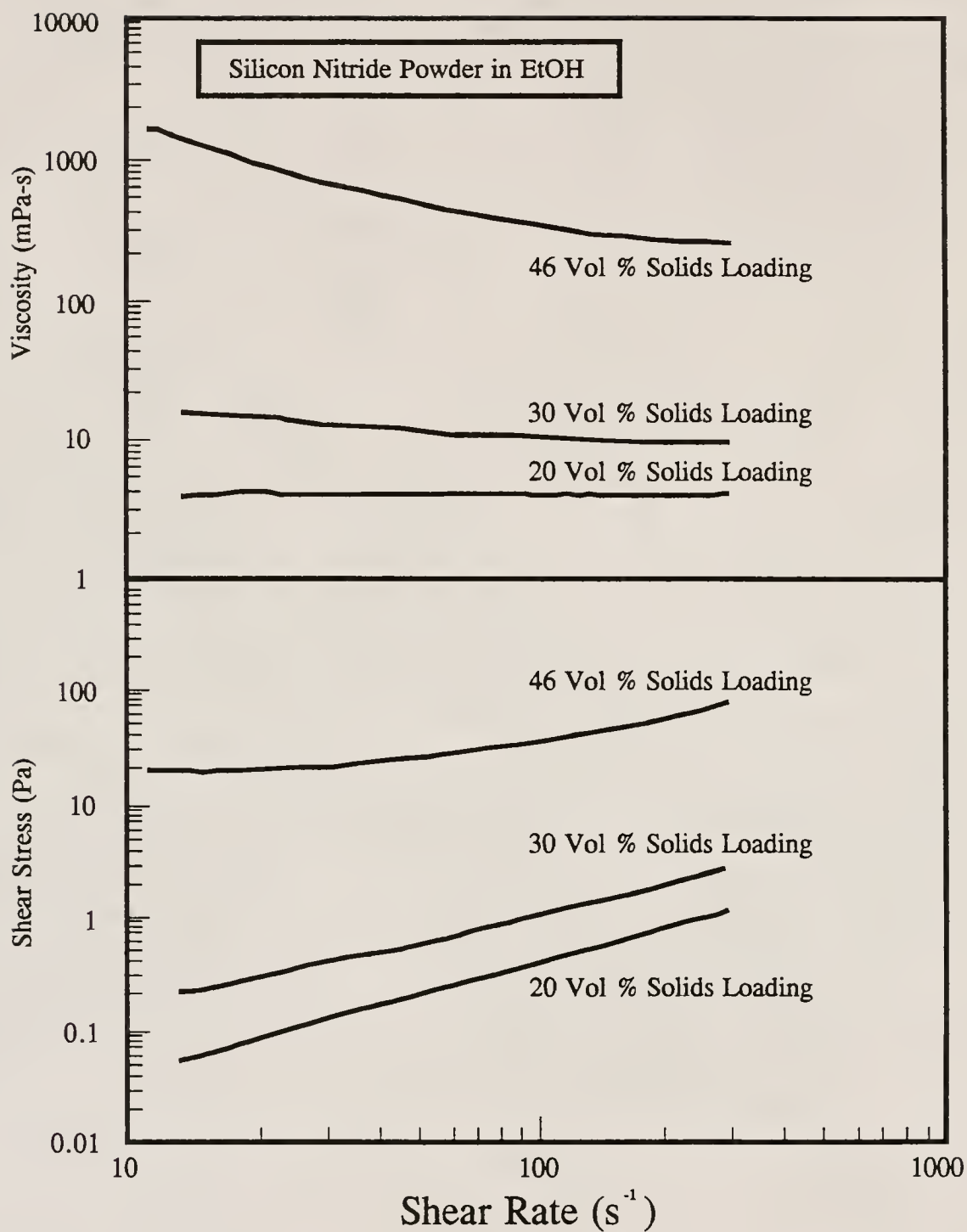


Figure 4.35

Viscosity and shear stress as functions of shear rate and solids loading of suspensions of pure  $Si_3N_4$  powder in EtOH



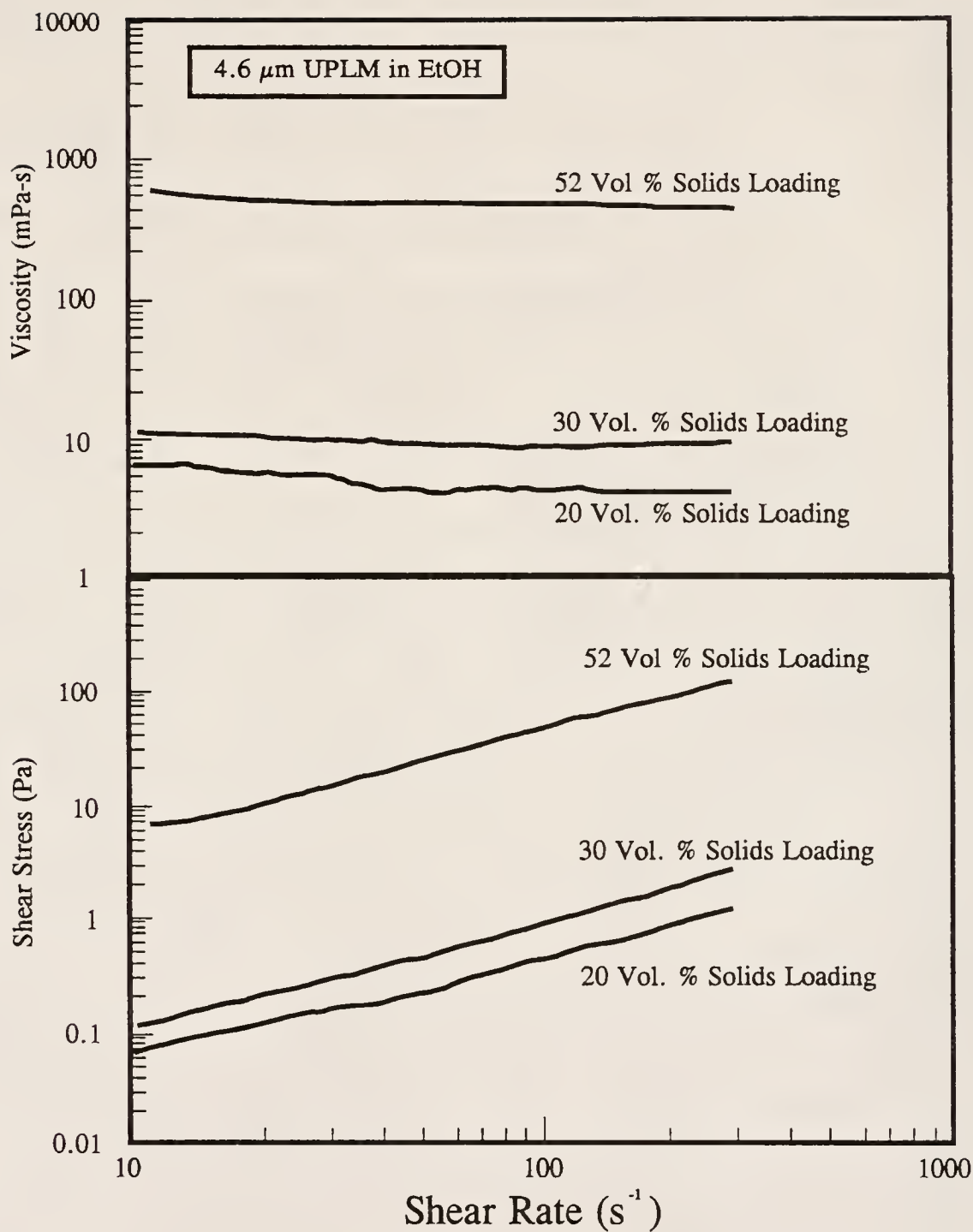


Figure 4.36

Viscosity and shear stress as functions of shear rate and solids loading of suspensions of pure UPLM powder in EtOH

thickening (dilatant) at a solids loading of 52 V%. Figure 4.35 indicates that the 20 and 30 V% solids loading, pure  $\text{Si}_3\text{N}_4$  suspensions in EtOH, are also nearly perfectly Newtonian. However, the 46 V% solids loading suspension of  $\text{Si}_3\text{N}_4$  powder in EtOH is slightly shear thinning (pseudoplastic). It should be noted that it was not possible to load the  $\text{Si}_3\text{N}_4$  suspension significantly beyond 46 V% solids loading and, thus, the  $\text{Si}_3\text{N}_4$  powder did not flow as efficiently in EtOH suspension as the other constituent powders did.

Figure 4.36 indicates that the suspensions of UPLM in EtOH are nearly perfectly Newtonian at all solids concentrations investigated. This is contradictory to other studies performed upon latex suspensions (both aqueous and nonaqueous) [70PAP,70WOO,72KRI]. This discrepancy may be due to the limited range of shear rates investigated in this study. For example, the data of Woods and Krieger indicate a near Newtonian, behavior in the shear rate range of approximately 10 to 300  $\text{s}^{-1}$  [70WOO]. Furthermore, none of the previously mentioned studies investigated latex suspensions in EtOH. Thus, the character of the dispersions studied could be somewhat different than those investigated by others. There are other differences between the above-mentioned studies and this one as well, such as synthesis techniques, etc. Also, these data are not normalized to the rheological character of the solvent-dispersant solution. Therefore, there may be effects of unadsorbed dispersant, etc. Finally, as mentioned above, the scale of viscosity used in this study is approximately two orders of magnitude coarser than the scales used in the studies [70WOO,70PAP].

Upon decreasing shear rate, a shear stress hysteresis was indicated in almost all of the high solids loading (i.e. >46 V% solids) suspensions investigated. Initially, this may appear to be an indicator of rheopexy (i.e. a hysteretic dilation of a suspension upon dynamic shear rate cycling [81SCH]). However, upon further cycling, the shear stress continued to increase, indicating that the increase in resistance

to shear is a result of solvent evaporation and not of the highly rare condition of rheopexy [81SCH].

Figure 4.37 illustrates the viscosity and shear stress of suspensions of as-received and ball milled BS glasses in EtOH. It is evident from Figure 4.37 that the BS glass does not flow as efficiently (i.e. exhibits greater shear stress and is dilatant) as the as-received BS glass in suspension. The as-received BS glass suspension is more nearly Newtonian than the ball milled BS glass suspension. This is most likely a result of the narrower particle size distribution of the ball milled BS glass.

Figure 4.38 illustrates the effect of volume percent latex addition upon the viscosity of co-dispersions of ball milled BS glass and  $\text{Si}_3\text{N}_4$  powders at shear rates of 100 and 300  $\text{s}^{-1}$ . The figure indicates that the viscosity decreases slightly as the volume percent UPLM is increased up to approximately 10 V% UPLM, then increases with increasing V% UPLM up to 20 V% UPLM. Furthermore, in suspensions of pure ball milled BS glass with UPLM, the suspension viscosity traverses another minimum from 15 to 30 V% UPLM, and decreases again as UPLM concentration increases toward 40 V%. These changes in viscosity do not correlate well with the minor fluctuations in measured solids loading (also shown in Figure 4.38). Thus, it may be concluded that said viscosity fluctuations, with changing UPLM concentration, are real.

Figure 4.39 illustrates the effect of latex powder mean size and size dispersity upon the viscosity of pure ball milled BS glass suspensions having 15 V% latex additions. It is illustrated that, within the confines of this study, the viscosity does not change greatly with the different latexes used (the dotted lines are shown as an indicator of relative relationships only). However, there apparently is a gradual decrease in viscosity as latex size is increased (with both monosized and polysized latexes). This relationship also does not correlate with fluctuations in total solids loading.

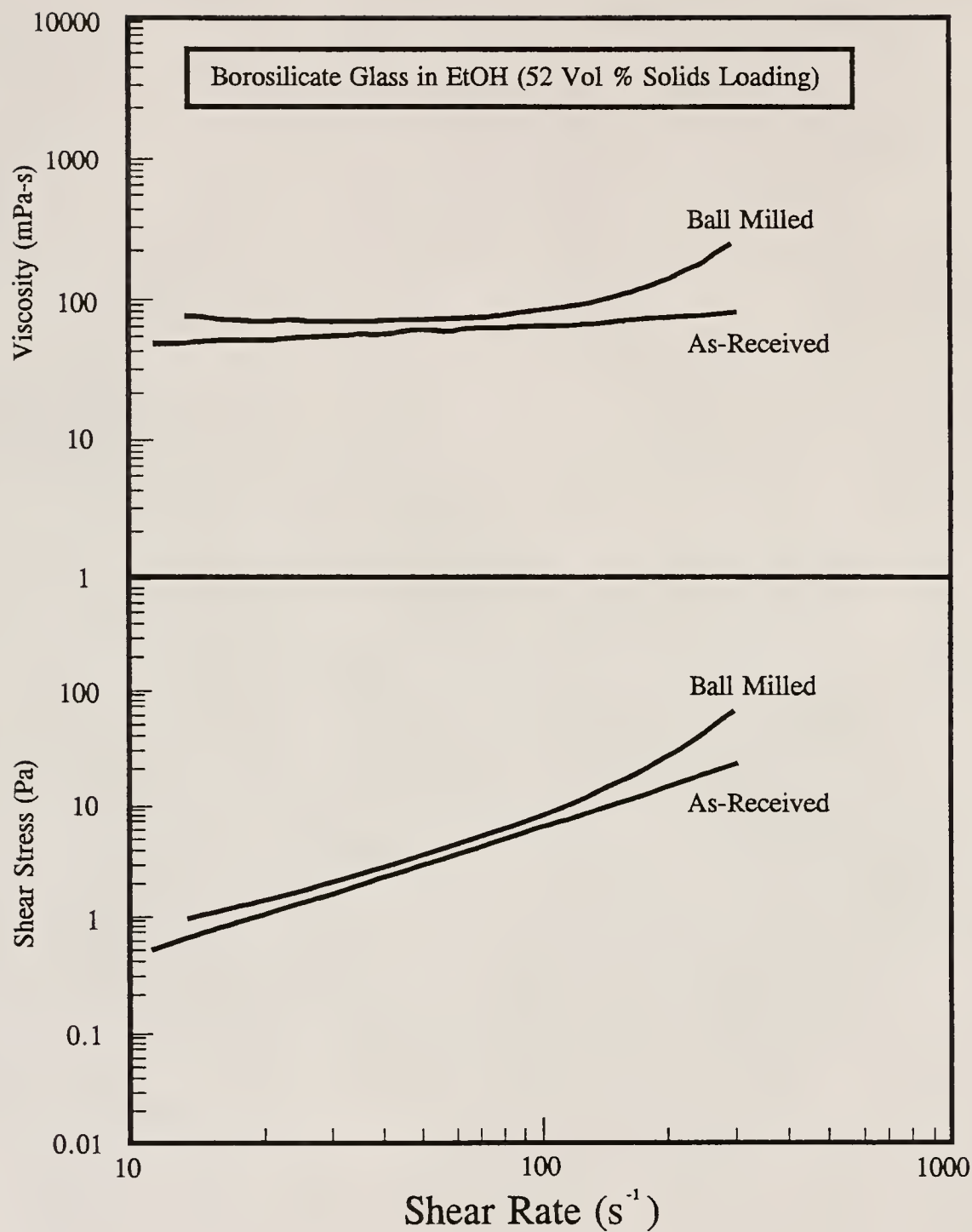
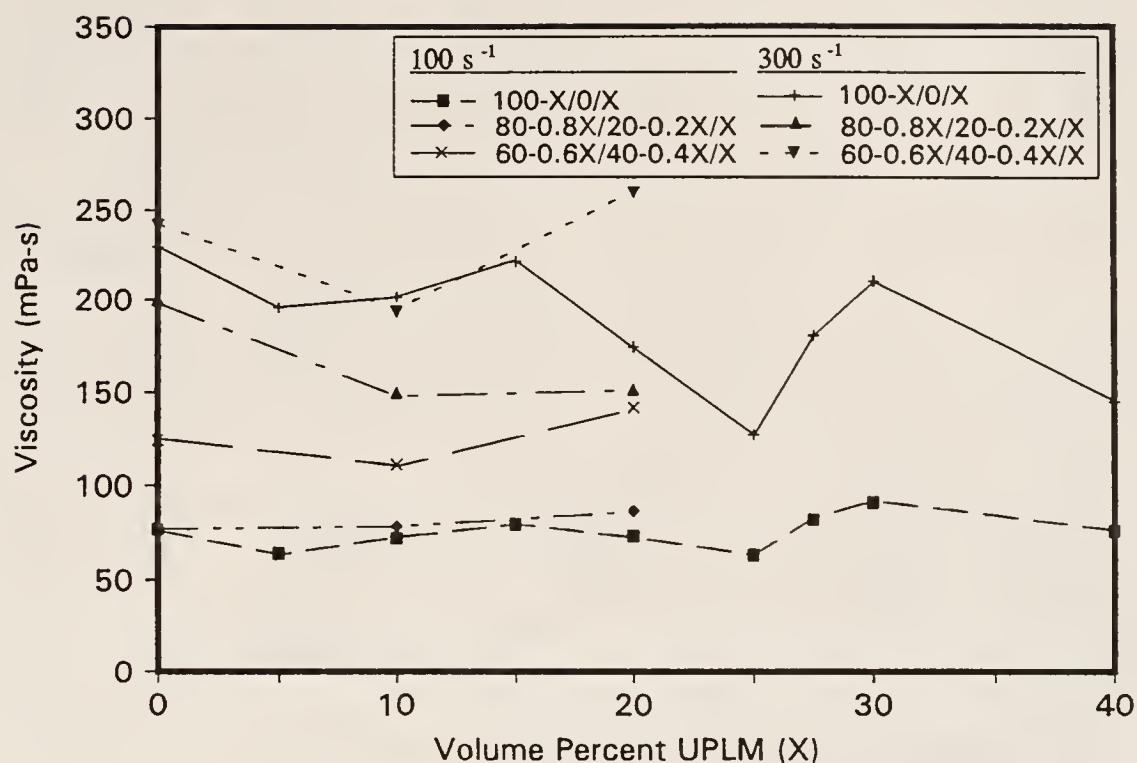


Figure 4.37

Viscosity and shear stress of suspensions of as-received versus ball milled BS glass powders in EtOH

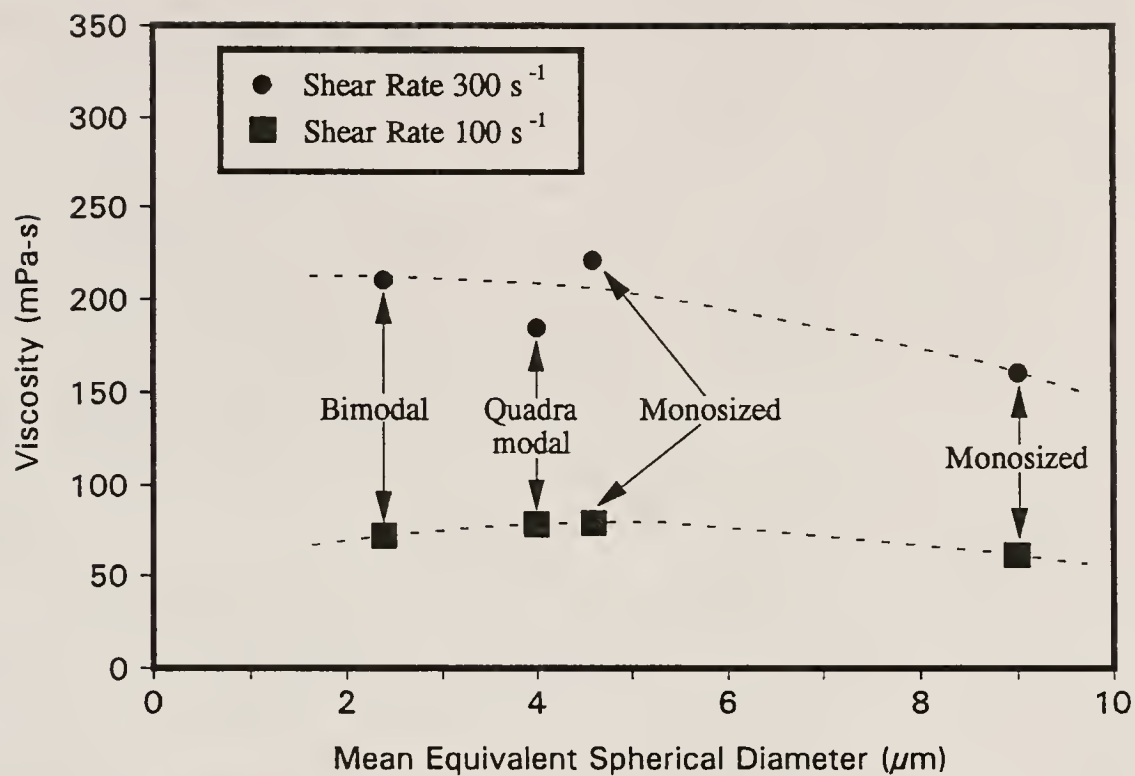


Note: First value denotes BS glass concentration, and  
Second value denotes Silicon Nitride concentration

	Measured Solids Loading (%)		
X	100-X/0/X	80-0.8X/20-0.2X/X	60-0.6X/40-0.4X/X
0	52.3	52.4	52.6
5	52.8		
10	52.7	52.8	52.3
15	52.6		
20	52.5	52.6	52.6
25	52.6		
27.5	52.7		
30	53.0		
40	52.8		

Figure 4.38

Viscosity as a function of volume percent UPLM concentration of the various suspensions used in this study



	Bimodal	Quadramodal	Monosized	
			4.6 $\mu\text{m}$	9.0 $\mu\text{m}$
Measured Vol % SL	52.8	52.7	52.6	52.7

Figure 4.39

Viscosity of 85 V% ball milled BS glass, 15V% latex suspensions as a function of latex size and size dispersity



Figure 4.40 illustrates the effect of normalized V%  $\text{Si}_3\text{N}_4$  upon the viscosity of ball milled BS glass and UPLM suspensions, where normalized V% ( $V_n^{SN}$ ) follows the relation:

$$V_n^{SN} = \frac{V_{\%}^{SN}}{V_{\%}^{BSglass}} \times 100$$

where:  $V_{\%}^{BSglass}$  is the actual V% of BS glass (total solids basis)

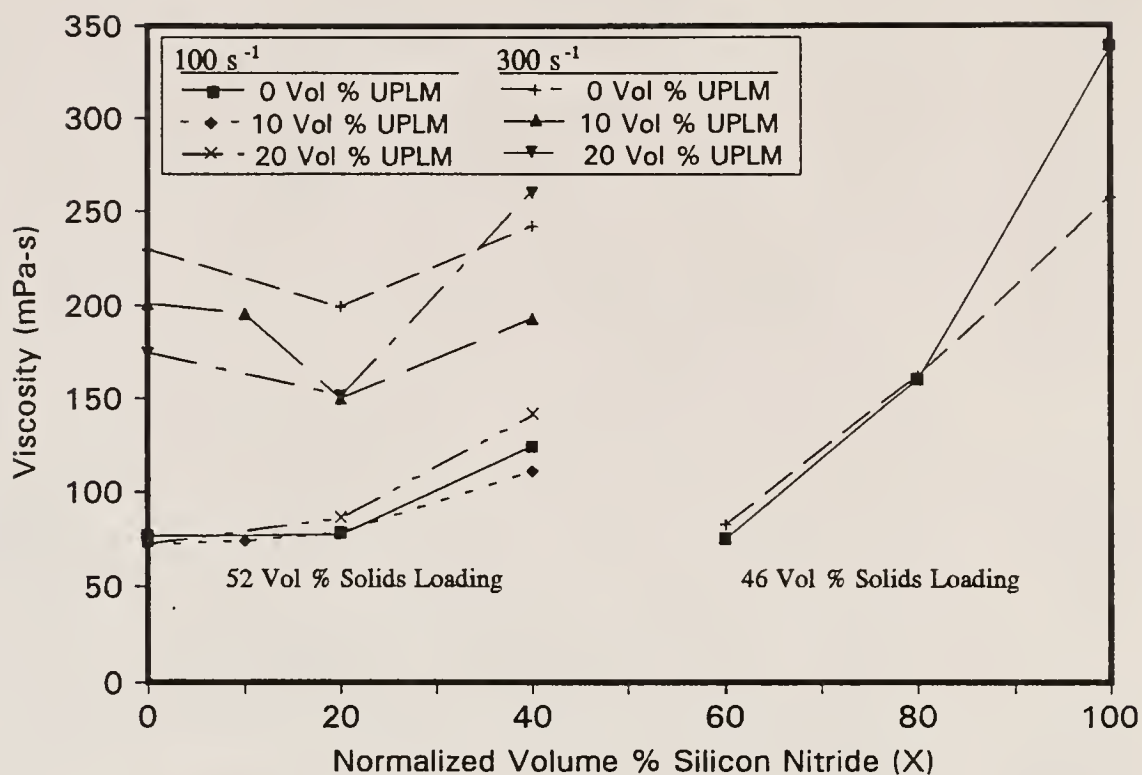
$V_{\%}^{SN}$  is the actual V%  $\text{Si}_3\text{N}_4$  (total solids basis)

similar to the relations in Figure 4.38, the viscosity traverses a minimum around 20 normalized V%. It is not known why this effect is greatest for suspensions containing 10 V% UPLM, while the 0 and 20 V% UPLM suspensions mirror each other closely (disregarding the actual difference in viscosity). The minimum is not as apparent at shear rates of  $100 \text{ s}^{-1}$  as it is at  $300 \text{ s}^{-1}$ .

Again, the above relation does not correlate with the measured variations in solids loadings and, thus, is also a real effect. It is not known why these minima in viscosity occur. It may be that they may truly exhibit more efficient flow behavior, or it may be a an effect of comparing raw viscosities as opposed to relative viscosities, as discussed above.

Furthermore, the viscosity of ball milled BS glass- $\text{Si}_3\text{N}_4$  suspensions increases greatly from 60 to 100 V%  $\text{Si}_3\text{N}_4$  concentration, and the BS glass- $\text{Si}_3\text{N}_4$  suspensions become pseudoplastic above a  $\text{Si}_3\text{N}_4$  concentration of approximately 80 V%. Again, this real effect does not correlate with the minor variations in measured solids loadings.

It should be noted that the above suspensions were formulated for this study, upon the basis of minimization of segregation, while attempting to maximize homogenization. These suspensions were not formulated for use in tape casting, or to be utilized as thick film dielectric inks. This was done in order to minimize the complexity of



	Measured Solids Loading (%)		
X	0 Vol % UPLM	10 Vol % UPLM	20 Vol % UPLM
0	52.3	52.7	52.5
10		52.8	52.6
20	52.4	52.8	52.6
40	52.6	52.3	
60	46.2		
80	46.1		
100	45.7		

Figure 4.40

Effect of normalized volume percent concentration of  $\text{Si}_3\text{N}_4$  upon the viscosity of suspensions characterized in this study

this system with respect to the number of organic suspension components, as well as to minimize the volume fraction of non-volatile organics.

In tape casting slurries, it is desirable that the suspension be pseudoplastic in the shear rate range of approximately 15 to 80  $\text{s}^{-1}$ , and have a viscosity between 1000 and 5000 mPa-s throughout said shear rate range [88REE,90MIS]. It is evident, from the above rheology data, that all of the suspensions produced for this study exhibit viscosity values well below 1000 mPa-s in the shear rate range of 15-80  $\text{S}^{-1}$ . Furthermore, all the suspensions used in this study were either nearly Newtonian or slightly shear thickening (i.e. dilatant) within the above-mentioned range of shear rates. Therefore, the suspension systems investigated in this study would require modification before they could be satisfactorily utilized in either tape casting or thick film processing. However, it is very encouraging that the viscosities of the suspensions, prepared for this study, were below the 1000 to 5000 mPa-s range, and that the rheological properties, by and large, were nearly Newtonian in the shear rate range of 15 to 80  $\text{s}^{-1}$ , since the viscosity properties of tape suspensions are largely determined by the binder/plasticizer system used [88REE,90MIS]. It is further encouraging that said suspension system could be loaded to (and somewhat in excess of) 52 V% non-volatile solids. The ability to pack a suspension at this great a solids loading indicates that the suspension is relatively well dispersed. Furthermore, highly loaded suspensions create dried tapes that experience relatively low drying shrinkages, thereby minimizing the stresses and defects that occur during drying.

Preliminary investigations also indicated that all of the powder precursors disperse quite well in basic (i.e.  $\text{pH} > 9$ ) aqueous media, thereby promoting the possibility of creating satisfactory tapes from aqueous suspensions. This is very important since aqueous systems are currently favored (and will be even more so in the future) due to environmental concerns and regulations [90NAH].

### 4.2.3 Green/Pyrolyzed Structure Characterization

#### 4.2.3.1 Overview

Green and pyrolyzed compact structures were characterized using both SEM and Hg porosimetry as discussed in sections 3.4.5.1 and 3.4.5.2. The first subsequent subsection (4.2.2.2) covers the green structure of pure latex compacts, in order to investigate the packing characteristics of said powders. The second subsequent sub-section (4.2.2.3) discusses the general characteristics of green and post pyrolyzed composite compacts, in order to investigate pore percolation, as well as the general packing characteristics and pore structures exhibited by the various compositions in the composite system as a whole. The third and final subsequent sub-section (4.2.2.4) discusses the effects of two processing parameters (i.e. sonication dispersion and suspension aging) upon the rheological and compact characteristics of representative composites investigated in this study. It is important to note that, with the exception of pure BS glass compacts, all composites investigated contained ball milled BS glass.

#### 4.2.3.2 Structural Characteristics of Polystyrene Latex Compacts

Figures 4.41 to 4.44 illustrate the representative surfaces of as-cast compacts of the smallest (2.4  $\mu\text{m}$ , bimodal, 07269001), medium sized (4.6  $\mu\text{m}$ , monomodal, 06199001-07+09), largest (9.0  $\mu\text{m}$ , monomodal, 07249001) and polysized (4.0  $\mu\text{m}$ , quadramodal, 05169101) latexes used in this study. It is interesting to note that none of the compact surfaces appear to have ordered packing. This is expected in this type of system. Furthermore, no ordered packing defects are evident in any of the micrographs. Similar behavior has been exhibited in slip cast compacts of monospherical silica [90VOR].

The packing efficiencies (green densities), as determined using Hg porosimetry (as outlined in section 3.4.5.2), of each of the slip cast



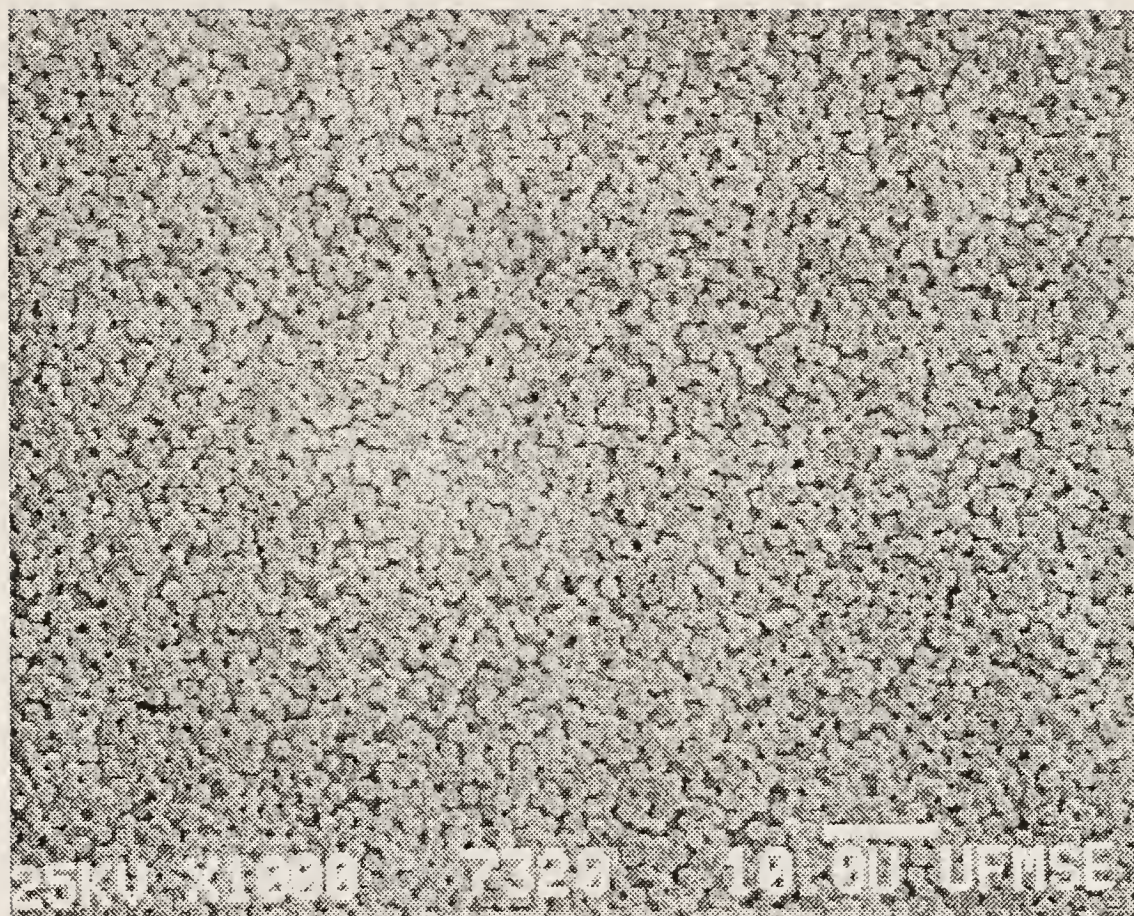


Figure 4.41

SEM micrograph of a representative surface of a slip cast compact of the smallest latex (2.4  $\mu\text{m}$ , bimodal, 07269001) used in this study



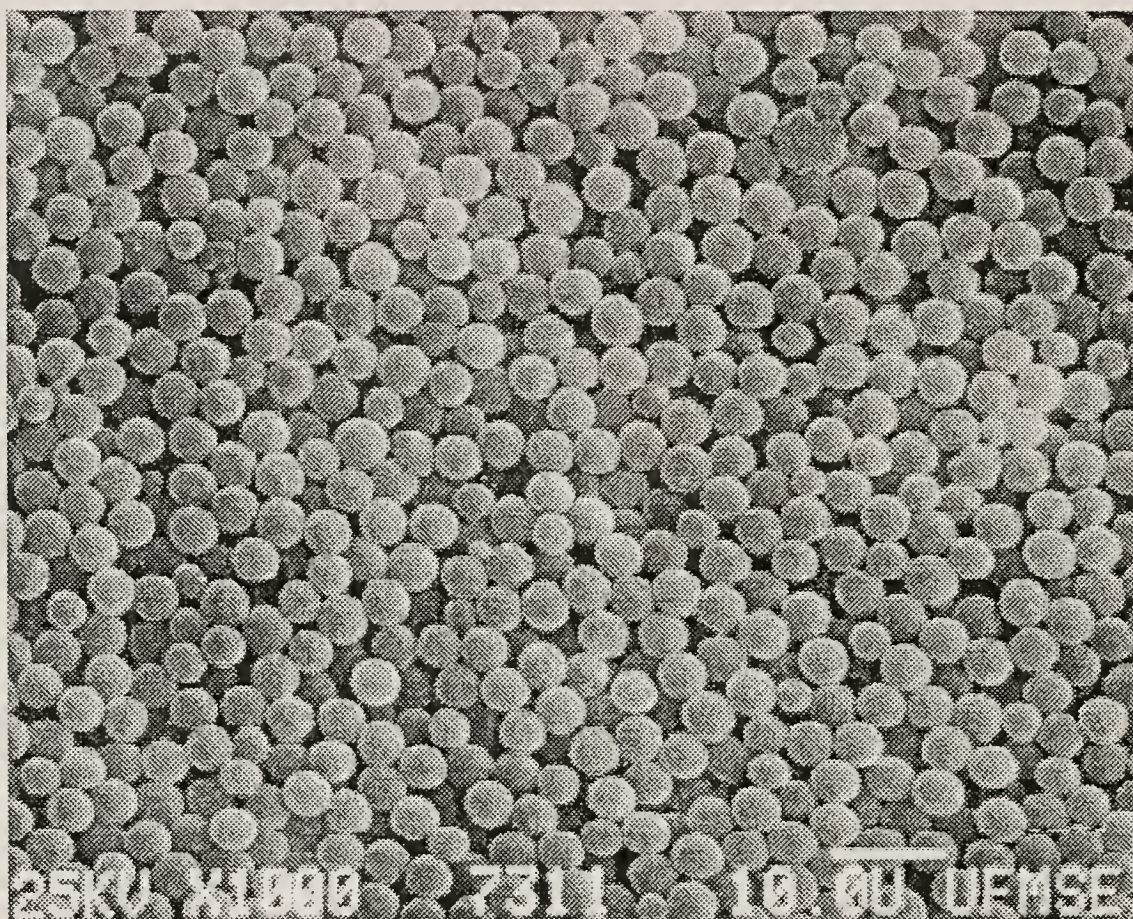


Figure 4.42

SEM micrograph illustrating a representative surface of a slip cast compact of the medium sized latex (4.6  $\mu\text{m}$ , monosized, 06199001-07+09) used in this study



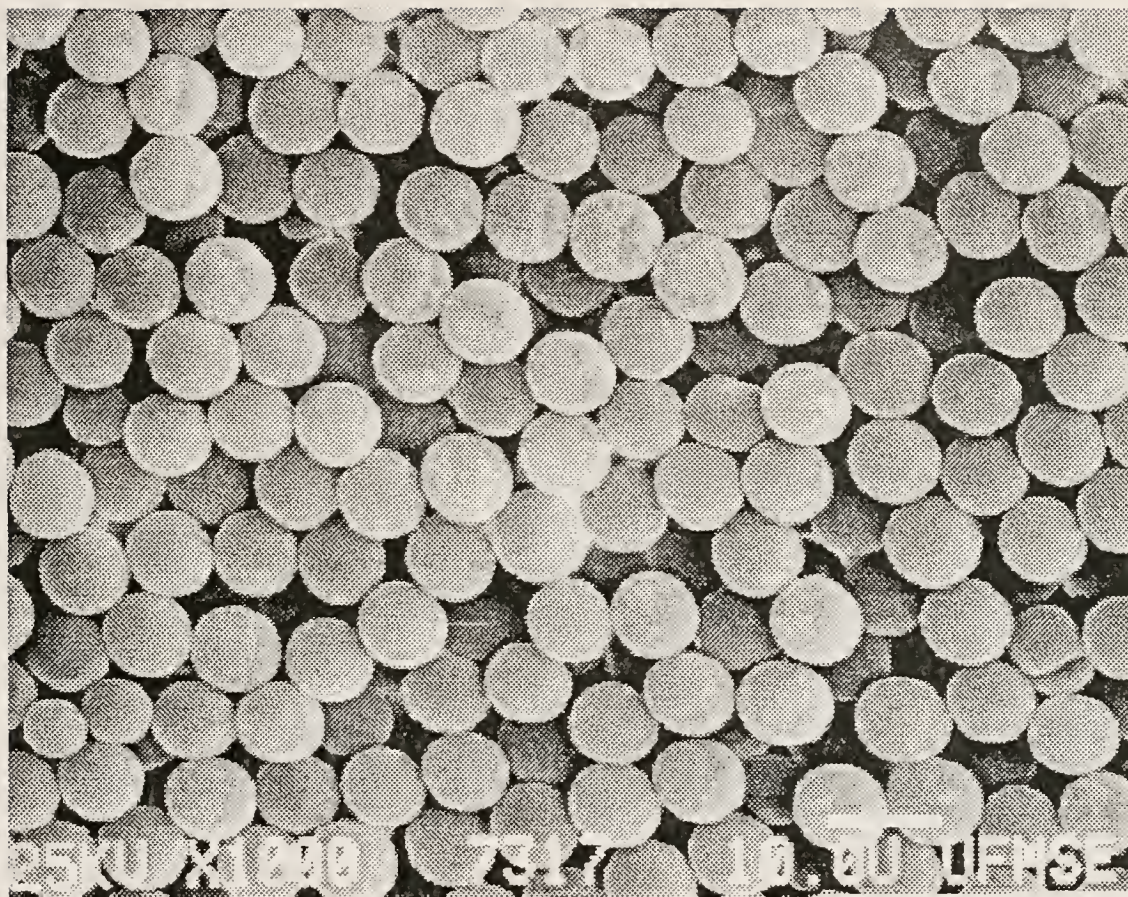


Figure 4.43

SEM micrograph illustrating a representative surface of a slip cast compact of the largest latex (9.0  $\mu\text{m}$ , monosized, 07249001) used in this study



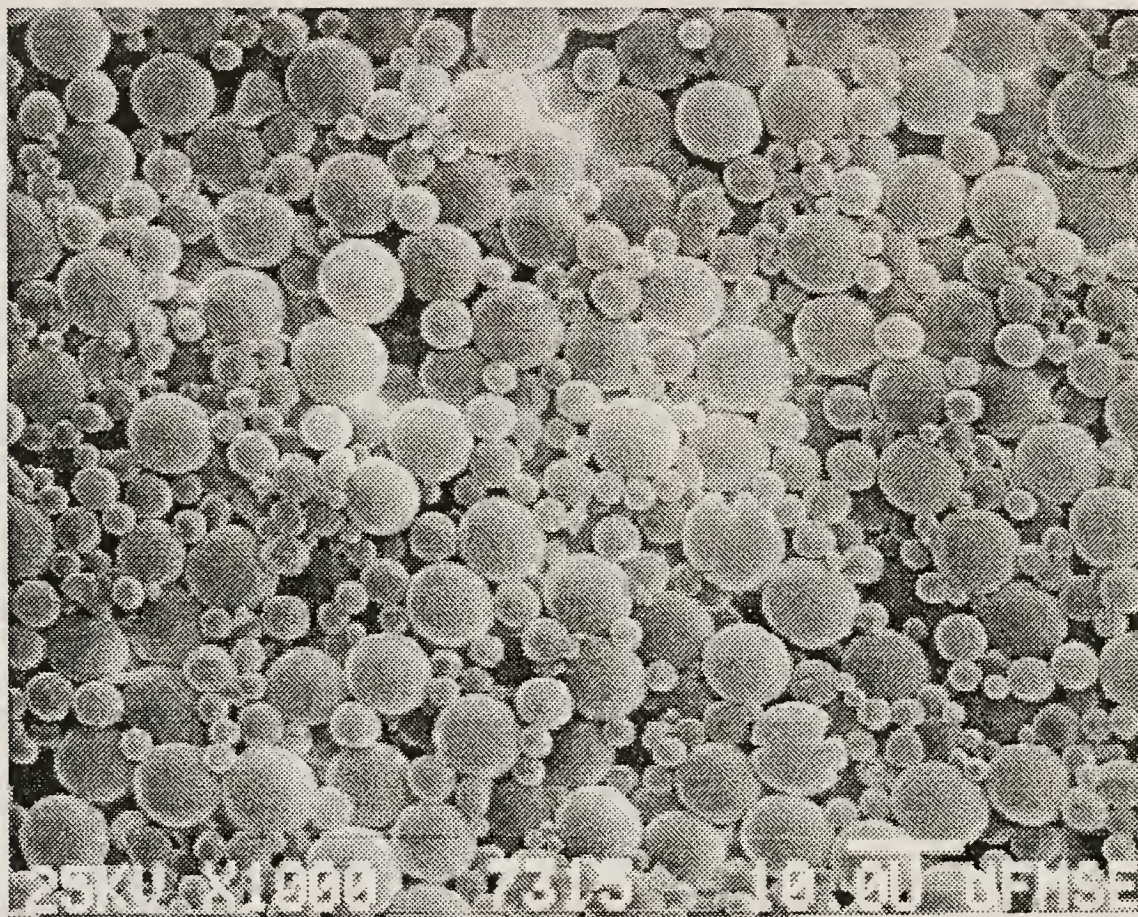


Figure 4.44

SEM micrograph illustrating a representative surface of a slip cast compact of the polysized latex ( $4.0\ \mu\text{m}$  (arithmetic mean), quadramodal, 05169101) used in this study

latexes are illustrated in Figure 4.45. It is evident that all of the monosized spheres packed to green densities between 61 and 63 % of theoretical density. This is in agreement with other investigations involving random close packing (RCP) of monosized spheres [30WES,60SCO,61MCG,88REE]. From these density data, it may be concluded that the containers (i.e. the slip casting mold rings) did not affect the measured PEs significantly. This is logical since the slip casting rings were over 3000 times larger in diameter than the largest size latex investigated. According to Figure 2.6, this container diameter to sphere diameter ratio should have little or no impact upon PE.

Figure 4.45 also indicates that the green density of slip cast UPLM compacts deviates slightly with changing latex sphere diameter. This is most likely an effect of deviations from monomodality rather than an effect of container-to-sphere-size ratio, since the size distributions of the 4.6, 6.1, 6.8 and 9.0  $\mu\text{m}$  diameter UPLMs get progressive narrower (with the exception of the 9.0  $\mu\text{m}$  UPLM, see Figures 4.13 to 4.16) should result in higher green densities, all other factors remaining equal). This effect is also responsible for the increase in green density with respect to increasing particle size modality. The bimodal compacts exhibited increased PEs as compared to the monomodal compacts, while the quadramodal compacts exhibited the greatest PE of all. Furthermore, Figure 4.45 indicates that the green density of the bimodal slip cast latex compacts increases with decreasing particle size. This is also resultant from increasing deviation from monomodality (see Figures 4.10 to 4.12).

It should be noted that the green densities of the slip cast bimodal and quadramodal latexes are less than 7 % greater than the green density of the monomodal latexes. This nominal increase in green density is due to the fact that the different modes of the respective size distributions do not differ enough in size. As indicated in Figure 2.8, in order to obtain the maximum PE in a multimodal packing of



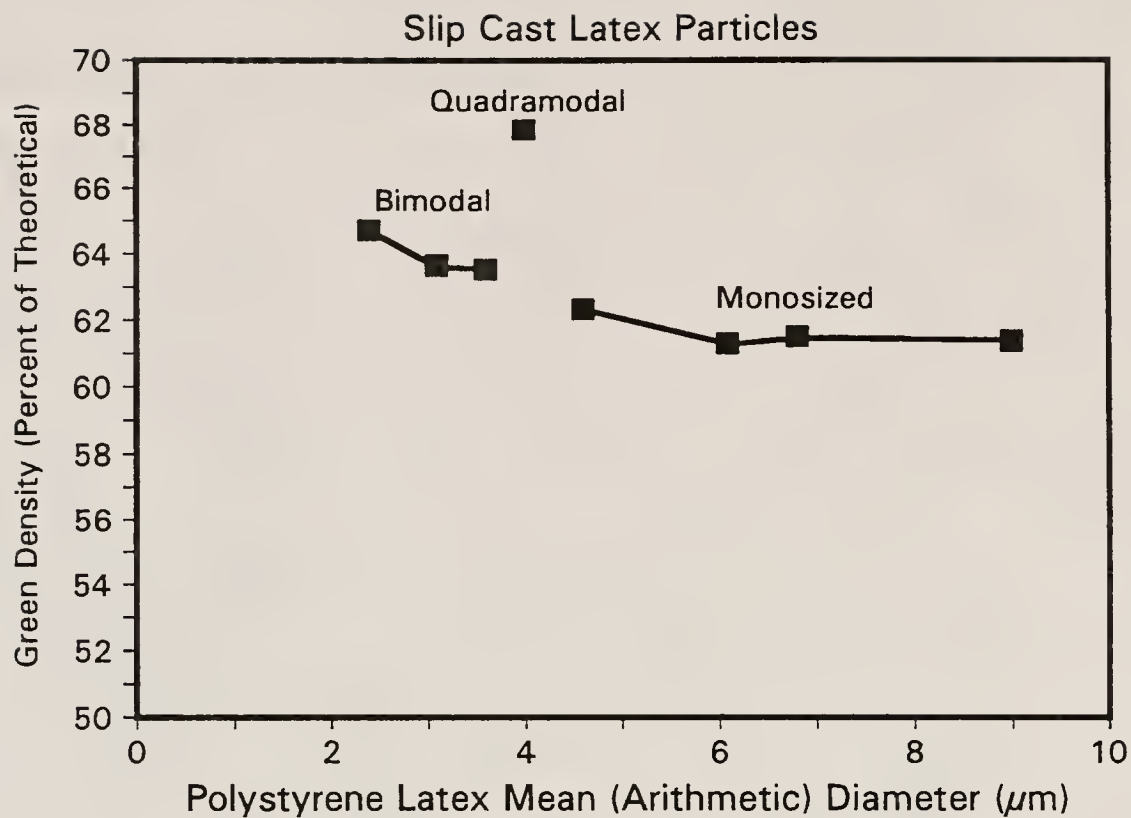


Figure 4.45

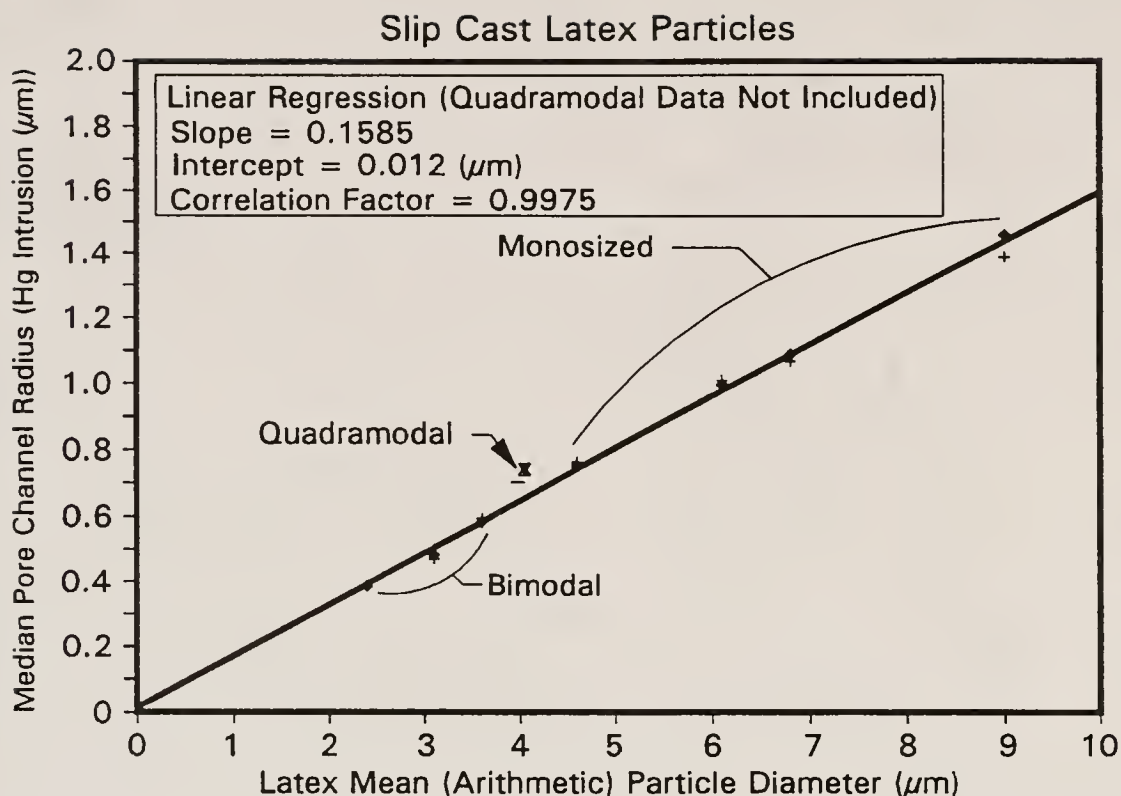
Green density (depicted as a percentage of theoretical density) as a function of mean sphere diameter of slip cast latex compacts

spheres, it is necessary that the diameter ratio of successively smaller size modes (i.e.  $D_{large}$  over  $D_{small}$ ) be at least 7 and preferably greater than 10 [61MCG,80PAT]. In this study, said size ratio is less than 2 in all cases. Again, referring to Figure 2.8, said diameter ratio is expected to increase green density only a few percent, at most (to a maximum of approximately 65 % of theoretical density for a bimodal mixture). As indicated in Figure 4.45 the increase in PE for the quadramodal distribution latex is higher than for the bimodal sphere distributions. This is expected as indicated by Table 2.4).

As shall be discussed below, this is a limitation to the investigation of the effect of latex size distribution upon maximization of closed porosity, in this study. However, this effect could not be avoided, due to the maximum size limitation of included porosity, as dictated by the maximum allowable surface flaw size as well as the minimum size limitation of included porosity, as determined by the BS glass powder size (as also shall be discussed below).

Figure 4.46 illustrates the relationship between latex mean (arithmetic) particle diameter and median pore channel radius (using Hg intrusion porosimetry). It is evident from Figure 4.46 that the median pore channel radius increases linearly with increasing particle size. Linear regression produced a fit with correlation of 0.9975, with an intercept of  $0.012 \mu\text{m}$ . This intercept value is quite close to 0.

It is interesting to note that the ratio of sphere diameter to median pore channel diameter ( $D/\text{MPCD}$ ), in the monomodal UPLM slip cast compacts, was a quite reproducible 3.0 to 3.1. This is a smaller ratio than would be expected in either square planar or triangular planar packing. Furthermore, this ratio is about one half that offered by McGeary [61MCG] and by Patankar and Mandal [80PAT], as the minimum ratio to allow smaller size spheres to pack within a bed of larger sized spheres (both used the model of triangular planar packing which gives a size ratio of 6.5, see Figure 2.7). However, when the third dimension



Latex	Mean Diameter ( $\mu\text{m}$ )	Pore Channel Size (Hg Intrusion, $\mu\text{m}$ )		Mean Diameter Pore Channel Diameter
		Radius	Diameter	
07269001 Bimodal	2.4	0.39	0.78	3.1
07309001 Bimodal	3.1	0.48	0.96	3.2
07199001 Bimodal	3.6	0.59	1.18	3.1
05169101 Quadramodal	4.0	0.74	1.48	2.7
06199001-07+09 Monomodal	4.6	0.75	1.50	3.1
07219001 Monomodal	6.1	1.01	2.02	3.0
08029001 Monomodal	6.8	1.08	2.16	3.1
07249001 Monomodal	9.0	1.43	2.86	3.1

Figure 4.46

Volume basis median pore channel radius (using Hg intrusion porosimetry) as a function of arithmetic mean latex sphere diameter of slip cast polystyrene latex compacts



of packing is considered, this value changes significantly. For example, the ratio of sphere diameter to pore entry diameter ( $D/P$ ) in cubic and tetrahedral packing of monosized spheres is 1.96 and 4.55 respectively, while the ratio of sphere diameter to entry sphere diameter ( $D/S$ ) is 2.38 and 6.67 respectively for cubic and tetrahedral packing [88REE]. These values are more realistic, since they involve three dimensional packing. The  $D/P$  value should represent a lower limit of validity for comparison with the ratio of sphere diameter to measured pore channel diameter ( $D/MPCD$ ), while the  $D/S$  value should provide upper limits for comparison. Whether the  $D/P$  versus PE or the  $D/S$  versus PE criterion is a better gauge of  $D/MPCD$  versus PE depends upon how the Hg intrudes the pore channels. If the Hg deforms to fit the pore channel, the  $D/P$  versus PE criterion is best. If the Hg remains circular in cross-section, upon infiltrating the pore, the  $D/S$  versus PE criterion is most correct.

The ratio of sphere diameter to pore channel diameter measured in the slip cast UPLM compacts with respect to PE is within both of these ranges. Figure 4.47 illustrates the relationship of pore channel size versus PE for cubic and tetrahedral packing, using the two criteria above. Figure 4.47 also shows the relationship of  $D/MPCD$  versus PE for the slip cast UPLM compacts. From the figure, it is obvious that the  $D/P$  versus PE criterion is most appropriate for comparison with  $D/MPCD$  versus PE. The UPLM data lie almost perfectly upon the theoretical interpolation between simple cubic and tetrahedral packing. This indicates that the Hg does conform to fit the pore channel. Furthermore, this relationship indicates that, even though the slip cast UPLMs are arranged in a random (i.e. RCP) fashion, the pore channel size may be accurately and reproducibly estimated using ordered packing theory. This is an extremely beneficial conclusion, since ordered systems may be characterized by exact mathematical models.

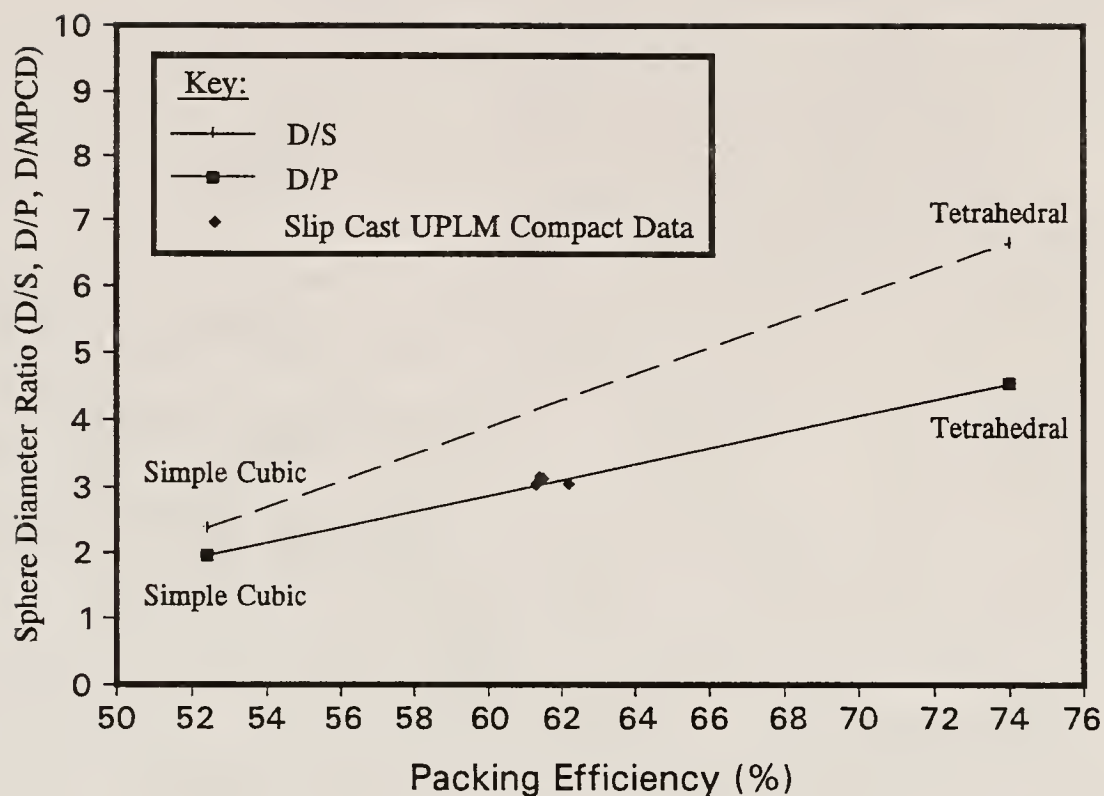


Figure 4.47

The relationship of D/S and D/P to PE for simple cubic and tetrahedral packing, the ratio of sphere diameter to pore channel diameter is also illustrated

It is also interesting to note that the bimodal compacts also fit the linear regression fit depicted in Figure 4.46. Finally, the quadramodal slip cast latex compact also fit the relationship illustrated in Figure 4.46, although not as well as either the UPLM compacts or the Bimodal latex compacts. It should be noted that the Hg intrusion curve was smooth for each of the latexes, regardless of modality, and the derivative curves showed only one peak. Therefore, it may be concluded that all of the slip cast latexes had only one distribution of pore channel sizes.

Unfortunately, it was not possible to investigate Hg intrusion-extrusion hysteresis, since ambient pressure was reached before the extrusion curve reached a median point (i.e. a change in concavity during the extrusion process) in all of the latex compacts investigated.

#### 4.2.3.3 Structural Characteristics of Green and Pyrolyzed Composites

An SEM micrograph of a representative green composite compact surface is illustrated in Figure 4.38. All three of the particulate constituents are apparent in this figure. The spherical particles are latex, the cubic or hexagonal particles are  $\text{Si}_3\text{N}_4$ , and the angular or non-symmetric particles are BS glass particles.

As predicted by both particle size/size distribution data and by rheometry data, the as-received BS glass packed to higher green density than the ball milled BS glass. The green/pyrolyzed density (as a percentage of theoretical density and determined using Hg intrusion porosimetry) of slip cast as-received BS glass compacts averaged  $72.0 \pm 0.1 \%$ , while the green/pyrolyzed density of the ball milled BS glass compacts averaged  $68.1 \pm 0.3 \%$ . The median pore channel radius (MPCR, volume basis, Hg intrusion) of the smaller particle size ball milled BS glass compacts was less than half that of the MPCR of the larger particle size as-received BS glass. Thus, it would be expected that the ball milled BS glass compacts sinter at a greater rate than the as-



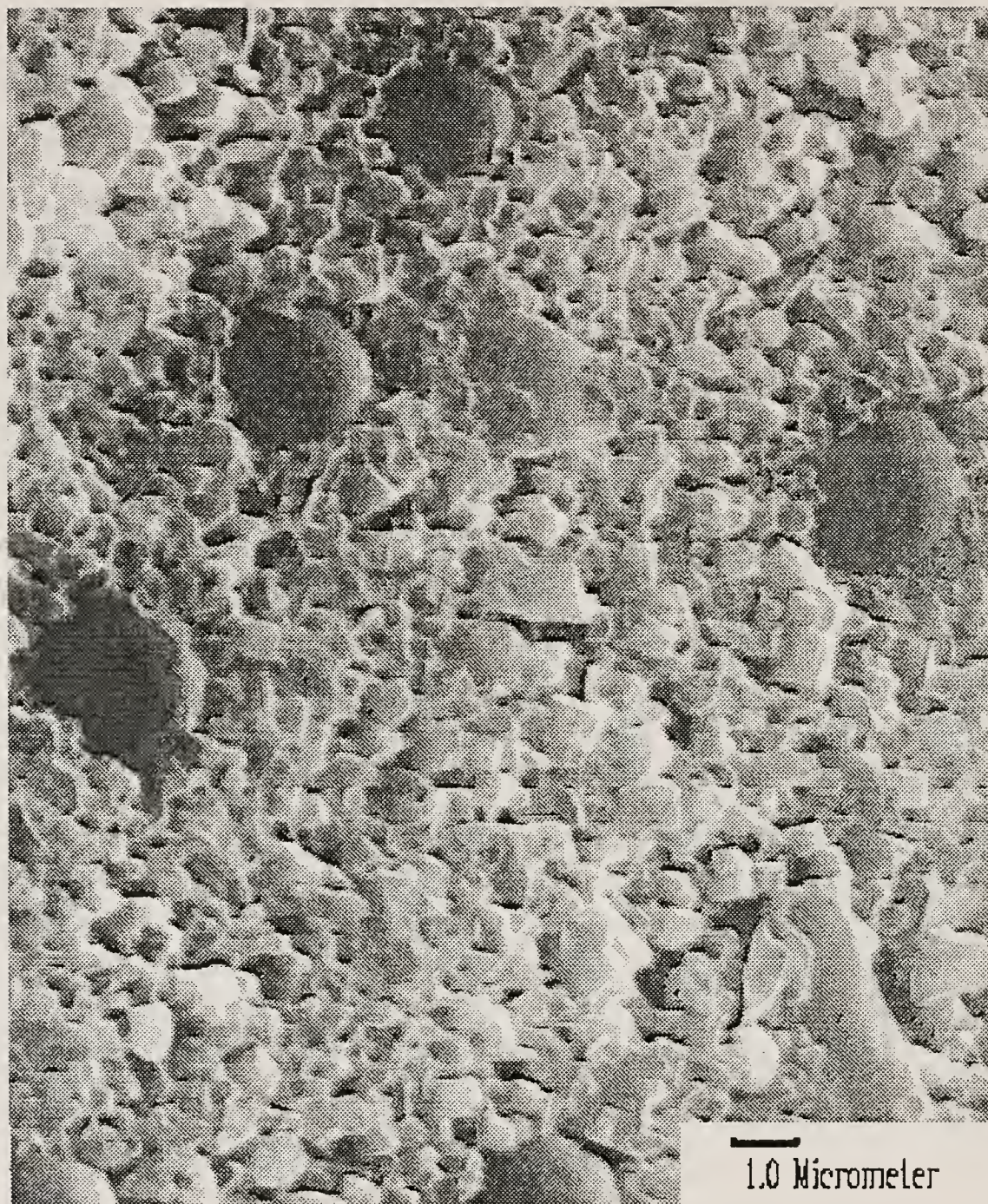


Figure 4.48

Micrograph of a representative surface of a green, Si<sub>3</sub>N<sub>4</sub> and UPLM filled, BS glass matrix composite



received BS glass powder compacts (all other factors remaining constant), despite the initially greater green density of the slip cast, as-received BS glass compacts.

In both categories of BS glass, there was a small (i.e. less than 0.5 %), but reproducible decrease in green density, as well as a correspondingly small (i.e. less than 0.01  $\mu\text{m}$ ) increase in median pore channel size, resulting from the process of organics pyrolyzation.

It was not possible to satisfactorily evaluate the Hg intrusion/extrusion hysteresis of the slip cast as-received BS glass compacts since the extrusion curves did not plateau to a stranded volume at ambient pressure. The slip cast ball milled BS glass compacts exhibited hysteresis behaviors that were not consistently reproducible as a result of inconsistencies in both the shapes and the final stranded volumes exhibited by the extrusion curves. However, the intrusion curves were quite reproducible.

Both slip cast BS glasses exhibited skewed pore channel size distributions. The distribution for the ball milled BS glass was much sharper as well as skewed toward smaller pore channel radii, as compared to the as-received BS glass. Figure 4.49 illustrates this effect.

In agreement with rheology data, the green density of slip cast composites in this system decreases with increasing  $\text{Si}_3\text{N}_4$  concentration. Figure 4.50 indicates that green density decreases monotonously from 68.1 % of theoretical density (pure ball milled BS glass compacts) to 51.5 % (pure  $\text{Si}_3\text{N}_4$  compacts). Figure 4.50 shows that this behavior is common in composites containing 10, 15 and 20 V%  $\text{Si}_3\text{N}_4$  as well. It is interesting to note that the green densities of composites in this system increase to approximately 71.5 % of theoretical with additions of 10, 15 and 20 V% of 4.6  $\mu\text{m}$  UPLM, and remain consistently greater than the green densities exhibited by the 0 V% UPLM system, throughout the entire range of normalized  $\text{Si}_3\text{N}_4$  concentrations investigated.

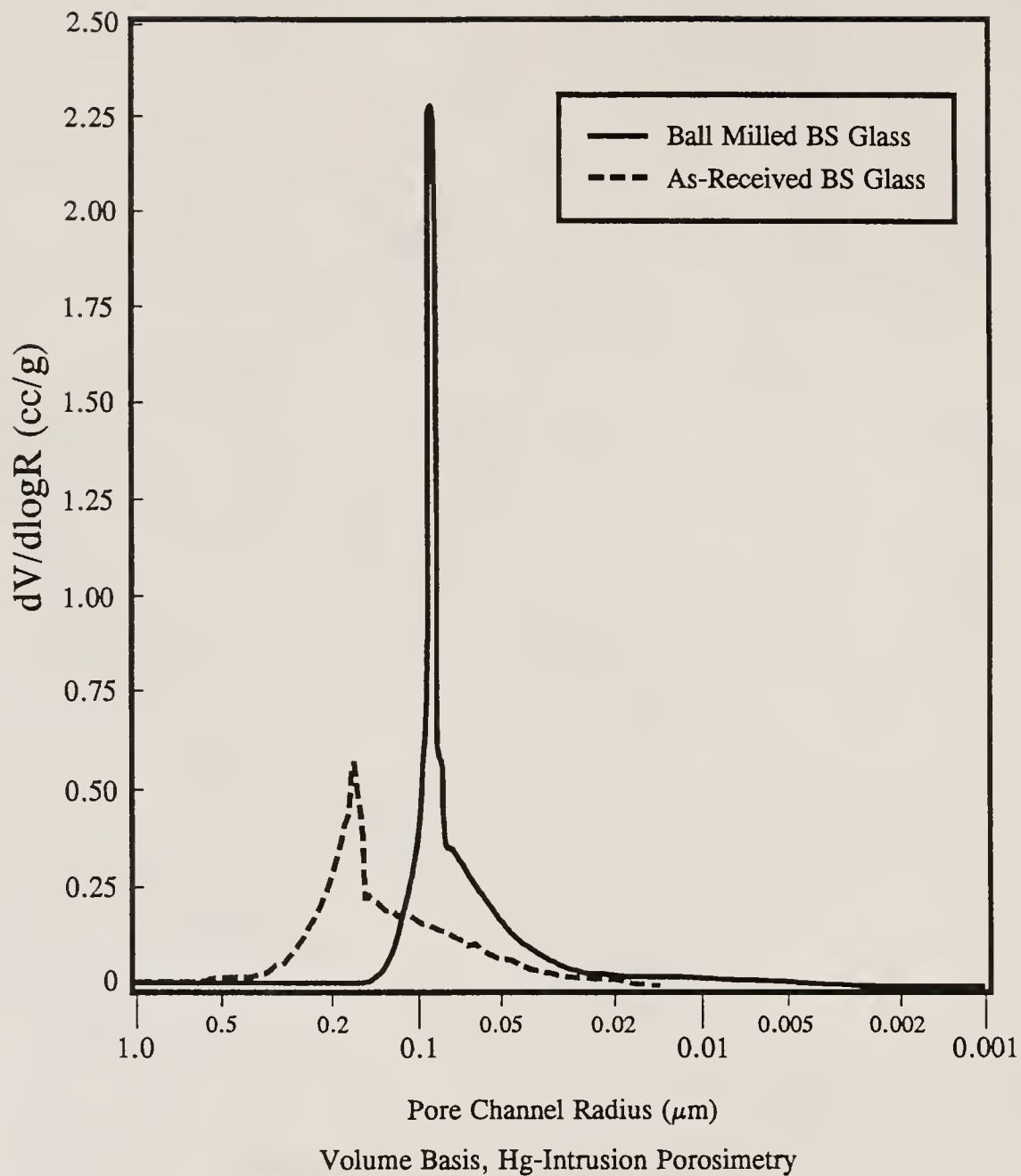


Figure 4.49

Pore channel radius distribution of slip cast as-received and ball milled BS glass samples



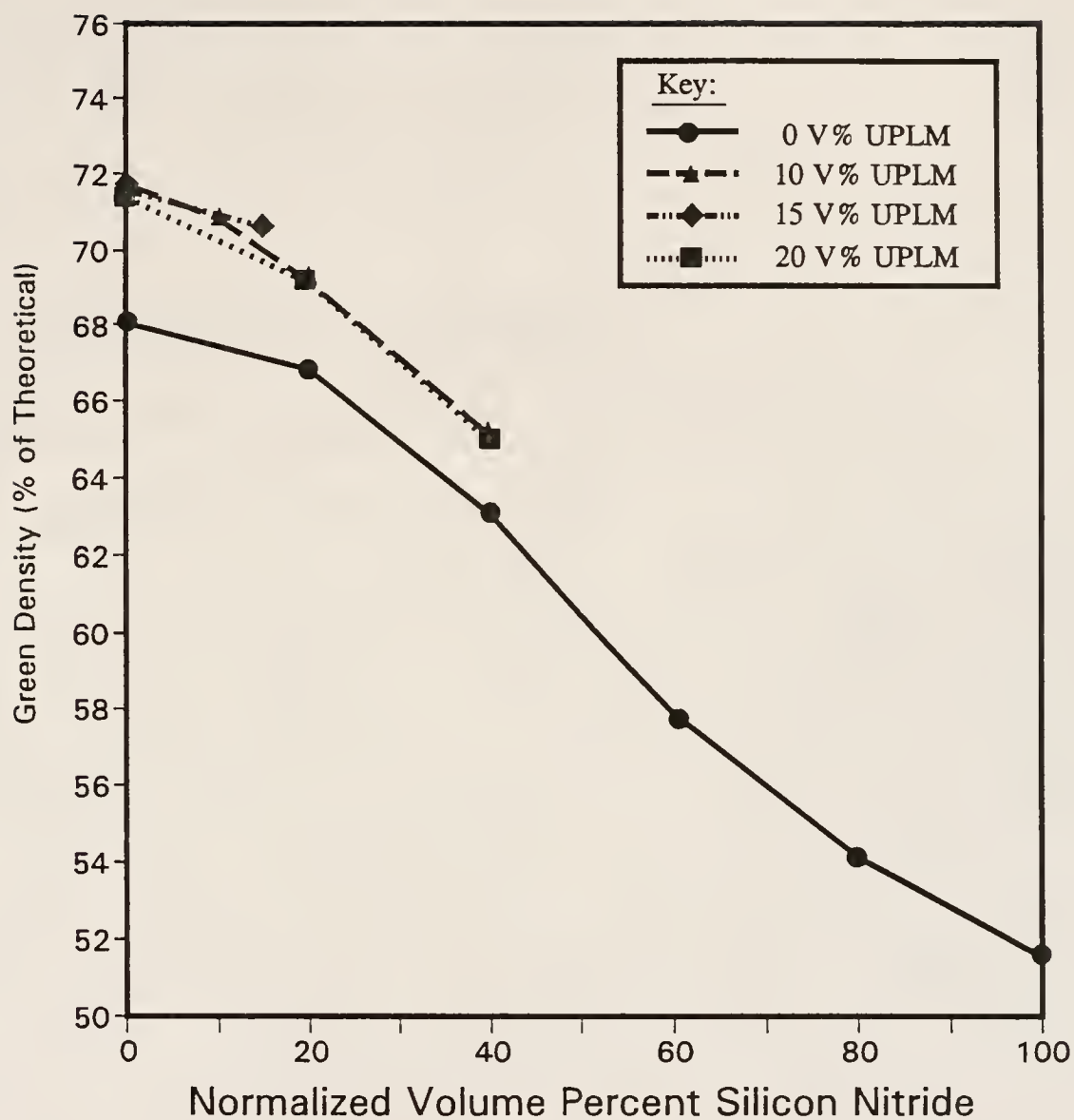


Figure 4.50

Green density (as a percent of theoretical density) of green (organics present) compacts with respect to normalized Si<sub>3</sub>N<sub>4</sub> concentration

This indicates that the particle size distribution is made progressively more favorable, from a packing standpoint, by the addition of 4.6  $\mu\text{m}$  UPLMs.

Figure 4.51 illustrates the effect of increasing  $\text{Si}_3\text{N}_4$  concentration upon pore channel radius, as measured via Hg intrusion analysis. It is evident from the figure that, in general, median pore channel size increases with increasing  $\text{Si}_3\text{N}_4$  concentration. The median pore channel radii do decrease slightly, with increasing  $\text{Si}_3\text{N}_4$  concentration in the 0 to 20 normalized V%  $\text{Si}_3\text{N}_4$  range, for most of the UPLM containing samples, however. It is interesting to note that, with one minor exception, the 0 V% UPLM samples consistently had the lowest median pore channel radii despite the fact that the 0 V% UPLM samples had the lowest green densities. This is due to the smaller average particle size of the 0 V% UPLM addition BS glass compacts. It is also interesting to note that the 0 V% UPLM compacts, exhibited very little difference in median pore channel radius between samples investigated before and after organics removal, via pyrolysis. This indicates that as the polymer latex is removed via pyrolysis, the pore channel structure enlarges. This effect is universally applicable to all the composite compositions studied.

Figure 4.52 illustrates the effect of increasing 4.6  $\mu\text{m}$  UPLM concentration upon green density for BS glass/UPLM composites in this system. The green density of the pure BS glass compacts in this system increases to a plateau at approximately 10 V% UPLM. The plateau continues to approximately 20 V% UPLM for 0, 20 and 40 normalized V%  $\text{Si}_3\text{N}_4$ . The green density values of the pure BS glass compositions continuously increase (with the exception of a dip at 27.5 V% UPLM) up to 40 V% UPLM, probably due to widening of the particle size distribution.

It is important to note that the PE value of the pure 4.6  $\mu\text{m}$  UPLM was approximately 62 %. Thus, the increase in PE with increasing UPLM

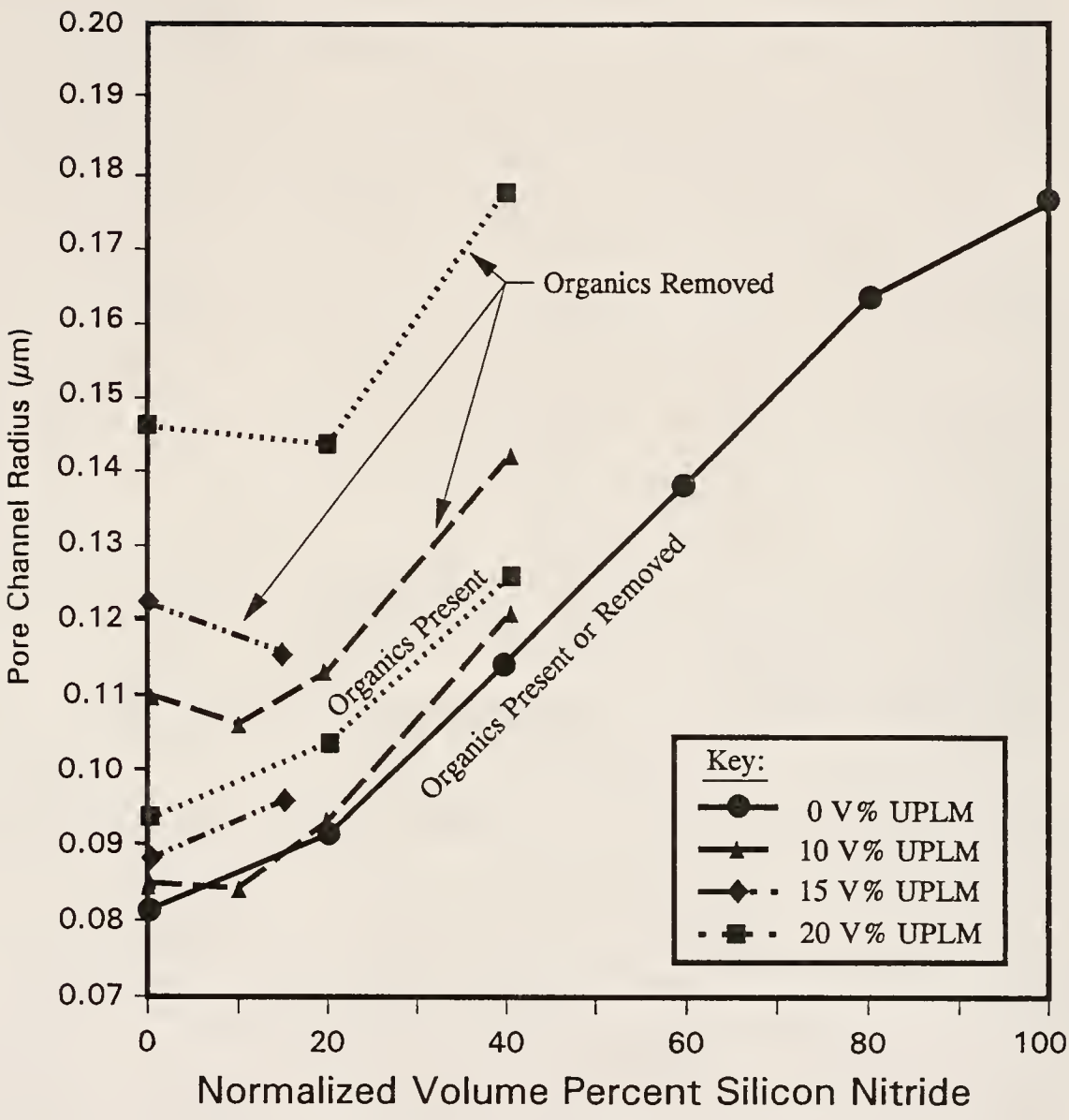


Figure 4.51 Median pore channel radius (volume basis, Hg-intrusion) with respect to normalized  $\text{Si}_3\text{N}_4$  concentration

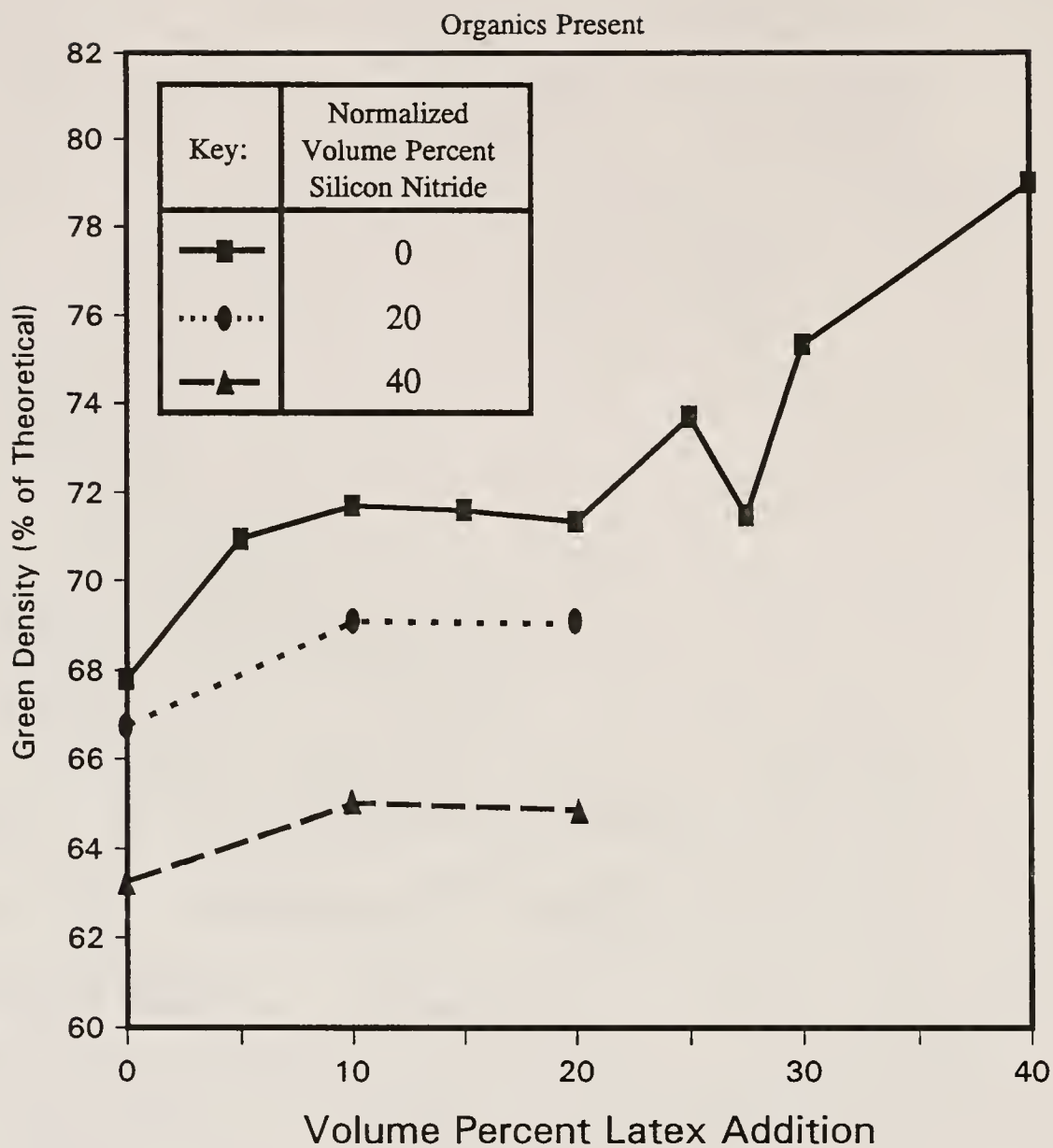


Figure 4.52

Green density (as a percent of theoretical density) with respect to V% UPLM for 0, 20, and 40 normalized V%  $\text{Si}_3\text{N}_4$  families

addition may be qualitatively explained by the Furnas model described in Chapter 2.

The dip in green density from 25 to 30 V% UPLM concentration corresponds somewhat to the dip in viscosity exhibited in the same system (see Figure 4.38). The minimum in viscosity with increasing V% UPLM concentration occurs over a larger range (i.e. 15 to 30 V% UPLM) however, and thus, does not exactly correlate with the dip in green density. It also should be noted that said dip is not apparent in the post pyrolysis Hg intrusion data (as shown below), and thus, may be an anomaly.

Figure 4.53 illustrates the increase in median pore channel radius (MPCR) with increasing UPLM concentration for the 0, 20 and 40 normalized V%  $\text{Si}_3\text{N}_4$  families of composites. Said increase is continuous, with one exception, throughout the range of samples studied.

Figure 4.54 illustrates the effect of both normalized V%  $\text{Si}_3\text{N}_4$  addition as well as V% UPLM addition upon green density and MPCR. As discussed above, green density (GD) increases to 10 V% (both UPLM and normalized V%  $\text{Si}_3\text{N}_4$ ), then plateaus to 15 V%. In this case, however, GD decreases slightly in the abscissa range from 15 to 20 V%. Again, MPCR increases with increasing concentration as well, with larger values being reported for samples having organics removed prior to testing.

Figure 4.55 illustrates the effect of latex size and size distribution upon GD and MPCR of compacts of BS glass containing 15 V% latex additions. The figure indicates that GD remains relatively constant with increasing latex size. Furthermore, dispersity seems to have little effect upon GD. However, MPCR does appear to be affected by the size and dispersity of the latex added. Pore channel radius continuously decreases with increasing size. This is important, since it is desirable that the ratio of MPCR to included pore size be as small as possible (as discussed below). This effect is most apparent in post-pyrolyzed samples, further amplifying the importance of this effect.



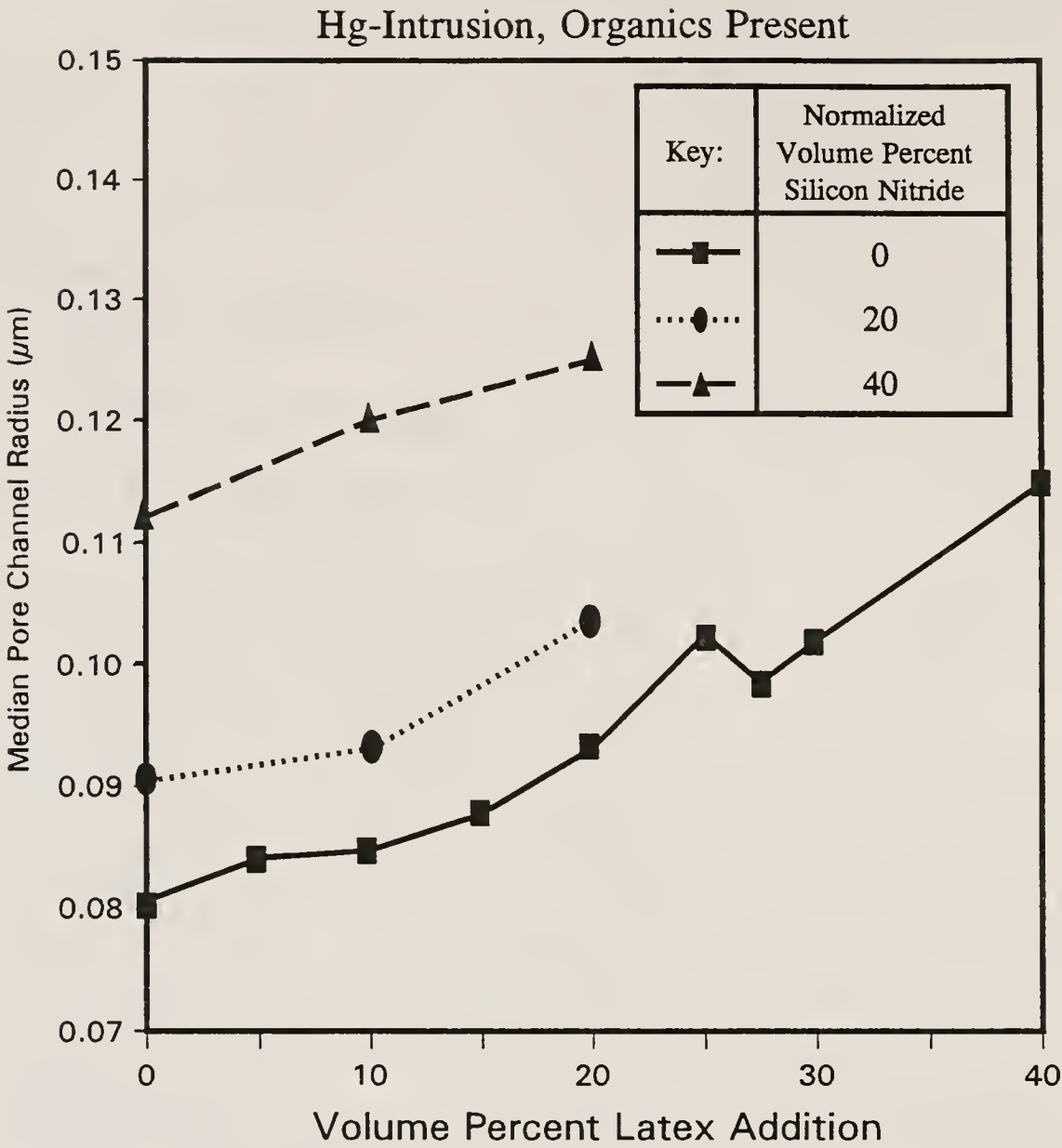


Figure 4.53      Illustration of the effect of V% UPLM addition upon median pore channel radius of green samples in 0, 20 and 40 normalized V% families of composites

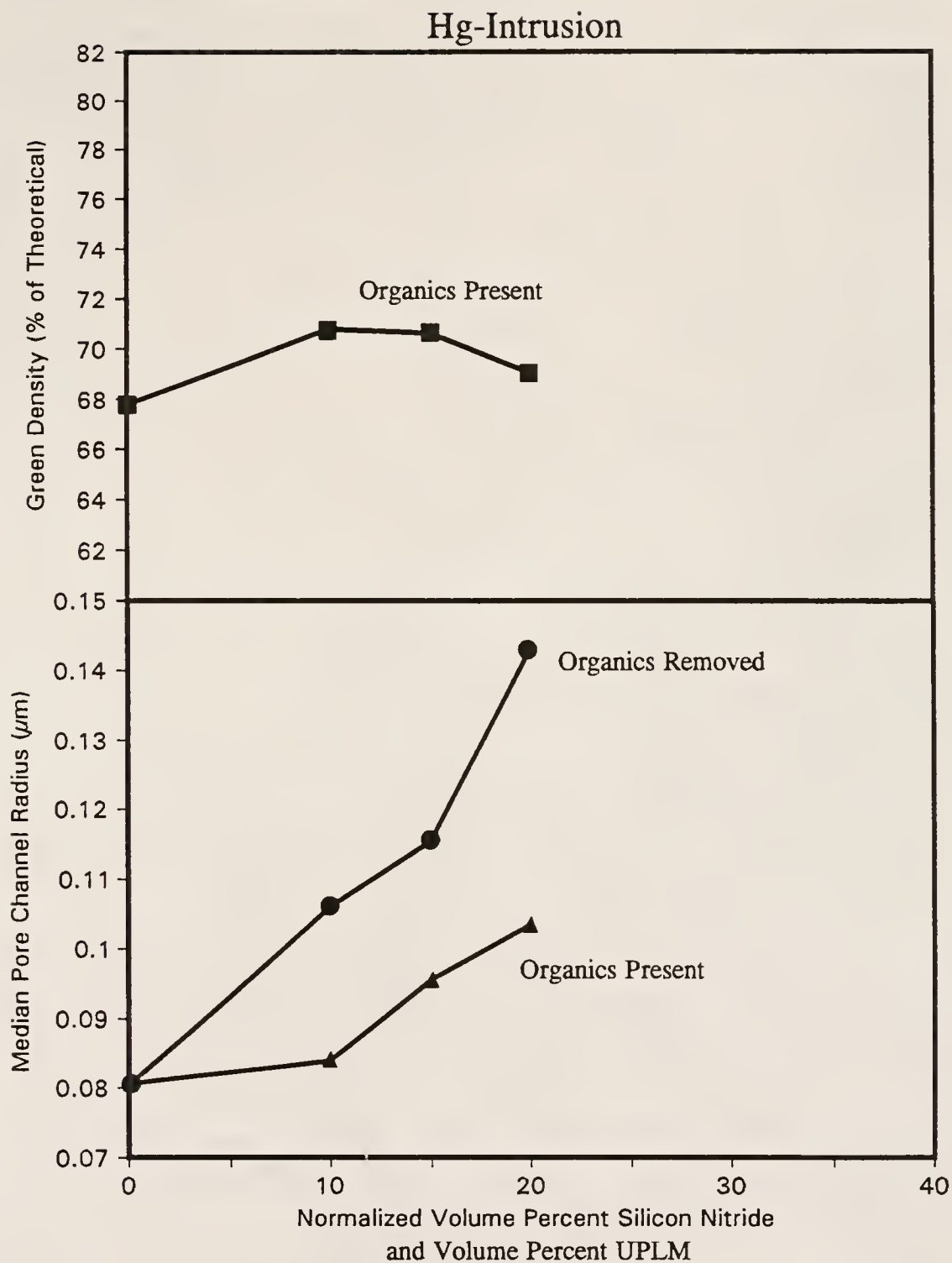


Figure 4.54

Illustration of the effect of both V% UPLM and normalized V%  $\text{Si}_3\text{N}_4$  additions on both GD and MPCR of composite compacts

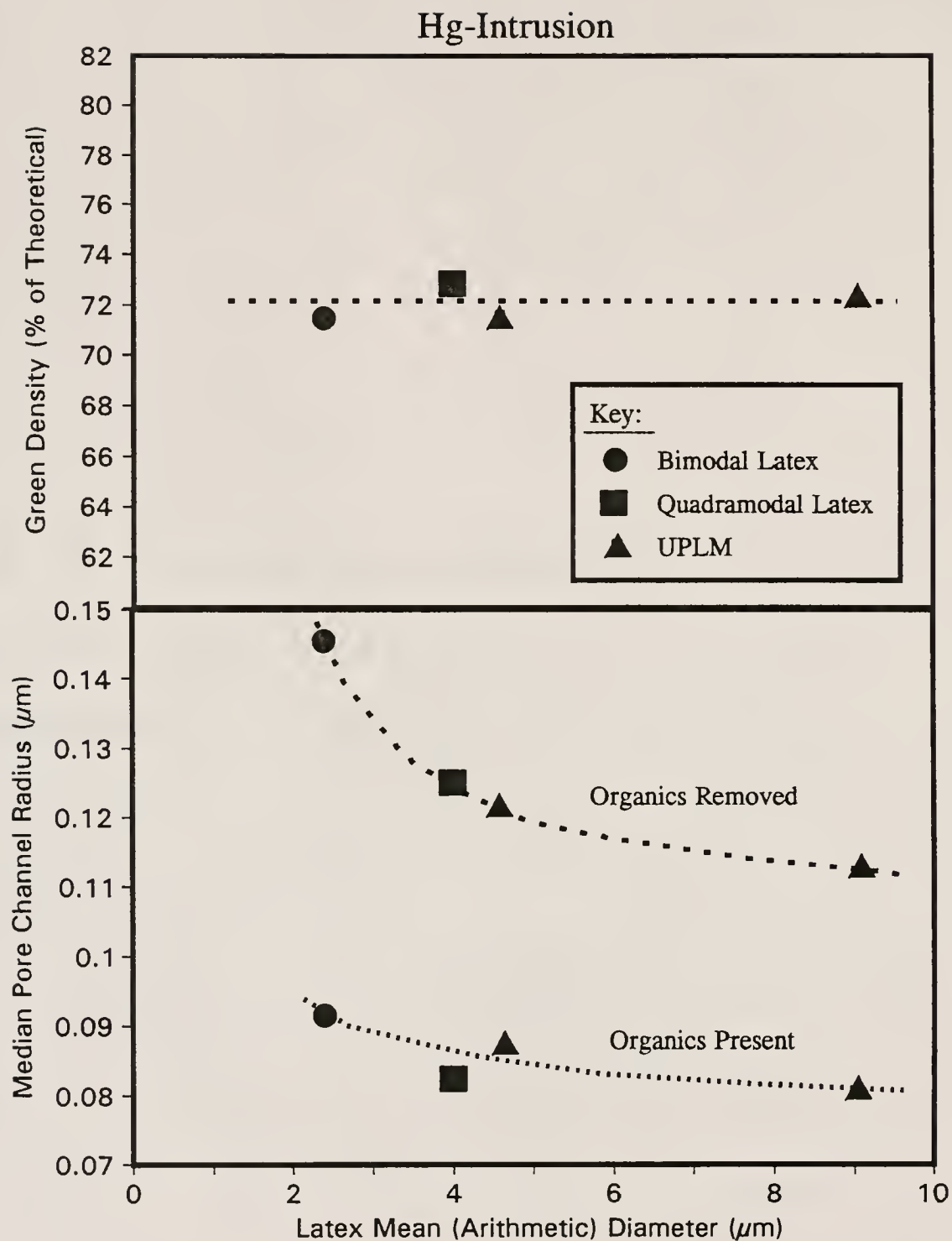


Figure 4.55

Illustration of the effect of size and size dispersity of added latex upon GD and MPCR for samples of ball milled BS glass containing 15 V% latex additions

Through the methodologies utilized in this study, it was possible to accurately predict the amount of porosity (for additions of up to 40 V% latex) added to the green structure via addition and subsequent pyrolysis of polystyrene latex microspheres. This was accomplished through the relation:

$$PPD = GD \times (1 - VF_{\text{Latex}})$$

where PPD is the predicted pyrolyzed density value, GD is the compact green density (pre-pyrolysis) and  $VF_{\text{Latex}}$  is the volume fraction of latex (solids basis).

Figure 4.56 illustrates these predictions. Figures 4.57 and 4.58 further confirm the ability to produce controlled amounts of porosity using the latex pyrolysis method outlined in this study. This is a very important factor in producing controlled porosity. In fact, after this step, it is necessary only to "sinter in" the porosity, to the final, desired porosity and pore structure.

Figure 4.59 illustrates that controlled amounts of porosity may be added to BS glass/latex composites regardless of latex size and size dispersity (within the size and size dispersity confines investigated in this study) via the methods used in this study.

A very interesting phenomenon is illustrated in Figure 4.60. The figure illustrates the difference between pre and post pyrolyzed MPCR as a function of UPLM (4.6  $\mu\text{m}$ ) concentration. It is evident that the difference between pre and post pyrolyzed MPCR increases monotonously with increasing UPLM concentration until a discontinuity, resultant from a dramatic increase in post pyrolysis MPCR, is encountered. This discontinuity results from the creation of a continuous pore structure. One that is a remnant of the pyrolyzed UPLMs. This is, in effect, a percolation onset, similar to that depicted in Figure 2.15.

Figure 4.60 shows that the extrapolated onset of the percolation occurs at approximately 23.5 V% UPLM. When multiplied by the

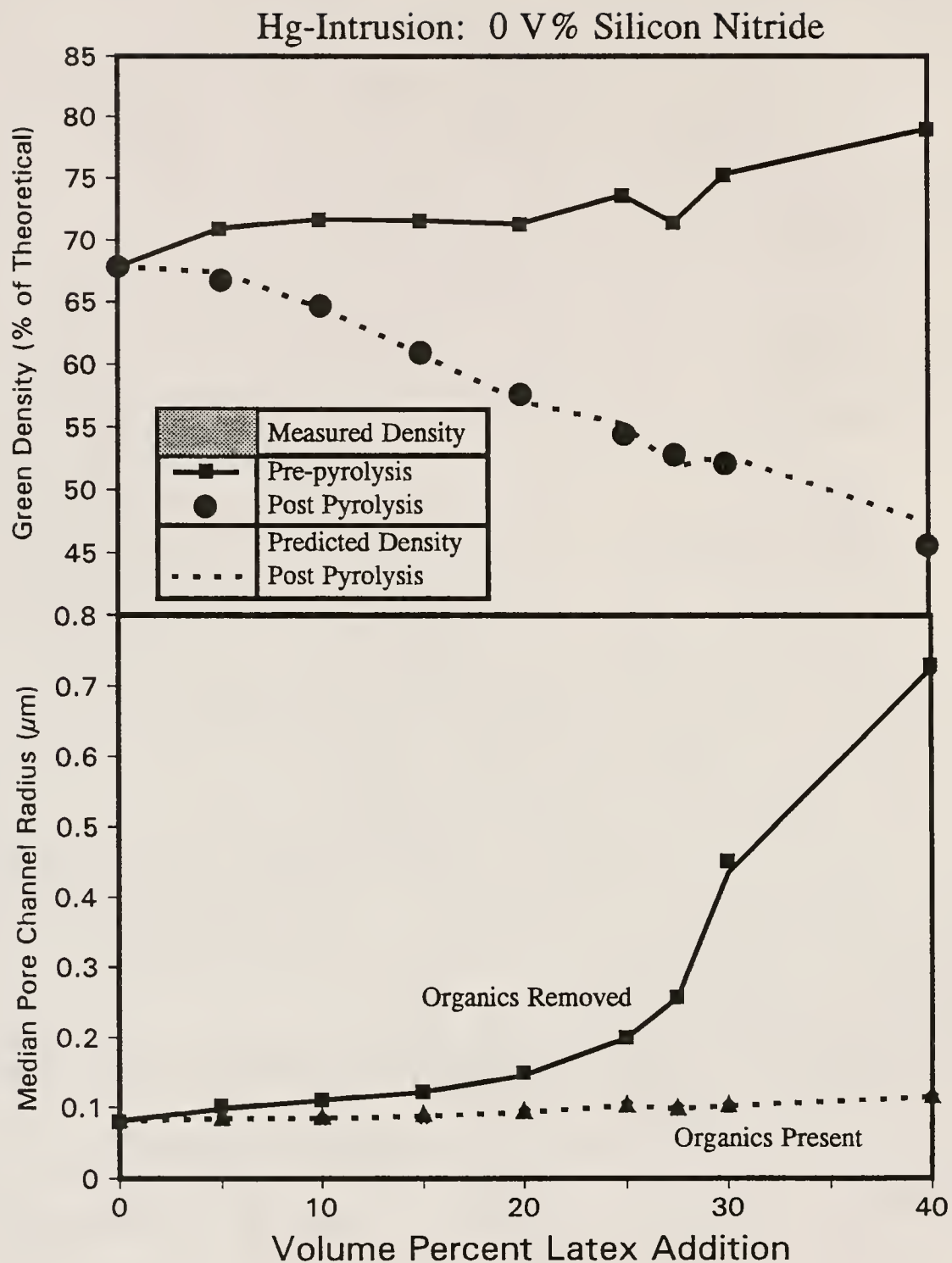


Figure 4.56

Illustration of the ability to produce controlled amounts of porosity in BS glass/UPLM composites via organics removal



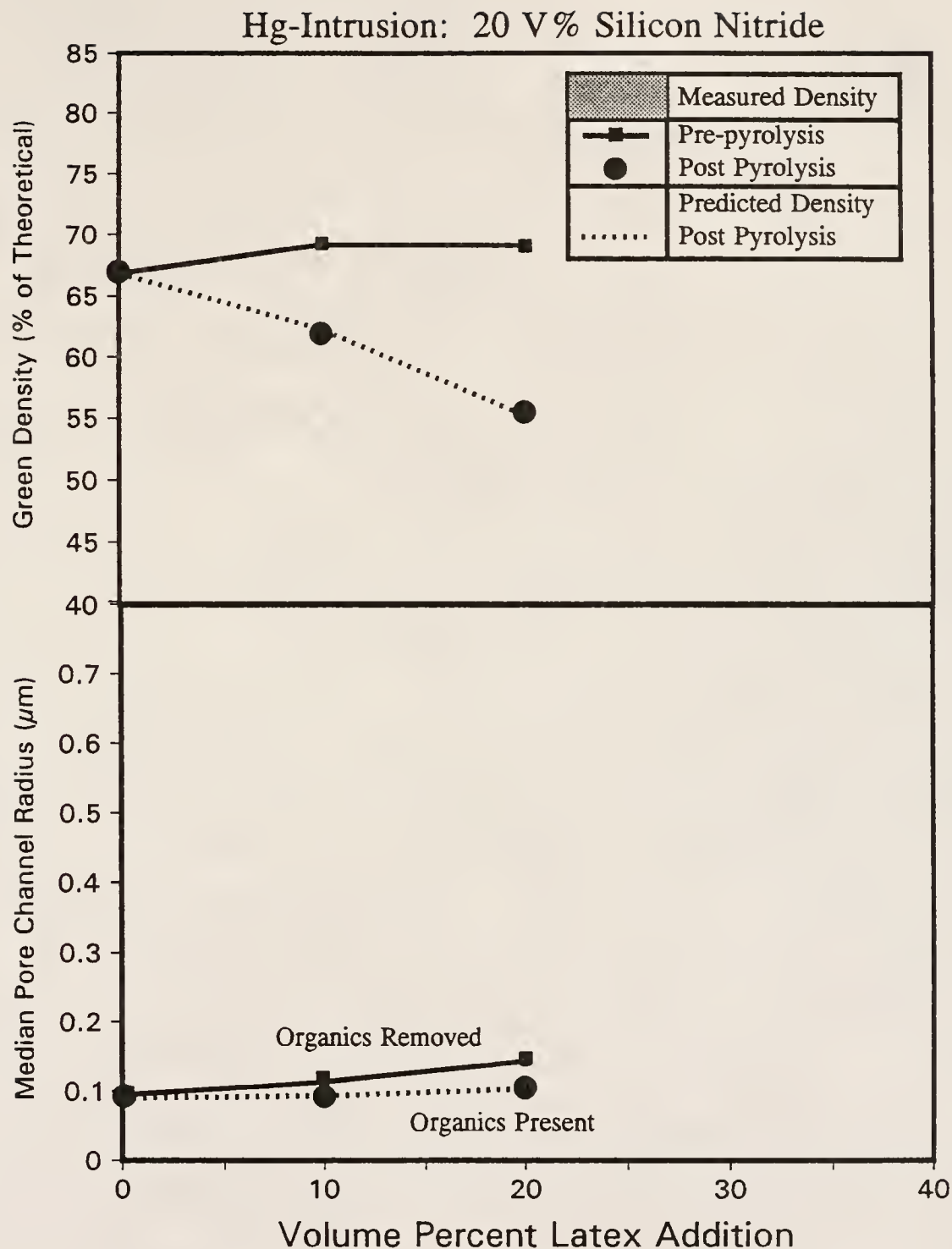


Figure 4.57

Illustration of the ability to create controlled amounts of porosity in BS glass/ $\text{Si}_3\text{N}_4$  (20 normalized V%)/UPLM composites via pyrolysis of latex

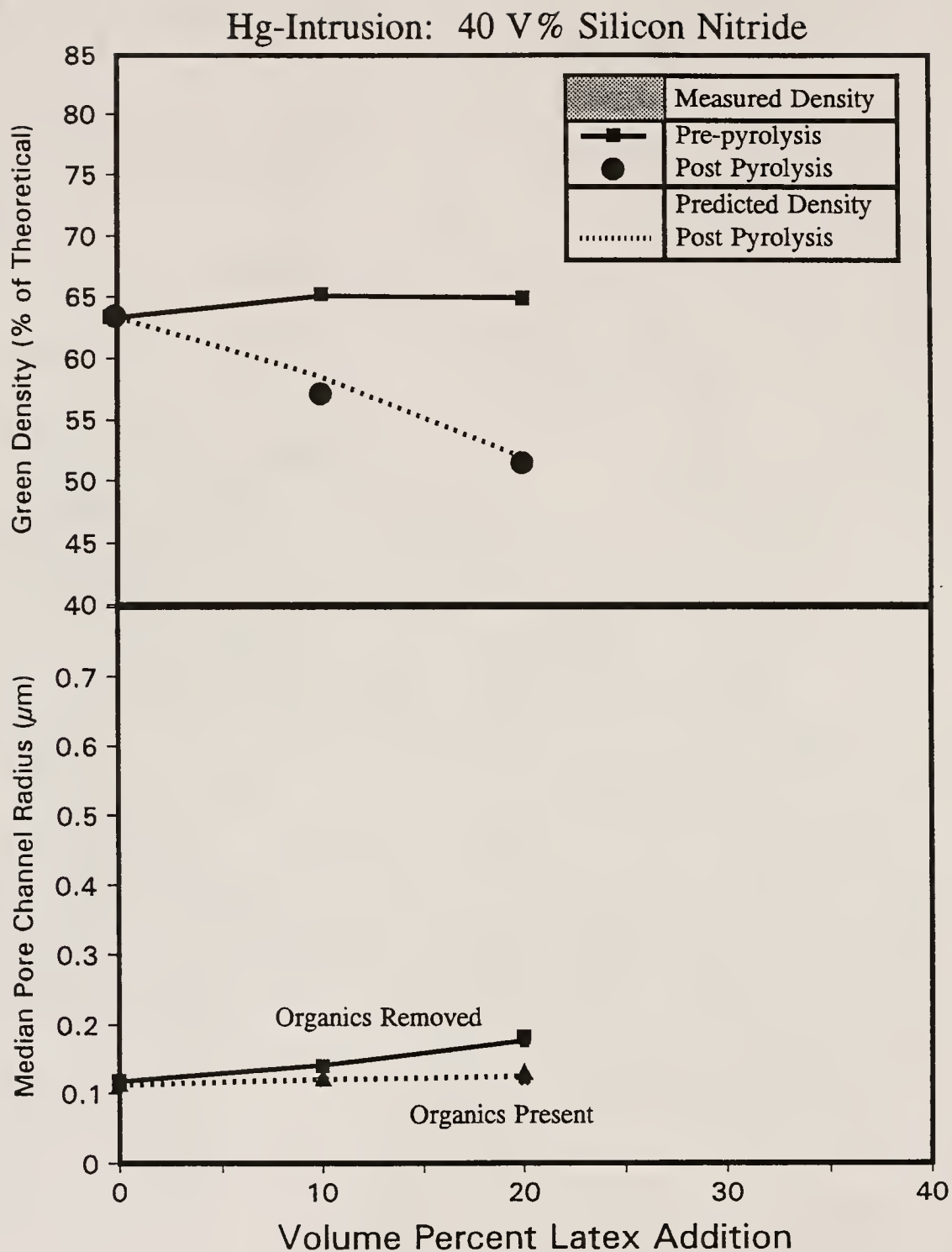


Figure 4.58

Illustration of the ability to produce controlled amounts of porosity in BS glass/Si<sub>3</sub>N<sub>4</sub> (40 normalized v%)/UPLM composites using organics removal methods

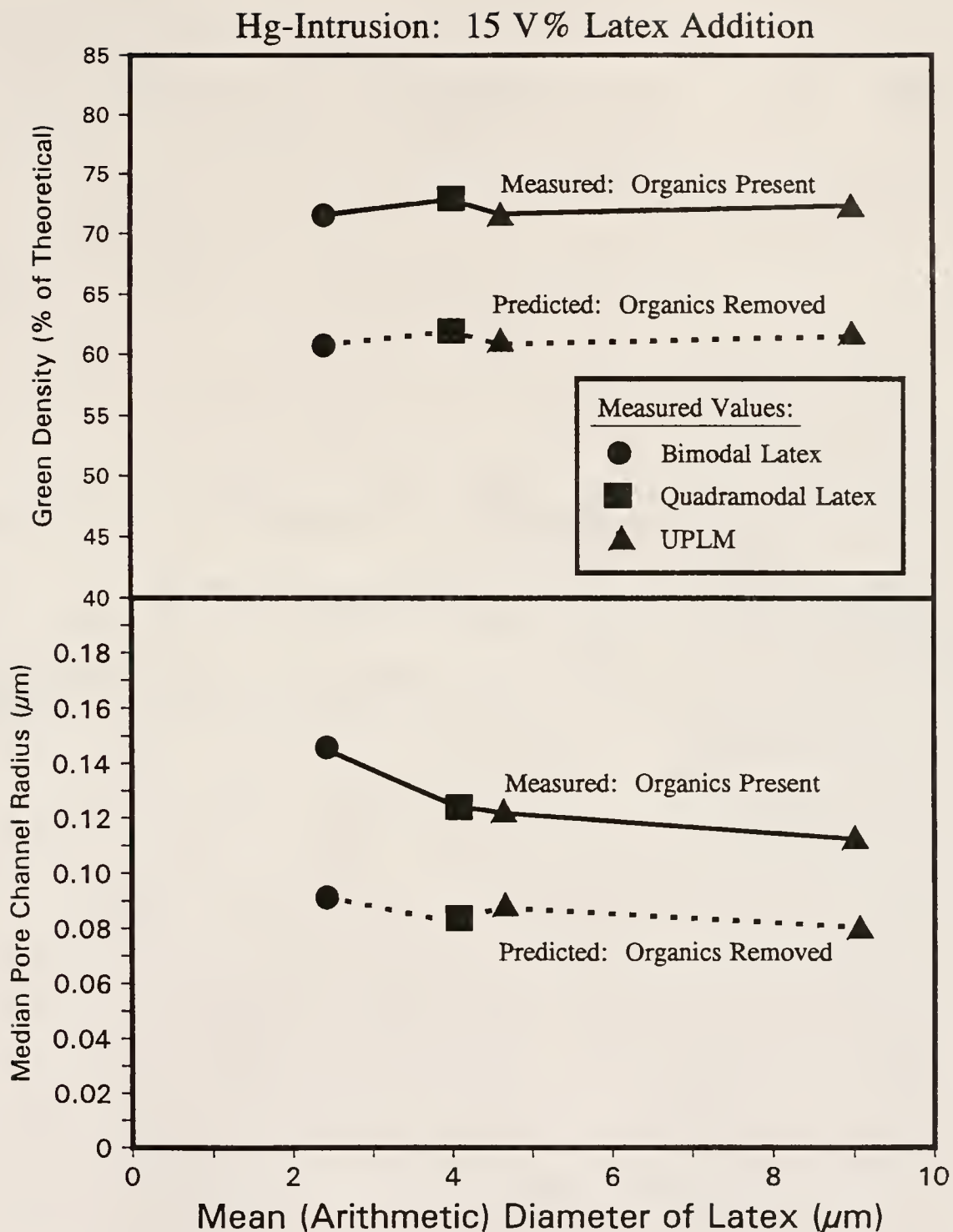


Figure 4.59

Illustration of the ability to produce controlled amounts of porosity over a range of latex sizes and size distributions, via the latex pyrolysis methods utilized in this study

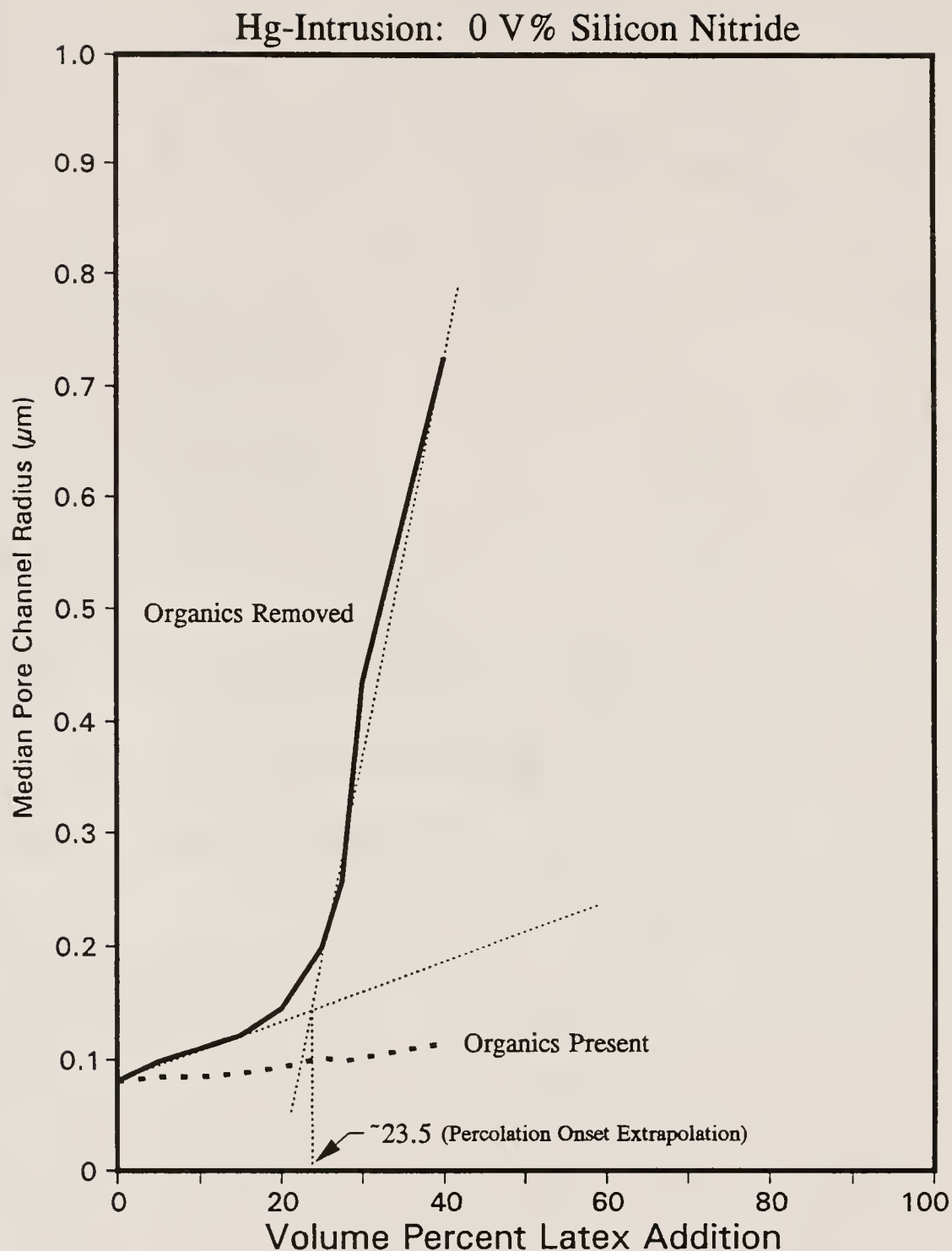


Figure 4.60

Illustration of the difference between pre and post pyrolysis MPCR as a function of V% UPLM concentration, the onset of discontinuity in post pyrolysis MPCR (~23.5 V% UPLM) is also depicted

interpolated green density of BS glass/UPLM composites at 23.5 V% UPLM (i.e. 0.732 or 73.2 % of space filled, see Figure 4.56), this value becomes approximately 17.2 % of the bulk space occupied by the compact. This value (17.2%) is very close to the value of 16 that has been experimentally measured for RCP structures (see Table 2.7 [83ZAL2]). It is also interesting to note, as mentioned in section 2.4.2, that all types of three dimensional packing (both repetitious and random) converge to a value of approximately 0.16 when PE is multiplied by the corresponding percolation onset (see Figure 2.16). Figure 4.60 adds further validity to the body of evidence that indicates that there is a universality of the value of PE multiplied by the percolation threshold.

These data further prove the existence of a percolation onset in this system, as well as the validity of applying percolation and related theories to the investigation of microstructure evolution in this system.

Representative pore channel radius distributions (Hg intrusion, post-pyrolysis) of BS glass/UPLM composites are depicted in Figure 4.61. The figure shows a change in the general shape of the pore channel size distribution with changing amounts of porosity additions via the latex addition/pyrolysis method used in this study. Relatively large amounts of included porosity (i.e. 25 V% or greater) tended to create a bimodality in the pore channel size distribution (PCSD), while smaller amounts of included porosity (i.e. below 25 V%) resulted in a skewed, monomodal PCSD. The transition concentration of included porosity occurred at approximately 25 V%, where it is evident that the PCSD is on the verge of becoming bimodal in nature.

It is interesting to note that the maximum of the larger mode of the 40 V% included porosity BS glass/UPLM composites occurs at approximately  $0.8\ \mu\text{m}$ , a value that is surprisingly close to the MPCR of pure  $4.6\ \mu\text{m}$  UPLM (the same UPLM used to make the above composite samples, compare Figures 4.46 and 4.61). This coincidence is surprising



## Hg-Intrusion, Post Pyrolysis

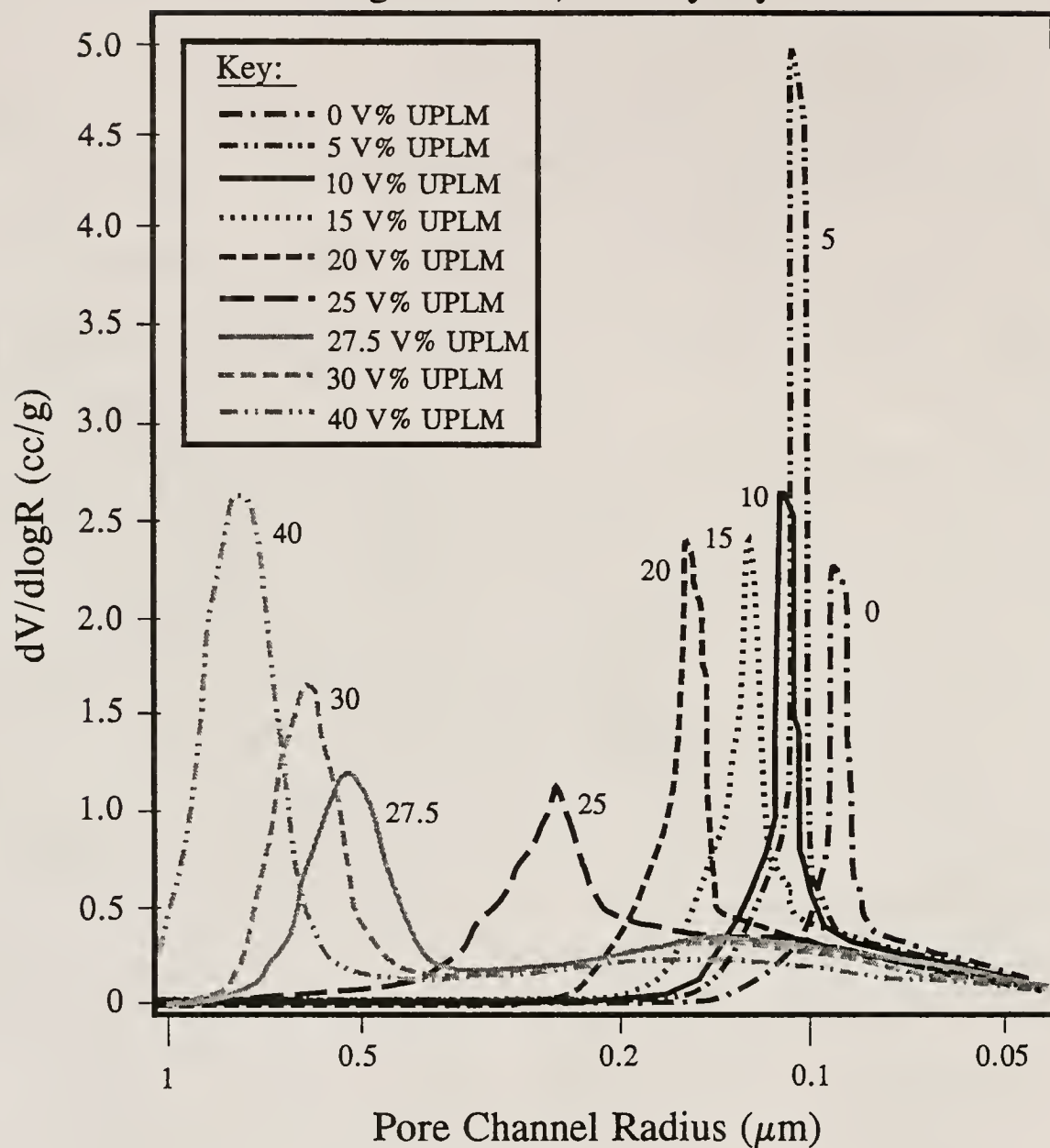


Figure 4.61

Hg intrusion (post-pyrolysis) pore channel size distributions (PCSDs) of BS glass/UPLM composites showing the changing nature of PCSD with changing amounts of included porosity

since the MPCR of the pure UPLM composites is a measure of the size of pore channels between UPLM spheres, while the PCSD of the BS glass/UPLM composites is a measure pore channels between ceramic particles, after pyrolysis (i.e. after thermal removal of UPLM additions). Thus, no physical relationship between the two analyses is apparent, and the phenomenon shall be considered only a coincidence.

It was not possible to directly compare the shapes and hystereses of the Hg intrusion/extrusion curves to the generic porosimetry hystereses of different microstructure categories, as illustrated in Figure 2.19, due to software and equipment limitations. However, several observations about the effect of this type of included porosity upon porosimetry hysteresis may be made. Table 4.4 depicts the pertinent available relationships between the porosimetry curves of the BS glass/UPLM composites produced. The stranded volume increases with an increasing amount of included porosity. It is not known whether this is a result of the larger MPCRs of the composite containing a larger amount of included porosity, or a result of the changing microstructure (i.e. from a spinodal-like structure to a ink-bottle type structure).

Second, the generic shape of all of the porosimetry hystereses differed somewhat from those depicted in Figure 2.19. The general shape of the porosimetry curves seemed to be that of a hybrid of a sphere microstructure (extrusion) and needle-like or a platey microstructure (intrusion).

The hysteresis was, by far, the smallest for the 0 V% UPLM composite. Said hysteresis increased with increasing V% UPLM up to about 20V% UPLM, then began to decrease above UPLM additions of 20 V%. Above 20V% UPLM addition, the porosimetry curves also changed shape somewhat.

The generic hystereses are what is generally expected from an ink bottle-type structure [88REE]. The small channels between ceramic particles impede Hg intrusion, while the spherical, included pores act as Hg reservoirs. Upon extrusion, these reservoirs must be emptied

Table 4.4

Pertinent Available Data for Porosimetry Curves  
of BS glass/UPLM Composites (Post-Pyrolysis)

I.D. Number	V% UPLM	Stranded Volume (%)	Relative Magnitude of Hysteresis	Hysteresis Shape
03209001	0	26.3	9	Needle/Platey (I/E)
05109102	5	32.3	5	Needle/Platey (I/E)
01039101	10	45.6	2	Needle/Platey (I) Rod/Sphere (E)
05069101	15	50.0	1	Needle/Platey (I) Rod/Sphere (E)
02069101	20	49.6	8	Needle/Platey (I) Rod/Sphere (E)
05109101	25	54.2	7	Needle/Rod (I) Sphere (E)
06019101	27.5	60.0	6	Needle/Rod (I) Sphere (E)
05079101	30	61.2	4	Needle/Rod (I) Sphere (E)
05079102	40	73.0	3	Needle/Rod (I) Sphere (E)

- Notes:
1. Stranded volume is displayed as a percent of total volume intruded.
  2. Relative magnitude of hysteresis is 1 for largest, 9 for smallest, there is little difference from 4 to 7.
  3. Hysteresis shape denotes a comparison with generic curves (see Figure 2.19), I denotes intrusion, E denotes extrusion.

through the relatively fine pore structure between ceramic particles. Thus a highly hysteretic porosimetry curve would be expected. This hysteretic structure changes depending upon the relative amounts of included porosity (reservoirs) and upon the relative size of the pore structure of the ceramic (which increases with increasingly large additions of UPLM, see Figure 4.61).

Table 4.5 shows a comparison between the densities of representative, non-latex-containing, green and pyrolyzed samples, measured using both Hg porosimetry and the Archimedes method. This table provides a measure of comparison between the Hg porosimetry values and the archimedes density values, as well as a measure of the difference between green versus pyrolyzed samples.

#### 4.2.3.4 Effects of Aging and Sonication Upon Green Properties

##### 4.2.3.4.1 Sonication

Sonic dismembration was utilized in this study to aid in proper dispersion. In order to determine the proper sonic dismembration treatment, a sonication experiment was performed as outlined in section 3.4.2.2.4.

Figure 4.62 illustrates the change in viscosity of the suspension tested, with increasing sonication duration. Figure 4.63 depicts the analogous relationship for properties measurable by Hg intrusion porosimetry (i.e. MPCR and GD). It is readily apparent that a minimal amount of sonication results in a significant reduction in viscosity as well as in an increase in both green density and median pore channel radius. From Figure 4.63, it is evident that the maximum green density increases monotonously up to approximately 90 m of sonication, then appears to plateau, hitting a relative maximum at approximately 120 m. It is also apparent that MPCR increases and GD decreases slightly after 120 m of sonication. This is most likely resultant from solvent evaporation, and not from an optimum value of sonication time, as the

Table 4.5

Comparison of Green and Pyrolyzed Densities  
and Measurement Method

Batch Number	Composition (BS Glass/SN)	Green Density (% Th, Hg Intrusion)	Pyrolyzed Density (% Th)	
			Hg Intrusion	Archimedes Method
03209001	100/0	67.8	68.3	68.2
12119001	100/0	72.0	71.9	71.8
03219001	80/20	66.8	66.7	66.8
03199001	60/40	63.3	62.7	62.5
02149101	40/60	58.2	57.3	*
02149102	20/80	54.5	53.5	*
01319101	0/100	51.9	51.0	*

Note: \* Indicates that sample was too delicate for archimedes  
method density analysis



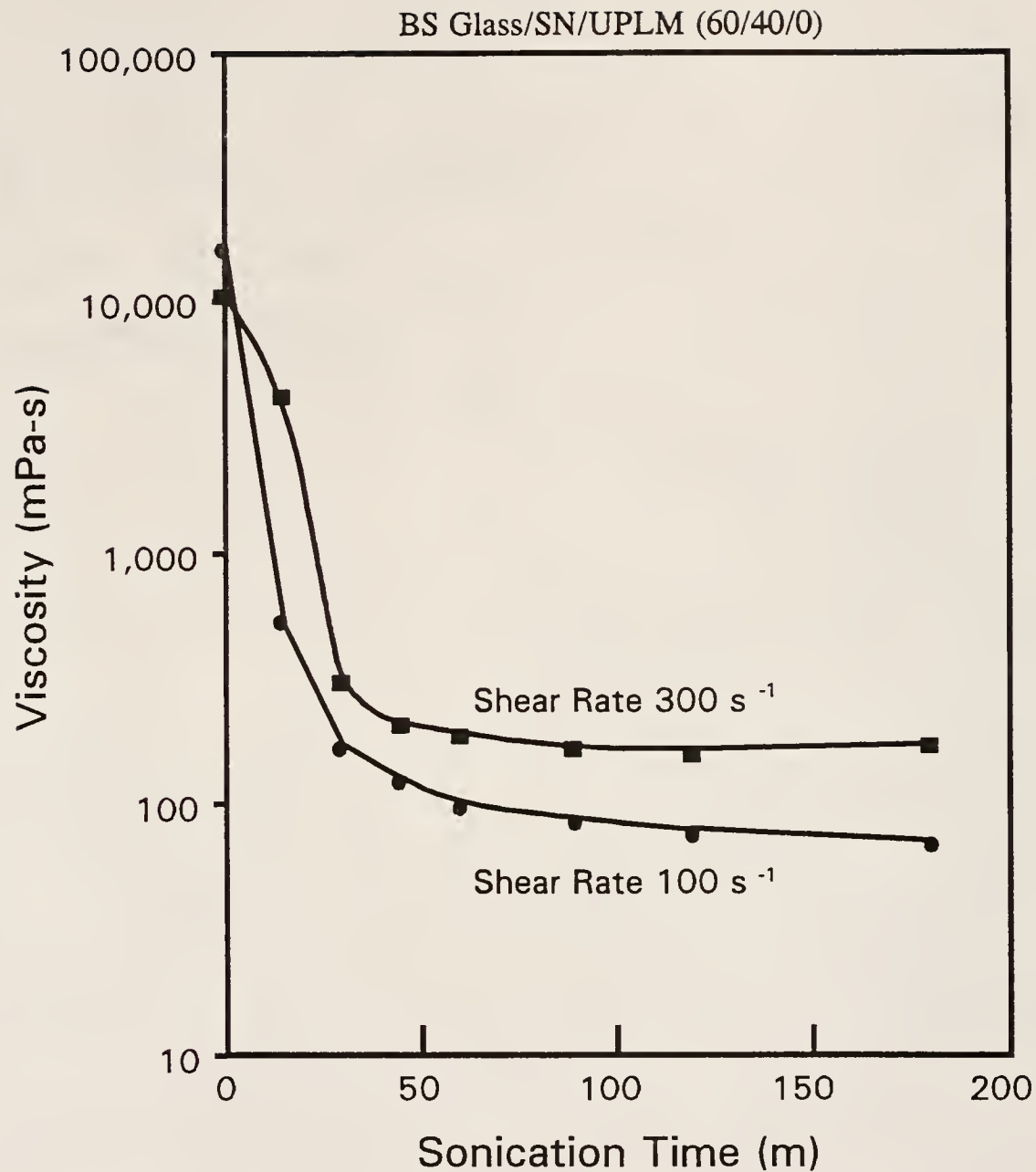


Figure 4.62      Effect of sonication duration upon suspension viscosity

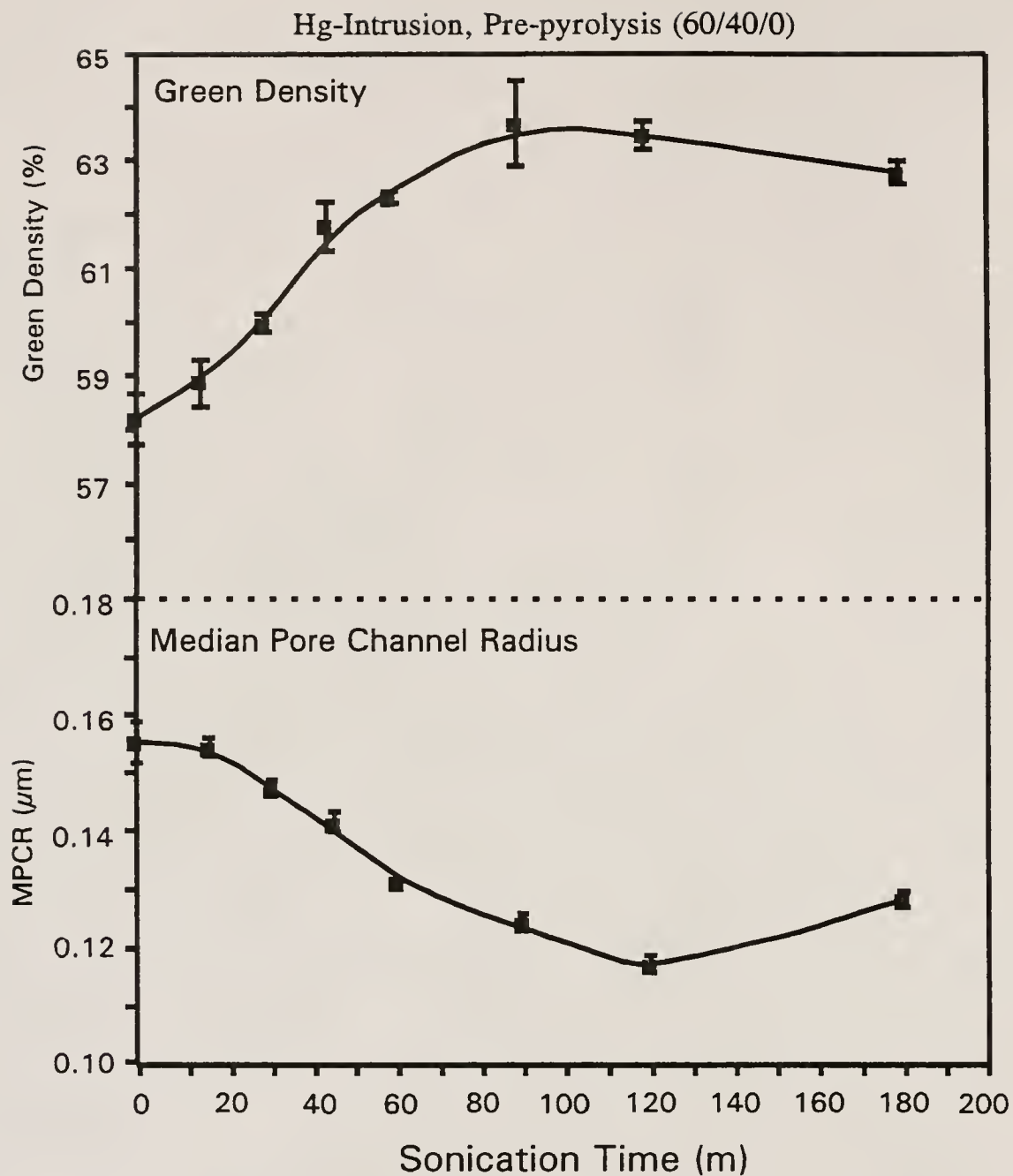


Figure 4.63

Effect of sonication duration upon GD and MPCR of the composite suspension tested

container was opened several times during the experiment. This effect is depicted in Figure 4.64.

Figures 4.65 to 4.68 depict micrographs of representative surfaces of green compacts treated to 0, 30, 60 and 120 m of sonication respectively. It is apparent from the figure that sonication enhances packing efficiency.

From these data (primarily green density data) it was decided to expose each ceramic loaded suspension, in this study, to no less than 120 m of sonic dismembration prior to casting compacts. This practice was adopted for all of the ceramic loaded suspensions investigated.

#### 4.2.3.4.2 Aging

Frequently it is desirable to age a suspension, in order to provide better homogenization of the dispersants, powders, solvent, etc. In this study, aging was performed on a rotisserie-type mixer. The optimum time for aging the suspensions was determined experimentally. The details of this experiment are outlined in section 3.4.2.2.4.

Figure 4.69 illustrates the effect of aging on suspension viscosity, while Figure 4.70 depicts the effect of suspension aging upon GD and MPCR. Both figures indicate that aging is immediately beneficial. The benefit from aging appears to plateau at about 24 h of aging. As in the sonication experiment, longer times appear to lead to slightly higher viscosity suspensions that make slightly less dense compacts having slightly larger MPCRs. Again, this is probably attributable to solvent evaporation rather than an optimum aging time. From these data, it was decided that all composite suspensions containing ceramic would be aged for no less than 48 h.

Figure 4.71 depicts solids loading with aging. The solids loading was measured only twice during this experiment. However the solids loading increased similar to the increase during the sonication experiment. Again, the suspension container was opened frequently

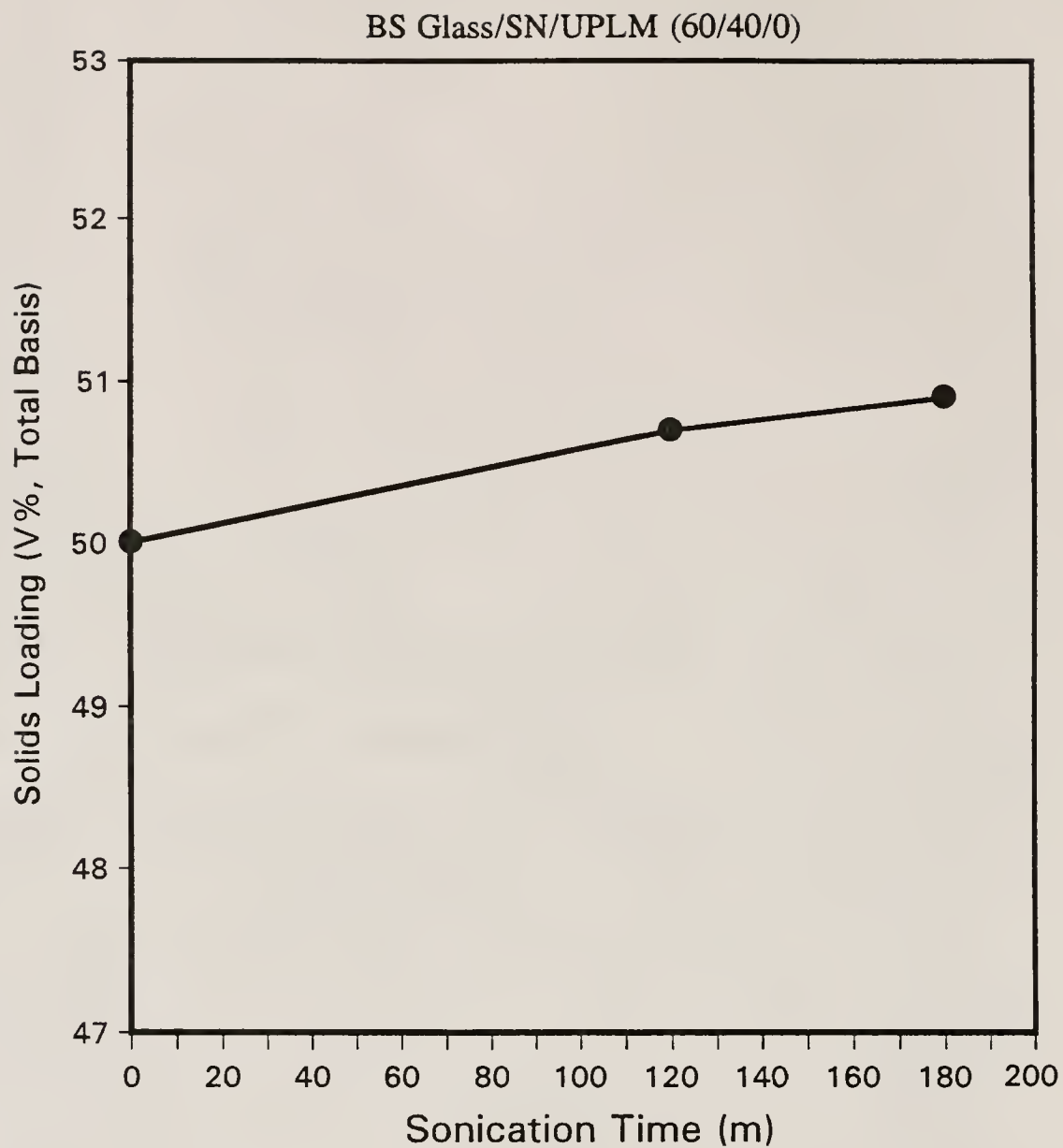


Figure 4.64

Measured change in percent solids loading occurring throughout the sonication study



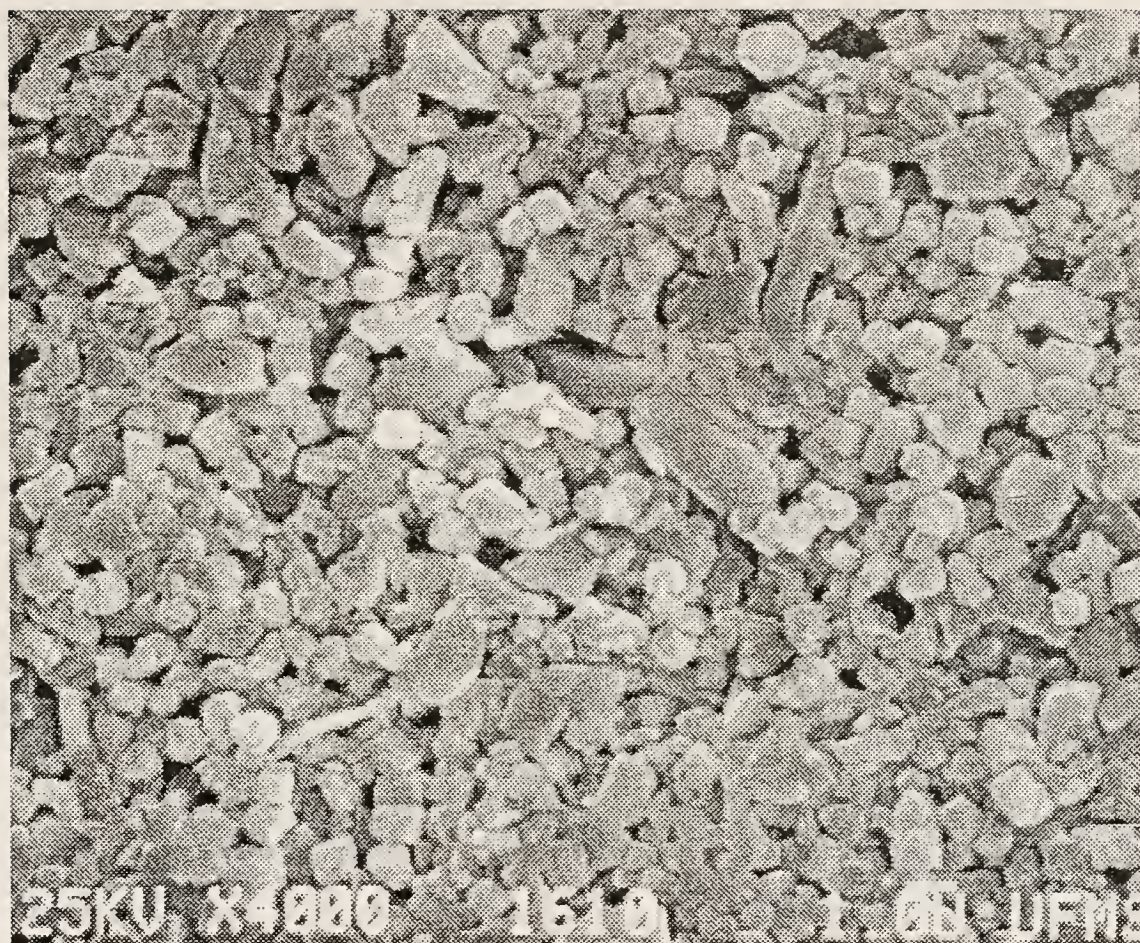


Figure 4.65

SEM micrograph of the surface of a compact subjected to 0 m of sonic dismembration (sonication study)



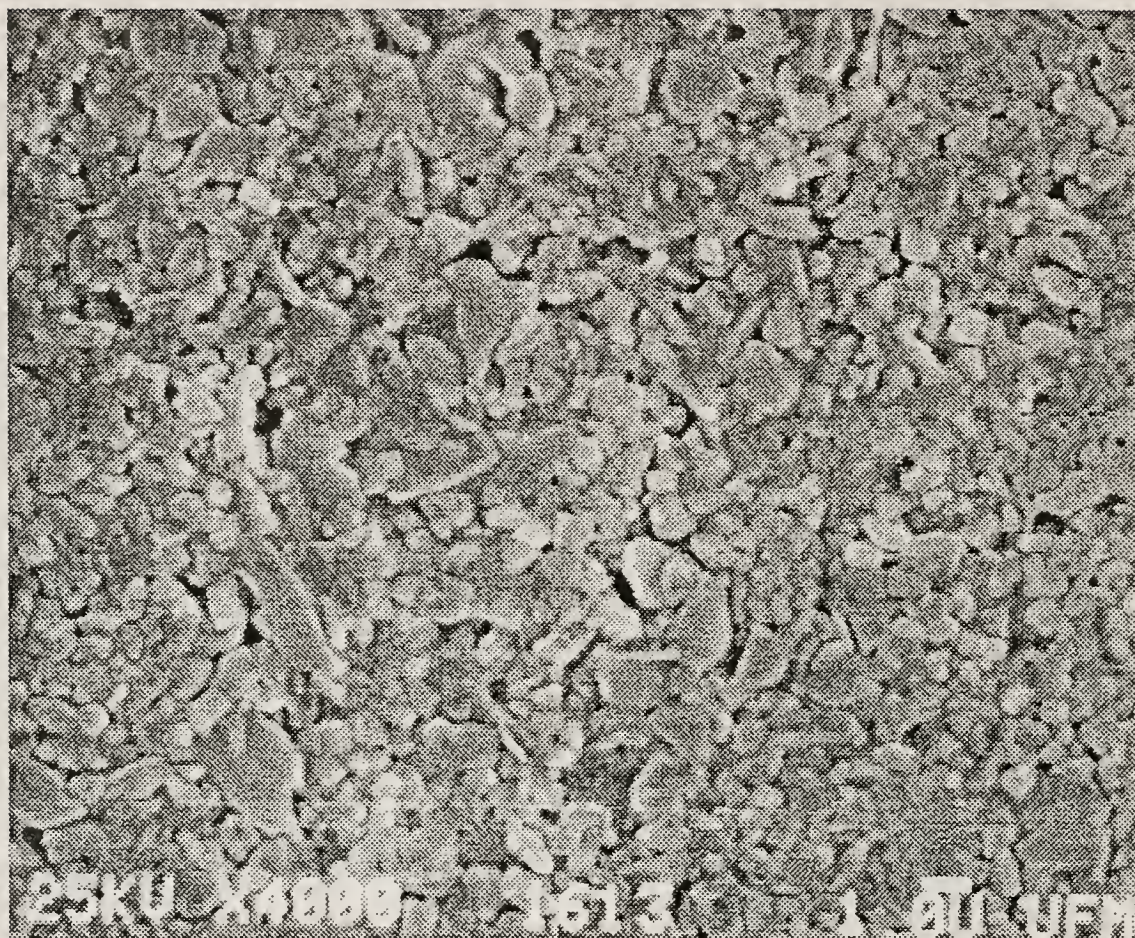


Figure 4.66

SEM micrograph of the surface of a compact, the anomalous suspension was subjected to 30 m of sonic dismembration



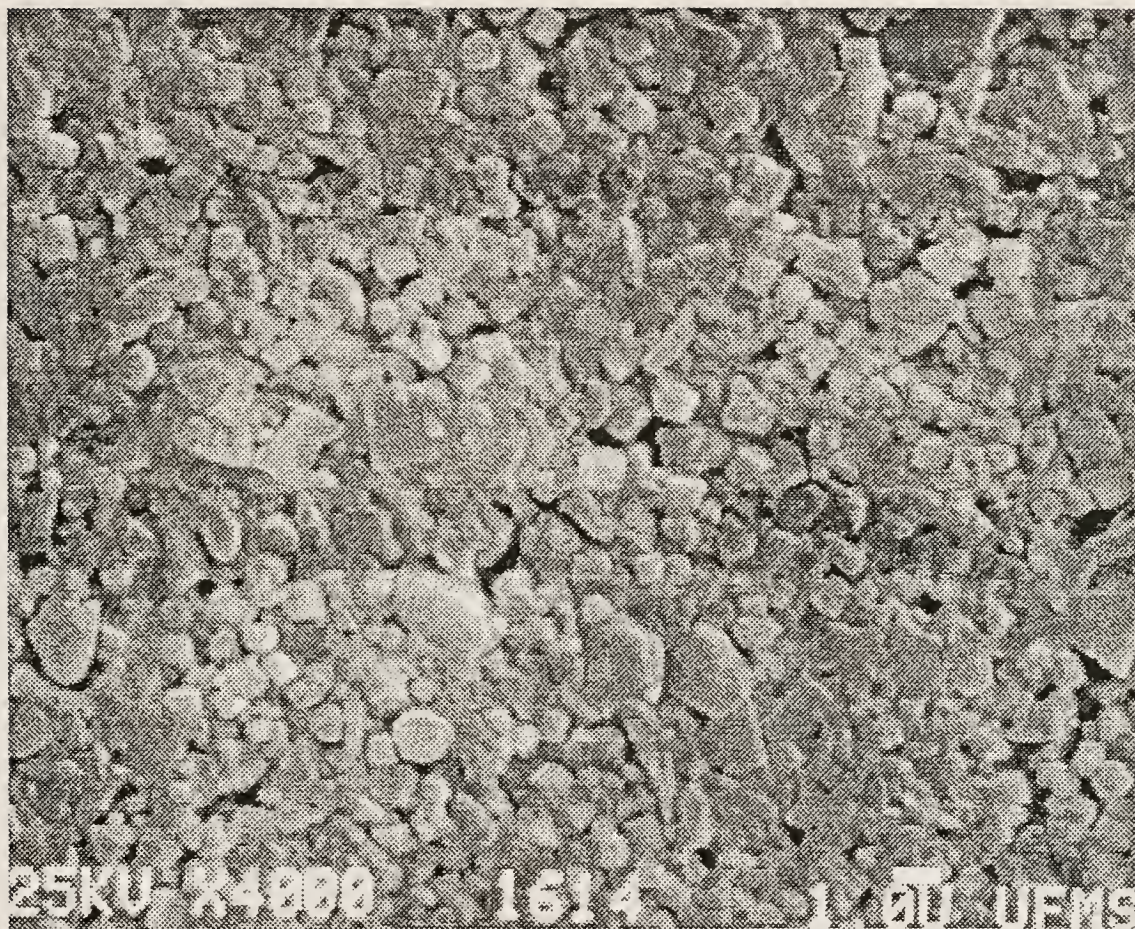


Figure 4.67

SEM micrograph illustrating the surface of a compact, the corresponding suspension was subjected to 60 m of sonic dismembration



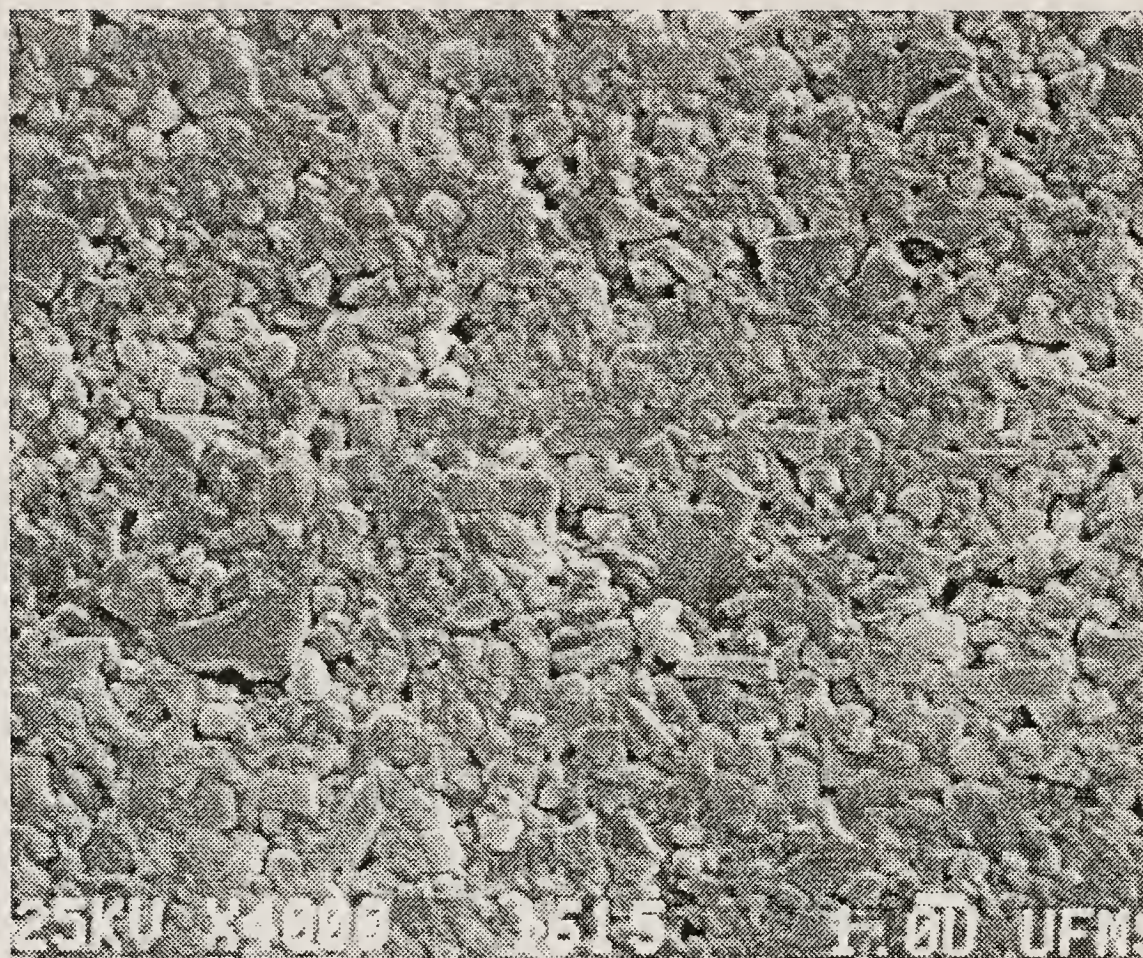


Figure 4.68

SEM micrograph depicting the surface of a compact, the analogous suspension was subjected to 120 m of sonic dismembration

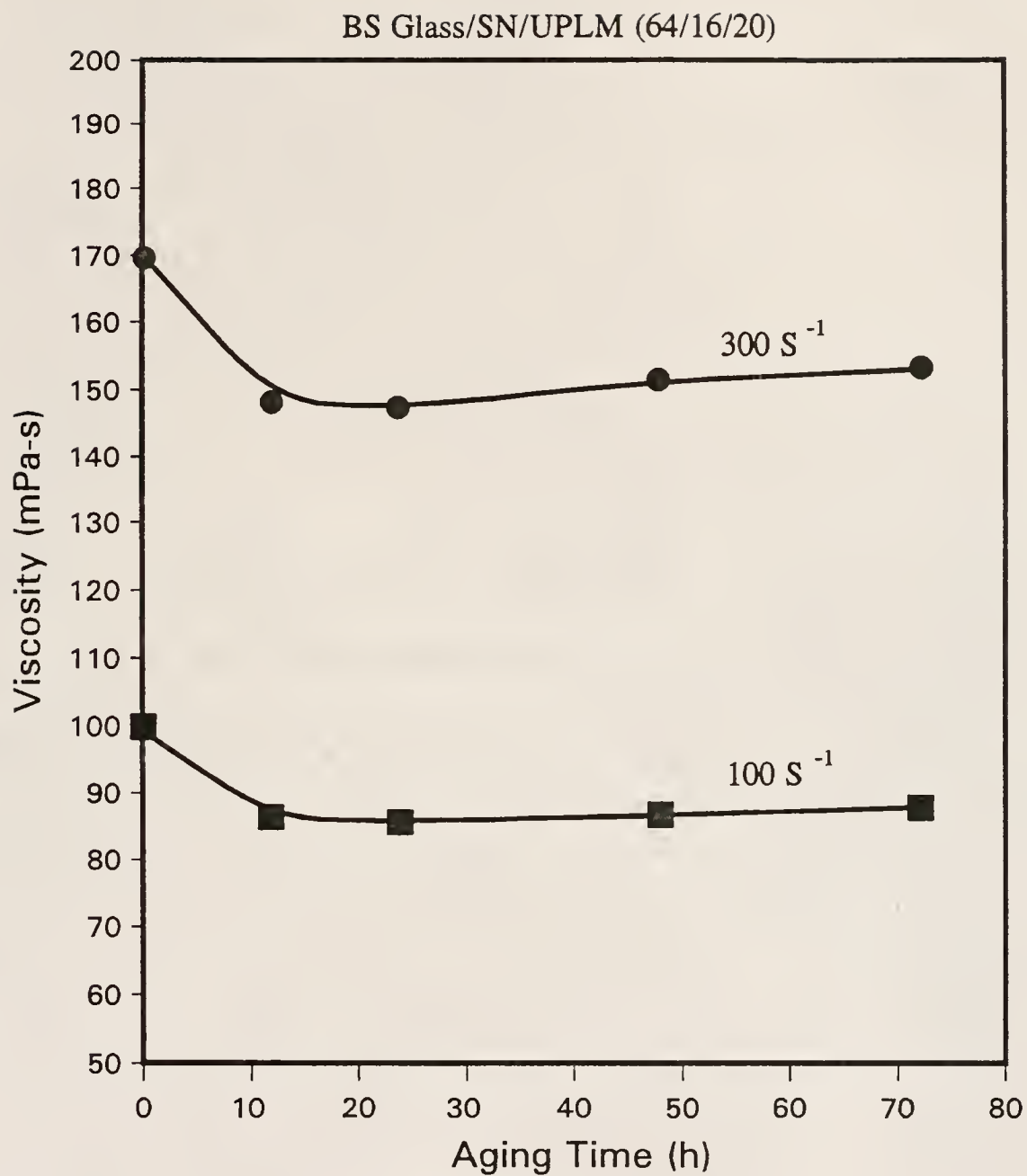


Figure 4.69

Illustration of the effect of aging upon suspension viscosity

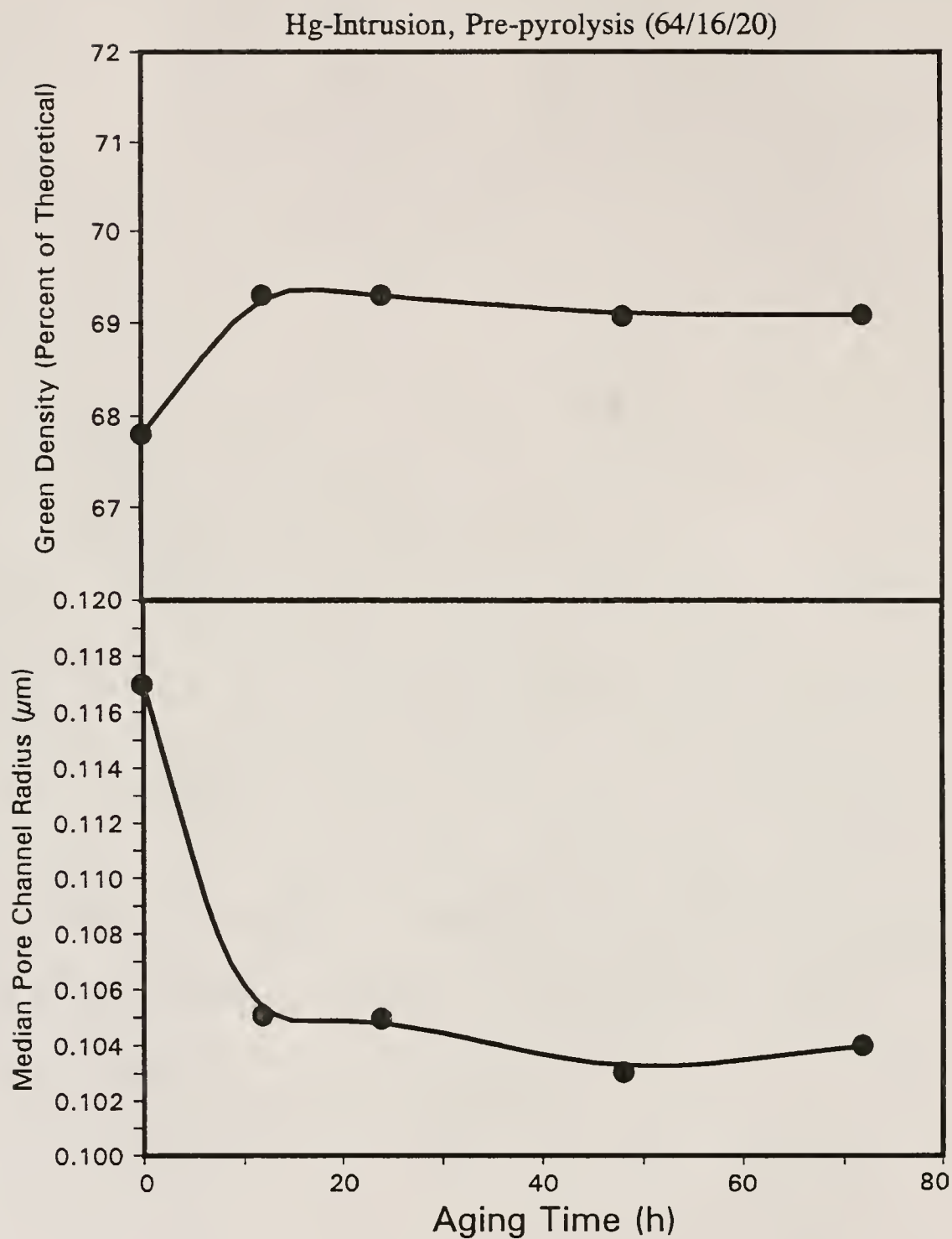


Figure 4.70

Illustration of the effect of suspension aging upon GD and MPCR of resulting compacts



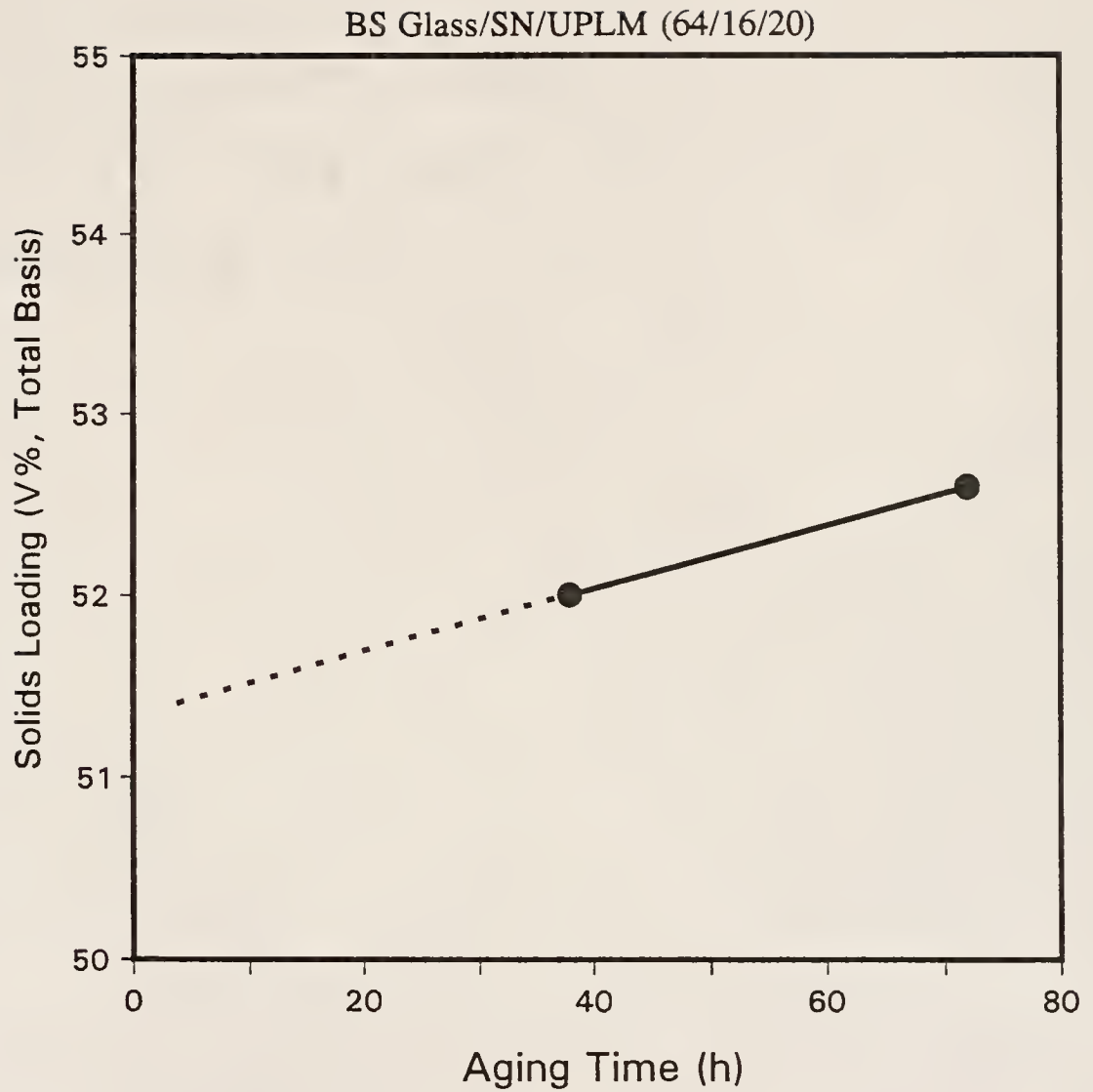


Figure 4.71

The increase in solids loading measured during the aging experiment

during the experiment, allowing evaporation. This study had the further disadvantage that, because this is a relatively low energy process, soft agglomerates that were created as suspension dried on the container walls would not necessarily be dismembrated (as in the sonication experiment).

### 4.3 Thermal Processing and Characterization

#### 4.3.1 Removal of Organics

In low dielectric loss insulator applications it is important that all organic materials and elemental carbon be removed to levels below 100 ppm (and ideally to below 30 ppm), prior to sintering, in order to insure that materials having favorable dielectric properties (i.e. insulation resistance and dielectric loss) were produced [91KUM2]. Unfortunately, residual carbon analysis (RCA) was not performed during this study. However, residual carbon levels above 100 ppm usually result in a slight discoloring of samples subsequent to the pyrolysis treatment [91KUM2].

For the experimental purposes of this study, it was most desired that all of the composite compositions experience the same pyrolysis heat treatment. Thus, the heat treatment schedule for organics removal was formulated to remove all amounts of latex used (i.e. up to 40 V%), and the same heat treatment schedule was used for all of the composite compositions. Therefore, it is important to note that the pyrolysis heat treatment schedule was longer than necessary in most cases.

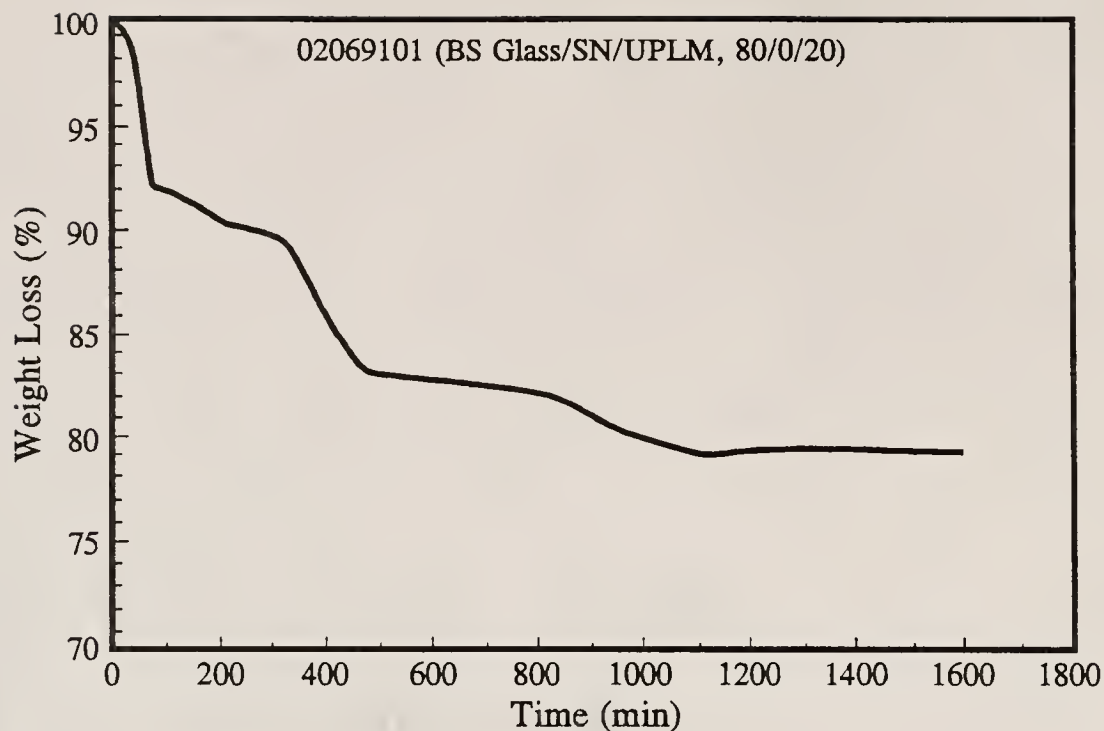
The methodology utilized to determine the pyrolysis schedule, as well as the actual pyrolysis schedule used, is described in sections 3.5 and 3.6. While not optimized, the heat treatment schedule proved adequate, providing samples having  $\tan(\delta)$  values comparable to literature values (as discussed below). This section presents thermal analysis data in order to better understand the organics removal process in this system.

Figure 4.72 illustrates time and temperature based TGA analyses of a sample (BS glass/SN/UPLM, 80/0/20) heat treated with the pyrolysis schedule used in this study (see Figure 3.10). This sample is representative of the entire composite system in that it contains an appreciable amount of latex UPLM as well as the proper amount of the dispersant (PVP K30). For the composition illustrated in Figure 4.72 a total weight loss of approximately 21 wt% is expected. It is interesting to note, from Figure 4.72, that approximately 8 weight % of the composite was lost at temperatures below 125 °C. This is probably due to evaporation of residual EtOH within the UPLM. This is logical since the precursor powders were carefully dried and kept in well-sealed storage containers prior to the batching process, while the compacts were formed from a wet (EtOH) process and were dried, at ambient temperature only, prior to the thermolysis treatment.

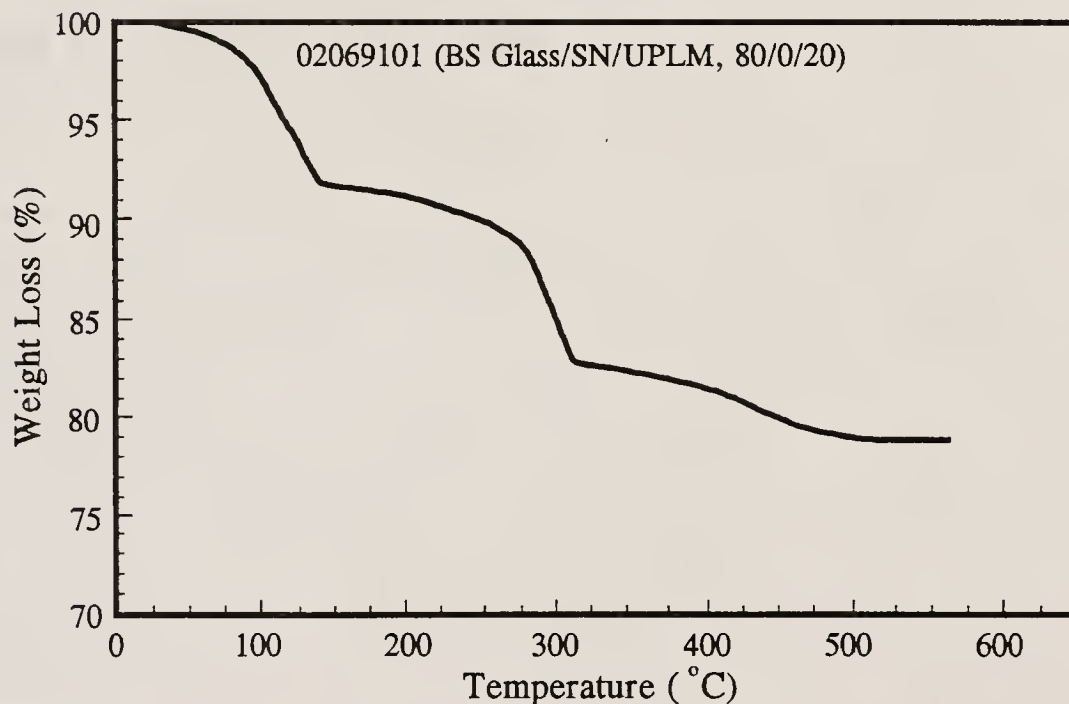
Figure 4.72 also illustrates a plateau toward the end of the pyrolysis treatment. This indicates that polymer removal is as complete as possible at the maximum temperature of heat treatment.

Figure 4.73 illustrates TGA and DTA analyses of the latex used in this study. Thermogravimetric analysis indicates that the UPLM powders pyrolyze over a sharp temperature range near 400 °C, leaving very little ash. It should be noted that the weight loss resultant from latex thermolysis, as indicated in Figure 4.72, occurred over a broader, lower temperature range (i.e. near 300 °C). Thus, it is important to note that the effects of both heating rate (i.e. 10 °C/min. versus 0.33 °C/min.) and (i.e. pyrolysis acceleration due to the presence of ceramic powder) can influence the pyrolysis process [88REE].

Differential thermal analysis of the latex powder indicates that the pyrolysis process is complex. The reaction corresponding to the major TGA weight loss is endothermic, indicating that the reaction mechanism is probably a type of polymer scission. At higher



A. Time Based



B. Temperature Based

Figure 4.72

Thermogravimetric data of a representative sample (80/0/20 BS Glass/SN/UPLM) heat treated using the pyrolysis schedule used in this study, A. time based, B. temperature based

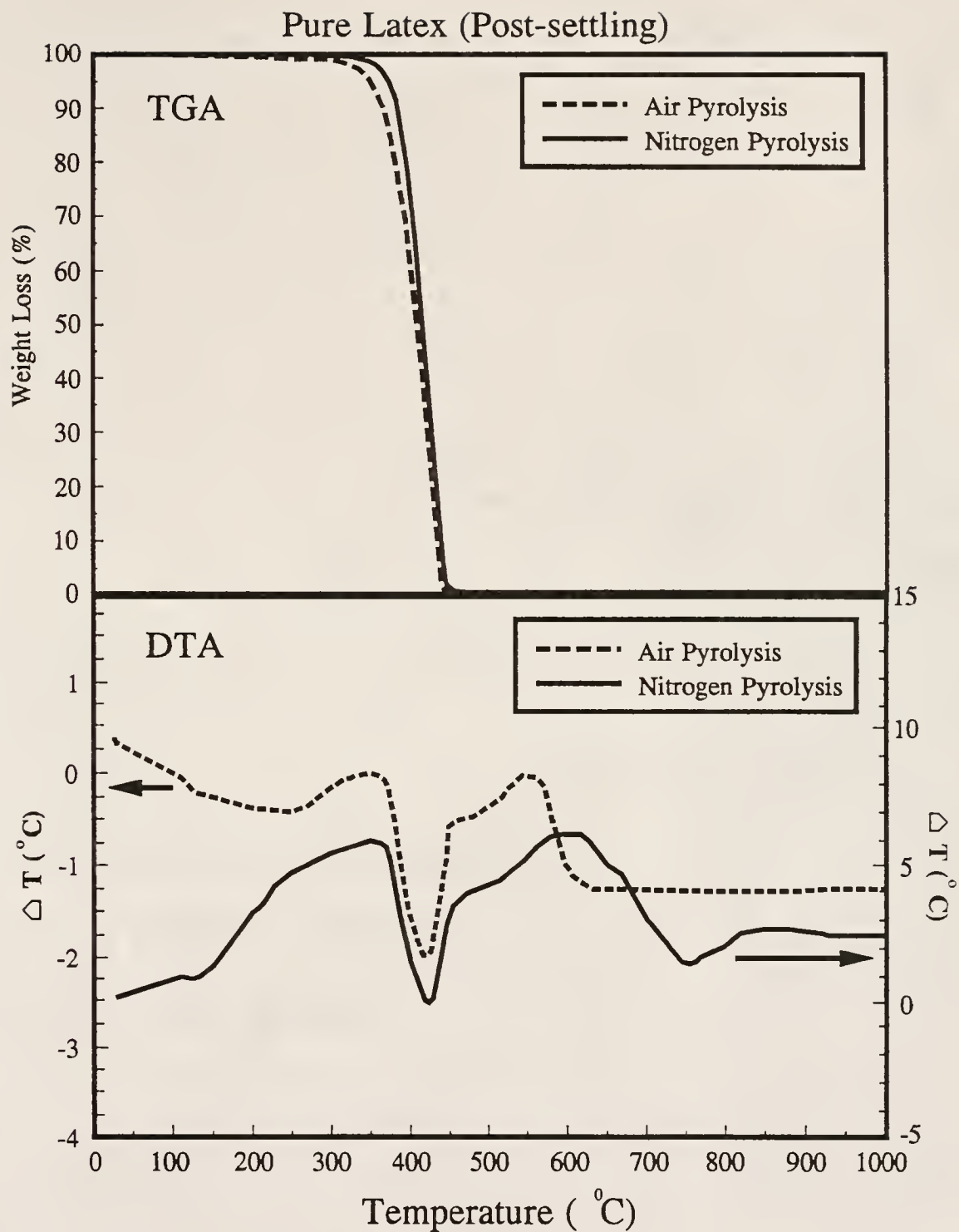


Figure 4.73

Illustration of TGA and DTA curves (10  $^{\circ}\text{C}/\text{min}$ ) for pure latex in air and in  $\text{N}_2$  gas atmosphere



temperatures the resulting organic residue burns off via an exothermic mechanism.

Figure 4.74 illustrates the TGA and DTA analyses of the dispersant polymer used. The dispersant has a significant amount of water (or solvent) adsorption, as indicated by the weight loss near 100 °C. This is reasonable since the powder was used as-received, and was not dried prior to the batching process. Thermogravimetric analysis indicates that the polymer is not completely removed until above 700 °C, and that a slight amount of residue may remain even at 1000 °C. Differential thermal analyses indicate that the reactions involved in the process of PVP pyrolysis are complex and continue to relatively high temperatures. These factors did not prove detrimental in this study however, since very little of the dispersant was used (i.e. 1 wt % of solids). Regardless, it would probably be beneficial to replace this dispersant with a less refractory system when developing thick film or tape cast systems.

Figures 4.73 and 4.74 also exhibit corresponding DTA and TGA data for pure latex and dispersant treated in N<sub>2</sub>. These analyses were included since it would be advantageous to change to nitrogen organics pyrolysis when using these materials in a cofirable system that uses non-noble metals such as Cu or Pd [91KUM1,91KUM2,91SHE2,91TUM]. It is interesting that the latex pyrolysis process in N<sub>2</sub> is quite similar to that in air. Nitrogen pyrolysis of the PVP dispersant is also somewhat similar to air pyrolysis. However, N<sub>2</sub> pyrolysis of the dispersant resulted in a significantly greater portion of residue than did the analogous air pyrolysis. This would add further impetus to change dispersant systems if developing these materials for N<sub>2</sub> thermolysis.

#### 4.3.2 Evolution of BS Glass Surface Area

It is important to know how surface area (SA) of a powder, or of powder compacts, is affected by thermal treatments. For example, as

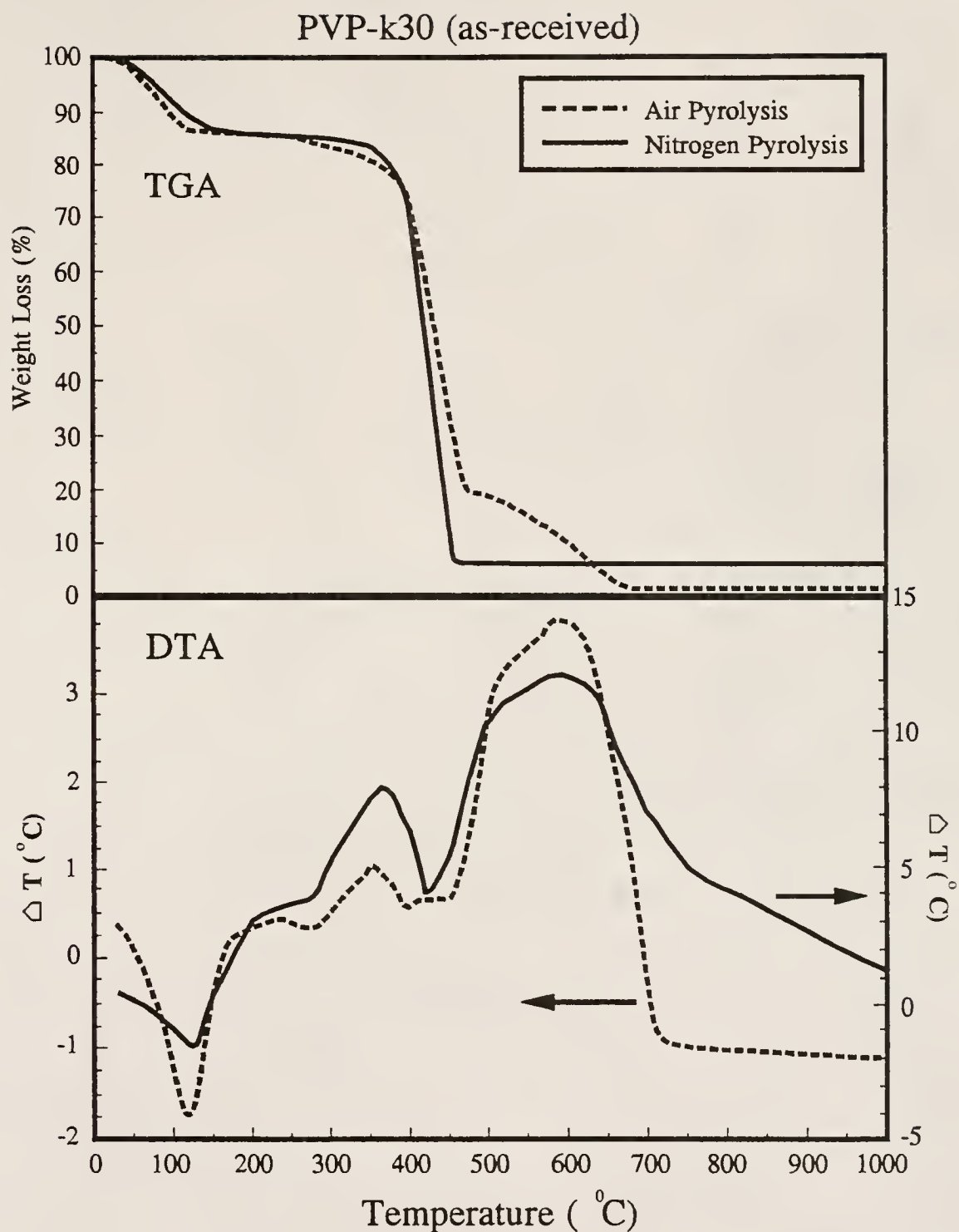


Figure 4.74

Illustration of both air and N<sub>2</sub> atmosphere TGA and DTA curves (10 °C/min) for the PVP dispersant used in this study

powder surface porosity is reduced, there is a possibility of entrapment of carbonaceous materials. It may also be important to know how SA evolves from a sintering standpoint. In the initial stages of sintering powder SA is reduced.

The SA evolution experiment was performed as outlined in section 3.3.5. The heat treatments used are depicted in Figure 3.4. Figure 4.75 illustrates the relationship of SA reduction with increasing heat treatment temperature maximum. It is evident, from the figure, that the SA of the ball milled BS glass powder decreases gradually up to the heat treatment maximum of 450 °C, then decreases at a greater rate, past the 450 °C heat treatment.

The SA of BS powder compacts is initially about one third that of the corresponding powder. It is not evident why this is the case, it may be an effect of dispersant coverage of the powder surface. This effect was not confirmed experimentally, however.

It is interesting to note that the general trend of the evolution of SA of the BS glass compacts with temperature is similar to that of the BS glass powder. In both cases, the SA reduction is greatest at heat treatment maximums exceeding 550 °C. It is interesting that the slip cast BS glass compacts did not exhibit significant densification when heat treated to these temperatures (see section 4.3.4), even though the SA of these compacts had decreased almost tenfold, using the 600 °C heat treatment. This reduction in surface area may be attributed to the elimination of the surface porosity, via a viscous flow mechanism, during these heat treatments. As mentioned earlier, the surface porosity resulted from corrosion during ball milling in MeOH.

Figure 4.76 illustrates the evolution of the ball milled BS glass powder pore structure (both 4 and 45 nm pore diameters) with successive thermal treatment, using gas desorption (similar to Figure 4.33). The figure shows a successive reduction in the height of the 4 nm pore diameter peak with increasing heat treatment temperature. The analogous

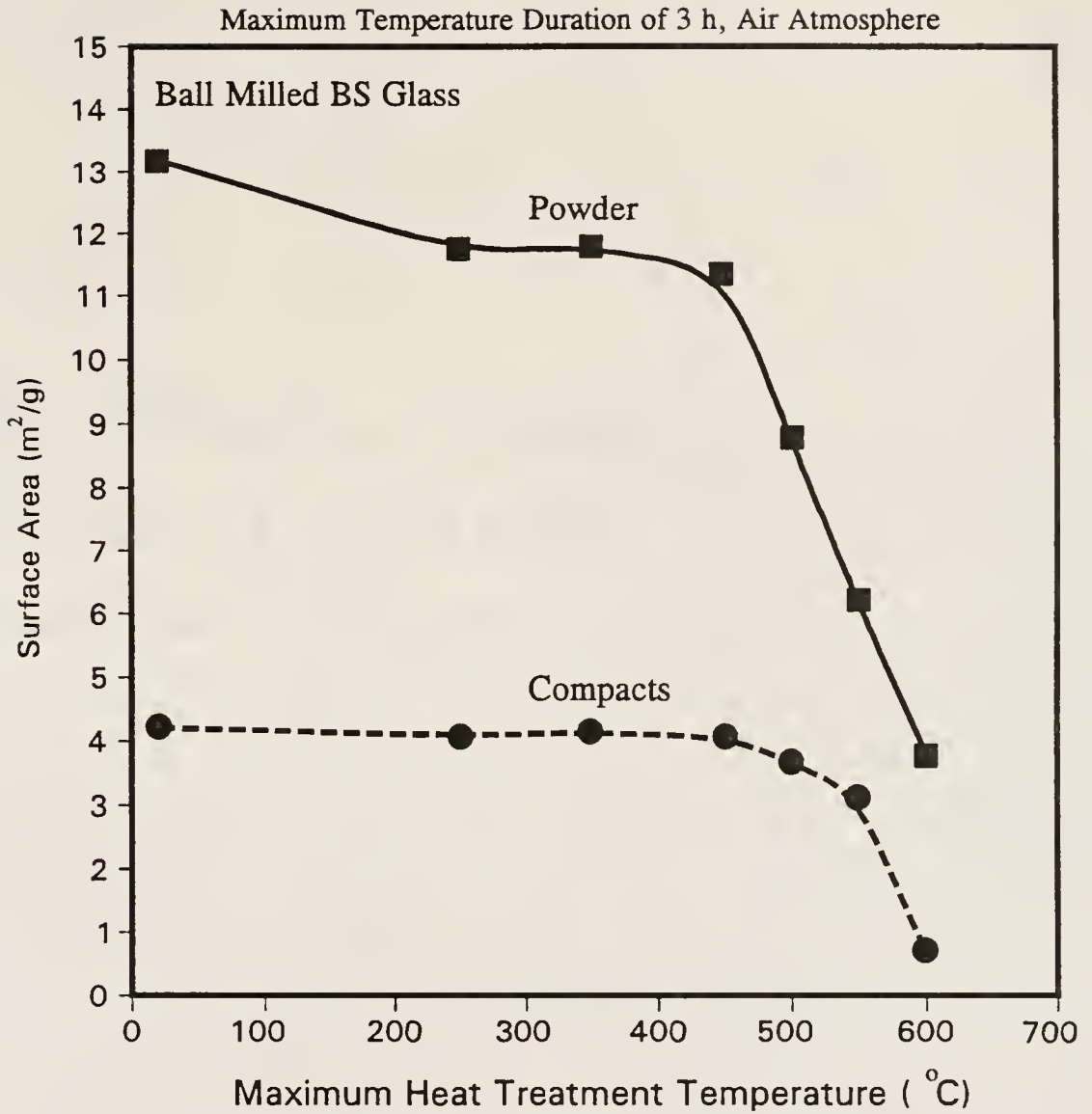


Figure 4.75

Illustration of the effect of heat treatment maximum temperature (for 3 h, in air) upon the measured surface areas of the ball milled BS glass powder and compacts investigated

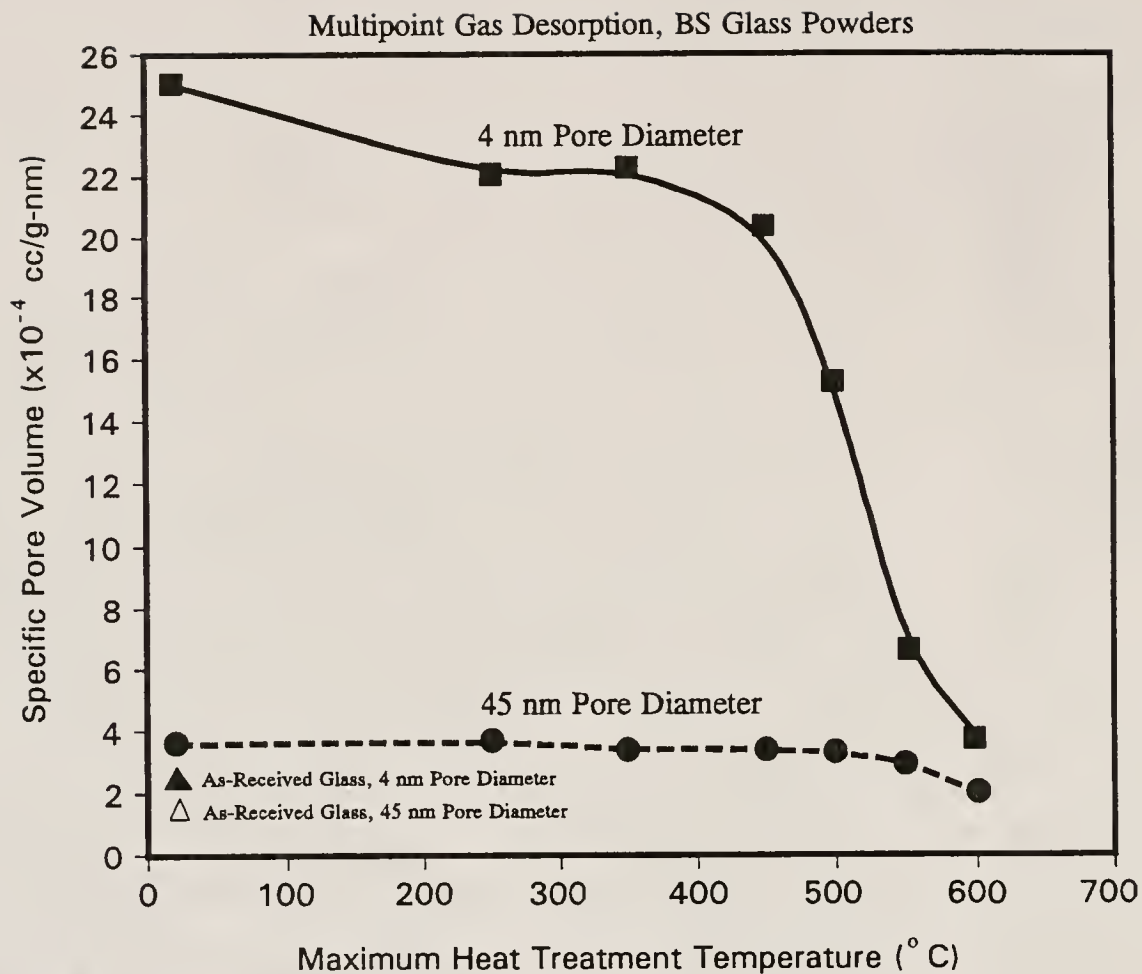


Figure 4.76

Illustration of the evolution of BS glass powder SA (4 and 45 nm pore diameter peak heights) with respect to heat treatment, using multipoint BET desorption



data for the as-received BS glass powder is included as well, for comparison. The desorption peaks (primarily the 4 nm peak), which resulted, or grew, from ball milling the BS glass powder in MeOH (see Figure 4.33), were reduced significantly with these heat treatments. Both peak heights values became more similar to those of the as-received BS glass powder with maximum heat treatment. The 45 nm peak height changed less with heat treatment than the 4 nm peak. This is logical since higher SA structures are more sensitive to temperature. It is interesting that the SA of the ball milled powder reverted to a value similar to that of the as-received powder (i.e. SA changes to  $3.8 \text{ m}^2/\text{g}$ , which is comparable to the  $3.4 \text{ m}^2/\text{g}$  value of the as-received glass).

This analysis was not performed upon the BS glass compacts, since the desorption peak at approximately 4 nm was never present. This fact gives further credence to the hypothesis that the polymer dispersant covered the powder particle surfaces during wet processing and casting.

Unfortunately, it is not possible to discuss the effects of these heat treatments upon measured particle size, because particle size analyses of the heat treated powders were not performed. This would be beneficial in order to compare the post heat treatment particle size to both the as-received and the ball milled BS glass powders. However, after the  $600^\circ\text{C}$  heat treatment was performed, a minor amount of agglomeration was observed. Thus, measurement of the particle size of this sample would have been sensitive to any regrinding process used.

#### 4.3.3 Oxidation of $\text{Si}_3\text{N}_4$ Powder

In this study it is important that the  $\text{Si}_3\text{N}_4$  powder used not oxidize appreciably. This is true because oxidation would alter the density of the  $\text{Si}_3\text{N}_4$  powder, thereby altering the density of the composite. This could become a significant source of error in determining percent of theoretical density when investigating sintered

composites containing  $\text{Si}_3\text{N}_4$ . Thus, oxidation experiments were performed on the  $\text{Si}_3\text{N}_4$  powder used in this study as outlined in section 3.5.2.

Figure 4.77 illustrates the TGA curve for  $\text{Si}_3\text{N}_4$  powder heated in air at a rate of  $10\text{ }^\circ\text{C}/\text{min}$ . The weight loss from RT to approximately  $1300\text{ }^\circ\text{C}$  was due mainly to baseline variance in the TGA instrument. This fact was determined from reference runs using reference alumina. However, the weight gain after approximately  $1300\text{ }^\circ\text{C}$  was real and is attributed to oxidation of the  $\text{Si}_3\text{N}_4$  powder.

The highest temperature used to sinter composites in this study was  $820\text{ }^\circ\text{C}$ . The relationship in Figure 4.77 seems to indicate that this temperature is well below the onset of oxidation of the  $\text{Si}_3\text{N}_4$  powder. However, as mentioned above, reactions tend to be shifted to lower temperatures when heating rates are decreased. In the case of sintering the  $820\text{ }^\circ\text{C}$  heat treatment was isothermal and lasted for relatively long periods.

Figure 4.78 illustrates isothermal TGA at  $820\text{ }^\circ\text{C}$  for the  $\text{Si}_3\text{N}_4$  powder. The reference curve (tabular alumina) is provided as a rudimentary means of baseline correction. It is evident from the figure, that little or no weight gain occurs over long periods of time at said temperature. The reference (baseline) curve has the same general shape and magnitude as the  $\text{Si}_3\text{N}_4$  curve. It is not known whether the relatively small difference between the curves is real or is a variable of the TGA apparatus, since the runs were not performed simultaneously (i.e. non-identical conditions). Thus, it may be hypothesized that  $\text{Si}_3\text{N}_4$  oxidation should not have significantly affected the various measurements (i.e. density, dielectric properties, etc.) taken during this study.

It should be noted that this experiment was performed upon pure  $\text{Si}_3\text{N}_4$  powder and, thus, is not indicative of any reactions between the BS

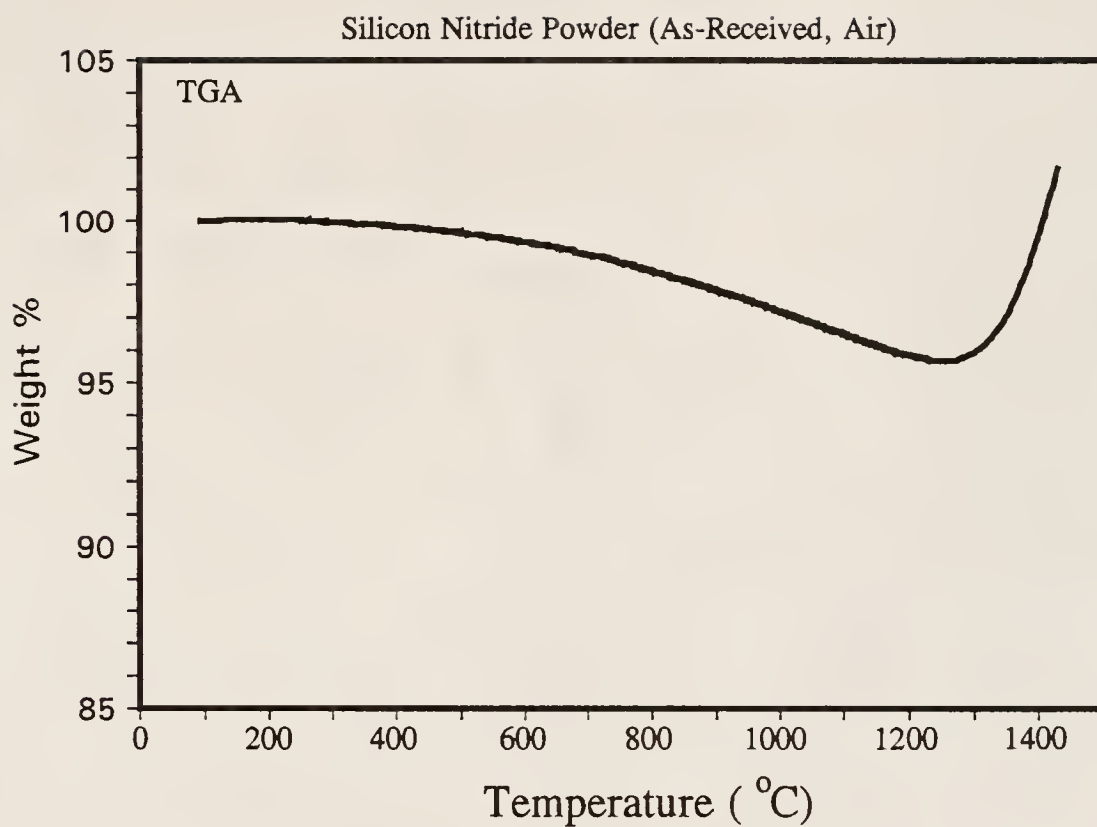


Figure 4.77

TGA curve of  $\text{Si}_3\text{N}_4$  powder heated to approximately 1500 °C, at a rate of 10 °C/min, in air

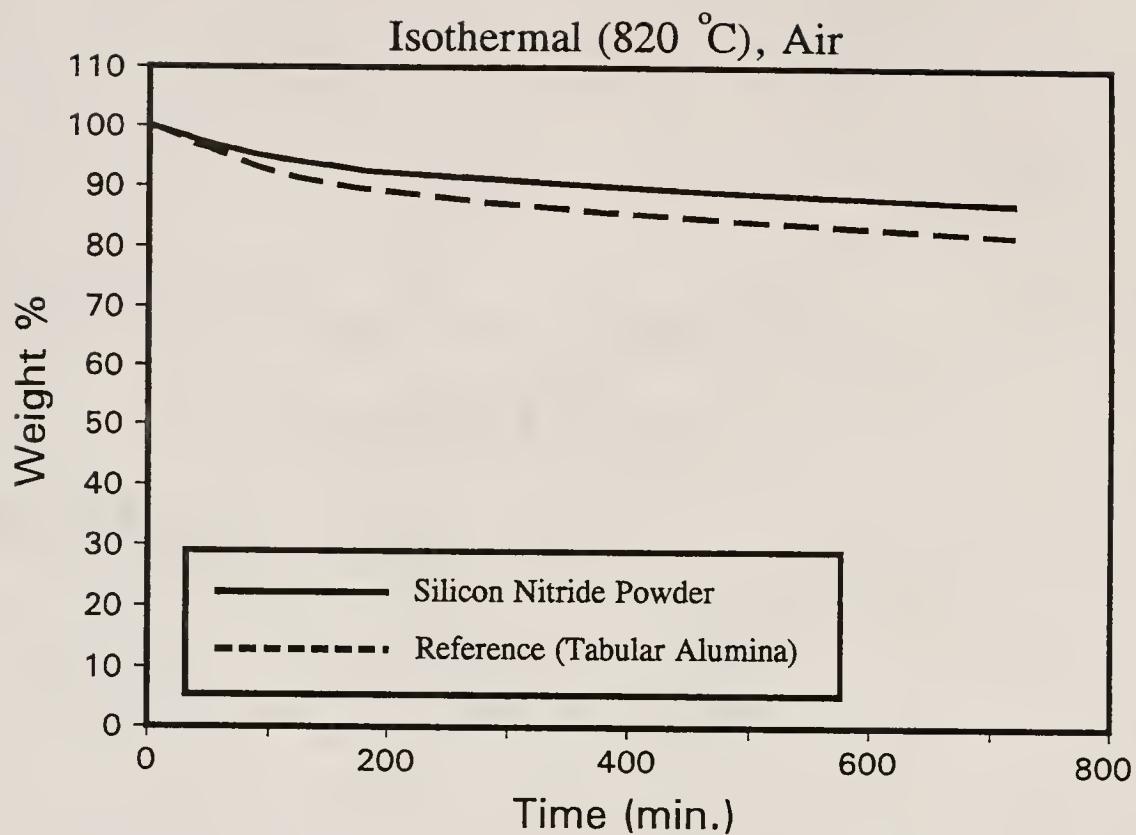


Figure 4.78

Isothermal TGA of  $\text{Si}_3\text{N}_4$  and reference powder (alumina) at 820 °C in air

glass and the  $\text{Si}_3\text{N}_4$  powder. As discussed below, microscopy studies indicate that there is little if any BS glass- $\text{Si}_3\text{N}_4$  interaction, however.

#### 4.3.4 Sintering

In studies of the densification of glass matrix composite materials it is important that sintering of the viscous matrix material is first understood. After this understanding is obtained, the effects of additions of porosity and of nonsintering particulates upon densification may be characterized.

Figure 4.79 illustrates isothermal densification curves of slip cast compacts made of pure, as-received and ball milled BS glass powders at 625 °C. Even though the as-received glass started with approximately 4% greater green density (~72 versus ~68 % of theoretical density), the ball milled BS glass sintered at a much greater rate, surpassing the density of the as-received compact in the initial stage of densification. This may be explained by the higher surface area and smaller MPCR of the ball milled BS glass compacts as compared to the as-received BS glass compacts.

Thus, the increased surface area of the ball milled glass powder greatly increased the rate of sintering of the BS glass. It should be noted that after the organics removal process the surface area of the ball milled BS glass was significantly reduced (see Figure 4.75). No analogous data is available upon the as-received BS glass, however, so it is difficult to gauge this effect. Regardless of the operant mechanism, the rate of sintering is significantly increased (i.e. 0.77 versus 3.05 % per hour for as-received and ball milled BS glass, in the initial stages, respectively) when the BS glass powder is ball milled.

The effect of  $\text{Si}_3\text{N}_4$  concentration upon the rate of densification is illustrated in Figures 4.80 and 4.81. Figure 4.80 depicts isothermal densification of BS glass/ $\text{Si}_3\text{N}_4$  compacts at 625 °C, while Figure 4.81 depicts isothermal sintering of BS glass/ $\text{Si}_3\text{N}_4$  composites at 650 °C.



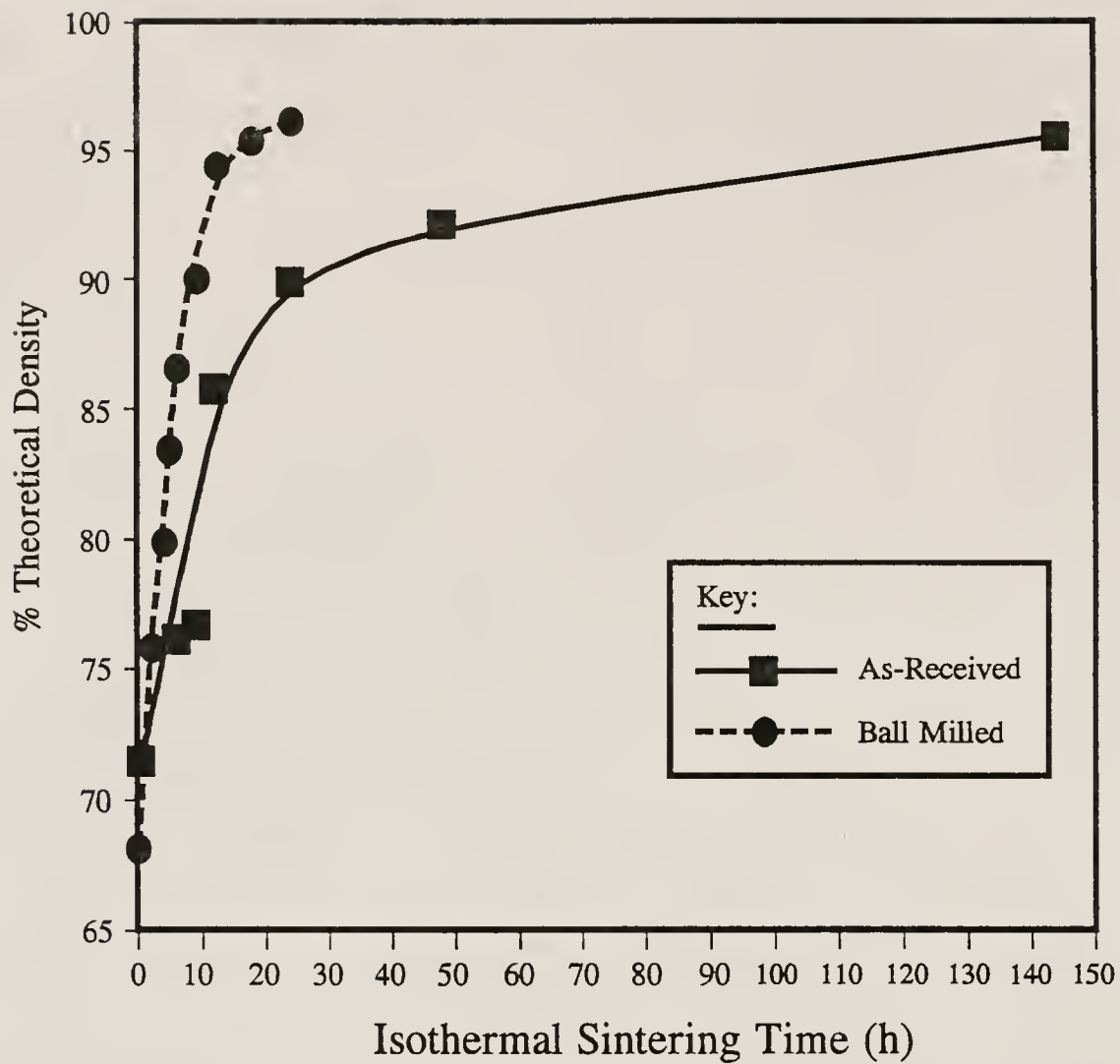


Figure 4.79

Isothermal densification of as-received and ball milled BS glass compacts at 625 °C

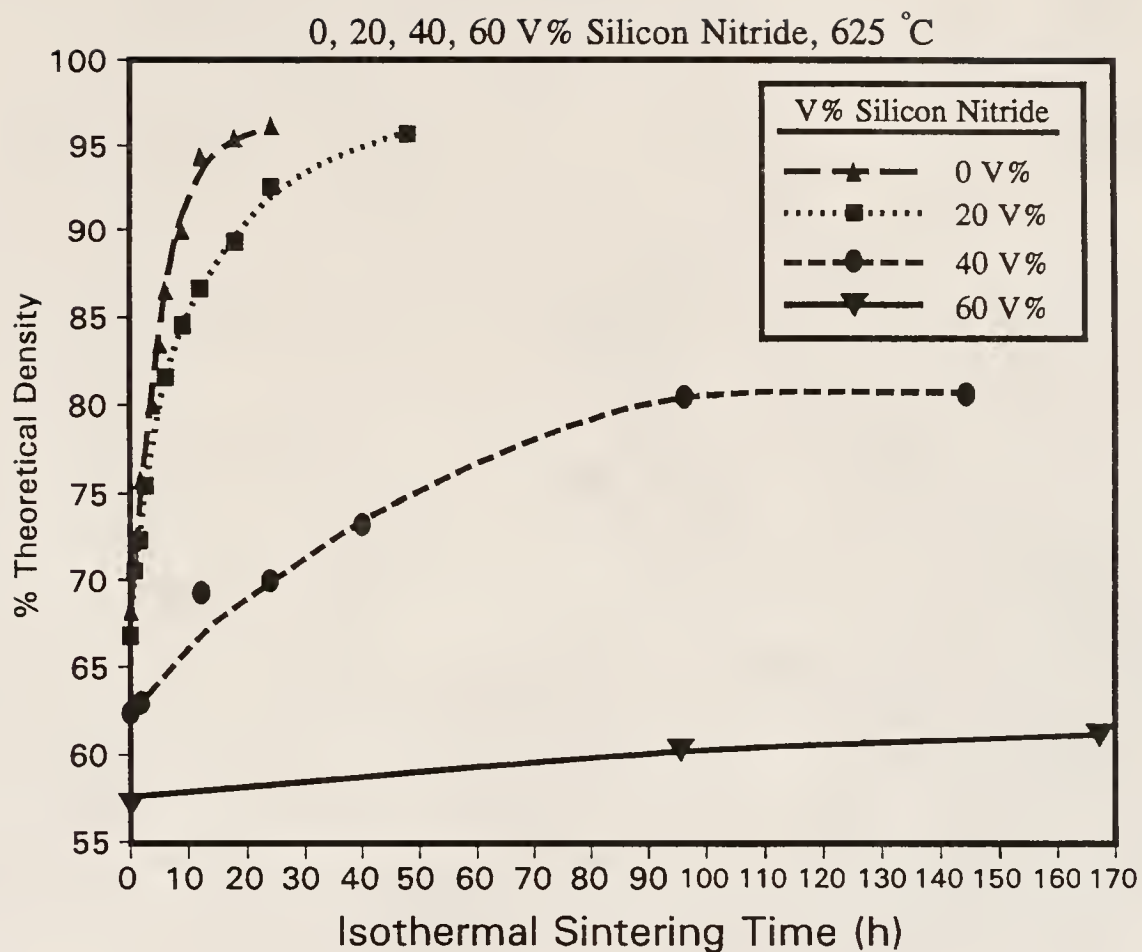


Figure 4.80

The effect of  $\text{Si}_3\text{N}_4$  concentration upon isothermal densification of BS glass/SN composites at 625 °C

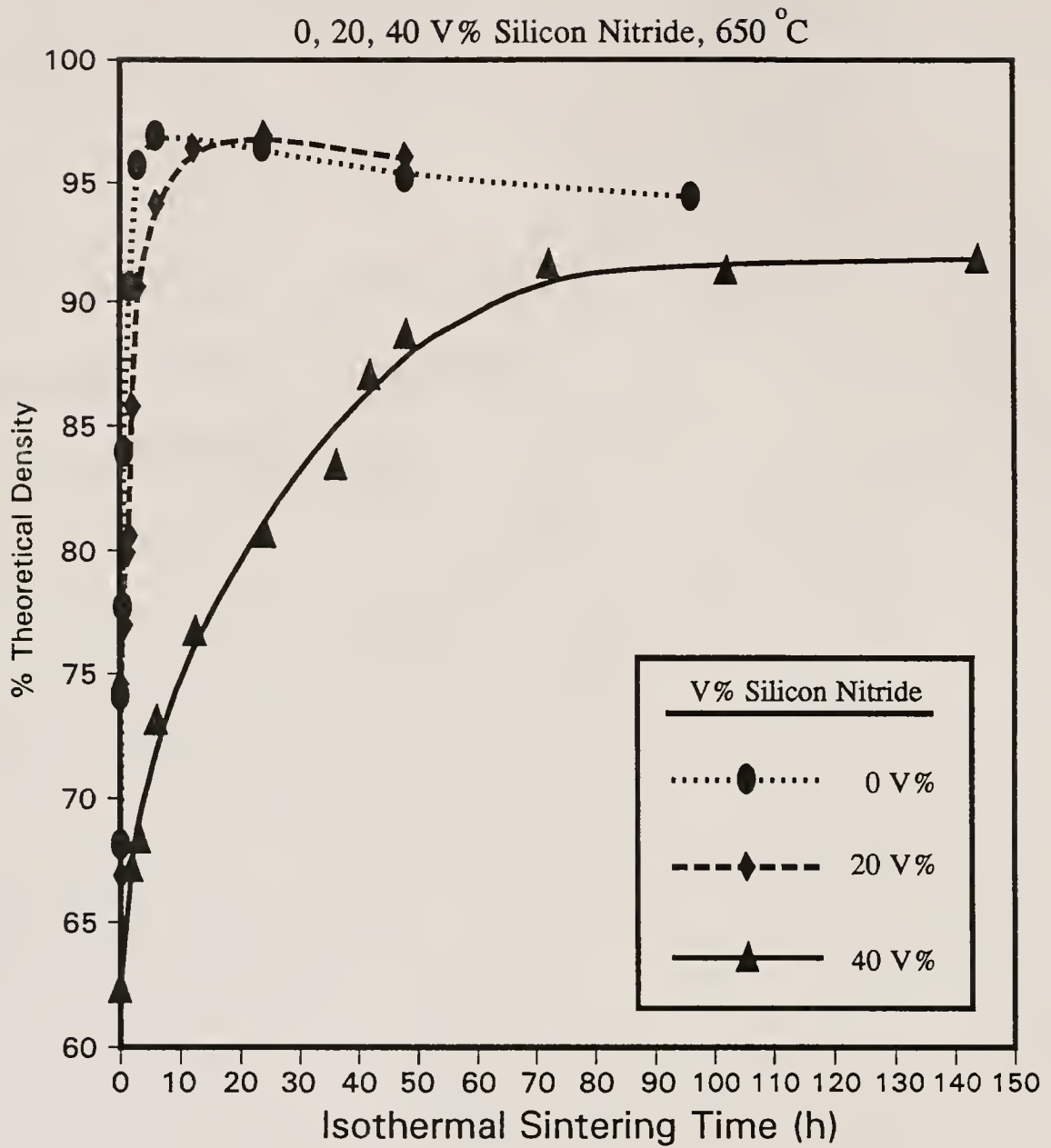


Figure 4.81

Effect of  $\text{Si}_3\text{N}_4$  concentration upon isothermal densification of BS glass/SN composites at 650 °C

From the figure, it is evident that densification is significantly retarded with  $\text{Si}_3\text{N}_4$  additions at and above 40 V%. In fact, with a  $\text{Si}_3\text{N}_4$  concentration of 60 V%, very little densification occurred. This is in agreement with theories presented in the literature [91SCH2].

It is interesting to note that, in both the 40 and 60 V%  $\text{Si}_3\text{N}_4$  addition samples, the maximum volume occupied by  $\text{Si}_3\text{N}_4$  is approximately 36 V% (i.e. 40 V% at a maximum observed density of approximately 90 % of theoretical density, and 60 V% at a maximum observed density of approximately 60 % of theoretical density). Thus, it may be hypothesized that the maximum  $\text{Si}_3\text{N}_4$  addition of approximately 36 V% may be used in order to produce compacts that may be sintered to near-full-density using pressureless sintering techniques. This is in general agreement with the available literature [87RAH1,87SCH3,88BOR3,90EWS,91EWS,91SCH2,91SCH3,91SCH4].

Conversely, concentrations of  $\text{Si}_3\text{N}_4$  at and below 20 V% affected densification of these composites relatively little. These  $\text{Si}_3\text{N}_4$  concentrations are below the percolation threshold (i.e.  $\sim 26$  V% for 60 % dense compacts) and thus, are not expected to affect densification greatly [91SCH2]. In fact, both the 0 and 20 V%  $\text{Si}_3\text{N}_4$  composites exhibited bloating (i.e. a reduction in density with increased sintering duration), which indicates that sintering proceeded relatively uninhibited.

The small amount of retardation in the rate of densification in the 20 V%  $\text{Si}_3\text{N}_4$  composites probably results from the fact that at approximately 80 % of theoretical density, the percolation threshold is reached and thus, sintering is inhibited. This is in agreement with Figures 4.80 and 4.81, where densification of the 20 V%  $\text{Si}_3\text{N}_4$  composites begins to differ from that of the pure BS glass at approximately 80 % of theoretical density.

It should be noted that investigation of compositions containing 20 to 36 or 40 V%  $\text{Si}_3\text{N}_4$  would be beneficial in order to further delineate

the composition at which severe retardation of sintering occurs. This would help to determine if significant sliding or sticking occurs between the  $\text{Si}_3\text{N}_4$  particles [91SCH2].

The effect of sintering temperature upon isothermal rate of densification is illustrated in Figures 4.82 through 4.85. Figure 4.82 illustrates this effect for pure ball milled BS glass, while Figures 4.83 and 4.84 depict these relationships for 80/20/0 and 60/40/0 BS Glass/SN/UPLM composites respectively. The figures indicate that an increase in temperature of 25 °C increases the initial rate of densification rate (i.e. in the first linear region) by factors of approximately 3.8, 3.2 and 2.8 (i.e. 9.15 versus 2.41 % per hour for pure, ball milled BS glass, 7.89 versus 2.44 % per hour for 80/20 BS glass/SN composites, and 1.78 versus 0.63 % per hour for 60/40 BS glass/SN composites) for 0, 20 and 40 V%  $\text{Si}_3\text{N}_4$  concentration composites, respectively.

Using interpolated viscosity values, depicted in Figure 4.85, it is evident that the viscosity of the bulk samples of the BS glass used in this study is reduced by a factor of approximately 4 when temperature is changed from 625 to 650 °C. This similarity to the above values is logical since viscous sintering is the operant densification mechanism in this system. Thus, the densification rate of the composites is expected to increase in direct proportion to the decrease in viscosity with temperature (all other factors remaining equal).

From Figure 4.84 it is evident that the 40 V%  $\text{Si}_3\text{N}_4$  concentration composites will not densify significantly in excess of 90 % of theoretical density using pressureless sintering. Furthermore, it is interesting to note that the compacts that were sintered at 820 °C did not achieve 90 % of theoretical density. Blistering was observed in these samples. Thus, it is assumed that 820 °C is too high a sintering temperature for effective sintering of these samples.



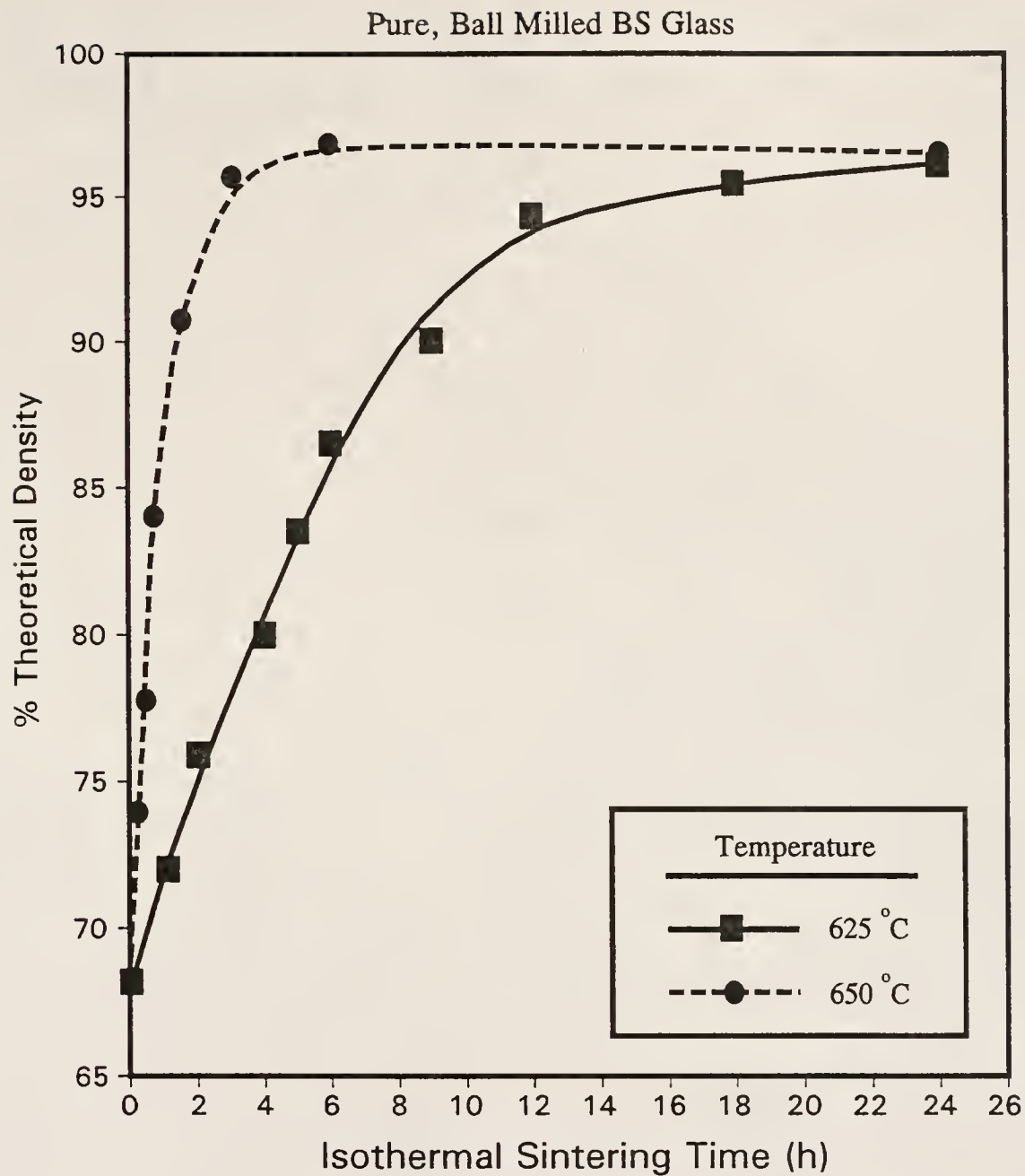


Figure 4.82

Illustration of the effect of isothermal sintering temperature upon densification rate of pure, ball milled BS glass compacts

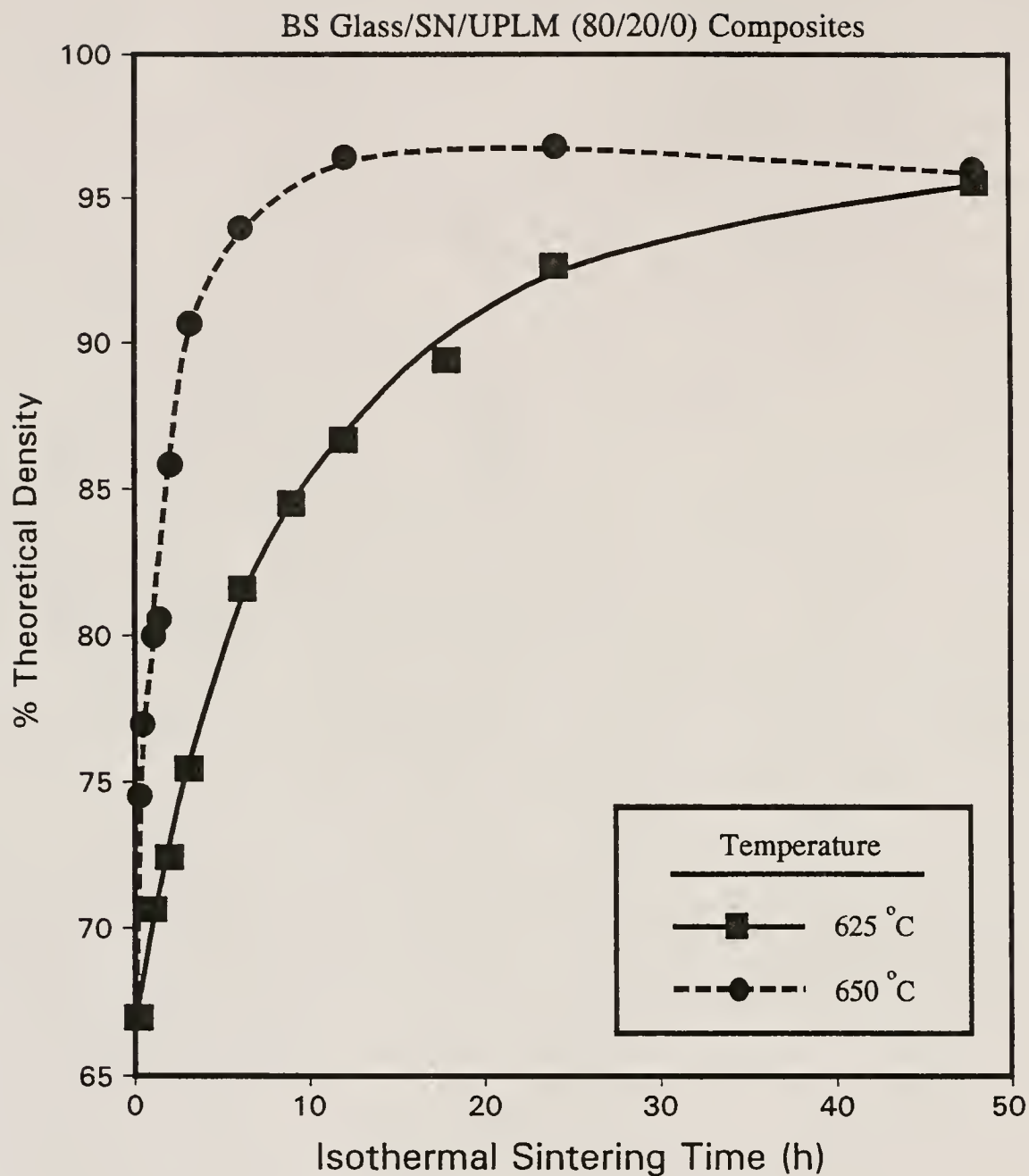


Figure 4.83

Illustration of the effect of isothermal sintering temperature upon the rate of densification of 80/20/0 BS glass/SN/UPLM composite compacts

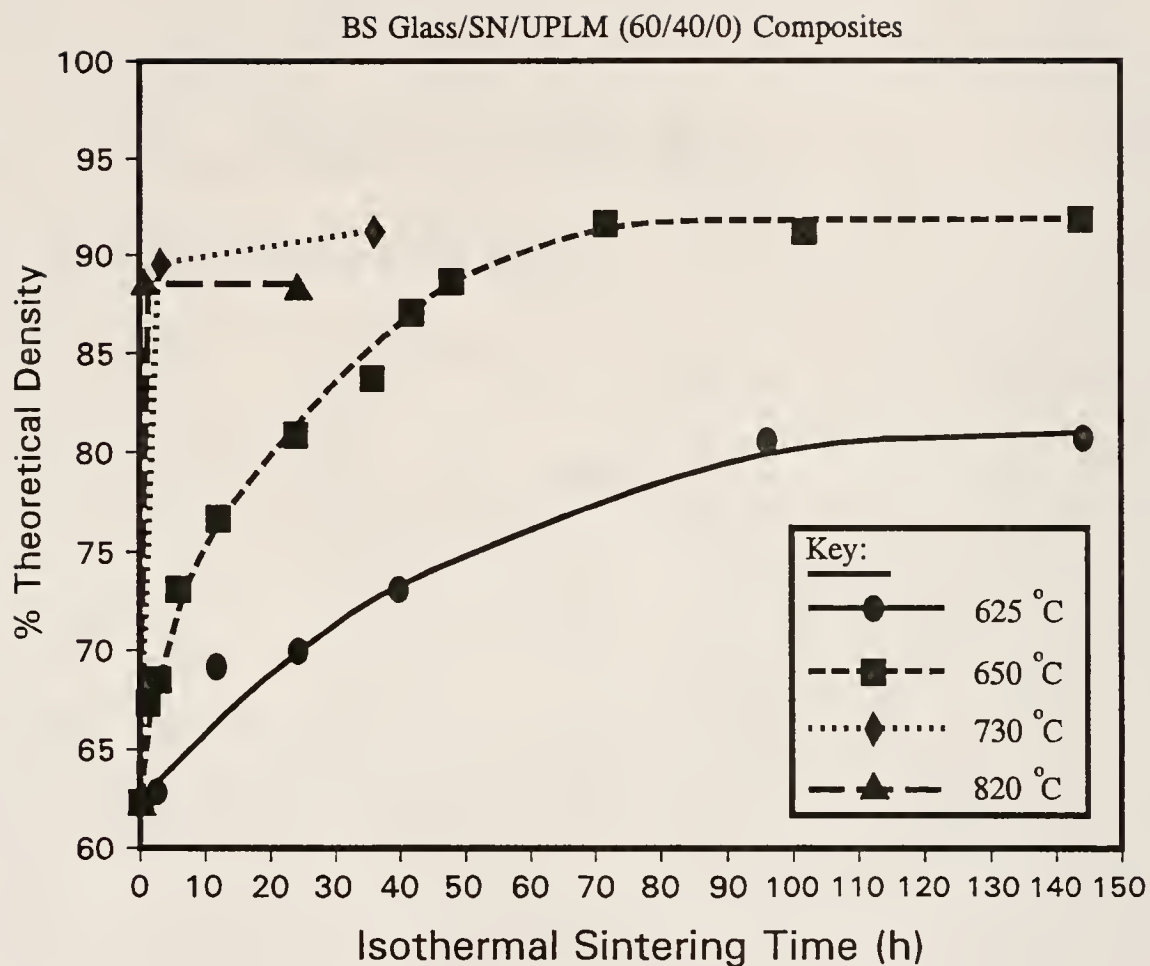


Figure 4.84

Illustration of the effect of isothermal sintering temperature upon the densification rate of 60/40/0 BS glass/SN/UPLM composite compacts

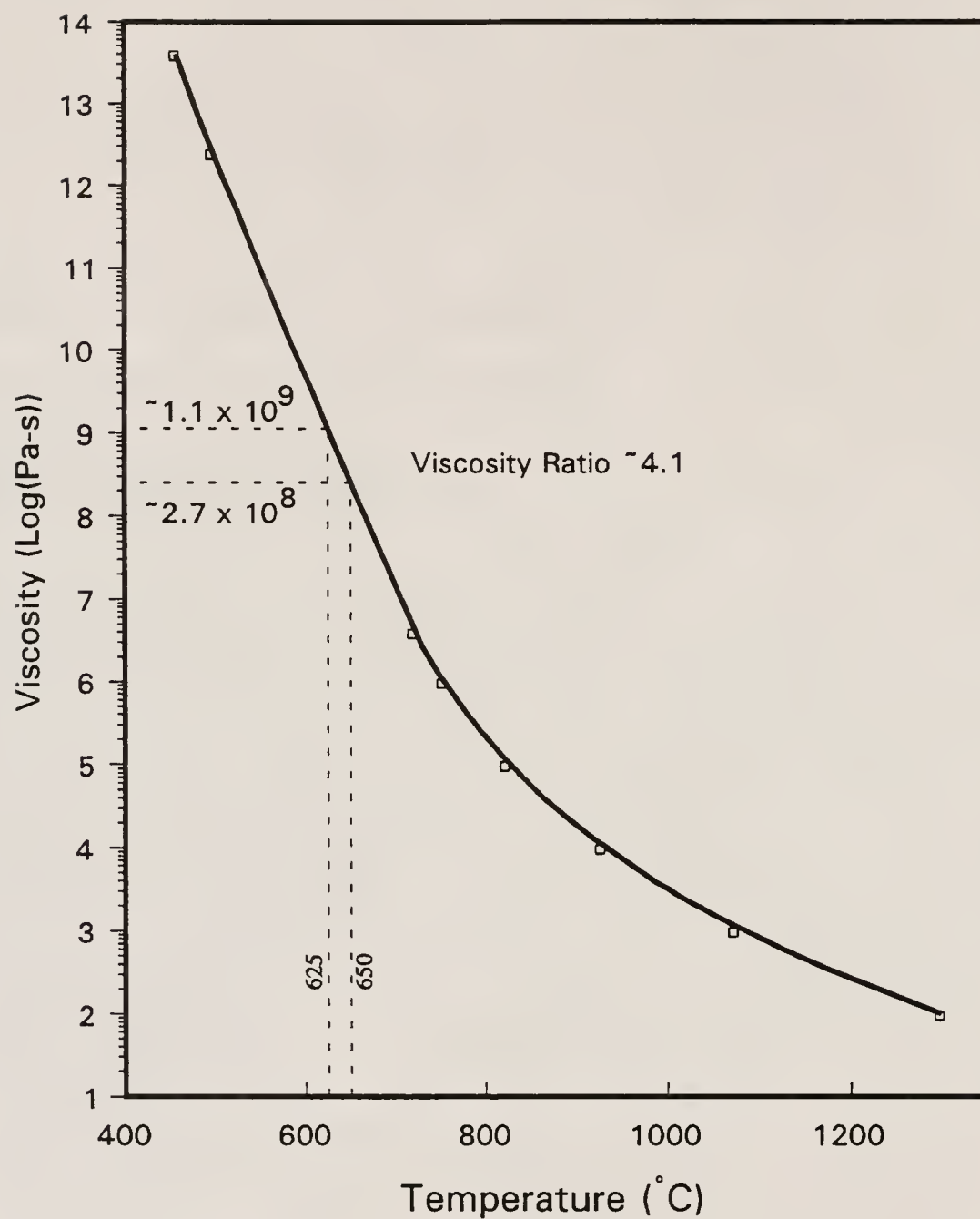


Figure 4.85

Illustration of the reduction in viscosity from 625 to 650 °C in the BS glass used in this study

The effect of porosity addition upon densification rate is illustrated in Figures 4.86 to 4.89. Figure 4.86 illustrates this effect for pure BS glass systems, while Figure 4.87 depicts this relationship for composites containing 20 normalized V%  $\text{Si}_3\text{N}_4$ . Similarly, Figures 4.88 and 4.89 depict the effect of added porosity concentration upon the densification behavior for composites containing 40 normalized V%  $\text{Si}_3\text{N}_4$ .

The effect of included porosity upon the densification behavior of the pure BS glass compacts is quite interesting. Sintering is not significantly impeded in samples containing 5 V% UPLM until densities in excess of 90 % of theoretical density are achieved. This behavior is imitated in samples containing 10 V% UPLM below approximately 80 % of theoretical density as well. Nearer the percolation threshold, densification is impeded almost from the onset of the sintering process. Beyond the percolation threshold (i.e 30 V% UPLM), densification occurs at a decreased rate. However, the densification behavior of the 30 V% UPLM addition compacts proceeds to higher densities than the BS glass compacts containing UPLM additions below the percolation threshold. In this sense, the general shape of the 30 V% UPLM addition curve is similar to the 0 V% UPLM addition curves (both as-received and ball milled BS).

The reason for this behavior is related to pore structure. The pore structure of the 30 V% UPLM addition material has considerably larger pore channels than the pore structures of the materials having latex additions below the percolation threshold (see Figures 4.60 and 4.61). The pore structures of the materials having UPLM additions below the percolation threshold have much smaller pore channels, and are similar to ink bottle-type pores. During densification the smaller pore channels close off first in ink bottle-type structures. If there is a large difference in size between the pores and the channels interconnecting the pores, the relatively large pores will become



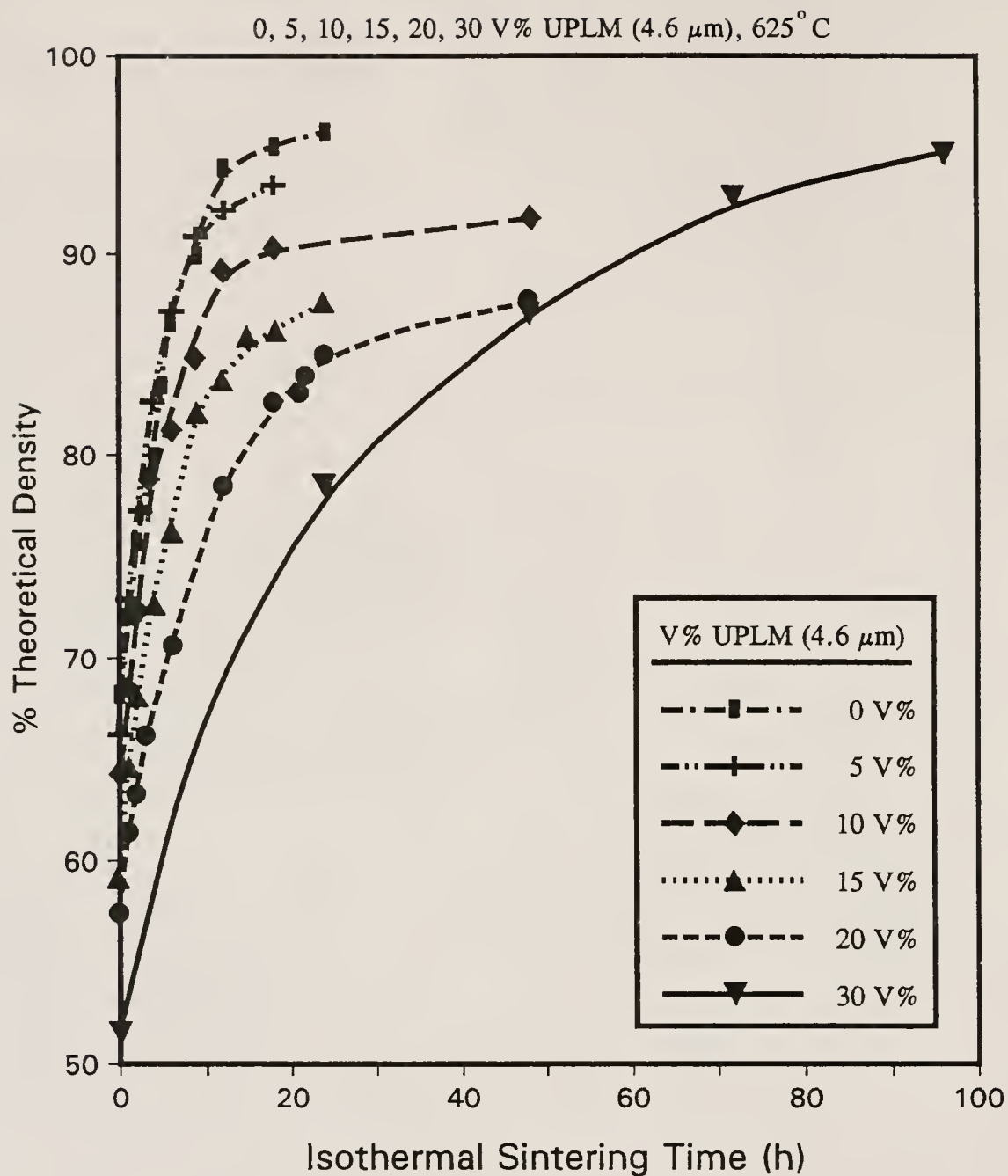


Figure 4.86

Illustration of the effect of added porosity concentration upon the densification behavior pure BS glass compacts at  $625^\circ\text{C}$

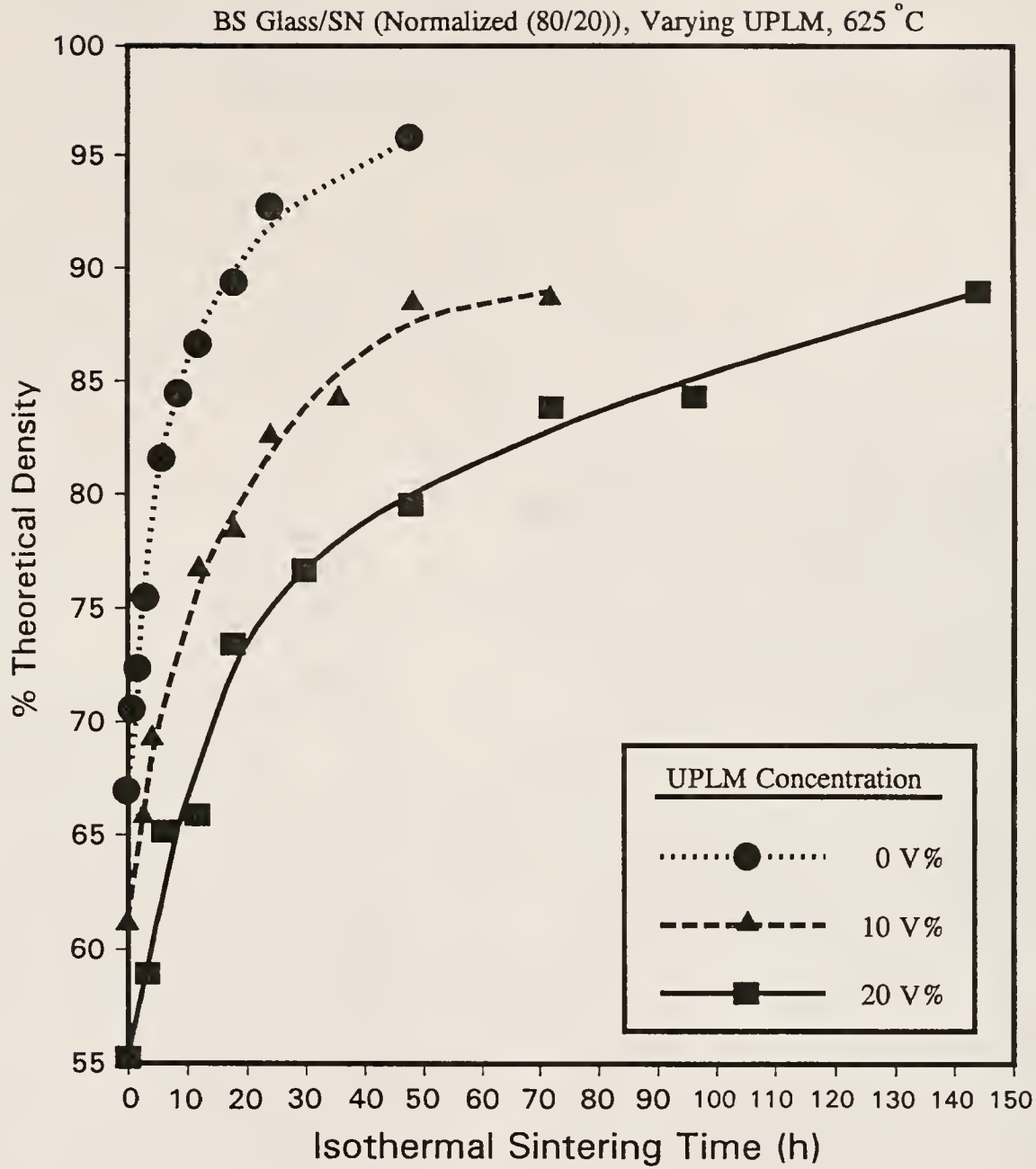


Figure 4.87

Illustration of the effect of added porosity concentration upon the densification behavior of normalized 80/20 BS glass/SN composite compacts at 625 °C

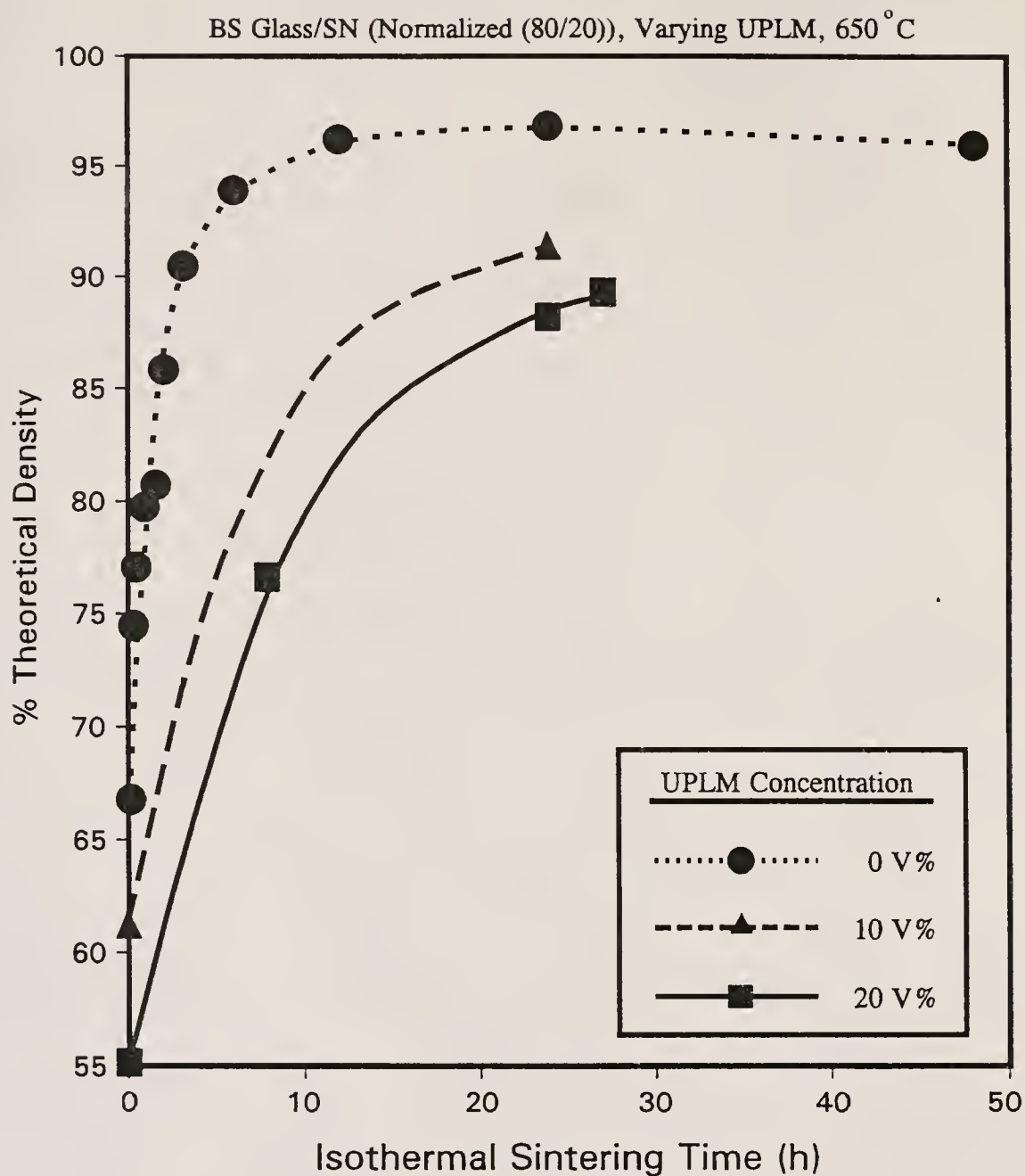


Figure 4.88

Illustration of the effect of added porosity concentration upon the densification behavior of normalized 80/20 BS glass/SN composite compacts at 650 °C

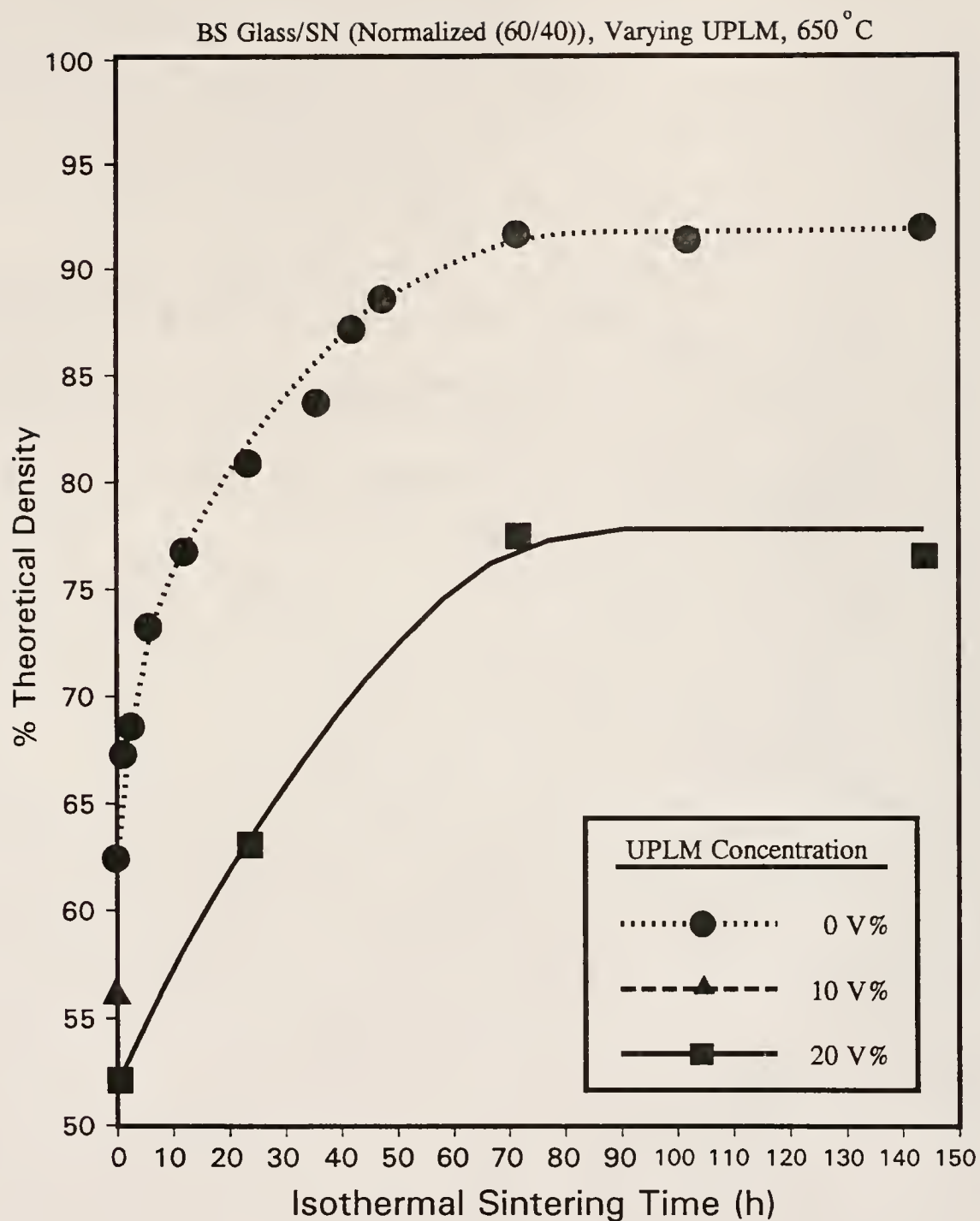


Figure 4.89

Illustration of the effect of added porosity concentration upon the densification behavior of normalized 60/40 BS glass/SN composite compacts at 650 °C

isolated during sintering. These isolated pores are tenacious and difficult to remove during sintering because transport to and from them is greatly impeded. In the case of large pores and large channels of pore interconnection, pore isolation does not occur until relatively high densities (i.e.  $> 94\%$  of theoretical density), because the pore channels do not sinter out of the structure prematurely as in ink bottle-type pores. Therefore, while the densification process is slowed in the 30 V% UPLM addition BS glass powder materials, it progresses to ultimate densities similar to those exhibited by the 0 V% latex addition curve (see Figure 4.86). This is not the case in materials having UPLM additions below the percolation threshold, where it appears that an asymptotic density level is approached (see 10 and 20 V% UPLM addition curves in Figure 4.86). Unfortunately data was not collected at longer sintering durations to further define these asymptotic values.

Figure 4.90 compares the densification curves for as-received and ball milled BS glass compacts as well as for 30 V% UPLM ball milled BS glass compacts. It is interesting that the as-received and the 30 V% UPLM curves match each other fairly closely at longer times, while the general shape of the 30 V% UPLM curve is similar to the densification curve for the ball milled BS glass. The common denominator among these materials (i.e. the 0 V% UPLM, as-received and ball milled BS glass compacts, as well as the 30 V%,  $4.6\ \mu\text{m}$  addition, ball milled BS glass compacts) is the presence of a continuous pore structure.

It is not known whether or not the asymptotic limits approached by the compacts having UPLM additions below the percolation threshold are real. Time did not permit such investigations. These compacts may sinter to greater densities. However, the closed-off porosity may become stable and may actually bloat in a manner similar to the behavior exhibited by the 0 V% latex addition ball milled BS glass compacts.

Bloating occurs as a result of pore ripening. Small, sealed pores have a higher surface curvature than larger, sealed pores.



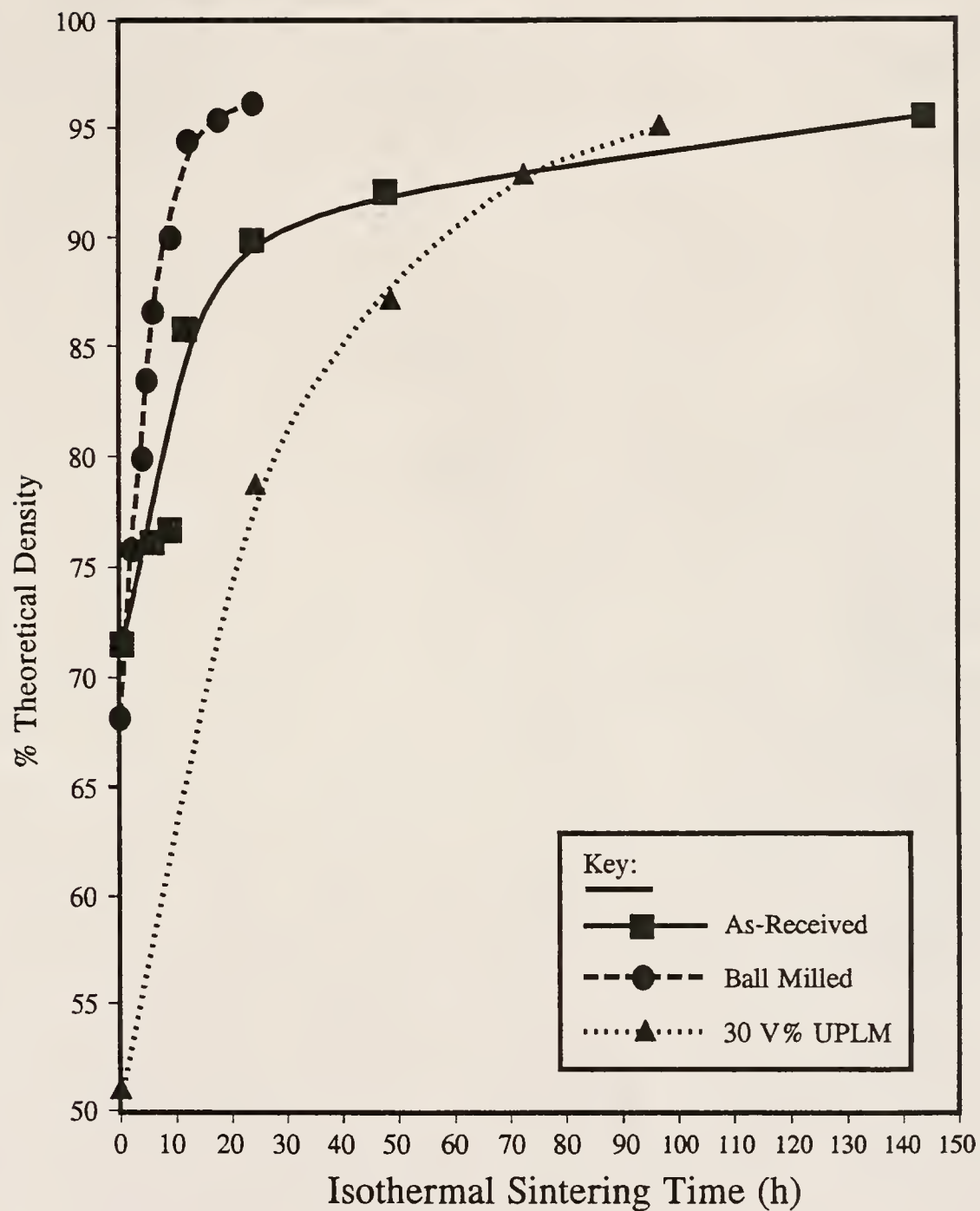


Figure 4.90

Illustration depicting the isothermal densification behaviors of pure as-received and ball milled BS glass compacts, as well as ball milled BS glass compacts with 30 V% UPLM additions at 625 °C

Therefore the sintering pressure (which is directly relatable to surface curvature) on smaller pores is greater than on larger pores, and a greater amount of gas pressure is required to stabilize a small pore against sintering. Thus, the same molar amount of gas trapped within a material, upon elimination of open porosity during the densification process, would create a greater volume of large porosity than smaller porosity, due to the pressure balance mentioned above. From Ostwald ripening theory [76KIN1], gases are expected to diffuse from small pores to local large pores. Thus, bloating would be expected in this system, if the amount of trapped gases remains constant. Conversely, if the trapped gases can diffuse to the material surface, bloating may be retarded or eliminated, depending upon the rate of trapped gas removal.

The densification behavior of the normalized 80/20 (BS glass/SN) composites containing UPLM additions do not seem to asymptotically approach a density limit as the above materials did (see Figures 4.87 and 4.88). It may be speculated that this is a result of the larger pore channels characteristic of the 20 normalized V%  $\text{Si}_3\text{N}_4$  composites (see Figure 4.51) as well as sintering for deficient sintering durations. Said larger pore channel structure would allow sintering behavior more similar to the continuous pore structure materials described above.

These densification behaviors introduce an important concept. The level of achievable closed porosity is affected not only by the amount of porosity addition, but by the pore structure itself. Specifically it is important that the ratio of the included pore size to the measured pore channel size be maximized, in order to achieve closed porosities similar to the porosity addition. This effect is called differential sintering, in that it allows densification of one aspect of an internal pore structure, with little or no densification of other aspects of the pore structure.

It is also important to note that, above the percolation threshold, this ratio is reduced significantly when using this method of porosity addition. Therefore, it is not possible to achieve fractions of closed porosity that exceed the percolation threshold (i.e. 16 V%) of the included porosity. This shall be discussed in further detail below.

Figure 4.89 illustrates that all normalized 40 V%  $\text{Si}_3\text{N}_4$  composites investigated achieve an asymptote. This results from the establishment of a continuous  $\text{Si}_3\text{N}_4$  structure. It is interesting that the asymptote achieved by the 20 V% UPLM addition composite is close to 0.8 of the asymptote achieved by the 60/40 composite with 0 V% UPLM addition. This further indicates that the asymptotes realized in the densification of the 40 normalized V%  $\text{Si}_3\text{N}_4$  samples are due to establishment of a stable, percolated  $\text{Si}_3\text{N}_4$  structure.

Figure 4.91 illustrates the effect of included porosity size and size distribution upon densification behavior. While there is not a great deal of difference between the curves, a couple of subtle observations may be made. All of the curves appear to approach an asymptote except for the smallest size of included porosity. The asymptote approached by the largest size of included porosity investigated is lowest in density of the groups. Unfortunately data were not taken at longer sintering durations. This would have helped to better establish the asymptotic relationships discussed above.

Figure 4.92 illustrates the densification behavior of composite compositions on the diagonal of the 4.6  $\mu\text{m}$  UPLM plane of the matrix of compositions investigated. It is evident from the figure that there is a large range in densification rate of these compositions.

It should also be noted that it was common, in those samples having nearly closed pore structures, for the relative amount of closed and opened porosity to change with the number of repetitions of density measurement used. In all cases, the amount of open porosity was observed to increase at the expense of closed porosity (without

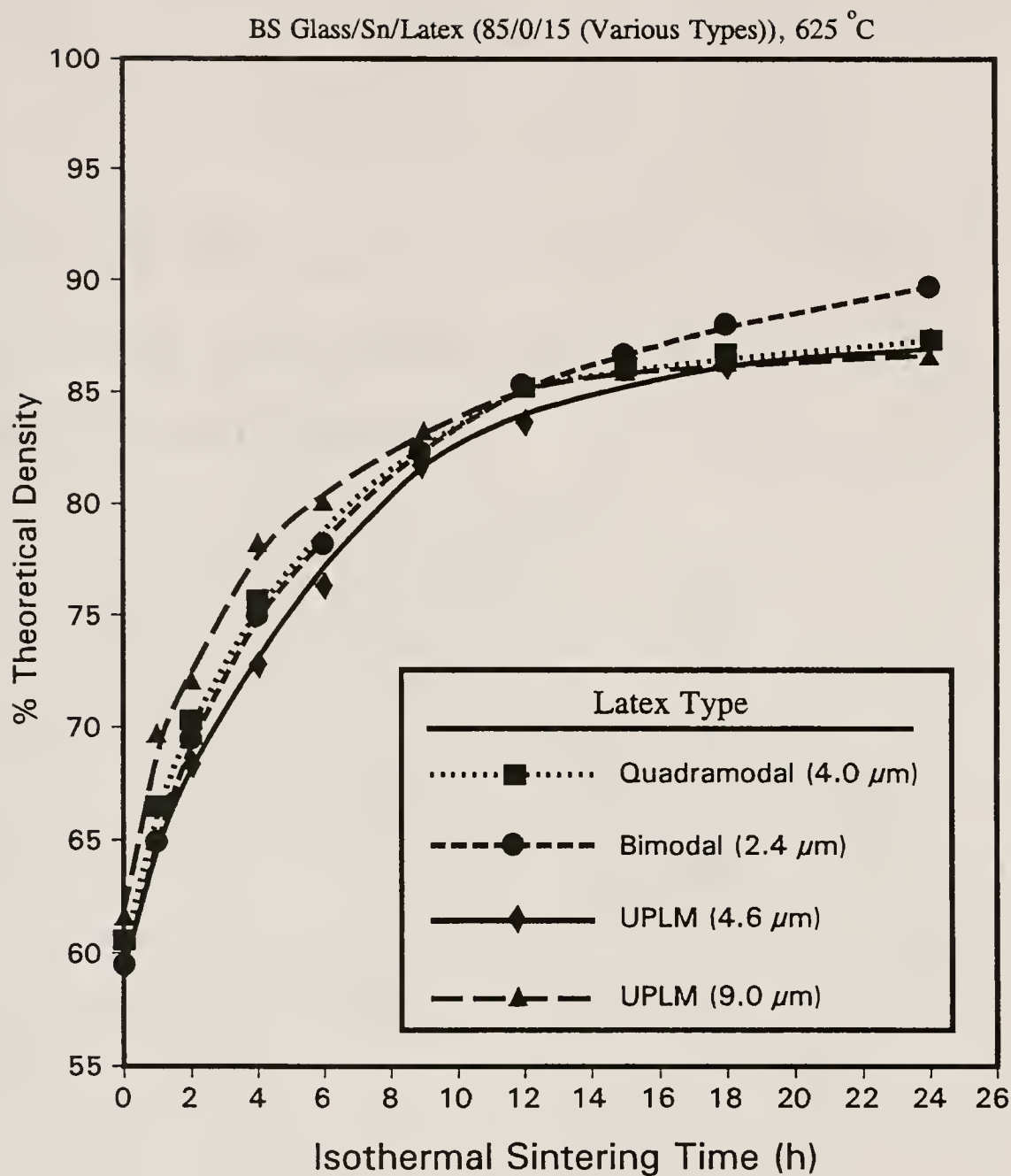


Figure 4.91

Illustration of the effect of included porosity size and size distribution upon the isothermal densification behavior of BS glass/SN/Latex (85/0/15) compacts at 625 °C

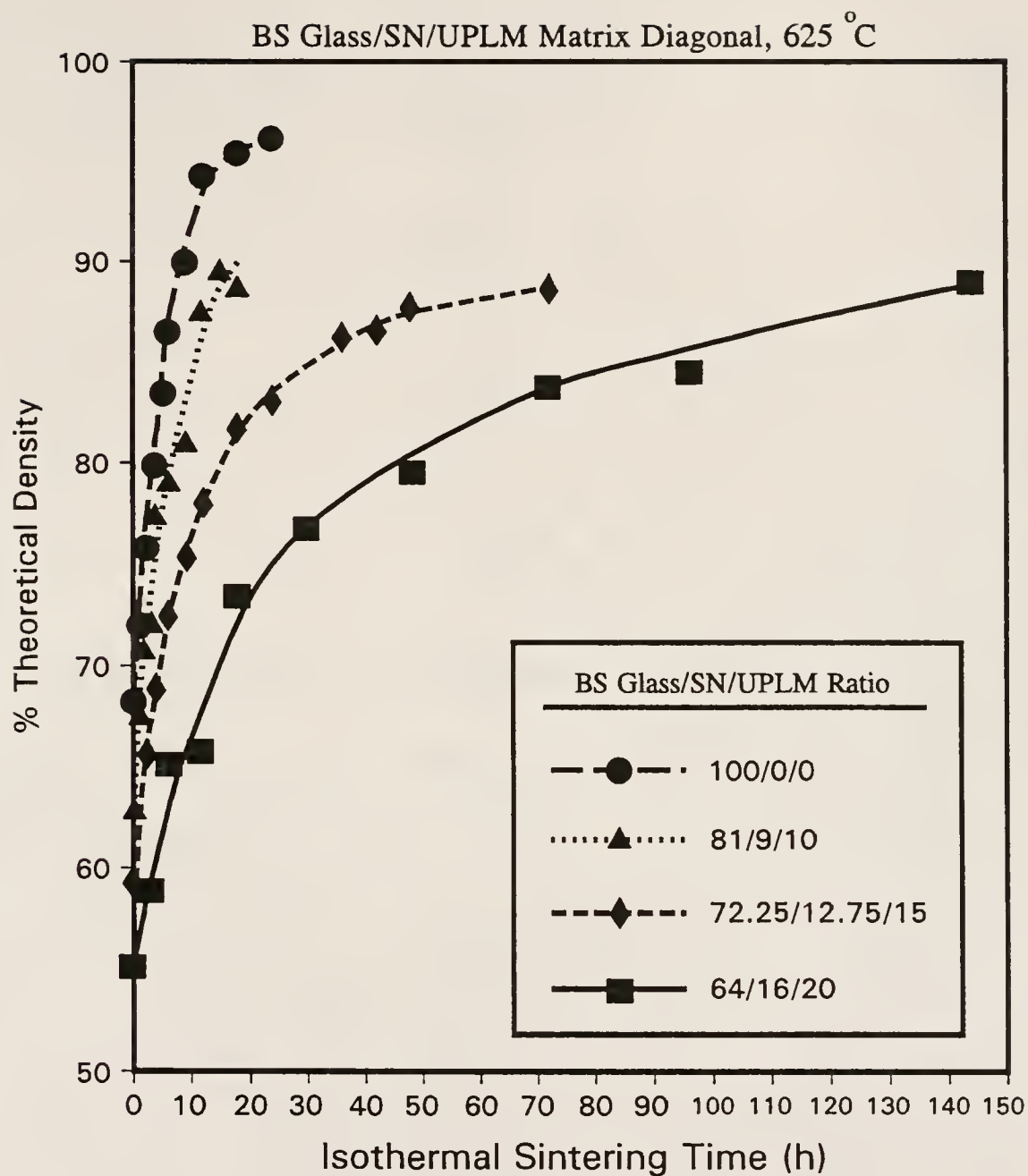


Figure 4.92

Illustration of the densification behavior of composite concentrations on the diagonal of the 4.6  $\mu\text{m}$  plane of the composition matrix investigated at 625 °C



noticeable change in total porosity). In extreme cases, this behavior necessitated up to 8 repetitions of density measurement before the criteria for reproducibility (see section 3.7.1) were met. Therefore, the open porosity stated for these samples represent the maximum amounts measured.

Possible reasons for this behavior include aqueous corrosion of the relatively thin and delicate regions of material between included pores, and/or erosion, of these interpore materials, due to the traumas experienced during Archimedes density measurements (i.e. aqueous infiltration and drying stresses, etc.). Using these explanations, it is reasonable to expect this type of behavior in samples in the initial stages of pore closure. This behavior decreased with further heat treatment (i.e. as the regions between included pores became more robust, and porosity became more closed off). Thus, investigation focusing upon maximization of closed porosity, concentrated upon samples having measured closed porosities at, or slightly after the curve maximum.

Another type of graph, that provides valuable representation of pore structure, is indicated in Figure 4.93. Figure 4.93 illustrates the total, open and closed porosities of as-received BS glass composites, as a function of sintered density, at 625 °C. The total porosity values were obtained by subtracting the percent density from 100 % (or full density). The open porosity was determined as outlined in section 3.7.1, and the closed porosity was obtained from the difference between the calculated total porosity and the measured open porosity. From this description, it is evident that two different techniques (as well as a couple of assumptions) are utilized to obtain these data. Therefore, possible errors are amplified. However, the amount of error may be determined by the graph itself using sintering criteria. First, it is assumed that negative porosities are impossible in reality. Also, in general, closed porosity does not occur until the

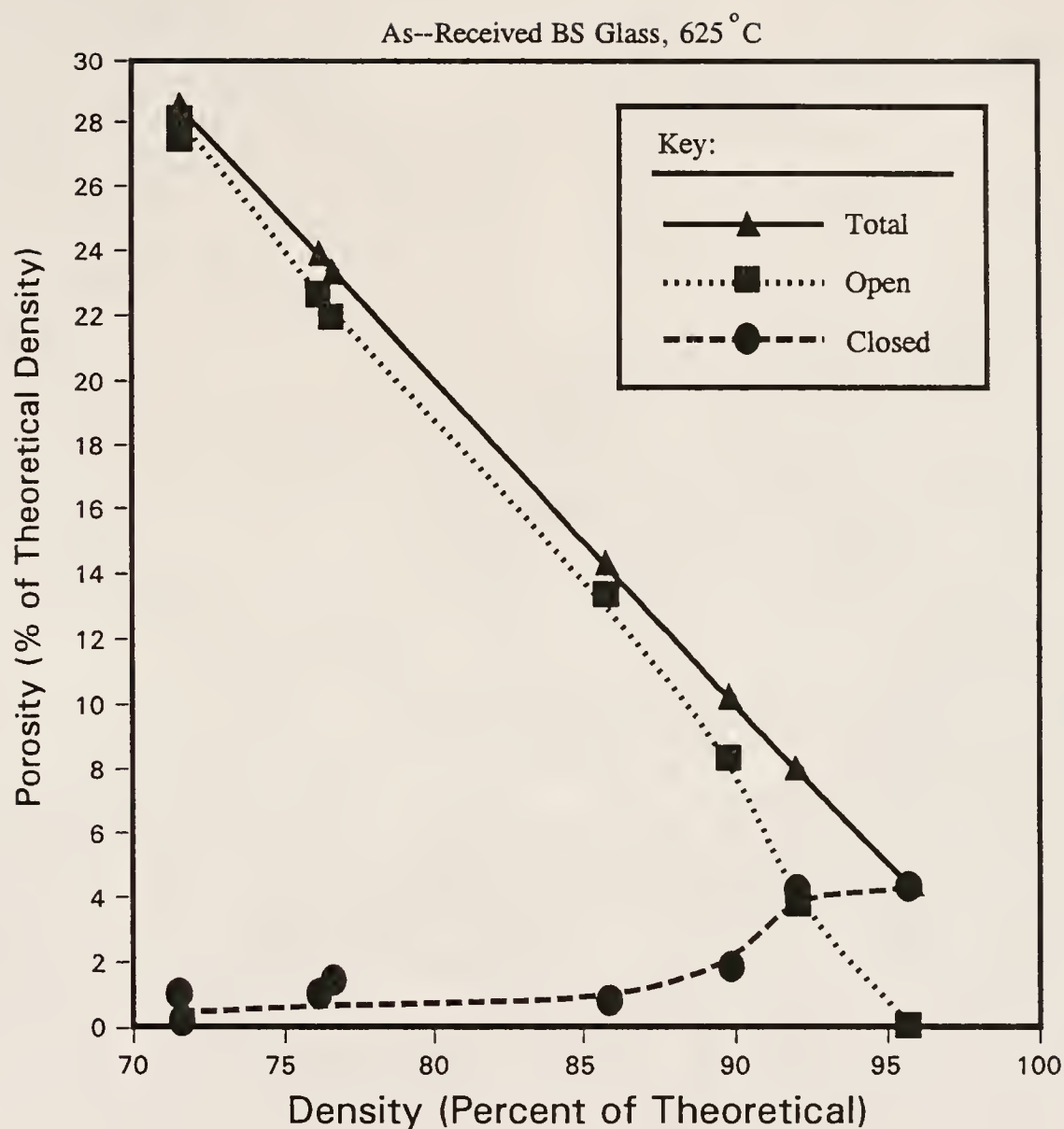


Figure 4.93

Illustration of the total, open and closed porosities of as-received BS glass compacts as a function of sintered density at 625 °C

matrix phase is densified in excess of 90 to 94 % of theoretical density. Using these criteria, it is evident that these values are accurate to within approximately 2 to 3 % at the initial stages of sintering, and improve significantly as densification progresses. This change in accuracy is also typically observed in buoyancy density measurements due to the delicateness of the low density samples as well as the hygroscopicity of the sample surfaces, etc.

Figure 4.93 illustrates behavior typical of the pure BS glass (no included porosity) samples investigated in this study. It is observed that the maximum closed porosity occurs at approximately 4 to 5 V%. Figure 4.94 indicates a similar relationship for the pure, ball milled BS glass (without porosity additions) compacts.

The effect of added porosity upon the total, open and closed porosities of ball milled BS glass compacts is illustrated in several, figures that follow. Figure 4.95 illustrates these relationships for ball milled BS glass compacts containing 5 and 10 V% UPLM additions, and sintered isothermally at 625 °C. It is evident from the figure that the total amount of closed porosity measured increases with increasing UPLM addition. It is also evident that the maximum measured amounts of closed porosity, exhibited by these curves, are not simply an addition of the included porosity (i.e. due to the addition of latex) plus the inherent porosity (i.e. the porosity native to the BS glass matrix). The maximum amounts of closed porosity measured for the 5 and 10 V% UPLM addition compacts were ~ 7.7 and ~ 10.3 respectively. Thus, it may be concluded that, as the amounts of porosity addition increase, the inherent porosity is eliminated. Eventually (i.e. around 10 V% addition), most or all of the inherent porosity is eliminated, and only included porosity remains to create the closed porosity observed.

This trend is observed with increased additions of porosity as well. Figures 4.96 and 4.97 illustrate the total, open and closed porosities of BS glass compacts containing 15 V% additions of the

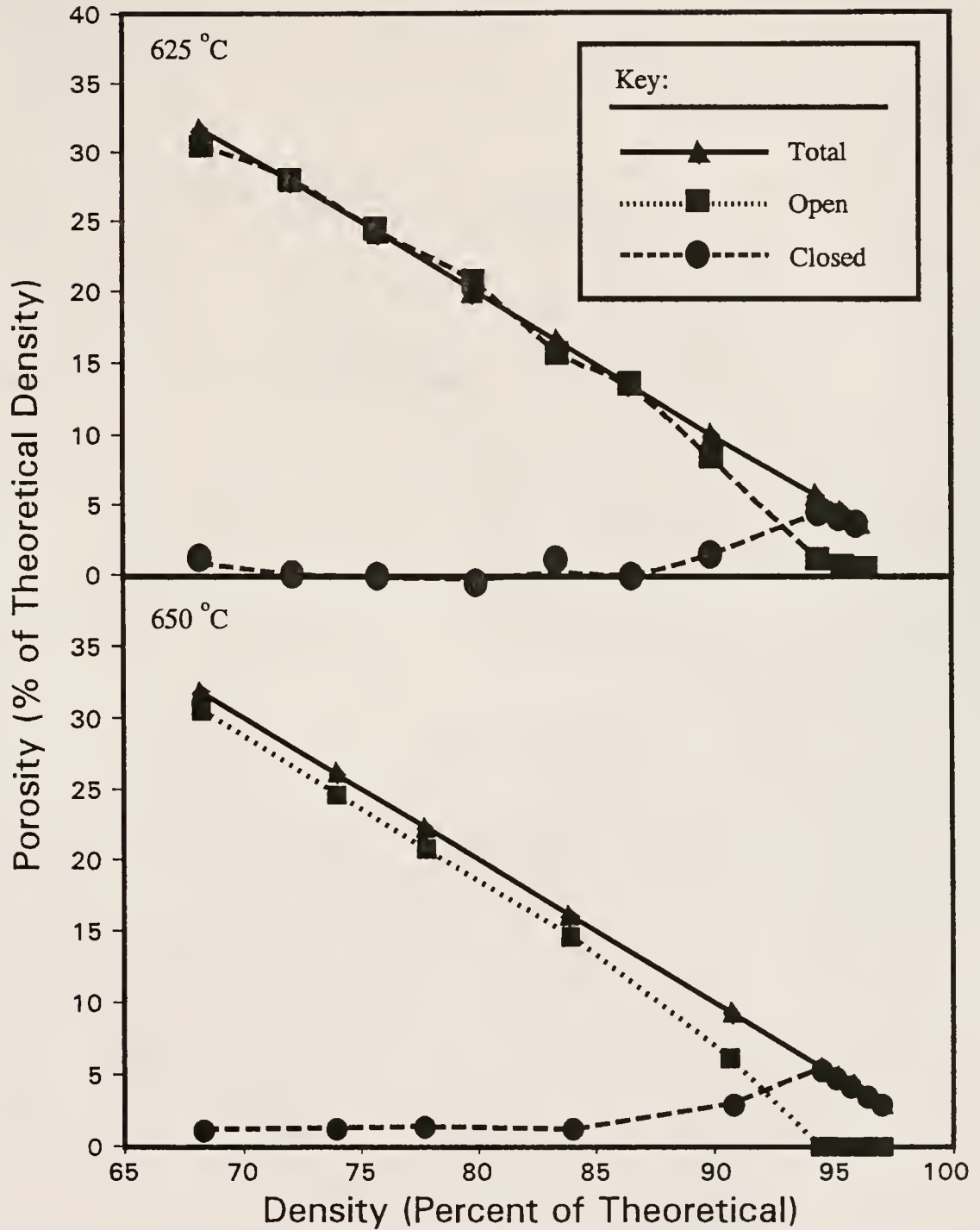


Figure 4.94

Illustration of the total, open and closed porosities, as a function of sintered density, for pure BS glass compacts sintered at 625 °C and 650 °C

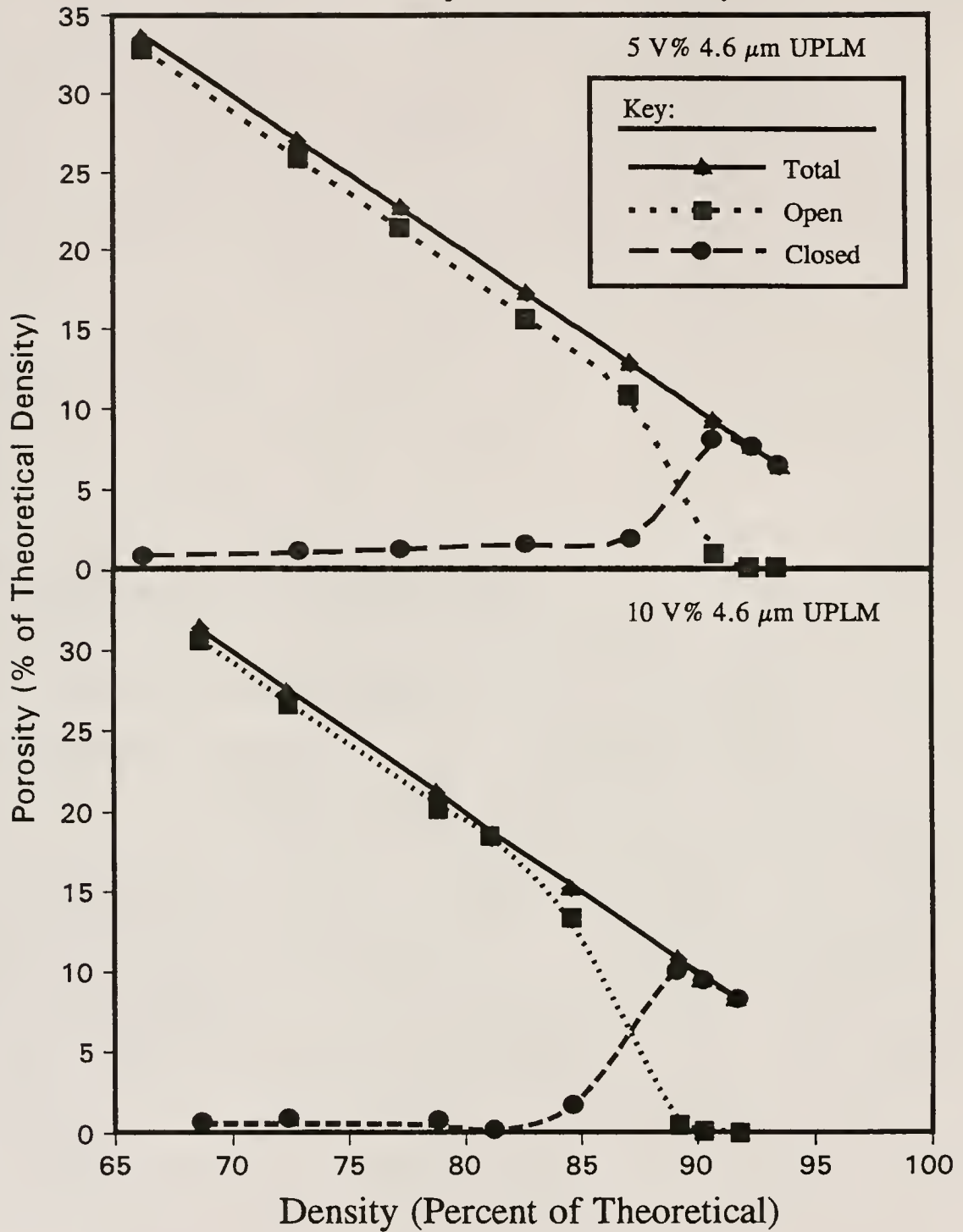


Figure 4.95

Illustration of the total, open and closed porosities versus sintered density of BS glass compacts containing 5 and 10 V% additions of 4.6  $\mu\text{m}$  UPLM isothermally sintered at 625  $^{\circ}\text{C}$



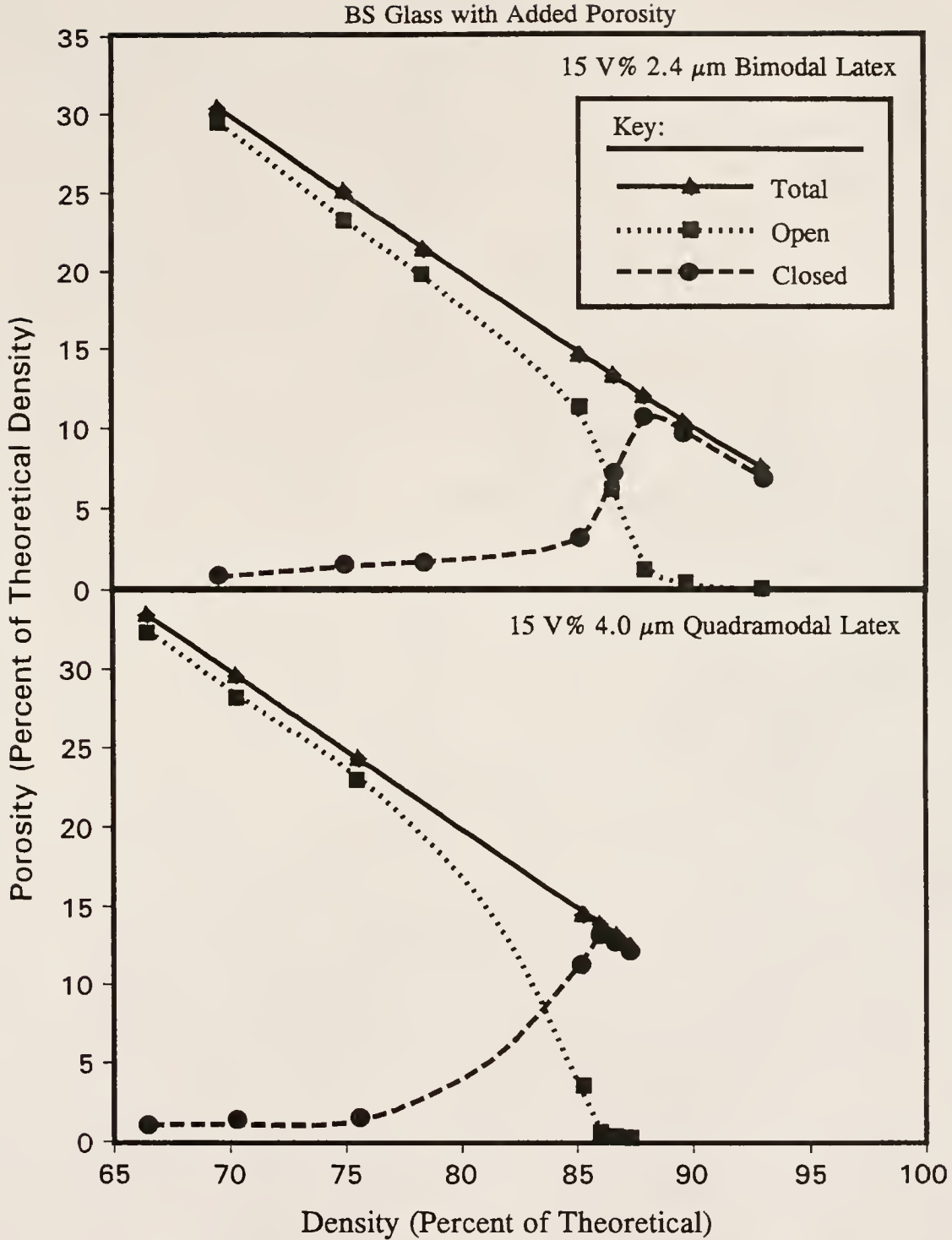


Figure 4.96

Illustration of the total, open and closed porosities of BS glass compacts containing 15 V% of 2.4  $\mu\text{m}$  bimodal and 4.0  $\mu\text{m}$  quadramodal respectively as a function of sintered density

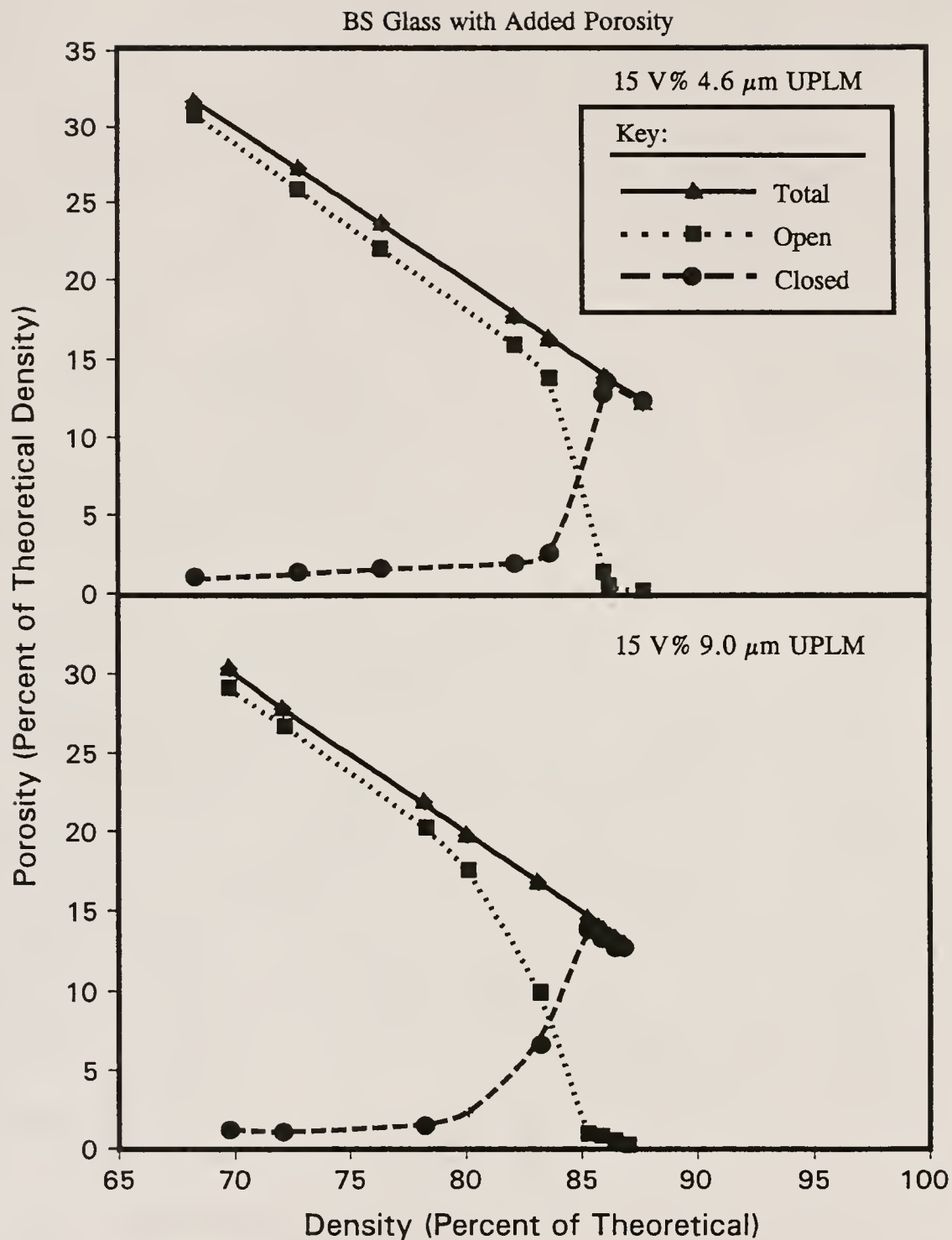


Figure 4.97

Illustration of total, open and closed porosities of BS glass compacts containing 15 V% additions of 4.6  $\mu\text{m}$  and 9.0  $\mu\text{m}$  UPLMs respectively, as a function of sintered density

various types of latex developed for this study. Figure 4.96 illustrates this behavior for the 2.4  $\mu\text{m}$  bimodal and the 4.0  $\mu\text{m}$  quadramodal additions, while Figure 4.97 illustrates these relations for the 15 V% additions of 4.6  $\mu\text{m}$  and 9.0  $\mu\text{m}$  UPLMs respectively. In fact, this figure indicates that even some of the added porosity is either eliminated or remains open, since 15 V% closed porosity is not achieved in any of these compacts.

There are two reasons to explain this. First, added porosity that is either at, or connected to, the sample surface through large pore channels, will always remain as open porosity. Second, the large pores may also decrease in size to some extent, as sintering proceeds. Thus, the actual volume of added porosity would be reduced due to size reduction in the added porosity. Both of these mechanisms will be shown to have an influence upon the maximum amount of porosity achievable, and will be discussed in further detail below.

It is also evident from Figures 4.96 and 4.97 that the maximum amount of closed porosity obtainable is also a function of the size of the latex added to create included porosity. The maximum amount of closed porosity achieved with 15 V% additions of 2.4  $\mu\text{m}$  latex was barely greater than the analogous amount for 10 V% additions of 4.6  $\mu\text{m}$  UPLM. Furthermore, the greatest amount of closed porosity of the 15 V% latex addition materials, was achieved using the additions of 9.0  $\mu\text{m}$  UPLM. Since the 9.0  $\mu\text{m}$  UPLM additions gave the highest performance, and since said additions resulted in nearly a 1 to 1 ratio in added to closed porosity, the following recommendation is made. The recommended added pore size to inherent, post-pyrolysis pore channel ratio should equal or exceed 40. This is the approximate value of the 9.0  $\mu\text{m}$  UPLM diameter divided by the 0.230  $\mu\text{m}$  post-pyrolysis pore channel diameter observed in the 15 V% 9.0  $\mu\text{m}$  UPLM addition compacts. It should be noted that the 4.6  $\mu\text{m}$  addition UPLM gave only slightly decreased performance, and had a

similar ratio of approximately 20. Thus, this value may vary somewhat, but should exceed at least 20.

This ratio is very valuable if it is desirable to design a system of known closed porosity (up to  $\sim 15$  V%) with minimal surface roughness. For example, if it is desirable to limit surface roughness to a maximum of  $5\text{ }\mu\text{m}$ , one would use a target included porosity diameter near to, or slightly less than,  $5\text{ }\mu\text{m}$  (assuming that no pore clustering occurs, less if it does). Thus, the glass matrix powder should pack to have a post-pyrolyzed pore channel diameter of less than  $0.25\text{ }\mu\text{m}$  (ideally less than  $0.125\text{ }\mu\text{m}$ ). If a monosized glass powder is utilized, and said powder packs according to RCP theory, the maximum powder size used should not exceed  $1.75\text{ }\mu\text{m}$  (ideally, it would not exceed  $0.875\text{ }\mu\text{m}$ ), using the pore channel size criteria outlined in section 2.3.

Figure 4.98 illustrates the total, open and closed porosity relationships, as a function of sintered density, of BS glass compacts having  $4.6\text{ }\mu\text{m}$  UPLM additions of 20 and 30 V%. It is evident from Figures 4.97 and 4.98 that there is little benefit from increasing the additions of UPLM from 15 V% to 20 V%. This is probably a result of included porosity exceeding the percolation threshold at the final stages of sintering. This also explains the longer times to achieve the maximum amount of closed porosity of the 20 V% UPLM addition compacts as compared to those containing 15 V% additions.

Furthermore, it is evident from Figure 4.98 that additions of latex, that surpass the percolation threshold in the green state, result in maximum closed porosities that are no greater than those observed in the pure glass compacts (i.e. without porosity additions). This is a result of the onset of a continuous included pore structure, as described above.

Therefore, it may be assumed that in order to maximize closed porosity (which will not exceed the percolation threshold of  $\sim 16$  V%), the UPLM addition should be between 15 and 20 V%, and should be of 9.0

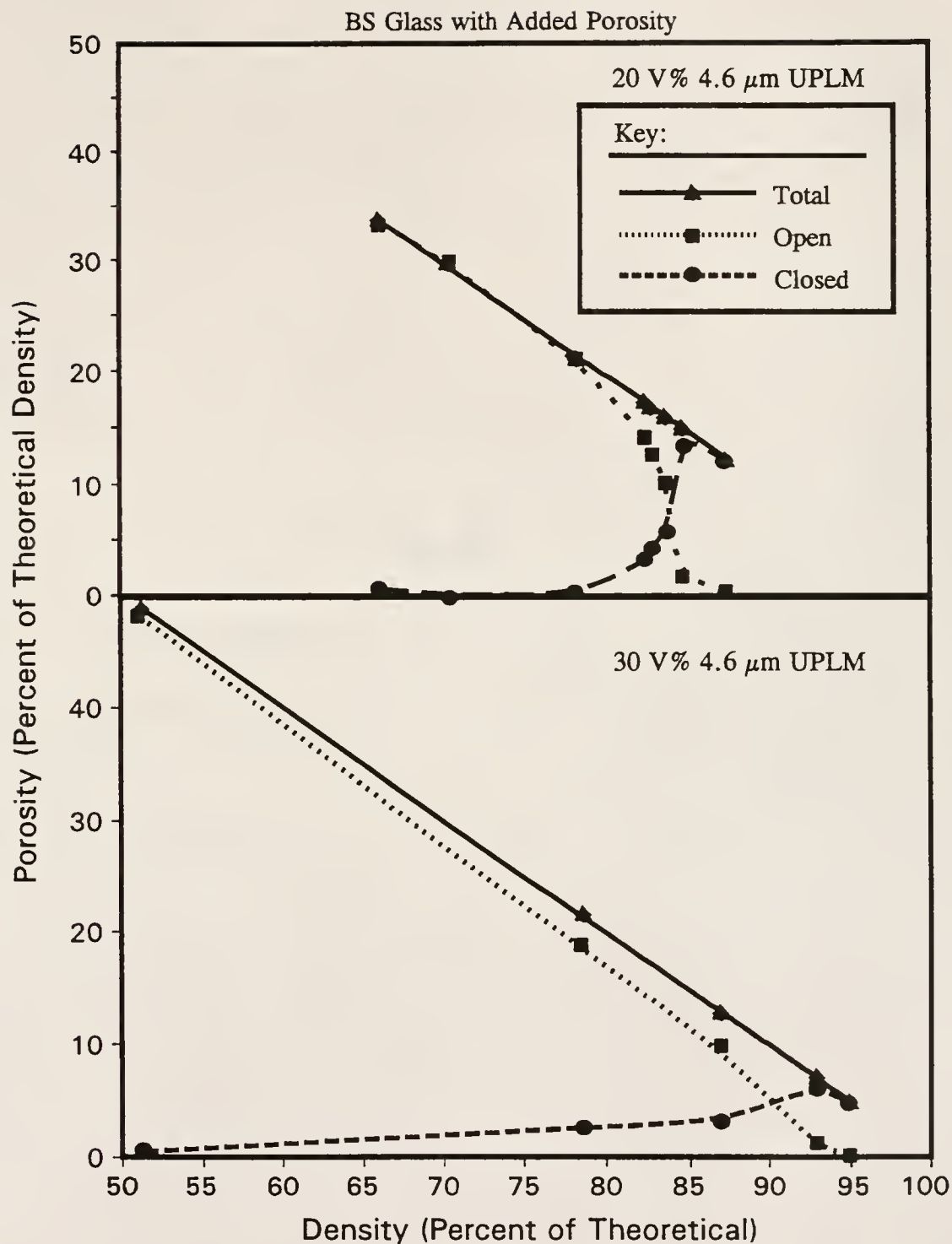


Figure 4.98

Illustration of the total, open and closed porosities, as a function of sintered density, of BS glass compacts containing 20 and 30 V% additions of 4.6  $\mu\text{m}$  UPLM



$\mu\text{m}$  UPLM (for this study). Using the feedback data obtained from this study, a batch of compacts of ball milled BS glass, containing 17.6 V% additions of 9.0  $\mu\text{m}$  UPLM were produced, processed and characterized. Figure 4.99 illustrates the analogous relationship for the 82.4/0/17.6 BS glass/ $\text{Si}_3\text{N}_4$ /9.0  $\mu\text{m}$  UPLM composition composite.

From Figure 4.99 it is evident that the maximum in closed porosity in this configuration is greater than in all other systems measured (i.e. approximately 15.6 V%) in this study. Thus, the feedback optimization used was successful, indicating that enough knowledge has been gained about this system to make precise and reasonably accurate predictions of pore structure. This is very important when designing materials for the properties desired. This is also very important in the sense of defining limitations of a technique or system, as has now been achieved for this system, in the sense of the maximization of closed porosity (for the techniques utilized in this study).

Figures 4.100 to 4.104 illustrate the total, open and closed porosity relationships, as a function of sintered density, for BS glass/ $\text{Si}_3\text{N}_4$ /4.6  $\mu\text{m}$  UPLM composites. Figures 4.100 and 4.101 depict these relationships for 80/20 normalized concentrations of BS glass/ $\text{Si}_3\text{N}_4$ . Figure 4.100 is for 80/20 BS glass/ $\text{Si}_3\text{N}_4$  composites without added porosity at isothermal sintering temperatures of 625 °C and 650 °C respectively, and Figure 4.100 is for the same, except with 10 and 20 V% additions of 4.6  $\mu\text{m}$  UPLM (sintered at 625 °C).

It is evident that these relationships are quite similar to the relationships in pure BS glass described above. The 10 V% UPLM addition has a slightly greater maximum closed porosity (i.e. ~ 10.3 versus ~ 10.5 V% respectively) however.

Figure 4.102 illustrates this relationship for the two remaining composite compositions on the diagonal of the 4.6  $\mu\text{m}$  UPLM plane of the composite composition volume (i.e. the 81/9/10 and the 72.25/12.75/15 compositions). From the figure, it is evident that the 10 V% UPLM

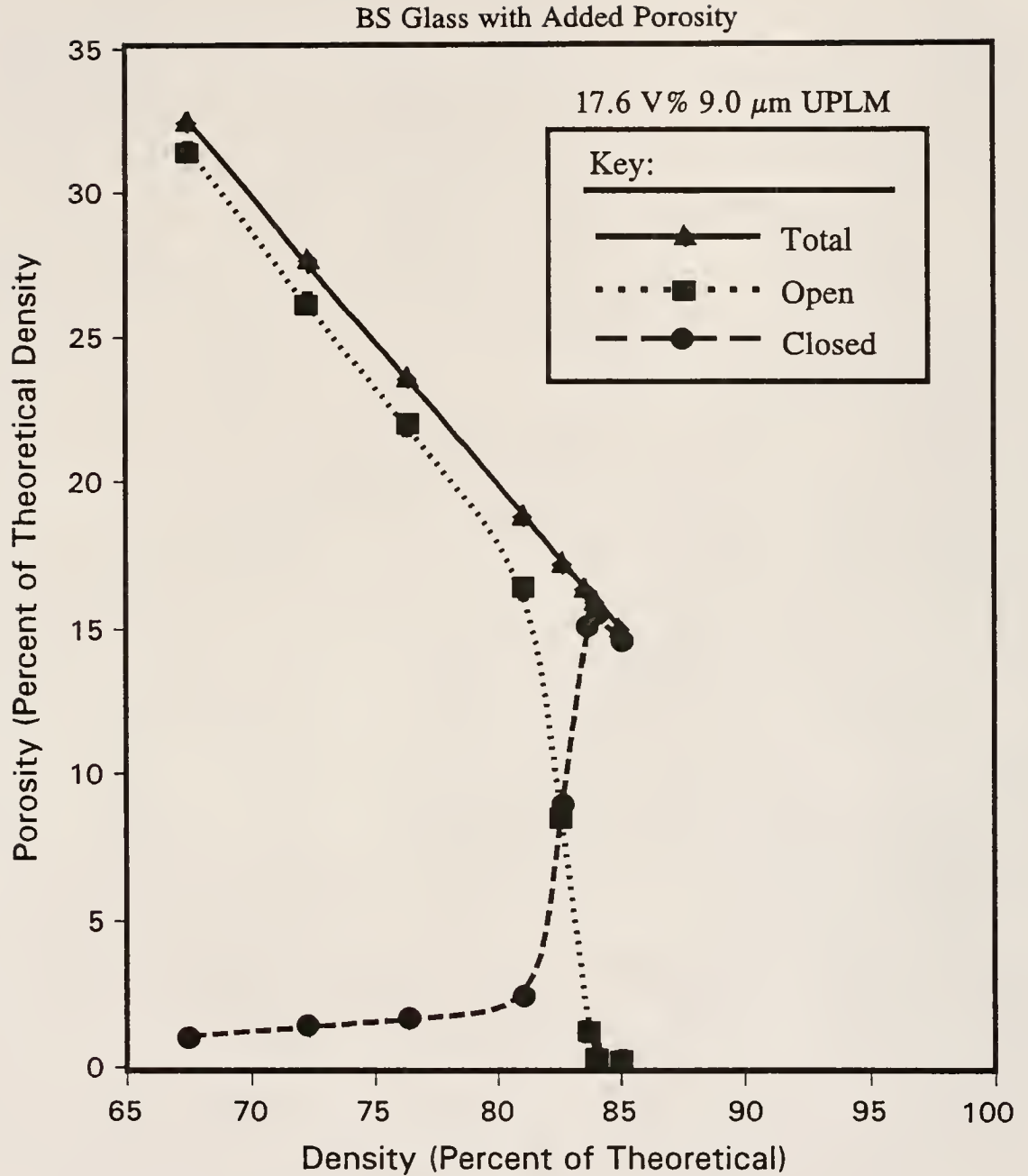


Figure 4.99

Illustration of the total, open and closed porosities, versus sintered density, of ball milled BS glass compacts containing 17.6 V% additions of 9.0  $\mu\text{m}$  UPLM, isothermally sintered at 625 °C

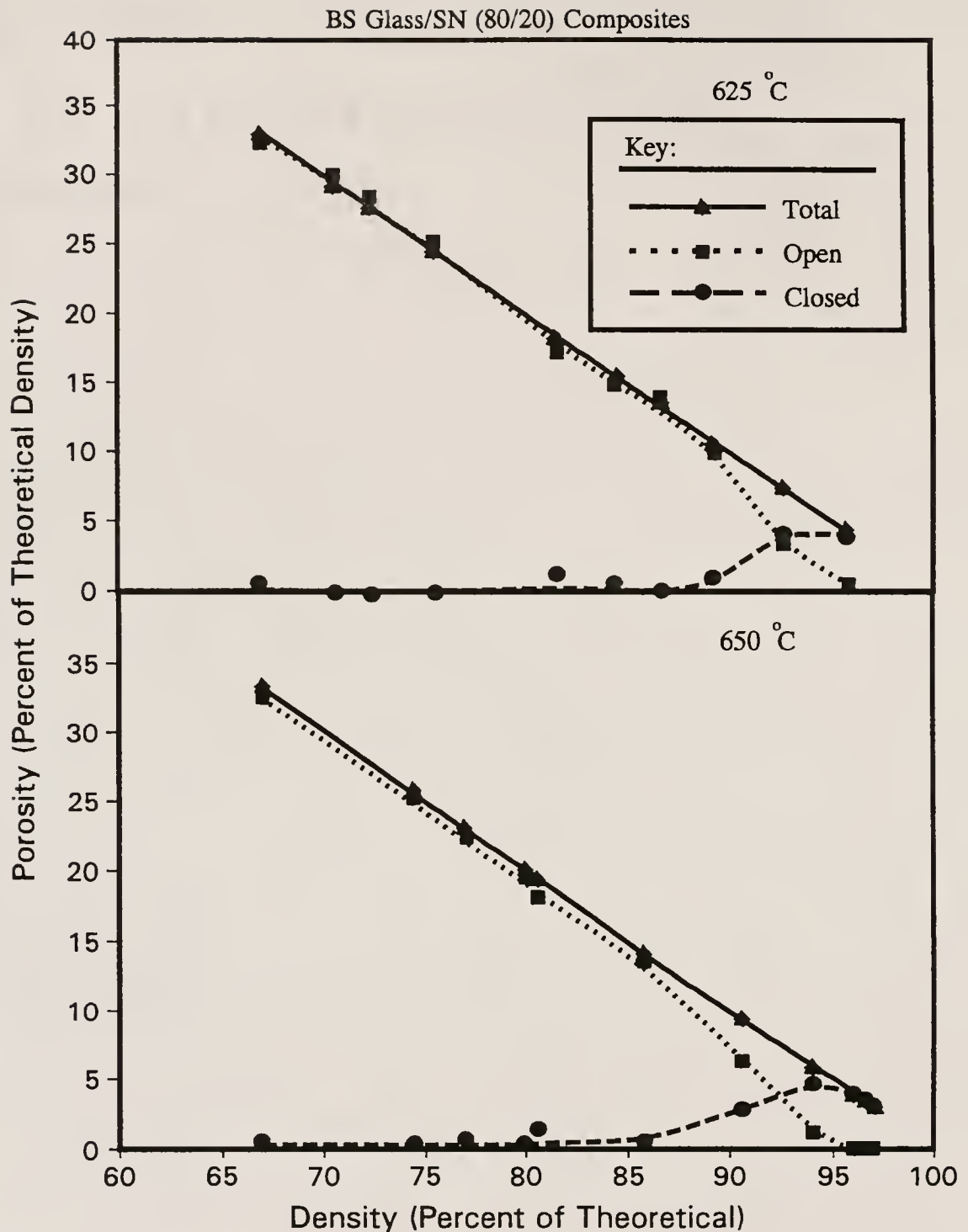


Figure 4.100

Illustration of total, open and closed porosities of 80/20 BS glass/SN composites, as a function of sintered density, isothermally sintered at 625 °C and 650 °C respectively

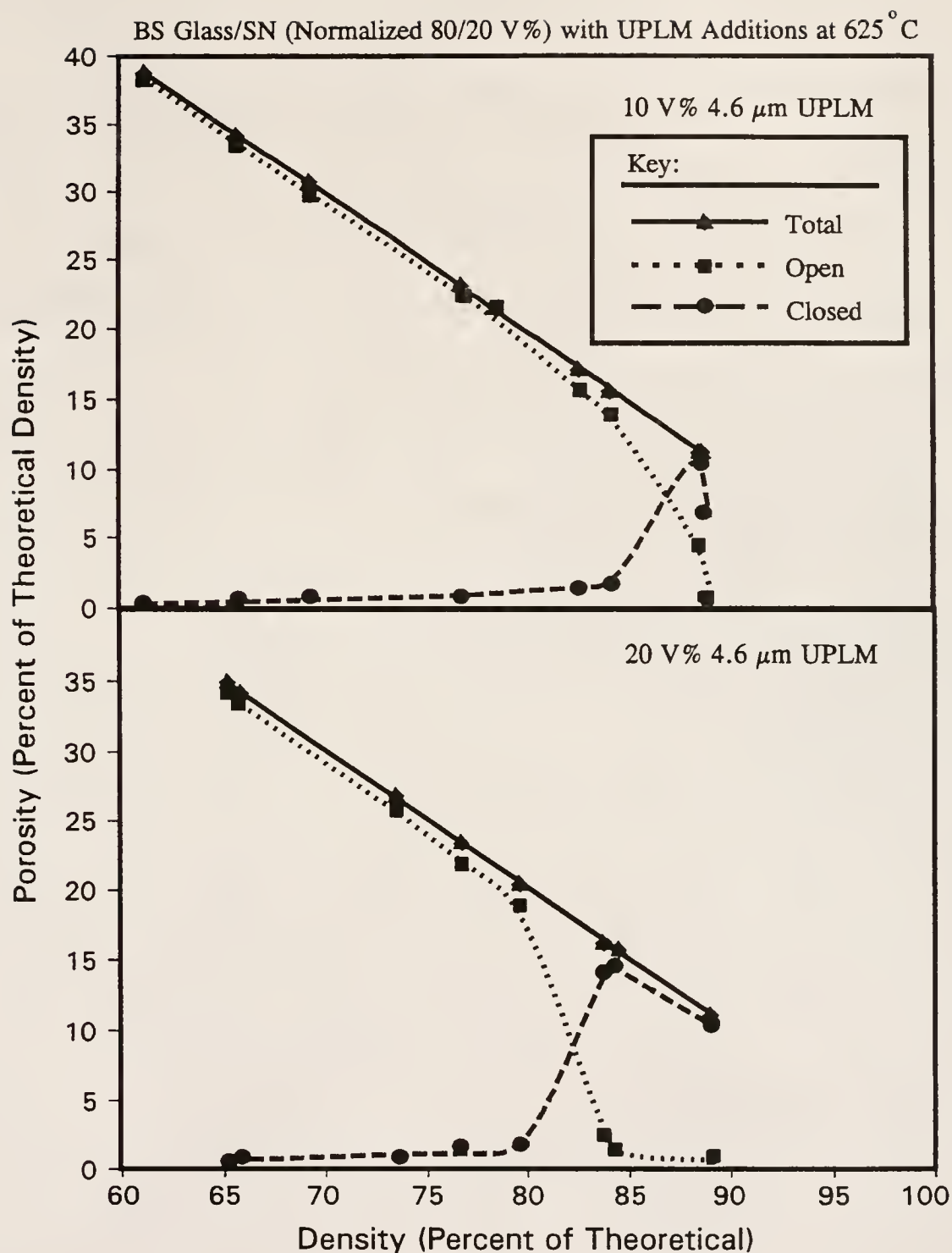


Figure 4.101

Illustration of total, open and closed porosities of normalized 80/20 (BS glass/SN) composites containing 10 and 20 V% 4.6  $\mu\text{m}$  UPLM, respectively, as a function of sintered density

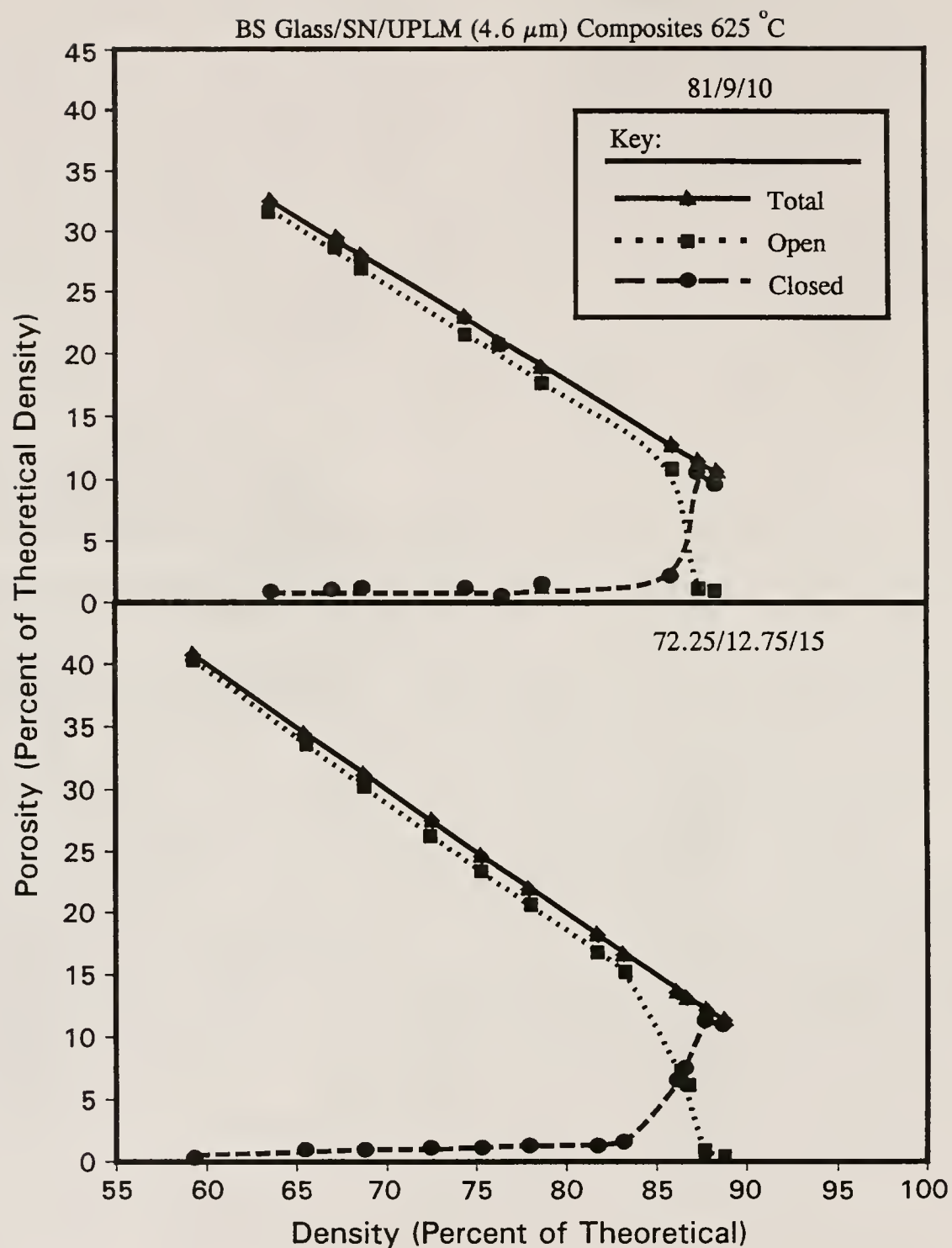


Figure 4.102

Illustration of the total, open and closed porosities of 81/9/10 and 72.25/12.75/15 (BS glass/SN/ $4.6\ \mu\text{m}$  UPLM) composite compositions, as a function of sintered density



addition gives a maximum in closed porosity that is comparable to both of the other 10 V% UPLM addition concentrations (i.e.  $\sim 10.5$  versus  $\sim 10.5$  versus  $\sim 10.3$  V% closed porosity maximum). However, the 72.25/12.75/15 (BS glass/ $\text{Si}_3\text{N}_4$ /4.6  $\mu\text{m}$  UPLM) composition curve does not exhibit as high a maximum in closed porosity as is expected (i.e.  $\sim 11.3$  versus  $\sim 13.4$ ). It is not known why this particular composition yielded a significantly lower maximum closed porosity.

Figures 4.103 and 4.104 illustrate the above relationship for the normalized 60/40 (BS glass/SN) family of composites produced for this study. Figure 4.103 depicts the total, open and closed porosities of 60/40 composites, without added porosities, at 625, 650 and 730  $^{\circ}\text{C}$  respectively. It is evident from the figure that a maximum in density is not achieved at 625  $^{\circ}\text{C}$  for these composites (at isothermal sintering times of up to 144 h) due to the lack of development of the pore structure to the final stages of sintering. It also is evident from the figure that the pore characteristics, of these samples, change when the isothermal sintering temperature is changed from 650  $^{\circ}\text{C}$  to 730  $^{\circ}\text{C}$ . This perceived effect may also be a result of the relatively limited data set obtained at 730  $^{\circ}\text{C}$ . However, this effect is also somewhat logical, since significant bloating was observed at 820  $^{\circ}\text{C}$ . Thus, gas evolution may be significant enough at 730  $^{\circ}\text{C}$  to keep porosity open to the more advanced stages of sintering.

It is also important to note that the 60/40 composites, sintered at 650  $^{\circ}\text{C}$ , exhibited a relatively high (i.e.  $\sim 7.5$  %) maximum in closed porosity. This may be a result of sealing-off of the relatively porous BS glass/ $\text{Si}_3\text{N}_4$  through viscous flow of the BS glass composite structure in the final stages of sintering.

Figure 4.104 indicates that the pore structure of the 48/32/20 (BS glass/SN/4.6  $\mu\text{m}$  UPLM) composites also remains relatively undeveloped after isothermal sintering times of 144 h. This is logical since 60/40/0 composition also exhibited this behavior. However, these

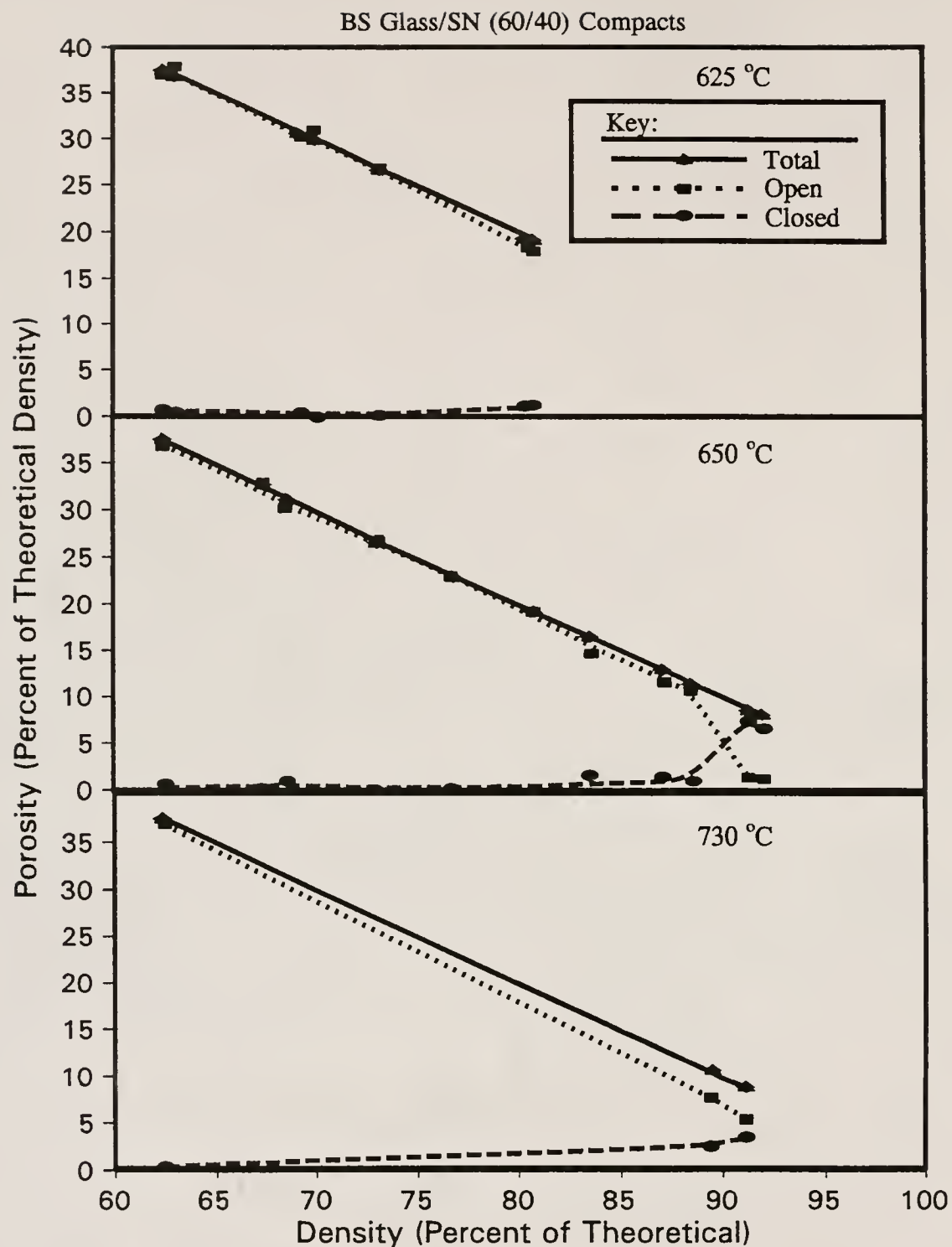


Figure 4.103

The total, open and closed porosity of 60/40/0 (BS glass/SN/UPLM) composites as a function of sintered density, at isothermal sintering temperatures of 625, 650 and 730 °C respectively

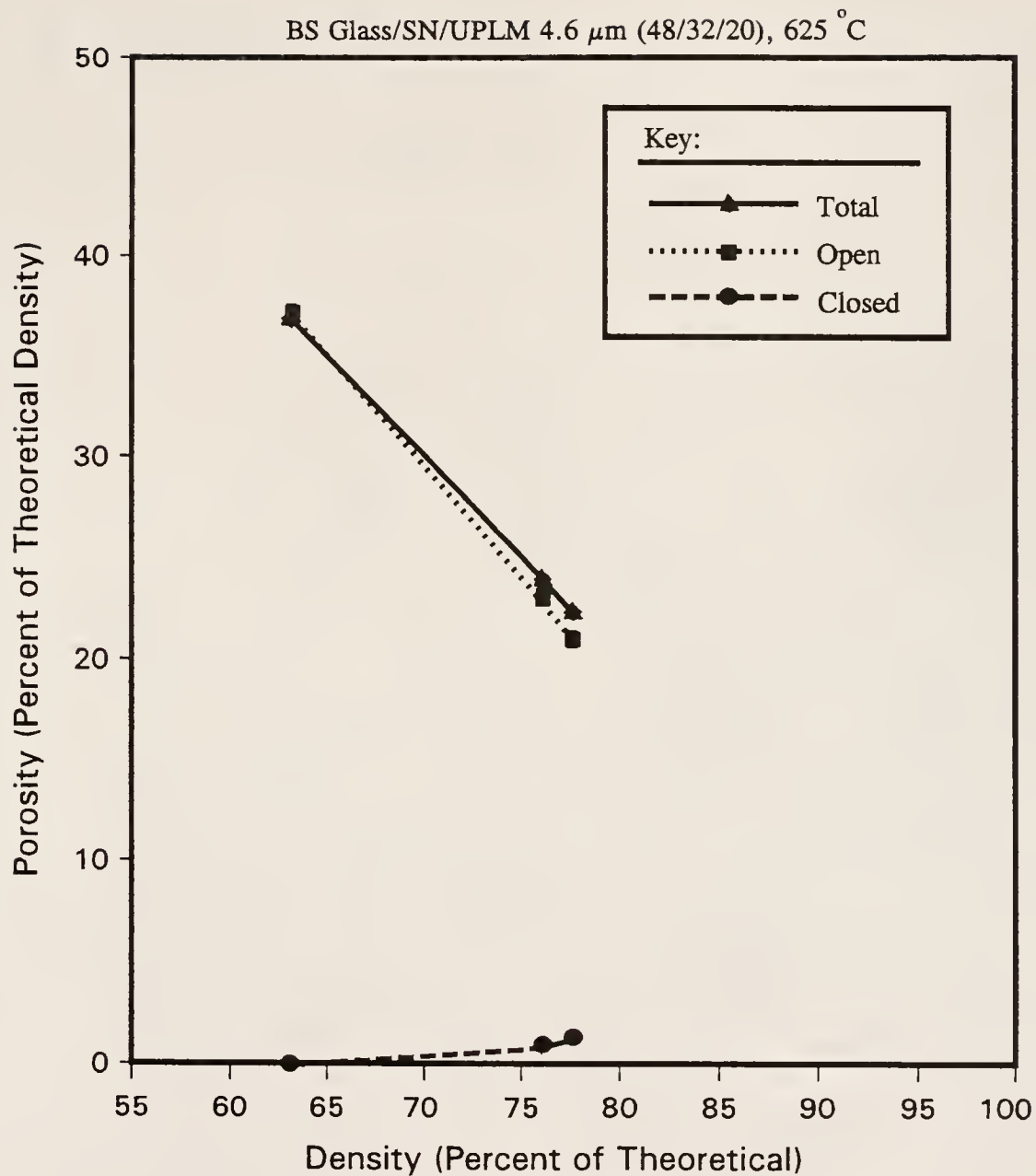


Figure 4.104

Illustration of the total, open and closed porosities of 48/32/20 (BS glass/SN/4.6  $\mu\text{m}$  UPLM) composites as a function of sintered density

compacts did sinter to a maximum observed density of approximately 76 % of theoretical density, indicating that some pore rearrangement must have occurred.

Table 4.6 depicts a summary of the data portrayed in the figures above. As mentioned above, the maximum closed porosity observed in this study is ~ 15.6 V%. The corresponding open porosity, at said maximum in closed porosity, was ~ 0.4 V%. Thus, the total porosity at the maximum in observed closed porosity is ~ 16 V%. This is in excellent agreement with literature values for the three-dimensional percolation threshold for monosized, randomly placed spheres in three dimensions (i.e. ~ 16 V% [83ZAL]), and indicates that the percolation onset probably cannot be exceeded using these techniques for additions of controlled porosity.

A comparison with pertinent literature indicates that the above values are reasonable. In a similar study, Kata, et al. noted that it was difficult to produce borosilicate glass-matrix composites (filled with either cordierite or quartz) with closed porosities in excess of 13 V% [90KAT]. Kata, et al. used 18  $\mu\text{m}$  average polystyrene microspheres having a relatively wide size distribution, as visually observed (exact data is not available as to the sizing basis used or the size distribution measured) in tape cast and laminated compacts. Polystyrene latex was used because the investigators found that it is a superior candidate from the standpoint of non-solubility in tape vehicles, as well as from the standpoint of thermolysis (in both  $\text{N}_2$  and in air).

The ceramic powders used had average diameters from 2.5 to 3.8  $\mu\text{m}$  in diameter. Thus, the average sphere diameter to pore channel diameter ratio ranged from approximately 33 to 50 (assuming that the packing of the ceramic powders can be reasonably modelled as monosized, spherical RCP structure). Due to the lamination process, the porosity additions were oval, or egg-shaped instead of spherical. Furthermore, the tape cast system had a relatively large amount of organic concentration,

Table 4.6

Maximum Closed Porosity Relationships for All  
Composite Compositions Investigated

I.D. #	Composition (V%)					Porosity (V%)			Sintering	
	BS <sup>1</sup>	SN	UPLM			Max. Clos ed	Open <sup>3</sup>	Tot <sup>3</sup>	Temp (°C)	Time (h)
			V%	S <sup>2</sup>	D <sup>2</sup>					
12119001	100 AR	0	0	NA	NA	4.9	2.9	7.8	625	48
03209001	100	0	0	NA	NA	5.6 <sup>4</sup>	0.0	5.6	650	96
03209001	100	0	0	NA	NA	4.8 <sup>4</sup>	1.1	5.9	625	12
05109102	95	0	5	4.6	M	8.1	1.1	9.2	625	9
01039101	90	0	10	4.6	M	10.3	0.6	10.9	625	12
05179102	85	0	15	2.4	B	10.9	1.2	12.1	625	18
05179101	85	0	15	4.0	Q	13.3	0.8	14.1	625	15
05069101	85	0	15	4.6	M	13.4	0.5	13.9	625	18
05099101	85	0	15	9.0	M	13.9	0.7	14.6	625	12
05069102	82.4	0	17.6	9.0	M	15.6	0.4	16.0	625	18
12109001	80	0	20	4.6	M	14.3	0.7	15.0	625	24
05079101	70	0	30	4.6	M	5.9	1.0	6.9	625	72
01049101	81	9	10	4.6	M	10.5	0.8	11.3	625	18
05119101	72.25	12.75	15	4.6	M	11.3	0.9	12.2	625	48
03219001	80	20	0	NA	NA	4.7	1.2	5.9	650	6
03219001	80	20	0	NA	NA	4.2	1.4	5.6	625	24
01249101	72	18	10	4.6	M	10.4	0.8	11.2	625	72
01069101	64	16	20	4.6	M	10.5	0.3	10.8	650	27
01069101	64	16	20	4.6	M	14.6	1.1	15.7	625	96
03199001	60	40	0	NA	NA	1.7	9.7	11.4 <sup>5</sup>	820	1
03199001	60	40	0	NA	NA	3.6	5.1	8.7	730	36
03199001	60	40	0	NA	NA	7.5	1.2	8.7	650	102
03199001	60	40	0	NA	NA	1.3	18.0	19.3 <sup>5</sup>	625	144
10109001	48	32	20	4.6	M	1.5	20.9	22.4 <sup>5</sup>	625	72



Table 4.6 (continued)

- Notes:
1. Borosilicate glass powder (AR denotes as-received, all others are ball milled)
  2. S is latex diameter, D is dispersity, B is bimodal, Q is quadramodal, M is monodisperse
  3. Open and Total porosities (in V%) are at the maximum observed in closed porosity
  4. Indicates value was influenced by bloating
  5. Indicates that the porosity in this system did not mature to the final stages of sintering

other than the latex (i.e. binder. plasticizer etc.), as compared to the current study. Other than these factors, the two studies are similar.

The maximum in closed porosity observed by Kata, et al. is remarkably close to that observed in this study. Percolation theory was not utilized to describe this phenomenon, however.

In a related study Yamamoto, et al. also investigated the effects of latex addition up on the amount of included porosity (and, ultimately dielectric properties) achievable [89YAM]. In this study, three different microsphere chemistries were utilized, polymethyl methacrylate (PMMA), polystyrene (PS), and polyethylene (PE). The PS spheres were found to function most satisfactorily of the three in this application as well. Two sizes of PS latex were investigated, one having an average size of 7  $\mu\text{m}$ , the other having an average size of 18  $\mu\text{m}$  (it is not known what the dispersity of these spheres were, or the basis used to determine the particle size). The samples were prepared similarly to those in the study of Kata, et al. Also, some samples were formed using dry pressing of intimately mixed powders.

The 7  $\mu\text{m}$  spheres were found unsatisfactory (they attribute this to agglomeration and segregation to the tape surface). The researchers in this study were able to produce samples having porosities as high as approximately 11 V%. Said additions were found to reduce dielectric constant by approximately 13%, and to slightly increase dielectric loss, due to residual Ca from the pyrolyzed latex (the manufacturer used  $\text{CaPO}_4$  in the fabrication of the latex).

#### 4.4 Characterization and Modelling of Processed Materials

##### 4.4.1 Characterization of Microstructure

Figures 4.105 and 4.106 illustrate representative microstructures of ball milled BS glass compacts. From the figure, it is evident that the microstructure of the 81 % dense sample includes porosity in the size regime of 1  $\mu\text{m}$ , while the porosity apparent in the 97 % dense

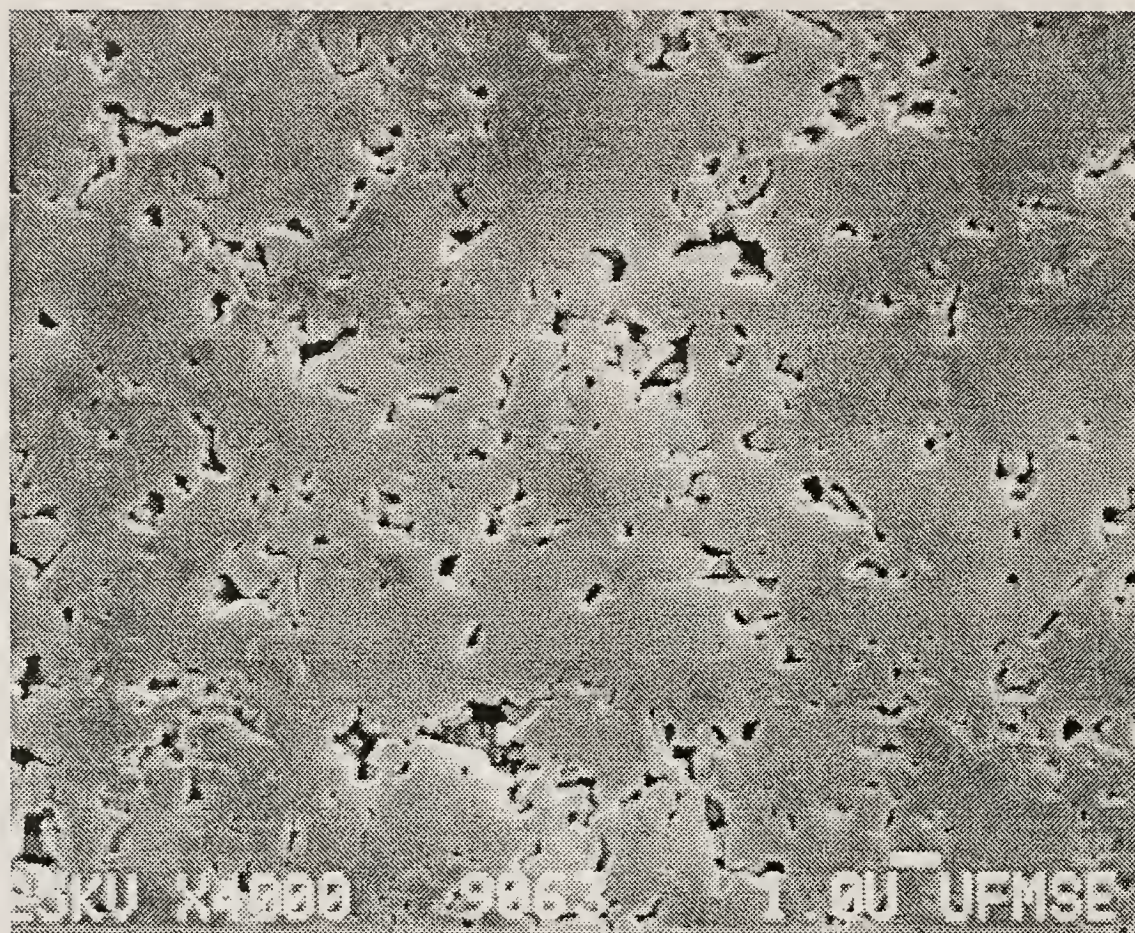


Figure 4.105

Micrograph illustrating the microstructure representative of a pure ball milled BS glass sintered to approximately 81 % density





Figure 4.106

Micrograph illustrating the microstructure representative of a pure, ball milled BS glass compact sintered to approximately 97 % of theoretical density

sample is much more sporadic, but is not significantly smaller in size. A major difference between these two samples is that the porosity in the 81 % dense sample is almost totally open (i.e. approximately 17.5 V% of the porosity is continuous, and connected to the sample surface), while almost all of the remaining 3 % of porosity in the 97 % dense sample is closed (i.e. the open porosity is less than 0.05 %).

Figure 4.107 depicts the relationship between the inherent porosity and the included porosity. The sample has a 10 V% addition of 4.6  $\mu\text{m}$  UPLM, and was sintered to approximately 72 % of theoretical density (approximately 27 and 1 V% open and closed porosities respectively). It is evident from the figure that the porosity created via the UPLM addition is significantly larger than the inherent porosity.

Figures 4.108 through 4.112 illustrate the representative microstructures of samples of sintered, ball milled, BS glass compacts containing 5, 10, 15, 20 and 30 V% of 4.6  $\mu\text{m}$  UPLM. These pictures are of fracture surfaces and represent various densities ranging from 86.2 to 92.2 % of theoretical density.

It is clearly evident from these pictures that the cluster size (i.e. the average of the number of interacting included pores in the plane of each, representative micrograph) increases as the amount of included porosity increases. As indicated above, the included porosity in the composition containing a 30 V% addition of 4.6  $\mu\text{m}$  UPLM is clearly interconnected. Relatively large clusters are apparent in the 20 V% UPLM addition samples as well. The cluster size decreases with decreasing UPLM addition, until no clusters larger than two included pores are evident in the sample containing 5 V% UPLM addition. A model that estimates the effect of volume fraction included porosity (monosized and randomly placed) upon pore cluster size, using pre-percolation, series cluster theory, is introduced in section 4.4.2 below.



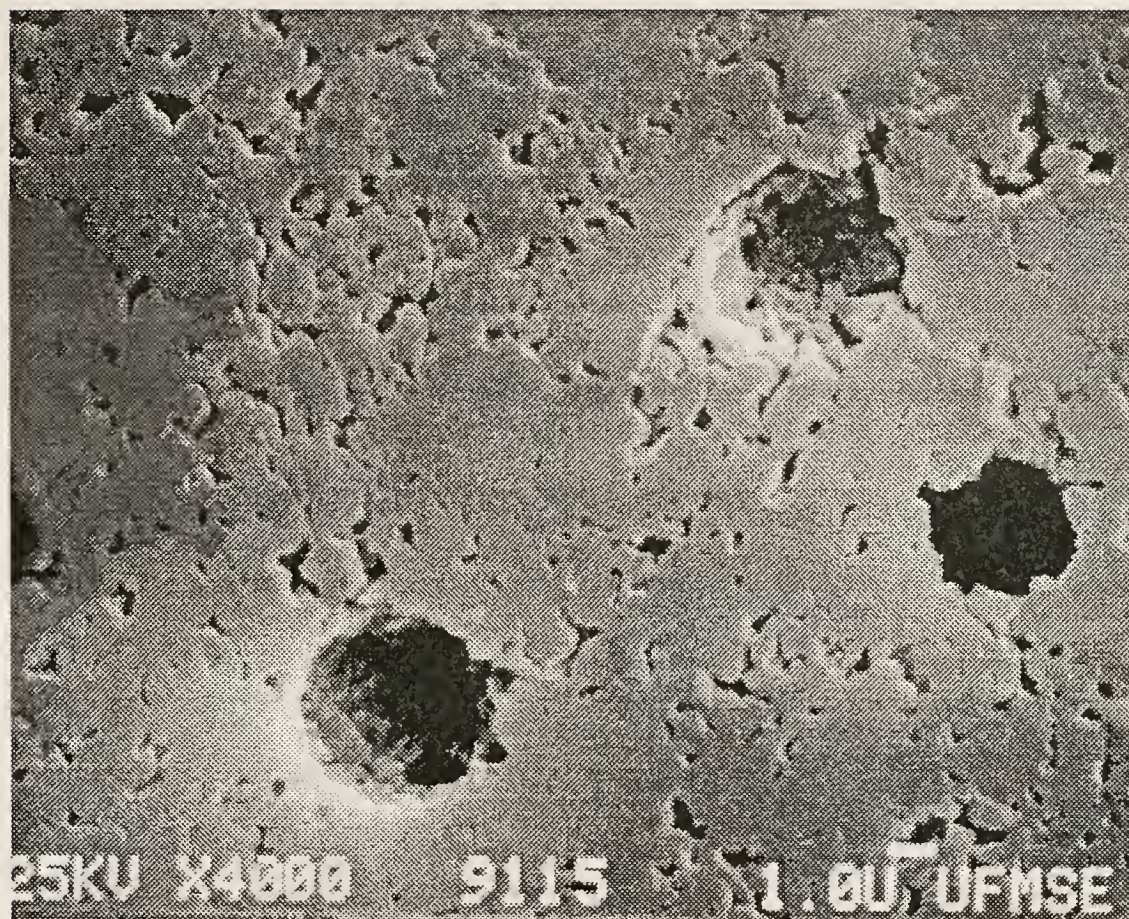


Figure 4.107

Micrograph illustrating the contrast between inherent and included porosity in a representative, ball milled BS glass compact, containing 10 V% of 4.6  $\mu\text{m}$  UPLM and sintered to approximately 72 % of theoretical density



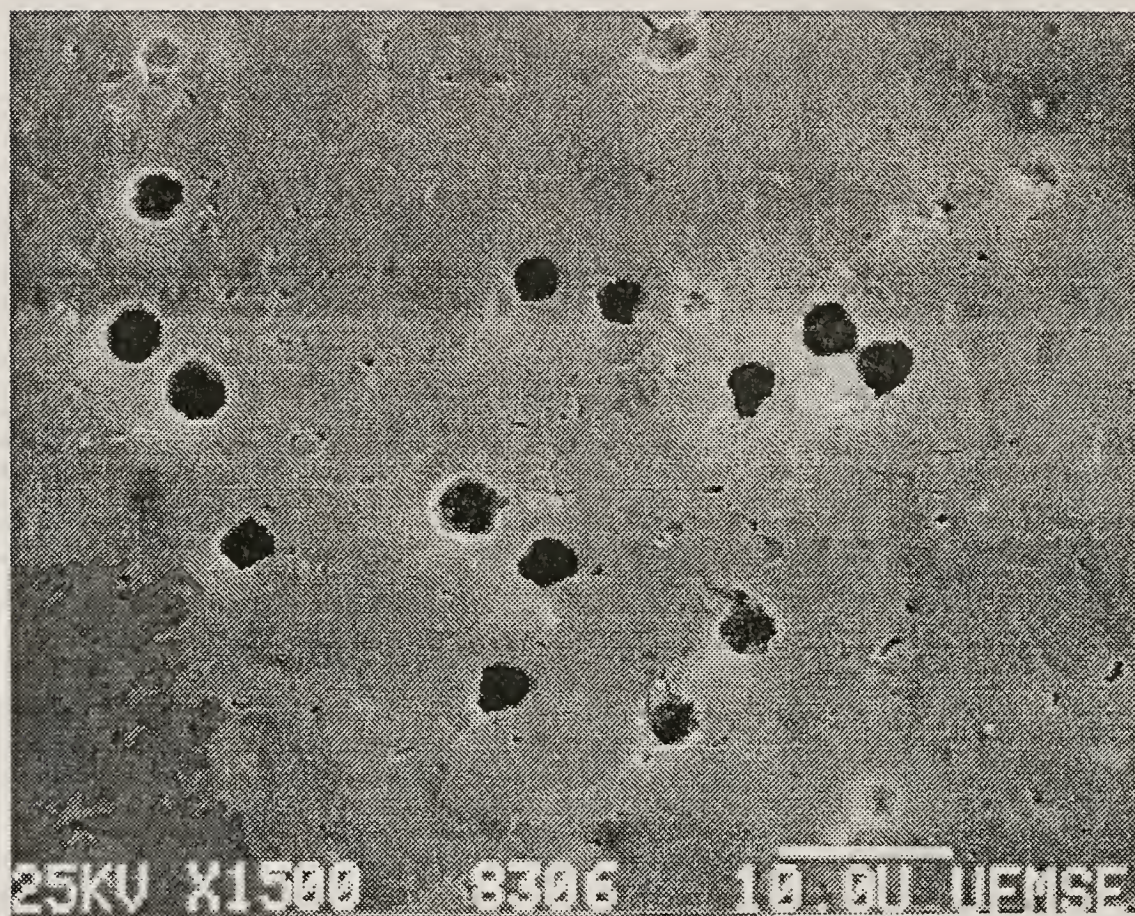


Figure 4.108

Illustration of the microstructure representative of a BS glass compact containing 5 V% of 4.6  $\mu\text{m}$  UPLM and sintered to 92.2 % of theoretical density (7.7 and 0.1 V% closed and open porosities respectively)



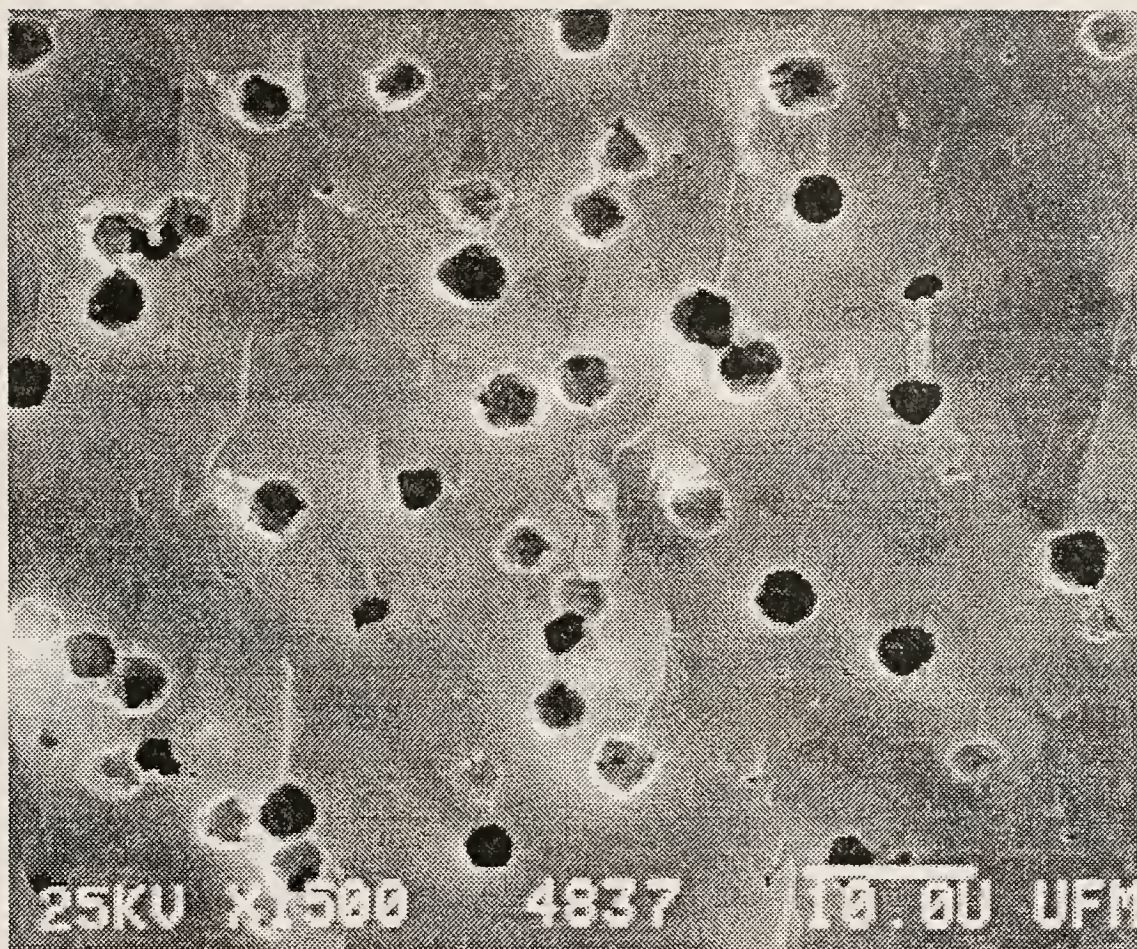


Figure 4.109

Illustration of the microstructure representative of a ball milled BS glass compact containing 10 V% of 4.6  $\mu\text{m}$  UPLM and sintered to 90.2 % density (9.7 and 0.1 V% closed and open porosities respectively)



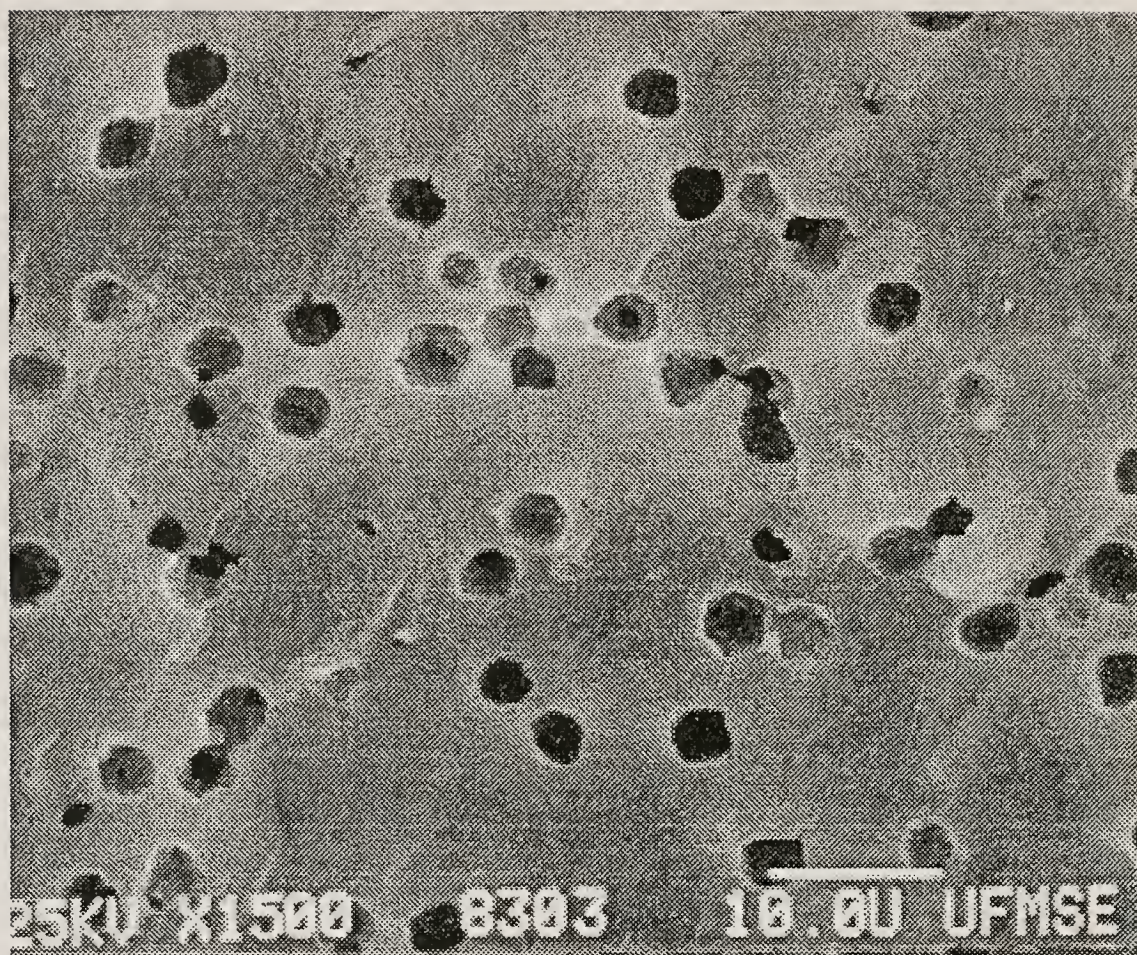


Figure 4.110

Illustration of the microstructure representative of a ball milled BS glass compact containing 15 V% of 4.6  $\mu\text{m}$  UPLM and sintered to 86.2 % density (13.4 and 0.4 V% closed and open porosities respectively)



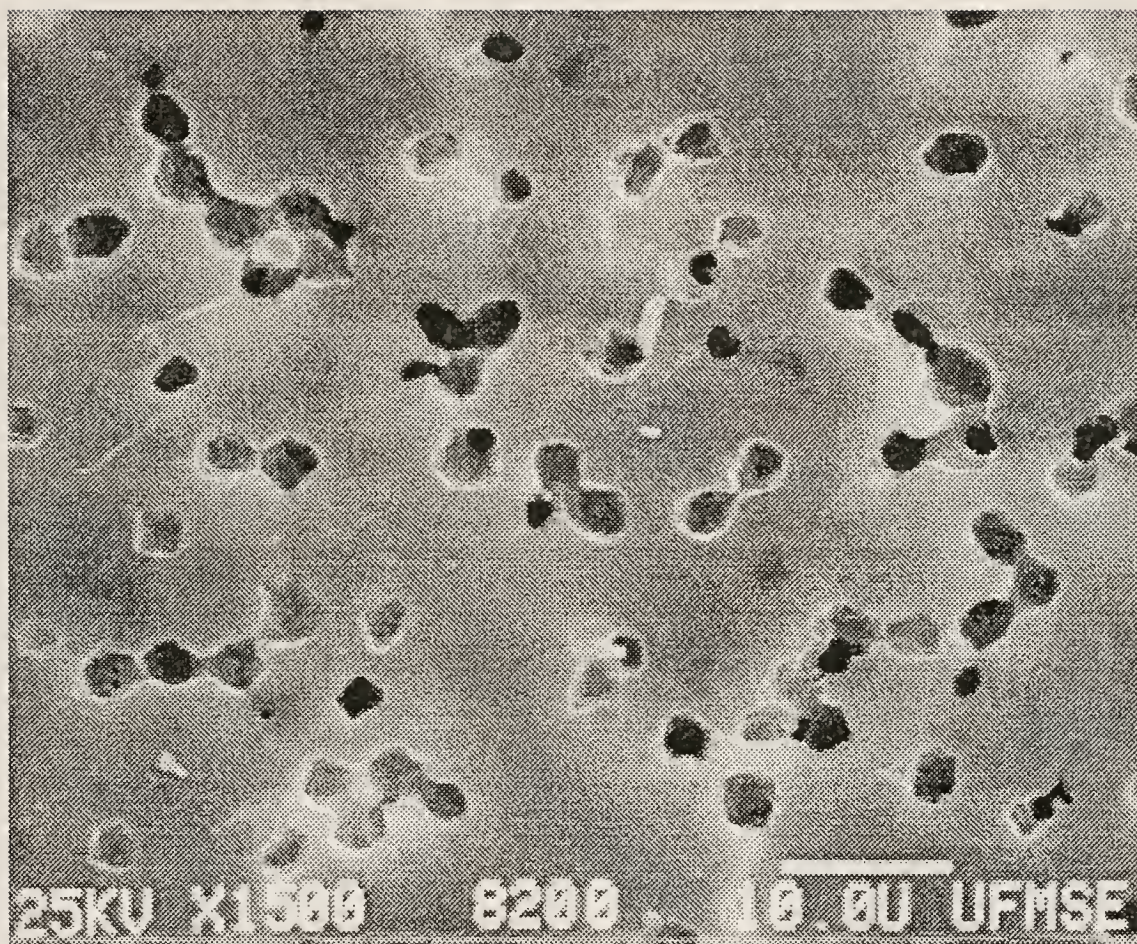


Figure 4.111

Illustration of the microstructure representative of a ball milled BS glass compact containing 20 V% of 4.6  $\mu\text{m}$  UPLM and sintered to 87.5 % density (12.1 and 0.4 V% closed and open porosities respectively)



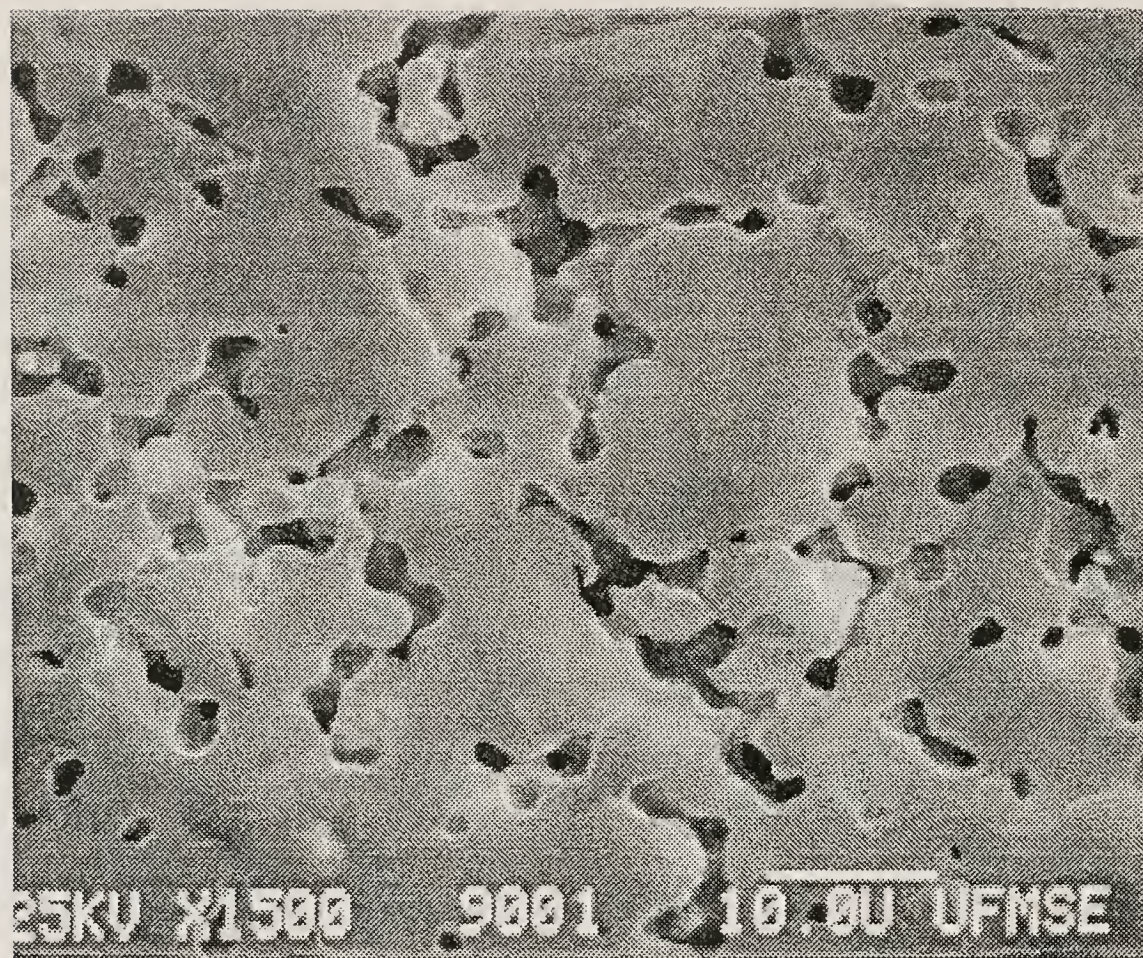


Figure 4.112

Illustration of the microstructure representative of a ball milled BS glass compact containing 30 V% of 4.6  $\mu\text{m}$  UPLM, sintered to 87.0 % density (3.0 and 10.0 V% closed and open porosities respectively)

Figures 4.113 through 4.116 illustrate representative microstructures of ball milled BS glass samples containing 15 V% additions of the four different size and size distributions of latex investigated, as included porosity, in this study. Figures 4.117 and 4.118 depict the difference between the smallest and largest included porosities of these same samples. It is quite evident, from these figures, that the shape and outline of the smaller included porosity is much less spherical than for the larger included porosity. This illustrates the concept of obscured porosity. In this context, obscured porosity is added porosity that is inefficient, from the standpoint of maximization of closed porosity, since the size of the added porosity is not large enough (i.e. the ratio of included porosity diameter to inherent pore channel size is not large enough to make satisfactory differential sintering occur). This phenomenon is described in section 4.3.4 above, in more detail.

Figure 4.119 illustrates the intersection of a polished surface with a top surface of a representative sample (80/0/15 BS glass/ $\text{Si}_3\text{N}_4$ /4.6  $\mu\text{m}$  UPLM), in order to provide a basis for comparison of surface roughness, included porosity size, and glass particle size. This figure also gives qualitative insight toward the connectivity of surface-connected pores with internal included porosity in the 15 V% 4.6  $\mu\text{m}$  UPLM compacts.

Figures 4.120 through 4.123 illustrate representative composites containing  $\text{Si}_3\text{N}_4$  as well as included porosity. Due to difficulties with particulate pullout during polishing and in sample etching, it was not possible to obtain satisfactory quantitative microscopy data pertaining to the included  $\text{Si}_3\text{N}_4$ . However, these investigations were important in that they indicated that there is little, if any, chemical reaction between the BS glass and the  $\text{Si}_3\text{N}_4$  (due to the relative ease of pullout of the  $\text{Si}_3\text{N}_4$  particulates, as well as to the sharp patterns that the pullouts left).



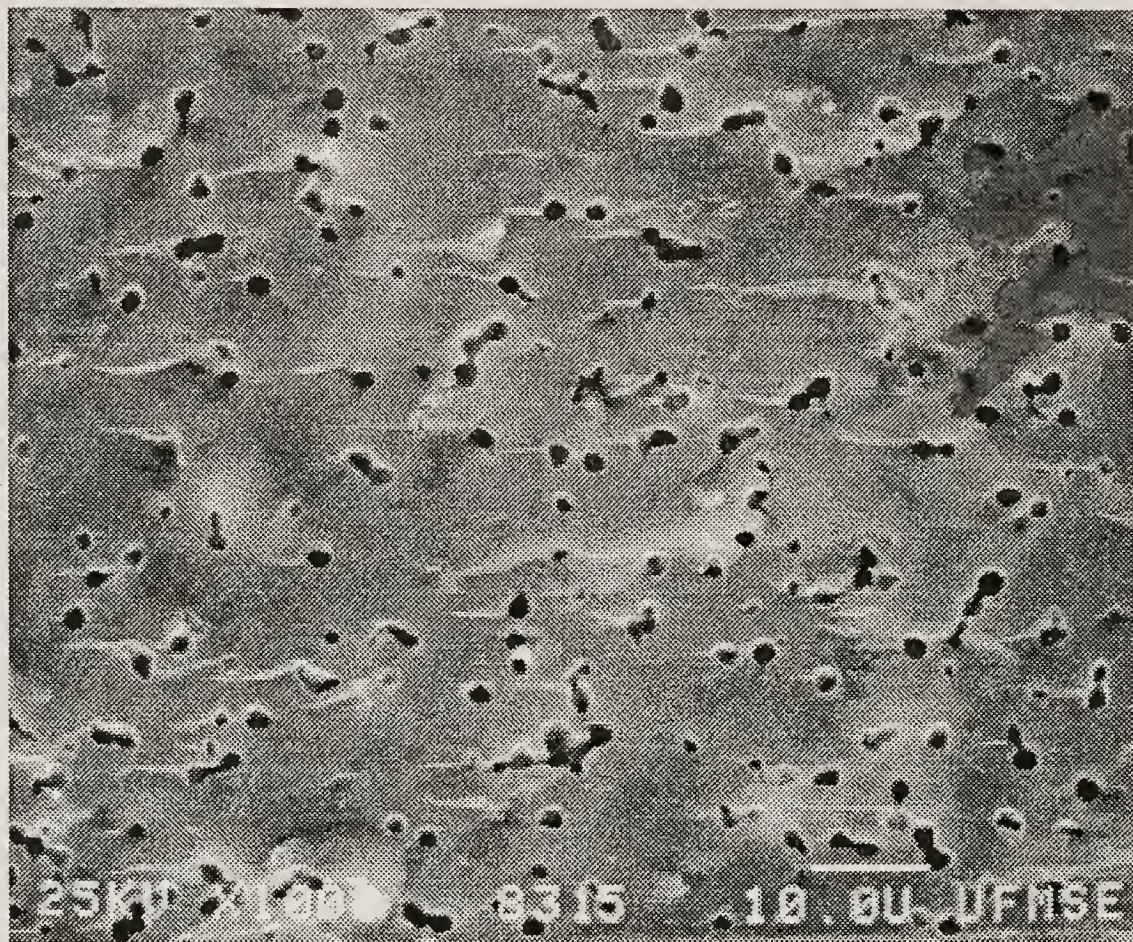


Figure 4.113

Illustration of the microstructure representative of a ball milled BS glass compact containing 15 V% of  $2.4\ \mu\text{m}$  bimodal latex, sintered to 87.3 % density (12.3 and 0.4 V% closed and open porosities respectively)



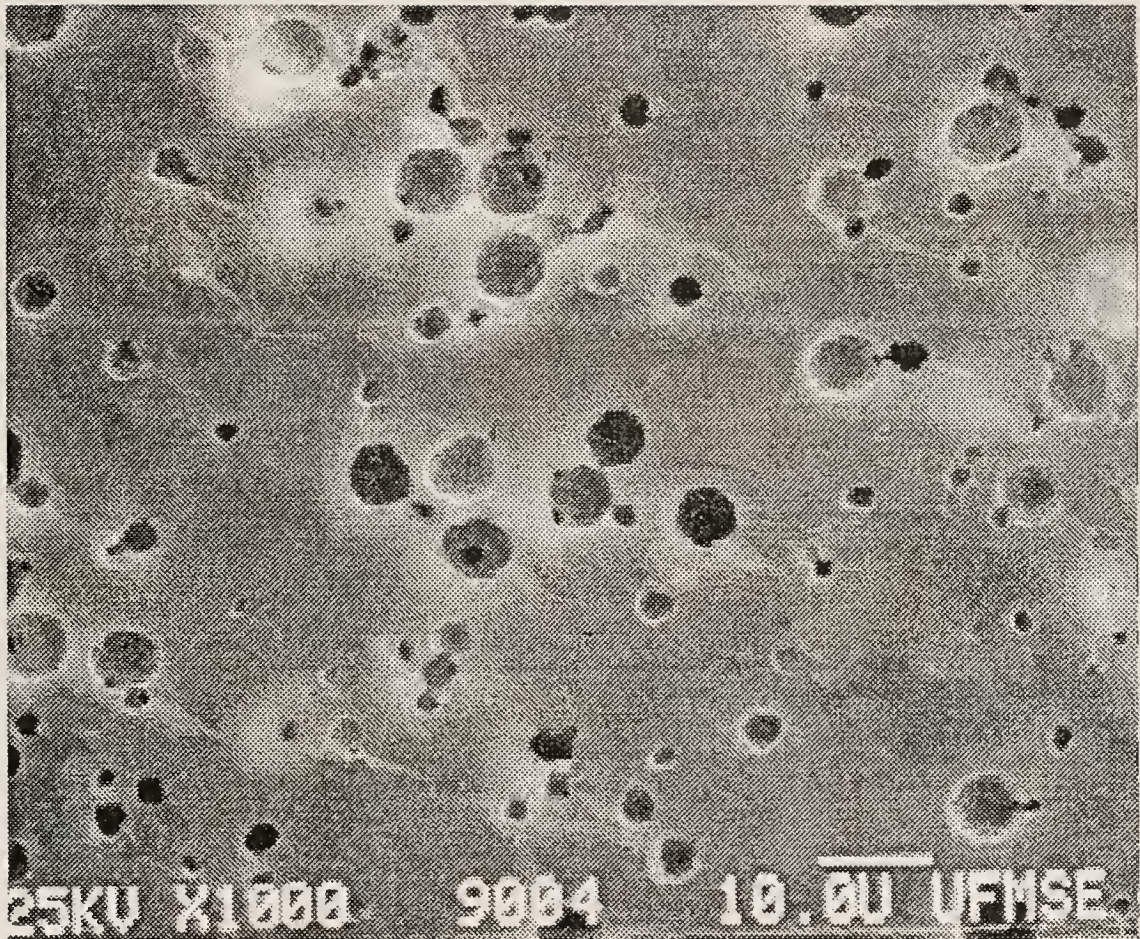


Figure 4.114

Illustration of the microstructure representative of a ball milled BS glass compact containing 15 V% of 4.0  $\mu\text{m}$  quadramodal latex, sintered to 86.0 % density (13.3 and 0.7 V% closed and open porosities respectively)



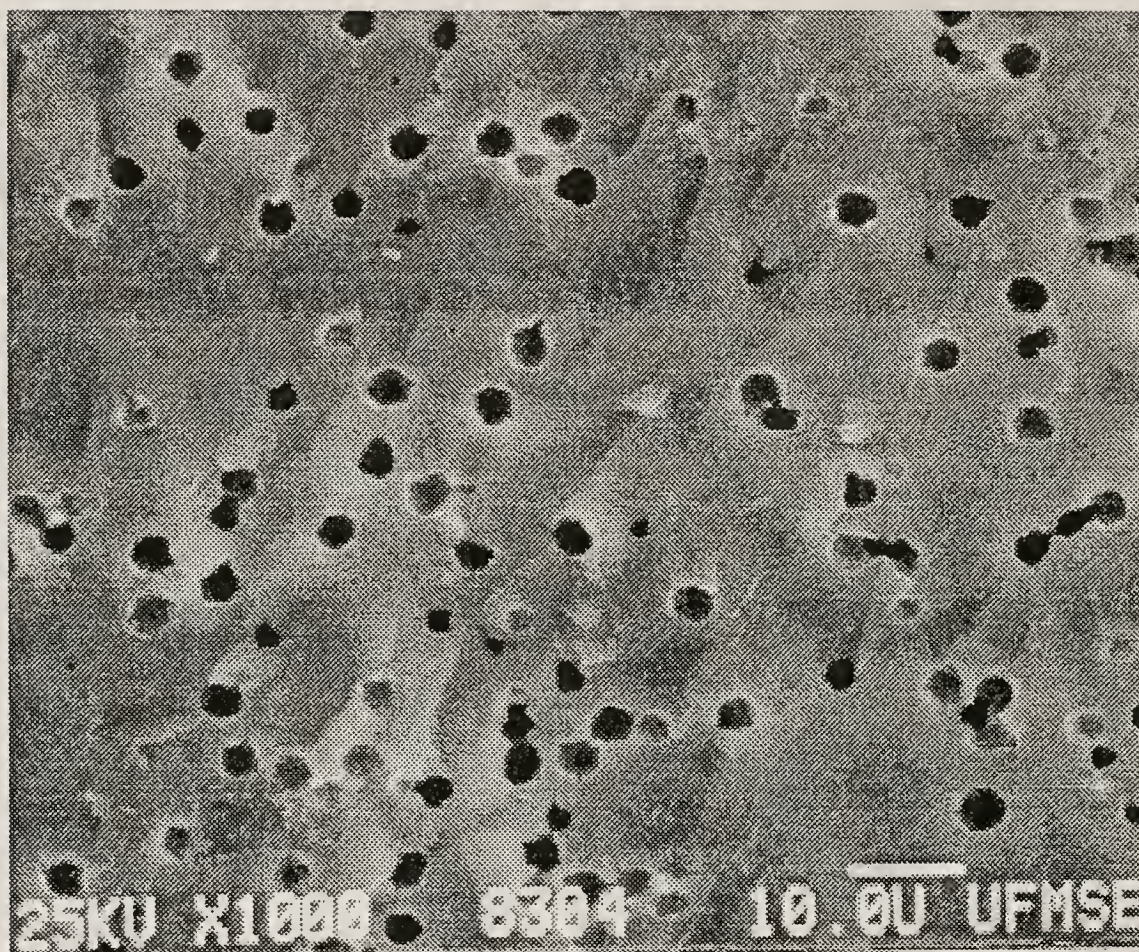


Figure 4.115

Illustration of the microstructure representative of a ball milled BS glass compact containing 15 V% of 4.6  $\mu\text{m}$  UPLM sintered to 86.2 % density (13.4 and 0.4 V% closed and open porosities respectively)



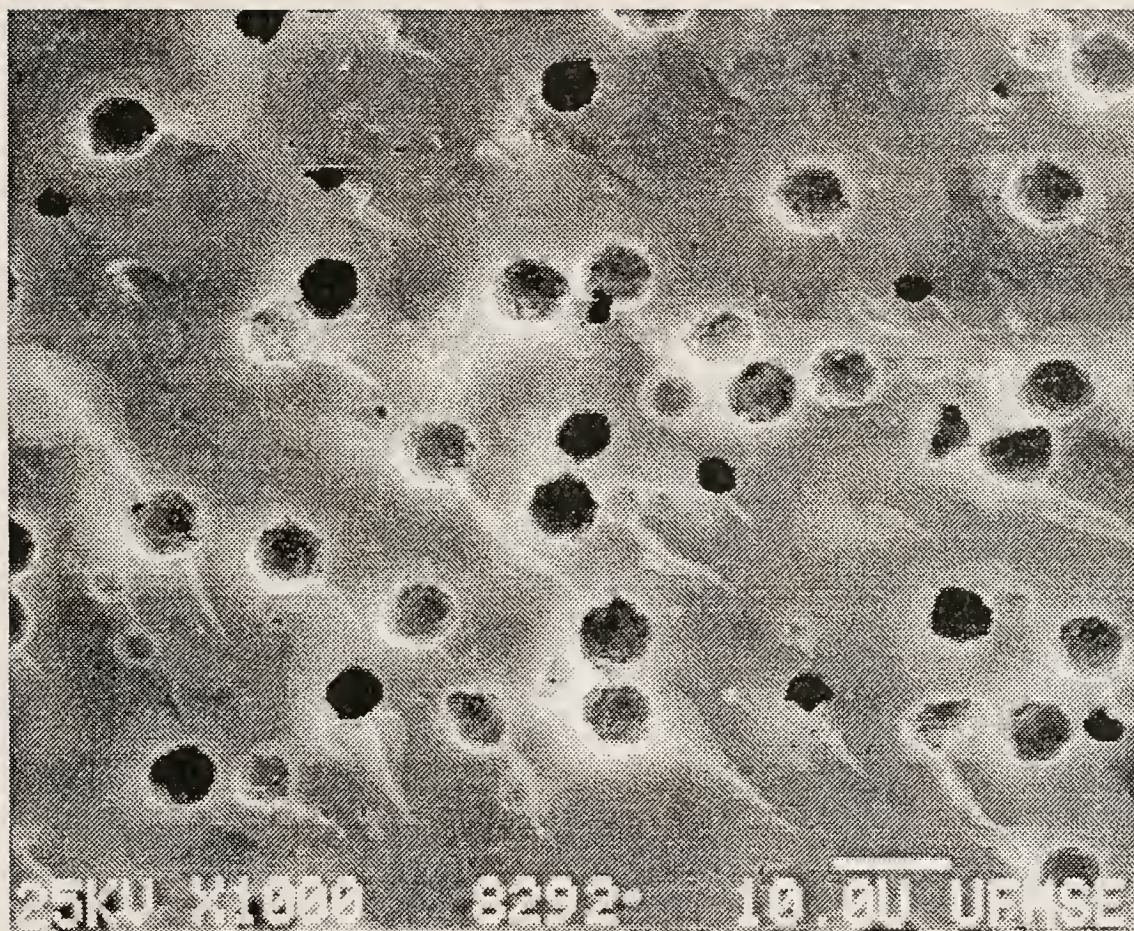


Figure 4.116

Illustration of the microstructure representative of a ball milled BS glass compact containing 15 V% of 9.0  $\mu\text{m}$  UPLM sintered to 85.4 % density (13.9 and 0.7 V% closed and open porosities respectively)



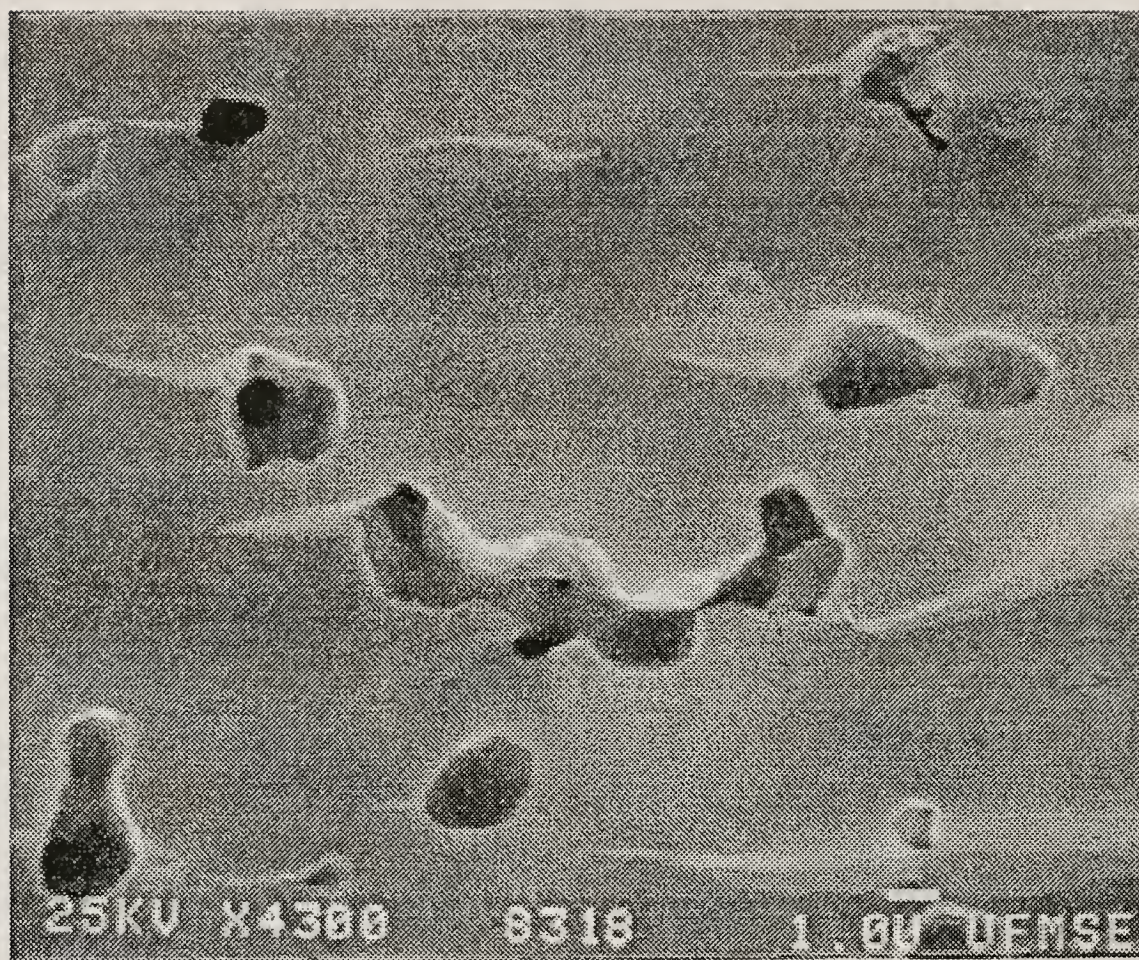


Figure 4.117

Close-up illustration of the included porosity resultant from additions of 2.4  $\mu\text{m}$  bimodal latex (the smallest size latex used)



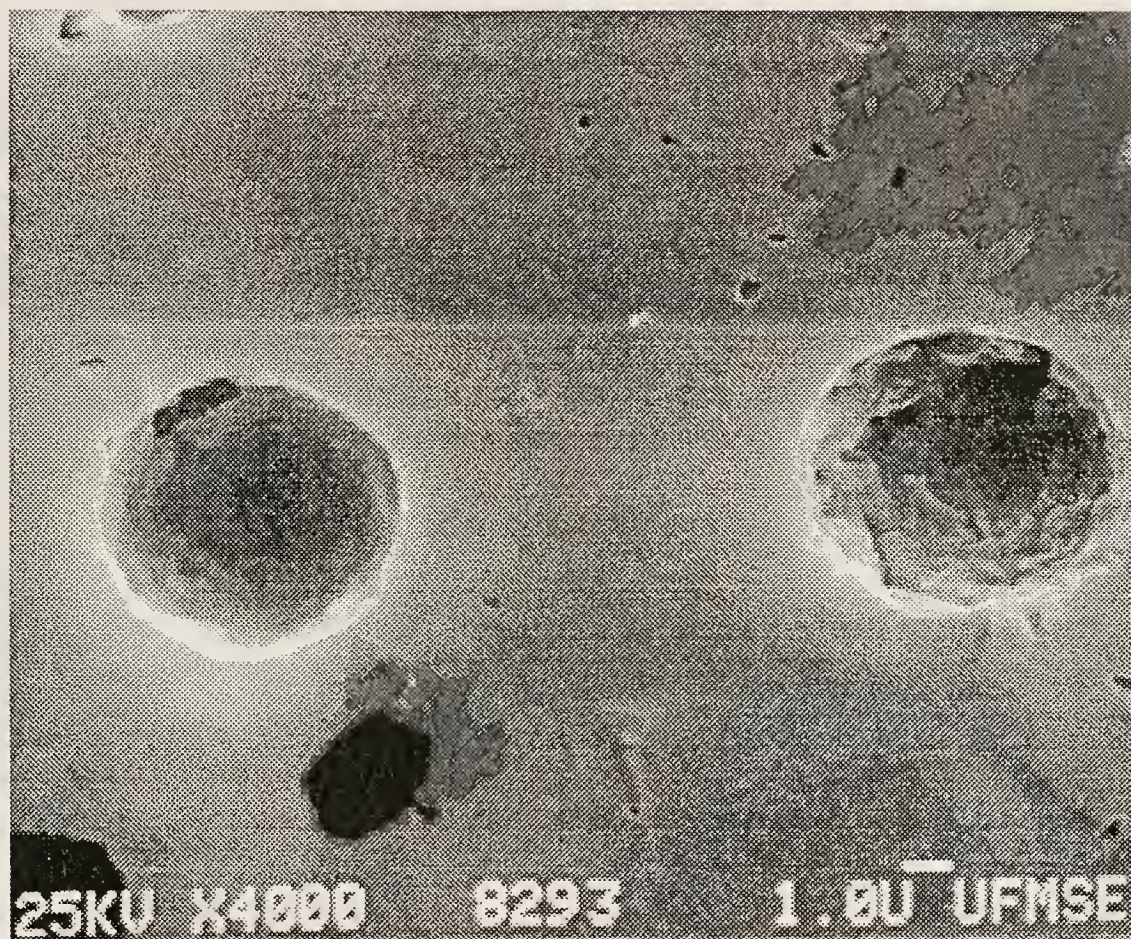


Figure 4.118

Close-up illustration of included porosity created using additions of  $9.0\ \mu\text{m}$  UPLM (the largest size latex used in this study)



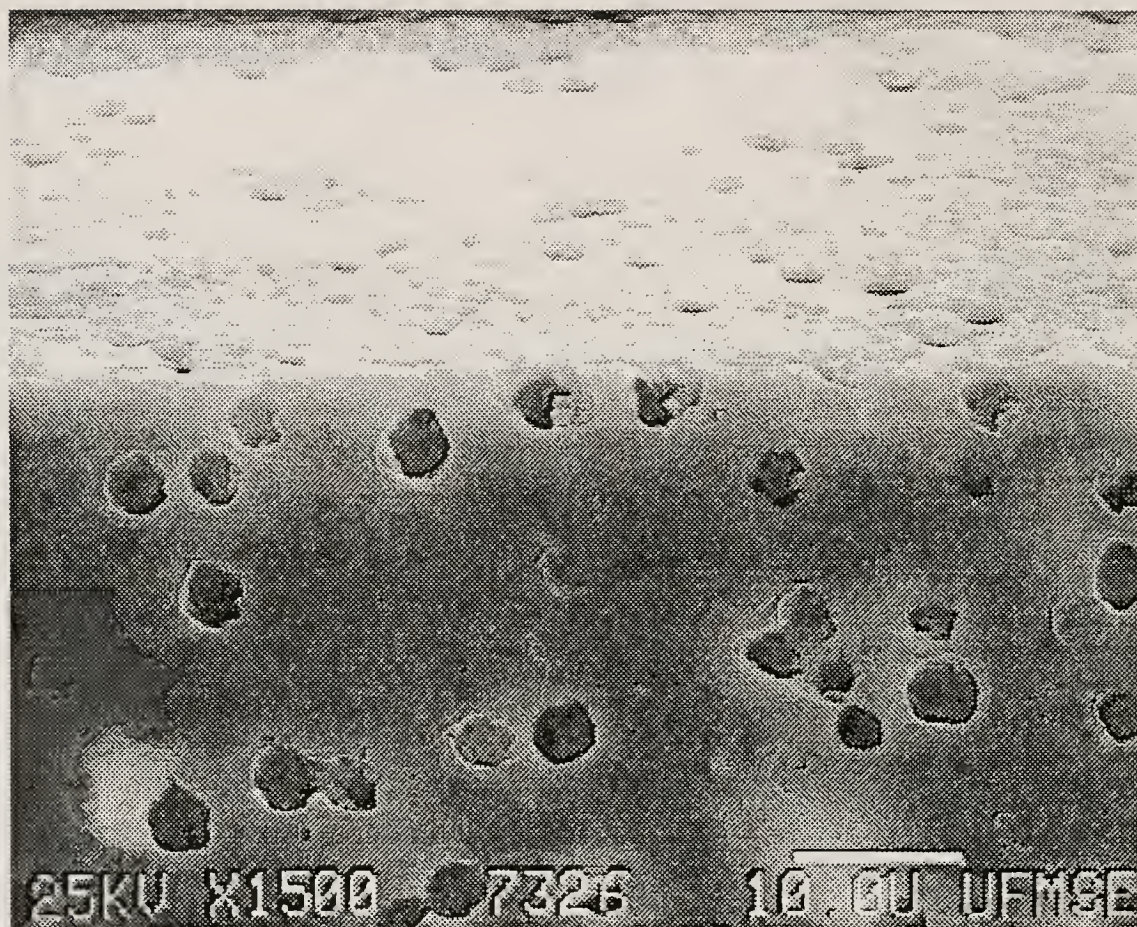


Figure 4.119

Illustration of the intersection of a polished surface with a top surface in a representative sample (BS glass/4.6  $\mu\text{m}$  UPLM 80/15)



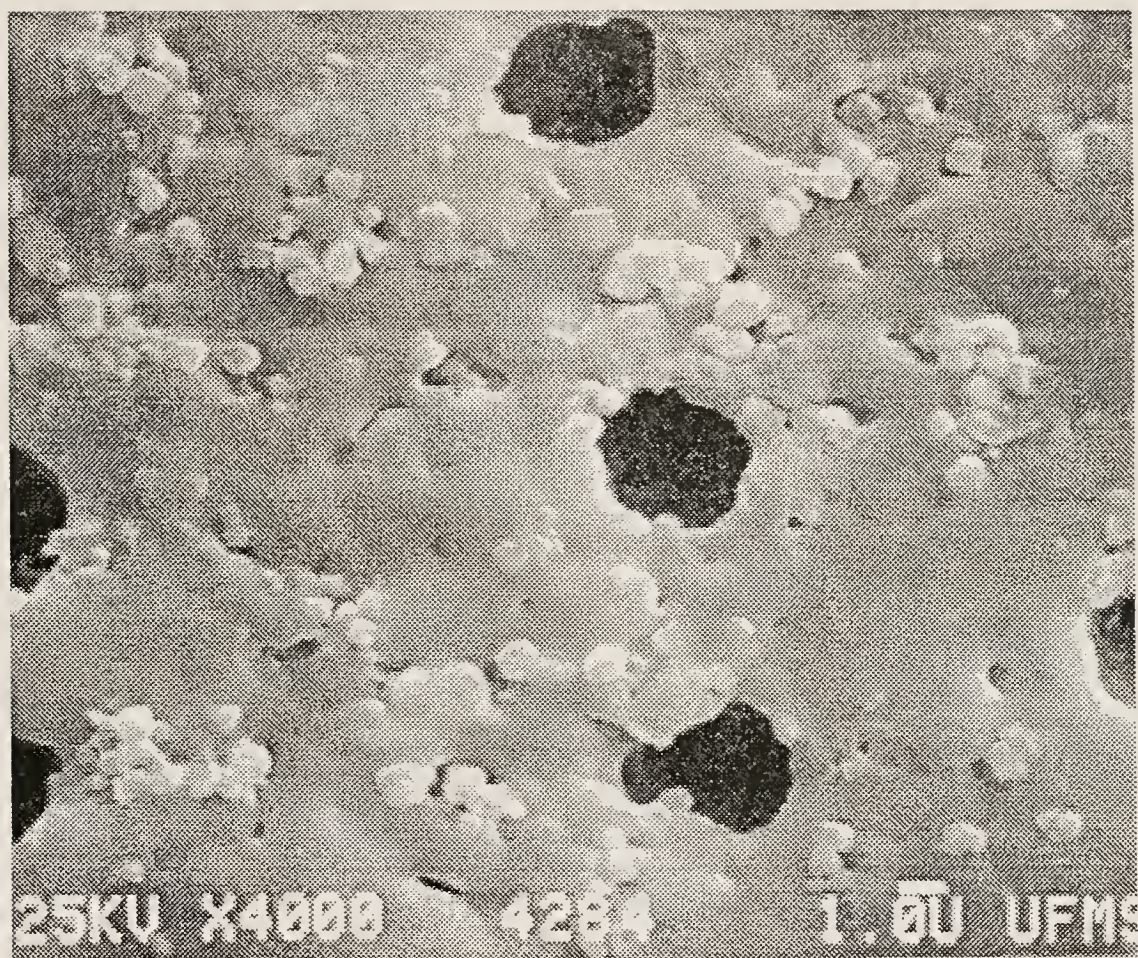


Figure 4.120

Illustration of the microstructure representative of the top surface of a composite containing ball milled BS glass, particulate silicon nitride and 4.6  $\mu\text{m}$  UPLM (72/18/10)



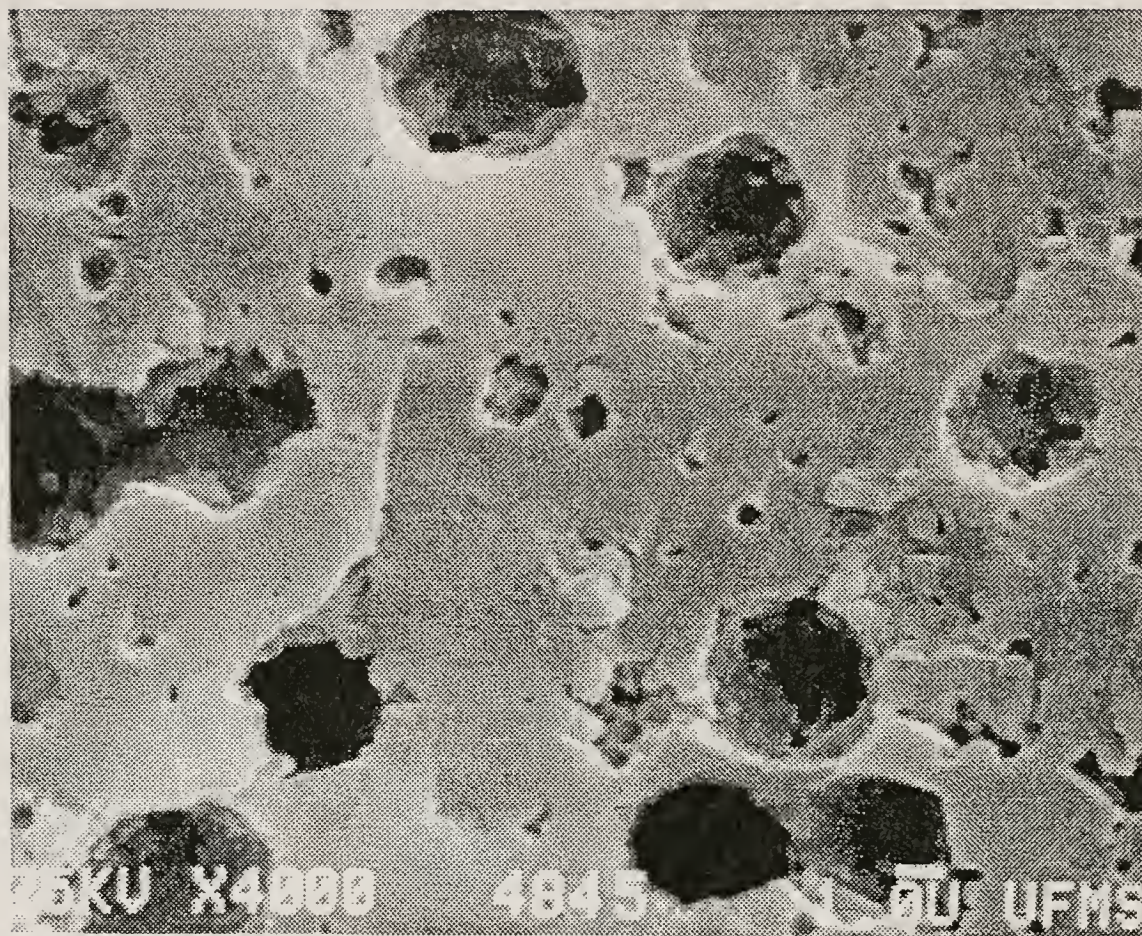


Figure 4.121

Illustration of the microstructure representative of an etched fracture surface of a composite containing ball milled BS glass compact,  $\text{Si}_3\text{N}_4$  and  $4.6\text{ }\mu\text{m}$  UPLM (81/9/10)



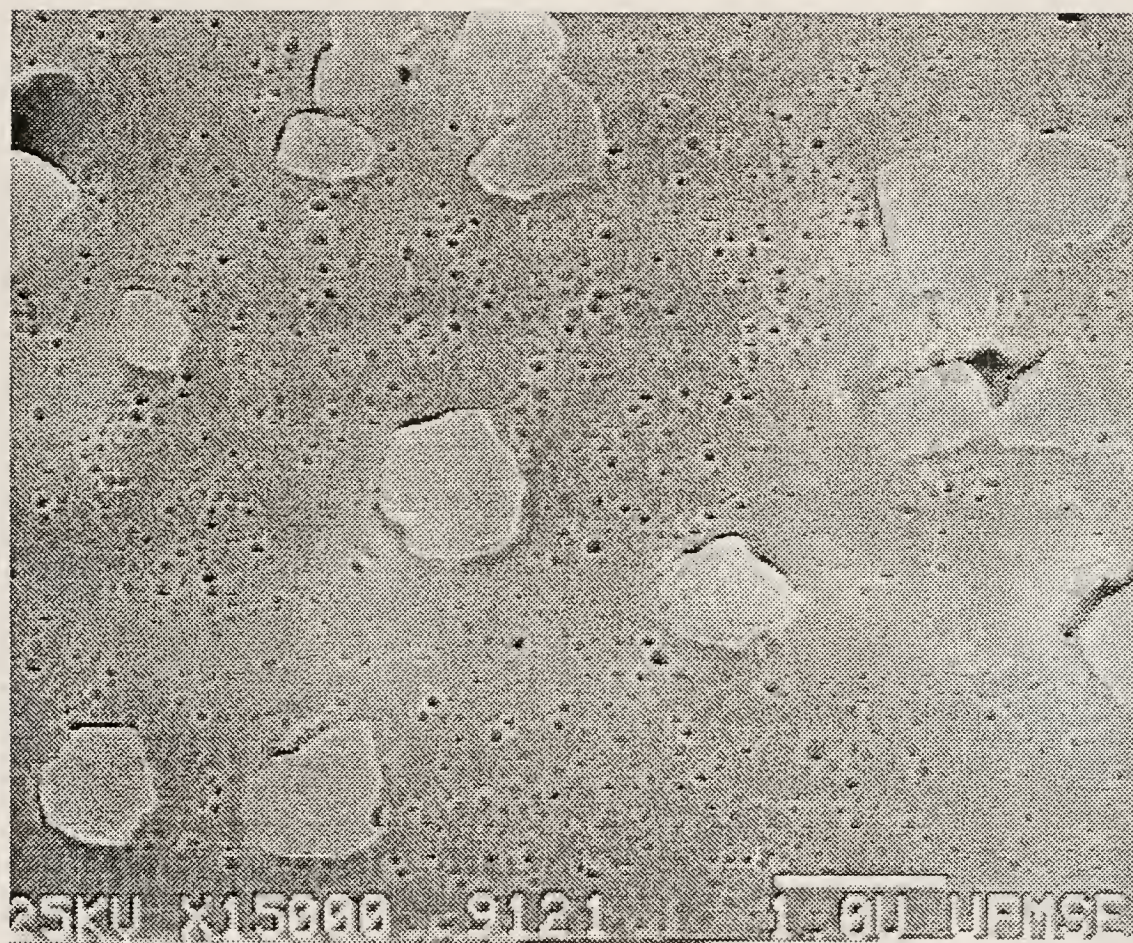


Figure 4.122

The microstructure of a polished and etched surface of a composite containing 80 V% BS glass and 20 V% Si<sub>3</sub>N<sub>4</sub> (small porosity is due to differential etching of the glass matrix)



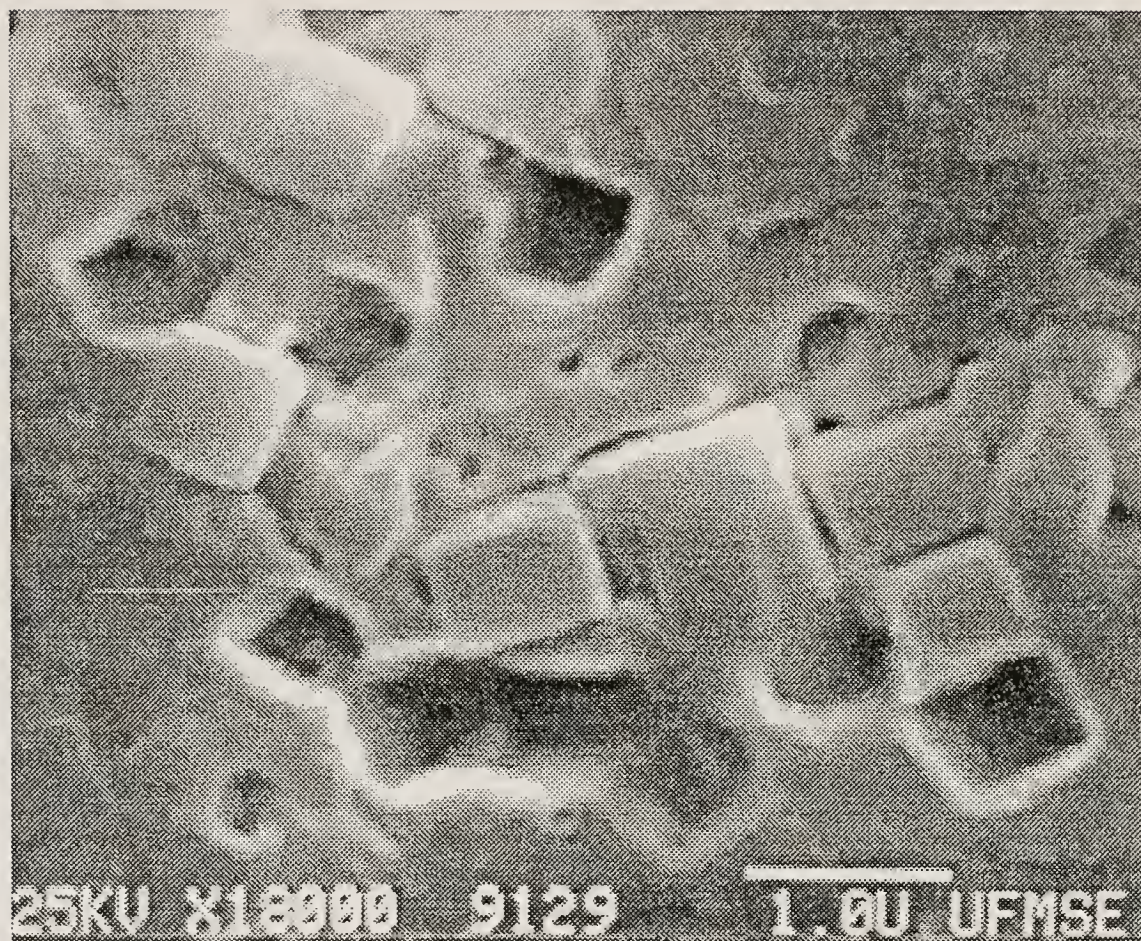


Figure 4.123

The microstructure of a polished and etched surface of a composite containing 60 V% BS glass and 40 V% Si<sub>3</sub>N<sub>4</sub> (showing pullout of the particulate Si<sub>3</sub>N<sub>4</sub>)

Thus, it was not possible to quantitatively monitor the various aspects associable with the particulate  $\text{Si}_3\text{N}_4$  additions investigated in this study. However, it was possible to monitor segregation of latex used in this study. It is also possible, using an extrapolation of Stoke's settling theory, to predict if appreciable segregation could be expected, of either of the other components in the composite system studied.

Segregation measurements for the  $4.6\text{ }\mu\text{m}$  UPLM used in this study, were performed by measuring the volume fraction of included porosity (using the grid technique) at the top, middle and bottom of an 80/0/20 BS glass/ $\text{Si}_3\text{N}_4$ / $4.6\text{ }\mu\text{m}$  UPLM compact. The sample surface was polished. This analysis also provided a basis for the comparison of porosities measured using Archimedes and quantitative microscopy techniques. The results are indicated in Table 4.7. Table 4.7 shows that the included porosities measured at the top, middle and bottom of the compact are within 0.8 V%. Since the standard deviation of the measurements varied from 2.4 to 3.4 V%, it may be concluded that no measurable segregation of the  $4.6\text{ }\mu\text{m}$  UPLM occurs within the samples investigated in this study. The amount of porosity measured in this compact using the Archimedes method was  $14.1 \pm 0.1\text{ V}\%$  ( $12.8 \pm 0.1\text{ V}\%$  closed porosity and  $1.3 \pm 0.1\text{ V}\%$  open porosity). Thus, the total porosity, measured by Archimedes density, agrees with the porosity measured using quantitative microscopy to within a standard deviation of the analyses, in all instances of measurement. Assuming that all of the porosity in the sample is attributable to included porosity (a reasonably valid assumption, see Figure 4.119), this indicates that the two techniques give comparable results. It is interesting to note that the measured porosity values were greater when quantitative microscopy (QM), in all instances. This may be a result of pore enlargement, due to polishing. It may also be due to both the grid line thickness as well as to the subjectivity of the experimenter.

Table 4.7  
Segregation Test Data

Area of Sample	Total Number of Grids Examined	Measured Porosity (V%)	Standard Deviation ( $\pm$ V%)
Top	2100	14.9	2.7
Middle	2100	15.7	3.4
Bottom	2100	15.3	2.4

Notes:

Sample Statistics:

85/0/15 (ball milled BS glass/Si<sub>3</sub>N<sub>4</sub>/4.6  $\mu$ m UPLM)

Measured Porosities (Archimedes method):

Total Porosity: 14.1  $\pm$  0.1 V%

Closed Porosity: 12.8  $\pm$  0.1 V%

Open Porosity: 1.3  $\pm$  0.1 V%



A representative fracture surface was also investigated using QM. The sample (90/0/10 BS glass/Si<sub>3</sub>N<sub>4</sub>/4.6  $\mu$ m UPLM) had a measured total porosity (using the Archimedes method) of 9.8 V% (9.7 and 0.1 V% closed and open porosities). The QM data (taken using 2000 grid points total) gave a total porosity of  $9.0 \pm 2.6$  V%. This indicates that the relatively large variation of measurement (and not necessarily pore enlargement) may be responsible for the higher porosities measured (combined with the effects of grid width and experimenter subjectivity mentioned above). It should be noted that the fracture surface may not be random due to the influence that inclusions may have upon the fracture path in a material [89JES]. Consequently, it is possible to hypothesize that the data obtained using the Archimedes technique is more accurate (from the basis of standard deviation).

In order to determine if either of the other composite constituents (i.e. either the BS glass powder or the Si<sub>3</sub>N<sub>4</sub> powder) would be expected to segregate, an extrapolation of Stoke's settling theory was used to provide an indication of relative settling rates within this composite system. It should be noted that Stoke's theory is quantitatively valid only for systems containing less than approximately 5 V% solids. For this application, Stoke's theory is extrapolated to the solids loadings used in this study (i.e. ~ 52 %). Another modification of the Stoke's theory for this application is that the suspension viscosity (rather than the suspension liquid viscosity) is used in the denominator of the Stoke's equation. Because these extrapolations are not legitimate, the data should be used in a qualitative sense only. These data are valuable only from the standpoint of relative settling velocity. However, since the particles within a highly loaded dispersion typically form an interconnected network that would trap other particles that would have settled at different rates, these data should represent a maximum in segregation potential. Thus, this application of modified Stoke's theory should be

legitimate for prediction of the degree of segregation, during slip casting, within this composite system. The modified Stoke's equation used for this exercise is

$$v = \frac{d^2 g (\rho_P - \rho_L)}{18 \eta_s}$$

where  $v$  is the particle settling velocity,  $d$  is the respective particle diameter,  $\rho_i$  is the density of the respective particle (P) or suspension liquid (L),  $g$  is the acceleration due to gravity and  $\eta_s$  is the viscosity of the suspension.

Table 4.8 depicts the relative velocities of the maximum, median and minimum particle sizes of each of the constituent powders used to make composites in this study. Said velocities were determined using the Stoke's equation depicted above, then normalizing the respective particle settling velocities to that of the median-sized 4.6  $\mu\text{m}$  UPLM. It is evident from the table that the wide size distribution powders (i.e. both BS glasses) have a very wide range of relative settling velocities (i.e up to six orders of magnitude variation in settling velocity). Thus, it is reasonable to expect segregation of the BS glass particles within the composites produced for this study. Similarly, the velocities predicted for the  $\text{Si}_3\text{N}_4$  powder used in this study vary up to three orders of magnitude. Conversely, the latexes used exhibit a maximum variation in relative settling velocity of approximately two orders of magnitude. However, using the calculated velocities for the median particle sizes of each of the composite constituents (e.g. 0.775, 0.620 and 1.000 for the ball milled BS glass powder, the  $\text{Si}_3\text{N}_4$  powder and the 4.6  $\mu\text{m}$  UPLM powder, respectively), only minor differences in settling velocity are to be expected for the major portions of each of the powder constituents. Thus, it is reasonable to assume that the segregation occurring within this composite system is less than or, at



Table 4.8  
Relative Settling Velocities of the Powders Used  
in this Study

Powder	Size ( $\mu\text{m}$ )		Relative Velocity
As-Received BS Glass	Maximum	58.00	802.06
	Median	5.03	6.032
	Minimum	0.18	0.007
Ball Milled BS Glass	Maximum	7.60	13.968
	Median	1.79	0.775
	Minimum	0.10	0.002
As-Received $\text{Si}_3\text{N}_4$	Maximum	4.73	9.168
	Median	1.23	0.620
	Minimum	0.48	0.094
2.4 $\mu\text{m}$ (Mean Size) Bimodal Latex	Maximum	4.88	1.104
	Median	3.05	0.432
	Minimum	1.13	0.059
4.0 $\mu\text{m}$ (Mean Size) Quadramodal Latex	Maximum	10.00	4.644
	Median	8.93	3.704
	Minimum	1.63	0.122
4.6 $\mu\text{m}$ (Mean Size) UPLM	Maximum	5.38	1.342
	Median	4.64	1.000
	Minimum	3.63	0.610
9.0 $\mu\text{m}$ (Mean Size) UPLM	Maximum	12.13	6.829
	Median	9.00	3.762
	Minimum	6.13	1.743

Notes: Maximum and minimum sizes are the largest and smallest sizes measured respectively

Median is the mass based median size

All relative velocities are normalized to the median velocity of the 4.6  $\mu\text{m}$  (mean size) UPLM powder

most, equal to the amount that would be observed within each of the ceramic powders (i.e. the ball milled BS glass powder and the  $\text{Si}_3\text{N}_4$  powder), under similar dispersion conditions.

In order to determine the relative amounts of included pore shrinkage in each of the compositions representative of this system, the average area of the included porosity in each of the representative compositions was measured in a manner similar to that used to measure latex sphere diameters (the optical comparator method), as described in section 3.2.2. The measured pore diameters were then converted to plane intersection areas (assuming a perfectly circular plane-pore intersection). These converted areas of intersection were then averaged ( $S^{ave}$ ) and converted to the equivalent pore diameter ( $D$ ) using the methods and assumptions of Fullman [53FUL]. These assumptions include monosized, perfectly spherical pores, intersected by a perfect plane, totally at random. The relationship involved is

$$D = \sqrt{\left(\frac{6}{\pi}\right) S^{ave}}.$$

Table 4.9 depicts the calculated equivalent pore diameters for the compositions tested. In all but two cases, monosized latex was used to create included porosity. Since the methods used to determine  $D$  are number based, they should be directly comparable to the number basis average size of each of the latexes used to create the included porosity.

The results indicated in Table 4.9 are enigmatic. In general, the standard deviations of these measurements are quite large, having a great affect upon the analysis of this data. The difference between the measured and calculated pore size and the included latex size apparently increases with increasing size. This is contrary to differential sintering theory (i.e. it is expected that the smallest included

porosity shrink the most during densification). This may be due to the fact that the two smallest latexes, used for added porosity (i.e. the 2.4  $\mu\text{m}$  bimodal distribution, and the 4.0  $\mu\text{m}$  quadramodal distribution latexes) are not monosized. Therefore, it is expected that the smallest included pores would densify first, thereby skewing the pore size distribution to larger sizes. One mode of the bimodal distribution of the 2.4  $\mu\text{m}$  latex is centered around 3.1  $\mu\text{m}$ , while the other was centered around approximately 1.8  $\mu\text{m}$ . If the 1.8  $\mu\text{m}$  mode pores were removed, the resulting measured included pore size (i.e. 2.2  $\mu\text{m}$ ) would make sense, indicating an approximate 30 % reduction in the diameter of the larger size mode of included porosity. This is enforced by the fact that the other 2.4  $\mu\text{m}$  included porosity sample investigated was not significantly densified, and had an average pore diameter of 2.4  $\mu\text{m}$  (which is in agreement with the average latex size).

This hypothesis is further reinforced through the examination of the standard deviations of the two 2.4  $\mu\text{m}$  bimodal samples investigated. The variance of the later sample was larger than for the former, indicating the tightening of the pore size distribution (as would be expected as a bimodal system evolves toward a more monomodal system).

A pore size increase was also observed in the 4.0  $\mu\text{m}$  quadramodal latex included porosity samples (05179101 group) as well. In this case, however, the standard deviation did not decrease with increasing density between the two samples. This may be due to the large statistical variance, since the amount of densification was small (i.e. 0.8 V%), and since both standard deviations are quite large.

Perhaps the most surprising result depicted in Table 4.9 is that of the measured pore diameter for the 9.0  $\mu\text{m}$  UPLM sample (05099101). The 6.9  $\mu\text{m}$  value represents a 23.3 % reduction in diameter from the 9.0  $\mu\text{m}$  UPLM addition used to create the included porosity. For comparison, an analogous 4.6  $\mu\text{m}$  UPLM sample experienced a reduction in diameter of only 13 %. This is definitely not expected. In order to determine if

Table 4.9

Calculated Equivalent Included Porosity Diameters  
of Representative Compositions

I.D. #	V% Lat	Latex Size		Porosity (V%)		Microscopic Measured/Calculated Data				
		(μm)	Ds	Closed	Open	S u r f a c e	S <sup>ave</sup> (μm <sup>2</sup> )		D (μm)	n
							S <sup>ave</sup>	σ <sub>n</sub>		
05109102	5	4.6	M	7.6	0.1	F	6.0	3.3	3.4	48
01039101	10	4.6	M	0.8	26.7	P	9.8	3.6	4.3	76
01039101	10	4.6	M	1.2	17.6	P	10.1	3.4	4.4	69
01039101	10	4.6	M	9.7	0.1	F	7.5	2.9	3.8	100
01049101	10	4.6	M	1.8	10.7	P	10.6	2.9	4.5	79
01049101	10	4.6	M	10.5	0.8	P	9.0	3.6	4.1	71
01049101	10	4.6	M	10.5	0.8	F	9.1	3.4	4.2	100
05179102	15	2.4	B	1.7	19.9	P	3.1	1.5	2.4	100
05179102	15	2.4	B	9.9	0.4	F	2.6	1.1	2.2	100
05179101	15	4.0	Q	13.3	0.8	F	11.5	11.2	4.7	100
05179101	15	4.0	Q	12.9	0.4	F	12.8	12.1	4.9	99
05069101	15	4.6	M	13.4	0.5	F	8.5	3.4	4.0	100
05119101	15	4.6	M	1.6	15.3	P	8.0	3.1	3.9	100
05099101	15	9.0	M	13.9	0.7	F	25.0	10.1	6.9	79
12109001	20	4.6	M	12.1	0.4	F	6.6	2.5	3.5	100
12109001	20	4.6	M	12.1	0.4	F	7.1	2.4	3.7	100
05079101	30	4.6	M	3.2	9.8	P	3.5	1.8	2.6	100

## Notes:

V% Lat is V% latex

σ<sub>n</sub> is standard deviation

Ds is distributions type (M = monosize, B = bimodal, Q = quadramodal)

Surface is viewed surface type (F = fracture, P = polished)

n is the number of pores measured

I.D. #'s 01049101 and 05119101 contain 9 and 12.75 V% Si<sub>3</sub>N<sub>4</sub> respectively

the sample investigated was representative, quantitative microscopy (standard point count method) was used to determine the volume fraction of included porosity. The measured volume fraction included porosity was  $15.5 \text{ V\%} \pm 1.78 \text{ V\%}$  (1000 point count). This agrees, to within a standard deviation, with the closed porosity measured using Archimedes techniques. Therefore, it was a representative sample from the standpoint of volume fraction porosity. However, this reduction in pore size correlates to a reduction of 45 V% of the pore volume. This would result in a maximum included porosity of only 6.8 V%. Since the measured porosities were in excess of 13 V%, this is impossible.

It should be noted that the standard deviation of  $S^{ave}$  in this sample is very large (as would be expected). The included sphere diameter would be  $8.2 \mu\text{m}$  considering the maximum  $S^{ave}$  allowed within one standard deviation. This would result in a sphere shrinkage of only 9% (volume shrinkage of 24 %, and included porosity reduction of 3.6 %), which is still too large, but more reasonable.

A possible explanation for this enigmatic behavior is that the path of the fracture surface is influenced by the included porosity, or that the standard deviations typical of this type of analysis are too large for accurate analyses. Thus, the analysis was probably skewed in some way.

Included pore clustering was determined by recording the average number of interacting included pores, per included pore cluster, in the plane of the micrograph. Table 4.10 depicts the clustering data of the included porosity of the samples investigated. Again, it is readily evident that the standard deviations of these measurements are relatively large. As above, this is also due to the method of the measurements (i.e. the measurement of a distribution of cluster sizes). However, the cluster size was observed to increase with increasing V% latex addition when comparing correlatable samples.



Table 4.10  
Cluster Data of Representative Samples

I.D. #	V% Lat	Latex Size		Porosity (V%)		Microscopic Measured/Calculated Data				
		(μm)	Ds	Closed	Open	S u r f a c e	Cluster Statistics			
							# Cl	# ISP	ACN	$\sigma_n$
05109102	5	4.6	M	7.6	0.1	F	52	61	1.17	0.47
01039101	10	4.6	M	0.8	26.7	P	44	52	1.18	0.66
01039101	10	4.6	M	1.2	17.6	P	48	58	1.21	0.41
01039101	10	4.6	M	9.7	0.1	F	189	267	1.41	0.69
01049101	10	4.6	M	1.8	10.7	P	61	71	1.16	0.37
01049101	10	4.6	M	10.5	0.8	P	113	149	1.32	0.62
01049101	10	4.6	M	10.5	0.8	F	138	193	1.40	0.71
05179102	15	2.4	B	1.7	19.9	P	90	140	1.56	0.79
05179102	15	2.4	B	9.9	0.4	F	235	404	1.71	1.16
05179101	15	4.0	Q	13.3	0.8	F	115	159	1.38	0.73
05179101	15	4.0	Q	12.9	0.4	F	99	157	1.59	0.93
05069101	15	4.6	M	13.4	0.5	F	120	172	1.43	1.01
05119101	15	4.6	M	1.6	15.3	P	94	122	1.33	0.59
05099101	15	9.0	M	13.9	0.7	F	58	80	1.38	0.76
12109001	20	4.6	M	12.1	0.4	F	272	491	1.81	1.22
12109001	20	4.6	M	12.1	0.4	F	226	391	1.73	1.16
05079101	30	4.6	M	3.2	9.8	P	208	522	2.51	1.95

## Notes:

V% Lat is V% latex

Ds is distributions type (M = monosize, B = bimodal, Q = quadramodal)

Surface is viewed surface type (F = fracture, P = polished)

# Cl is the total number of clusters measured

# ISP is the number of included spherical pore units measured

ACN is the average cluster number calculated

 $\sigma_n$  is standard deviation of the ACNI.D. #'s 01049101 and 05119101 contain 9 and 12.75 V% Si<sub>3</sub>N<sub>4</sub> respectively

Furthermore, it is evident that there is little if any dependence of average cluster number (ACN) upon included sphere size or size distribution (it is possible that the smaller, wider size distribution latexes had a slightly larger ACN, but this is not conclusive, since all are within one standard deviation of each other).

#### 4.4.2 Modelling of Included Porosity

Series cluster theory, as outlined in section 2.4.1 may be used to predict the average cluster number of randomly placed spheres upon a three dimensional lattice structure [64SYK]. The mean cluster size, as a function of sphere concentration ( $S_p$ ), may be determined by the relationship

$$S_p = 1 + \sum_{n=2}^{n=\infty} a_n p^n$$

where  $n$  is the number of spheres in the cluster of interest,  $a_n$  is the number of possible configurations for a cluster of size  $n$  and  $p$  is the fraction of the lattice or space occupied by the spheres. The number of configurations of each cluster size for both bond and site clustering of diamond, simple cubic (SC), body centered cubic (BCC) and face centered cubic (FCC) lattices are depicted in Table 2.6. It is now proposed that this model may be utilized to predict the average cluster number for random close packed (RCP) systems as well. This is an extension of the theories covered in section 2.4.2.

Zallen showed that, even though RCP structures do not exhibit a characteristic lattice structure (as do the ordered structures mentioned above), they may be modelled as an interpolation between SC and BCC structures (see Figure 2.15) [83ZAL2]. Figure 4.124 illustrates the Napierian logarithm of the number of possible configurations of cluster size  $n$  as a function of cluster size  $n$  for bond and site cluster models, for the packing types mentioned above. The interpolated estimate for

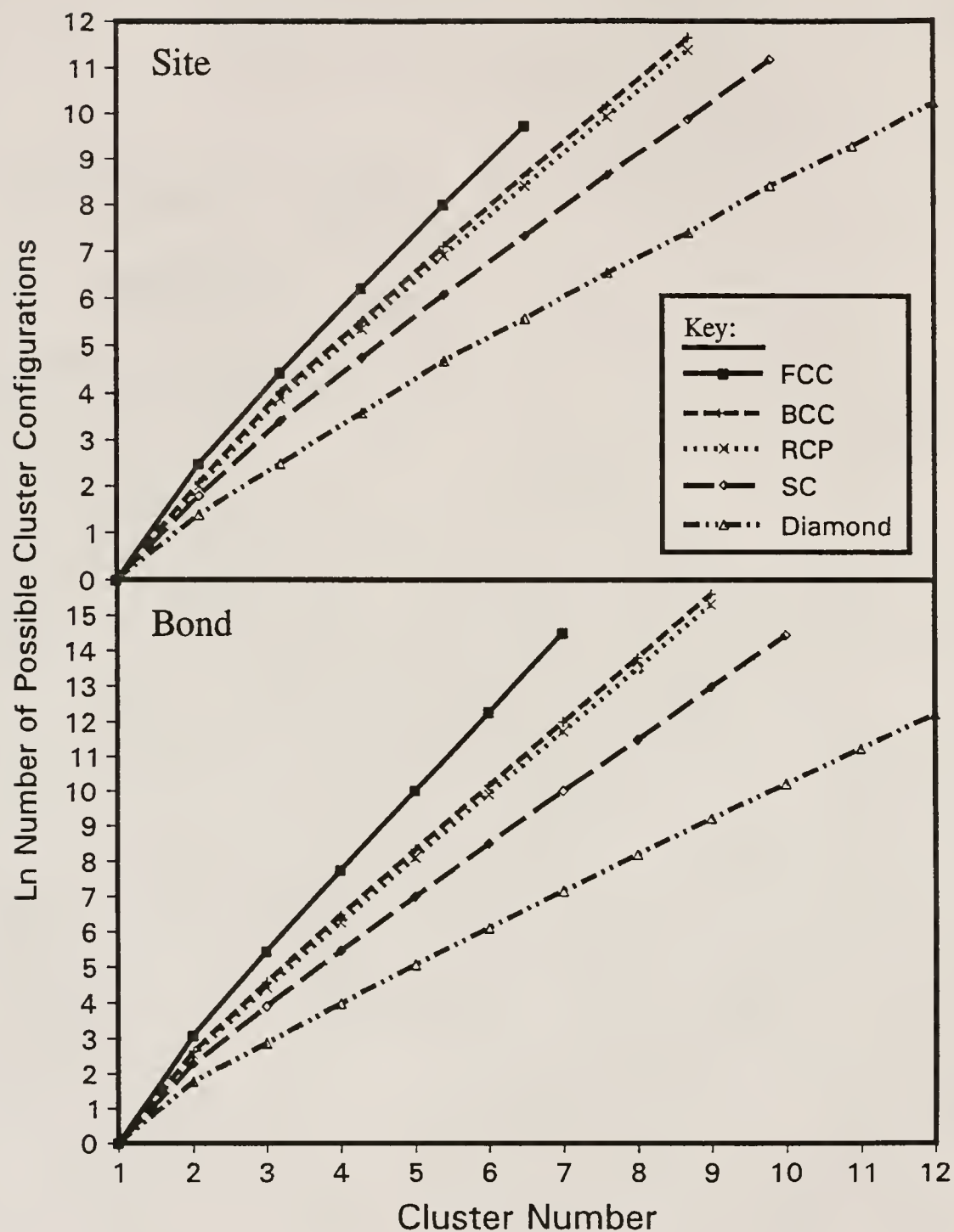


Figure 4.124

Natural logarithm of the number of cluster configurations ( $\ln(a_n)$ ) possible versus cluster size ( $n$ ) for site and bond clustering of diamond, SC, RCP, BCC and FCC "structures"

RCP packing structures is also included. The interpolation was obtained by standard weighted averaging between SC and BCC values (based upon relative packing efficiencies (PEs)). It is evident from the figure that this relationship is well defined, becoming linear, for each type of packing, at cluster sizes larger than 2 for FCC site and bond, and BCC bond, 3 for BCC site and RCP and SC bond, 4 for RCP site and diamond bond, and 5 for SC and diamond site. The corresponding interpolated RCP values ( $a_n$ 's) for bond and site clustering are depicted in Table 4.11. This table indicates the equivalent next-nearest-neighbor coordination number for RCP packed structures may be estimated by  $\sim 7.5$  for site clustering and  $\sim 13$  for bond clustering. The values for  $a_n$  for the other types of packing are located in Table 2.6.

Table 4.12 depicts the linear regression modelling data for each type of packing. It is evident from the table that the linear correlations of these relationships are excellent. These data may be utilized, in a novel manner, to estimate the onset of percolation. Due to the linear relationship described above

$$\ln(a_n) \approx mn + b$$

where  $n$  is the cluster number,  $m$  is slope and  $b$  is the intercept at the ordinate. This may be modified to

$$a_n \approx C \exp^{mn}$$

where

$$C = \text{constant} = \exp^b.$$

Thus, the relation for mean cluster size ( $S_p$ ) becomes

$$S_p \approx 1 + \sum_{n=2}^{n=\infty} C \exp^{mn} p^n$$

where  $p$  is the fraction of the lattice filled. The relation of  $p^n$  may also be modified to

Table 4.11

Interpolated Cluster Number Values for RCP Packing

Cluster Number (n)	$a_n$	
	Site	Bond
1	1	1
2	7.5	12.9
3	48.8	84.8
4	211.0	536.3
5	1013.0	3350.1
6	4545.7	20323.7
7	20875.4	124370.0
8	87676.7	739709.5
9		4476031.2



Table 4.12  
Linear Regression Data of  $a_n$

Site Clustering					
Packing Type	Regression Range		Regression Data		
	Minimum n	Maximum n	Slope ( $\ln(a_n)/n$ )	Intercept ( $\ln(a_n)$ )	Correlation Coefficient (R)
FCC	2	6	1.810830	-1.06373	0.99978
BCC	3	8	1.532376	-0.57278	0.99992
RCP	4	8	1.508447	-0.64621	0.99989
SC	5	9	1.275351	-0.29632	0.99996
Diamond	5	10	0.929321	0.024476	0.99990
Bond Clustering					
Packing Type	Regression Range		Regression Data		
	Minimum n	Maximum n	Slope ( $\ln(a_n)/n$ )	Intercept ( $\ln(a_n)$ )	Correlation Coefficient (R)
FCC	2	7	2.280134	-1.40713	0.99994
BCC	2	9	1.848492	-0.96318	0.99992
RCP	3	9	1.810573	-0.96055	0.99999
SC	3	10	1.501755	-0.52993	0.99994
Diamond	4	12	1.029219	-0.06587	0.99993

Notes:  $a_n$  is the possible number of cluster configurations of size n

$$p^n = \exp^{n \ln(p)}$$

thus allowing manipulation of  $S_p$  to the desired form of

$$S_p = 1 + \sum_{n=2}^{\infty} C \exp^{[n(m + \ln(p))]}.$$

The percolation onset ( $p_c$ ) is defined as the lattice fraction at which  $S_p$  becomes infinite, or undefined. Therefore,  $p_c$  for each lattice type (as well as for the interpolated RCP packing structure) occurs at the value of  $p$  that delineates where the series for  $S_p$  changes from a convergent series approximation to a divergent one. Said change from convergence to divergence may be found using the integral test [81GIL], which states that if a series converges, so will its corresponding integral. Since the 1 in front of the series is irrelevant, with regard to convergence or divergence of the series, it is sufficient to solve the following integral

$$S_p \approx \int_2^{\infty} C \exp^{[n(m + \ln(p))]} dn$$

then to determine the divergence boundary from the solution of,

$$S_p \approx \frac{C}{m + \ln(p)} \exp^{[n(m + \ln(p))]} \Big|_{n=2}^{n=\infty}.$$

The above solution shall be convergent (with respect to  $p$ ) when

$$m + \ln(p) \leq 0$$

Table 4.13 shows the results of the above solution, as well as a comparison of the results of the above method with those in the literature [83ZAL2]. From the table, it is evident that the solutions agree closely, but not exactly with published values. These variances range from ~ 8 % to ~ 18 %. It is interesting to note that the general trends in these values mirror each other closely. This gives further credence to the general accuracy of the above, series divergence model.

Table 4.13  
Estimated Percolation Onsets

Site Mechanism					
Packing Type	$p_c$ Site		PE	$PEp_c^{\text{Site}}$	
	Calculated	Literature		Calculated	Literature
FCC	0.164	0.198	0.7405	0.121	0.147
BCC	0.216	0.245	0.6802	0.147	0.167
RCP	0.221	0.27*	0.637*	0.141	0.16*
SC	0.279	0.311	0.5236	0.146	0.163
Diamond	0.395	0.428	0.3401	0.134	0.146
Bond Mechanism					
Packing Type	$p_c$ Bond		$Z$	$Zp_c^{\text{Bond}}$	
	Calculated	Literature		Calculated	Literature
FCC	0.102	0.119	12	1.23	1.43
BCC	0.158	0.179	8	1.26	1.43
RCP	0.164	N/A	7.5	1.22	N/A
SC	0.223	0.247	6	1.34	1.48
Diamond	0.357	0.388	4	1.43	1.55

Notes: \* Indicates experimental (not calculated) literature values

It is interesting that the literature values represent an upper limit of the measured porosity values in Table 4.6, while the values calculated, using the above methods, indicate a lower limit (of the group of samples giving the greatest closed porosities (i.e. the 15 V% 4.6  $\mu\text{m}$ , 9.0  $\mu\text{m}$  UPLM and 4.0  $\mu\text{m}$  quadramodal latex additions, the 17.6 V% 9.0  $\mu\text{m}$  UPLM addition and the 20 V% 4.6  $\mu\text{m}$  UPLM addition samples) to the measured porosity values.

The source of the differences between the solution values and the published values is not known, since the linear approximations were extremely accurate. However, there is also some discrepancy in the literature regarding the exact values of percolation onsets. Regardless, the above method represents a novel and greatly simplified method of determining percolation onsets. This method also is (to the knowledge of the author) the only non-experimental method, currently available, through which the onset of percolation may be estimated for RCP structures.

The above model may also be modified to approximate cluster numbers in RCP structures of pores. The expected value of  $S_p$  may be calculated using the interpolated values indicated in Table 4.11. In order to accurately estimate the average cluster number ( $S_p$ ) for this approximation, it is necessary to use a nominal number of terms in the series. It also is evident, from the series equation for  $S_p$ , that the necessary number of terms in the series increases with increasing  $p$ , requiring infinitely many terms at the percolation threshold. The necessary number of the terms in the series may be determined using a modification of the integral test utilized in the convergence/divergence test discussed above [81GIL]. The integral test, when used in this context, states that the error of a convergent series, computed to the  $N^{\text{th}}$  term, is no greater than the corresponding integral computed from  $N + 1$  to infinity. For purpose of this discussion, it

will be assumed that it is sufficient to model  $S_p$  using the interpolated terms in Table 4.11 (an estimate of error is included).

From Table 4.13, it is evident that both the 20 and 30 V% UPLM addition materials are in excess of the calculated bond percolation threshold ( $p_c$  bond), and that the 30 V% UPLM addition exceeds  $p_c$  site as well. It is interesting to note, however, that in the green state, the actual  $p$  of the 30 and 20 V% UPLM addition samples is approximately 22.5 and 14.4 V% respectively. Therefore, percolation of the pore structure, in the 20 V% UPLM samples, does not necessarily occur until significant densification (i.e. to ~ 80 % of theoretical density) of the structure occurs. In the 30 V% UPLM samples percolation is probably (but not necessarily, see Table 4.13,  $p_c$  site literature value) present from the green stage of processing.

It is evident, from the above discussion, that the type of clustering occurring in this system (i.e. site versus bond clustering) may be postulated by using the cluster number model discussed above, then comparing these predictions with the measured  $S_p$ s (from the ACN column of Table 4.10). Figure 4.125 illustrates the relationship of  $S_p$  as a function of  $p$ , using the series method for RCP (both site and bond clustering mechanisms). Figure 4.125 shows that  $S_p$  bond increases at a greater rate than does  $S_p$  site. This also accounts for the lower  $p_c$  characteristic of the bond mechanism. Also apparent in the figure is the two dimensional approximation of  $S_p$  (i.e. the three  $S_p^{2/3}$ ) as well as the estimate of error of both the two and three dimensional  $S_p$  approximations. The estimate of error is defined (in this case) as the value of the last term calculated. This value increases greatly as  $p_c$  is approached, and thus, is an indicator of the inaccuracy of the approximation. The accuracies of these approximations are adequate for the purpose of this comparison, however.

Figure 4.126 shows the above-mentioned two dimensional approximations of  $S_p$  (site and bond, for RCP structures) as well as



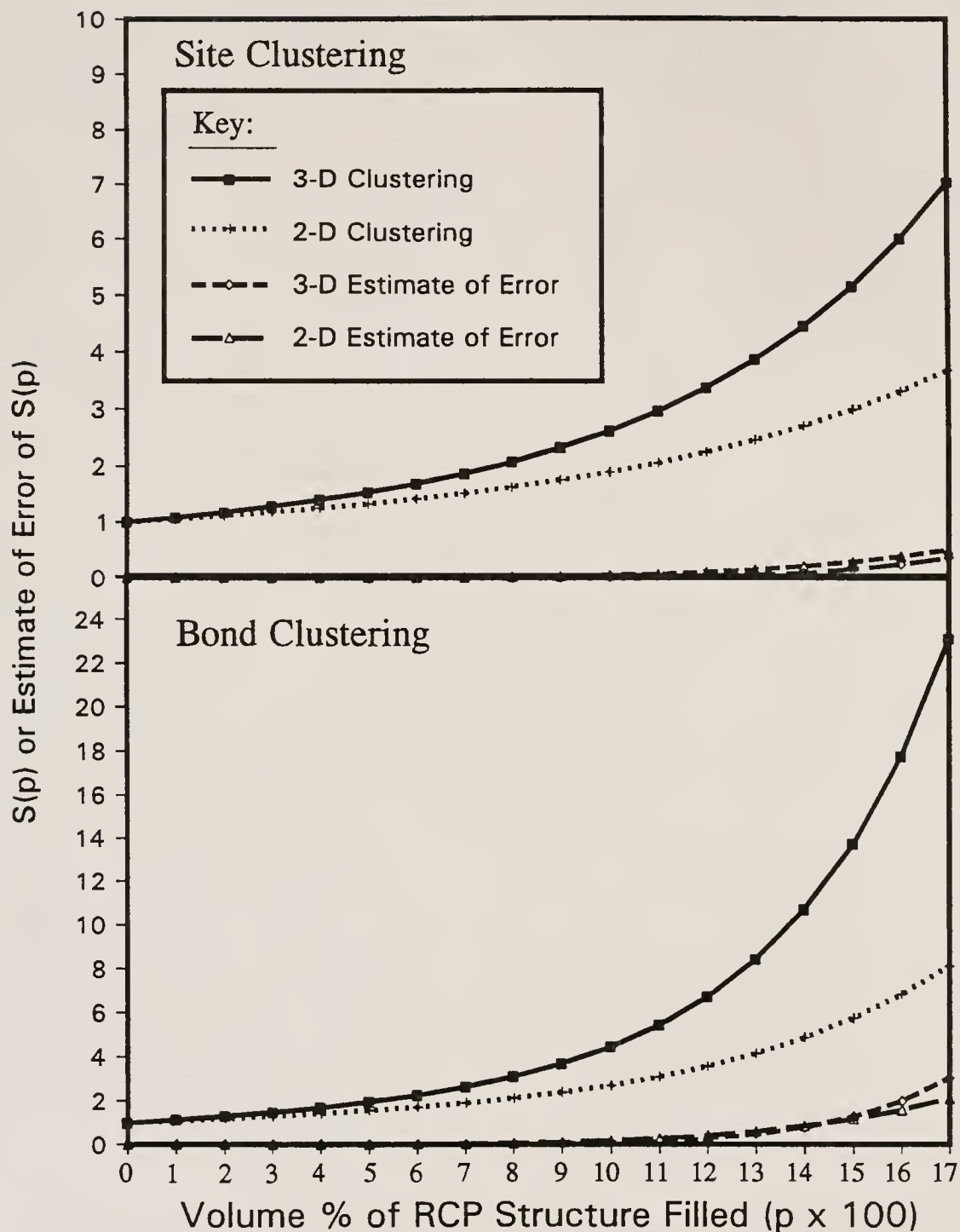


Figure 4.125

$S_p$  as a function of  $p$  (predicted using the series approximation method) for both two and three dimensional site and bond clustering mechanisms in RCP structures, with associated estimates of error

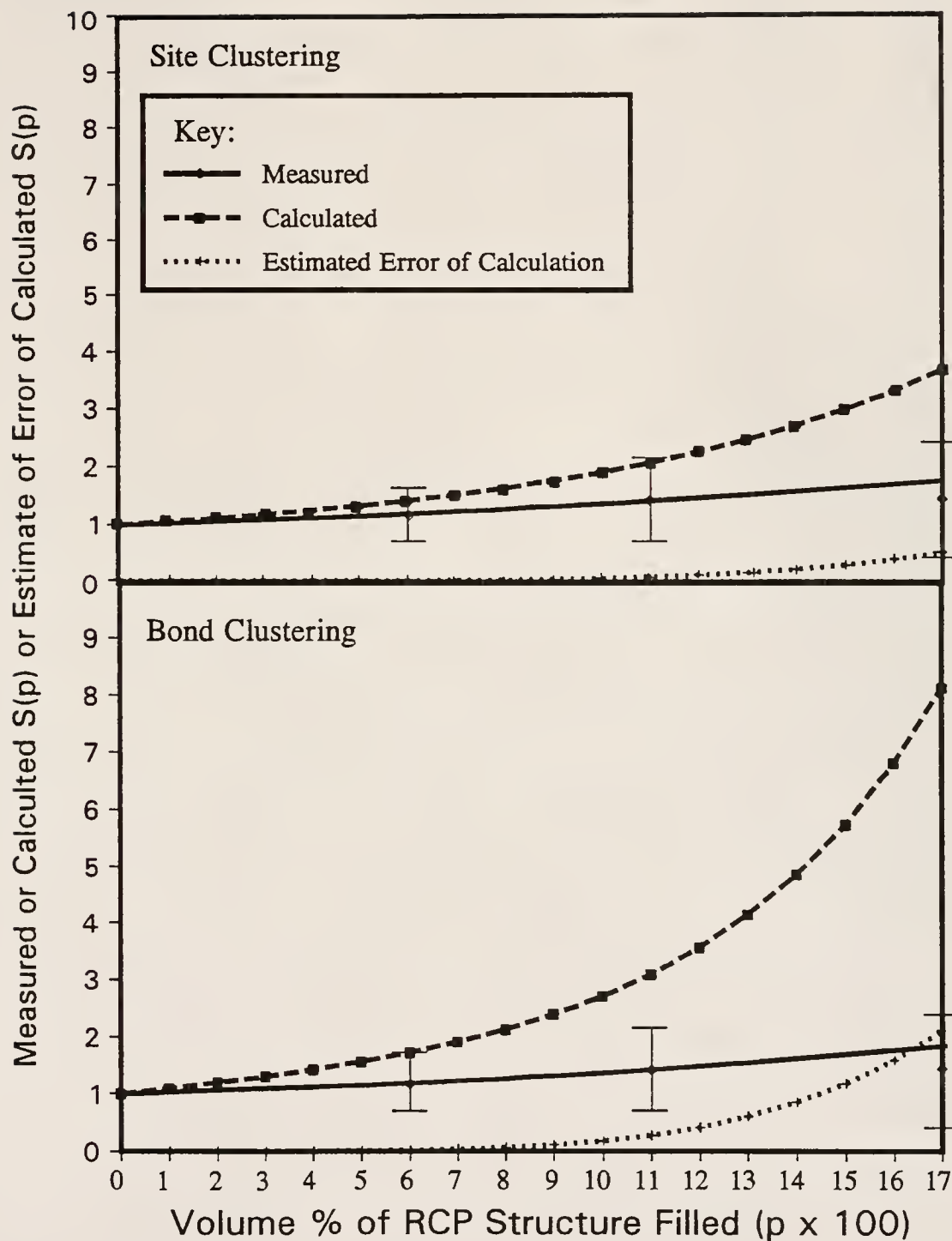


Figure 4.126

Measured versus calculated cluster size as a function of percent of RCP "structure" filled for representative BS glass/4.6  $\mu\text{m}$  UPLM composites, below the onset of percolation

representative values measured from microscopic samples (4.6  $\mu\text{m}$  UPLM at 5, 10 and 15 V% additions, see Table 4.10). The approximation is limited to V% values near the onset of percolation for the bond clustering mechanism. Furthermore, the measured values are corrected for the  $p$  values through the relation

$$p = \frac{VF_{\text{UPLM addition}} \times \rho_{\text{green compact}}}{PE_{\text{RCP}}}$$

where  $p$  is the volume fraction of the RCP "structure" filled,  $VF_{\text{UPLM addition}}$  is the volume fraction UPLM addition,  $PE_{\text{RCP}}$  is the packing efficiency of RCP structures (0.637 was used), and  $\rho_{\text{green compact}}$  is the fraction of theoretical density of the green compact of the particular composite composition of interest (see Figure 4.52). This model assumes that the clustering configuration does not change between the green and densified states. This potential source of error was minimized by using data from samples having volume fraction additions of UPLM below the percolation onset for either clustering mechanism. From the figure, it is apparent that the site clustering mechanism models the measured cluster number much better than does the two dimensional, bond clustering approximation. Thus, it may be surmised that the site mechanism of clustering was measured in this study. This is logical, since it is expected that site filling (and not necessarily bonding between previously filled sites) of the RCP "structure" is responsible for the percolation phenomena observed. The source of the difference between measured and approximated, two dimensional  $S_p$  values at higher  $p$  values is not known, but is probably relatable to the microstructural changes that occur during thermal processing.

The above model may also be used to predict maxima in closed porosity. In materials that are isomorphous in three dimensions, the volume fraction of an included phase is equivalent to the area fraction

of a plane randomly placed through the sample [68DEH]. This fact is commonly used in the field of quantitative microscopy to correlate measured area fractions of phases to actual volume fractions (and was used above to determine included porosity concentrations). This phenomenon, coupled with the relationship between uniform sphere diameter and measured crosssectional area of planes, randomly placed through said spheres (discussed above) may be used to determine the number of spheres intersecting the surface ( $N_{sis}$ ) of a unit volume (in  $\text{cm}^3$ ) of a compact of known surface area to volume ratio ( $S/V$  in  $\text{cm}^{-1}$ ) through the equation

$$N_{sis} = \frac{(VF_{pore} \times \frac{S}{V})}{((\frac{\pi}{6}) (\frac{D}{10000})^2)}$$

where  $VF_{pore}$  is the volume fraction of included porosity, and  $D$  is the UPLM diameter in  $\mu\text{m}$ . The value of  $N_{sis}$  is equivalent to the number of clusters intersecting ( $N_{sic}$ ) the surface (assuming no interaction between surface connected clusters). Cluster theory is then utilized to determine the number of surface connected spheres ( $N_{scs}$ ) per unit volume ( $\text{cm}^3$ ) through the relation

$$N_{scs} \approx N_{sis} \times (\frac{S_p}{2}) .$$

The corresponding volume (in  $\text{cm}^3$ ) of the surface connected spheres ( $V_{scs}$ ) per unit volume is determined through the relation

$$V_{scs} \approx (\frac{4\pi}{3}) \times (\frac{D}{20000})^3 \times (\frac{1}{2} + N_{scs}) .$$

These equations are based upon the assumption that the average volume of a surface intersected sphere is equal to one half of the volume of the corresponding sphere. Another assumption is that the average number of spheres connected to the surface is equal to one half the average

cluster number ( $S_p$ ).

The volume percent total porosity ( $V\%_{tot}$ ) of the compact is

$$V\%_{tot} = 100 \times VF_{pore}$$

and the volume percent open porosity ( $V\%_{op}$ ) is

$$V\%_{op} = 100 \times V_{scs}.$$

Finally, the volume percent closed porosity is equal to

$$V\%_{cp} = V\%_{tot} - V\%_{op}.$$

Figure 4.127 depicts these relationships as a function of volume percent total porosity, and as a function of RCP (site) spaces filled ( $p$ ) for a representative hypothetical series of samples (i.e. 4.6 UPLM included porosity in a disk-shaped compact of 25.4 x 2 mm) containing only included porosity. Since a greater accuracy is required with these approximations than with the cluster measurement investigations discussed above, the number of terms used to determine  $S_p$  was increased to 30, from 8 (the linear regression outlined in Table 4.12 (RCP site) was extrapolated to an  $n$  value of 30). This afforded acceptable accuracy slightly below  $p_c$ . However, at  $p_c$  an infinite number of terms is required to determine  $S_p$  (which is also infinity). Again, it should be noted that this model assumes no interaction between clusters. This assumption is not valid as  $p$  approaches  $p_c$ . However, from Figure 4.127, it is evident that the error resultant from said simplification is not detrimental for  $p$  slightly below  $p_c$ .

Table 4.14 depicts the maxima in  $V\%$  closed porosities and other relevant data for compacts of discoidal shape and constant diameter, but of varying thicknesses. Data for monospherical included pore sizes of



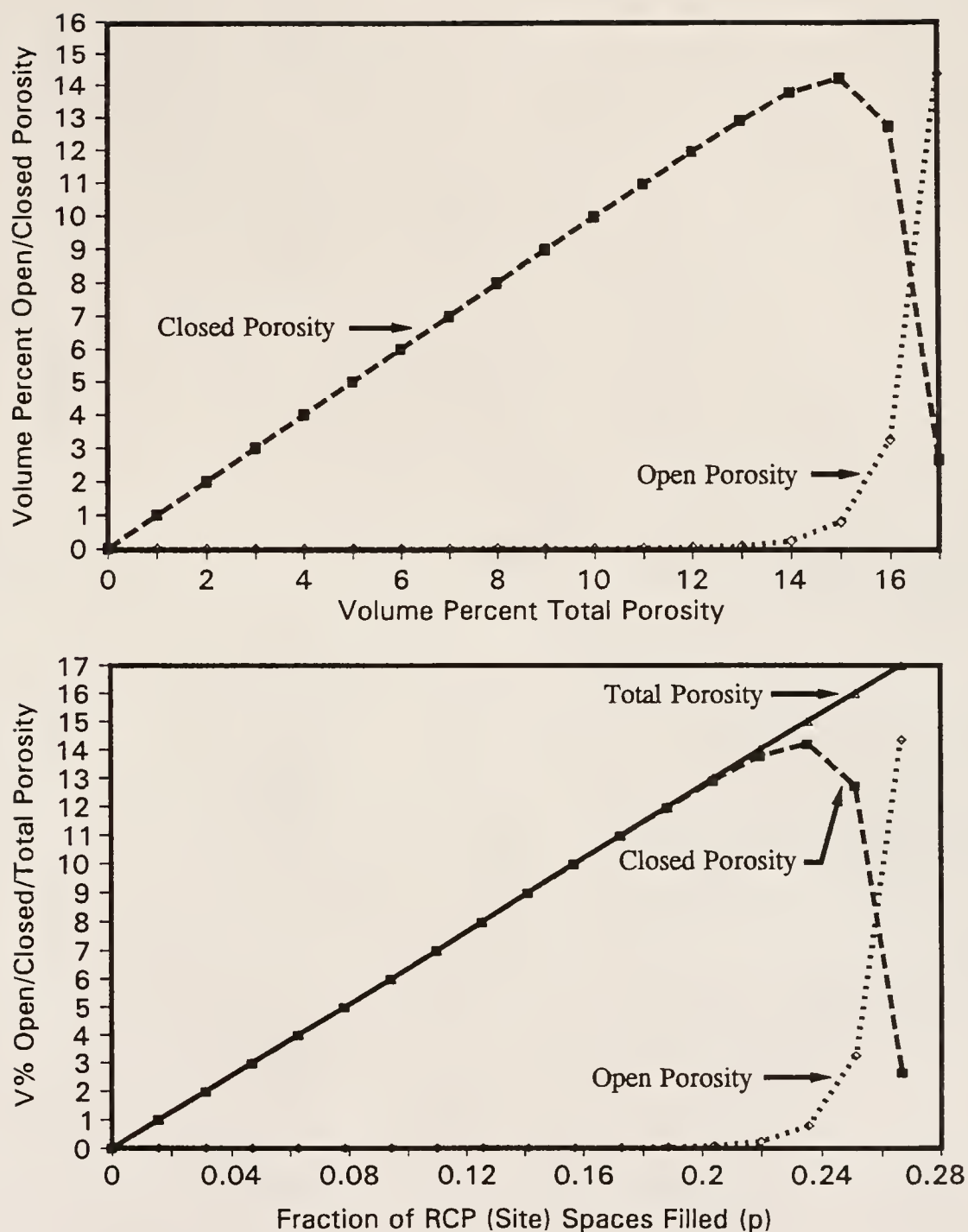


Figure 4.127

Illustration of closed and open porosities versus  $V\%$  total porosity and of total, closed and open porosities versus  $p$  calculated using pre-percolation cluster theory

Table 4.14

Effects of Disk Thickness and Included Sphere Size  
Upon Maximum Closed Porosity

Disk Thickness (mm)	Included Sphere Diameter ( $\mu\text{m}$ )	Maximum Calculated V% CP	Calculated Percent Porosities at Maximum Closed Porosity		p at Maximum Closed Porosity
			Total Porosity	Open Porosity	
0.1	4.6	11.51	13.00	1.49	0.204
1.0	4.6	13.57	14.00	0.43	0.220
2.0	4.6	14.21	15.00	0.79	0.235
5.0	2.0	15.31	16.00	0.69	0.251
5.0	4.6	14.62	15.00	0.38	0.235
5.0	9.0	14.25	15.00	0.75	0.235
10.0	4.6	14.99	16.00	1.01	0.251
100.0	4.6	15.49	16.00	0.51	0.251

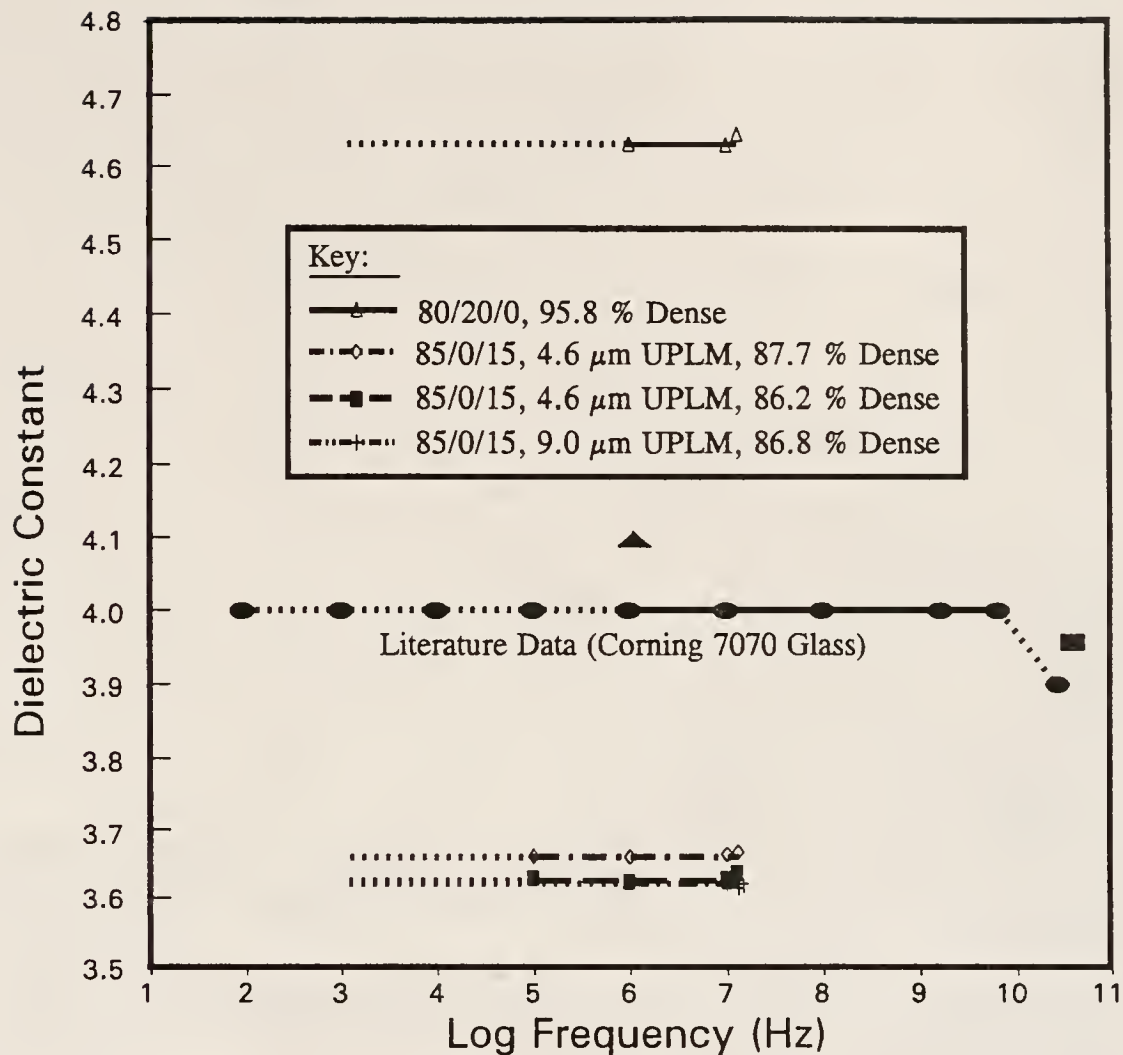
2.0, 4.6 and 9.0  $\mu\text{m}$  is also included. From Table 4.14 it is evident that the maximum amount of closed porosity (as well as  $p$  at said maximum) decreases with decreasing disk thickness. The maximum amount of closed porosity also decreases with increasing included pore diameter. The former effect is reasonable, since the surface area to volume ratio increases as disk thickness is decreased. Furthermore, it is expected that clusters of spheres would interact more with the surfaces of a thinner compact. This should be a caveat when designing included pore systems for thin substrate applications (which is common in high speed electronic packaging). The later effect was not observed experimentally, however. This is because the model does not take the effects of differential sintering into consideration. Therefore, increasing the included porosity size serves only to reduce the thickness to diameter ratio where this model is concerned. This is important in that it provides further impetus to use included sphere sizes that are small compared to the sample thickness. Thus, when designing included porosity multilayer packages, with the goal of maximization of closed porosity, it is important to maximize the ratio of layer thickness to included pore diameter. It is interesting to note that, with the exception of the first two entries, the value of  $p$  at maximum calculated closed porosity in Table 4.14 is always between the calculated and the literature values of  $p_c$  (site) for the RCP structure (see Table 4.13). This gives further credence to the accuracy of the series approximation model.

Again, it should be noted that all of the above quantitative analyses were not possible for the  $\text{Si}_3\text{N}_4$  additions, due to problems related to sample preparation and quantitative microscopic analysis of composites containing  $\text{Si}_3\text{N}_4$ . This should be an area of focus for future research.

#### 4.4.3 Characterization of Dielectric Properties

Both dielectric constant ( $K$ ) and dielectric dissipation factor ( $\tan(\delta)$ ) were measured as explained in section 3.7.2. Figure 4.128 illustrates the dielectric constant of several representative (hermetic) samples, investigated in this study, as a function of frequency. Figure 4.129 illustrates the loss tangent for the above representative samples as a function of frequency. For comparative purposes literature values for the pure, bulk BS glass are also included. The dotted portions of the data in Figure 4.128 indicate that the accuracy of the impedance analyzer-test fixture was questionable, therefore, the lines are extrapolated at frequencies below 100 kHz, and none of the data measured below 100 kHz are included. From Figure 4.128, it is evident that the dielectric constants of the specimens prepared for this study do not change appreciably with changing frequency. It is also evident that the dielectric property characteristics of these materials closely follow the general character of the corresponding literature data. It is interesting to note the effects of included porosity, and of  $\text{Si}_3\text{N}_4$  inclusions upon dielectric constant.

The dissipation factor data (Figure 4.129) agrees well with the available literature data. The sporadic nature of the data (see closeup of test data, Figure 4.129) is probably due somewhat to errors associable with measurement. However, a general trend of increasing  $\tan(\delta)$  with increasing frequency is also indicated in the literature data. This should be considered when designing for high frequency, low loss packaging applications. However, the excellent agreement with the  $\tan(\delta)$  literature data, in general, indicates that the specimens were not contaminated during processing. This is important in that it indicates that the organics were removed sufficiently during thermal processing. It also indicates that ball milling and subsequent processing did not introduce significant contamination to the system.



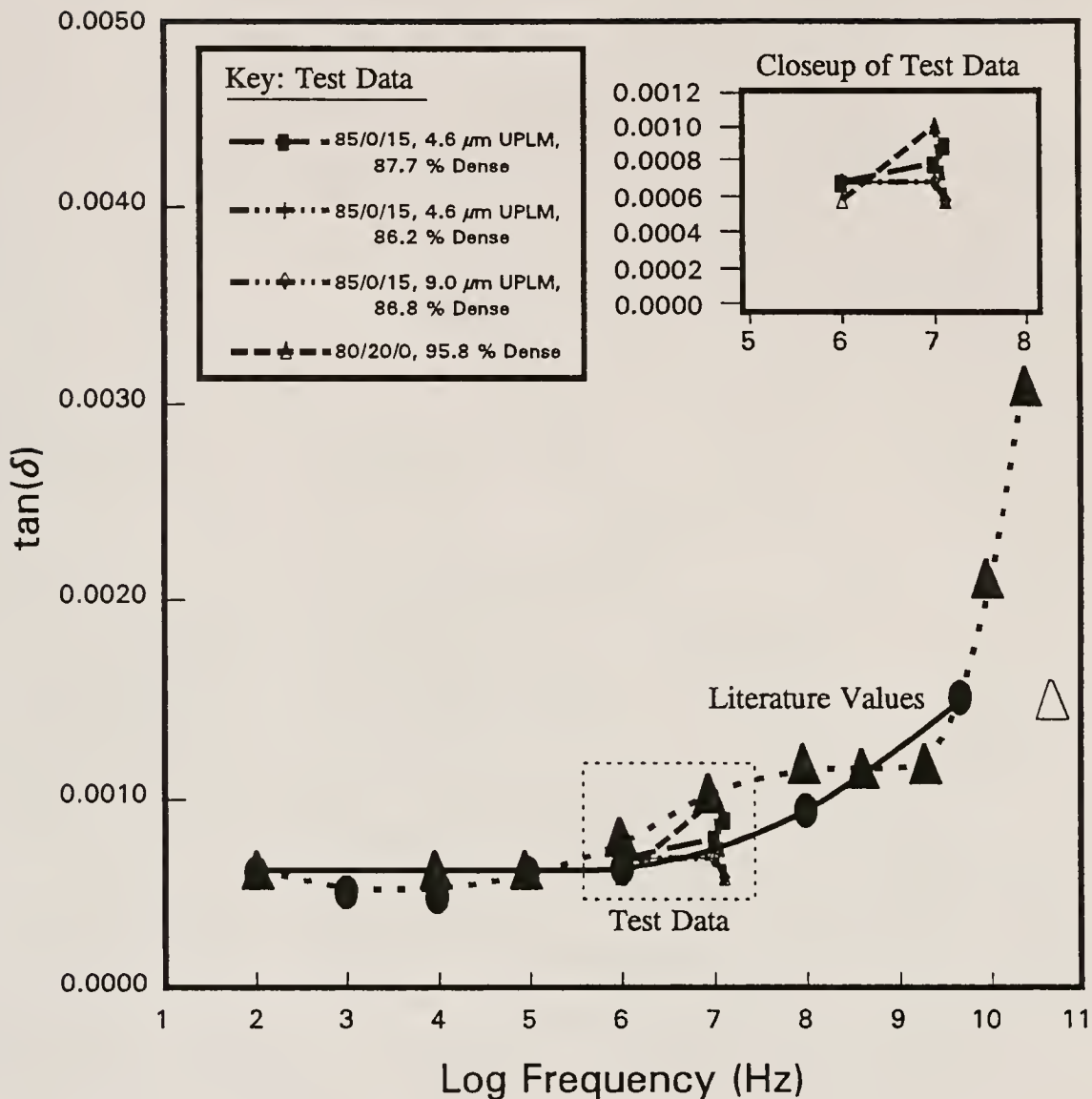
Source for Literature Values:

Air Force Materials Laboratory (prepared by the  
Electronic Properties Information Center,  
Hughes Aircraft Company, Culver City, CA)

Figure 4.128

Dielectric constant (K) as a function of frequency for representative samples investigated in this study as well as pertinent literature data





Source for Literature Values:

Air Force Materials Laboratory (prepared by the  
Electronic Properties Information Center,  
Hughes Aircraft Company, Culver City, CA)

Figure 4.129

Dielectric dissipation factor ( $\tan(\delta)$ ) as a function of frequency for representative hermetic samples investigated in this study, pertinent literature values are also included

Figures 4.130 and 4.131 illustrate measured dielectric constant data of the pure BS glass system (both with and without  $4.6\ \mu\text{m}$  included porosity). Figure 4.130 depicts this data with corresponding traditional modelling (parallel and perpendicular slabs, logarithmic and Maxwell models), while Figure 4.131 models the data using effective medium theory (EMT). The dielectric constant values of 4.1 and 1 were used for the BS glass and porosity phases respectively. From the figures it is evident that, with few exceptions, the dielectric constant data follow the same relation, regardless of the type of porosity. Said relation is quite linear and generally falls between the Maxwell and logarithmic models (see Figure 4.130). This linear relation is also well modelled by the EMT approximation for perfectly spherical pores within a matrix (i.e.  $c/a = 1$ ). It is interesting to note that there is a slight difference between the Maxwell and EMT ( $c/a = 1$ ) models.

The dielectric constant data fall between the Maxwell and logarithmic models at lower densities, and are well modelled by the Maxwell equation at higher densities, as is expected from the evolution in pore structure during sintering. During the densification process the pore structure changes from a continuous structure to a discrete dispersion of spheres. The logarithmic model approximates a continuous structure, while the Maxwell model approximates a discrete distribution of spheres within a matrix. Therefore, "switching" of these data, from logarithmic to Maxwell models, is expected.

Data from other studies have indicated similar relationships between percent density and  $K$ . The  $K$  data, in a study by Cross and Gururaja on microballoon-filled cement composites, fit well between relations modelled by logarithmic and Maxwell models [86CRO]. The  $K$  data of Cao, et. al, found during a study of porous colloidal silica, had greater scatter, but still fit mostly between the Maxwell and log model relations [89CAO]. Other data on porous silica shows a deviation of  $K$  from the Maxwell model at very low densities ( $\sim 20\%$  dense), but a

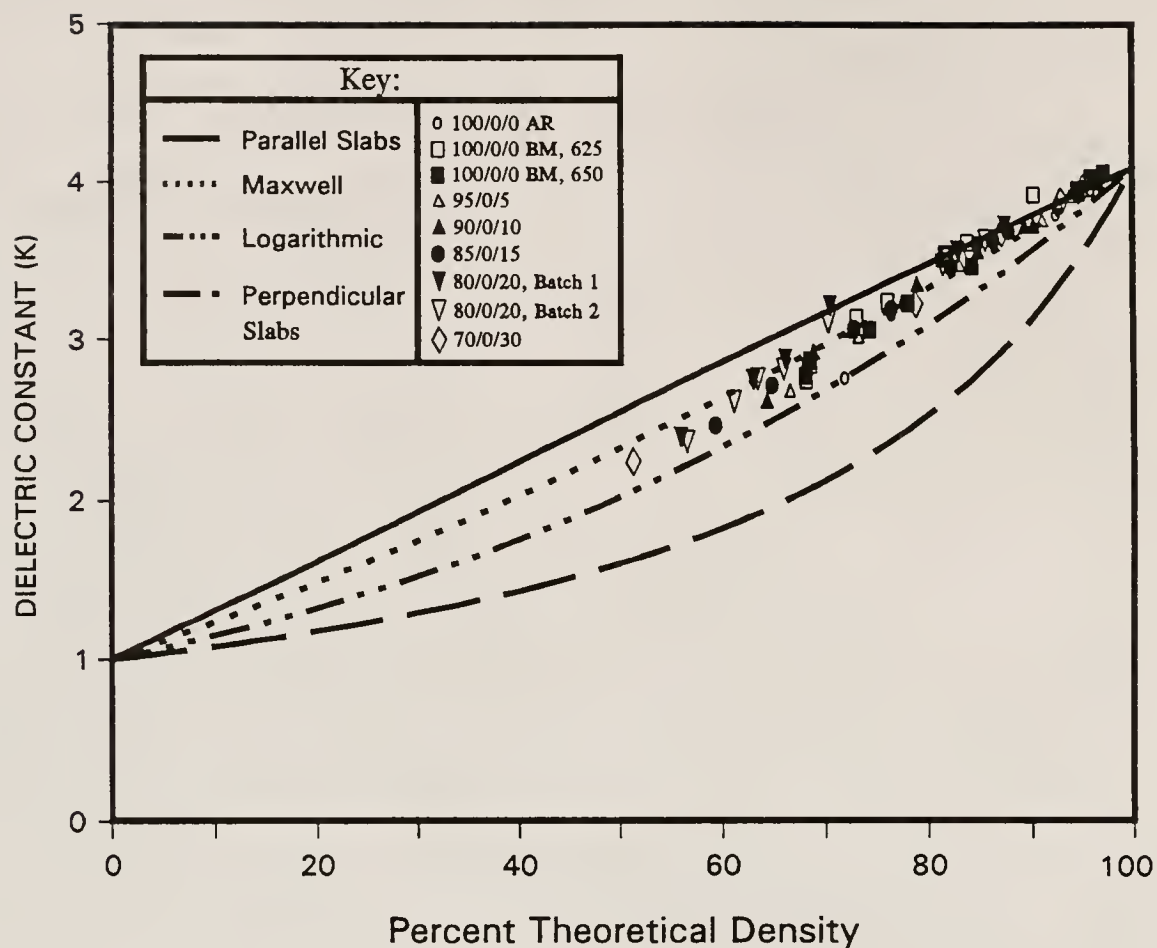


Figure 4.130

Measured dielectric constant data as a function of percent density for all pure BS glass compositions (with and without  $4.6\ \mu\text{m}$  included porosity), with associate traditional models

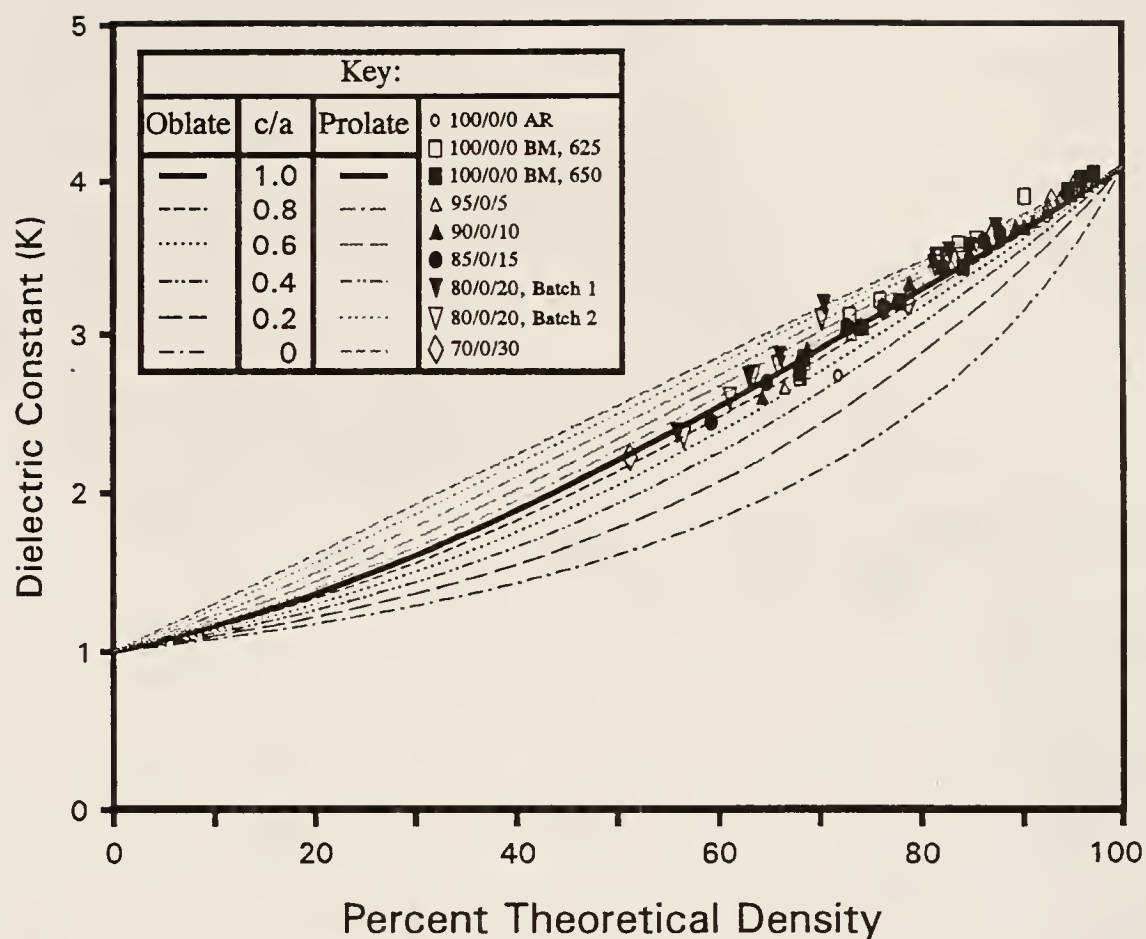


Figure 4.131

Measured dielectric constant data as a function of percent density for all pure BS glass compositions (with and without 4.6  $\mu\text{m}$  included porosity) modelled using EMT theory

general agreement with the Maxwell model at densities higher than ~ 20 % [88GER3]. The data of Leap, et. al, extracted from a study of composites with a silica matrix with embedded Pb glass microspheres, fit between Maxwell and parallel slabs models and thus, was slightly higher [89LEA]. Sacks, et. al, found a linear relation between K and percent density [91SAC1]. No further modelling was performed, however. Unfortunately, EMT modelling was not performed in any of the above studies.

Since the EMT model accounts for sphere overlapping at higher fractions of spherical phase, it models both situations well. Thus, it may be concluded that the EMT model ( $c/a = 1$ ) is best for modelling K, in this system, at all stages of densification. Furthermore, it is logical that the compositions bereft of included porosity also follow this relation, since the final stages of sintering of this type of microstructure also involves changing from a continuous pore structure to a discrete spheroidal pore structure. In order to better understand the dielectric properties of this (and similar) composite system, it would be interesting to model, using EMT, controlled porosity materials such as those studied by Yamamoto, et al., and Kata, et al. [89YAM,90KAT]. The pore shape within the materials investigated in these studies was ellipsoidal, due to a unidirectional (Z-axis) lamination step. Thus, the  $c/a$  value would be  $< 1$  (prolate or oblate depending upon sample orientation). This would be valuable for determination of the validity of EMT theory for values of  $c/a$  near (but not equal to) one. Modelling of the K values of tubular fiber composites would also be beneficial in order to determine the validity of EMT theory for ellipsoids having  $c/a$  values close to 0.

Figures 4.132 and 4.133 illustrate K data for 15 and 17.6 V% included porosity compositions (2.4  $\mu\text{m}$  bimodal, 4.0  $\mu\text{m}$  quadramodal and 4.6  $\mu\text{m}$  and 9.0  $\mu\text{m}$  monomodal included porosity). It is evident from these figures that included porosity size and size distribution have no



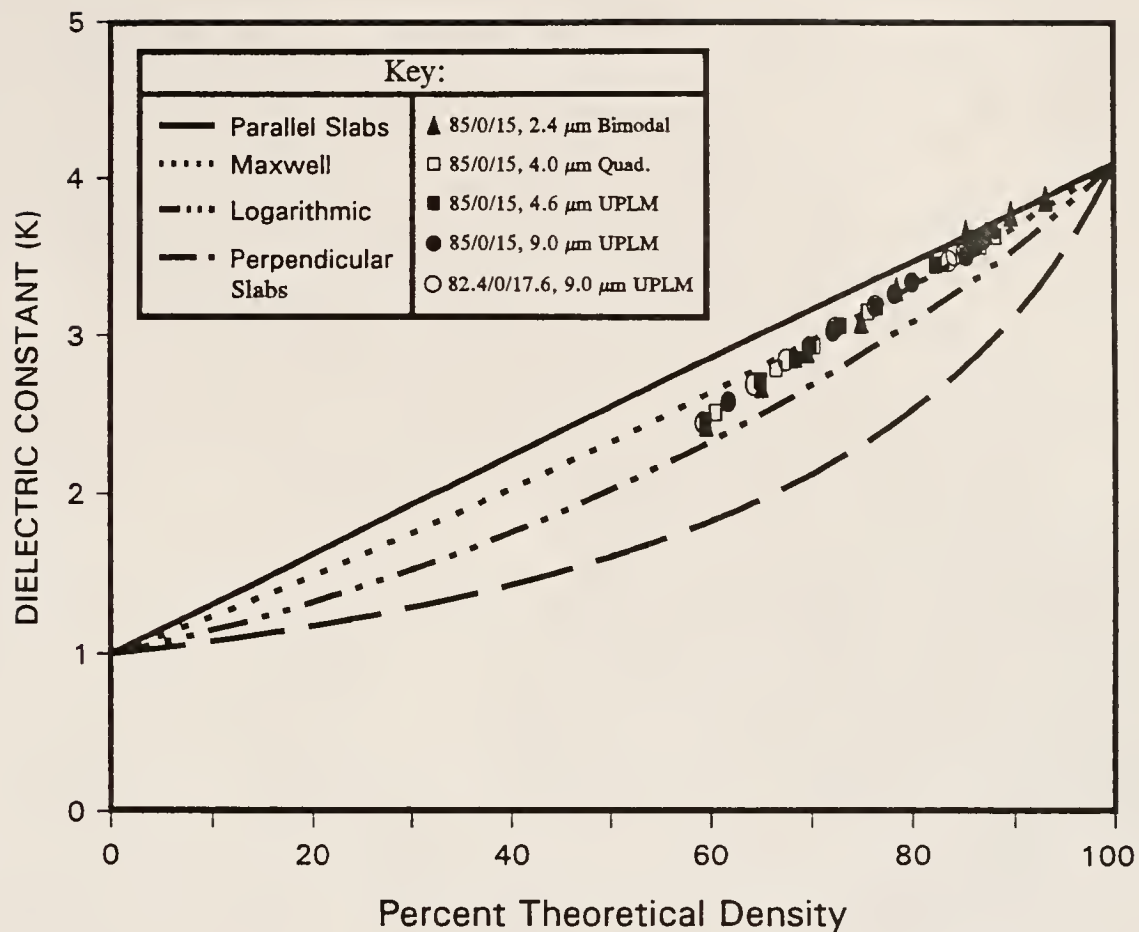


Figure 4.132

Measured K values as a function of percent density for 15 or 17.6 V% (2.4  $\mu\text{m}$  bimodal, 4.0  $\mu\text{m}$  quadramodal and 4.6  $\mu\text{m}$  and 9.0  $\mu\text{m}$  monomodal included porosity) compositions, with associable traditional models

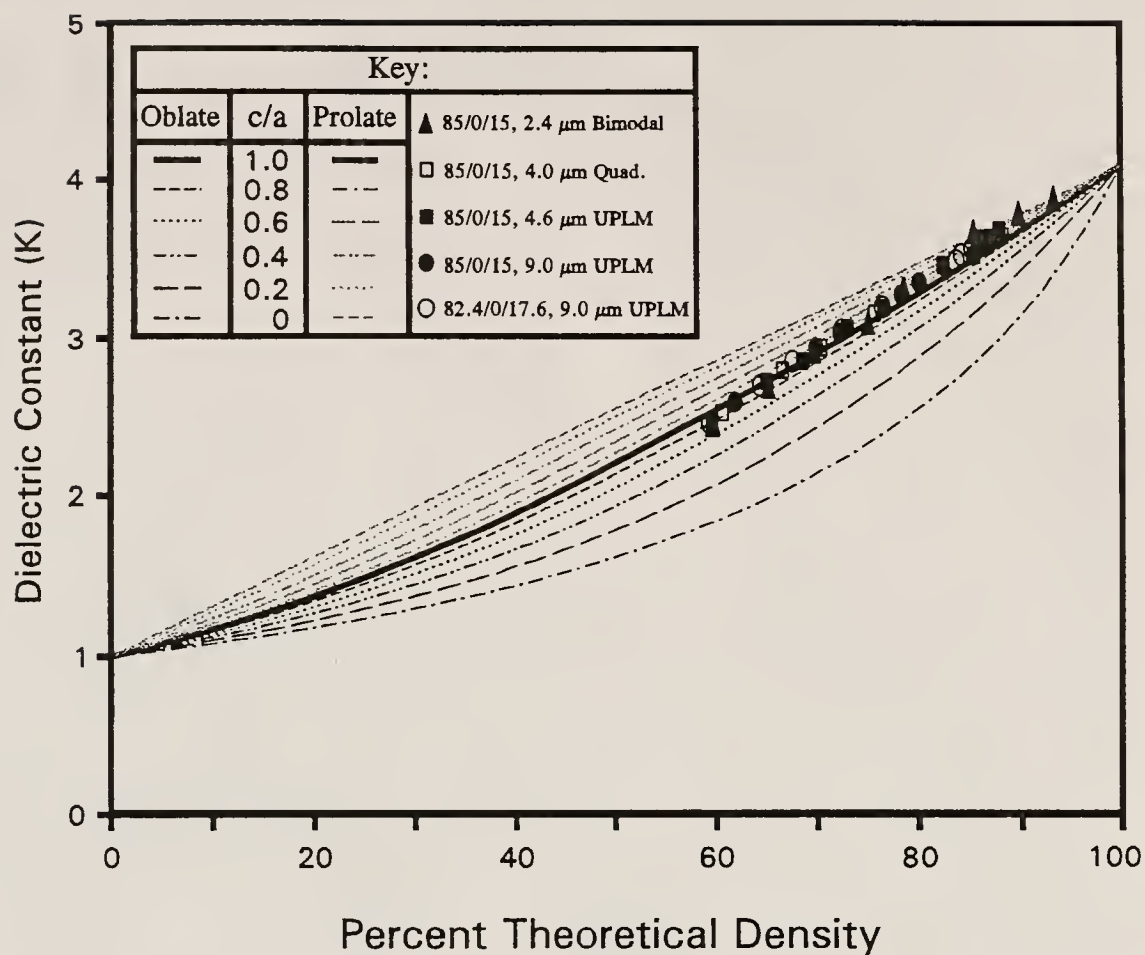


Figure 4.133

Measured K values with respect to density for 15 or 17.6 V% (2.4  $\mu\text{m}$  bimodal, 4.0  $\mu\text{m}$  quadramodal and 4.6  $\mu\text{m}$  and 9.0  $\mu\text{m}$  monomodal) compositions, modelled with EMT

significant effect upon K. Again, the K values of these compositions falls between the logarithmic and Maxwell predictions, coming closer to the logarithmic model at lower densities and being more closely approximated by the Maxwell model at higher densities. Again, EMT ( $c/a = 1$ ) most closely models the K values for these compositions over all densities investigated.

Figures 4.134 and 4.135 depict the K data as well as the traditional and EMT predictions for the 10 V% (final)  $\text{Si}_3\text{N}_4$  concentration samples studied. Again, both figures indicate that the data fits between the logarithmic and Maxwell models (favoring the log model at lower densities and the Maxwell model at higher densities, as above), and is well modelled over all densities (except the lowest ones investigated) by EMT predictions. Figures 4.136 and 4.137, 4.138 and 4.139, and 4.140 and 4.141 illustrate analogous relationships for the composites containing 15, 20 and 40 V% (final)  $\text{Si}_3\text{N}_4$  concentrations. Again, the above observations hold true, with the exception that the K data for the 40 V% (final)  $\text{Si}_3\text{N}_4$  concentration samples is more scattered and generally more over-estimated by the models than the other compositions. This is because the regression data for said compositions also had a relatively large amount of scatter. The K values used for the fully dense glass- $\text{Si}_3\text{N}_4$  composites were obtained from linear regression analysis and subsequent extrapolation to full density. This extrapolation represents a potential (albeit small) source of error in K modelling of these compositions. The K values used for the fully dense BS glass- $\text{Si}_3\text{N}_4$  particulates were 4.53, 4.65, 4.85 and 5.68 for the 10, 15, 20 and 40 V% (final)  $\text{Si}_3\text{N}_4$  concentration composites respectively.

It should be noted that the corresponding extrapolated linear regression value for pure BS glass compositions was 4.19. This value is approximately 2 % greater than the literature value used for said glass (i.e. 4.1). The standard deviation of the average of the extrapolated linear regression values is 0.04 (13 data sets). This increase in K is

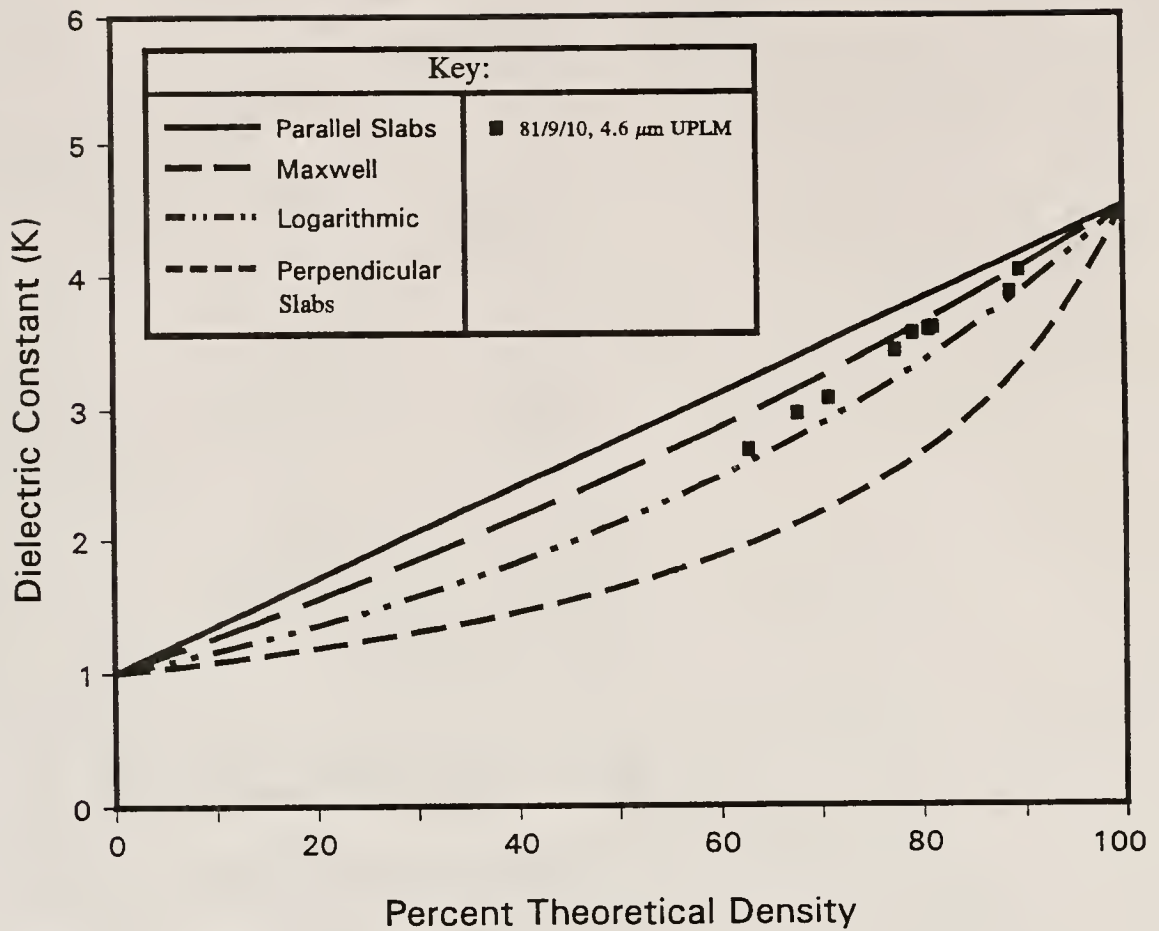


Figure 4.134

Measured dielectric constant as a function of percent density, with traditional modelling, for the 10 V% (final) concentration silicon nitride composition

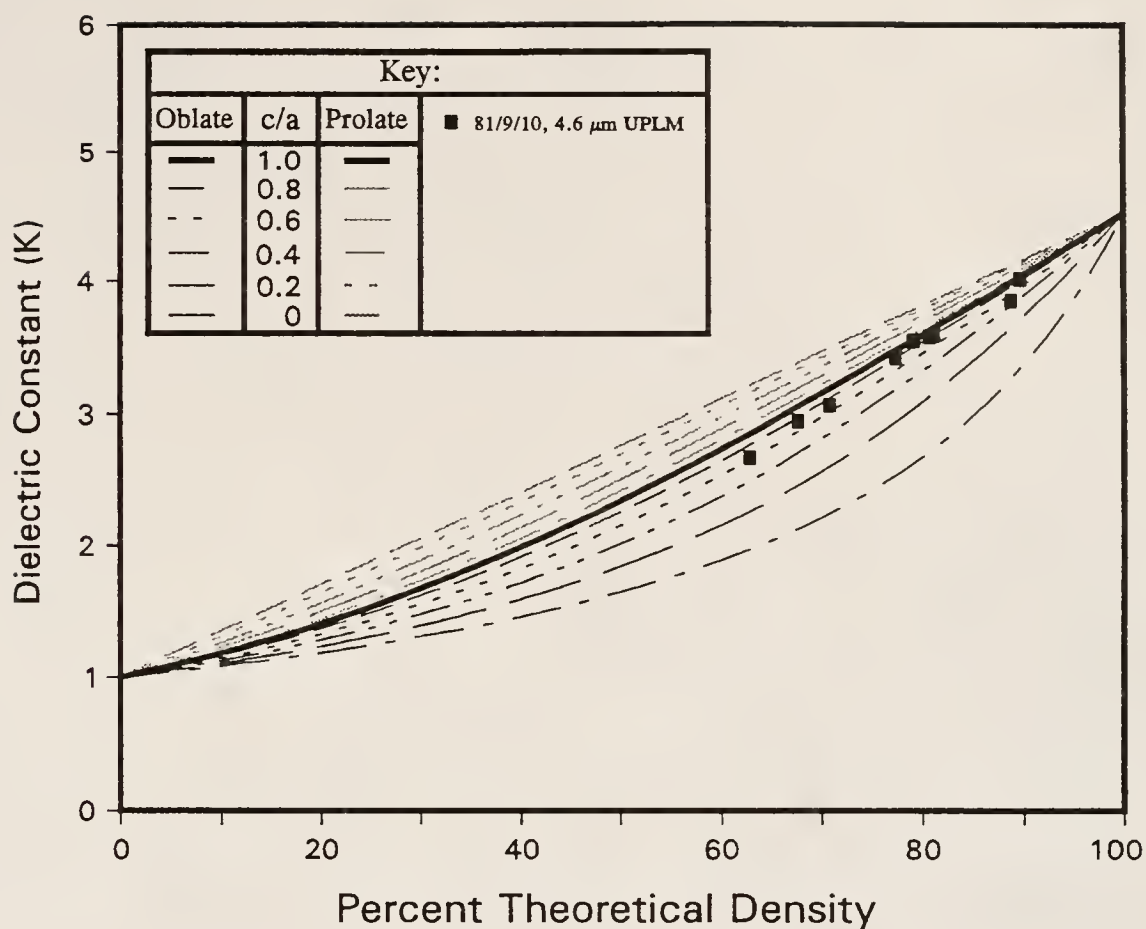


Figure 4.135

Measured dielectric constant as a function of percent density, with EMT modelling, for the 10 V% (final) concentration silicon nitride composition



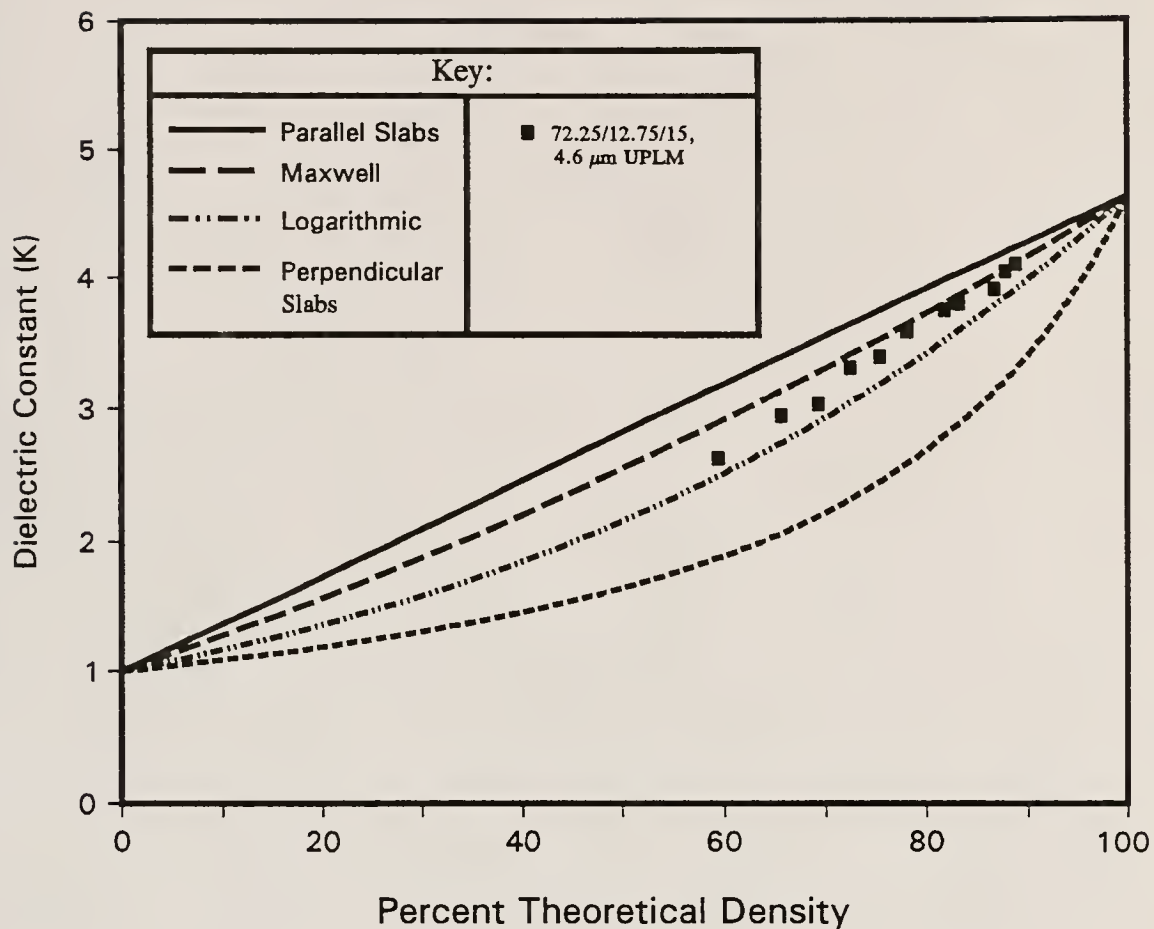


Figure 4.136

Measured dielectric constant as a function of percent density, with traditional modelling, for the 15 V% (final) concentration silicon nitride compositions

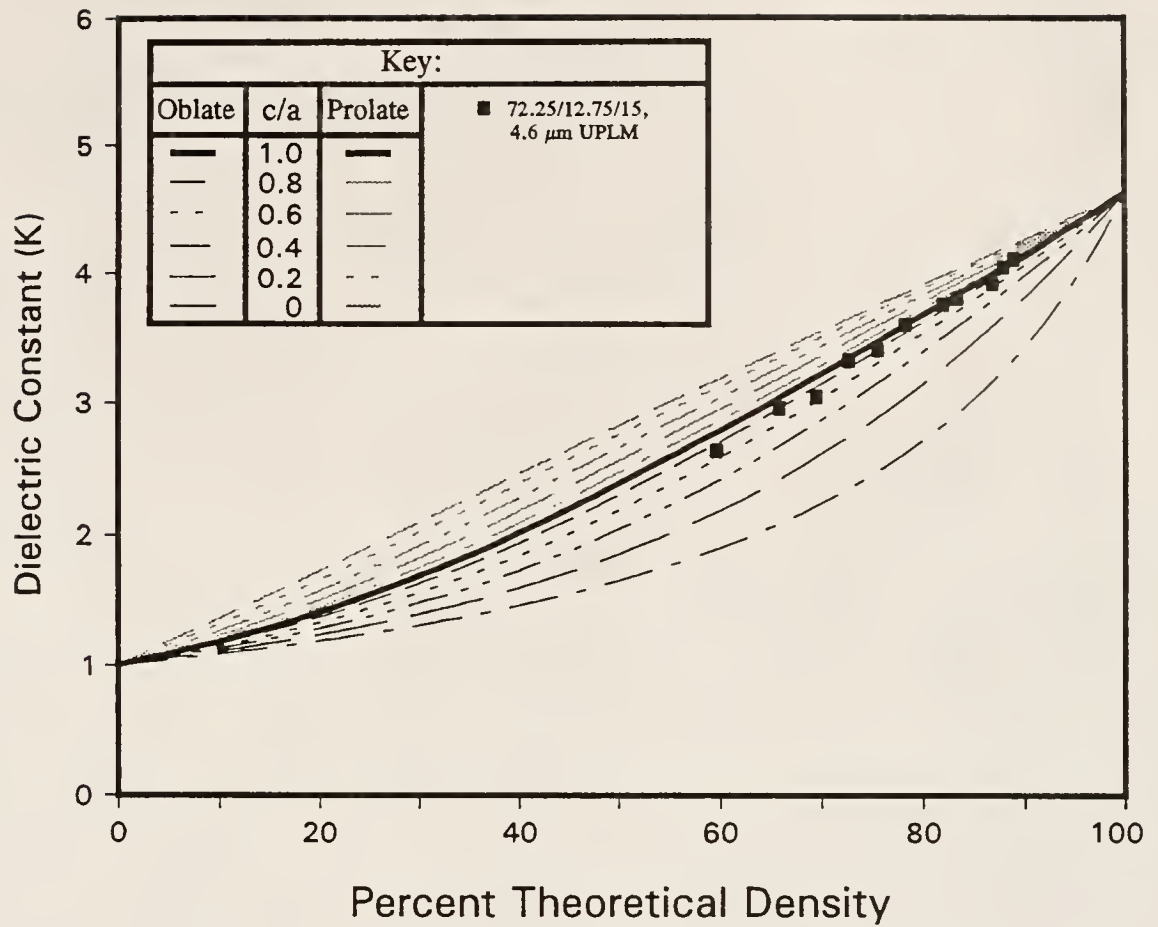


Figure 4.137

Measured dielectric constant as a function of percent density, with EMT modelling, for the 15 V% (final) concentration silicon nitride composition

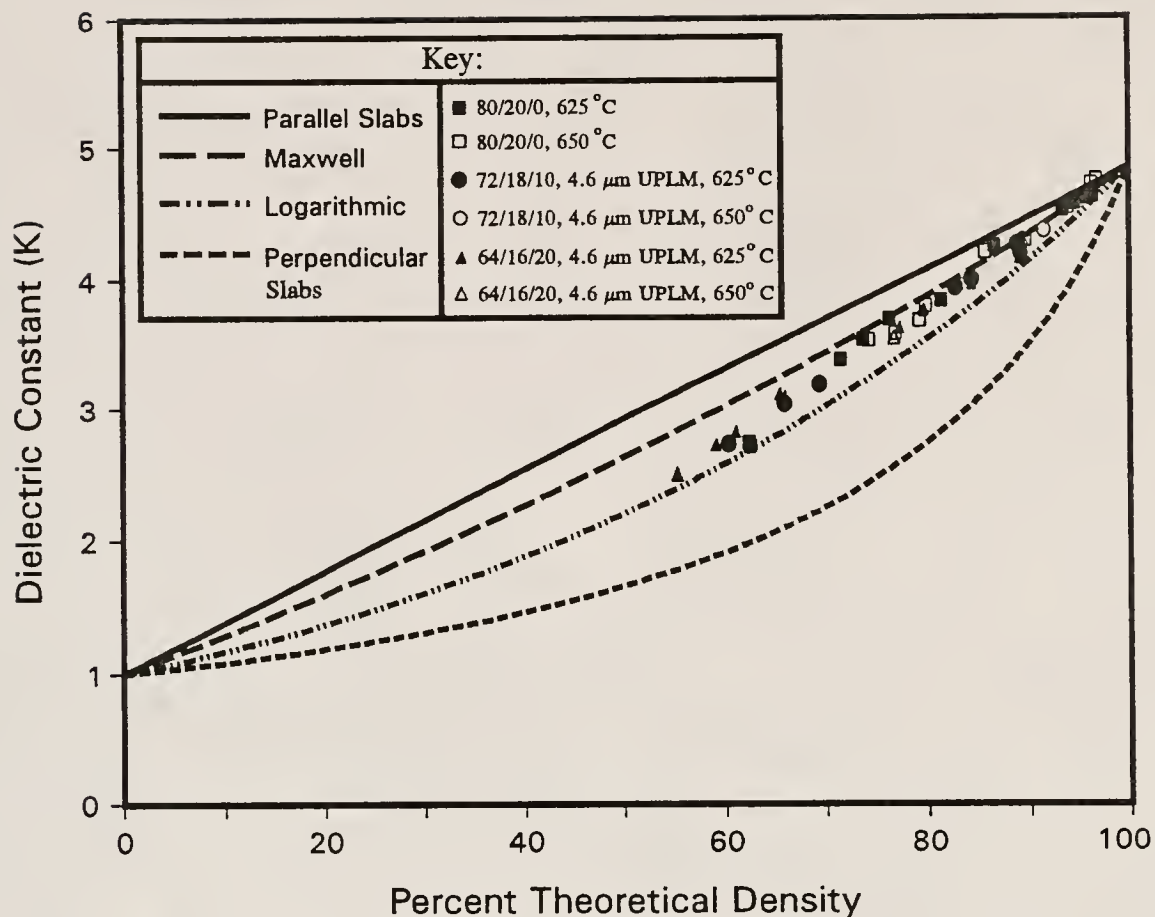


Figure 4.138

Measured dielectric constant as a function of percent density, with traditional modelling, for the 20 V% (final) concentration silicon nitride composition

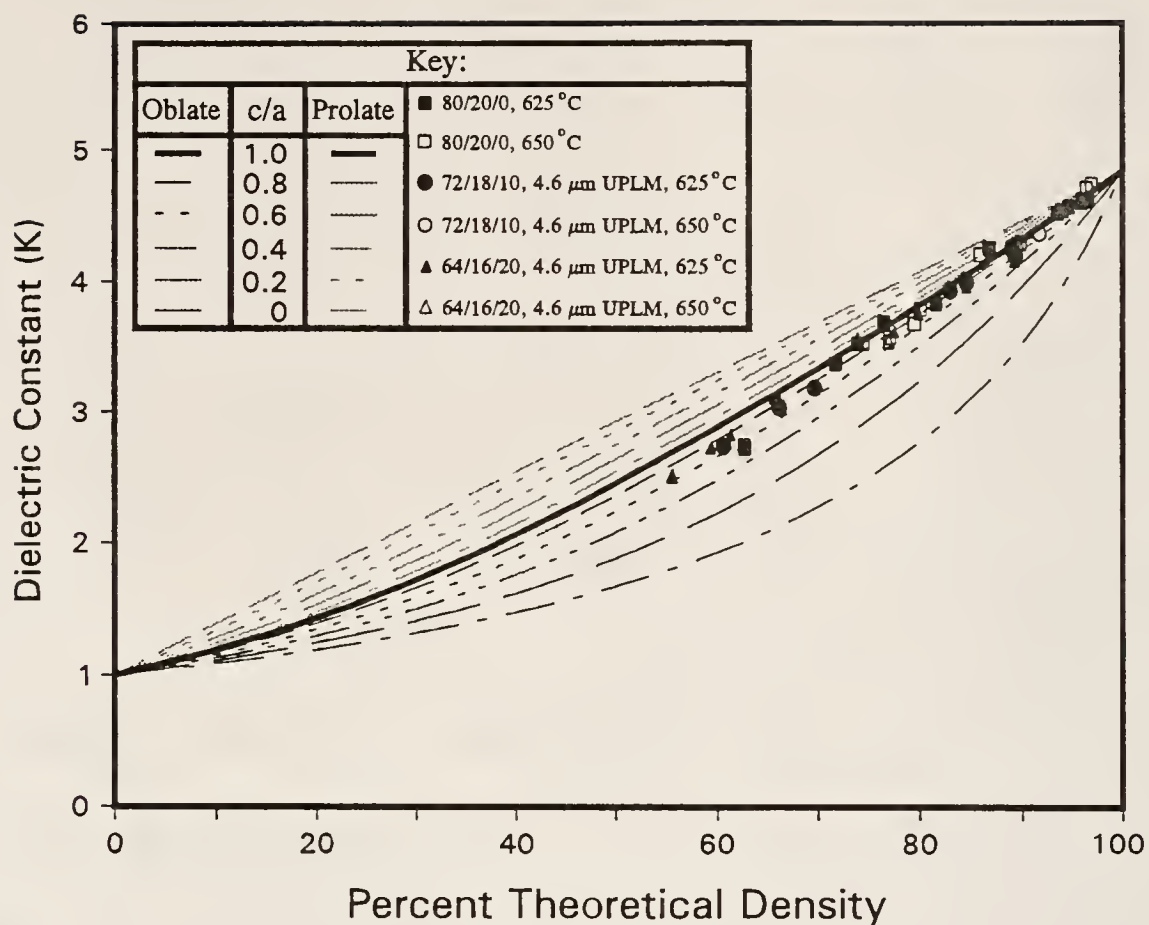


Figure 4.139

Measured dielectric constant as a function of percent density, with EMT modelling, for the 20 V% (final) concentration silicon nitride composition

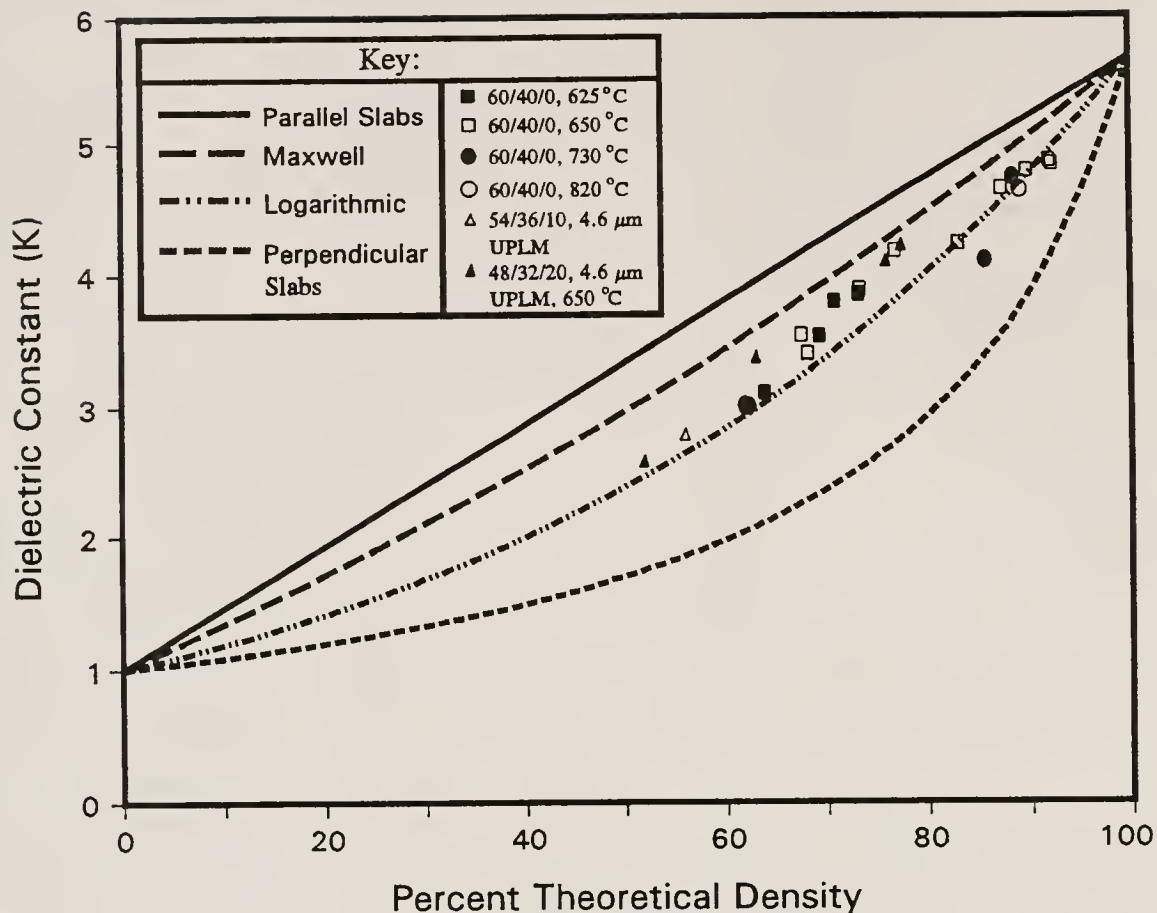


Figure 4.140

Measured dielectric constant as a function of percent density, with traditional modelling, for the 40 V% (final) concentration silicon nitride composition



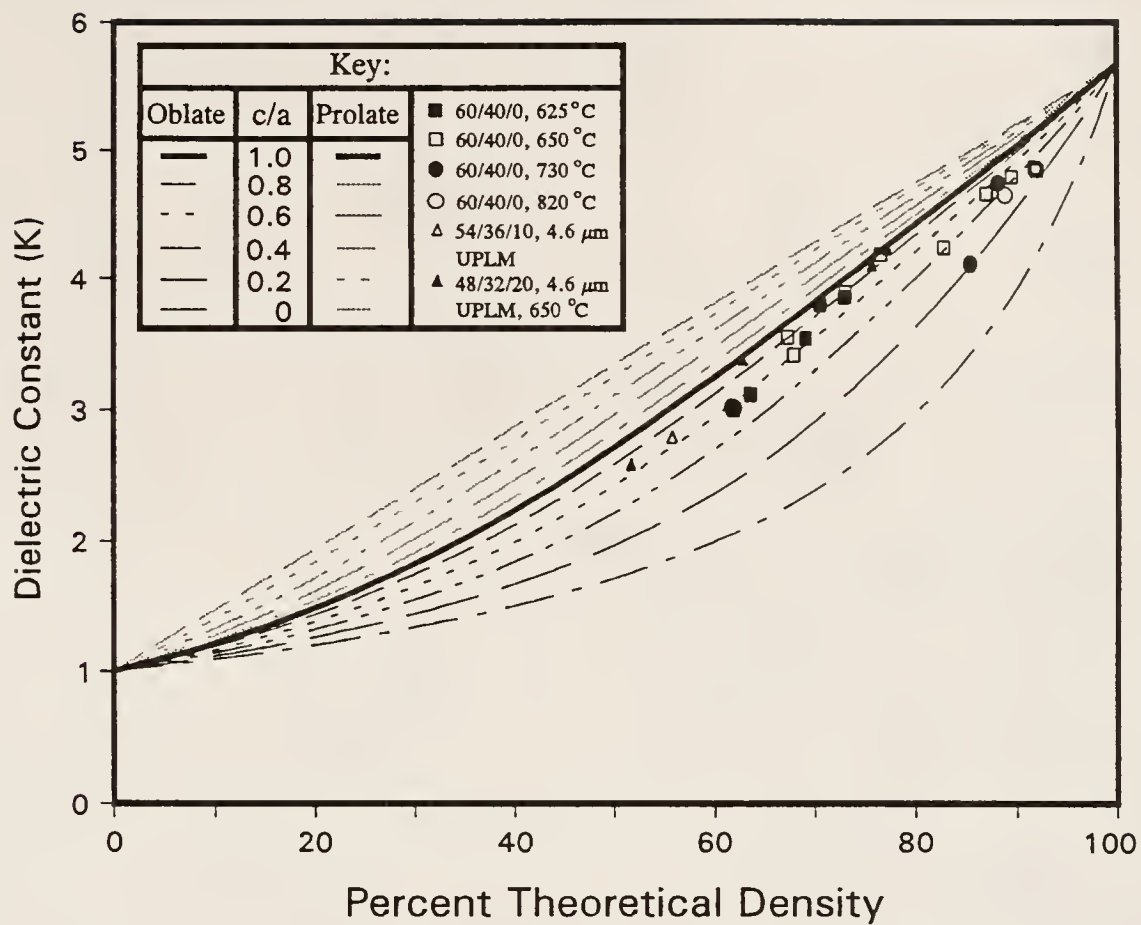


Figure 4.141

Measured dielectric constant as a function of percent density, with EMT modelling, for the 40 V% (final) concentration silicon nitride composition

not a result of changes experienced during ball milling, since the extrapolated value for the as-received BS glass is well within a standard deviation of the average (i.e. 4.17). It is possible that the impedance analyzer and test fixture consistently indicated high. However, it is more likely that the values are genuine, since the density value used to determine percent of theoretical density was that of the ball milled BS glass powder (i.e. 2.20 g/cm<sup>3</sup>) and not the literature value of (2.13 g/cm<sup>3</sup>). The manufacturer's value (2.13 g/cm<sup>3</sup>) was confirmed to be valid via the Archimedes method. Also, none of the sintered densities of the pure BS glass powder compacts exceeded 2.13 g/cm<sup>3</sup> during this investigation. However, none of the samples became optically transparent after densification. Bloating was observed as well. Thus, it is not likely that the samples reverted to the manufacturer's value of bulk density (i.e. 2.13 g/cm<sup>3</sup>).

Using the extrapolated 100 % density value for K of the pure BS glass, the data depicted in Figures 4.130 and 4.131, and 4.132 and 4.133 was replotted using the maximum K value of 4.19 (instead of 4.1). Figures 4.142 and 4.143 and 4.144 and 4.145 depict these relations. From the figures, it is evident that the above discussions, correlating these data to values between the Maxwell and logarithmic models as well as to the EMT model ( $c/a = 1$ ), still apply, having even better fits to the data to than originally discussed.

It is interesting that the above-mentioned extrapolated data for each group of increasing Si<sub>3</sub>N<sub>4</sub> concentration, do not fit the prediction of any of the composite dielectric constant models well, if literature values for pure Si<sub>3</sub>N<sub>4</sub> are used. Figures 4.146 through 4.151 delineate this relationship. From the figures, it is evident that 8.6 is the best value for modelling the K of Si<sub>3</sub>N<sub>4</sub> (assuming that the EMT model is best for this application).

All available literature values for the K value of Si<sub>3</sub>N<sub>4</sub> are between 6 and 7 (see Table 1.4). Most of these references cited a K

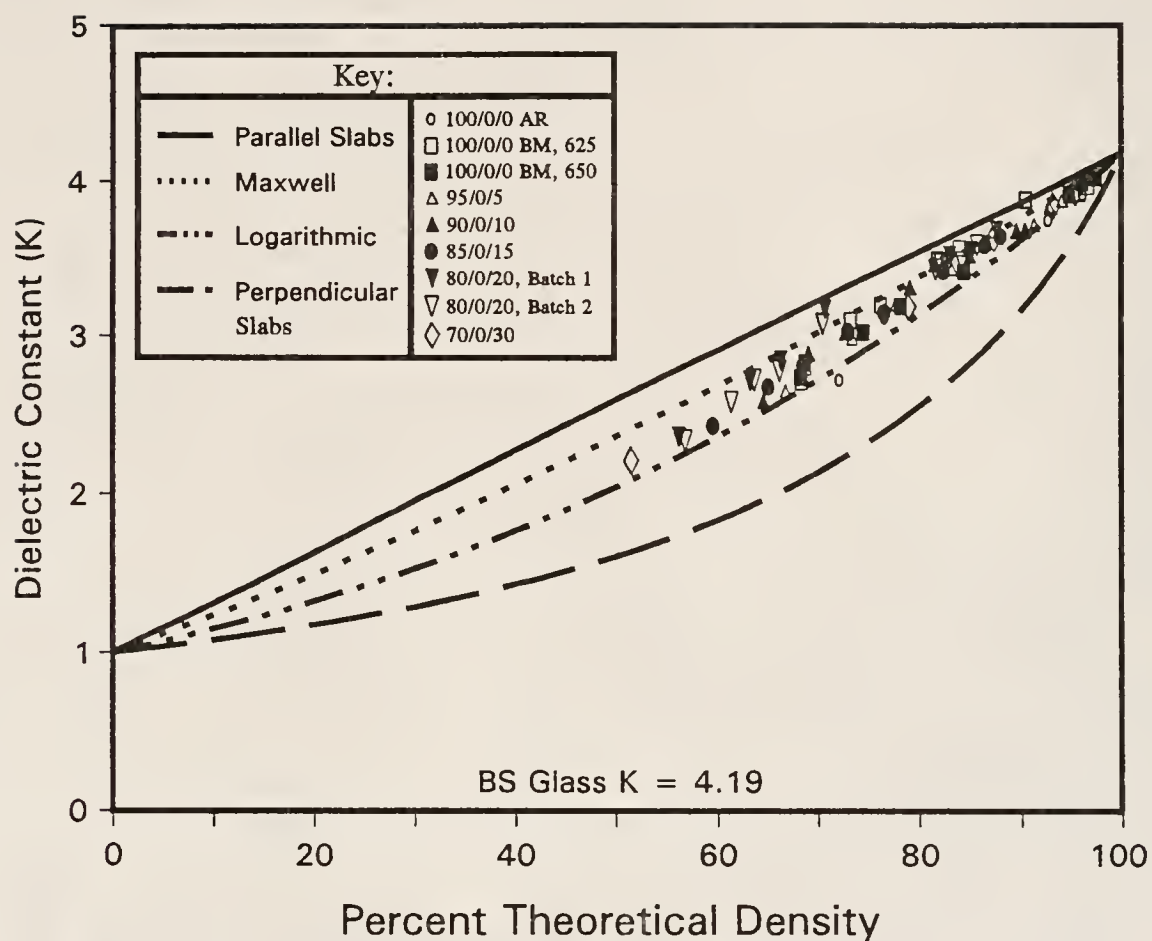


Figure 4.142

Measured K data as a function of percent density for all pure BS glass compositions (with and without 4.6  $\mu\text{m}$  included porosity) with traditional models, BS glass K = 4.19

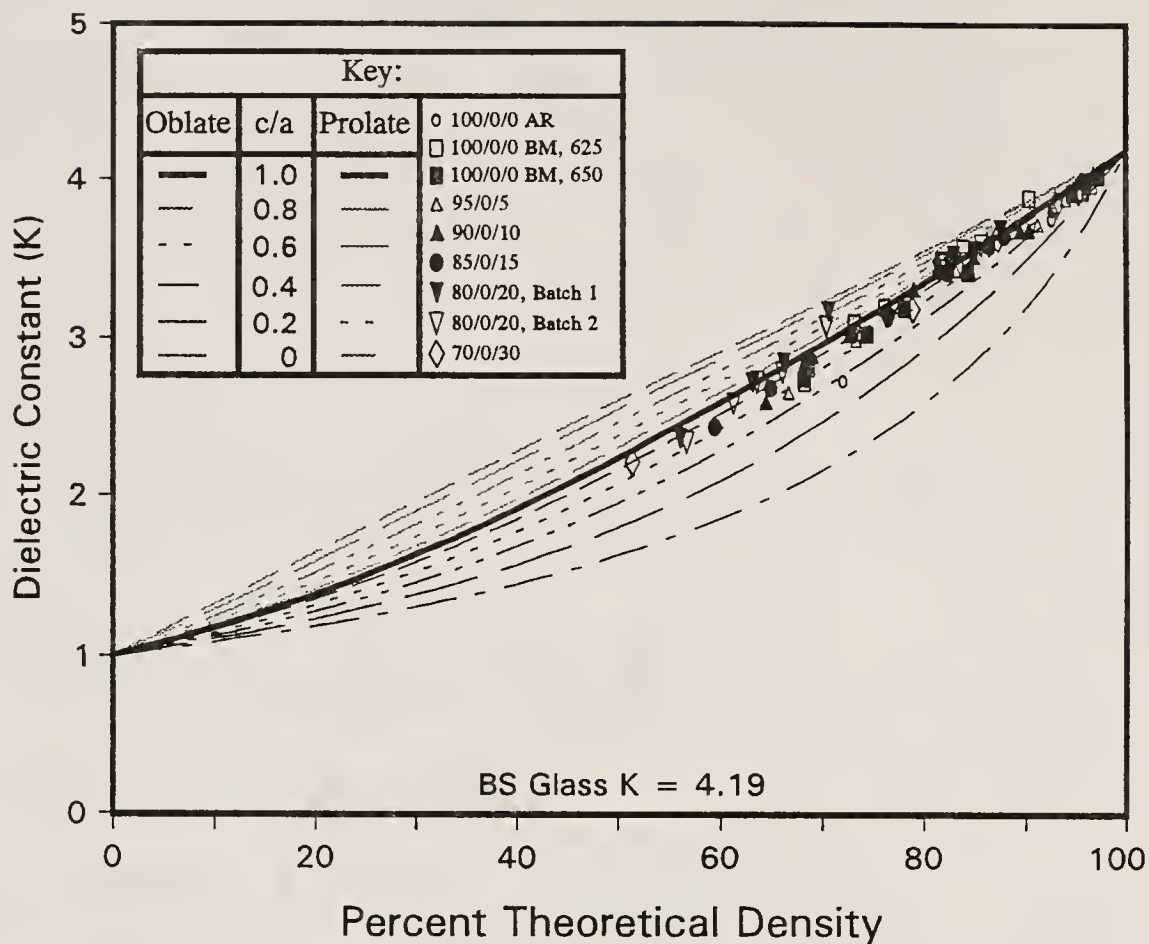


Figure 4.143

Measured K values as a function of percent density for all pure BS glass compositions (with and without 4.6  $\mu\text{m}$  included porosity) with EMT models, BS glass K = 4.19

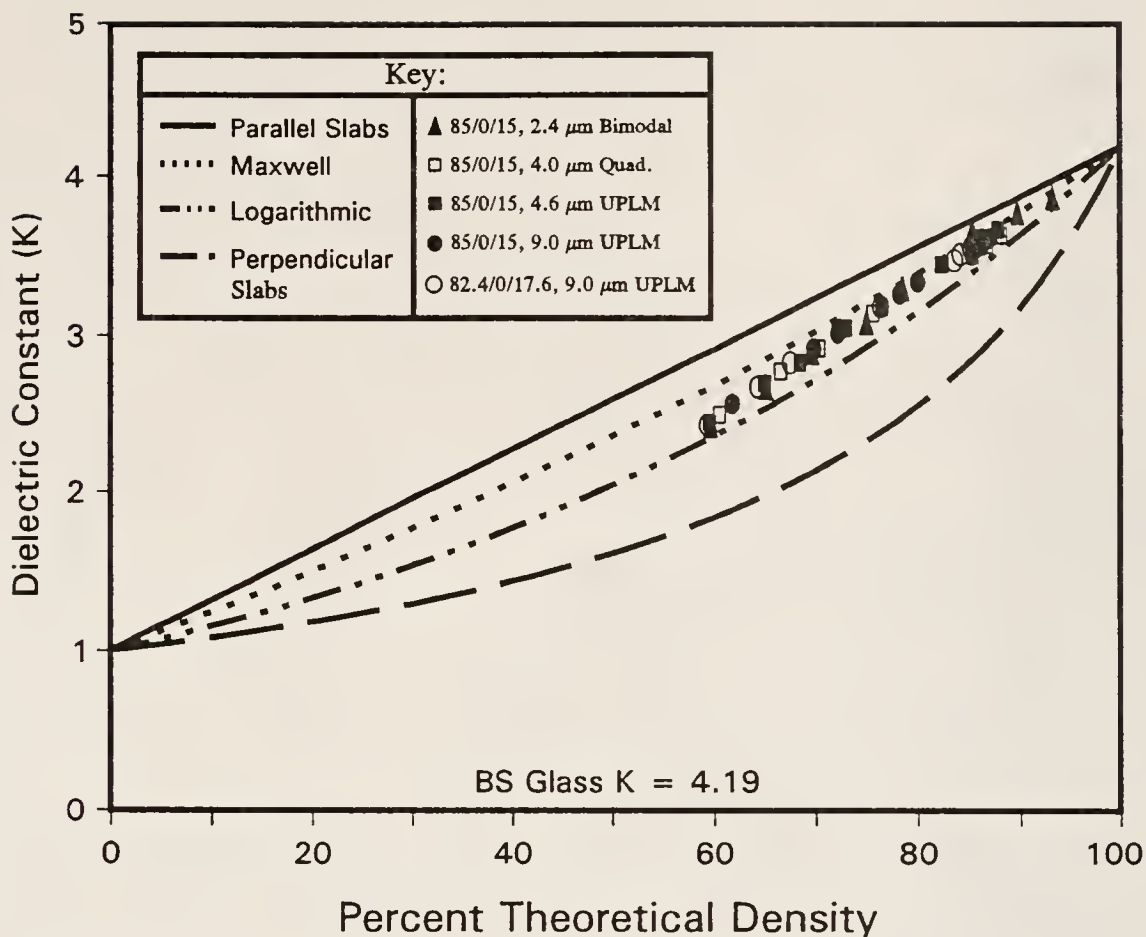


Figure 4.144

Measured K values as a function of percent density for (2.4  $\mu\text{m}$  bimodal, 4.0  $\mu\text{m}$  quadramodal and 4.6  $\mu\text{m}$  and 9.0  $\mu\text{m}$  monosized included porosity) compositions with traditional models, BS glass K = 4.19



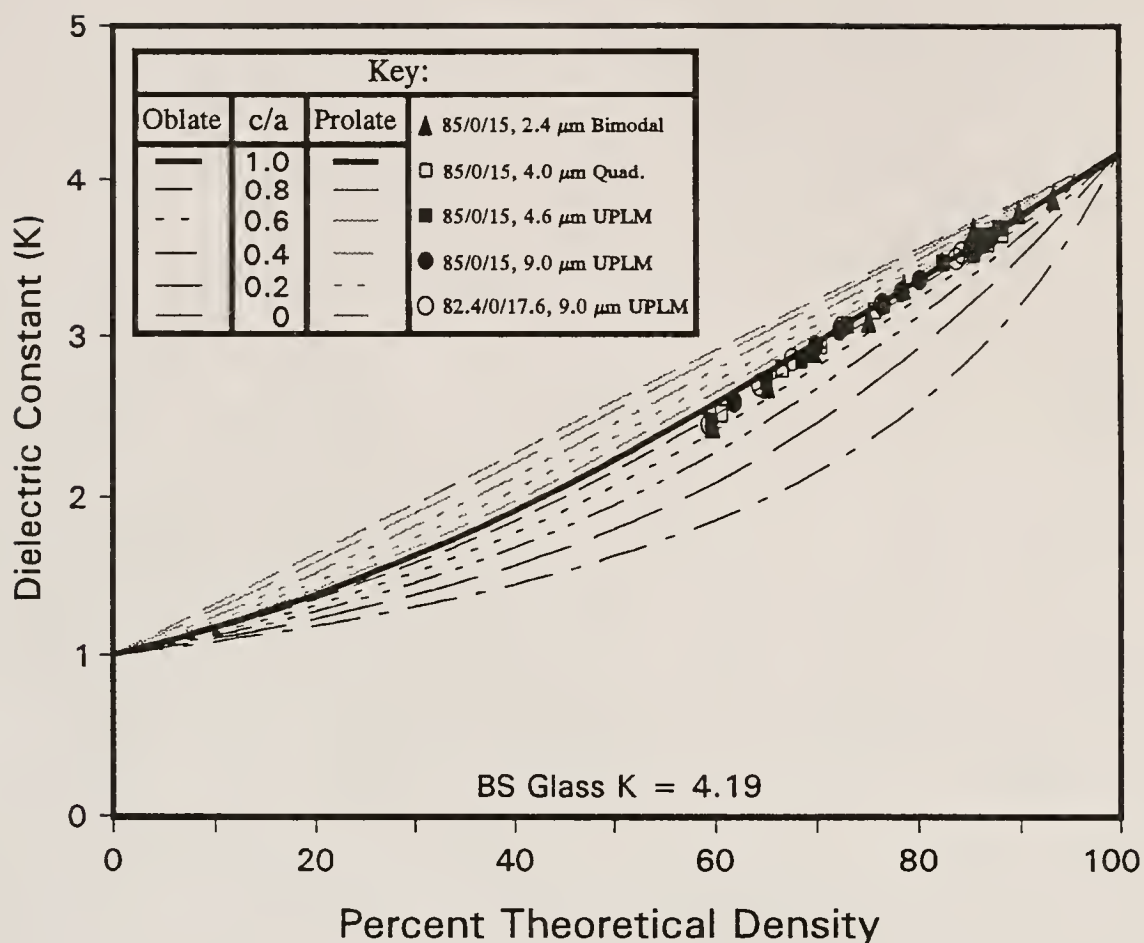


Figure 4.145

Measured K values as a function of percent density for (2.4  $\mu\text{m}$  bimodal, 4.0  $\mu\text{m}$  quadramodal and 4.6  $\mu\text{m}$  and 9.0  $\mu\text{m}$  monosized included porosity) compositions with EMT modelling, BS glass K = 4.19

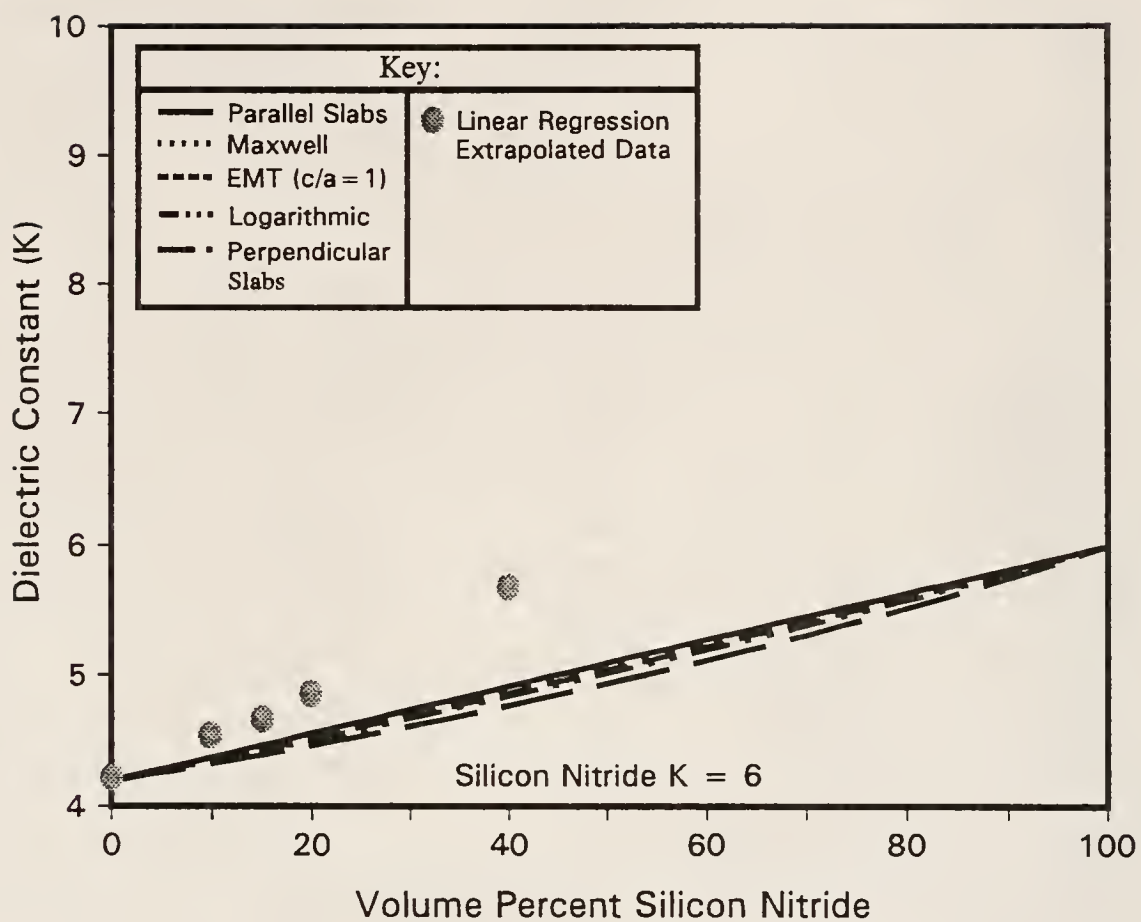


Figure 4.146

Extrapolated K values for 0 V%, 10 V%, 15 V%, 20 V% and 40 V% (final) silicon nitride concentration samples, modelled using a K value of 6 for silicon nitride

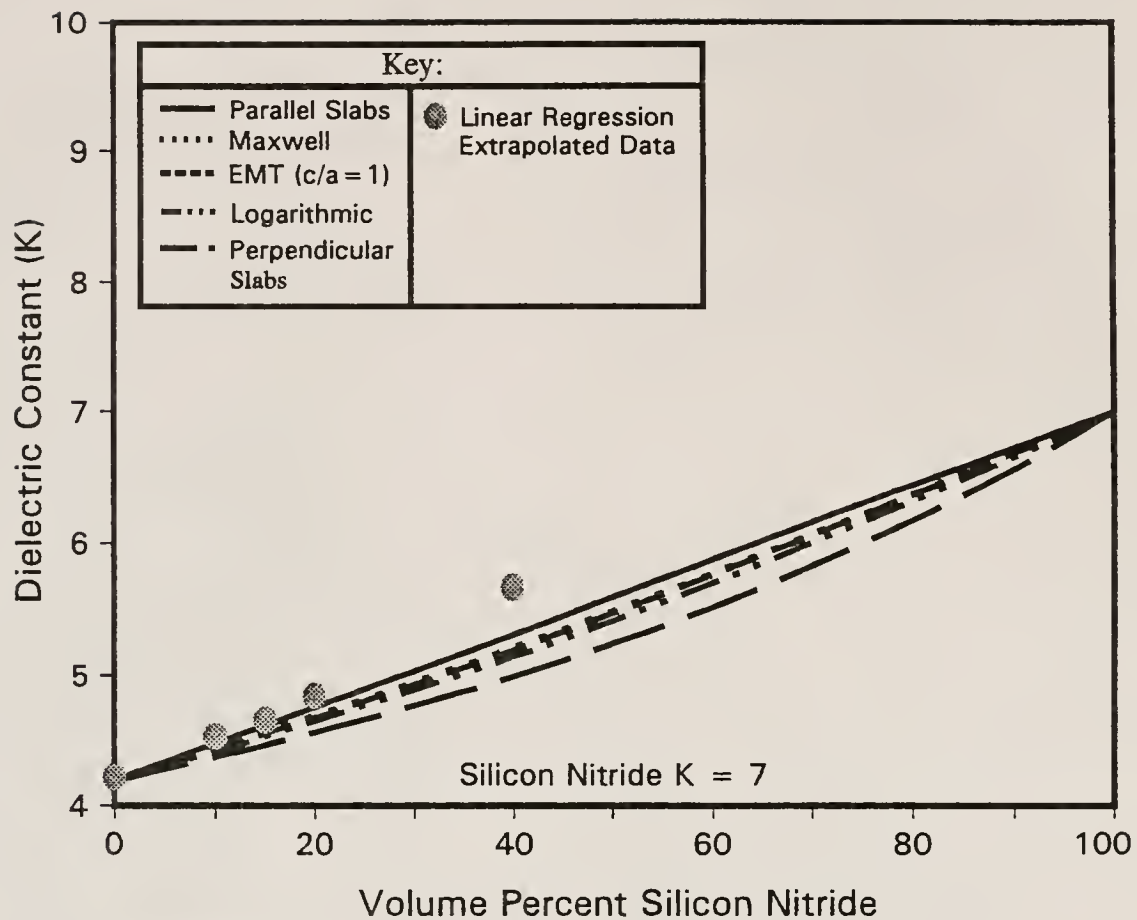


Figure 4.147

Extrapolated K values for 0 V%, 10 V%, 15 V%, 20 V% and 40 V% (final) silicon nitride concentration samples, modelled using a K value of 7 for silicon nitride

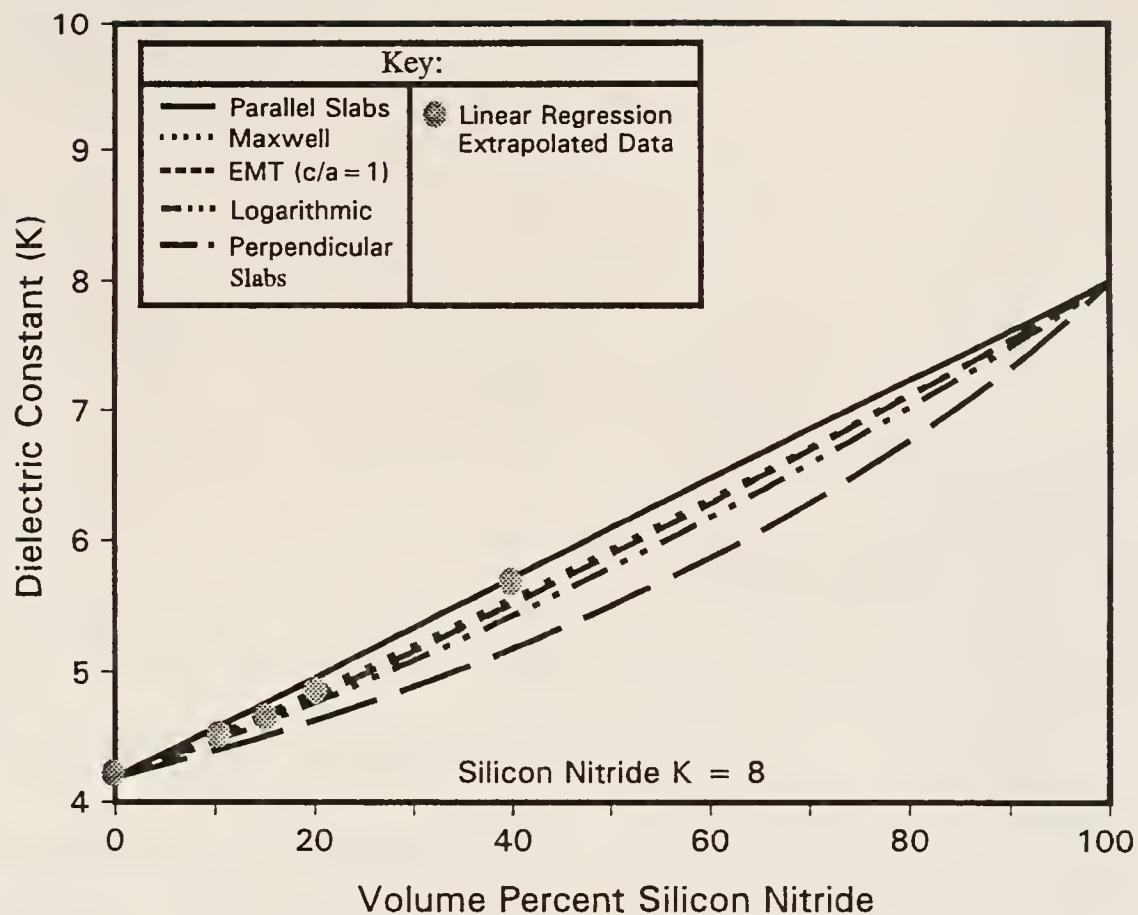


Figure 4.148

Extrapolated K values for 0 V%, 10 V%, 15 V%, 20 V% and 40 V% (final) silicon nitride concentration samples, modelled using a K value of 8 for silicon nitride

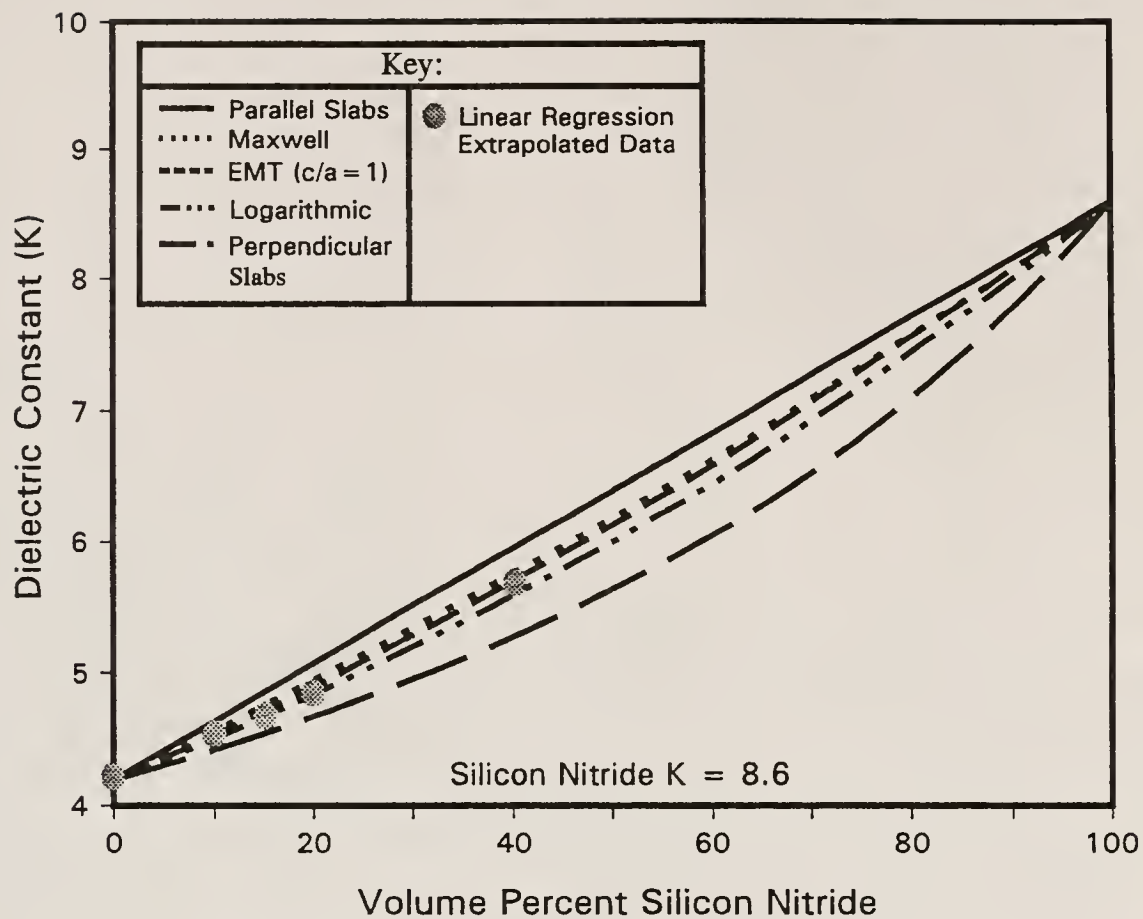


Figure 4.149

Extrapolated K values for 0 V%, 10 V%, 15 V%, 20 V% and 40 V% (final) silicon nitride concentration samples, modelled using a K value of 8.6 for silicon nitride



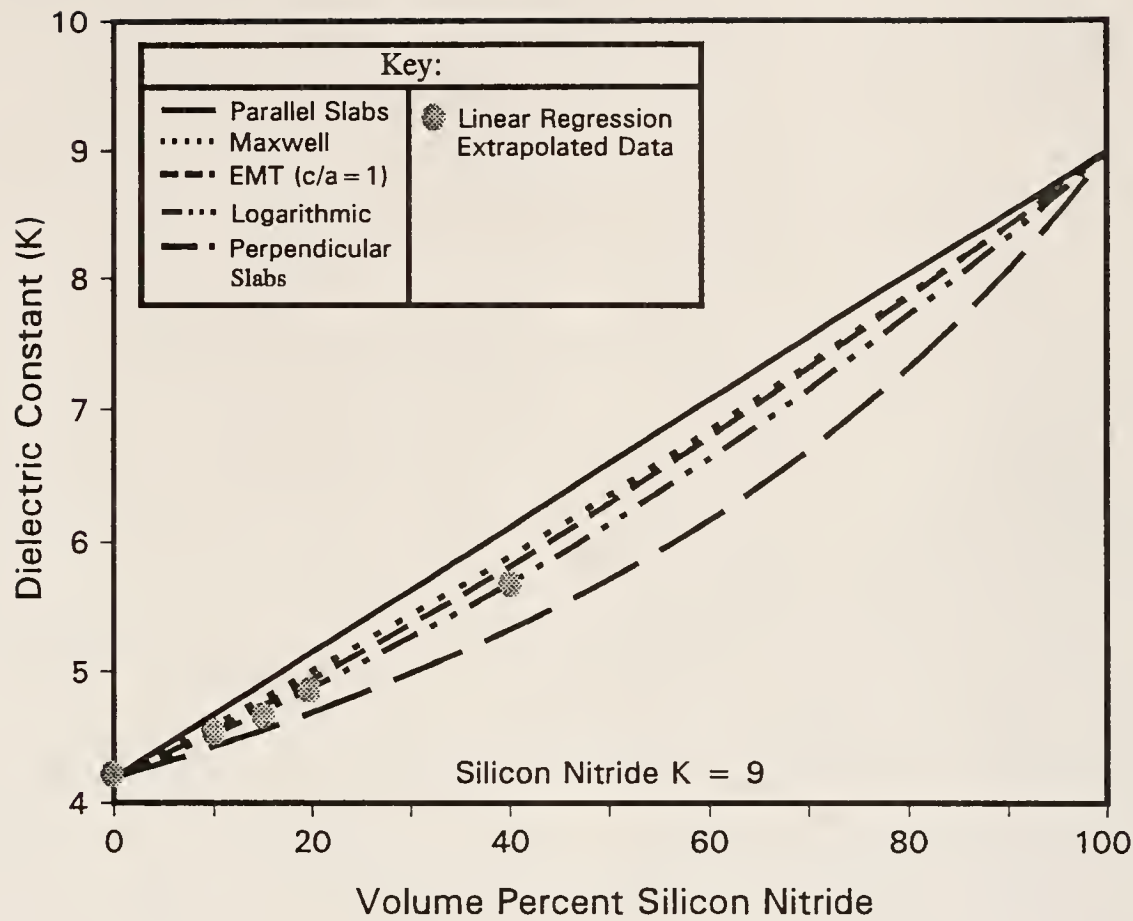


Figure 4.150

Extrapolated K values for 0 V%, 10 V%, 15 V%, 20 V% and 40 V% (final) silicon nitride concentration samples, modelled using a K value of 9 for silicon nitride

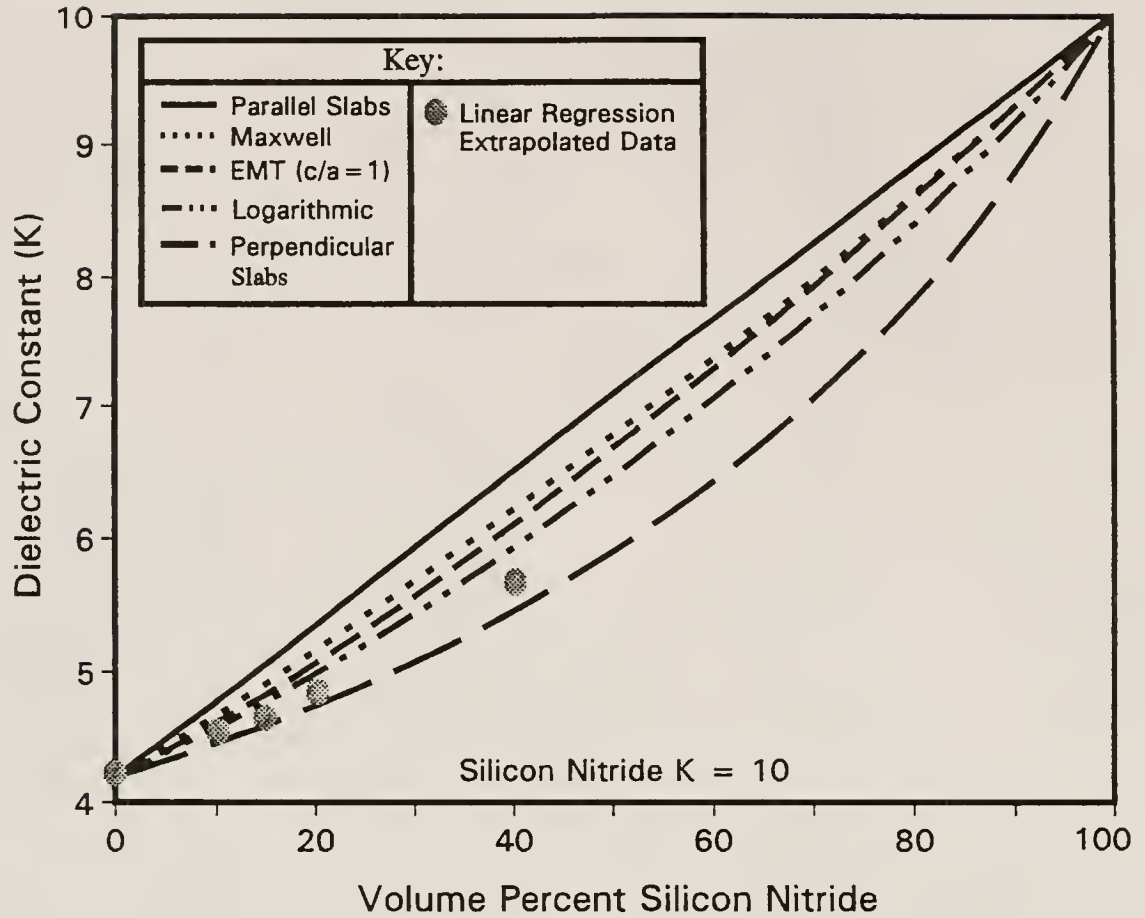


Figure 4.151

Extrapolated K values for 0 V%, 10 V%, 15 V%, 20 V% and 40 V% (final) silicon nitride concentration samples, modelled using a K value of 10 for silicon nitride

value of 6 for  $\text{Si}_3\text{N}_4$ . However, the references did not specify the purity, density or phase purity of the  $\text{Si}_3\text{N}_4$  investigated. To the knowledge of the author, bulk samples of fully dense, ultra pure and phase correct  $\alpha\text{-Si}_3\text{N}_4$  have not yet been synthesized. This could help explain the difference between predicted and literature K values for  $\text{Si}_3\text{N}_4$ .

Another explanation is that the particulate  $\text{Si}_3\text{N}_4$  used in this study may have reacted with the BS glass matrix, creating a high K phase at the BS glass  $\text{Si}_3\text{N}_4$  interfaces. However, this is not likely due to the relatively poor adherence of the  $\text{Si}_3\text{N}_4$  particles to the glass matrix. It is also unlikely that internal boundary layers were formed since the K values remained constant with frequency over the range measured. Therefore, further investigation which focuses upon measurement of the actual dielectric constant of pure fully dense  $\alpha\text{-Si}_3\text{N}_4$ , is warranted.

The goal of this study was to produce hermetic materials having minimized K values. Table 4.15 depicts the lowest K value measured for a hermetic sample of each of the composite compositions investigated. As mentioned above, the interpretation of hermeticity, for this study, is a material having an open porosity value of  $\leq 1$ . The table indicates that, using the methods and materials of this study, hermetic materials having K values as low as 3.5 may be produced. Similarly, hermetic, or nearly hermetic, samples containing 10 V%, 15 V% 20 V% and 40 V% final concentration of  $\text{Si}_3\text{N}_4$  were produced having K values of 3.89, 4.05, 3.99 and 4.87 respectively. The relatively low value for the 20 V%  $\text{Si}_3\text{N}_4$  concentration composite results from a greater amount of total porosity, resultant from a greater controlled porosity addition. Thus, it should be possible to consistently produce controlled porosity BS glass- $\text{Si}_3\text{N}_4$  composites having K values of  $\sim 4.0$  with final  $\text{Si}_3\text{N}_4$  concentrations as high as 20 V%. It was not possible to produce hermetic samples in the 40 V%  $\text{Si}_3\text{N}_4$  composition series. However, it is interesting to note that

Table 4.15

## Dielectric Constant Data of Hermetic Samples

Composition (V%)					Porosity (V%)			Dielectric Data (1 MHz)	
BS <sup>1</sup>	SN	UPLM			Max. Closed	Open <sup>3</sup>	Tot <sup>3</sup>	K	tan( $\delta$ ) (%)
		V%	S <sup>2</sup>	D <sup>2</sup>					
100 AR	0	0	NA	NA	4.9	2.9 <sup>6</sup>	7.8	3.79	0.11
100	0	0	NA	NA	5.6 <sup>4</sup>	0.0	5.6	3.93	0.11
95	0	5	4.6	M	8.1	1.1 <sup>6</sup>	9.2	3.74	0.07
90	0	10	4.6	M	10.3	0.6	10.9	3.71	0.08
85	0	15	2.4	B	10.9	1.2 <sup>6</sup>	12.1	3.67	0.37
85	0	15	4.0	Q	13.3	0.8	14.1	3.56	0.07
85	0	15	4.6	M	13.4	0.5	13.9	3.62	0.07
85	0	15	9.0	M	13.9	0.7	14.6	3.52	0.06
82.4	0	17.6	9.0	M	15.6	0.4	16.0	3.51	0.07
80	0	20	4.6	M	14.3	0.7	15.0	3.56	0.07
70	0	30	4.6	M	5.9	1.0	6.9	3.87	0.08
81	9	10	4.6	M	10.5	0.8	11.3	3.89	0.06
72.25	12.75	15	4.6	M	11.3	0.9	12.2	4.05	0.06
80	20	0	NA	NA	4.7	1.2 <sup>6</sup>	5.9	4.53	0.16
80	20	0	NA	NA	4.2	1.4 <sup>6</sup>	5.6	4.59	0.06
72	18	10	4.6	M	10.4	0.8	11.2	4.27	0.06
64	16	20	4.6	M	10.5	0.3	10.8	4.31	0.10
64	16	20	4.6	M	14.6	1.1 <sup>6</sup>	15.7	3.99	0.05
60	40	0	NA	NA	1.7	9.7 <sup>6</sup>	11.4 <sup>5</sup>	4.64	0.14
60	40	0	NA	NA	7.5	1.2 <sup>6</sup>	8.7	4.87	0.12
48	32	20	4.6	M	1.5	20.9 <sup>6</sup>	22.4 <sup>5</sup>	4.22	0.21

- Notes: 1. BS glass (AR is as-received, all others are ball milled)
2. S is latex diameter, D is dispersity, B is bimodal, Q is quadramodal, M is monodisperse
3. Open and Total porosity, at maximum observed closed porosity
4. Value was influenced by bloating
5. The porosity did not reach the final stages of sintering
6. Does not meet the hermeticity criterion (i.e. % OP  $\leq$  1)

it was possible to form 7.5 V% closed porosity in the 60/40/0 (BS glass/Si<sub>3</sub>N<sub>4</sub>/Latex). This is probably due to the porous, bridging structure of the Si<sub>3</sub>N<sub>4</sub> at 40 V% concentration.

The effect of atmospheric exposure upon the dielectric properties and sample weights of both hermetic and non-hermetic materials representative of this system was investigated as outlined in section 3.7.2. The relative humidity (RH) varied from approximately 70 to 74 % over the duration of this study. Figure 4.152 depicts the effects of atmospheric exposure duration upon the dielectric constant of hermetic and non-hermetic samples. Figure 4.153 depicts the effects of atmospheric exposure duration upon  $\tan(\delta)$ , and Figure 4.154 illustrates the evolution of the normalized weight of the respective samples over the time period of the investigation.

The above figures indicate that the dielectric properties (both  $K$  and  $\tan(\delta)$ ) as well as normalized weight of the non-hermetic samples increase with increasing atmospheric exposure time, while the analogous values for the hermetic samples remain constant throughout the time period of the investigation. This indicates that, when using the materials investigated in this study, for low loss dielectric applications, said materials must be hermetic in order to meet dielectric stability requirements.

It is interesting to note that the dielectric data of the non-hermetic samples experience maxima between approximately 15 and 150 min. During this period, the normalized weights of the non-hermetic samples also go through similar (albeit smaller) maxima. After this period, the dielectric properties and the normalized weight of the non-hermetic samples increases monotonously. The reason for this behavior is not known. It may be relatable to changes in RH during the experiment, or it may be due to the mechanism of moisture sorption operant in these samples. This topic has been addressed for pure silica glasses [91WAL], and would be an interesting topic for future investigation.



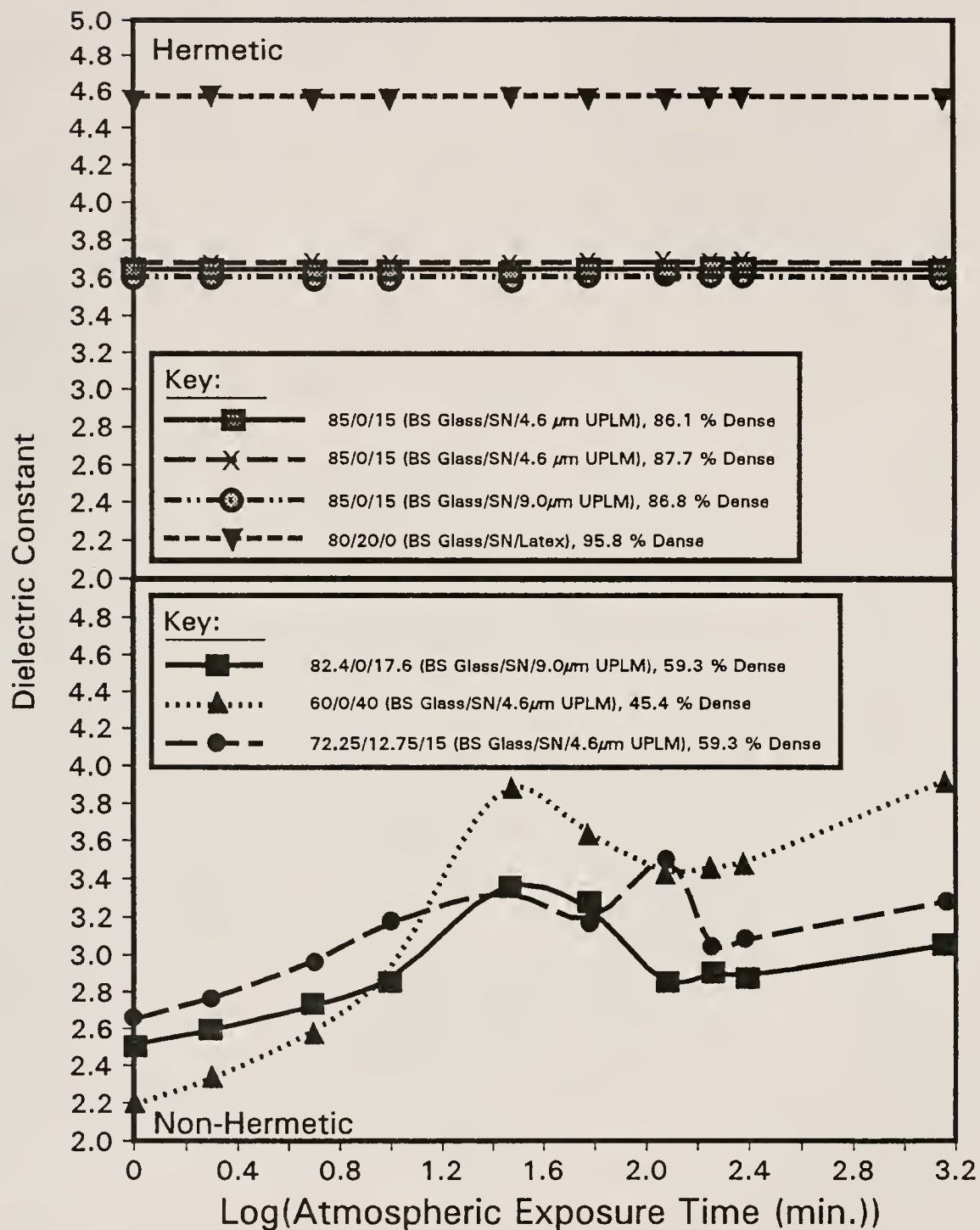


Figure 4.152

Dielectric constant as a function of atmospheric exposure time for representative hermetic and non-hermetic samples

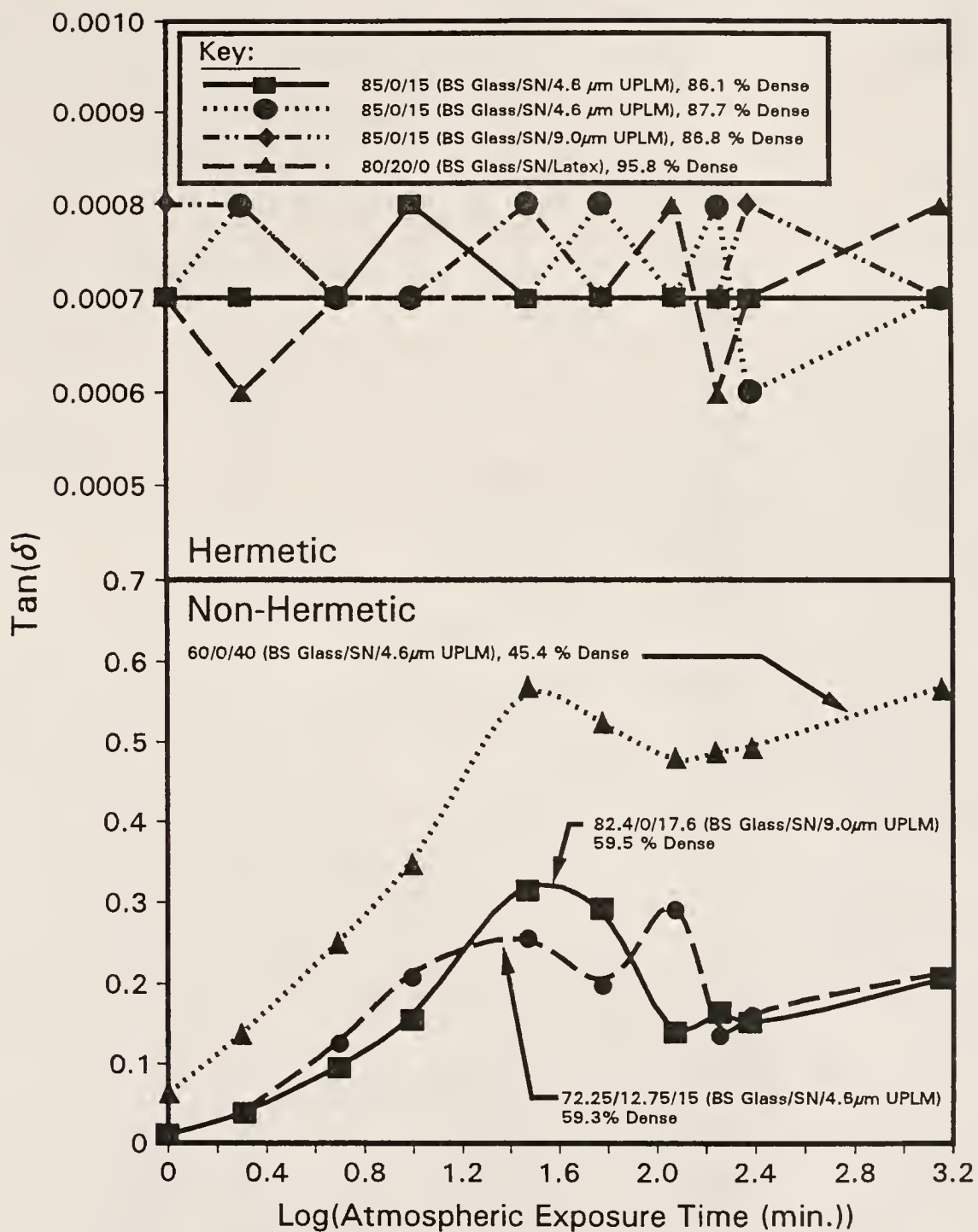


Figure 4.153

Loss tangent as a function of atmospheric exposure duration for representative hermetic and non-hermetic samples

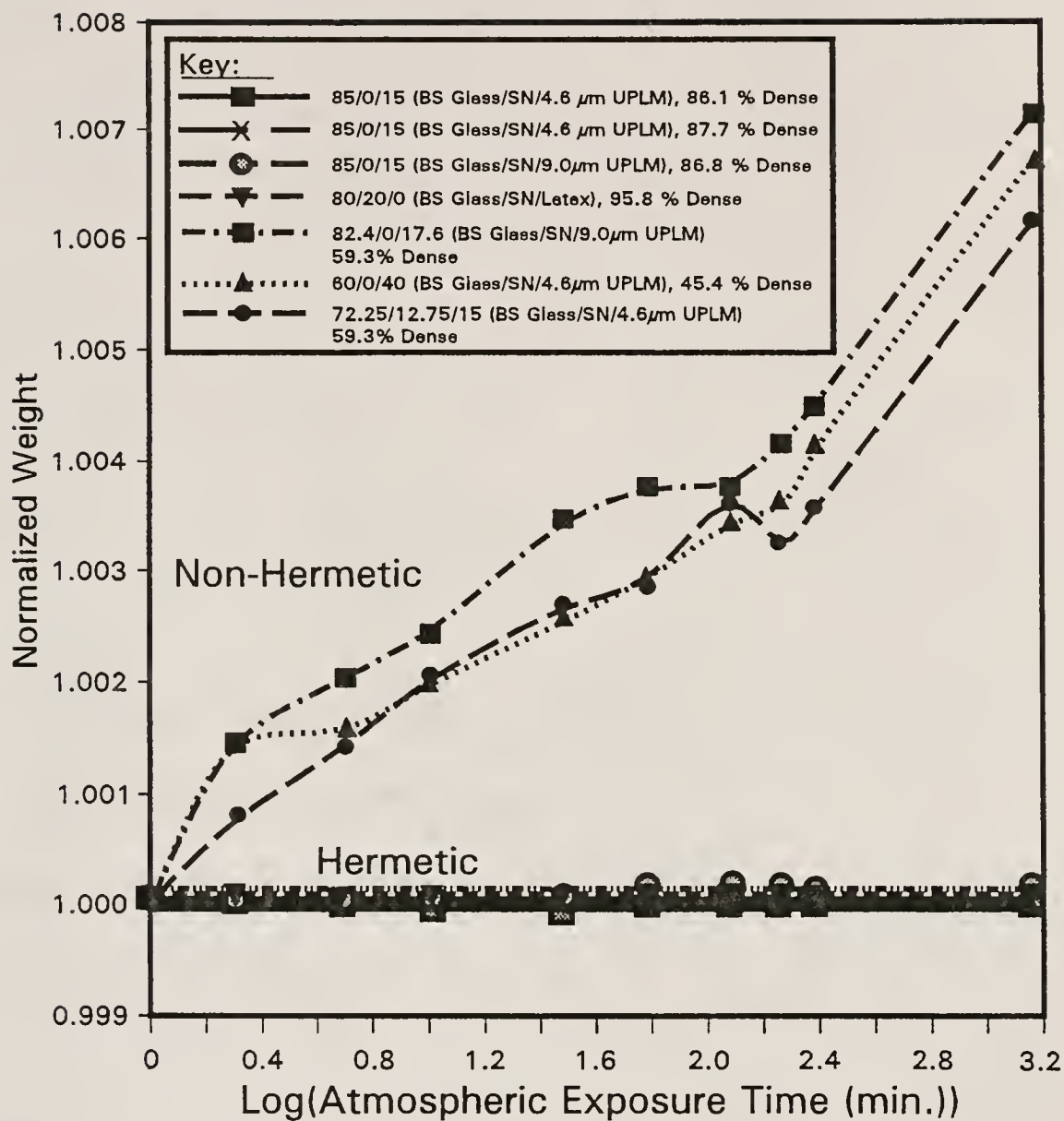


Figure 4.154

Normalized weight as a function of atmospheric exposure time for the representative hermetic and non-hermetic samples studied

#### 4.4.4 Microhardness Characterization

Microhardness and elastic modulus data were obtained from representative samples as outlined in section 3.7.4. As noted in said section, it was not possible to determine fracture toughness using microhardness indentation techniques. Table 4.16 shows the compiled data from the microhardness investigation. The statistical variance of the data is relatively high. This is expected, since the microstructures of the materials tested was of a size regime similar to that of the indentations characterized. This factor could affect the variation in indentation size considerably, and thus, the statistical variation of the material properties measured. The lowest porosity, BS glass samples exhibited somewhat lower statistical variance, as expected. The hardness and elastic modulus of the sintered, BS glass sample is quite close to the values measured for the manufacturer's BS glass ingot. This is logical, since they had almost identical bulk density values (i.e. both bulk densities were  $2.13 \text{ g/cm}^3$  as measured using the Archimedes method). Although the measured bulk densities were identical, the calculated % densities were not, due to the different bases used to calculate % density values (i.e.  $2.13 \text{ g/cm}^3$  for the bulk BS glass versus  $2.20 \text{ g/cm}^3$  for the ball milled BS glass powder). This relationship was discussed in section 4.4.3 above.

No literature hardness data was available for this particular composition of BS glass. However, the Knoop hardness values obtained are similar to literature values of similar BS glasses (i.e.  $\sim 360 \pm 10 \text{ kg/mm}^2$  for both the BS glass samples versus 375, 418 and 442  $\text{kg/mm}^2$  for Corning 7052, 7740 and 7760 BS glasses respectively [79COR]).

The elastic modulus literature value for the BS glass used [79COR] is  $5200 \text{ kg/mm}^2$  versus 6071 and 6083  $\text{kg/mm}^2$  ( $\pm 1825$  and  $1436 \text{ kg/mm}^2$ ) for the manufacturer's and sintered samples respectively. The literature value is within one standard deviation of each of the measured values, and thus, is comparable. The measured values agree even more closely

Table 4.16  
Microhardness Data Culmination

Composition			Lat. Dia. ( $\mu\text{m}$ )	Bulk $\rho$ %ThD	Vicker's Hardness (GPa)		Knoop Hardness (GPa)		Elastic Modulus (GPa)	
BSG	SN	LTX			Ave	$\sigma_n$	Ave	$\sigma_n$	Ave	$\sigma_n$
100 <sup>3</sup>	0	0	NA	100	4.0	0.2	3.5	0.1	59.5	17.9
100	0	0	NA	97.0	4.1	0.1	3.5	0.1	59.6	14.1
95	0	5	4.6	92.2	3.8	0.4	3.2	0.2	66.1	34.2
90	0	10	4.6	90.2	4.1	0.8	3.2	0.3	39.1	8.0
85	0	15	4.6	86.2	3.8	0.5	2.7	0.3	34.0	7.9
85	0	15	2.4	89.7	3.8	0.5	3.0	0.2	34.2	7.2
85	0	15	9.0	85.9	3.8	0.7	3.0	0.5	34.2	6.3
85	0	15	POLY	86.7	3.6	0.8	2.7	0.3	32.8	6.8
80	20	0	NA	96.9	6.0	0.6	4.7	0.4	121.1	6.3
72	18	10	4.6	91.4	5.3	0.5	4.5	0.4	74.0	25.0
64	16	20	4.6	89.0	5.3	1.1	4.1	0.5	60.2	8.4
60	40	0	NA	89.6	5.1	0.7	3.8	0.4	120.1	8.2
81	9	10	4.6	88.7	4.7	0.6	3.3	0.4	46.9	1.2
72.25	12.75	15	4.6	87.7	4.5	0.5	3.4	0.6	61.3	24.7

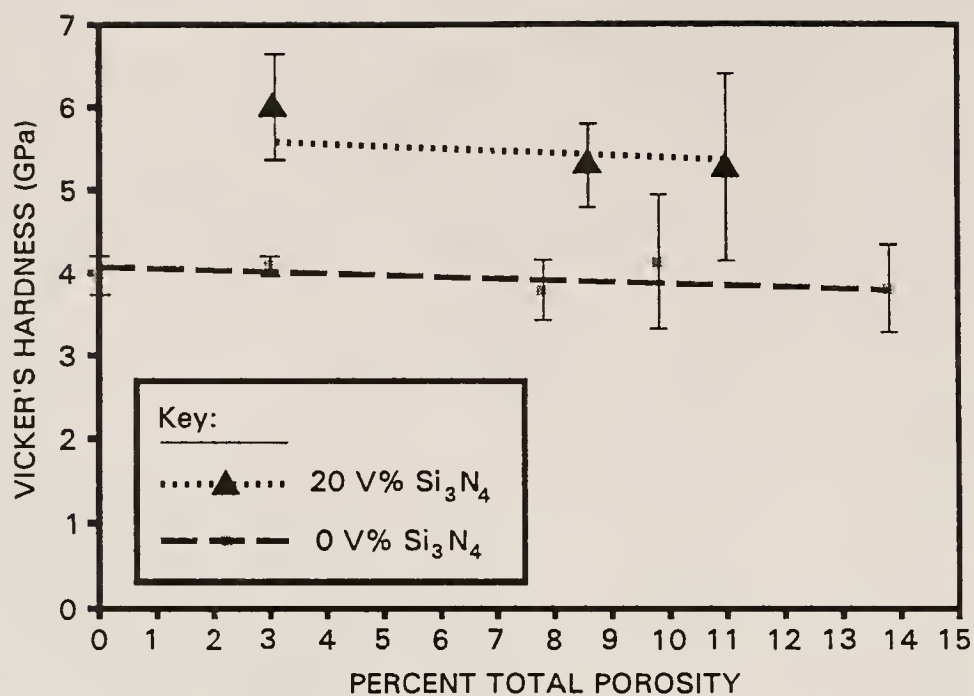
- Notes:
1. Lat. Dia. is the number basis mean UPLM diameter (POLY means polydisperse latex).
  2. NA means Not Applicable
  3. Manufacturer's Sample
  4. BSG is ball milled borosilicate glass powder, SN is as-received  $\text{Si}_3\text{N}_4$  powder, LTX is polystyrene latex.



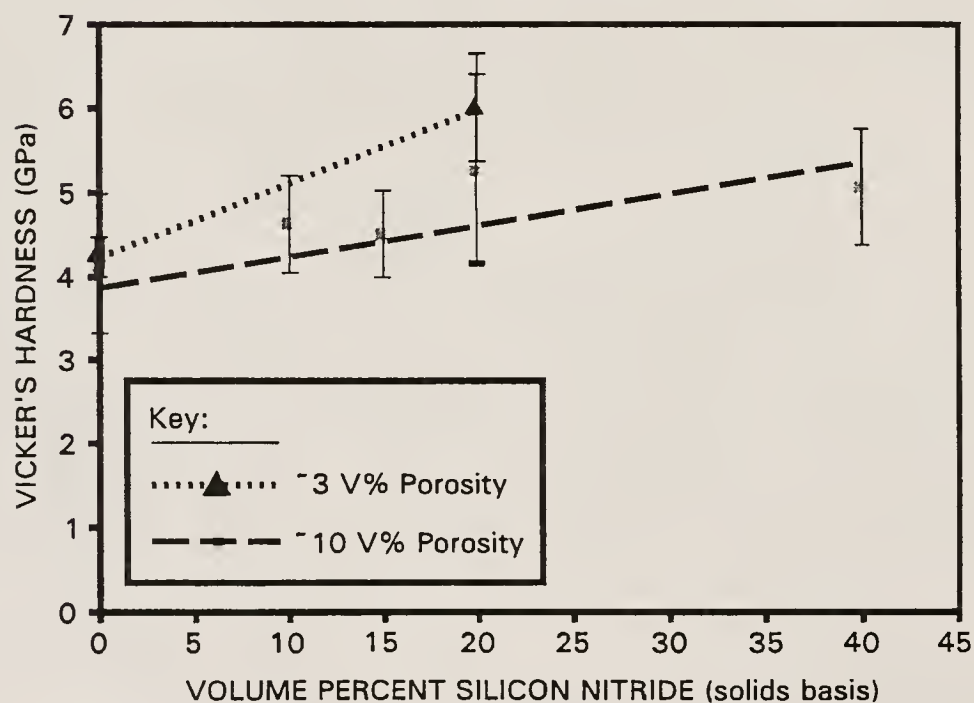
with literature values for the elastic modulus of generic borosilicate glasses [74MEC] (i.e. 63.7 GPa for the literature value versus  $59.5 \pm 17.9$  and  $59.7 \pm 14.1$  GPa for the manufacturer's and sintered samples respectively). As expected, the hardness and elastic modulus values increase with increasing  $\text{Si}_3\text{N}_4$  concentration. Similarly, these values decrease with increasing porosity concentration. The standard deviations of these values are large, indicating that perhaps, other methods of mechanical properties evaluation should be investigated in future study.

Figure 4.155A demonstrates the Vicker's hardness of the samples with respect to percent total porosity, while Figure 4.155B illustrates the Vicker's hardness as a function of  $\text{Si}_3\text{N}_4$  concentration. Figure 4.156 shows the above relationships using Knoop hardness data. It should be noted that the Knoop data is probably more accurate, due to the larger size of the Knoop indentations measured (i.e. the Knoop indentations were larger with respect to the  $\text{Si}_3\text{N}_4$  inclusions as well as the included porosity). Furthermore, the Vicker's indentations tended to be difficult to read if they interacted with the included porosity.

Figure 4.157 illustrates the decrease in elastic modulus (E) with increasing porosity, as well as the increase in elastic modulus with increasing silicon nitride content. The figures also illustrate the MacKenzie, Voigt and Reuss models [76KIN1] for comparison of said models with the experimental data. The Voigt model characterizes the increase in E with increasing additions of  $\text{Si}_3\text{N}_4$  better than the Reuss model. With one exception however, the Reuss model is within one standard deviation of the measured data as well. The data for the ~10 V% porosity set seem to mostly fit between the Voigt and Reuss bounds (i.e. they follow an intermediate path between the extrema of the Voigt and Reuss models). This is expected in a real composite system [76KIN1], and may indicate that said system has neither a constant stress nor a constant strain between components (or that the effects of each state



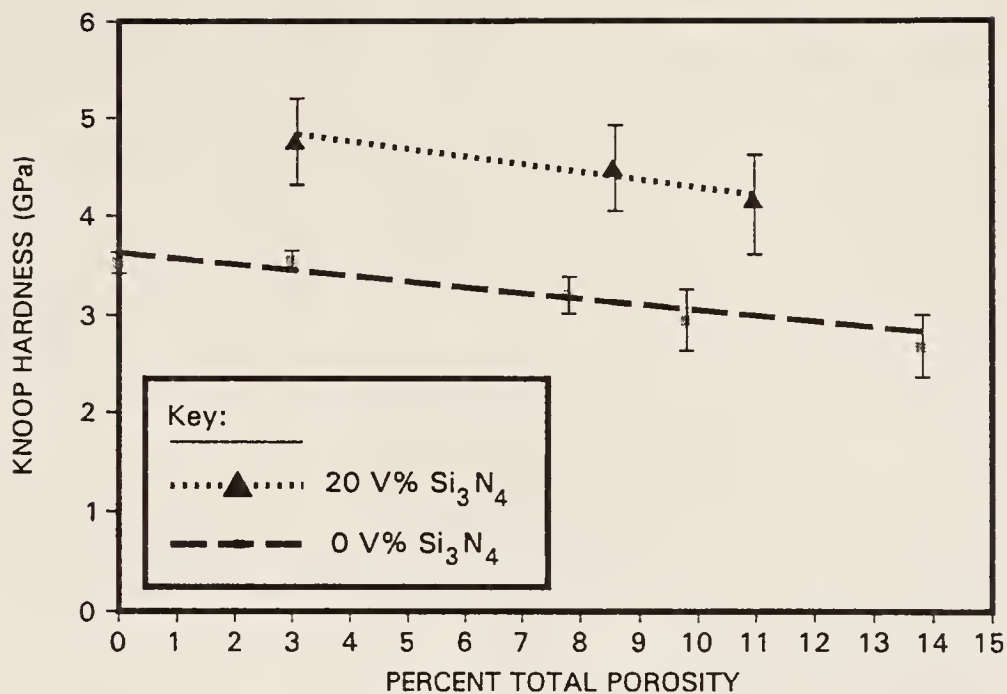
A. Vicker's Hardness as a Function of Porosity



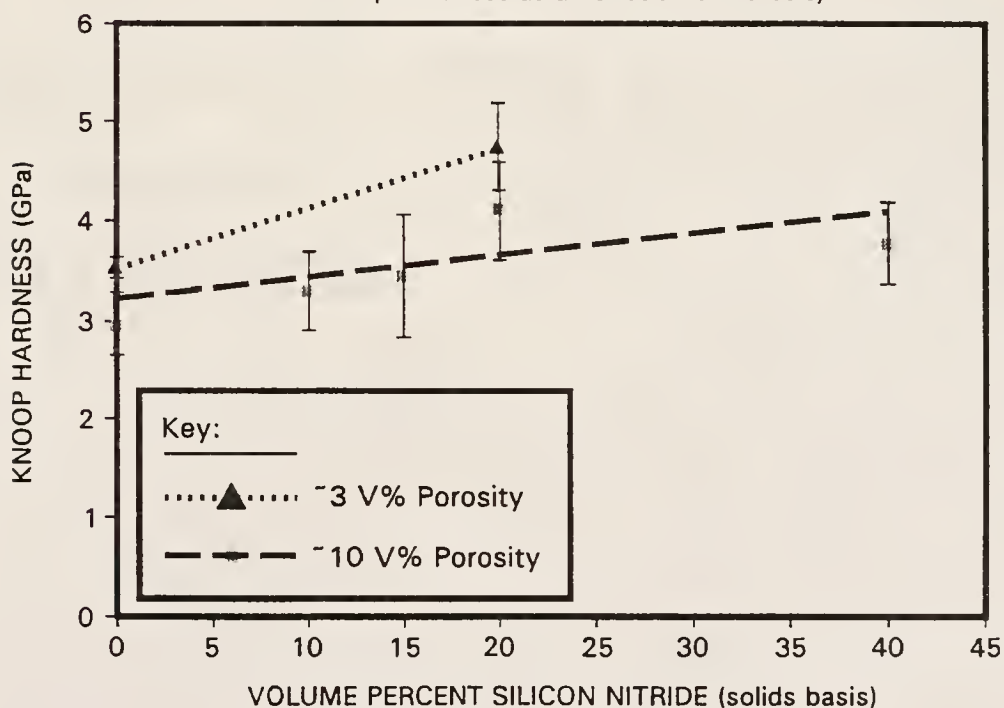
B. Effect of Silicon Nitride Concentration Upon Vicker's Hardness

Figure 4.155

The effects of included porosity (A) and  $\text{Si}_3\text{N}_4$  (B) additions upon the Vicker's hardness values of BS glass-silicon nitride composites



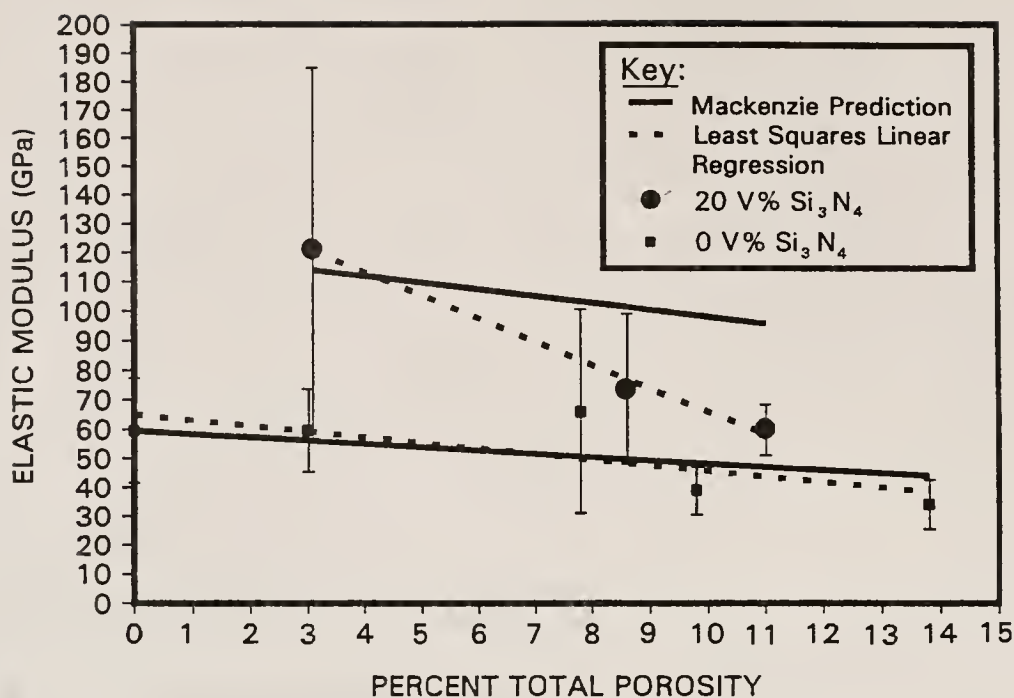
A. Knoop Hardness as a Function of Porosity



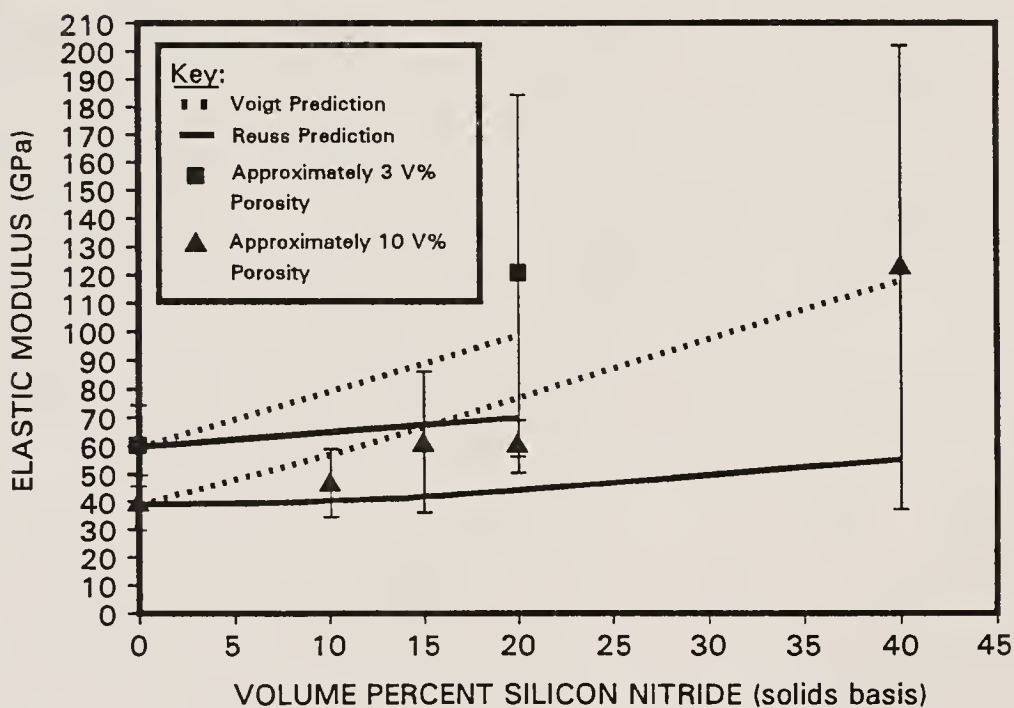
B. Effect of Silicon Nitride Content Upon Knoop Hardness

Figure 4.156

The effects of included porosity (A) and  $\text{Si}_3\text{N}_4$  (B) additions upon the Knoop hardness values of BS glass-silicon nitride composites



A. Effect of Porosity Upon Elastic Modulus



B. Effect of Silicon Nitride Concentration Upon Elastic Modulus

Figure 4.157

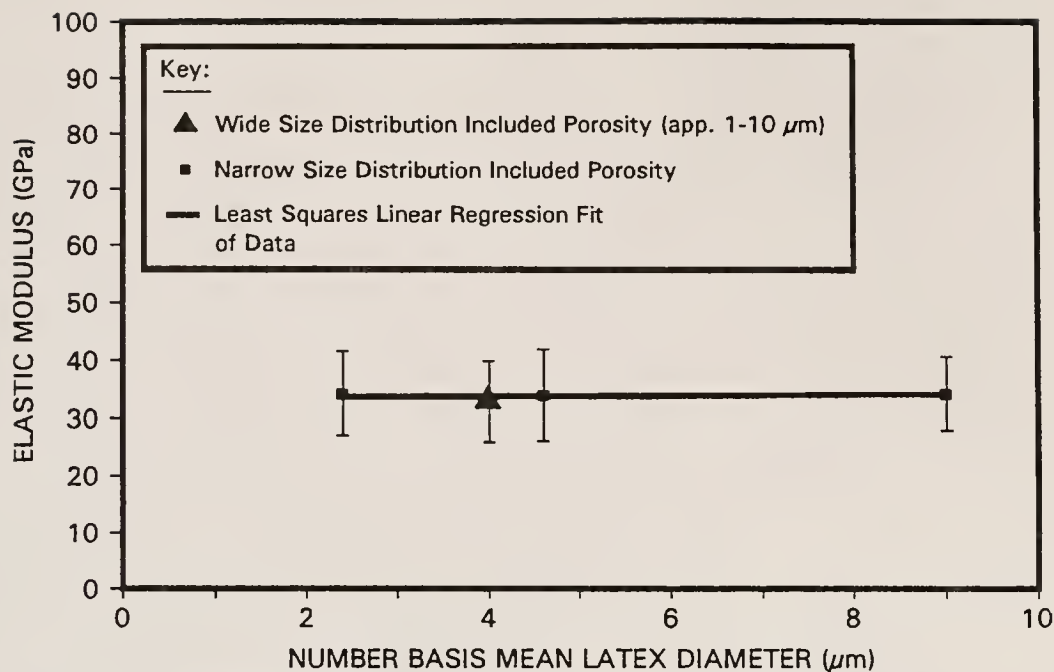
The effects of included porosity (A) and  $\text{Si}_3\text{N}_4$  (B) additions upon the elastic modulus of BS glass-silicon nitride composites

are balanced in the system). The ~3 V% porosity data do not fit between the Voigt and Reuss limits, however. This may be due to the limited data set.

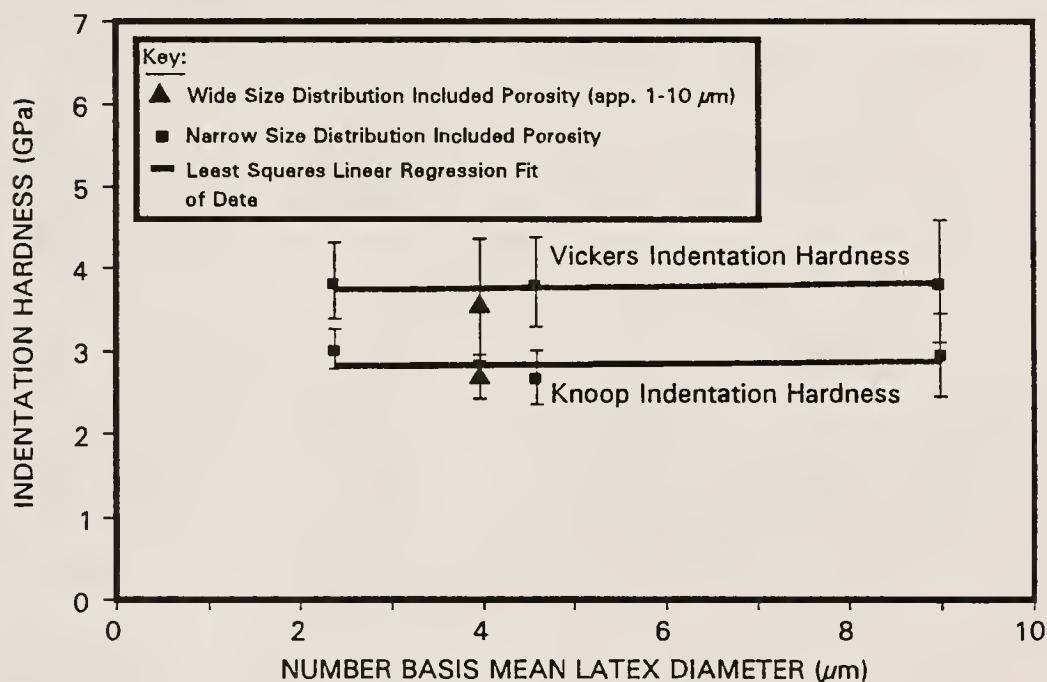
Linear regression analysis proved better than the Mackenzie model at predicting E with respect to porosity concentration. The MacKenzie model assumes that the material of interest has a Poisson's ratio ( $\alpha$ ) of approximately 0.3 and that the porosity is closed and isolated within a continuous matrix. The porosity is closed and reasonably well isolated within the composites investigated. However, the Poisson's ratio of the BS glass is 0.22 [79COR], representing a greater than 25 % deviance from this value. Also, the Poisson's ratio of  $\alpha$ -Si<sub>3</sub>N<sub>4</sub> is 0.27 [81ANS]. The greatest deviation from the MacKenzie model was in the system containing 20 V% Si<sub>3</sub>N<sub>4</sub>. These differences in  $\alpha$  may be a source of deviation of the experimental values from those predicted via the MacKenzie model.

The size and/or dispersity of included porosity had no effect upon the mechanical properties measured (within the regime of sensitivity of the measurement technique used) as indicated in Figure 4.158. The data in the figure are fitted using least squares linear regression. These fits are almost perfectly horizontal. Therefore, it is concluded that, within this size regime of porosity at least, pore size and/or size dispersity has very little, if any, effect upon the elastic modulus, Vicker's hardness or Knoop hardness. It seems to be simply a matter of constituent concentration.





A. Elastic Modulus as a Function of Included Porosity Size/Dispersity



B. Hardness as a Function of Included Porosity Size/Dispersity

Figure 4.158

The effects of included pore size and/or pore size distribution upon the mechanical properties (A. Elastic Modulus, B. Indentation Hardness) of pure BS glasses containing included porosity

decreased then began to increase again as sphere diameter increased from 4.6 to 9.0  $\mu\text{m}$ .

Along with the particle size and particle size distribution, the composition, surface structure and density of the borosilicate glass changed with ball milling, in MeOH (methanol). These changes were found to affect green density slightly as well as measured powder density (compared to the as-received glass). However, no other noticeable changes in materials properties were evident.

The  $\text{Si}_3\text{N}_4$  powder was used as-received, and was observed to contain a small amount (not observed via sedigraph or CPSA (centrifugal particle size analysis), but observed microscopically) of agglomeration. It was observed that the  $\text{Si}_3\text{N}_4$  powder did not oxidize measurably at the temperatures, and in the atmospheres, used to process the composites. Visual inspection, as well as mechanical polishing investigation, indicated that the  $\text{Si}_3\text{N}_4$  powder did not react appreciably with the BS glass matrix material.

### 5.3 Green Processing and Characterization

Both sonication and rotisserie aging were found to significantly improve both the suspension and green properties of these composites. It can be safely assumed that these two treatments also improve the final properties of the final composites.

All measured rheological properties were found to increase with increased solids loading in all suspensions investigated. It was possible to load both latex and BS glass suspensions in excess of 52 V% solids. However, it was not possible to load the  $\text{Si}_3\text{N}_4$  suspensions significantly in excess of 46 V% solids. Poor behavior of the  $\text{Si}_3\text{N}_4$  powder was also exhibited during green structure characterization as well, leading to the conclusion that the  $\text{Si}_3\text{N}_4$  powders are not well dispersed using the EtOH-PVP (ethanol-polyvinyl pyrrolidone) dispersion system used in this study. The latex microspheres exhibited near-

Newtonian, rheological behavior as opposed to the characteristically dilatant behavior of the ceramic powders investigated.

The BS glass was found to pack very well using the dispersion medium and dispersants investigated in this study. The as-received BS glass packed more efficiently than the ball milled BS glass, as predicted from pertinent literature [30AND,88REE,90ZHE]. The packing behavior of the latexes investigated in this study was modelled both accurately and predictably using random close packing theory [30WES,60SCO,61MCG,88REE].

In general, increased latex concentration was found to increase green density as well as to slightly decrease suspension viscosity. Overall, the opposite behavior was found with increasing  $\text{Si}_3\text{N}_4$  concentration.

It was demonstrated that the removal of latex additions (via pyrolysis) produces accurately predictable, as well as consistently reproducible amounts of included porosity in all of the composite compositions studied, up to 40 V%, at the post-pyrolysis stage of processing. The onset of a percolated pore structure was observed to occur in the regime of 25 V% UPLM addition. This is in close agreement with the, universally accepted, 16 V% for random placement on all types of lattices (periodic or random) for structures of three dimensions, when corrected for non-filled space. Above the percolation value, the pore channel size was observed to increase at an accelerated rate with increasing latex addition. The pore structure was also observed to become bimodal after the percolation threshold of latex was exceeded.

#### 5.4 Thermal Processing and Characterization

The polystyrene latex used in this study was observed to pyrolyze adequately in both air and  $\text{N}_2$  atmospheres at temperatures below those used for sintering. However, the dispersant (PVP k-30) was observed to leave a small amount of residual ash in both  $\text{N}_2$  and air atmospheres.

The ash was only removable in air at temperatures above the onset of sintering for this glass system, and thus, could be problematic. The onset temperature of sintering, within reasonable timespans, was found to be 625 °C. The ball milled BS glass was observed to densify at a greater rate than the as-received BS glass, despite the higher packing efficiency of the latter.

Increasing temperature was observed to increase the rate of densification of the glass composites studied. The magnitude of densification acceleration was found to be in agreement with reduction in viscosity, indicating that the sintering mechanism is purely viscous.

Silicon nitride additions at and above the percolation threshold (i.e. ~ 16 V% of total space) was found to retard sintering. At and above  $\text{Si}_3\text{N}_4$  additions of ~ 36 V% of total space, the sintering process was arrested. For example, in the case of 40 V%  $\text{Si}_3\text{N}_4$  additions, it was not possible to densify the composite significantly in excess of 90 % of theoretical density using pressureless sintering techniques. Furthermore, in the case of 60 V%  $\text{Si}_3\text{N}_4$  addition, sintering was limited to only a few percent increase in density, as predicted by Scherer [91SCH2].

It was possible to create materials having closed porosities of ~ 15.6 V% (at ~ 16.0 V% total porosity) via the techniques utilized during this study. This value is in excellent agreement with the percolation threshold (~ 16 V% of total space) for three dimensional percolation [83ZAL2]. It was found that increasing the ratio of included pore size to native pore size (i.e. to approximately 20 or 40 to 1) increased the maximum amount of closed porosity attainable. It was also found that quadramodal sphere additions did not noticeably change the amount of maximum attainable closed porosity. However, it was denoted that this experiment should be repeated using a different size distribution of

spheres (i.e. larger overall, with at least a 7 to 1 ratio in successive sphere size) in order to be conclusive.

The greatest amount of closed porosity achieved in this study was 15.6 V% (16.0 V% total porosity) using additions of 17.6 V% 9.0  $\mu\text{m}$  UPLM. This is in excellent agreement with the onset of percolation in randomly filled, three-dimensional space. Smaller amounts of closed porosity (i.e. up to 14.6 V%) were observed in the systems using additions of 4.6  $\mu\text{m}$  UPLM in both pure BS glass and in composites containing  $\text{Si}_3\text{N}_4$  additions of 20 normalized V% or below. It is assumed that the maximum-observed value of 15.6 V% could also be attained in these systems if the 9.0  $\mu\text{m}$  UPLM was utilized for the porosity additions.

It was found that the densification behavior of BS glass compacts containing additions of UPLM beyond the percolation onset (i.e. 30 V%) was quite different than for UPLM additions below the percolation threshold. The shape of the rate of densification curve was found to be somewhat similar to the compacts that did not contain latex additions. This behavior was attributed to the previously-mentioned percolated (continuous) structure of the added porosity.

### 5.5 Characterization and Modelling of Densified Compacts

Quantitative microscopy results indicated that there is no measurable segregation of the 4.6  $\mu\text{m}$  UPLMs in this systems. Modified Stokes' settling theory indicates that this should be the case. It also indicates that there should be minimal segregation of all of the composite components, with the possible exceptions of the large versus small BS glass particles. Porosities measured using quantitative microscopy techniques (QMTs) were slightly greater (but within the variance) of data obtained via the Archimedes density technique. The calculated diameters using QMTs were also smaller than expected. Pore size measurements of both polished and fractured surfaces agreed within



the variance of the measurements. It was not possible to model pore shrinkage during densification accurately using these techniques.

Series modelling was used to predict the 3 and 2 dimensional average cluster numbers of included porosities, and to compare the predicted 2-D values with those obtained using QMTs. It was found that, before percolation, the data was modelled much more accurately via the site clustering series model. The series clustering model was also found to accurately predict the maximum amount of closed porosity (and the associable open and total porosities at said maximum) obtainable in the type of system studied.

An extrapolation of the series model proved accurate at predicting the onset of percolation in this system. These predictions were found to represent the lower limit to said onset. To the knowledge of the author, this is the first successful application of percolation modelling to random packed systems. The model used was accurate, as well as relatively simple to use.

Measured dielectric properties ( $K$  and  $\tan(\delta)$ ) agreed well with literature values over the frequency range investigated. Effective medium theory (EMT), applied to perfectly spherical pore geometries, was found to model the composite  $K$  values the most accurately. Using traditional models, the data was best modelled as an intermediate fit between the logarithmic and Maxwell models. Using these modelling techniques, the literature  $K$  (dielectric constant) value (i.e. 4.1) for the BS glass was found to be quite accurate. However, the literature  $K$  values for  $\text{Si}_3\text{N}_4$  (i.e. 6 to 7) were disputed using composite dielectric modelling. Using EMT modelling, the  $K$  value of phase pure, fully dense  $\alpha\text{-Si}_3\text{N}_4$  was predicted to be approximately 8.6.

Using the methods of this study, it was possible to produce hermetic materials with  $K$  values as low as 3.51. It was also possible to produce hermetic composites, containing 20 V%  $\text{Si}_3\text{N}_4$  inclusions, with  $K$  values of approximately 4.0. During these investigations, the  $K$  and

$\tan(\delta)$  values of hermetic samples were found to be stable with atmospheric exposure, while the  $K$  and  $\tan(\delta)$  values of non-hermetic samples were observed to increase significantly with atmospheric exposure time.

Microhardness indentation techniques were used to quantify the hardness and elastic modulus ( $E$ ) values of representative materials within this composite system. It was not possible to monitor fracture toughness via these techniques, however. The variances of the data were quite large, increasing with increasing included porosity and/or  $\text{Si}_3\text{N}_4$  additions.

The Knoop hardness values were found to agree with literature values within the  $\sigma_n$  values of the experimental data. The  $E$  data were also found to agree well with the literature values of similar BS glasses. The size and size distribution of included porosity was found to have no appreciable effect upon any of the mechanical properties measured.

As expected, the hardness and  $E$  values decreased with increasing porosity concentrations, and increased with increasing  $\text{Si}_3\text{N}_4$  concentrations. However, the Mackenzie model did not predict the decrease in  $E$  with increasing porosity well. The relationship of  $E$  with respect to increasing  $\text{Si}_3\text{N}_4$  concentration was found to generally fit between the extrema predictions of the Voigt (upper limit) and Reuss (lower limit) predictions.

## CHAPTER SIX

### SUGGESTIONS FOR FUTURE WORK

As in all studies, a complete knowledge is never truly achieved. Many questions remain unanswered. This chapter, discusses some recommended suggestions and experiments that, if employed, should help to answer many of these questions. This discussion is intended to be an addition to those suggestions contained within previous chapters.

The BS (borosilicate) glass used in this study should be either modified or replaced to obtain more suitable properties. The glass particle size should be reduced. This would promote surface smoothness as well as allow the use of smaller latexes. The use of smaller latexes would reduce the maximum surface flaw size of the resulting packaging material. The modified or replacement glass should also sinter at a higher temperature, in order to further augment removal of organic materials from the ceramic body. A possible candidate for this replacement would be boron-doped Stober's silica, which has been fully densified below the melting point of Cu [89SAN1,89SAN2], thereby allowing cofiring with Cu. Other candidates exist as well. Also, the BS glass used could be modified chemically (i.e. lower [B], higher [Si], reduce or eliminate Al, K, Na and Li) and classified/milled to smaller particle size.

The investigation of wide size distribution latex additions should be repeated using latex size modes having a consecutive mode size ratio greater than 7 to 1. For example, a binary (or ternary), discrete size distribution having size modes of approximately 35 and 5  $\mu\text{m}$  (or 245, 35 and 5  $\mu\text{m}$ ) should be investigated to determine, conclusively, whether or not the size distribution of the added porosity has an effect upon maximization of closed porosity. This study probably would not give

insight into decreasing the size of surface flaws, but the resulting knowledge could be invaluable from the standpoint of maximization of closed porosity.

Alternative methods of porosity addition should also be investigated. Theoretically, additions of hollow spherical shells of a low loss, higher sintering temperature material (i.e.  $\text{SiO}_2$ ) would allow hermetic composites of higher porosity to be produced. Potentially, this would also reduce the amounts of organic in the green system, thereby simplifying the thermolysis process.

Further characterization of the composite system with respect to  $\text{Si}_3\text{N}_4$  fillers should also be performed. The BS glass- $\text{Si}_3\text{N}_4$  binary of this composite system should be further investigated in order to determine the maximum  $\text{Si}_3\text{N}_4$  concentration that would allow full densification using pressureless sintering techniques. It would also be interesting to determine, more closely, the  $\text{Si}_3\text{N}_4$  concentration at which no densification occurs via pressureless sintering.

Studies should be performed characterizing the effects of  $\text{Si}_3\text{N}_4$  powder size as well as agglomeration index upon green and mechanical properties as well as densification characteristics. Additions of microcomposite glass- $\text{Si}_3\text{N}_4$  powders, currently under development [91SAC1] should also be investigated. The potential benefit of using said microcomposites would be the ability to obtain fully dense composites, having higher concentrations of  $\text{Si}_3\text{N}_4$ , without resorting to pressurized sintering techniques.

Different ceramic filler candidates should be investigated in this system. Diamond and cubic BN (boron nitride) should be usable in this system with little processing modification. Other materials, such as cordierite, quartz, etc., may also be of interest. Other shapes of ceramic filler (i.e. whiskers or fibers, etc.) should also be investigated in order to further advance the state of knowledge of ceramic-filled, glass matrix composites containing controlled porosity.

An investigation of the effect of atmosphere on sintering should also be performed. A potential benefit, from this experimentation, would be the ability to enhance added porosity volume through the evolution of previously dissolved gases, in the final stage of sintering. The ability to sinter in an inert atmosphere is also necessary if the ceramic is to be cofired with Cu metallization.

This composite system should be developed for tape and thick film application. These tape and film systems should be formulated with EPA/OSHA approved dispersant and solvent systems. The composite system should be developed for use with metallization systems commonly used in low loss electronic packaging. This development would include characterization of thermolysis in low [O<sub>2</sub>] atmospheres (i.e. steam-hydrogen systems, etc. [91KUM2,91TUM]) as well as studies attempting to investigate the chemical compatibility of metallizations with the ceramic composite system, etc.

The methods of testing and evaluation, used in this study, should also be enhanced. Porosimetry characterization should be extended beyond green and post pyrolysis samples. Mercury porosimetry would be a valuable diagnostic tool for characterization of pore structures during densification. This would give further insight into the evolution of the pore structure during processing.

Dielectric data should be obtained at higher frequencies (i.e. to > 10 GHz) using resonant cavity or low frequency Kramer's-Kronig techniques [88EWS2,89YAM1,90SAD,91GIP,91SU1]. Further mechanical testing should be performed. Analysis of fracture strength and fracture toughness should be performed using pure tension or other techniques having sound fundamental bases (i.e. diametral compression, etc. [67KIR,72WAC,81ANS,81CHA,83SHE,84SIM,89BER]). Theoretical strengths could also be investigated using controlled flaw techniques [74MEC].

Also, polishing and etching techniques of these composites should be improved in order to improve upon the ability to perform various



types of microstructure evaluation (i.e. determination of volume fractions of  $\text{Si}_3\text{N}_4$ , more accurate pore diameter measurements and volume fraction determinations, etc.).

Finally, other material properties should be evaluated (including the above-mentioned properties), such as thermal conductivity, thermal expansion, thermal shock resistance, insulation resistance, residual carbon content, etc. This would help to provide a data-base, for this system, that would prove to be a valuable resource when engineering composites for specific applications. It would also be valuable in identifying properties that need improvement for specific or general applications.

All of these recommended experiments/studies would help to promote a better understanding of BS glass matrix composites having non-sintering ceramic inclusions, and/or controlled porosity.

APPENDIX I  
MANUFACTURER'S DATA FOR CERAMIC CONSTITUENT POWDERS

I. Corning 7070 Borosilicate Glass [79COR,88COR]

1. Composition:

Composition: Constituent Based		
Constituent	Weight Percent	Mole Percent
Silica ( $\text{SiO}_2$ )	72.0 (70.0)	74.8
Boria ( $\text{B}_2\text{O}_3$ )	25.0 (28.0)	22.4
Alumina ( $\text{Al}_2\text{O}_3$ )	1.0 (1.1)	0.61
Potassia ( $\text{K}_2\text{O}$ )	1.0 (0.5)	0.66
Soda ( $\text{Na}_2\text{O}$ )	0.5 (0)	0.5
Lithia ( $\text{Li}_2\text{O}$ )	0.5 (1.2)	1

Note: The values in parentheses are those provided by Air Force Materials Laboratories (prepared by the Electronic Properties Information Center, Hughes Aircraft Company, Culver City, CA). Note that the parenthetical values sum to 100.8 wt%.

Composition: Element Based		
Element	Weight Percent	Mole Percent
Silicon (Si)	33.7	31.8
Boron (B)	7.8	19
Aluminum (Al)	0.53	0.52
Potassium (K)	0.83	0.56
Sodium (Na)	0.4	0.4
Lithium (Li)	0.2	0.9
Oxygen ( $\text{O}_2$ )	56.6	46.9

Note: Calculated values are based on the assumption that all the constituent oxides are stoichiometric.

## 2. Description:

Glass Type: Borosilicate

Class: I

Corrosion Resistance:

Weathering: Class 2, (will occasionally show problem with atmospheric liquids and gases if corrosion products may not be used)

Water: Class 2, (see above)

Acid: Class 2, ( $10^{-6}$ - $10^{-5}$  inches lost when subjected to 5% HCl @ 95°C, for 24h)

Color: Clear

Forms Available: Blown, Multiform, Powder, Pressed, Tubing

Principal Uses: Low Loss Electrical, Seals to Tungsten, used with 3320, 7740, 7574

Materials Properties		
Property	Metric Value	English Value
Mechanical		
Density	2.13 g/cm <sup>3</sup>	132.9 lb/ft <sup>3</sup>
Young's Modulus	$5.2 \times 10^3$ kg/mm <sup>2</sup>	$7.4 \times 10^6$ psi
Poisson's Ratio	0.22	0.22
Viscosity		
Working Point ( $10^4$ Poises)	1068°C	1954°F
Annealing Point ( $10^{13}$ Poises)	496°C	925°F
Set Point	461°C	862°F
Strain Point ( $10^{14}$ Poises)	456°C	853°F
Thermal		
Coefficient of Expansion (0-300°C)	$32.0 \times 10^{-7}/^\circ\text{C}$	$17.7 \times 10^{-7}/^\circ\text{F}$
Coefficient of Expansion (25°C to Set Point, 461°C)	$39.0 \times 10^{-7}/^\circ\text{C}$	$21.7 \times 10^{-7}/^\circ\text{F}$
Upper Working Temperature (Annealed, Normal Service)	230°C	446°F
Upper Working Temperature (Annealed, Extreme Service)	430°C	806°F

Materials Properties		
Property	Metric Value	English Value
Upper Working Temperature (Tempered, Normal Service)	230°C	446°F
Upper Working Temperature (Tempered, Extreme Service)	230°C	446°F
Thermal Stress Resistance	66°C	151°F
Optical		
Refractive Index (at $\lambda=589.3$ nm)	1.469-1.47	1.469-1.47
Electrical		
$\text{Log}_{10}$ Volume Resistivity @ 25°C	17+ ohm-cm	
$\text{Log}_{10}$ Volume Resistivity @ 250°C	11.2 ohm-cm	
$\text{Log}_{10}$ Volume Resistivity @ 350°C	9.1 ohm-cm	
Dielectric Constant @ 20°C, 1MHz	4.1	4.1
Power Factor or Loss Tangent @ 20°C, 1MHz	0.06%	0.06%
Loss Factor @ 20°C, 1MHz	0.25%	0.25%

The following figures further outline the materials properties of Corning 7070 borosilicate glass (note: some of this information is not manufacturer's data)

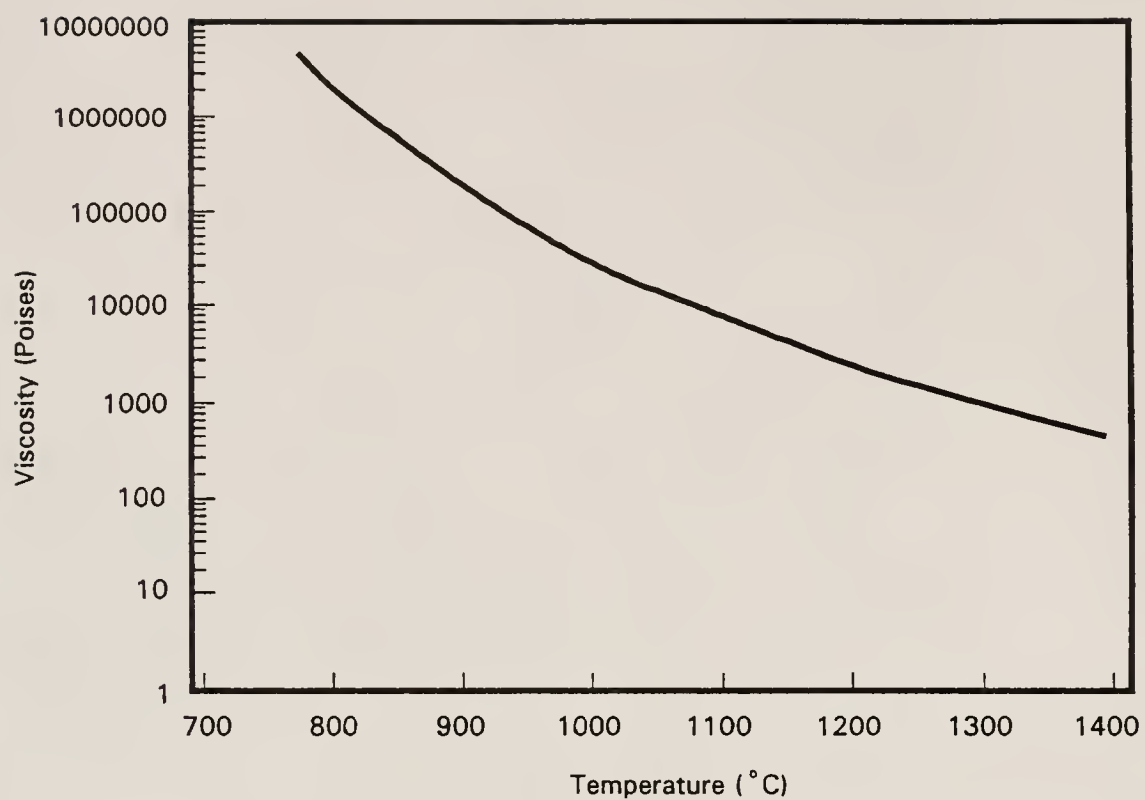


Figure A1.1

Viscosity of Corning 7070 as a function of temperature  
[88COR]



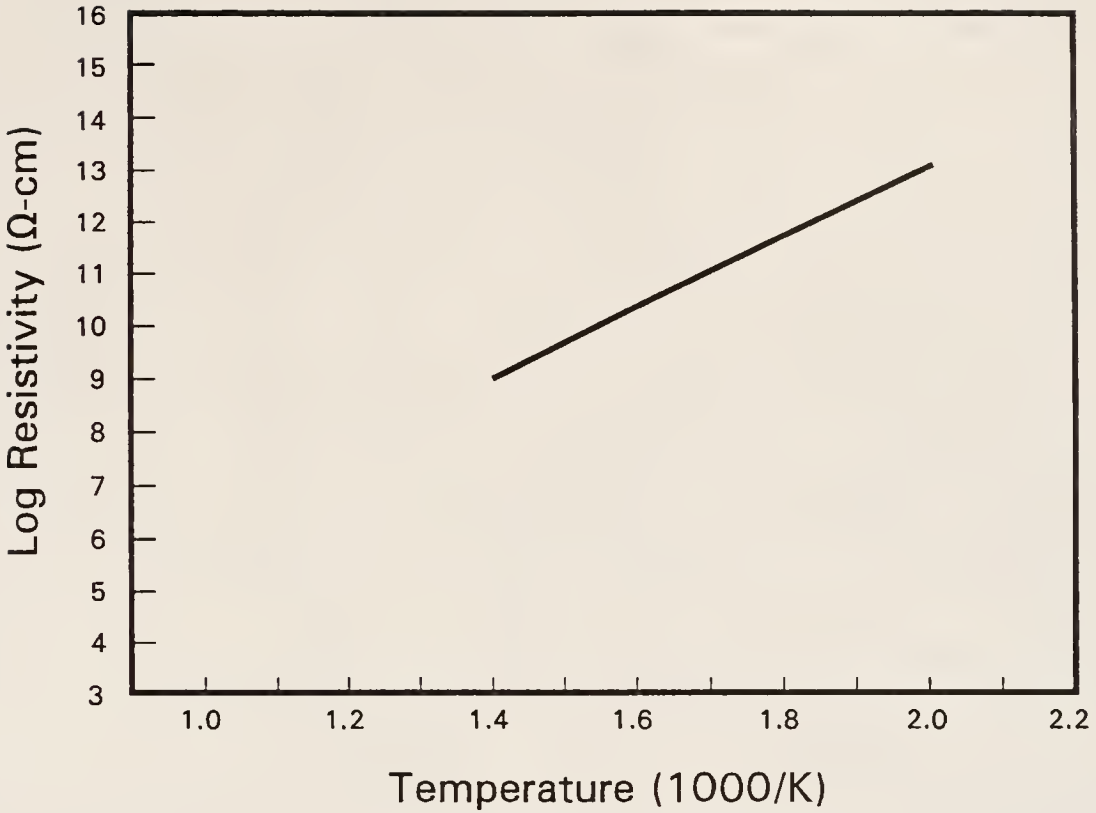


Figure AI.2 Resistivity of Corning 7070 as a function of reciprocal temperature [88COR]

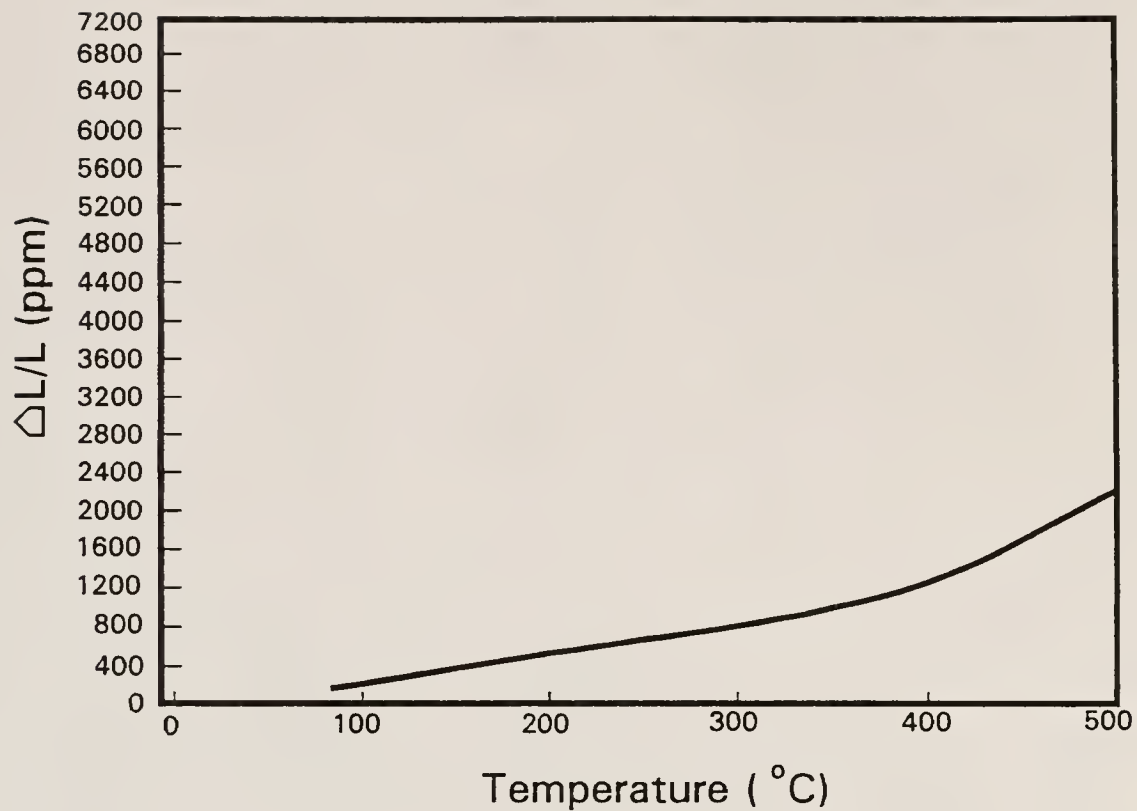


Figure AI.3

Thermal expansion of Corning 7070 borosilicate glass  
[88COR]

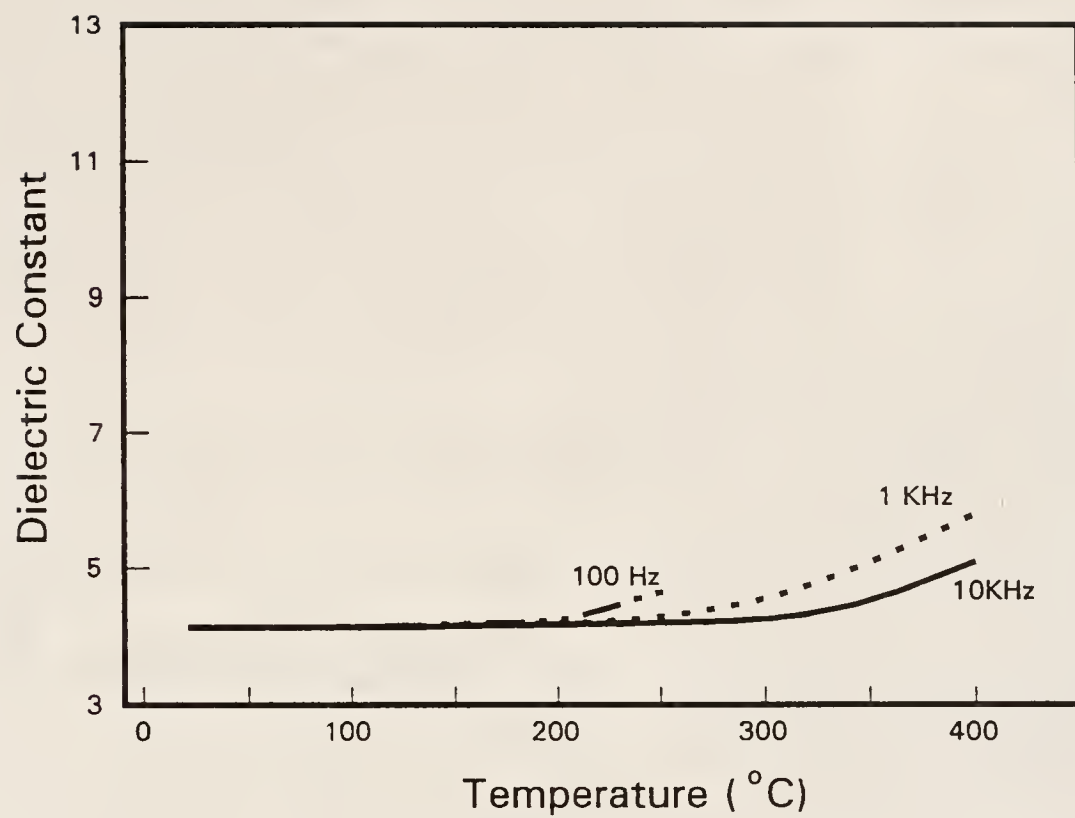


Figure AI.4

Dielectric Constant of Corning 7070 as a function of temperature [88COR]

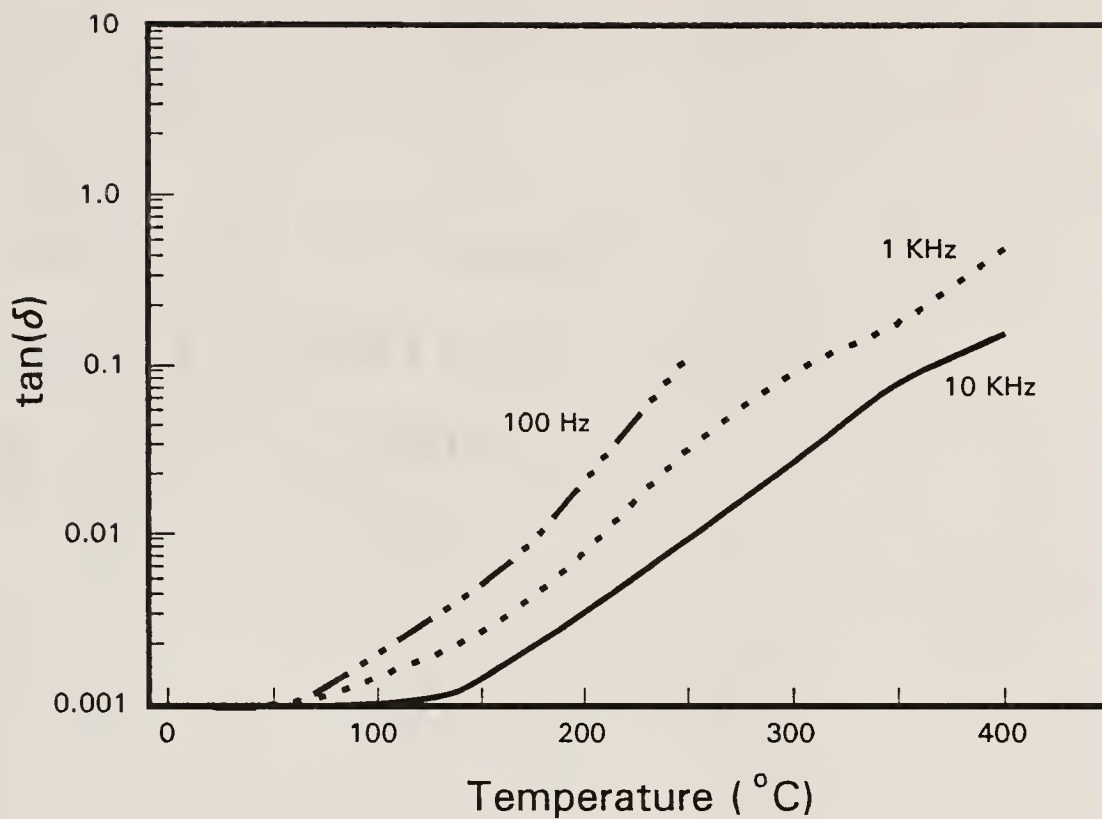
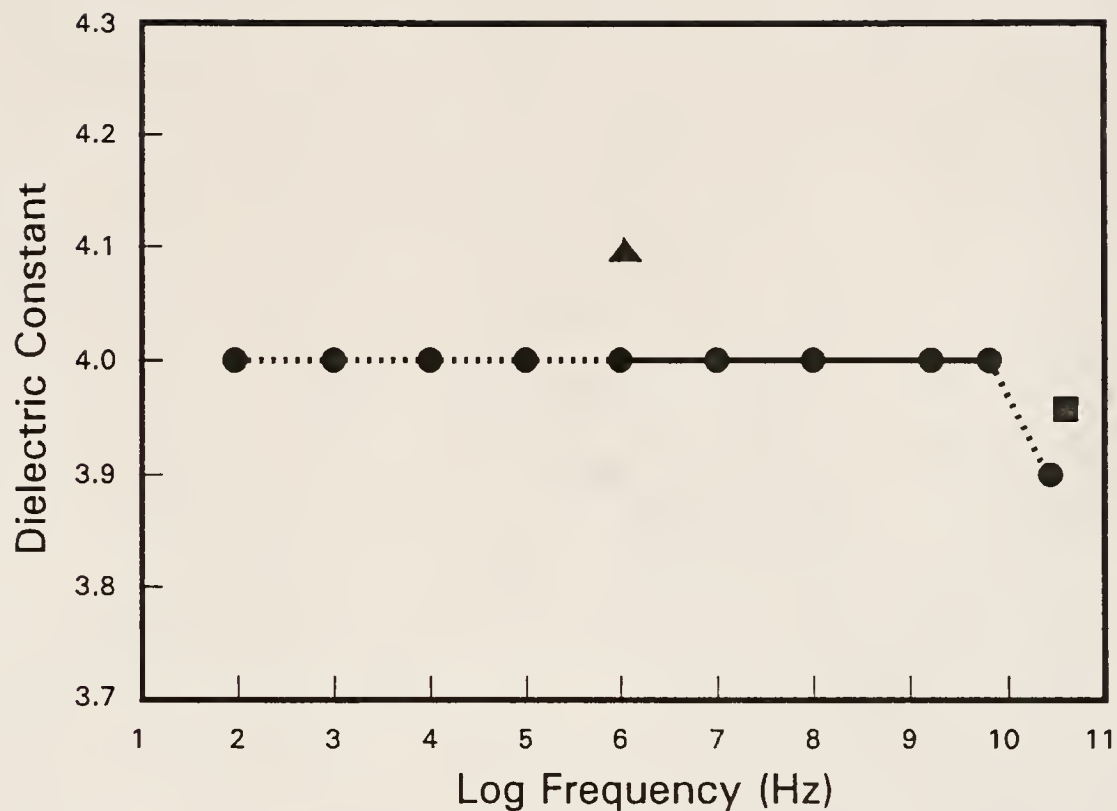


Figure AI.5

Loss tangent of Corning 7070 borosilicate glass as a function on temperature [88COR]

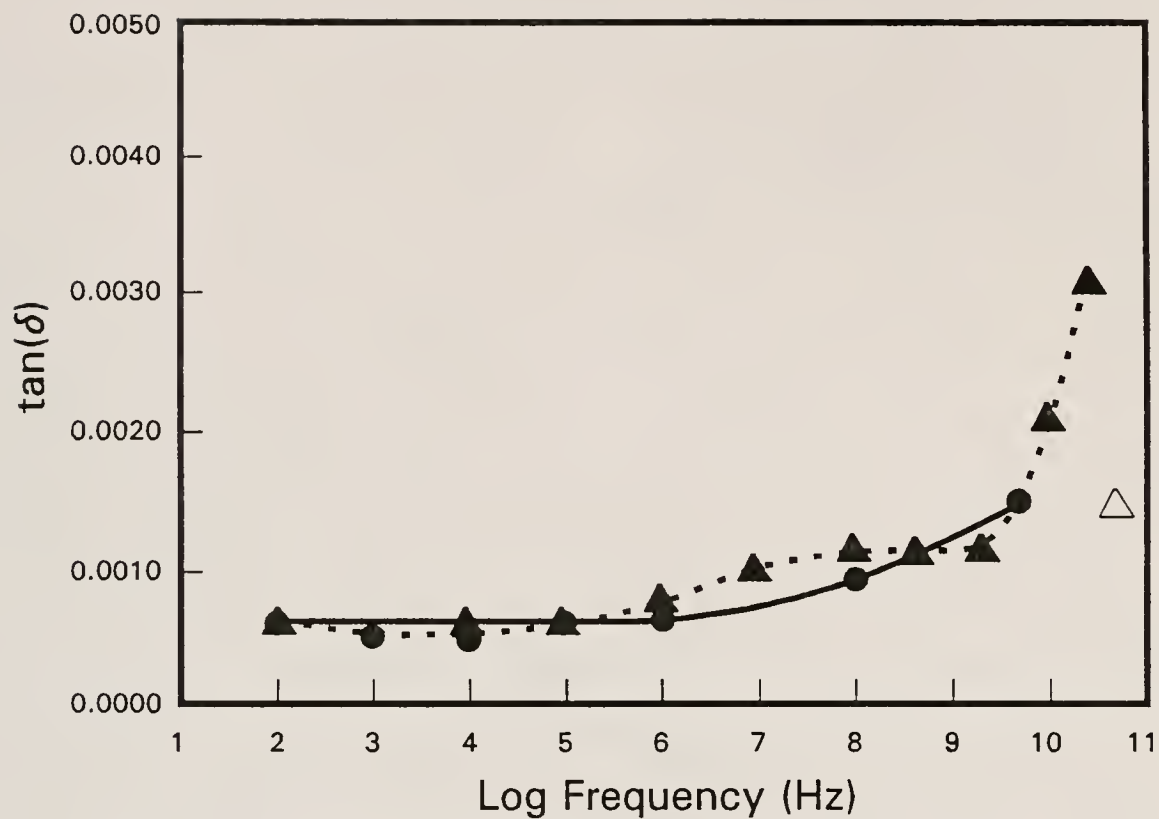


Source: Air Force Materials Laboratory  
(prepared by the Electronic Properties Information Center,  
Hughes Aircraft Company, Culver City, CA)

Figure AI.6

Dielectric constant of Corning 7070 borosilicate glass  
as a function of frequency





Source: Air Force Materials Laboratory  
(prepared by the Electronic Properties Information Center,  
Hughes Aircraft Company, Culver City, CA)

Figure AI.7

Loss tangent of Corning 7070 borosilicate glass as a  
function of frequency

## II. UBE SNE03 Silicon Nitride Powder

(Data obtained from UBE Industries Limited Quality Certificate for UBE SN-series  $\text{Si}_3\text{N}_4$  Powders and From Reference [89SOM])

Product Characteristics	
Identification	
Grade	SNE03
Lot Number	B 910062
Chemical	
Nitrogen (N, Weight Percent)	>38.0
Oxygen (O, Weight Percent)	0.83
Chlorine (Cl, PPM)	<100
Iron (Fe, PPM)	<100
Calcium (Ca, PPM)	<50
Aluminum (Al, PPM)	<50
Crystal	
Crystallinity (Weight Percent)	>99.5
Major Phase	$\alpha$
$\frac{\beta}{(\alpha+\beta)}$	<5
Physical	
Specific Surface Area ( $\text{m}^2/\text{g}$ )	3.5
Specific Gravity ( $\text{g}/\text{cm}^3$ )	3.18

APPENDIX II  
PARTICLE SIZE AND SIZE DISTRIBUTION DATA OF  
UNSETTLED 4.6  $\mu\text{m}$  REGIME (061990 SERIES) UPLM SPHERES

Batch 06199001, Unsettled

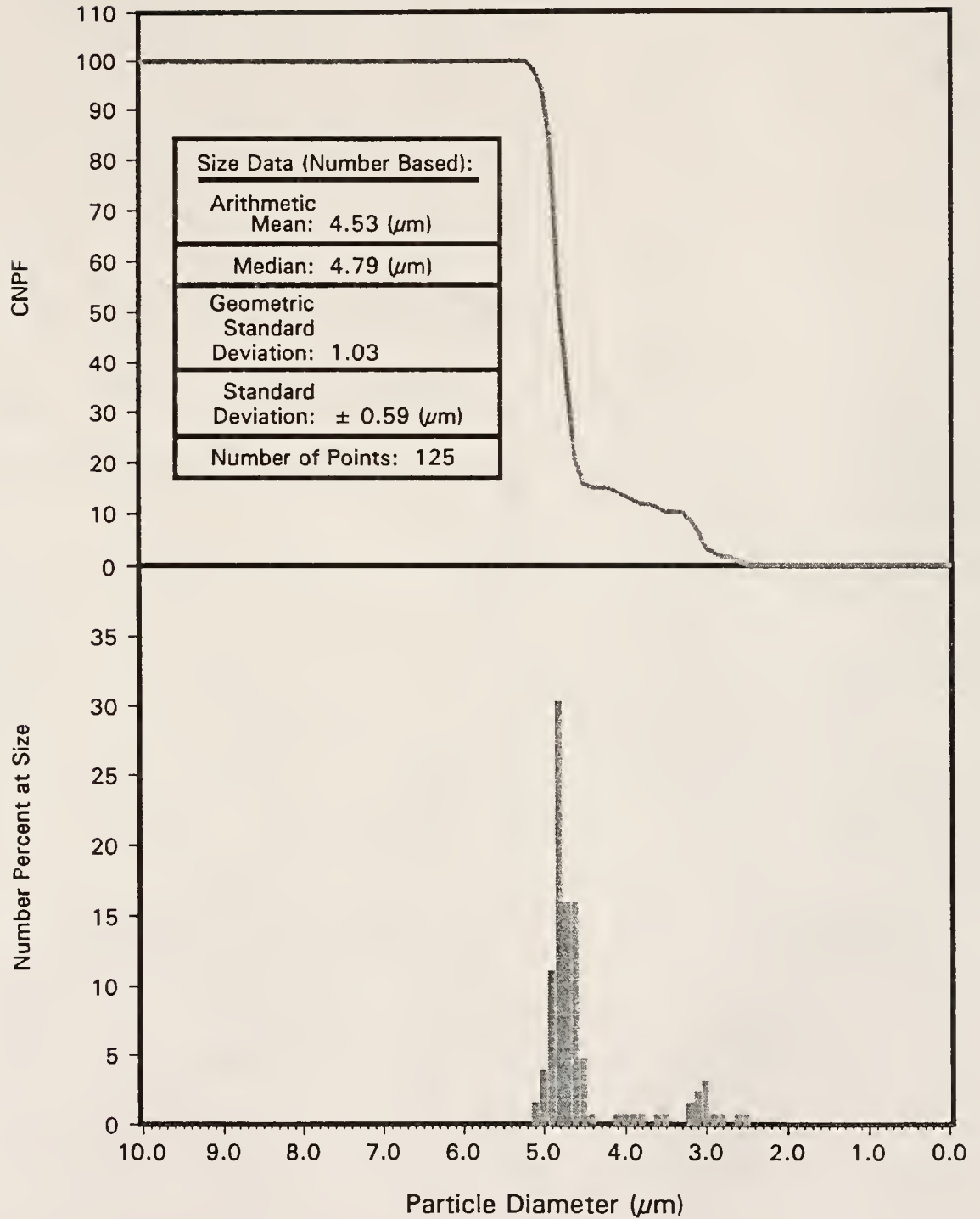


Figure AII.1

Number basis particle size data for batch number one of 061990 series UPLMs (4.6  $\mu\text{m}$  size regime, unclassified)  
565

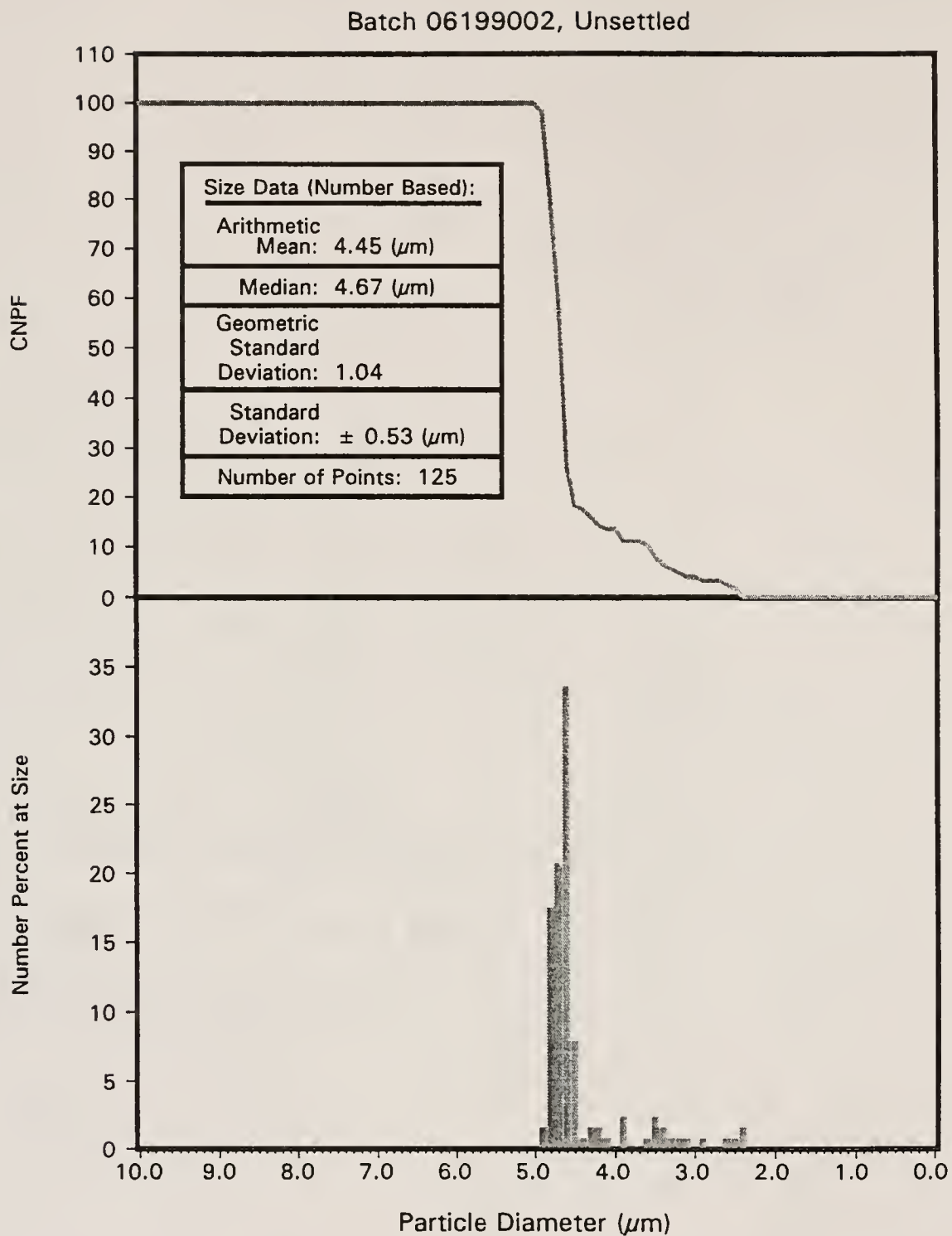


Figure AII.2

Number basis particle size data for batch number two of 061990 series UPLMs (4.6  $\mu\text{m}$  size regime, unclassified)



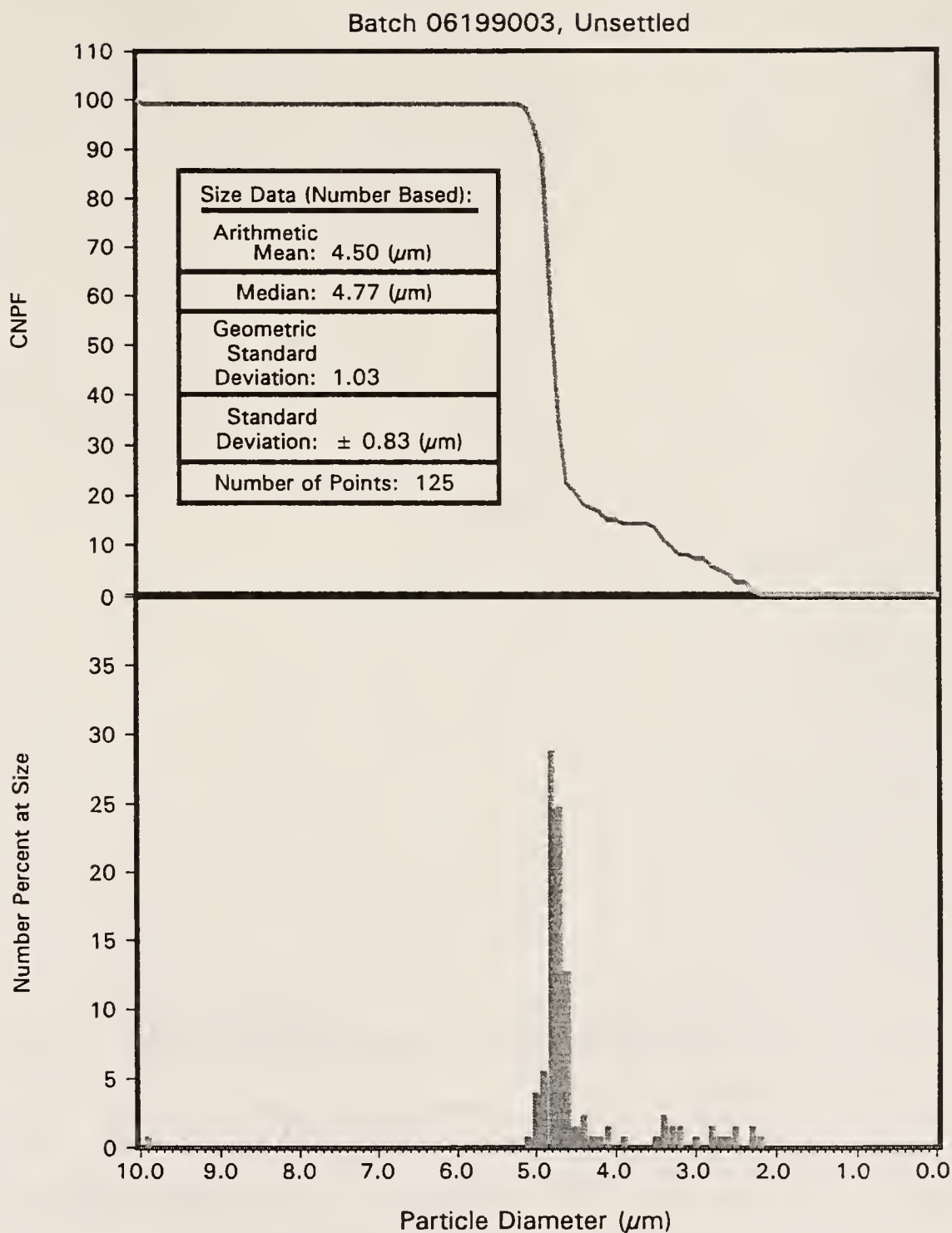


Figure AII.3

Number basis particle size data for batch number 3 of 061990 series UPLMs (4.6  $\mu\text{m}$  size regime, unclassified)

## Batch 06199004, Unsettled

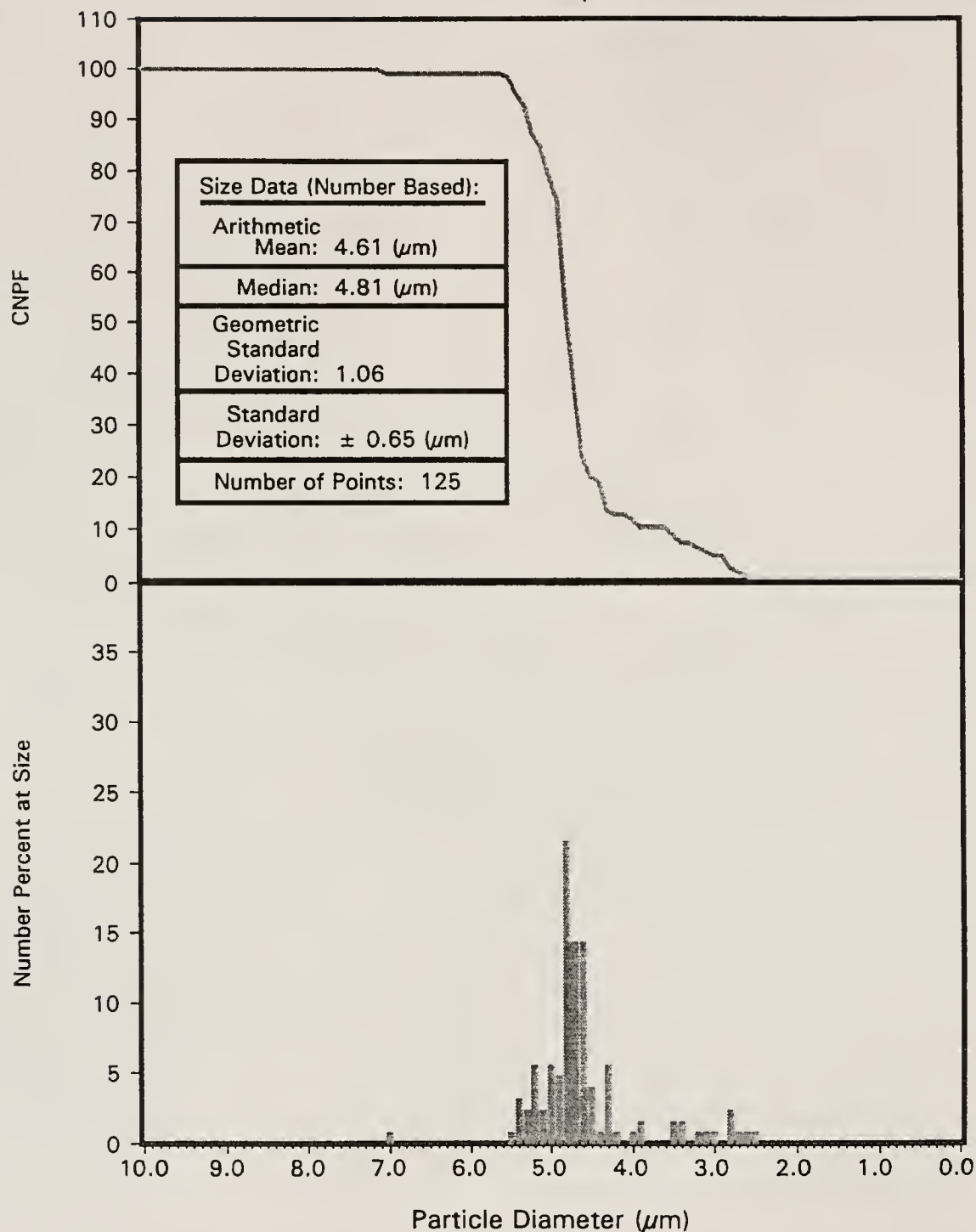


Figure AII.4

Number basis particle size data for batch number four of 061990 series UPLMs (4.6  $\mu\text{m}$  size regime, unclassified)

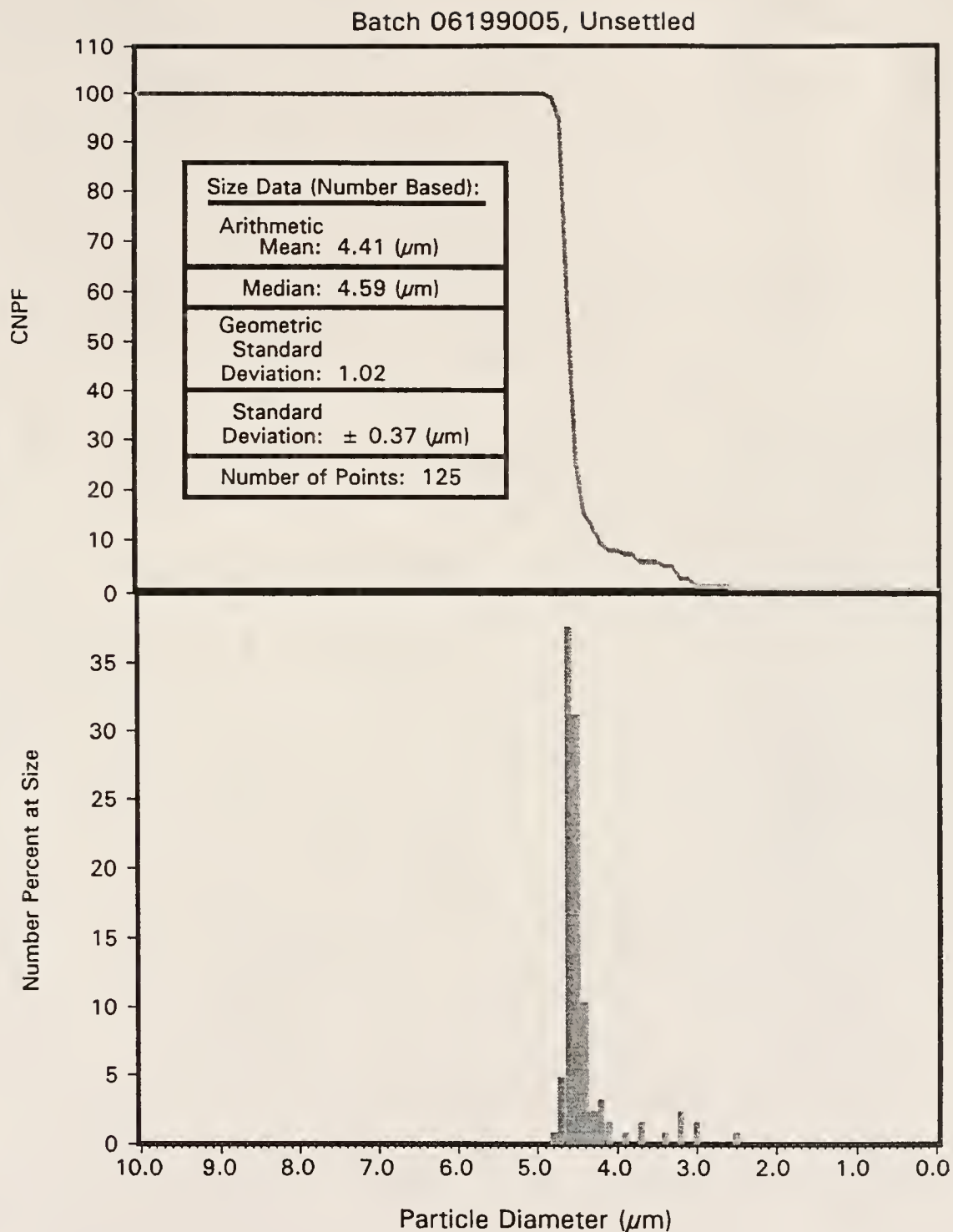


Figure AII.5

Number basis particle size data for batch number five of 061990 series UPLMs (4.6  $\mu\text{m}$  size regime, unclassified)

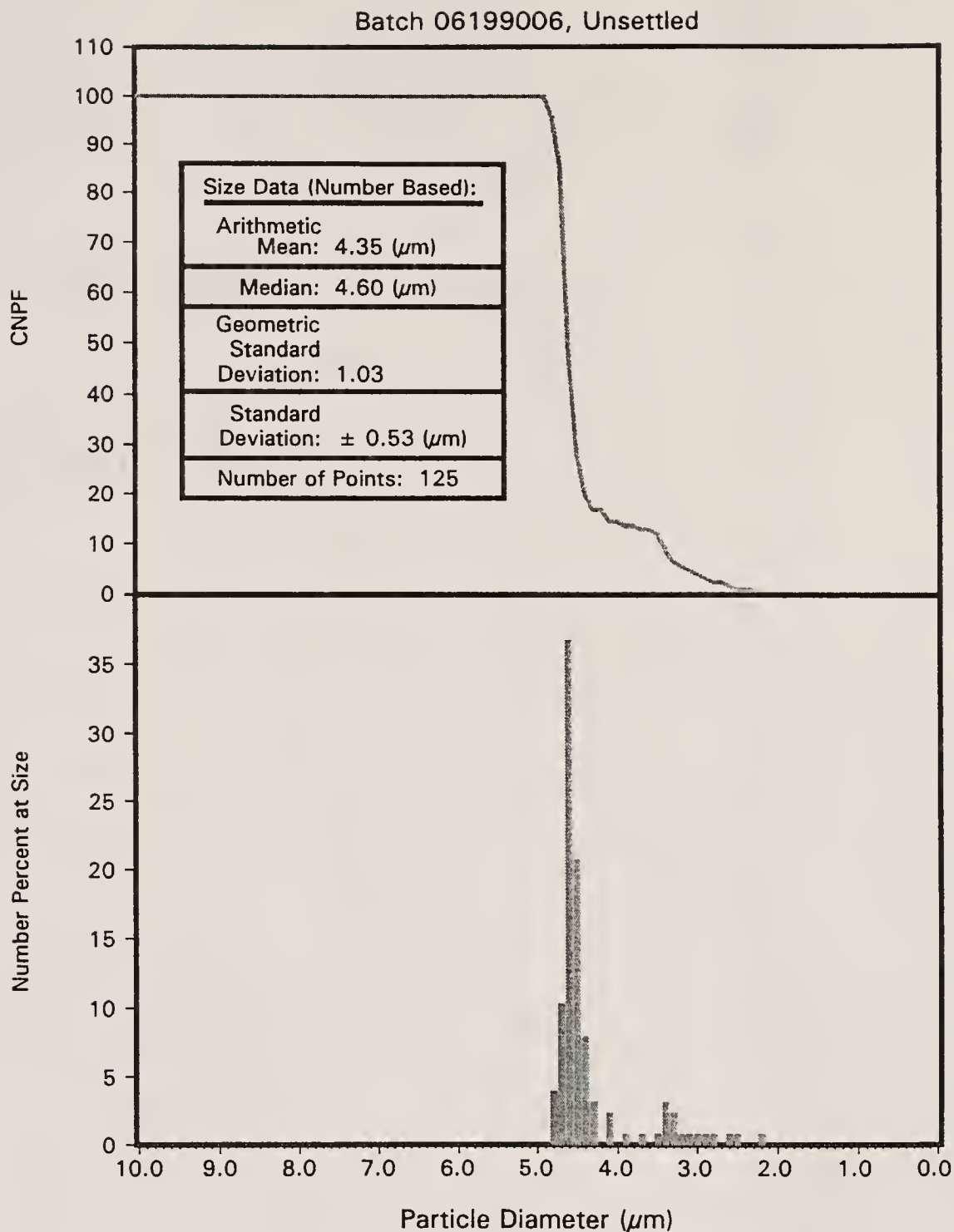


Figure AII.6

Number basis particle size data for batch number six of 061990 series UPLMs (4.6  $\mu\text{m}$  size regime, unclassified)

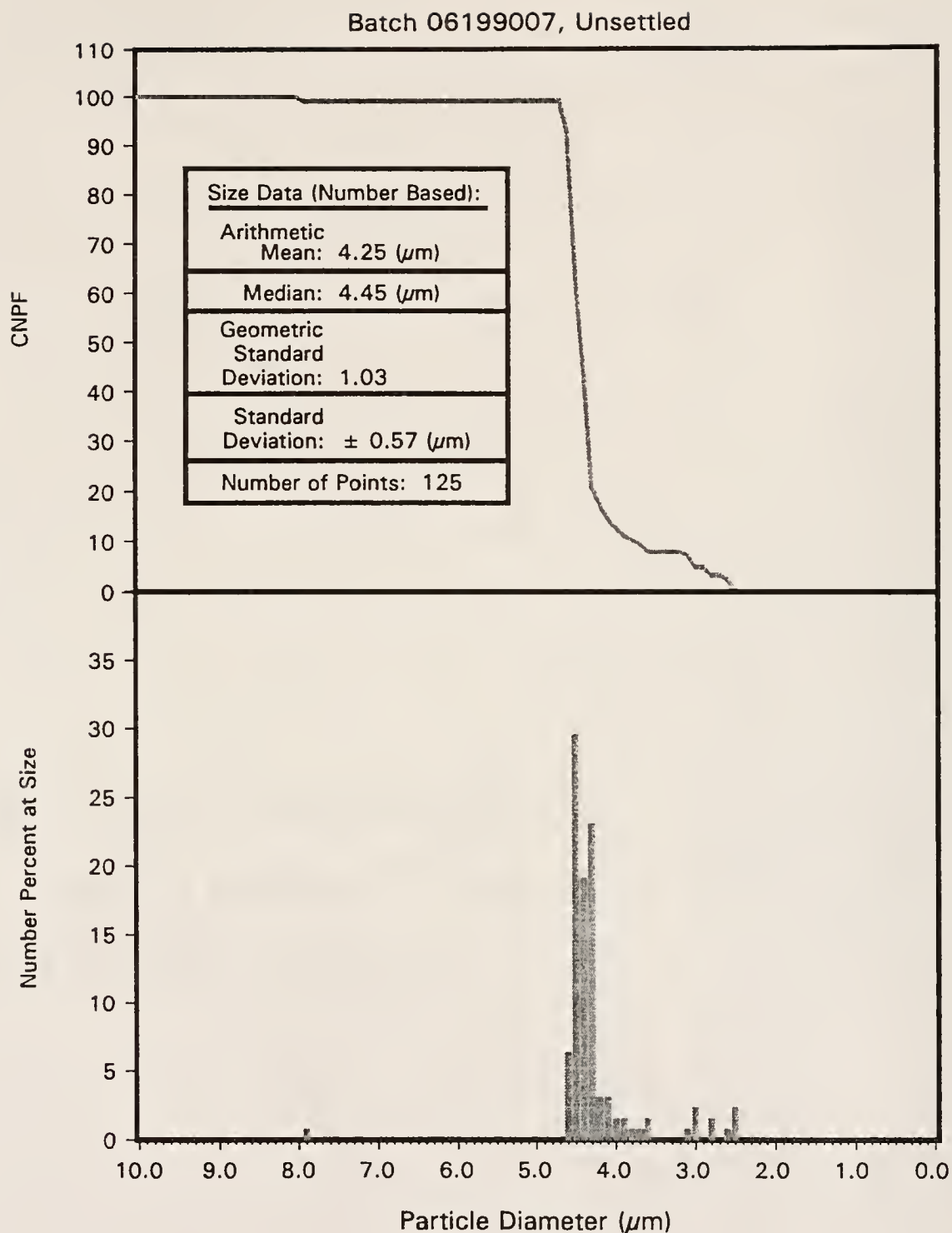


Figure AII.7

Number basis particle size data for batch number seven of 061990 series UPLMs (4.6  $\mu\text{m}$  size regime, unclassified)



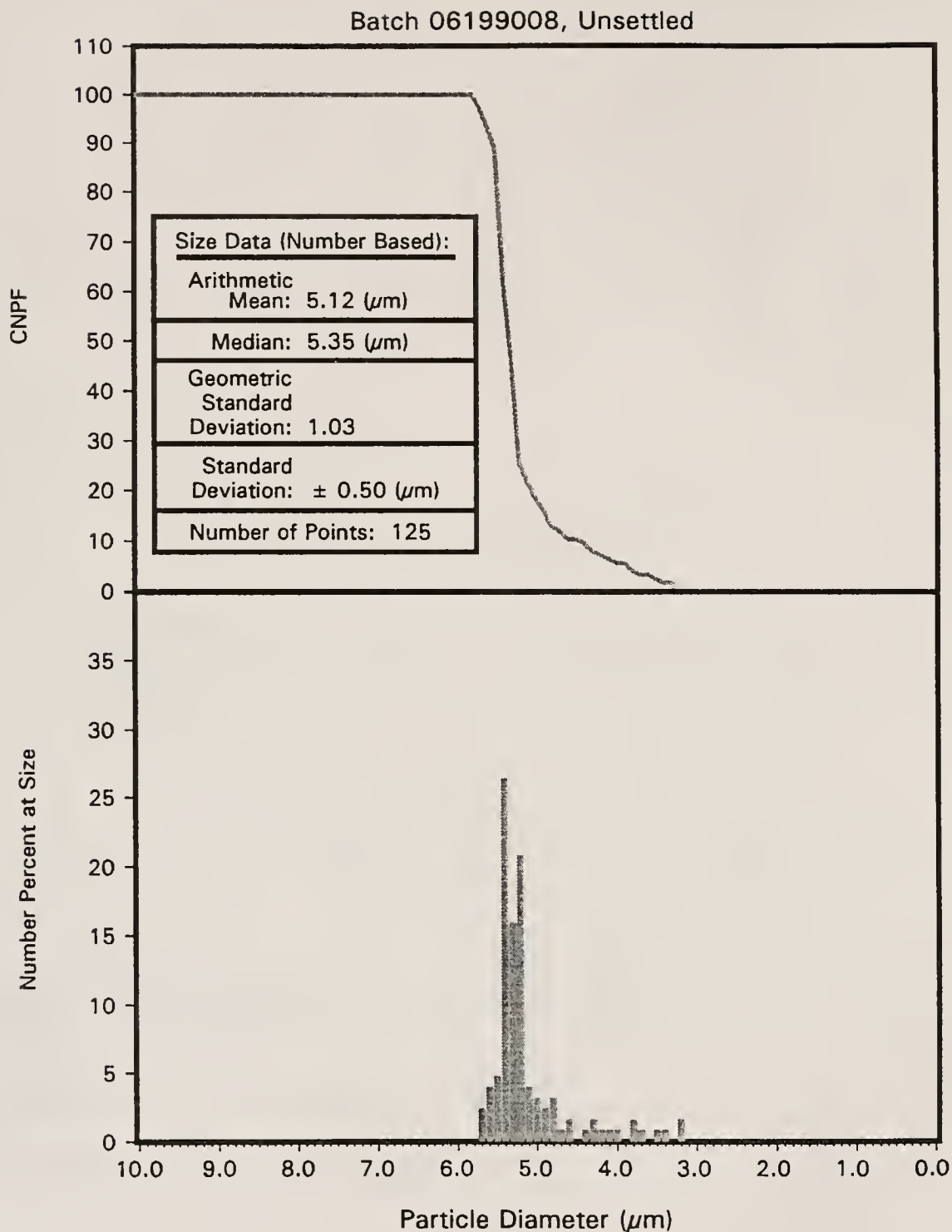


Figure AII.8

Number basis particle size data for batch number eight of 061990 series UPLMs (4.6  $\mu\text{m}$  size regime, unclassified)

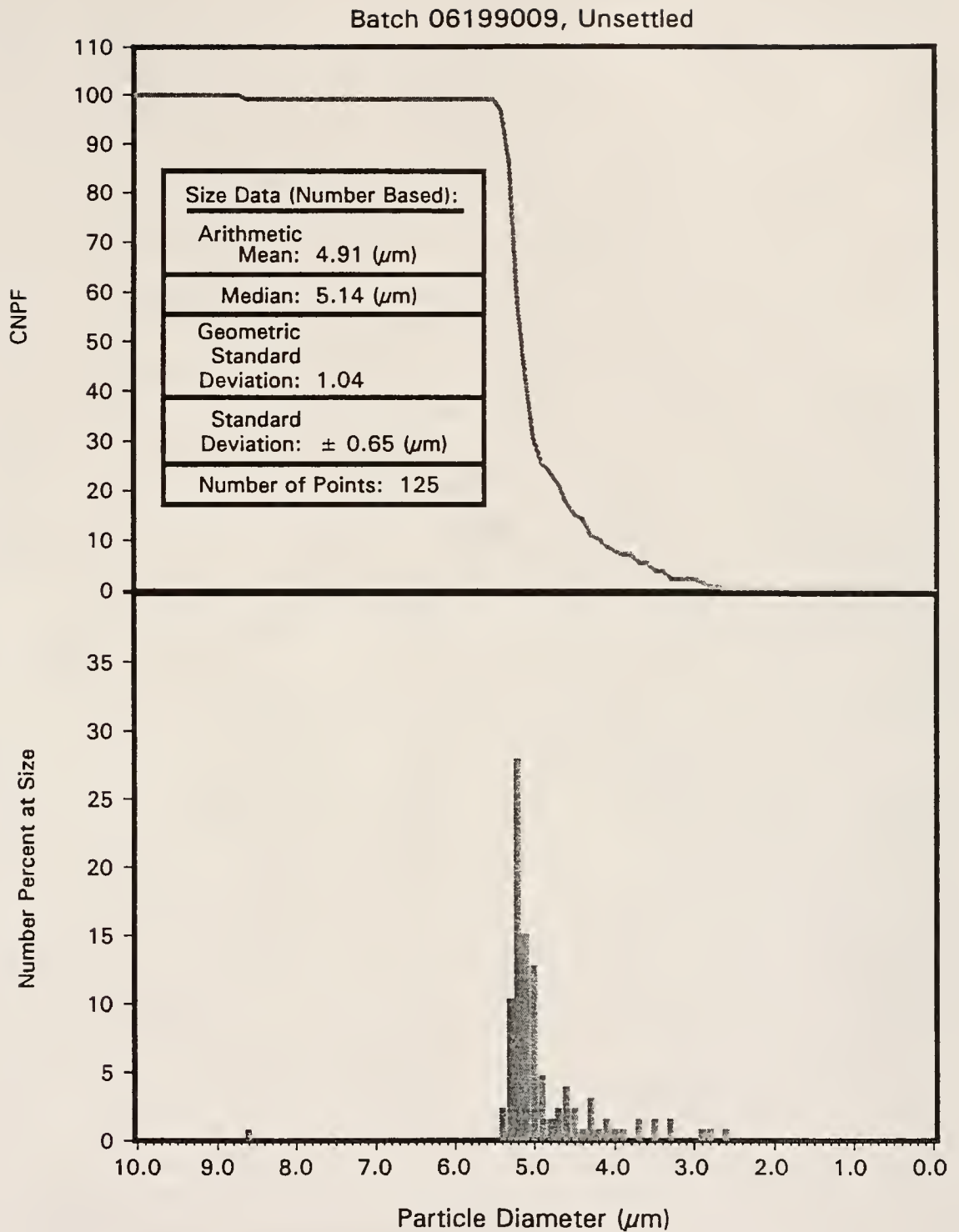


Figure AII.9

Number basis particle size data for batch number nine of 061990 series UPLMs (4.6  $\mu\text{m}$  size regime, unclassified)

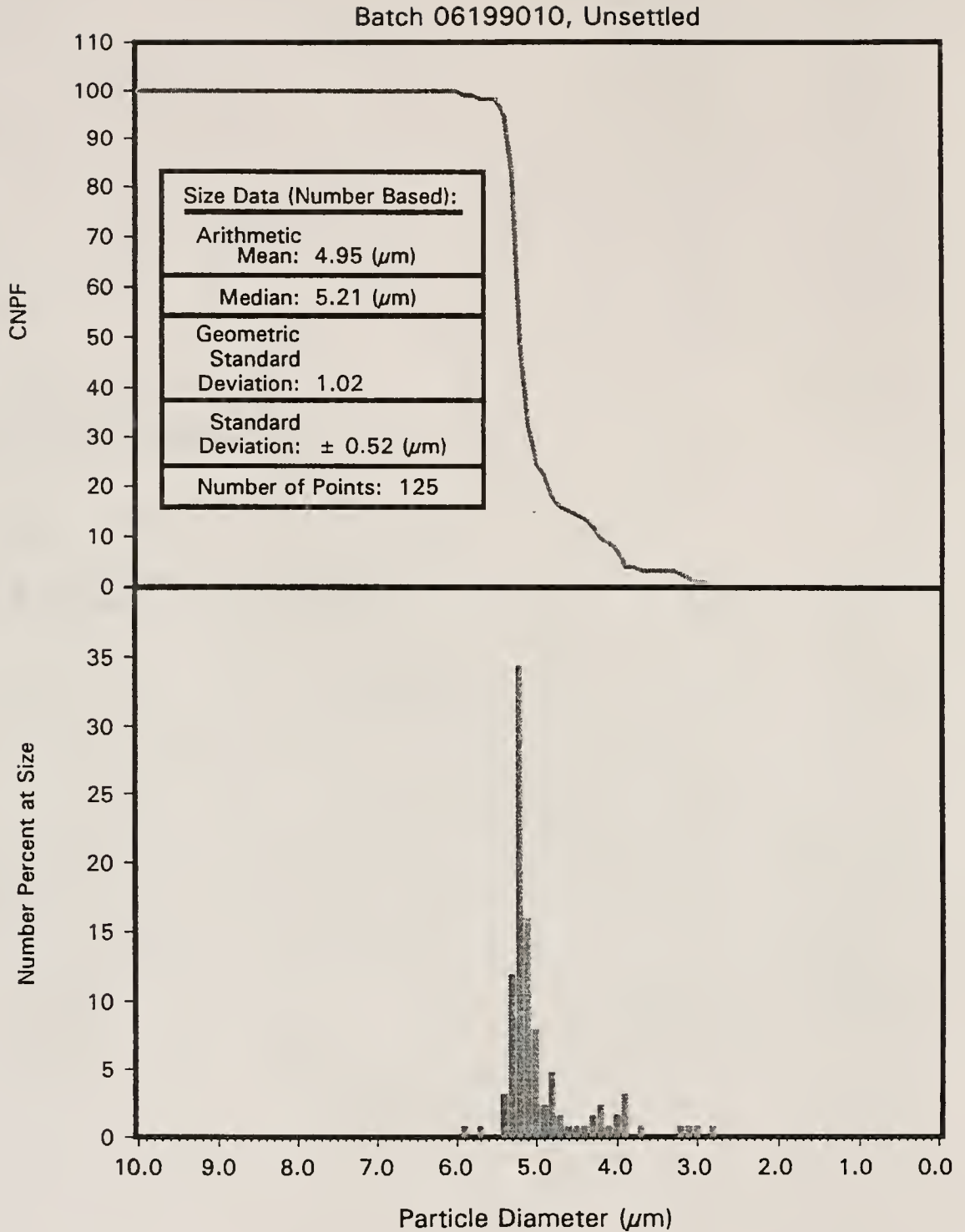


Figure AII.10

Number basis particle size data for batch number ten of 061990 series UPLMs (4.6  $\mu\text{m}$  size regime, unclassified)

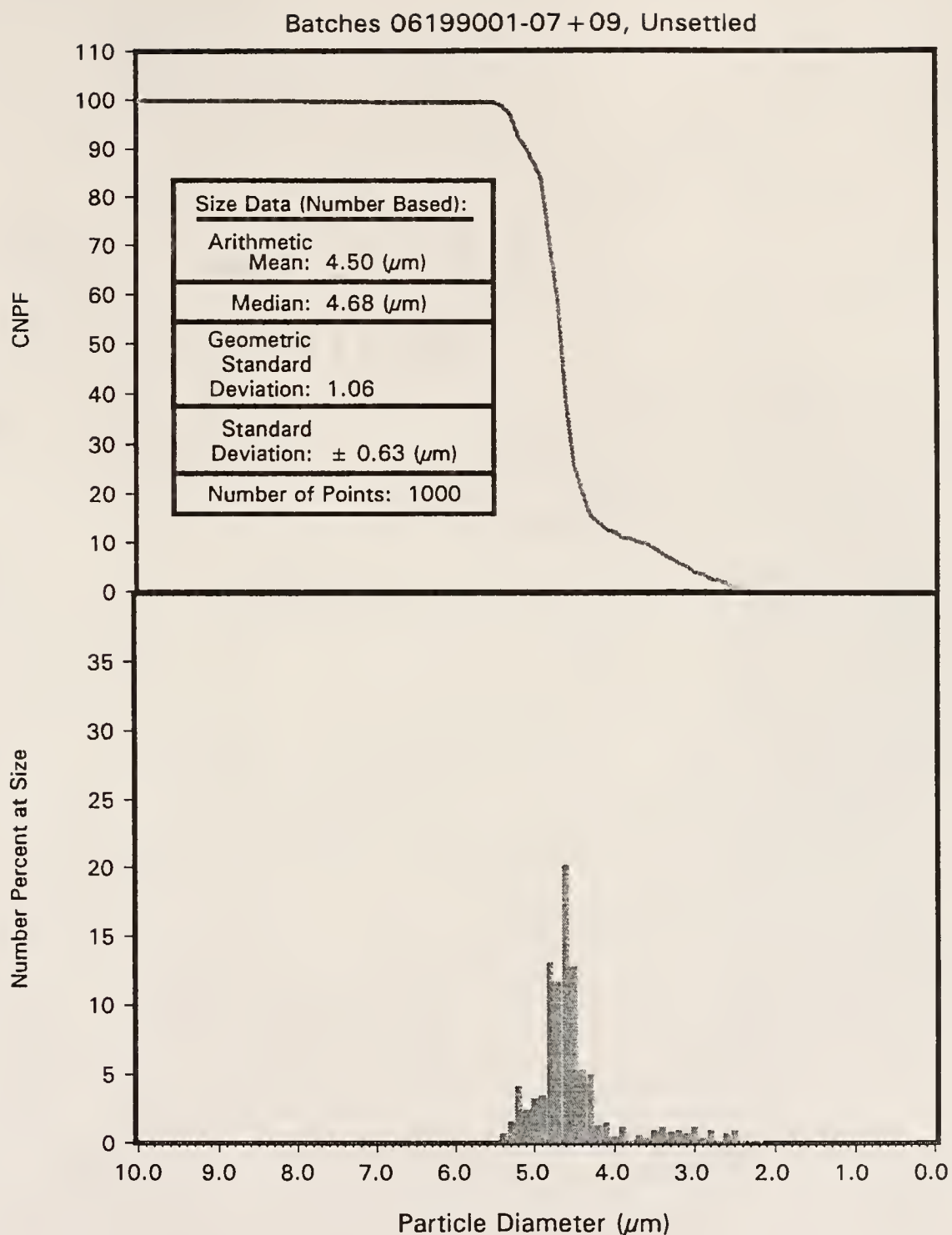


Figure AII.11

Number basis particle size data for combined batches 1-7+9 of 061990 series UPLMs (4.6  $\mu\text{m}$  size regime, unclassified)

APPENDIX III  
LEAST SQUARES POLYNOMIAL REGRESSION  
DATA CURVE FITTING PROGRAM (BASIC)

```

10  CLS
20  COLOR 13,1
30  PRINT "
40  PRINT
50  PRINT "
60  PRINT
70  DIM A(25), R(13,14), T(14)
80  PRINT "DEGREE OF EQUATION";
90  INPUT D
100 PRINT "NUMBER OF KNOWN POINTS";
110 PRINT "
120 INPUT N
130 A (1) = N
140 INPUT "TYPE 1 TO USE OLD FILE OR 2 TO START NEW FILE";L
150 IF L=1 GOTO 350
160 INPUT "WHAT IS THE FILE NAME FOR X";X$
170 INPUT "WHAT IS THE FILE NAME FOR Y";Y$
180 OPEN X$ FOR OUTPUT AS #1
190 OPEN Y$ FOR OUTPUT AS #2
200 FOR I=1 TO N
210 PRINT "X,Y OF POINT";I;
220 INPUT X,Y
230 WRITE #1,X
240 WRITE #2,Y
250 FOR J=2 TO 2*D+1
260 A(J) = A(J) + X^(J-1)
270 NEXT J
280 FOR K=1 TO D+1
290 R(K,D+2) = T(K) + Y*X^(K-1)
300 T(K) = T(K) + Y*K^(K-1)
310 NEXT K
320 T(D+2) = T(D+2) + Y^2
330 NEXT I
340 GOTO 510
350 INPUT "WHAT IS THE FILE NAME FOR X";X$
360 INPUT "WHAT IS THE FILE NAME FOR Y";Y$
370 OPEN X$ FOR INPUT AS #1
380 OPEN Y$ FOR INPUT AS #2
390 FOR I=1 TO N
400 INPUT #1,X
410 INPUT #2,Y
420 FOR J=2 TO 2*D+1
430 A(J) = A(J) + X^(J-1)
440 NEXT J
450 FOR K=1 TO D+1
460 R(K,D+2) = T(K) + Y*X^(K-1)
470 T(K) = T(K) + Y*X^(K-1)
480 NEXT K
490 T(D+2) = T(D+2) + Y^2
500 NEXT I

```



```

510  CLOSE
520  FOR J=1 TO D+1
530  FOR K=1 TO D+1
540  R(J,K) = A(J+K-1)
550  NEXT K
560  NEXT J
570  FOR J=1 TO D+1
580  K=J
590  IF R(K,J) <> 0 THEN 640
600  K=K+1
610  IF K <= D+1 THEN 590
620  PRINT "NO UNIQUE SOLUTION"
630  GOTO 1220
640  FOR I=1 TO D+2
650  S = R(J,I)
660  R(J,I) = R(K,I)
670  R(K,I) = S
680  NEXT I
690  Z = 1/R(J,J)
700  FOR I=1 TO D+2
710  R(J,I) = X*R(J,I)
720  NEXT I
730  FOR K=1 TO D+1
740  IF K=J THEN 790
750  Z = -R(K,J)
760  I=1 TO D+2
770  R(K,I) = R(K,I) + Z*R(J,I)
780  NEXT I
790  NEXT K
800  NEXT J
810  INPUT "1 FOR PRINTOUT OF X AND Y OR 2 FOR PRINTOUT OF STATISTICS
ONLY";M
820  IF M=2 GOTO 920
830  OPEN X$ FOR INPUT AS #1
840  OPEN Y$ FOR INPUT AS #2
850  LPRINT " X Y "
860  NEXT I
870  INPUT #1,X
880  INPUT #2,Y
890  LPRINT X,Y
900  NEXT I
910  CLOSE
920  LPRINT
930  LPRINT " CONSTANT =";R(1,D+2)
940  FOR J=1 TO D
950  LPRINT J; "DEGREE COEFFICIENT ="; R(J+1,D+2)
960  NEXT J
970  LPRINT
980  P=0
990  FOR J=2 TO D+1
1000  P = P + R(J,D+2)*(T(J) - A(J)*T(1)/N)
1010  NEXT J
1020  Q = T(D+2) - T(1)^2/N
1030  Z = Q - P
1040  I = N - D -1
1050  LPRINT
1060  J = P/Q
1070  LPRINT "COEFFICIENT OF DETERMINATION (R^2) = ";J
1080  LPRINT "COEFFICIENT OF CORRELATION ="; SQR (J)
1090  LPRINT "STANDARD ERROR OF ESTIMATE ="; SQR (ABS(Z/I))
1100  LPRINT

```

```
1110 PRINT "INTERPOLATION: (ENTER 0 TO END PROGRAM)"
1120 P = R(1,D+2)
1130 PRINT "X =";
1140 INPUT X
1150 IF X = 0 THEN 1220
1160 FOR J=1 TO D
1170 P = P + R(J+1,D+2)*X^J
1180 NEXT J
1190 PRINT "Y ="; P
1200 PRINT
1210 GOTO 1120
1220 RUN "POLYREGR"
```

APPENDIX IV  
LIST OF ACRONYMS

<u>Acronym:</u>	<u>Definition:</u>
AC	Alternating Current
ACN	Average Cluster Number
AI	Artificial Intelligence
AIBN	Azobis (2-methyl-propionitrile)
ASG	Apparent Specific Gravity
ASLT	Advanced Solid Logic Technology
BCB	Bisbenzocyclobutene
BCC	Body-Centered Cubic
BPO	Benzoyl Peroxide
BS	Borosilicate glass
C4	Controlled Collapse Chip Connection
CFG	Ceramic-Filled Glass
CMOS	Complimentary Metal Oxide Semiconductor
CMPF	Cumulative Mass Percent Finer than
CMPL	Cumulative Mass Percent Larger than
CNPF	Cumulative Number Percent Finer than
CNPL	Cumulative Number Percent Larger than
COB	Card On Board
CP	Closed Porosity
CPSA	Centrifugal Particle Size Analysis
CSSA	Cumulative Spherical equivalent Surface Area
CTE	Coefficient of Thermal Expansion
CVFF	Cumulative Volume Fraction Finer than
CVPF	Cumulative Volume Percent Finer than
CVPL	Cumulative Volume Percent Larger than
DIP	Dual In-line Package
DTA	Differential Thermal Analysis
ELSI	Early Large Scale Integration
EMT	Effective Medium Theory
EtOH	Ethanol
FCC	Face-Centered Cubic
FRU	Field Replaceable Unit
FTIR	Fourier Transform Infrared spectroscopy
GD	Green Density
GEM	General Effective Medium theory
GNP	Gross National Product
GSD	Geometric Standard Deviation
HGM	Hollow Glass Microspheres
ICP	Inductively Coupled Plasma spectroscopy
ISDN	Integrated Services Digital Network
LCM	Liquid Cooled Module
LSI	Large Scale Integration
MC	Metallized Ceramic

<u>Acronym:</u>	<u>Definition:</u>
MCP	Metallized Ceramic-Polyimide
MeOH	Methanol
MIBK	Methyl Isobutyl Ketone
MLC	Multilayer Ceramic
MMA	Methyl Methacrylate
MPCD	Median Pore Channel Diameter
MPCR	Median Pore Channel Radius
MS	Mackenzie-Shuttleworth
MUT	Material Under Test
NLPS	Nonreactive Liquid Phase Sintering
NSRI	Nonsintering Rigid Inclusions
OP	Open Porosity
PCSD	Pore Channel Size Distribution
PDN	Power Distribution Network
PE	Packing Efficiency
PE	Polyethylene
PF	Power dissipation Factor
PLII	Platinel Two thermocouple
PM	Photomultiplier tube
PMMA	Polymethyl Methacrylate
PMP	Polymethylpentene
PS	Polystyrene
PTFE	Polytetrafluoroethylene
PVB	Polyvinyl Butyral
PVP	Polyvinyl Pyrrolidone
QM	Qualitative Microscopy
QMT	Qualitative Microscopy Techniques
RC	Resistive Capacitance
RCP	Random Close Packing
RH	Relative Humidity
RNSPAS	Relative Number of Spherical Particles at Size
RP	Random Packing
SA	Surface Area
SC	Simple Cubic
SEM	Scanning Electron Microscopy
SLT	Solid Logic Technology
SMS	Standard Modular System
SSA	Specific Surface Area
SSAAS	Specific Surface Area At Size
TCM	Thermal Conduction Module
TDR	Time Domain Reflectometry
TEM	Transmission Electron Microscopy
TGA	Thermogravimetric Analysis
ThD	Theoretical Density
TOF	Time Of Flight spectroscopy
TP	Total Porosity
TRNP	Total Relative Number of spherical Particles
ULSI	Ultra-Large Scale Integration
UPLM	Uniform Polystyrene Latex Microspheres
VF	Volume Fraction
VLSI	Very-Large Scale Integration
VTL	Vendor Transistor Logic
WSI	Wafer Scale Integration

## REFERENCES

- [28FUR] C.C. Furnas, "Relation Between Specific Volume, Voids and Size Composition in Systems of Broken Solids of Mixed Sizes," Report of Investigations No. 2894, Department of Commerce, Bureau of Mines, (Oct., 1928).
- [29SMI] W.O. Smith, P.D. Foote, P.F. Busang, "Packing of Homogeneous Spheres," Phys. Rev., 24, pp. 1271-74, (November, 1929).
- [30AND] A.H.M. Andreasen, J. Andersen, "Relation Between Grain Size and Interstitial Space in Products of Unconsolidated Granules," Kolloid-Z., 50, pp. 217-28, (1930, German).
- [30WES] A.E.R. Westman, H.R. Hugill, "The Packing of Particles," J. Am. Cer. Soc., 13, [10], pp. 767-79, (1930).
- [31FUR] C.C. Furnas, "Grading Aggregates, I-Mathematical Relations for Beds of Broken Solids of Maximum Density," Ind. Eng. Chem., 23, [9], pp. 1052-58, (1931).
- [37WHI] H.E. White, S.F. Walton, "Particle Packing and Particle Shape," J. Am. Cer. Soc., 20, pp. 155-66, (1937).
- [45FRE] J. Frenkel, "Viscous Flow of Crystalline Bodies Under the Action of Surface Tension," Journal of Physics, 2, [5], pp. 385-91, (1945).
- [49KUC] G.C. Kuczynski, "Study of the Sintering of Glass," Journal of Applied Physics, 20, pp. 1160-63, (1949).
- [49MAC] J.K. MacKenzie, R.L. Shuttleworth, "A Phenomenological Theory of Sintering," The Proceedings of the Physical Society: B, 62, 833-52, (1949).
- [50HER] C. Herring, "Effect of Change of Scale on Sintering Phenomena," Journal of Applied Physics, 21, pp. 301-03, (1950).
- [53FUL] R.L. Fullman, "Measurement of Particle Sizes in Opaque Bodies," Journal of Metals, pp. 447-52, (1953).
- [54VON] A.R. Von Hippel, editor, Dielectric Materials and Applications, MIT Press, Inc., Cambridge, MA, (1954).
- [55KIN] W.D. Kingery, M. Berg, "Study of the Initial Stages of Sintering Solids by Viscous Flow, Evaporation-Condensation, and Self Diffusion," Journal of Applied Physics, 26, [10], pp. 1205-12, (1955).
- [56FAT1] I. Fatt, "The Network Model of Porous Media: I. Capillary Pressure Characteristics," Petroleum Transactions of the AIME, 207, pp. 144-59, (1956).



- [56FAT2] I. Fatt, "The Network Model of Porous Media: II. Dynamic Properties of a Single Size Tube Network," Petroleum Transactions of the AIME, 207, pp. 160-63, (1956).
- [56FAT3] I. Fatt, "The Network Model of Porous Media: III. Dynamic Properties of Networks with Tube Radius Distribution," Petroleum Transactions of the AIME, 207, pp. 164-81, (1956).
- [56TEM] C.C. Templeton, S.S. Rushing, Jr., "Oil-Water Displacements in Microscopic Capillaries," Petroleum Transactions of the AIME, 207, pp. 211-14, (1956).
- [57WAC] J.B. Wachtman, Jr., L.H. Maxwell, "Plastic Deformation of Ceramic-Oxide Single Crystals, II," J. Am. Cer. Soc., 40, [11], pp. 377-85, (1957).
- [59BRO] S.D. Brown, S.S. Kistler, "Devitrification of High-SiO<sub>2</sub> Glasses of the System Al<sub>2</sub>O<sub>3</sub>-SiO<sub>2</sub>," J. Am. Cer. Soc., 42, [6], pp. 263-70, (1959).
- [59DOM] C. Domb, On the Theory of Cooperative Phenomena in Crystals, Advances in Physics, VIII., [29-32], Taylor and Frances Ltd., London, England, pp. 149-361, (1959).
- [59FIS] M.E. Fisher, M.F. Sykes, Excluded-Volume Problem and the Ising Model of Ferromagnetism," Phys. Rev., 114, [1], pp. 45-58, (1959).
- [60BER] J.D. Bernal, J. Mason, "Co-ordination of Randomly Packed Spheres," Nature, 188, pp. 910-11, (1960).
- [60SCO] G.D. Scott, "Packing of Equal Spheres," Nature, 188, pp. 908-909, (1960).
- [61DOM] C. Domb, M.F. Sykes, "Cluster Size in Random Mixtures and Percolation Processes," Phys. Rev., 122, [1], pp. 77-78, (1961).
- [61FIS1] M. E. Fisher, J.W. Essam, "Some Cluster Size and Percolation Problems," Journal of Mathematical Physics, 2, [4], pp. 609-19, (1961).
- [61FIS2] M.E. Fisher, "Critical Probabilities for Cluster Size and Percolation Problems," Journal of Mathematical Physics, 2, [4], pp. 620-27, (1961).
- [61FRI] H.L. Frisch, E. Sonnenblick, V.A. Vyssotsky, "Critical Percolation Probabilities (Site Problem)," Phys. Rev., 124, [4], pp. 1021-22, (1961).
- [61MCG] R.K. McGeary, "Mechanical Packing of Spherical Particles," J. Am. Cer. Soc., 44, [10], pp. 513-22, (1961).
- [61SEL] J. Selsing, "Internal Stress in Ceramics," J. Am. Cer. Soc.-Discussions and Notes, 44, [8], p. 419, (1961).
- [62EPS] N. Epstein, M.J. Young, "Random Loose Packing of Binary Mixtures of Spheres," Nature 196, pp. 885-86, (1962).

- [62HET] G. Hetherington, K.H. Jack, "Water in Vitreous Silica: Part I. Influence of 'Water' Content on the Properties of Vitreous Silica," *Physics and Chemistry of Glasses*, 3, [4], pp. 129-33, (1962).
- [62KIN] W.D. Kingery, The Thermal Conductivity of Ceramic Dielectrics, Chap. 4, Progress in Ceramic Science, Volume 2, Edited by J.E. Burke, Pergamon Press, Inc., New York, NY, (1962).
- [63DOM] C. Domb, "Excluded-Volume Effect for Two- and Three-Dimensional Lattice Models," *The Journal of Chemical Physics*, 38, [12], pp. 2957-63, (1963).
- [63FRI] H.L. Frisch, J.M. Hammersley, "Percolation Processes and Related Topics," *J. Soc. Indust., Appl. Math.*, 11, [4], pp. 894-918, (1963).
- [64HET] G. Hetherington, K.H. Jack, J.C. Kennedy, "The Viscosity of Vitreous Silica," *Physics and Chemistry of Glasses*, 5, [5], pp. 130-36, (1964).
- [64SYK] M.F. Sykes, J.W. Essam, "Critical Percolation Probabilities by Series Methods," *Phys. Rev.*, 133, [1A], pp. A310-15, (1964).
- [65AYE] J.E. Ayer, F.E. Soppet, "Vibratory Compaction: I, Compaction of Spherical Shapes," *J. Am. Cer. Soc.*, 48, [4], pp. 180-83, (1965).
- [65LEV] M.M. Levine, J. Chernick, "A Numerical Model of Random Packing of Spheres," *Nature*, 208, pp. 68-69, (1965).
- [65ROS] H.E. Rose, D.J. Robinson, "The Density of Packing of Two-Component Powder Mixtures," *Powder Metallurgy*, 8, [15], pp. 20-37, (1965).
- [66AYE] J.E. Ayer, F.E. Soppet, "Vibratory Compaction: II, Compaction of Angular Shapes," *J. Am. Cer. Soc.*, 49, [4], pp. 207-10, (1966).
- [66WAG] F.E. Wagstaff, K.J. Richards, "Kinetics of Crystallization of Stoichiometric SiO<sub>2</sub> Glass in H<sub>2</sub>O Atmosphere," *J. Am. Cer. Soc.*, 49, [3], pp. 118-21, (1966).
- [66WEB] Webster's Third New International Dictionary, Published for Encyclopedia Britannica, Inc. by William Benton, Chicago, IL, (1966).
- [67KIR] A.F. Kirstein, R.M. Woolley, "Symmetrical Bending of Thin Circular Elastic Plates on Equally Spaced Point Supports," *Journal of Research of the National Bureau of Standards-C. Engineering and Instrumentation*, 71C, [1], pp. 1-10, (1967).
- [67VAN] L.K.H. van Beek, Dielectric Behavior of Heterogeneous Systems, Chap. 3, Progress in Dielectrics, 7, Edited by J.B. Birks, CRC Press, Cleveland, OH, pp. 71-114, (1967).
- [68CUT] I.B. Cutler, R.E. Henrichsen, "Effect of Particle Shape on the Kinetics of Sintering of Glass," *J. Am. Cer. Soc.*, 51, [10], pp. 604-05, (1968).

- [68DEH] R.T. DeHoff, F.N. Rhines, Quantitative Microscopy, McGraw-Hill Book Company, New York, NY, (1968).
- [68LYK] J. Lyklema, "Principles of the Stability of Lyophobic Colloidal Dispersions in Non-Aqueous Media," Advances in Colloid and Interface Science, 2, pp. 65-114, (1968).
- [68SOH] H.Y. Sohn, C. Moreland, "The Effect of Particle Size Distribution on Packing Density," The Canadian Journal of Chemical Engineering, 46, pp. 162-67, (June, 1968).
- [68STO] W. Stober, A. Fink, E. Bohn, "Controlled Growth of Monodisperse Silica Spheres in the Micron Size Range," Journal of Colloid and Interface Science, 26, pp. 62-69, (1968).
- [69CUT1] I.B. Cutler, "Effect of Water Vapor on the Sintering of Glass Powder Compacts," J. Am. Cer. Soc., 52, [1], pp. 11-13, (1969).
- [69CUT2] I.B. Cutler, "Sintering of Glass Powders During Constant Rates of Heating," J. Am. Cer. Soc., 52, [1], pp. 14-16, (1969).
- [69SCO] G.D. Scott, D.M. Kilgour, "The Density of Random Close Packing of Spheres," Brit. J. Appl. Phys (J. Phys. D), Ser. 2, 2, pp. 863-66, (1969).
- [70KAR] K. Karlsson, L. Spring, "Packing of Irregular Particles," Journal of Materials, 5, pp. 340-44, (1970).
- [70LEE] D.I. Lee, "Packing of Spheres and Its Effect on the Viscosity of Suspensions," Journal of Paint Technology, 42, [550], pp. 579-87, (1970).
- [70PAP] Y.S. Papir, I.M. Krieger, "Rheological Studies on Dispersions of Uniform Colloidal Spheres, II: Dispersion in Nonaqueous Media," Journal of Colloid and Interface Science, 34, [1], pp. 126-30, (1970).
- [70SCH] H. Scher, R. Zallen, "Critical Density in Percolation Processes," J. Chem. Phys., 53, pp. 3759-61, (1970).
- [70WOO] M.E. Woods, I.M. Kreiger, "Rheological Studies of Uniform Colloidal Spheres, I: aqueous Dispersions in Steady Shear Flow," Journal of Colloid and Interface Science, 34, [1], pp. 91-99, (1970).
- [71BOR] R.K. Bordia, R. Raj, "Sintering of  $TiO_2$ - $Al_2O_3$  Composites: A Model Experimental Investigation," J. Am. Cer. Soc., 71, [4], pp. 302-10, (1988).
- [71RHI] F.N. Rhines, R.T. DeHoff, "A Topological Approach to the Study of Sintering," Modern Developments in Powder Metallurgy, 4, Processes, Edited by H.H. Hausner, Plenum, Press, New York, NY, pp. 173-88, (1971).
- [72KRI] I.M. Krieger, "Rheology of Monodisperse Latices," Advan. Colloid, Interface Sci., 3, pp. 111-36, (1972).

- [72WAC] J.B. Wachtman, Jr., W. Capps, J. Mandel, "Biaxial Flexure Tests of Ceramic Substrates," *Journal of Materials*, 7, pp. 188-94, (1972).
- [73COB] R.L. Coble, "Effects of Particle-Size Distribution in Initial-Stage Sintering," *J. Am. Cer. Soc.*, 56, [9], pp. 461-66, (1973).
- [73EXN] H.E. Exner, G. Petzow, P. Wellner, "Problems in the Extension of Sintering Theories to Real Systems," *Sintering and Related Phenomena*, Materials Science Research, 6, Edited by G.C. Kuczynski, Plenum Press, New York, NY, pp. 351-62, (1973).
- [73JOH] D.L. Johnson, "Interpretation of Sintering Kinetics Data," *Sintering and Related Phenomena*, Materials Science Research, 6, Edited by G.C. Kuczynski, Plenum Press, New York, NY, pp. 363-68, (1973).
- [73KIR] S. Kirkpatrick, "Percolation and Conduction," *Reviews of Modern Physics*, 45, [4], pp. 574-88, (1973).
- [73KUC] G.C. Kuczynski, "Pore Shrinkage and Ostwald Ripening," *Sintering and Related Phenomena*, Materials Science Research, 6, Edited by G.C. Kuczynski, Plenum Press, New York, NY, pp. 217-24, (1973).
- [73ORM] T.J. Ormiston, O.J. Whittemore, Jr., "Sintering of Silica Fiber Compacts," *Ceramic Bulletin*, 52, [3], pp. 247-54, (1973).
- [74DUN] B. Dunn, F. Chen, J.D. Mackenzie, "Preparation of Low Dielectric Constant Glasses," *J. Non. Cryst. Sol.*, 16, pp. 313-14, (1974).
- [74MEC] J.J. Mecholsky, R.W. Rice, S.W. Freiman, "Prediction of Fracture Energy and Flaw Size in Glasses from Measurements of Mirror Size," *J. Am. Cer. Soc.*, 57, [10], pp. 440-43, (1974).
- [75EXN] H.E. Exner, G. Petzow, "Shrinkage and Rearrangement During Sintering of Glass Spheres," *Sintering and Catalysis*, Edited by G.C. Kuczynski, Plenum Press, New York, NY, pp. 279-93, (1975).
- [76HAL] D.K. Hale, "Review: The Physical Properties of Composite Materials," *Journal of Materials Science*, 11, pp. 2105-41, (1976).
- [76KIN1] W.D. Kingery, H.K. Bowen, D.R. Uhlmann, *Introduction to Ceramics*, J. Wiley & Sons, New York, NY, (1976).
- [76KIN2] W.D. Kingery, B. Francois, "The Sintering of Crystalline Oxides, I. Interaction Between Grain Boundaries and Pores," *Sintering and Related Phenomena*, Edited by G.C. Kuczynski, N.A. Hooton, C.F. Gibbon, Gordon and Breach Science Publishers, Inc., New York, pp. 471-96, (1976).
- [76MEC] J.J. Mecholsky, Jr., R.W. Rice, G.W. Anderson, G.H. Sigel, Jr., "Effect of Sputtering on the Strength of Silicate Glasses," *Journal of Applied Physics*, 47, [7], pp. 2972-74, (1976).



- [77MAS] W.L. Masterson, Chemical Principles, W.B. Saunders Co., Philadelphia, PA, pp. 25-26, (1977).
- [77SCH1] G.W. Scherer, "Sintering of Low-Density Glasses: I, Theory," J. Am. Cer. Soc., 60, [5-6], pp. 236-39, (1977).
- [77SCH2] G.W. Scherer, D.L. Bachman, "Sintering of Low-Density Glasses: II, Experimental Study," J. Am. Cer. Soc., 60, [5-6], pp. 239-43, (1977).
- [77SCH3] G.W. Scherer, "Sintering of Low-Density Glasses: III, Effect of a Distribution of Pore Sizes," J. Am. Cer. Soc., 60, [5-6], pp. 243-46, (1977).
- [78MES1] G.L. Messing, G.Y. Onoda, Jr., "Inhomogeneity-Packing Density Relations in Binary Powders," J. Am. Cer. Soc., 61, [1-2], pp. 1-5, (1978).
- [78MES2] G.L. Messing, G.Y. Onoda, Jr., "Inhomogeneity-Packing Density Relations in Binary Powders-Experimental Studies," J. Am. Cer. Soc., 61, [7-8], pp. 363-66, (1978).
- [78NEW] R.E. Newnham, D.P. Skinner, L.E. Cross, "Connectivity and Piezoelectric-Pyroelectric Composites," Mat. Res. Bul., 13, [5], pp. 525-36, (1978).
- [78RAO] G.R. Rao, S.A. Kohktev, R.E. Loehman, "Electrical and Thermal Conductivity of Sialon Ceramics," Ceramic Bulletin, 57, [6], pp. 592-95, (1978).
- [78RYA1] B. Ryan, B. Tardy, Solid Spherical Fillers, Chap. 18, Handbook of Fillers and Reinforcements for Plastics, Edited by H.S. Katz, J.V. Milewski, Van Nostrand Reinhold, New York, NY, pp. 301-17, (1978).
- [78RYA2] B. Ryan B. Tardy, Hollow Spherical Fillers, Chap. 19, Handbook of Fillers and Reinforcements for Plastics, Edited by H.S. Katz and J.V. Milewski, Van Nostrand Reinhold, New York, NY, pp. 317-30, (1978).
- [79BOS] S. Boskovic, L.J. Gauckler, G. Petzow, T.Y. Tien, "Reaction Sintering of  $\beta$ - $\text{Si}_3\text{N}_4$  Solid Solution in the System Si,Al/N,O," Sintering Processes, Materials Science Research, 13, Edited by G.C. Kuczynski, Plenum Press, New York, NY, pp. 295-302, (1979).
- [79COR] Corning Glass Works, Inc., Materials for the Design Engineer: Properties of Corning's Glass and Glass Ceramic Families, Corning, NY, (December, 1979).
- [79FED] R.F. Fedors, R.F. Landel, "An Empirical Method of Estimating the Void Fraction in Mixtures of Uniform Particles of Different Size," Powder Technology, 23, pp. 225-231, (1979).
- [79HAU] H.H. Hausner, "Discussion on the Definition of the Term 'Sintering'," Sintering-New Developments, Materials Science Monographs, 4, Edited by M.M. Ristic, Elsevier Scientific Publishing Company, New York, NY, pp. 3-7, (1979).



- [79HEN] L.L. Hench, R.G. Newton, S. Bernstein, "Use of Infrared Reflection Spectroscopy in Analysis of Durability of Medieval Glasses, with Some Comments on Conservation Procedures," *Glass Technology*, 20, [4], pp. 144-48, (1979).
- [79KIP] Kiparisov S.S., Levinskiy, Y.V., "The Role of Gas in the Behaviour of a Closed Porosity Body," Sintering-New Developments, Materials Science Monographs, 4, Edited by M.M. Ristic, Elsevier Scientific Publishing Company, New York, NY, pp. 41-45, (1979).
- [79SBR] N.M. Sbrockey, D.L. Johnson, "Influence of Second Phase Particles to Retard Surface Smoothing and Sintering," Sintering Processes, Materials Science Research, 13, Edited by G.C. Kuczynski, Plenum Press, New York, NY, pp. 177-86, (1979).
- [79SIM] J.H. Simmons, P.B. Elterman, C.J. Simmons, R.K. Mohr, "Dielectric Relaxation in High-Silica Borosilicate Glasses," *J. Am. Cer. Soc.*, 62, [3-4], pp. 158-61, (1979).
- [79THU] F. Thummler, "Sintering and High Temperature Properties of  $\text{Si}_3\text{N}_4$  and  $\text{SiC}$ ," Sintering Processes, Materials Science Research, 13, Edited by G.C. Kuczynski, Plenum Press, New York, NY, pp. 247-77, (1979).
- [79USK] D. Uskokovic, V. Petrovic, M.M. Ristic, "Interdependence of the Porosity, Grain Size and Pore Size During Intermediate Stage of Sintering," Sintering Processes, Materials Science Research, 13, Edited by G.C. Kuczynski, Plenum Press, New York, NY, pp. 471-77, (1979).
- [79WHI] O.J. Whittemore, J.A. Varela, "The Initial Stages of Sintering," Sintering Processes, Materials Science Research, 13, Edited by G.C. Kuczynski, Plenum Press, New York, NY, pp. 51-60, (1979).
- [79ZAG] L. Zagar, "Theoretical Aspects of Sintering Glass Powders," Sintering-New Developments, Materials Science Monographs, 4, Edited by M.M. Ristic, Elsevier Scientific Publishing Company, New York, NY, pp. 57-64, (1979).
- [80PAT] A.N. Patankar, G. Mandal, "The Packing of Solid Particles: A Review," *Transactions of the Indian Ceramic Society*, 39, [4], pp. 109-19, (1980).
- [80SAC] M.D. Sacks, Sintering Behavior of Mullite-Containing Materials, Ph. D. Dissertation, University of California, Berkeley, (1980).
- [80SHA] M. Shahinpoor, "Statistical Mechanical Considerations on the Random Packing of Granular Materials," *Powder Technology*, 25, pp. 163-176, (1980).
- [80UGE] J. Ugelstad, P.C. Mork, "Swelling of Oligomer-Polymer Particles. New Methods of Preparation of Emulsions and Polymer Dispersions," *Advances in Colloid and Interface Science*, 13, pp. 101-40, (1980).

- [81ANS] G.R. Anstis, P. Chantikul, B.R. Lawn, D.B. Marshall, "A Critical Evaluation of Indentation Techniques for Measuring Fracture Toughness: I, Direct Crack Measurements," J. Am. Cer. Soc., 64, [9], pp. 533-38, (1981).
- [81BIS] D.R. Biswas, "Crack-Void Interaction in Polycrystalline Alumina," Journal of Materials Science, 16, pp. 2434-38, (1981).
- [81CHA] P. Chantikul, G.R. Anstis, B.R. Lawn, D.B. Marshall, "A Critical Evaluation of Indentation Techniques for Measuring Fracture Toughness: II, Strength Method," J. Am. Cer. Soc., 64, [9], pp. 539-43, (1981).
- [81FLI] R.A. Flinn, A.K. Trojan, "Chapter 3: Effects of Stress and Temperature, Engineering Materials and Their Applications, 2nd Ed., Houghton Mifflin Co., Boston, MA, pp. 79-82, (1981).
- [81GIL] P. Gillett, Calculus and Analytic Geometry, Chapter 11, "More About Limits," pp. 444-483, D.C. Heath and Company, Lexington, MA, (1981).
- [81HAN] K.W. Hang, J. Andrus, W.M. Anderson, "High-Temperature Porcelain-Coated-Steel Electronic Substrates-Composition and Properties," RCA Review, 42, pp. 159-77, (June, 1981).
- [81KIR] H.P. Kirchner, R.M. Gruver, M.V. Swain, R.C. Garvie, "Crack Branching in Transformation-Toughened Zirconia," J. Am. Cer. Soc., 64, [9], pp. 529-33, (1981).
- [81KRS] V.V. Krstic, P.S. Nicholson, R.G. Hoagland, "Toughening of Glasses by Metallic Particles," J. Am. Cer. Soc., 64, [9], pp. 499-504, (1981).
- [81MEC] J.J. Mecholsky, "Intergranular Slow Crack Growth in  $MgF_2$ ," J. Am. Cer. Soc., 64, [9], pp. 563-66, (1981).
- [81SCH] G. Schramm, Introduction to Practical Viscometry, Gebruder Haake GmbH, West Germany, (1981).
- [81SEI] M.A. Seitz, S.Y. Yang, "Thermal Conductivity of Ceramic Varistors," Advances in Ceramics, 7, The American Ceramic Society, Inc., Westerville, OH, pp. 438-44, (1981).
- [82AHM] M. Ahmadzadeh, A.W. Simpson, "Critical Concentrations for the Site Percolation in the Dense-Random-Packed Hard-Sphere Bernal Model," Physical Review B, 25, [7], pp. 4633-38, (1982).
- [82BLO] A.J. Blodgett, D.R. Barbour, "Thermal Conduction Module: A High-Performance Multilayer Ceramic Package," IBM Journal of Research and Development, 26, [1], pp. 30-36, (1982).
- [82CHA] N.C. Chao, "Duality in Three Dimensions," J. Phys. C: Solid State Phys., 15, pp. L1263-67, (1982).
- [82EVA] A.G. Evans, "Consideration of Inhomogeneity Effects in Sintering," J. Am. Cer. Soc., 65, [10], pp. 497-501, (1982).
- [82NIE] L.F. Nielsen, "Elastic Properties of Two Phase Materials," Materials Science and Engineering, 52, pp. 39-62, (1982).

- [82OVE] J.T.G. Overbeek, "Monodisperse Colloidal Systems, Fascinating and Useful," *Advances in Colloid and Interface Science*, 15, pp. 251-77, (1982).
- [83BAR] A. Bar-Cohen, W.M. Rohsenow, "Thermally Optimum Arrays of Cards and Fins in Natural Convection," *IEEE Transactions on Components, Hybrids, and Manufacturing Technology*, CHMT-6, [2], pp. 154-58, (1983).
- [83BER] H.M. Berg, D.L. Shealy, C.M. Mitchell, D.W. Stevenson, L.C. Lofgran, "Optical Computing in Fiber Optics Packages with Surface Emitting LEDs," *IEEE Transactions on Components, Hybrids, and Manufacturing Technology*, CHMT-6, [3], pp. 334-42, (1983).
- [83BLO] A. J. Blodgett, Jr., "Microelectronic Packaging," *Scientific American*, 249, pp. 86-96, (1983).
- [83DAV1] W.S. Davis, Computers and Business Information Processing, 2nd Ed., Addison-Wesley Publishing, Reading, MA, pp. 73-91, (1983).
- [83DAV2] E.E. Davidson, "Electrical Design of a High Speed Computer Packaging System," *IEEE Transactions on Components, Hybrids, and Manufacturing Technology*, CHMT-6, [3], pp. 272-82, (1983).
- [83DEA] E.A. Dean, J.A. Lopez, "Empirical Dependence of Elastic Moduli on Porosity for Ceramic Materials," *J. Am. Cer. Soc.*, 66, [5], pp. 366-70, (1983).
- [83DOU] W.E. Dougherty, S.E. Greer, "An Alternate Method of Fabricating Multilayer-Multichip Ceramic Substrates," *IEEE Transactions on Components, Hybrids, and Manufacturing Technology*, CHMT-6, [2], pp. 150-53, (1983).
- [83GHA] S.K. Ghandi, VLSI Fabrication Principles, Wiley and Sons, New York, NY, p. 1, (1983).
- [83HAL] P.M. Hall, T. D Dudderar, J.F. Argyle, "Thermal Deformations Observed in Leadless Ceramic Chip Carriers Surface Mounted to Printed Wiring Boards," *IEEE Transactions on Components, Hybrids, and Manufacturing Technology*, CHMT-6, [4], pp. 544-52, (1983).
- [83HSU] W.Y. Hsu, T.D. Gierke, C.J. Molnar, "Morphological Effects on the Physical Properties of Polymer Composites," *Macromolecules*, 16, [12], pp. 1945-47, (1983).
- [83JOH] D.W. Johnson, E.M. Rabinovich, J.B. MacChesney, E.M. Vogel, "Preparation of High-Silica Glasses from Colloidal Gels: II, Sintering," *J. Am. Cer. Soc.*, 66, [10], pp. 688-93, (1983).
- [83KOH] M. Kohara, S. Nakao, K. Tsutsumi, H. Shibata, H. Nakata, "High Thermal Conduction Package Technology for Flip Chip Devices," *IEEE Transactions on Components, Hybrids, and Manufacturing Technology*, CHMT-6, [3], pp. 267-71, (1983).

- [83MAH] L.M. Mahalingham, J.A. Andrews, J.E. Drye, "Thermal Studies on Pin Grid Array Packages for High Density LSI and VLSI Logic Circuits," IEEE Transactions on Composites, Hybrids, and Manufacturing Technology, CHMT-6, [3], pp. 246-56, (1983).
- [83POB] R.L. Pober, Ceramic Technology for Electronics, ISHM, Reston, VA, (1983).
- [83SCH] L.W. Schaper, D.I. Amey, "Improved Electrical Performance Required for Future MOS Packaging," IEEE Transactions on Components, Hybrids, and Manufacturing Technology, CHMT-6, [3], pp. 283-289, (1983).
- [83SHE] D.K. Shetty, A.R. Rosenfield, W.H. Duckworth, P.R. Held, "A Biaxial-Flexure Test for Evaluating Ceramic Strengths," J. Am. Cer. Soc., 66, [1], pp. 36-42, (1983).
- [83SHI] Y. Shimada, K. Utsumi, M. Suzuki, H. Takamizawa, M. Nitta, T. Watari, "Low Firing Temperature Multilayer Glass-Ceramic Substrate," IEEE Transactions on Components, Hybrids, and Manufacturing Technology, CHMT-6, [4], pp. 382-88, (1983).
- [83VEN] P.N. Venkatachalam, "Pulse Propagation Properties of Multilayer Ceramic Multichip Modules for VLSI Circuits," IEEE Transactions on Components, Hybrids, and Manufacturing Technology, CHMT-6, [4], pp. 480-84, (1983).
- [83WAL] D.L. Waller, L.R. Fox, R.J. Hannemann, "Analysis of Surface Mount Thermal and Thermal Stress Performance," IEEE Transactions on Components, Hybrids, and Manufacturing Technology, CHMT-6, [3], pp. 257-66, (1983).
- [83ZAL1] R. Zallen, Amorphous Morphology, Chap. 2, Section 2.4, The Physics of Amorphous Solids, J. Wiley and Sons, New York, NY, pp. 48-60, (1983).
- [83ZAL2] R. Zallen, The Percolation Model, Chap. 4, The Physics of Amorphous Solids, J. Wiley and Sons, New York, NY, pp. 135-204, (1983).
- [83ZIM] D.D. Zimmerman, D.H. Lewin, editor, The Fundamentals of Microjoining Processes, ISHM, Reston, VA, (1983).
- [84ANT] V.W. Antonetti, M. Yovanovich, "Thermal Contact Resistance in Microelectronic Equipment," Thermal Management Concepts in Microelectronic Packaging, Edited by S.S. Furkay, R.F. Kilburn, G. Monti, Jr., The International Society for Hybrid Microelectronics, Silver Spring, MD, pp. 135-51, (1984).
- [84BAR] J. Bartoszek, "Thermal Management in Small Systems," Thermal Management Concepts in Microelectronic Packaging, Edited by S.S. Furkay, R.F. Kilburn, G. Monti, Jr., The International Society for Hybrid Microelectronics, Silver Spring, MD, pp. 215-25, (1984).
- [84BIL] R.T. Bilson, M.R. Hephner, J.P. McCarthy, "The Impact of Surface Mounted Chip Carrier Packaging on Thermal Management in Hybrid Microcircuits," Thermal Management Concepts in Microelectronic Packaging, Edited by S.S. Furkay, R.F. Kilburn, G. Monti, Jr., The International Society for Hybrid Microelectronics, Silver Spring, MD, pp. 185-91, (1984).



- [84CAD] R.L. Cadenhead, Assuring the Integrity of Multilayer Substrates Prior to Assembly, ISHM, Reston, VA, (1984).
- [84CHU] R.C. Chu, R.E. Simons, "Thermal Management of Large Scale Digital Computers," Thermal Management Concepts in Microelectronic Packaging, Edited by S.S. Furkay, R.F. Kilburn, G. Monti, Jr., The International Society for Hybrid Microelectronics, Silver Spring, MD, pp. 193-214, (1984).
- [84DEH] R.T. DeHoff, "A Cell Model for Microstructural Evolution During Sintering," Sintering and Heterogenous Catalysis, Edited by G.C. Kuczynski, A.E. Miller, G.A. Sargent, Plenum Publishing Corp., pp. 23-34, (1984).
- [84DOM] H. Domingos, "Transient Temperature Rise in Microelectronic Components," Thermal Management Concepts in Microelectronic Packaging, Edited by S.S. Furkay, R.F. Kilburn, G. Monti, Jr., The International Society for Hybrid Microelectronics, Silver Spring, MD, pp. 67-82, (1984).
- [84FEN] S. Feng, P.N. Sen, "Percolation on Elastic Networks: New Exponent and Threshold," Phys. Rev. Letters, 52, [3], pp. 216-19, (1984).
- [84FUR] S.S. Furkay, "Convective Heat Transfer in Electronic Equipment: An Overview," Thermal Management Concepts in Microelectronic Packaging, Edited by S.S. Furkay, R.F. Kilburn, G. Monti, Jr., The International Society for Hybrid Microelectronics, Silver Spring, MD, pp. 153-71, (1984).
- [84MUS] B.H. Mussler, M.W. Shafer, "Preparation and Properties of Mullite-Cordierite Composites," Ceramic Bulletin, 63, [5], pp. 705-10, (1984).
- [84NOB] W.P. Noble, A.R. Ellenberger, "Temperature Effects on Device Functionality," Thermal Management Concepts in Microelectronic Packaging, Edited by S.S. Furkay, R.F. Kilburn, G. Monti, Jr., The International Society for Hybrid Microelectronics, Silver Spring, MD, pp. 45-65, (1984).
- [84PAT] B.R. Patterson, L.A. Benson, "The Effect of Powder Size Distribution on Sintering," Progress in Powder Metallurgy, 39, pp. 215-30, (1984).
- [84RAJ] R. Raj, R.K. Bordia, "Sintering Behavior of Bi-Modal Powder Compacts," Acta. Metall., 32, [7], pp. 1003-19, (1984).
- [84RIC] R.W. Rice, "Pores as Fracture Origins in Ceramics," Journal of Materials Science, 19, pp. 895-915, (1984).
- [84SAC1] M.D. Sacks, T.Y. Tseng, "Preparation of SiO<sub>2</sub> Glass from Model Powder Compacts: I, Formation and Characterization of Powders, Suspensions, and Green Compacts," J. Am. Cer. Soc., 67, [8], pp. 526-31, (1984).
- [84SAC2] M.D. Sacks, T.Y. Tseng, "Preparation of SiO<sub>2</sub> Glass from Model Powder Compacts: II, Sintering," J. Am. Cer. Soc., 67, [8], pp. 532-37, (1984).
- [84SCH1] G.W. Scherer, J.C. Luong, "Glasses from Colloids," Journal of Non-Crystalline Solids, 63, pp. 163-72, (1984).



- [84SCH2] G.W. Scherer, "Viscous Sintering of a Bimodal Pore-Size Distribution," J. Am. Cer. Soc., 67, [11], pp. 709-15, (1984).
- [84SCH3] B. Schwartz, "Microelectronics Packaging: II," Ceramic Bulletin, 63, [4], pp. 577-81, (1984).
- [84SCH4] B. Schwartz, "Review of Multilayer Ceramics for Microelectronic Packaging," J. Phys. Chem. Solids, 45, [10], 1051-68, (1984).
- [84SIM] E. Simiu, D.A. Reed, C.W.C. Yancey, J.W. Martin, E.M. Hendrickson, A.C. Gonzalez, M. Koike, J.A. Lechner, M.E. Batts, Ring-on-Ring Tests and Load Capacity of Cladding Glass, National Bureau of Standards Building Science Series 162, (August, 1984).
- [84SMI] J.P. Smith, G.L. Messing "Sintering of Bimodally Distributed Alumina Powders," J. Am. Cer. Soc., 67, [4], pp. 238-42, (1984).
- [84TAY] B.E. Taylor, R.R. Getty, J. Henderson, C.R.S. Needes, "Air and Nitrogen-Fireable Multilayer Systems: Materials and Performance Characteristics, Part II," Solid State Technology, pp. 291-95 (April, 1984).
- [84WAG1] A.J. Wagner, H.C. Cook, "Modeling the Temperature Dependence of Integrated Circuit Failures," Thermal Management Concepts in Microelectronic Packaging, Edited by S.S. Furkay, R.F. Kilburn, G. Monti, Jr., The International Society for Hybrid Microelectronics, Silver Spring, MD, pp. 1-43, (1984).
- [84WAG2] G.R. Wagner, "Circuit Board Material/Construction and its Effect on Thermal Management," Thermal Management Concepts in Microelectronic Packaging, Edited by S.S. Furkay, R.F. Kilburn, G. Monti, Jr., The International Society for Hybrid Microelectronics, Silver Spring, MD, pp. 173-84, (1984).
- [84WEB] Webster's Illustrated Dictionary Encyclopedia, Crescent Books, New York, NY, (1984).
- [85BAR] D.R. Barbour, "Multichip Module Technology," Advances in Ceramics, 19, The American Ceramic Society, Inc., Westerville, OH, pp. 15-30, (1985).
- [85BLA] J.R.H. Black, "Technology and Market Trends in Multilayer Ceramic Devices," Advances in Ceramics, 19, The American Ceramic Society, Inc., Westerville, OH, pp. 3-11, (1985).
- [85BOR] R.K. Bordia, R. Raj, "Sintering Behavior of Ceramic Films Constrained by Rigid Substrate," J. Am. Cer. Soc., 68, [6], pp. 287-92, (1985).
- [85BUG] A.L.R. Bug, S.A. Safran, G.S. Grest, I. Webman, "Do Interactions Raise or Lower a Percolation Threshold?" Physical Review Letters, 55, [18], pp. 1896-99, (1985).
- [85CAN] W.R. Cannon, J.R. Morris, K.R. Mikeska, "Dispersants for Nonaqueous Tape Casting," Advances in Ceramics, 19, The American Ceramic Society, Inc., Westerville, OH, pp. 161-74, (1985).

- [85CHI] Y.C. Chiew, G. Stell, E.D. Glandt, "Clustering and Percolation in Multicomponent Systems of Randomly Centered and Permeable Spheres," *J. Chem. Phys.*, 83, [2], pp. 761-67, (1985).
- [85FRE] S.W. Freiman, A.C. Gonzalez, "Electrical Failures Due to Cracks in Multilayer Ceramic Capacitors," Advances in Ceramics, 19, The American Ceramic Society, Inc., Westerville, OH, pp. 191-201, (1985).
- [85HOD] J.D. Hodge, "Densification and Microstructural Aspects of Mullite-Cordierite Ceramics," Advances in Ceramics, 19, The American Ceramic Society, Inc., Westerville, OH, pp. 117-29, (1985).
- [85HSU] W.Y. Hsu, T. Berzins, "Percolation and Effective-Medium Theories for Perfluorinated Ionomers and Polymer Composites," *Journal of Polymer Science: Polymer Physics Edition*, 23, pp. 933-53, (1985).
- [85KAH] M. Kahn, "Effects of Partial Oxygen Pressure During Burnout of Multilayer Structures," Advances in Ceramics, 19, The American Ceramic Society, Inc., Westerville, OH, pp. 185-88, (1985).
- [85KAW] K. Kawakami, M. Takabatake, T. Minowa, J. Chiba, M. Sasaki, "A Low-Temperature Cofired Multilayer Ceramic Substrate," Advances in Ceramics, 19, The American Ceramic Society, Inc., Westerville, OH, pp. 95-102, (1985).
- [85KON] K. Kondo, M. Okuyama, Y. Shibata, "Low Firing Temperature Ceramic Material for Multilayer Ceramic Substrates," Advances in Ceramics, 19, The American Ceramic Society, Inc., Westerville, OH, pp. 77-87, (1985).
- [85KUC] G.C. Kuczynski, "Towards the Understanding of the Process of Sintering," Sintering '85, Edited by G.C. Kuczynski, D.P. Uskokovic, H. Palmour III, M.M. Ristic, Plenum Press, New York, NY, pp. 3-16, (1985).
- [85LEE1] C.T. Lee, D.E. Clark, "Characterization of Glass Surfaces," *Applications of Surface Science*, pp. 397-412, (1985).
- [85LEE2] H.Y. Lee, L.C. Button, "Influence of Electrode-Ceramic Interface on MLC Leakage Current," Advances in Ceramics, 19, The American Ceramic Society, Inc., Westerville, OH, pp. 219-27, (1985).
- [85LOK] K.P. Lok, C.K. Ober, "Particle Size Control in Dispersion Polymerization of Polystyrene," *Can. J. Chem.*, 63, pp. 209-16, (1985).
- [85OGI] S. Ogihara, T. Yasuda, K. Otsuka, F. Kobayashi, "Application to LSI Packages of SiC Ceramics with High Thermal Conductivity," *The International Journal for Hybrid Microelectronics*, 8, [2], pp. 16-20, (1985).
- [85NEE] C.R.S. Needes, D.P. Button, "Reliability Testing of Thick Film Multilayer Materials," *Proceedings of the 35th Electronic Components Conference*, Washington, DC, IEEE, New York, NY, pp. 505-11, (1985).

- [85NIW] K. Niwa, N. Kamehara, H. Yokoyama, K. Yokouchi, K. Kurihara, "Multilayer Ceramic Circuit Board with Copper Conductor," Advances in Ceramics, 19, The American Ceramic Society, Inc., Westerville, OH, pp. 41-47, (1985).
- [85PAT] B.R. Patterson, V.D. Parkhe, J.A. Griffin, "Effect of Particle Size Distribution on Sintering," Sintering '85, Edited by G.C. Kuczynski, D.P. Uskokovic, H. Palmour III, M.M. Ristic, Plenum Press, New York, NY, pp. 43-51, (1985).
- [85RAB] E.M. Rabinovich, "Review: Preparation of Glass by Sintering," Journal of Materials Science, 20, pp. 4259-97, (1985).
- [85RIK] P.A. Rikvoid, G. Stell, "Porosity and Specific Surface for Inpenetrable-Sphere Models of Two-Phase Random Media," J. Chem. Phys., 82, [2], pp. 1014-20, (1985).
- [85SAC] M.D. Sacks, G.W. Scheiffele, "Polymer Adsorption and Particulate Dispersion in Nonaqueous Al<sub>2</sub>O<sub>3</sub> Suspensions Containing Poly(vinyl butyral) Resins," Advances in Ceramics, 19, The American Ceramic Society, Inc., Westerville, OH, pp. 175-84, (1985).
- [85SCH1] G.W. Scherer, "Sol-Gel-Glass: III. Viscous Sintering," Journal of Non-Crystalline Solids, 72, pp. 369-89, (1985).
- [85SCH2] G.W. Scherer, Relaxation in Glass and Composites, J. Wiley & Sons, New York, NY, (1985).
- [85SCH3] G.W. Scherer, T. Garino, "Viscous Sintering on a Rigid Substrate," J. Am. Cer. Soc., 68, [4], pp. 216-20 (1985).
- [85SCH4] B. Schwartz, "Multilayer Ceramics," Advances in Ceramics, 19, The American Ceramic Society, Inc., Westerville, OH, p. 13, (1985).
- [85SHA] D.J. Shanefield, "Competing Adsorptions in Tape Casting," Advances in Ceramics, 19, The American Ceramic Society, Inc., Westerville, OH, pp. 155-60, (1985).
- [85SIE] K. Sieradzki, "The Fracture Strength of Solids Near the Percolation Threshold," J. Phys. C: Solid State Phys., 18, pp. L855-56, (1985).
- [85STA] D. Stauffer, Introduction to Percolation Theory, Taylor and Francis, Inc., Philadelphia, PA, (1985).
- [85STE] J.I. Steinberg, S.J. Horowitz, R.J. Bacher, "Low-Temperature Cofired Tape Dielectric Material Systems for Multilayer Interconnections," Advances in Ceramics, 19, The American Ceramic Society, Inc., Westerville, OH, pp. 31-39, (1985).
- [85VER] H. Verweij, G. De, D. Veeneman, "Hollow Glass Microsphere Composites: Preparation and Properties," Journal of Materials Science, 20, pp. 1069-78, (1985).
- [85WEA] R.C. Weast, editor, CRC Handbook of Chemistry and Physics, 66, CRC Press, Boca Raton, FL, (1985-86).
- [85WEB] J. Weber, Tomorrow's World: Computers, The Next Generation, ARCO Publishing, Inc., New York, NY, (1985).

- [86BLE] P. Bless, L. Ugol, C. Huang, S.J. Stein, "Reliable Multilayer Thick Films Made with Low Impedance Ag-Based Conductors," Proceedings of the 19th International Symposium on Microelectronics, Atlanta, GA, ISHM, Reston, VA, pp. 450-60, (1986).
- [86BUC] R.C. Buchanan, C.V. Beck, "Glass Films and Interfaces in Microelectronic Applications," Mat. Res. Soc. Symp. Proc., 72, pp. 41-45, (1986).
- [86CHA] G.V. Chandrashekar, M.W. Shafer, "Dielectric Properties of Sol-Gel Silica Glasses," Mat. Res. Soc. Symp., pp. 705-10, (1986).
- [86CRO] L.E. Cross, T.R. Gururaja, "Ultra-Low Dielectric Permittivity Ceramics and Composites for Packaging Applications," Mat. Res. Soc. Symp. Proc., 72, pp. 53-65, (1986).
- [86DAS] A. Das, R. Messier, T.R. Gururaja, L.E. Cross, "Low Permittivity, SiO<sub>2</sub>/Void Nanocomposite Films," Mat. Res. Soc. Proc., 72, pp. 27-33, (1986).
- [86DEJ] L.C. DeJonge, M.N. Rahaman, C.H. Hsueh, "Transient Stresses in Bimodal Compacts During Sintering," Acta. Metall., 34, [7], pp 1467-71, (1986).
- [86GEN] G. Gensse, U. Chowdry, "Non-Conventional Route to Glass-Ceramics for Electronic Packaging," Mat. Res. Soc. Symp., 73, pp. 693-703, (1986).
- [86HAM] Y. Hamano, M. Terasawa, "Advanced Packaging for High Integration and High Speed Applications," Mat. Res. Soc. Symp. Proc., 72, pp. 3-13, (1986).
- [86HSU1] C.H. Hsueh, A.G. Evans, R.M. Cannon, R.J. Brook, "Viscoelastic Stresses and Sintering Damage in Heterogeneous Powder Compacts," Acta. Metall., 34, [5], pp. 927-36, (1986).
- [86HSU2] C.H. Hsueh, A.G. Evans, R.M. McMeeking, "Influence of Multiple Heterogeneities on Sintering Rates," J. Am. Cer. Soc., 69, [4], pp. C-64-C-66, (1986).
- [86IWA] Y. Iwata, S. Saito, Y. Satoh, F. Okamura, "Development of Ceramic-Composite (Porous-Ceramic & Resin Composite with Copper Foil)," IMC 1986 Proceedings, Kobe, Japan, pp. 65-70, (1986).
- [86KAH] M. Kahn, B. Kriese, "Patterned Macrovoids for Dielectric Constant Control of High Frequency Circuit Substrates," Mat. Res. Soc. Symp. Proc., 72, pp. 35-40, (1986).
- [86KHA] A.K. Khaund, C.L. Cutts, "Defect Free Al<sub>2</sub>O<sub>3</sub> Substrates for Thin Film Applications," Proceedings of the 19th International Symposium on Microelectronics, Atlanta, GA, ISHM, Reston, VA, pp. 209-16, (1986).
- [86LAN] A. Lane, N. Shah, W.C. Conner, Jr., "Measurement of the Morphology of High-Surface-Area Solids: Porosimetry as a Percolation Process," Journal of Colloid and Interface Science, 109, [1], pp. 235-42, (1986).



- [86LEV] R.A. Levy, K. Nassau, "Viscous Behavior of Phosphosilicate and Borophosphosilicate Glasses in VLSI Processing," Solid State Technology, pp. 123-30, (October, 1986).
- [86MAC] R.B. Maciolek, "Packaging Very High I/O Chips with Tab/Solder Reflow Technology, Electronic Packaging: Materials and Processes, Edited by J.A. Sartell, ASM International, Metals Park, OH, pp. 15-18, (1986).
- [86NIS] S. Nishigaki, J. Fukuta, S. Yano, H. Kawabe, K. Noda, M. Fukaya, "A New Low Temperature Fireable Ag Multilayer Ceramic Substrate Having Post-Fired Cu Conductor (LFC-2), Proceedings of the 19th International Symposium on Microelectronics, Atlanta, GA, ISHM, Reston, VA, pp. 429-49, (1986).
- [86PON] R. G. Pond, C.J. Sabo, W.A. Vitriol, R.L. Brown, "Processing and Reliability of Resistors Incorporated within Low Temperature Cofired Ceramic Structures," Proceedings of the 19th International Symposium on Microelectronics, Atlanta, GA, ISHM, Reston, VA, pp. 461-72, (1986).
- [86RAH1] M.N. Rahaman, L.C. DeJonghe, R.J. Brooke, "Effect of Shear Stress on Sintering," J. Am. Cer. Soc., 69, [1], pp. 53-58, (1986).
- [86RAH2] M.N. Rahaman, L.C. DeJonghe, C.H. Hsueh, "Creep During Sintering of Porous Compacts," J. Am. Cer. Soc., 69, [1], pp. 58-60, (1986).
- [86RAO] M.K. Rao, K.Y. Chua, S.L. Lim, "Effects of Infra-Red Firing on the Properties of Low-K Thick Film Dielectric Compositions," Proceedings of the 19th International Symposium on Microelectronics, Atlanta, GA, ISHM, Reston, VA, pp. 119-23, (1986).
- [86SAT] T. Satoh, K. Akiyama, Y. Fujita, N. Ebina, Y. Fukuda, "Properties of Copper Plated Metal Core Ceramic Substrates," Proceedings of the 19th International Symposium on Microelectronics," Atlanta, GA, ISHM, Reston, VA, pp. 203-07, (1987).
- [86SAW] H.T. Sawhill, A.L. Eustice, S.J. Horowitz, J. Gar-El, A.R. Travis, "Low Temperature Co-Fireable Ceramics with Co-Fired Resistors," Proceedings of the 19th International Symposium on Microelectronics, Atlanta, GA, ISHM, Reston, VA, pp. 473-80, (1986).
- [86SCH1] G.W. Scherer, "Viscous Sintering Under a Uniaxial Load," J. Am. Cer. Soc., 69, [9], pp. C-206-C-207, (1986).
- [86SCH2] G.W. Scherer, Relaxation in Glass and Composites, Wiley & Sons, New York, NY, (1986).
- [86SMI] L.H. Smith, "Hollow Microspheres: More Than Just Fillers," Materials Engineering, 103, pp. 27-30, (February, 1986).
- [86TEA] W.H. Teat, B.L. Marten, D.C. Blazej, R. Oboodi, "Properties of a New Selective Ceramic-Coated Metal Substrate," Proceedings of the 19th International Symposium on Microelectronics, Atlanta, GA, ISHM, Reston, VA, pp. 196-202, (1986).



- [86THO] S.C. Thorstenson, "Compatible Substrates for Surface Mounting Technology-A PWB Industry Review," Electronic Packaging: Materials and Processes, ASM International, Metals Park, OH, pp. 1-7, (1986).
- [86TSE1] C.M. Tseng, Y.Y. Lu, M.S. El-Aasser, J.W. Vanderhoff, "Uniform Polymer Particles by Dispersion Polymerization in Alcohol," *Journal of Polymer Science: Part A: Polymer Chemistry Edition*, 24, pp. 2995-3007, (1986).
- [86TSE2] T.Y. Tseng, J.J. Yu, "Various Atmospheric Effects on Sintering of Compacts of SiO<sub>2</sub> Microspheres," *Journal of Materials Science*, 21, pp. 3615-3624, (1986).
- [86UTS] K. Utsumi, Y. Shimada, H. Takamizawa, "Monolithic Multicomponents Ceramic (MMC) Substrate," *Mat. Res. Soc. Symp. Proc.*, 72, pp. 15-26, (1986).
- [86VEN] K. R. Venkatachari, R. Raj, "Shear Deformation and Densification of Powder Compacts," *J. Am. Cer. Soc.*, 69, [6], pp. 499-506, (1986).
- [86VES] G.M. Vest, V.P. Cone, C.J. Herzfeld, A.K. Bansali, "Metallo-Organic Decomposition (MOD) Films for Electronic Packaging," *Mat. Res. Soc. Symp. Proc.*, 72, pp. 47-52, (1986).
- [86YAN] M. Yanuka, F.A.L. Dullien, D.E. Elrick, "Percolation Processes and Porous Media, I: Geometrical and Topological Model of Porous Media Using a Three-Dimensional Joint Pore Size Distribution," *Journal of Colloid and Interface Science*, 112, [1], pp. 24-41, (1986).
- [87ALF] N.M. Alford, J.D. Birchall, K. Kendall, "High-Strength Ceramics through Colloidal Control to Remove Defects," *Nature*, 330, [5], 51-53, (1987).
- [87BAN1] H. Banno, "Effects of Shape and Volume Fraction of Closed Pores on Dielectric, Elastic, and Electromechanical Properties of Dielectric and Piezoelectric Ceramics-A Theoretical Approach," *Ceramic Bulletin*, 66, [9], pp. 1332-37, (1987).
- [87BAN2] L.B. Bangs, Uniform Latex Particles, Seragen Diagnostics, Inc., Indianapolis, IN, (1987).
- [87BEL] F.J. Belcourt, "Electrical Issues Associated with High Density Packaging," Electronic Packaging and Corrosion in Microelectronics, Edited by M.E. Nicholson, ASM International, Metals Park OH, pp. 71-77, (1987).
- [87BEN] L. Benguigui, J. Yacubowicz, M. Narkis, "On the Percolative Behavior of Carbon Black Cross-Linked Polyethylene Systems," *Journal of Polymer Science: Part B: Polymer Physics*, 25, pp. 127-35, (1987).
- [87BER] K.A. Berry, "Corrosion Resistance of Military Microelectronic Packages at the Lead-Glass Interface," Electronic Packaging and Corrosion in Microelectronics, Edited by M.E. Nicholson, ASM International, Metals Park, OH, pp. 55-61, (1987).

- [87CAH] D.G. Cahill, R.O. Pohl, "Thermal Conductivity of Amorphous Solids above the Plateau," *Physical Review B*, 35, [8], pp. 4067-73, (1987).
- [87CHO] U. Chowdry, A.W. Sleight, "Ceramic Substrates for Microelectronic Packaging," *Ann. Rev. Mater. Sci.*, 17, pp. 323-40, (1987).
- [87CLA] R. Clasen, "Preparation and Sintering of High-Density Green Bodies to High-Purity Silica Glasses," *Journal of Non-Crystalline Solids*, 89, pp. 335-44, (1987).
- [87COR1] M. Corke, K. Sweeney, R. Prater, J. Muhs, K. Schmidt, "Fiber Optic Components for Communications Applications," *Proceedings of the 37th Electronic Components Conference*, Boston, MA, IEEE, New York, NY, pp. 243-53, (1987).
- [87COR2] M. Corke, P. Akhavan-Leilabady, "Fiber Optic Components For Sensor Applications," *Proceedings of the 37th Electronic Components Conference*, Boston, MA, IEEE, New York, NY, pp. 254-64, (1987).
- [87DET] E.S. Dettmer, H.K. Charles, Jr., "Fundamental Characterization of Aluminum Nitride and Silicon Carbide for Hybrid Substrate Applications," *The International Journal for Hybrid Microelectronics*, 10, [2], pp. 9-17, (1987).
- [87FOS] E.M. Foster, "The Electrical Effect of Single-Chip CMOS Packages," *Proceedings of the 37th Electronic Components Conference*, Boston, MA, IEEE, New York, NY, pp. 342-53, (1987).
- [87FRA] R.P. Frankenthal, "Corrosion in Microelectronics Current Status and Future Directions," Electronic Packaging and Corrosion in Microelectronics, Edited by M.E. Nicholson, ASM International, Metals Park, OH, pp. 295-96, (1987).
- [87GEH] R.W. Gehman, "Materials Selection for Failure Prevention in Hybrids," Electronic Packaging and Corrosion in Microelectronics, Edited by M.E. Nicholson, ASM International, Metals Park, OH, pp. 103-10, (1987).
- [87IWA1] N. Iwase, T. Yanazawa, M. Nakahashi, K. Shinozaki, A. Tsuge, K. Anzai, "Aluminum Nitride Multilayer Pin Grid Array Packages," *Proceedings of the 37th Electronic Components Conference*, Boston, MA, IEEE, New York, NY, pp. 384-91, (1987).
- [87IWA2] Y. Iwata, S. Saito, "New Ceramic and Plastic Composite Substrate for Face Down Bonding & Large Silicon Chip Mounting," *Proceedings of the 37th Electronic Components Conference*, Boston, MA, IEEE, New York, NY, pp. 392-97, (1987).
- [87JIN] S. Jinsheng, C. Shanxiang, "A New Type of Optical and Electric Hybrid Switch," *Proceedings of the 37th Electronic Components Conference*, Boston, MA, IEEE, New York, NY, pp. 265-68, (1987).

- [87KEL] D.W. Kellerman, "The Development and Characterization of a Low Dielectric Constant Thick Film Material," Proceedings of the 37th Electronic Components Conference, Boston, MA, IEEE, New York, NY, pp. 316-27, (1987).
- [87KIN] K.R. Kinsman, "Integrated Circuit Packaging-A Materials Microcosm," Electronic Packaging and Corrosion in Microelectronics, Edited by M.E. Nicholson, ASM International, Metals Park OH, pp. 1-10, (1987).
- [87KUR] Y. Kurokawa, H. Hamaguchi, Y. Shimada, K. Utsumi, H. Takamizawa, "Highly Thermal Conductive Aluminum Nitride Substrates," Proceedings of the 20th International Symposium on Microelectronics, Minneapolis, MN, ISHM, Reston, VA, pp. 654-61, (1987).
- [87LIN] E. Liniger, R. Raj, "Packing and Sintering of Two-Dimensional Structures Made from Bimodal Particle Size Distributions," J. Am. Cer. Soc., 70, [11], pp. 843-49, (1987).
- [87MOH] U. Mohideen, T.R. Gururaja, L.E. Cross, W. Yarbrough, A. Das, J. Yamamoto, R. Roy, "Ultra-Low Dielectric Permittivity Ceramics and Composites for High Speed IC Packaging Applications," Proceedings of the 37th Electronic Components Conference, Boston, MA, IEEE, New York, NY, pp. 406-12, (1987).
- [87NIS] S. Nishigaki, S. Yano, H. Kawabe, J. Fukuta, T. Nonomura, S. Hebishima, "LFC-III: A New Low Temperature Multilayered Ceramic Substrate with Au(top)-Ag(internal)-Ti/Mo/Cu(bottom) Conductor System," Proceedings of the 20th International Symposium on Microelectronics, Minneapolis, MN, ISHM, Reston, VA, pp. 400-07 (1987).
- [87OKA] H. Okamura, T. Fukuba, Y. Fujita, "The High Thermal Conductive Ceramic Coated Substrate," Proceedings of the 20th International Symposium on Microelectronics, Minneapolis, Minn., ISHM, Reston, VA, p. 386-99, (1987).
- [87POR] G. Poreux, P.C., "Transport in Heterogeneous Porous Media," Physica Scripta, T19, pp. 524-30, (1987).
- [87RAH1] M.N. Rahaman, L.C. DeJonghe, "Effect of Rigid Inclusions on the Sintering of Glass Powder Compacts," J. Am. Cer. Soc., 70, [12], pp. C-348-C-351, (1987).
- [87RAH2] M.H. Rahaman, L.C. DeJonghe, G.W. Scherer, R.J. Brook, "Creep and Densification During Sintering of Glass Powder Compacts," J. Am. Cer. Soc., 70, [10], pp. 766-74, (1987).
- [87RAJ] R. Raj, "Analysis of the Sintering Pressure," J. Am. Cer. Soc., 70, [9], pp. C-210-C-211, (1987).
- [87RIC] E.L. Rich, III, S.K. Suko, A.J. Martin, B.H. Smith, D.G. Onn, A.J. Whittaker, R.E. Giedd, "Thermal Management Considerations for a Low-Temperature, Co-Fireable Ceramic System," Proceedings of the 20th International Symposium on Microelectronics, Minneapolis, MN, ISHM, Reston, VA, pp. 408-18, (1987).

- [87ROM] B.M. Romensko, G.V Clatterbaugh, H.K. Charles, Jr., "Design, Fabrication and Performance Testing of Large Area Multilevel Thick Film Surface Mount Assemblies," Proceedings of the 37th Electronic Components Conference, Boston, MA, IEEE, New York, NY, pp. 269-81, (1987).
- [87RUS] L.M. Russell, L.F. Johnson, D.P.H. Hasselman, "Thermal Conductivity/Diffusivity of Silicon Carbide Whisker Reinforced Mullite," J. Am. Cer. Soc., 70, [10], pp. C-226-C-229, (1987).
- [87SCH1] M. Scheinfein, J. Prince, "Electrical Performance of Integrated Circuit Packages: Three Dimensional Structures," Proceedings of the 37th Electronic Components Conference, Boston, MA, IEEE, New York, NY, pp. 377-83, (1987).
- [87SCH2] M.A. Schmitt, B.K. Bhattacharyya, "Electrical Characterization of a Multilayer Ceramic Pin Grid Array Package," Proceedings of the 37th Electronic Components Conference, Boston, MA, IEEE, New York, NY, pp. 370-76, (1987).
- [87SCH3] G. W. Scherer, "Sintering With Rigid Inclusions," J. Am. Cer. Soc., 70, [10], pp. 719-25, (1987).
- [87SEN] R. Senthinathan, J. Prince, M. Scheinfein, "Characteristics of Coupled, Buried Microstrip Lines by Modelling and Simulation," Proceedings of the 37th Electronic Components Conference, Boston, MA, IEEE, New York, NY, pp. 362-69, (1987).
- [87SHI] Y. Shimada, Y. Yamashita, Y. Shiozawa, M. Suzuki, H. Takamizawa, "Low Dielectric Constant Multilayer Glass-Ceramic Substrate with Ag-Pd Wiring for VLSI Package," Proceedings of the 37th Electronics Component Conference, Boston, MA, IEEE, New York, NY, pp. 398-405, (1987).
- [87SHU] V.N. Shukla, P. Hingorany, A. Amin, "CERCIC-A Hybrid Substrate," Proceedings of the 20th International Symposium on Microelectronics, Minneapolis, MN, ISHM, Reston, VA, pp. 392-99, (1987).
- [87THO] R.G. Thompson, D.L. Shealy, H.T. Tohver, "Compatibility Studies in Metal-Cordierite Systems For Electronic Packaging," Proceedings of the 37th Electronic Components Conference, Boston, MA, IEEE, New York, NY, pp. 420-26, (1987).
- [87YAR] W.A. Yarbrough, T.R. Gururaja, L.E. Cross, "Materials for IC Packaging with Very Low Permittivity via Colloidal Processing," Ceramic Bulletin, 66, [4], pp. 692-98, (1987).
- [87WHI] H.S. White, "Corrosion Principles in Microelectronics," Electronic Packaging and Corrosion in Microelectronics, Edited by M.E. Nicholson, ASM International, Metals Park, OH, pp. 33-34, (1987).
- [87ZHD] V.P. Zhdanov, V.B. Fenelonov, D.K. Efremov, "Determination of Pore-Size Distribution from Sorption Isotherms: Application of Percolation Theory," Journal of Colloid and Interface Science, 120, [1], pp. 218-23, (1987).



- [88ANG] G. Angenieux, J. Chillo, "Dynamic Behavior of Interconnection Lines in Wafer Scale Integration Circuits," Proceedings of the 21st International Symposium on Microelectronics, Seattle, WA, ISHM, Reston, VA, pp. 498-504, (1988).
- [88ARI] H. Arikawa, S. Hanada, T. Yokoi, T. Sekino, "Low Thermal Resistance Hybrid IC Package," Proceedings of the 21st International Symposium on Microelectronics, Seattle, WA, ISHM, Reston, VA, pp. 160-63, (1987).
- [88ANZ] K. Anzai, T. Takahashi, T. Yasumoto and N. Iwase, "Thin Film Metallization on AlN Substrate," Paper No. 31-E-88, Annual National Convention of The American Ceramic Society, Cincinnati, OH, (1988).
- [88BAB1] K. Baba, N. Shohata and M. Yonezawa, "Preparation and Properties of Ultrafine AlN Powder by RF Plasma," Paper No. 27-E-88, Annual National Convention of The American Ceramic Society, Cincinnati, OH, (1988).
- [88BAB2] Y. Baba, K. Higashiyama, S. Segawa, "Co-Fireable Copper Multilayer Ceramic Substrates," Proceedings of the 21st International Symposium on Microelectronics, Seattle, WA, ISHM, Reston, VA, pp. 405-13, (1988).
- [88BAL] J.W. Balde, "Small Dimensions or Low Dielectric Constant: The Competing Approaches to High Density Interconnect," Mat. Res. Soc. Symp. Proc., 108, pp. 61-71, (1988).
- [88BEN] M.F. Bender, F.K. Patterson, E.A. Kemp, J.E. Gantzhorn, Jr., "Low Temperature Cofired Ceramic Tape System: A Cost Effective Solution for Multilayer Packaging," Proceedings of the 21st International Symposium on Microelectronics, Seattle, WA, ISHM, Reston, VA, pp. 12-24, (1988).
- [88BIR] D.P. Birnie, III, "The Effect of an Intergranular Liquid Phase on Thermal Conduction in Aluminum Nitride," Paper No. 30-E-88, Annual National Convention of The American Ceramic Society, Cincinnati, OH, (1988).
- [88BOR1] R.K. Bordia, G.W. Scherer, "On Constrained Sintering-I. Constitutive Model for a Sintering Body," Acta. Metall., 36, [9], pp. 2393-97, (1988).
- [88BOR2] R.K. Bordia, G.W. Scherer, "On Constrained Sintering-II. Comparison of Constitutive Models," Act. Metall., 36, [9], pp. 2399-409, (1988).
- [88BOR3] R.K. Bordia, G.W. Scherer, "On Constrained Sintering-III. Rigid Inclusions," Acta. Metall., 36, [9], pp. 2411-16, (1988).
- [88BOR4] R.K. Bordia, R. Raj, "Sintering of  $\text{TiO}_2\text{-Al}_2\text{O}_3$  Composites: A Model Experimental Investigation," J. Am. Cer. Soc., 71, [4], pp. 302-10, (1988).
- [88BOR5] W. Borland, V.P. Suita, "Materials Interactions in the Firing of Copper Thick Film Multilayer Ceramics," Mat. Res. Soc. Symp. Proc., 108, pp. 287-300, (1988).



- [88CAO] W. Cao, R. Gerhardt and J.B. Wachtman, Jr., "Effects of Alkali Ions and Water Adsorption on the Dielectric Properties of Bulk Porous Silica by a Colloidal Processing Method," Paper No. 21-E-88, Annual National Convention of The American Ceramic Society, Cincinnati, OH, (1988).
- [88CAR] G. Carruth, E. Ehrlich, editors, The Harper Book of American Quotations, Harper & Row, New York, NY, 84.8, (1988).
- [88CER] E.W. Smothers, editor, Ceramic Source '88, The American Ceramic Society, Inc., Westerville, OH, p. 198, (1988).
- [88CLA] S. Clark and R. Gerhardt, "Glass: Boron Nitride Composites for Electronic Substrate Applications," Paper No. 94-E-88, Annual National Convention of The American Ceramic Society, Cincinnati, OH, (1988).
- [88COR] Corning Glass Works, Inc., Materials Information, MI-7070-88, Materials Business, Corning, NY, (1988).
- [88COW] C. Cowen, M.Y. Xu, H. Jain and M.R. Notis, "Structure and Dielectric Behavior of Composite Oxide Ceramics," Paper No. 37-E-88, Annual National Convention of The American Ceramic Society, Cincinnati, OH, (1988).
- [88DET] E.S. Dettmer, H.K. Charles, Jr., S.J. Mobley, B.M. Romanesko, "Hybrid Design and Processing Using Aluminum Nitride Substrates," Proceedings of the 21st International Symposium on Microelectronics, Seattle, WA, ISHM, Reston, VA, pp. 545-53, (1988).
- [88DIN] R.K. Dinsmore, "MIL-H-38534: Military Specifications for Hybrid Microcircuits," Proceedings of the 21st International Symposium on Microelectronics, Seattle, WA, ISHM, Reston, VA, pp. 475-79, (1988).
- [88ECK] C. Eckert, K. Chan and D. Bausback, "Business Assessment of Electronic Ceramics," Paper No. 34-E-88, Annual National Convention of The American Ceramic Society, Cincinnati, OH, (1988).
- [88EWS1] K.G. Ewsuk, L.W. Harrison and F.J. Walczak, "Thermal Conductivity of Glass-Filled Ceramic Composites," Paper No. 39-E-88, Annual National Convention of The American Ceramic Society, Cincinnati, OH, (1988).
- [88EWS2] K. Ewsuk, "High Frequency Dielectric Properties of Pure and Magnesia-Doped, Polycrystalline Alumina," Paper No. 118-E-88, Annual National Convention of The American Ceramic Society, Cincinnati, OH, (1988).
- [88FAR] W.E. Farneth, R.H. Staley, T. Budzichowski, "Reaction Mechanisms in Organic Binder Removal During Ceramic Processing: PMMA/Cordierite as a Prototype System," Mat. Res. Soc. Symp. Proc., 108, pp. 95-99, (1988).
- [88FRE] R.H. French, D.J. Jones, W.Y. Hsu, B.A. Yost and M.A. Subramanian, "Percolation Effects in the Dielectric Properties of Polymer Ceramic Composite Systems," Paper No. 88-E-88, Annual National Convention of The American Ceramic Society, Cincinnati, OH, (1988).

- [88FUN] J.E. Funk, D.R. Dinger, "Slip Control Using Particle-Size Analysis and Specific Surface Area," *Ceramic Bulletin*, 67, [5], pp. 890-94, (1988).
- [88GER1] R. Gerhardt, "Influence of Geometric Factors on Dielectric Constant," Paper No. 69-E-88, Annual National Convention of The American Ceramic Society, Cincinnati, OH, (1988).
- [88GER2] R. Gerhardt, "Composites for Electronic Substrate Applications," *Mat. Res. Soc. Symp. Proc.*, 108, pp. 101-06, (1988).
- [88GER3] F.J. German, B. Dillard, L. S. Riggs, R.W. Johnson, "Transmission Line Matrix Method for Modelling the Electrical Performance of Interconnections," *Proceedings of the 21st International Symposium on Microelectronics*, Seattle, WA, ISHM, Reston, VA, pp. 492-97, (1988).
- [88GIL] B.K. Gilbert, G.W. Pan, "The Application of Gallium Arsenide Integrated Circuit Technology to the Design and Fabrication of Future Generation Digital Signal Processors, Promises and Problems," *Proceedings of the IEEE*, 76, [7], pp. 816-34, (1988).
- [88GJE] P. Gjerde, W.D. Scott, "Binder Burnout in Multilayer Capacitors," *Proceedings of the 21st International Symposium on Microelectronics*, Seattle, WA, ISHM, Reston, VA, pp. 79-83, (1988).
- [88GLA] W.R. Glave, L.J. Hagerty, J.D. Grier, Sr., R.E. Park, Jr., "Characterization of Nitrogen Furnace Atmospheres in Copper Thick Film Multilayer Ceramic Board Manufacturing," Advances in Ceramics, 26, The American Ceramic Society, Inc., Westerville, OH, pp. 414-20, (1989).
- [88HAE] C. Haertling, S. Yoshikawa and R. Newnham, "Patterned Ceramics Through Ultraviolet Curable Pastes," Paper No. 48-EP-88, Annual National Convention of The American Ceramic Society, Cincinnati, OH, (1988).
- [88HAM] M. Hama, W.Y. Shih, R. Kikuchi and I.A. Aksay, "Low Temperature (1250°C) Sintering of High Purity  $\alpha$ -Al<sub>2</sub>O<sub>3</sub>," Paper No. 18-E-88, Annual National Convention of The American Ceramic Society, Cincinnati, OH, (1988).
- [88HAY] K. Hayashi, M. Sugie, and T. Hirao, "CVD-Silicon Nitride with High Thermal Conductivity," Paper No. 33-E-88, Annual National Convention of The American Ceramic Society, Cincinnati, OH, (1988).
- [88HIR] S. Hirano, K. Ibata, T. Toyosawa, K. Togawa, "Three-Dimensional Thermal Conduction Analysis on Thick Film Thermal Head Using Finite Element Method," *Proceedings of the 21st International Symposium on Microelectronics*, Seattle, WA, ISHM, Reston, VA, pp. 480-84, (1988).
- [88HOF] L. Hoffman, "Crystallizable Dielectrics in Multilayer Structures for Hybrid Circuits," Paper No. 36-E-88, Annual National Convention of The American Ceramic Society, Cincinnati, OH, (1988).

- [88HON] S. Hong, J.C. Bravman, T.P. Weihs, O.K. Kwon, "Materials and Structures for High Density I/O Interconnection Systems," Mat. Res. Soc. Symp. Proc., 108, pp. 309-17, (1988).
- [88HUT] L.D. Hutcheson, "Integrated Optoelectronic Materials and Circuits for Optical Interconnects," Mat. Res. Soc. Symp. Proc., 108, pp. 407-18, (1988).
- [88IBR] A.M. Ibrahim, "Surface Mount Technology (SMT) Substrate Material Requirements- A Brief Review," Mat. Res. Soc. Symp. Proc., 108, pp. 159-68, (1988).
- [88ISH] J. Ishigama, T. Kubota, S. Sekihara, K. Fujimara, "Technological Advances of Thick Film Resistors for Aluminum Nitride Substrates with New Conductive Compositions," Proceedings of the 21st International Symposium on Microelectronics, Seattle, WA, ISHM, Reston, VA, pp. 149-57, (1988).
- [88IYE] L. Iyengar, Y. Berta and V.R.W. Amarakoon, "Dense-Homogeneous Ceramics at Low Temperature via Sol-Gel Coating of Powders," Paper No. 22-E-88, Annual National Convention of The American Ceramic Society, Cincinnati, OH, (1988).
- [88JAF] D. Jaffe, "Materials and Processes for High Functionality Hybrid Circuit Packages," Mat. Res. Soc. Symp. Proc., 108, pp. 301-08, (1988).
- [88JEN] R.J. Jensen, "Recent Advances in Thin Film Multilayer Interconnect Technology for IC Packaging," Mat. Res. Soc. Symp. Proc., 108, pp 73-79, (1988).
- [88KAC] K.K. Kachelries, J.A. Olenick, S.G. Konsowski, "Evaluation of Thick Film Multilayers on AlN," Proceedings of the 21st International Symposium on Microelectronics, Seattle, WA, ISHM, Reston, VA, pp. 170-82, (1988).
- [88KEY] R.W. Keyes, "Device Limitations," Mat. Res. Soc. Symp. Proc., 108, pp. 3-13, (1988).
- [88KIN] J.A. King, Materials Handbook for Hybrid Microelectronics, Artech House, Boston, MA, (1988).
- [88KUN] A. Kunioka, "Current Situation of Japanese Hybrid Microelectronics," Proceedings of the 21st International Symposium on Microelectronics, Seattle, WA, ISHM, Reston, VA, pp. 203-05, (1988).
- [88KUS] A.G. Kusmierczyk, A.D. Snicer, "Calculation of Extremely High Temperature Effects in Conductors Suffering Electromigration," Proceedings of the 21st International Symposium on Microelectronics, Seattle, WA, ISHM, Reston, VA, pp. 377-80, (1988).
- [88LEA1] M. Leap and W. Huebner, "Electrical Properties of Tape Cast Hollow Glass Microsphere 0-3 Composites," Paper No. 38-E-88, Annual National Convention of The American Ceramic Society, Cincinnati, OH, (1988).

- [88LEA2] M. Leap, A. Das, L. Cross and W. Huebner, "Thin and Thick Film Technology for Novel Approaches in Microelectronic Packaging," Paper No. 46-EP-88, Annual National Convention of The American Ceramic Society, Cincinnati, OH, (1988).
- [88LEE] S.B. Lee, S. Torquato, "Pair Connectedness and Mean Cluster Size for Continuum-Percolation Models: Computer-Simulation Results," J. Chem. Phys., 89, [10], pp. 6427-33, (1988).
- [88LIC] J.J. Licari, L.R. Enlow, Hybrid Microcircuit Technology Handbook: Materials, Processes, Design, Testing and Production, Noyes Publications, Park Ridge, NJ, (1988).
- [88LU] Y.Y. Lu, M.S. El-Aasser, J.W. Vanderhoff, "Dispersion Polymerization of Styrene in Ethanol: Monomer Partitioning Behavior and Locus of Polymerization," Journal of Polymer Science: Part B: Polymer Physics, 26, pp. 1187-1203, (1988).
- [88MAC] D. MacCaulay, The Way Things Work, Houghton Mifflin Company, Boston, MA, (1988).
- [88MAD] C. Madhavan, T. Srinivasan, Q. Xu and R. Newnham, "Fired 0-3 Piezoelectric Composite Materials for Biomedical Ultrasonic Imaging Applications," Paper No. 49-EP-88, Annual National Convention of The American Ceramic Society, Cincinnati, OH, (1988).
- [88MIC] Seradyn, Inc., Microparticle Immunoassay Techniques, Particle Technology Division, Seradyn, Inc., Indianapolis, IN, (1988).
- [88MIE] K.M. Miessen and D.J. Shanefield, "Sintering Aids and Grain Boundary Compositions in Aluminum Nitride," Paper No. 29-E-88, Annual National Convention of The American Ceramic Society, Cincinnati, OH, (1988).
- [88MOH] U. Mohideen, T.R. Gururaja, L.E. Cross, R. Roy, "Ultra-Low Dielectric Constant Porous Silica Thick Films for High-Speed IC Packaging," IEEE Transactions on Components, Hybrids, and Manufacturing Technology, 11, [1], pp. 159-162, (1988).
- [88MRO] C.M. Mroz and J.A.T Taylor, "Characterization of Aluminum Nitride-Metal Interface in Electronic Aluminum Nitride Ceramics," Paper No. 6-EP-88, Annual National Convention of The American Ceramic Society, Cincinnati, OH, (1988).
- [88NEU] C.A. Neugebauer, "Materials Limitations in the Higher Electronic Packaging Levels," Mat. Res. Soc. Symp. Proc., 108, pp. 13-25, (1988).
- [88NEW] C.E. Newberg and S.H. Risbud, "Interfacial Reactions of Thick Film Metallizations and Aluminum Nitride Substrates," Paper No. 32-E-88, Annual National Convention of The American Ceramic Society, Cincinnati, OH, (1988).
- [88OHU] F. Ohuchi, M. Bortz, "Synthesis and Characterization of Cordierite-Based Ceramic Thin Films," Paper No. 97-E-88, Annual National Convention of The American Ceramic Society, Cincinnati, OH, (1988).



- [88ONN] D.G. Onn, H.M. Zhang, R.E Giedd and O. Guerrero, "Percolation Effects in the Thermal Diffusivity of Polymer/Ceramic Composites," Paper No. 89-E-88, Annual National Convention of The American Ceramic Society, Cincinnati, OH, (1988).
- [88PAG] R.A. Page, S. Spooner, W.B. Sanderson, D.L. Johnson, "Pore Evolution During Glow Discharge Sintering of Alumina," J. Am. Cer. Soc., 71, [12], pp. 1125-29, (1988).
- [88PAR] N.A. Park, T.F. Irvine, Jr., "Measurements of Rheological Fluid Properties with the Falling Needle Viscometer," Re. Sci. Instrum., 59, [9], pp. 2051-58, (1988).
- [88PHU] P.P. Phule and S.H. Risbud, "Chemically Derived Electroceramic Powders," Paper No. 19-E-88, Annual National Convention of The American Ceramic Society, Cincinnati, OH, (1988).
- [88PIL] V. Pilletteri and E. Case, "Laser Surface Melting and Cutting of Cordierite Substrates," Paper No. 7-EP-88, Annual National Convention of The American Ceramic Society, Cincinnati, OH, (1988).
- [88REE] J.S. Reed, Introduction to the Principles of Ceramic Processing, J. Wiley & Sons, New York, NY, (1988).
- [88ROB] M.J. Robinson, C. Tsay, M. Buynoski, R. Pendse, "Measurement of Die Stress From Packaging and Effects of Thermal Cycling," Mat. Res. Soc. Symp. Proc., 108, pp, 43-46, (1988).
- [88ROO] A. Roosen, H.K. Bowen, "Influence of Various Consolidation Techniques on the Green Microstructure and Sintering Behavior of Alumina Powders," J. Am. Cer. Soc., 71, [11], pp. 970-77, (1988).
- [88SAC] M.D. Sacks, S.D. Vora, "Preparation of SiO<sub>2</sub> Glass from Model Powder Compacts: III, Enhanced Densification by Sol Infiltration," J. Am. Cer. Soc., 71, [4], pp. 245-49, (1988).
- [88SAE] M.A. Saed, A.Y. Almazroo, A. Elshabini-Riad, S.M. Riad, "Wideband (DC-10) GHz Characterization of Thick Film Dielectric and Ferrite Materials," Proceedings of the 21st International Symposium on Microelectronics, Seattle, WA, ISHM, Reston, VA, pp. 340-44, (1988).
- [88SAW] H.T. Sawhill, "Materials Compatibility and Sintering in Low Temperature Co-Fired Ceramic Packages," Paper No. 129-E-88, Annual National Convention of The American Ceramic Society, Cincinnati, OH, (1988).
- [88SCH1] G. Scherer, K. Mikeska and R Bordia, "Warping During Cofiring," Paper No. 130-E-88 , Annual National Convention of The American Ceramic Society, Cincinnati, OH, (1988).
- [88SCH2] G.W. Scherer, "Viscous Sintering with a Pore-Size Distribution and Rigid Inclusions," J. Am. Cer. Soc., 71, [10], pp. C-447-C-448, (1988).



- [88SCH3] M. Schober, "Electronics Market Strives for Higher Marks," Ceramic Bulletin, 67, [4], pp. 722-23, (1988).
- [88SEI] R.W. Seibold, R.T. Lamoureux, S.H. Goodman, "Materials for High Speed Circuit Boards," Mat. Res. Soc. Symp. Proc., 108, pp. 141-52, (1988).
- [87SEV] E.M. Sevick, P.A. Monson, J.M. Ottino, "Monte Carlo Calculations of Cluster Statistics in Continuum Models of Composite Morphology," J. Chem. Phys., 88, [2], pp. 1198-1206, (1988).
- [88SHA1] P.T.B Shafer and S. Majorowski, "High Thermal Conductivity AlN," Paper No. 28-E-88, Annual National Convention of The American Ceramic Society, Cincinnati, OH, (1988).
- [88SHA2] M. Shah and J. Rigsbee, "Microstructural Characterization of Vapor Deposited Ni/Al<sub>2</sub>O<sub>3</sub> Composites," Paper No. 108-E-88, Annual National Convention of The American Ceramic Society, Cincinnati, OH, (1988).
- [88SHA3] A. Shaikh, D. Hankey, D. Leandri, G. Roberts, "A Hermetic Low K Dielectric for Alumina Substrates," Proceedings of the 21st International Symposium on Microelectronics, Seattle, WA, ISHM, Reston, VA, pp. 189-95, (1988).
- [88SHE] L.M. Sheppard, "Automation of Particle Size Analysis," Ceramic Bulletin, 67, [5], pp. 878-83, (1988).
- [88SHI] Y. Shimada, Y. Yamashita, H. Takamizawa, "Low Dielectric Constant Multilayer Glass-Ceramic Substrate with Ag-Pd Wiring for VLSI Package," IEEE Transactions on Components, Hybrids, and Manufacturing Technology, 11, [1], pp. 163-70, (1988).
- [88SHU] V. Shukla, "Thin Oxide Films in Electronic Applications," Paper No. 96-E-88, Annual National Convention of The American Ceramic Society, Cincinnati, OH, (1988).
- [88SIM] Y. Simpson and C. Carter, "The Influence of Al<sub>2</sub>O<sub>3</sub> Substrate Orientations on the Kinetics of NiAl<sub>2</sub>O<sub>4</sub> Growth in Thin-Film Reactions," Paper No. 106-E-88, Annual National Convention of The American Ceramic Society, Cincinnati, OH, (1988).
- [88SLI] P. Sliva, M. Leffler, M. Bliss, L.E. Cross, B.E. Scheetz, "High Frequency Dielectric Response of Calcium Aluminate Cements: Potential Packaging Substrate Materials," Mat. Res. Soc. Symp. Proc., 108, pp. 467-74, (1988).
- [88SOR] D.J. Sordelet, M. Akinc, "Sintering of Monosized, Spherical Yttria Powders," J. Am. Cer. Soc., 71, [12], pp. 1148-53, (1988).
- [88SPE] K.E. Spear, M. Frenklach, A. Badzian, T. Badzian, R. Messier, "Vapor Deposition of Crystalline Diamond," Ceram. Eng. Sci. Proc., 9, [9-10], pp. 1095-1102, (1988).
- [88SRI] S. Sriram, R.L. Holman, "Packaging of Components for Optical Fiber Technology," Mat. Res. Soc. Symp. Proc., 108, pp. 419-30, (1988).

- [88STE] C.A. Steidel, "Mechanical Interconnects to Silicon Integrated Circuits," Mat. Res. Soc. Symp. Proc., 108, pp. 347-57, (1988).
- [88STO1] R.A. Storer, editor, American Society for Testing and Materials, "Standard Test Methods for A-C Loss Characteristics and Permittivity (Dielectric Constant) of Solid Electrical Insulating Materials, Designation: D 150-87," Annual Book of ASTM Standards, Easton, MD, Section 9, 9.02, pp. 27-45, (1988).
- [88STO2] R.A. Storer, editor, American Society for Testing and Materials "Standard Test Method for Water Absorption, Bulk Density, Apparent Porosity, and Apparent Specific Gravity of Fired Whiteware Products, Designation: C 373-72 (Reapproved 1982)," Annual Book of ASTM Standards, Storer, Easton, MD, Section 15, 15.02, pp. 105-06, (1988).
- [88TAK] Y. Takeuchi, "New Nitrogen-Fireable Material Designed for Use as a Crossover Dielectric," The International Journal for Hybrid Microelectronics, 11, [4], pp. 93-98, (1988).
- [88TED] S. Tedjini, N. Daoud, E. Pic, "Dynamic Modelling of Interconnection Lines for Sub-Nanosecond Applications," Proceedings of the 21st International Symposium on Microelectronics, Seattle, WA, ISHM, Reston, VA, pp. 485-91, (1988).
- [88TEN] K.F. Teng, P.O. Drawer, "Theoretical Model and Rheology in Thick Film Orifice Printing Technology," Proceedings of the 21st International Symposium on Microelectronics, Seattle, Washington, ISHM, Reston, VA, pp. 88-94, (1988).
- [88TUM] R.R. Tummala, "Ceramics in Microelectronic Packaging," Ceramic Bulletin, 67, [4], pp. 752-58, (1988).
- [88UNG] R.F. Unger, P.N. Migdal, R. Redemske, "Overview of the Navy's IFAHMM Program," Proceedings of the 21st International Symposium on Microelectronics, Seattle, WA, ISHM, Reston, VA, pp. 510-18, (1988).
- [88VOG] M.M. Vogel and R.C. Buchanan, "Low Melting Glass Films for Microelectronic Applications," Paper No. 14-EP-88, Annual National Convention of The American Ceramic Society, Cincinnati, OH, (1988).
- [88WAN] D.W. Wang, "Advanced Materials for Printed Circuit Boards," Mat. Res. Soc. Symp. Proc., 108, pp. 125-39, (1988).
- [88WEN] S.H. Wen, J.I. Kim, "Thin Film Wiring for Integrated Electronic Packages," Mat. Res. Soc. Symp. Proc., 108, pp 81-87, (1988).
- [88WHI] D. Whitman, "Mechanisms of Char Formation in Nitrogen Fired Thick Film Materials," Proceedings of the 21st International Symposium on Microelectronics, Seattle, WA, ISHM, Reston, VA, pp. 421-25, (1988).
- [88WON] V. Wong, "Leach Resistance End Terminations for Multilayer Ceramic Capacitors Used in Surface Mount Applications," Paper No. 29-EP-88, Annual National Convention of The American Ceramic Society, Cincinnati, OH, (1988).

- [88YAN] M.F. Yan, W.W. Rhodes, "Ceramic Optical Package Material Requirements and Guidelines for Material Selection," *Mat. Res. Soc. Symp. Proc.*, 108, pp. 439-53, (1988).
- [88YEH1] T.S. Yeh, M.D. Sacks, "Effect of Particle Size Distribution on the Sintering of Alumina," *J. Am. Cer. Soc.*, 71, [12], pp. C-484-C-487, (1988).
- [88YEH2] T.S. Yeh, M.D. Sacks, "Low-Temperature Sintering of Aluminum Oxide," *J. Am. Cer. Soc.*, 71, [10], pp. 841-44, (1988).
- [88YOS] F.G. Yost, A.D. Romig, Jr., "Thermodynamics of Wetting by Liquid Metals," *Mat. Res. Soc. Symp. Proc.*, 108, pp. 385-90, (1988).
- [88YU] Y.F. Yu, S. Heng, L. Boothe and T.I. Mah, "Sol-Gel Processing of Spinel and Cordierite," Paper No. 20-E-88, Annual National Convention of The American Ceramic Society, Cincinnati, OH, (1988).
- [88ZHA] J. Zhao, M.P. Harmer, "Effect of Pore Distribution on Microstructure Development: II, First and Second Generation Pores," *J. Am. Cer. Soc.*, 71, [7], pp. 530-39, (1988).
- [89AND] R.M. Anderson, R. Gerhardt, J.B. Wachtman, Jr., D. Onn, S. Beecher, "Thermal, Mechanical, and Dielectric Properties of Mullite-Cordierite Composites," Advances in Ceramics, 26, The American Ceramic Society, Inc., Westerville, OH, pp. 265-77, (1989).
- [89BAC] B.J. Bachman, C.A. Pryde, E.T. Johnson, D.A. Simoff, V.W. Ryan, "Evaluation of Polyimide as a Dielectric for Multichip Packaging," Proceedings of the 22nd International Symposium on Microelectronics, Baltimore, MD, ISHM, Reston, VA, pp. 462-69, (1989).
- [89BAN] N. Bandyopadhyay, S. Tamhankar, M. Kirschner, "Process Conditions for Hermetic Sealing of KOVAR to Borosilicate Glass," Advances in Ceramics, 26, The American Ceramic Society, Inc., Westerville, OH, pp. 597-604, (1989).
- [89BEE] S.C. Beecher, R.E. Giedd, D.G. Onn, "Thermal Properties of Mullite-Cordierite Composites," Thermal Conductivity 20, Edited by D.P.H. Hasselman and J.R. Thomas, Jr., Plenum Press, New York, NY, pp. 119-27, (1989).
- [89BER] W. Berweiler, J.R. Varner, H. Riedel, "Processing Defects and Strength of Alumina Substrates," Advances in Ceramics, 26, The American Ceramic Society, Inc., Westerville, OH, pp. 557-67, (1989).
- [89BUT] D.P. Button, B.A. Yost, R.H. French, W.Y. Hsu, J.D. Bolt, M.A. Subramanian, H.M. Zhang, R.E. Geidd, A.J. Whittaker, D.G. Onn, "Ceramic-Fiber/Polymer Laminates: Thermally Conductive Composites with Low Dielectric Constants," Advances in Ceramics, 26, The American Ceramic Society, Inc., Westerville, OH, pp. 353-73, (1989).
- [89CAO] W. Cao, R. Gerhardt, J.B. Wachtman, Jr., "Low-Permittivity Porous Silica by a Colloidal Processing Method," Advances in Ceramics, 26, The American Ceramic Society, Inc., Westerville, OH, pp. 409-18, (1989).

- [89CAW] J.D. Cawley, "Joining of Ceramic-Matrix Composites," *Ceramic Bulletin*, 69, [9], pp. 1619-23, (1989).
- [89CHI] Y.C. Chiew, G. Stell, "Connectivity and Percolation of Randomly Centered Spheres: Correction to the Percus-Yevick Approximation," *J. Chem. Phys.*, 90, [9], pp. 4956-59, (1989).
- [89CLE] W.J. Clegg, N.M. Alford, J.D. Birchall, K. Kendall, "Improved Process for Making Dense Vitreous Silica from Submicrometer Particles by Sintering Near 1000°C," *J. Am. Cer. Soc.*, 72, [3], pp. 432-36, (1989).
- [89DAS] A. Das, R. Messier, L.E. Cross, "A Morphological Study of Low-Dielectric Permittivity Substrates for Packaging VLSIs," Advances in Ceramics, 26, The American Ceramic Society, Inc., Westerville, OH, pp. 419-30, (1989).
- [89DEH] R.T. DeHoff, "Stereological Theory of Sintering," Science of Sintering: New Directions for Materials Processing and Microstructural Control, Edited by D.P. Uskokovic, H. Palmour III, R.M. Spriggs, Plenum Press, New York, NY, pp. 55-71, (1989).
- [89DIG] G. DiGiacomo, "Copper Diffusion Kinetics Through Mo, Co, Ti Barriers and the Gold Surface Layer," *Proceedings of the 22nd International Symposium on Microelectronics*, Baltimore, MD, ISHM, Reston, VA, pp. 227-36, (1989).
- [89DIN1] D.R. Dinger, J.E. Funk, "Particle-Size Analysis Routines Available on CERABULL," *Ceramic Bulletin*, 68, [8], pp. 1406-07, (1989).
- [89DIN2] R. Dinwiddle, A. Whittaker, D.G. Onn, "Effect of Processing Conditions on Thermal Conduction in Alumina," Thermal Conductivity 20, Edited by D.P.H. Hasselman and J.R. Thomas, Jr., Plenum Press, New York, NY, pp. 129-38, (1989).
- [89DUF] S.F. Duffy, J.M. Manderscheid, J.L. Palko, "Analysis of Whisker-Toughened Ceramic Components-A Design Engineers Point of View," *Ceramic Bulletin*, 68, [12], pp. 2078-83, (1989).
- [89DUP] R.W. Dupon, R.L. McConville, M.S. Thompson, "Low Temperature Route to Cordierite Ceramics Using a Reactive Liquid Phase Sintering Aid, Dense Body Preparation and Green Tape Fabrication," *Mat. Res. Soc. Symp. Proc.*, 154, pp. 351-56, (1989).
- [89ELS] A. Elshabini-Riad, N.M. Muthukrishnan, "An Overview of Wideband Characterization and Modelling of Thick Film Materials and Components," *Proceedings of the 22nd International Symposium on Microelectronics*, Baltimore, MD, ISHM, Reston, VA, pp. 400-15, (1989).
- [89EMU] H. Emura, K. Onituka, H. Maruyama, "Multilayered Ceramic Substrates with Low Dielectric Constants," Advances in Ceramics, 26, The American Ceramic Society, Inc., Westerville, OH, pp. 375-85, (1989).



- [89FER] M. R. Ferrick, J. Murtagh, J.K. Thomas, "Synthesis and Characterization of Polystyrene Latex Particles," Macromolecules, 22, [4], pp. 1515-17, (1989).
- [89GIE] R.E. Geidd, D.G. Onn, "Electronic Flash: A Rapid Method for Measuring the Thermal Conductivity and Specific Heat of Dielectric Materials," Thermal Conductivity 20, Edited by D.P.H. Hasselman and J.R. Thomas, Jr., Plenum Press, New York, NY, pp. 339-46, (1989).
- [89GLA] J.J. Glatz, J.F. Leon, "Passive Thermal Management of Excess Heat From Electronic Devices," Mat. Res. Soc. Symp. Proc., pp. 461-71, (1989).
- [89HAN] S. Hanada, H. Arikawa, "Thin Film Circuits Formed on a Co-fired Alumina Multilayer Substrate," Proceedings of the 22nd International Symposium on Microelectronics, Baltimore, MD, ISHM, Reston, VA, pp. 431-34, (1989).
- [89HAS] D.P.H. Hasselman, "Thermal Diffusivity and Conductivity of Composites with Interfacial Thermal Contact Resistance," Thermal Conductivity 20, Edited by D.P.H. Hasselman and J.R. Thomas, Jr., Plenum Press, New York, NY, pp. 405-21, (1989).
- [89HER] M. Herrmann, S. Hess, H. Kessler, J. Pabst, W. Hermel, "Microstructural Development in Dense  $\text{Si}_3\text{N}_4$  Ceramics," Science of Sintering: New Directions for Materials Processing and Microstructural Control, Edited by D.P. Uskokovic, H. Palmour III, R.M. Spriggs, Plenum Press, New York, NY, pp. 421-27, (1989).
- [89HEW1] Hewlett Packard Company, HP 16451B Dielectric Test Fixture, Operation and Service Manual, Yokagawa-Hewlett-Packard, LTD., pp. 3.6-3.27, 3.31-34, 3.37-52, (1989).
- [89HEW2] Hewlett Packard Company, Dielectric Constant Measurement of Solid Material, Application Note 380-1, (October 1989).
- [89HIM] R.P. Himmel, J.J. Licari, "Fabrication of Large-Area, Thin-Film Multilayer Substrates," Proceedings of the 22nd International Symposium on Microelectronics, Baltimore, MD, ISHM, Reston, VA, pp. 454-61, (1989).
- [89HIR] S.I. Hirano, N. Fujii, A. Fujii, S. Naka, "Processing and Properties of Cubic BN Disks under Pressure," Advances in Ceramics, 26, The American Society, Inc., Westerville, OH, pp. 55-61, (1989).
- [89HOF] L.C. Hoffman, "Crystallizable Dielectrics in Multilayer Structures for Hybrid Microcircuits: A Review," Advances in Ceramics, 26, The American Ceramic Society, Inc., Westerville, OH, pp. 249-53, (1989).
- [89JES] T.L. Jessen, J.J. Mecholsky, "Viscoelastic Effect of Heat Treatment on the Fracture Toughness of Metal-Particle/Glass-Matrix Composites," J. Am. Cer. Soc., 72, [11], pp. 2094-97, (1989).
- [89JUN] R. Jung, R. Litman, D. Kellerman, "Development of a Low K Thick Film Dielectric Paste," Proceedings of the 22nd International Symposium on Microelectronics, Baltimore, MD, ISHM, Reston, VA, pp. 590-97, (1989).



- [89KON] K. Kondo, M. Hattori, Y. Matsuo, Y. Shibata, "Low-Temperature, Cofired, Multilayer Ceramic Packages Containing Copper Conductors and AlN Heat Sinks," Advances in Ceramics, 26, The American Ceramic Society, Inc., Westerville, OH, pp. 229-38, (1989).
- [89LEA] M.J. Leap, W. Huebner, I. Eicher, "Low-Permittivity, Silica, Hollow-Glass-Microsphere 0-3 Composites," Advances in Ceramics, 26, The American Ceramic Society, Inc., Westerville, OH, pp. 399-407, (1989).
- [89LEI] D.W. Leigh, D.A. Payne, J.F. Young, "Preparation and Properties of Hardened DSP Cement Materials for Electrical Applications," Advances in Ceramics, 26, The American Ceramic Society, Inc., Westerville, OH, pp. 255-63, (1989).
- [89LU] S. Lu, M. Hayes, K.M. Fidanboyly, A. Elshabini-Riad, "Modelling of Geometrical Effects of Thick Film Components on Their Microwave Performance," Proceedings of the 22nd International Symposium on Microelectronics, Baltimore, MD, ISHM, Reston, VA, pp. 385-89, (1989).
- [89LYN] J.F. Lynch, A.M. Gaibrois, W.F. Lands, P.M. Vernon, Jr., "Material Properties of TapeCast BeO," Advances in Ceramics, 26, The American Ceramic Society, Inc., Westerville, OH, pp. 577-82, (1989).
- [89MAT] D.M. Mattox, S.R. Gurkovich, J.A. Olenick, K.M. Mason, "Low-Dielectric-Constant, Alumina-Compatible, Cofired, Multilayer Substrate," Advances in Ceramics, 26, The American Ceramic, Inc., Westerville, OH, pp. 431-43, (1989).
- [89MCE] D.L. McElroy, F.J. Weaver, M. Shapiro, A.W. Longest, D.W. Yarbrough, "The Thermal Conductivity of Beds of Spheres," Thermal Conductivity 20, Edited by D.P.H. Hasselman and J.R. Thomas, Jr., Plenum Press, New York, NY, pp. 423-33, (1989).
- [89MCL] D.S. McLachlan, "The Complex Permittivity of Emulsions: An Effective Media-Percolation Equation," Solid State Communications, 72, [8], pp. 831-34, (1989).
- [89MIT] W. Mitch, "Low K Dielectric Developed for Thick-Film and Transfer-Tape Process," Ceramic Bulletin, 68, [9], p. 1564, (1989).
- [89NEU] W. Neumann, A. Hallen, "Changes in Thermal Diffusivity During Heating of PM Powder Compacts," Thermal Conductivity 20, Edited by D.P.H. Hasselman and J.R. Thomas, Jr., Plenum Press, New York, NY, pp. 71-80, (1989).
- [89NIS1] S. Nishigaki, J. Fukuta, "Low-Temperature, Cofireable, Multilayered Ceramics Bearing Pure-Ag Conductors and Their Sintering Behavior," Advances in Ceramics, 26, The American Ceramic Society, Inc., Westerville, OH, pp. 199-214, (1989).
- [89NIS2] K. Nishiwaki, K. Okuno, Y. Moritsu, N. Konaga, Y. Nokami, "High Density Circuit on Ceramics: Material, Process, Applications," Proceedings of the 22nd International Symposium on Microelectronics, Baltimore, MD, ISHM, Reston, VA, pp. 305-12, (1989).

- [89NIW] K. Niwa, Y. Imanaka, N. Kamehara, S. Aoki, "Low-K and Low-T Sintering Materials for Multilayer Circuit Boards," Advances in Ceramics, 26, The American Ceramic Society, Inc., Westerville, OH, pp. 323-37, (1989).
- [89PAB] J. Pabst, M. Herrmann, "On The Kinetics of Densification During Liquid Phase Sintering of  $\text{Si}_3\text{N}_4$ ," Science of Sintering: New Directions for Materials Processing and Microstructural Control, Edited by D.P. Uskokovic, H. Palmour III, R.M. Spriggs, Plenum Press, New York, NY, pp. 607-12, (1989).
- [89PAN] P.C. Panda, R. Raj, "Sintering and Crystallization of Glass at Constant Heating Rates," J. Am. Cer. Soc., 72, [8], pp. 1564-66, (1989).
- [89PER1] M. Perez-Pena, D.M. Roy, P. Kistler, M.T. Lanagan, L.E. Cross, "Cementitious Materials for Electronic Packaging, I. Processing, Electrical, and Mechanical Properties of Chemically Bonded Ceramics:  $\text{SiO}_2$ -Amorphous/ $\text{Ca}_3\text{SiO}_5$ ," Advances in Ceramics, 26, The American Ceramic Society, Inc., Westerville, OH, pp. 279-85, (1989).
- [89PER2] M. Perez-Pena, D.M. Roy, M.T. Lanagan, L.E. Cross, "Cementitious Materials for Electronic Packaging, II. Low-Temperature, Sintered Wollastonite Substrates with Relatively Low Dielectric Permittivity and High Tensile Strength," Advances in Ceramics, 26, The American Ceramic Society, Inc., Westerville, OH, pp. 287-306, (1989).
- [89SAB] C.J. Sabo, W.A. Vitriol, C.L. Slaton, D.L. Rychlick, "The Use of Low-Temperature, Cofired Ceramic Technology for the Fabrication of High-Density, Hermetic, Multicavity Modules," Advances in Ceramics, 26, The American Ceramic Society, Inc., Westerville, OH, pp. 217-28, (1989).
- [89SAN1] L.E. Sanchez, "Electrical, Mechanical, and Thermal Characterization of a Cofired, Multilayer Substrate Processed from Sol-Gel Silica," Advances in Ceramics, 26, The American Ceramic Society, Inc., Westerville, OH, pp. 387-97, (1989).
- [89SAN2] L.E. Sanchez, D. Ngo, "Electrical Characterization of Matched Impedance, Cofired, High-Speed, Microelectronic Packages Made From Low Dielectric Constant, Boron-Doped, Sol-Gel," The International Journal for Hybrid Microelectronics, 12, [2], pp. 95-101, (1989).
- [89SAN3] C.V. Santilli, S.H. Pulcinelli, J.A. Varela, J.P. Bonnet, "Effect of Green Compact Pore Size Distribution on the Sintering of  $\alpha\text{-Fe}_2\text{O}_3$ ," Science of Sintering: New Directions for Materials Processing and Microstructural Control, Edited by D.P. Uskokovic, H. Palmour III, R.M. Spriggs, Plenum Press, New York, NY, pp. 519-27, (1989).
- [89SAW] H.T. Sawhill, "Materials Compatibility and Cosintering Aspects of Shrinkage Control in Low-Temperature Cofired Ceramic Packages," Advances in Ceramics, 26, The American Ceramic Society, Inc., Westerville, OH, pp. 307-19, (1989).

- [89SCH] N.N. Schulz, R.W. Hendricks, A. Elshabini-Riad, "Role of Residual Stresses in Ceramic Substrate Materials for Hybrid Thick Film Applications," Proceedings of the 22nd International Symposium on Microelectronics, Baltimore, MD, ISHM, Reston, VA, pp. 220-26, (1989).
- [89SCO] G.C. Scott, G. Astfalk, "A Model of Thermal Stress Development in Microelectronic Components," Mat. Res. Soc. Symp. Proc., 154, pp. 473-78, (1989).
- [89SER] D.P. Seraphim, R. Lasky, C.Y. Li, Principles of Electronic Packaging, McGraw-Hill Book Company, New York, NY, (1989).
- [89SHA] A. Shaikh, K. Allison, G. Ackerman, G. Sarkar, "Thick Film Interfacial Interactions and Resultant Effects on Fired Film Properties," Proceedings of the 22nd International Symposium on Microelectronics, Baltimore, MD, ISHM, Reston, VA, pp. 568-76, (1989).
- [89SLI] P. Sliva, G.O. Dayton, L.E. Cross, B.E. Scheetz, "Tapecast Calcium Aluminate Cement Substrates for Microelectronic-Packaging Applications," Advances in Ceramics, 26, The American Ceramic Society, Inc., Westerville, OH, pp. 583-597, (1989).
- [89SOM] S. Somiya, M. Mitomo, M. Yoshimura, editors, Silicon Nitride-1, Elsevier Applied Science, New York, NY, (1989).
- [89STE] J. Steinberg, K. Kistler, "The Battery Effect in Thick Film Multilayer Circuits," Proceedings of the 22nd International Symposium on Microelectronics, Baltimore, MD, ISHM, Reston, VA, pp. 237-42, (1989).
- [89SUB] M.A. Subramanian, D.R. Corbin, U. Chowdry, "Zeolites as Precursors to Aluminosilicate-Based Ceramics for Microelectronic Packaging," Advances in Ceramics, 26, The American Ceramic Society, Inc., Westerville, OH, pp. 239-47, (1989).
- [89TAK] T. Takahashi, N. Iwase, A. Tsuge, M. Nagata, "Properties and Reliability of AlN Ceramics for Power Devices," Advances in Ceramics, 26, The American Ceramic, Inc., Westerville, OH, pp. 159-69, (1989).
- [89TAM] S.S. Tamhankar, R.J. Wolf, M.T. Marczi, R.L. Keusseyan, "An Atmosphere System for Firing Copper Compatible Dielectrics," Proceedings of the 22nd International Symposium on Microelectronics, Baltimore, MD, ISHM, Reston, VA, pp. 577-84, (1989).
- [89TAN] J. Tanak, S. Kajita, M. Terasawa, "Mullite Ceramics for the Application to Advanced Packaging Technology," Mat. Res. Soc. Symp. Proc., pp. 369-78, (1989).
- [89TED] S. Tedjini, M. Van Veen, "Empirical Formulas for MIS Microstrip Parameters," Proceedings of the 22nd International Symposium on Microelectronics, Baltimore, MD, ISHM, Reston, VA, pp. 422-30, (1989).
- [89TUM1] R.R. Tummala, "Ceramics in Microelectronic Packaging," Advances in Ceramics, 26, The American Ceramic Society, Inc., Westerville, OH, pp. 3-16, (1989).

- [89TUM2] R.R. Tummala, "Ceramics in Microelectronics Packaging: Past, Present and Future," Mat. Res. Soc. Symp. Proc., pp. 379-86, (1989).
- [89TUM3] R.R. Tummala, E.J. Rymaszewski, editor, Microelectronics Packaging Handbook, Van Nostrand Reinhold, New York, NY, (1989).
- [89TYL] J.R. Tyler, D.J. Gasper, "Evaluation and Characterization of Low-Temperature Cofired Ceramic Structures for Microwave Applications," Proceedings of the 22nd International Symposium on Microelectronics, Baltimore, MD, ISHM, Reston, VA, pp. 390-99, (1989).
- [89WES] A.D. Westwood, M.R. Notis, "Metallization Issues in Advanced Ceramic Substrates:-Microstructural, Microchemistry, and Thermal Conductivity in AlN," Mat. Res. Soc. Symp. Proc., 154, pp. 479-85, (1989).
- [89WU] G.H. Wu, Y.C. Chiew, "Selective Particle Clustering and Percolation in Binary Mixtures of Randomly Centered Spheres," J. Chem. Phys., 90, [9], pp. 5024-29, (1989).
- [89YAM1] J.K. Yamamoto, M.T. Lanagan, A.S. Bhalla, R.E. Newnham, L.E. Cross, "Dielectric Properties of Microporous Glass In the Microwave Region," J. Am. Cer. Soc., 72, [6], pp. 916-21, (1989).
- [89YAM2] J.K. Yamamoto, K. Kata, Y. Shimada, "Fabrication of Controlled Porosity In a Tape Cast Glass Ceramic Substrate Material," Materials Letters, 8, [8], pp. 278-282, (1989).
- [89ZHE] J. Zheng, J.S. Reed, "Effects of Particle Packing Characteristics on Solid-State Sintering," J. Am. Cer. Soc., 72, [5], pp. 810-17, (1989).
- [90ANG] G. Angenieux, B. Flechet, P. Ferrari, J. Chilo, "Broad Band Dielectric Characterization of Substrates for Sub-Nanosecond Hybrid Circuits," Proceedings of the 23rd International Symposium on Microelectronics, Chicago, IL, ISHM, Reston, VA, pp. 518-28, (1990).
- [90BLE] J. Ble'try, "Sphere and Distance Models for Binary Disordered Systems," Philosophical Magazine B, 62, [5], pp. 469-508, (1990).
- [90BOR] W. Borland, "New Materials for Advanced Consumer Microelectronic Applications," Ceramic Transactions, 15, The American Ceramic Society, Inc., Westerville, OH, pp. 555-73, (1990).
- [90BUR] I. Burn, W.C. Porter, "Processing Multilayer Ceramics with Internal Copper Conductors," Ceramic Transactions, 15, The American Ceramic Society, Inc., Westerville, OH, pp. 375-90, (1990).
- [90CAM] C.P. Cameron, R. Raj, "Better Sintering Through Green-State Deformation Processing," J. Am. Cer. Soc., 73, [7], pp. 2032-37, (1990).



- [90CAN] R.E. Canright, Jr., "Capacitance: Relationships and Measurements," Proceedings of the 40th Electronic Components and Technology Conference, 1, New York, NY, IEEE, New York, NY, pp. 163-68, (1990).
- [90DAV] E.E. Davidson, "The Performance Choice: A Study of Chip and Package Densities," Proceedings of the 40th Electronic Components and Technology Conference, 1, New York, NY, IEEE, New York, NY, pp. 147-49, (1990).
- [90DUP] Dupont Electronics, Technology Handbook: Ceramic Printed Wiring Boards For the Military Market, pp. 1-8, (1990).
- [90EWS] K.G. Ewsuk, "Ceramic-Filled-Glass Composite Sintering," Ceramic Transactions, 15, The American Ceramic Society, Inc., Westerville, OH, pp. 279-95, (1990).
- [90GAG] J. A. Gaglani, M.A. Kuhlman, "Thermal Management of Low-Temperature Co-Fired Ceramic," Proceedings of the 23rd International Symposium on Microelectronics, Chicago, IL, ISHM, Reston, VA, pp. 410-15, (1990).
- [90GEI] G. Geiger, "Glass in Electronic Packaging Applications," Ceramic Bulletin, 69, [7], pp. 1131-36, (1990).
- [90GIE] E.A. Giess, J.M. Roldan, P.J. Bailey, E. Goo, "Microstructure and Dielectric Properties of Mullite Ceramics," Ceramic Transactions, 15, The American Ceramic Society, Inc., Westerville, OH, pp. 167-77, (1990).
- [90GOO] J.W. Goodwin, "Rheology of Ceramic Materials," Ceramic Bulletin, 69, [10], pp. 1694-98, (1990).
- [90HEN] L.L. Hench, J.K. West, Principles of Electronic Ceramics, John Wiley & Sons, New York, NY, (1990).
- [90HOF] M.S. Hoffman, editor, The World Almanac and Book of Facts, 1990, Pharos Books, New York, NY, (1989).
- [90HUS] M.M. Hussein, D.J. Nelson, A. Elshabini-Riad, "Thermal Management of Hybrid Circuits: Effect of Metallization Layer, Substrate Material and Thermal Environment, Proceedings of the 23rd International Symposium on Microelectronics, Chicago, IL, ISHM, Reston, VA, pp. 389-94, (1990).
- [90JAG1] A. Jagota, K.R. Mikeska, R. K. Bordia, "Isotropic Constitutive Model for Sintering Particle Packings," J. Am. Cer. Soc., 73, [8], pp. 2266-73, (1990).
- [90JAG2] A. Jagota, P.R. Dawson, "Simulation of the Viscous Sintering of Two Particles," J. Am. Cer. Soc., 73, [1], pp. 173-77, (1990).
- [90JOH] D.L. Johnson, "Sintering-Mechanistic Implications," Ceramic Transactions, 15, The American Ceramic Society, Inc., Westerville, OH, pp. 77-90, (1990).
- [90KAH] M. Kahn, R. Nelson, "Internally Cooled Substrates for High Power Density Packaging," Ceramic Transactions, 15, The American Ceramic Society, Inc., Westerville, OH, pp. 527-53, (1990).



- [90KAT] K. Kata, A. Sasaki, Y. Shimada, K. Utsumi, "New Fabrication Technology of Low Dielectric Permittivity Multilayer Ceramic Substrate," Proceedings of the 23rd International Symposium on Microelectronics, Chicago, IL, ISHM, Reston, VA, pp. 308-15, (1990).
- [90KEL] D. Kellerman, R. Peluso, "The Application of Low Dielectric Constant Thick Film Material on Low Temperature Cofired Glass/Ceramic Material," Proceedings of the 23rd International Symposium on Microelectronics, Chicago, IL, ISHM, Reston, VA, pp. 345-51, (1990).
- [90KUR] T. Kurihara, M. Horiuchi, Y. Takeuchi, S.I. Wakabayashi, "Mullite Ceramic Substrate for Thin-Film Application," Proceedings of the 40th Electronic Components and Technology Conference, 1, New York, NY, IEEE, New York, NY, pp. 68-75, (1990).
- [90LEE1] H.H. Lee, Fundamentals of Microelectronics Processing, McGraw-Hill Publishing Company, New York, NY, (1990).
- [90LEE2] H.H.D. Lee, "Validity of Using Mercury Porosimetry to Characterize the Pore Structure of Ceramic Green Compacts," J. Am. Cer. Soc., 73, [8], pp. 2309-15, (1990).
- [90LEV] L.M. Levinson, C.W. Eichelberger, R.J. Wojnarowski, R.O. Carlson, "High-Performance Packaging Using Laser Lithography," Ceramic Transactions, 15, The American Ceramic Society, Inc., Westerville, OH, pp. 405-16, (1990).
- [90MAC] J.F. MacDowell, G.H. Beall, "Low K Glass-Ceramics for Microelectronic Packaging," Ceramic Transactions, 15, The American Ceramic Society, Inc., Westerville, OH, pp. 259-77, (1990).
- [90MAN] L.T. Manzione, Plastic Packaging of Microelectronic Devices, Van Nostrand Reinhold, New York, NY, (1990).
- [90MAZ] G. Maze, S. Tedjini, J.L. Bonnefoy, "Substrate Anisotropy Effects on the Electrical Parameters of the Interconnection Lines," Proceedings of the 23rd International Symposium on Microelectronics, Chicago, IL, ISHM, Reston, VA, pp. 507-12, (1990).
- [90MCL1] D.S. McLachlan, "A Quantitative Analysis of the Volume Fraction Dependence of the Resistivity of Cermets Using the General Effective Media Equation," J. Appl. Phys., 68, [1], pp. 195-99, (1990).
- [90MCL2] D.S. McLachlan, M. Blaszkiewicz, R.E. Newnham, "Electrical Resistivity of Composites," J. Am. Cer. Soc., 73, [8], pp. 2187-2203, (1990).
- [90MID] S. Middleman, B. Heble, H.C.T. Cheng, "Improved Uniformity of Densification of Ceramic Composites Through Control of the Initial Preform Porosity Distribution," J. Mater. Res., 5, [7], pp. 1544-48, (1990).
- [90MIK] K.R. Mikeska, R.H. Jensen, "Pressure-Assisted Sintering of Multilayer Packages," Ceramic Transactions, 15, The American Ceramic Society, Inc., Westerville, OH, pp. 629-50, (1990).

- [90MIS] R.E. Mistler, "Tape Casting: The Basic Process for Meeting the Needs of the Electronics Industry," Ceramic Bulletin, 69, [6], pp. 1022-26, (1990).
- [90NAH] P. Nahass, W.E. Rhine, R.L. Pober, H.K. Bowen, W.L. Robbins, "A Comparison of Aqueous and Non-Aqueous Slurries for Tape-Casting, and Dimensional Stability in Green Tapes," Ceramic Transactions, 15, The American Ceramic Society, Inc., Westerville, OH, pp. 355-64, (1990).
- [90NEB] W.J. Nebe, "Ceramic Photolithography," Ceramic Transactions, 15, The American Ceramic Society, Inc., Westerville, OH, pp. 417-26, (1990).
- [90OHS] T. Ohsaka, "Electronic Packaging in the 90's-A Perspective from Asia," Proceedings of the 40th Electronic Components and Technology Conference, 1, New York, NY, IEEE, New York, NY, pp. 1-8, (1990).
- [90OKA] K. Okazaki, "Recent Topics of Electronic Ceramics in Japan," Ceramic Transactions, 15, The American Ceramic Society, Inc., Westerville, OH, pp. 11-22, (1990).
- [90RAM] N Ramakrishnan, V.S. Arunachalam, "Effective elastic Moduli of Porous Solids," Journal of Materials Science, 25, pp. 3930-37, (1990).
- [90RAN] M.S. Randall, M.D. Sacks, J.H. Simmons, "Processing of Borosilicate Glass-Silicon Nitride Composites Containing Controlled Porosity," Poster, Presented at the Second International Ceramic Science and Technology Congress and Electronics Division Meeting, The American Ceramic Society, Inc., Orlando, FL, November 12-15, (1990).
- [90REC] J. Reche, P. Garrou, J. Carr, P. Townsend, "High Density Multichip Module Fabrication," The International Journal for Hybrid Microelectronics, 13, [4], pp. 91-99, (1990).
- [90RIC] E.L. Rich, A.J. Martin, T.M. Lengel, J.J. Stewart, S.A. Gallo, "Low Temperature Co-fired Glass-Ceramic, High-Density-Interconnect, Substrate with Improved Thermal Management," Proceedings of the 40th Electronic Components and Technology Conference, 1, New York, NY, IEEE, New York, NY, pp. 122-30, (1990).
- [90RIN] T.A. Ring, "Processing of Fine Ceramic Powders," MRS Bulletin, pp. 34-40, (January, 1990).
- [90RUS] G.R. Ruschau, S. Yoshikawa, R.E. Newnham, "Effects of Filler Particle Size on the Resistivity of Conductive Composites," The International Journal for Hybrid Microelectronics, 13, [4], pp. 100-04, (1990).
- [90RUY] A.J. Ruys, C.C. Sorrell, "Slip Casting of High Purity Alumina Using Sodium Carboxymethylcellulose as a Deflocculant/Binder," Ceramic Bulletin, 69, [5], pp. 828-32, (1990).
- [90SAW] H.T. Sawhill, R.H. Jensen, K.R. Mikeska, "Dimensional Control in Low-Temperature Co-Fired Multilayers," Ceramic Transactions, 15, The American Ceramic Society, Inc., Westerville, OH, pp. 611-28, (1990).

- [90SAD] H. Sadri, "High Frequency Dielectric and Loss Tangent Properties of Aluminum Nitride Over Temperature Range," Proceedings of the 23rd International Symposium on Microelectronics, Chicago, IL, ISHM, Reston, VA, pp. 503-06, (1990).
- [90SCH] G.W. Scherer, "Effect of Inclusions on Shrinkage," Mat. Res. Soc. Symp. Proc., 180, pp. 503-14, (1990).
- [90SHE1] L. M. Sheppard, "The Changing Demand for Ceramic Additives," Ceramic Bulletin, 69, [5], pp. 802-6, (1990).
- [90SHE2] C.J. Sheu, R.F. Scratton, "Quenching, Polishing, and Grinding Reaction-Bonded Silicon Nitride," Ceramic Bulletin, 69, [7], pp. 1148-51, (1990).
- [90SHI1] Y. Shimada, Y. Kobayashi, K. Kata, M. Kurano, H. Takamizawa, "Large Scale Multilayer Glass-Ceramic Substrate For Supercomputer," IEEE Transactions on Components, Hybrids, and Manufacturing Technology, 13, [4], pp. 751-58, (1990).
- [90SHI2] Y. Shimada, Y. Kobayashi, K. Kata, M. Kurano, H. Takamizawa, "Large Scale Multilayer Glass-Ceramic Substrate for Supercomputer," Proceedings of the 40th Electronic Components and Technology Conference, 1, New York, NY, IEEE, New York, NY, pp. 76-83, (1990).
- [90SHO] G.P. Shorthouse, L. Bricknell, R.W.J. Russell, R.J. Morris, "High Density High Speed Thick Film Interconnections Incorporating a New, Low Permittivity, High Resolution Dielectric," Proceedings of the 23rd International Symposium on Microelectronics, Chicago, IL, ISHM, Reston, VA, pp. 216-23, (1990).
- [90SIN] D. Singh, D. Shetty, "Subcritical Crack Growth in Soda-Lime Glass in Combined Mode I and Mode II Loading," J. Am. Cer. Soc., 73, [12], pp. 3597-3606, (1990).
- [90STE] S.J. Stein, R.L. Wahlers, K.Y.D. Huang, T. Grunstein, G.P. Sykora, "Controlled Porosity Dielectrics and Etchable Conductors for High Density Packages," Proceedings of the 23rd International Symposium on Microelectronics, Chicago, IL, ISHM, Reston, VA, pp. 725-32, (1990).
- [90TUM] R.R. Tummala, "Electronic Packaging in the 90's-A Perspective from America," Proceedings of the 40th Electronic Components and Technology Conference, 1, New York, NY, IEEE, New York, NY, pp. 9-15, (1990).
- [90VAR] A.K. Varshneya, S.C. Cherukuri, "Glass in Microelectronic Packaging: A Review," Ceramic Transactions, 15, The American Ceramic Society, Inc., Westerville, OH, pp. 217-43, (1990).
- [90VOR] S.D. Vora, Effect of Green Microstructure on the Sintering of Model Silica Compacts, Ph. D. Dissertation, University of Florida, (1990).
- [90WAH] R.L. Wahlers, S.J. Stein, G.P. Sykora, "Tapes and Thick Films for High Frequency Packaging," Proceedings of the 40th Electronic Components and Technology Conference, 1, New York, NY, IEEE, New York, NY, pp. 116-21, (1990).

- [90WAR] D.A. Warner, C.C. Hung, M.J. Munson, J.F. Wang, R.E. Riman, "Preparation and Characterization of Ceramic Powders for Electronics," *Ceramic Transactions*, 15, The American Ceramic Society, Inc., Westerville, OH, pp. 51-68, (1990).
- [90WEI] A. Weinberg, "High Density Electronic Packaging Utilizing Vertical Integration and Low Temperature Cofired Ceramics," *Proceedings of the 23rd International Symposium on Microelectronics*, Chicago, IL, ISHM, Reston, VA, pp. 618-25, (1990).
- [90WES] H. Wessely, O. Fritz, P. Klimke, W. Koschnick, K.H. Schmidt, "Electronic Packaging in the 90's-A Perspective from Europe," *Proceedings of the 40th Electronic Components and Technology Conference*, 1, New York, NY, IEEE, New York, NY, pp. 16-33, (1990).
- [90WRI] J.W. Wright, editor, The Universal Almanac, 1990, Universal Press, New York, NY, p. 283, (1989).
- [91ALE] J.H. Alexander, S.K. Muralidhar, G.J. Roberts, T.J. Vlach, "A Low Temperature Cofiring Tape System Based on a Crystallizing Glass," *Proceedings of the 24th International Symposium on Microelectronics*, Orlando, FL, ISHM, Reston, VA, pp. 414-17, (1991).
- [91AOY] S. Aoyama, M. Kishimoto, T. Manabe, "Influence of Solvent on Dispersability of Ceramic Particles in Polymer Solution," *Ceramic Transactions*, 19, The American Ceramic Society, Inc., Westerville, OH, pp. 67-73, (1991).
- [91ARG] J.F. Argillier, M. Tirrell, "Manipulating Solid-Surface Properties with Polymeric Agents," *Ceramic Transactions*, 19, The American Ceramic Society, Inc., Westerville, OH, pp. 167-82, (1991).
- [91ART] D.J. Arthur, G.S. Swei, "Fluoropolymer Composites with Tailored Properties for High Performance Electronic Packaging," *Ceramic Transactions*, 19, The American Ceramic Society, Inc., Westerville, OH, pp. 397-405, (1991).
- [91AUB] J.N. Auborn, R.A. Haber, "The Effects of Particulate Grain Size and Volume Fraction on the Mechanical Properties of Alumina-Glass Composites," *Ceramic Transactions*, 19, The American Ceramic Society, Inc., Westerville, OH, pp. 789-95, (1991).
- [91BAB] Y. Baba, K. Hagashiyama, S. Segawa, S. Fukanaga, J. Shigemi, "High Density Multilayer Substrate," *Proceedings of the 24th International Symposium on Microelectronics*, Orlando, FL, ISHM, Reston, VA, pp. 498-501, (1991).
- [91BLA] D.C. Blazej, Microelectronics Packaging/Interconnect: An Industry in Transition, Chap. 14, Electronics Packaging Forum, 2, Edited by J.E. Morris, Van Nostrand Reinhold, New York, NY, pp. 437-49, (1991).
- [91BRI] J.D. Bright, S. Danchaivijit, D.K. Shetty, "Interfacial Sliding Friction in Silicon Carbide-Borosilicate Glass Composites: A Comparison of Pullout and Pushout Tests," *J. Am. Cer. Soc.*, 74, [1], pp. 115-22, (1991).



- [91BRU] R. Bruckner, H. Hegeler, "One and Two Dimensionally Reinforced Glasses with Long and Short Fibers," *Ceramic Transactions*, 19, The American Ceramic Society, Inc., Westerville, OH, pp. 797-808, (1991).
- [91CAL] J.M. Calvert, C.S. Dulcey, M.C. Peckerar, J.M. Schnur, J.H. Georger, Jr., G.S. Calabrese, P. Sricharoenchaikit, "New Surface Imaging Techniques for Sub-0.5 Micrometer Optical Lithography," *Solid State Technology*, 34, [10], pp. 77-82, (1991).
- [91CAR] P.J.M. Carrott, M.B. Kenny, R.A. Roberts, K.S.W. Sing, C.R. Theocharis, "The Adsorption of Water Vapour by Microporous Solids," Characterization of Porous Solids II, Edited by F. Rodriguez-Reinoso, J. Roquerol, K.S.W. Sing, K.K. Ungar, Elsevier Science, Amsterdam, pp. 685-92, (1991).
- [91CAS] J.A. Castrovilla, "Thin Films, Thick Films and Multichip Modules," *JOM*, p. 25, (June, 1991).
- [91CAT] M.E. Cather, N.R. Morrow, I. Klich, "Characterization of Porosity and Pore Quality in Sedimentary Rocks," Characterization of Porous Solids II, Edited by F. Rodriguez-Reinoso, J. Roquerol, K.S.W. Sing, K.K. Ungar, Elsevier Science, Amsterdam, pp. 727-36, (1991).
- [91CER] L.M. Sheppard, editor, Ceramic Source, Vol. 7, American Ceramic Society, Inc., (1991).
- [91CHA] N. Chandra, R. Chella, K.L. Chen, "Effect of Cracks on the Mechanical Behavior of Materials-A Finite Element Approach," *Ceramic Transactions*, 19, The American Ceramic Society, Inc., Westerville, OH, pp. 493-501, (1991).
- [91DAY] M. Day, I.B. Parker, J. Bell, M. Thomas, R. Fletcher, J. Duffie, "Modelling of Mercury Intrusion and Extrusion," Characterization of Porous Solids II, Edited by F. Rodriguez-Reinoso, J. Roquerol, K.S.W. Sing, K.K. Ungar, Elsevier Science, Amsterdam, pp. 75-84, (1991).
- [91DEA] J.M. Dealy, "Rheology of Molten Polymers," *MRS Bulletin*, pp. 24-26, (August, 1991).
- [91DEM] U. Demlehner, "The Contact Angle of Liquids in Porous Media," Characterization of Porous Solids II, Edited by F. Rodriguez-Reinoso, J. Roquerol, K.S.W. Sing, K.K. Ungar, Elsevier Science, Amsterdam, pp. 97-104, (1991).
- [91DIL] J.F. DiLazzaro, D.G. Naumann, "Low Temperature Co-Fired Multilayer Ceramics for High Performance Packages," *Proceedings of the 24th International Symposium on Microelectronics*, Orlando, FL, ISHM, Reston, VA, pp. 409-13, (1991).
- [91DIN] D.R. Dinger, J.E. Funk, "Version 2 of Particle-Size Analysis Routines Available on CERABULL," *Ceramic Bulletin*, 70, [4], pp. 669-70, (1991).



- [91DOL] L.E. Dolhert, J.W. Lau, J.H. Enloe, E.Y. Luh, A.L. Kovacs, J. Stephan, "Performance and Reliability of Metallized Aluminum Nitride for Multichip Module Applications," *The International Journal for Hybrid Microelectronics*, 14, [4], pp. 113-20, (1991).
- [91EFR] D.K. Efremov, V.B. Fenelonov, "Adsorption-Desorption Hysteresis in Porous Networks," Characterization of Porous Solids II, Edited by F. Rodriguez-Reinoso, J. Roquerol, K.S.W. Sing, K.K. Ungar, Elsevier Science, Amsterdam, pp. 115-22, (1991).
- [91EME] "Emerging Technologies: What the Experts Say!," *Inside ISHM*, pp. 5-12, November/December, (1991).
- [91EWS] K.G. Ewsuk, "Sintering Maps for Ceramic-Filled-Glass Composites," *Ceramic Transactions*, 19, The American Ceramic Society, Inc., Westerville, OH, pp. 125-35, (1991).
- [91FEI] E. Feit, H. Shaw, "Advances in Thermal Properties Testing at Oak Ridge National Laboratories," *Ceramic Bulletin*, 70, [1], pp. 125-28, (1991).
- [91FIE] J.T. Fielding, Jr., W.S. Hackenberger, T.R. Shrout, R.F. Speyer, "Rate-Controlled Sintering or "Smart Processing" for Electronic Packaging," *Proceedings of the 24th International Symposium on Microelectronics*, Orlando, FL, ISHM, Reston, VA, pp. 387-91, (1991).
- [91FRA1] A.S. Francomacaro, N.A. Blum, G.V. Clatterbaugh, T.R. Sanderson, "Packaging Bare Chip Gallium Arsenide Devices Using Low K, Low Temperature Cofired Ceramic (LTCC) Substrates," *Proceedings of the 24th International Symposium on Microelectronics*, Orlando, FL, ISHM, Reston, VA, pp. 392-96, (1991).
- [91FRA2] A.B. Frazier, M.G. Allen, "Hybrid Multichip Packaging for Micromachined Systems," *Inside ISHM*, pp. 23-26, November/December, (1991).
- [91FUJ] T. Fujita, S. Ishihara, S. Ogiwara, G. Toda, Y. Watanabe, "Multilayer Mullite-Glass Ceramic Substrate for Mainframe Computers," *Proceedings of the 24th International Symposium on Microelectronics*, Orlando, FL, ISHM, Reston, VA, pp. 187-90, (1991).
- [91GIP] J.W. Gippich, K.A. Leahy, A.J. Martin, E.L. Rich, III, K.W. Sparks, "Microwave Dielectric Constant of a Low Temperature Cofired Ceramic," *IEEE Transactions on Components, Hybrids, and Manufacturing Technology*, 14, [4], pp. 732-37, (1991).
- [91GLA] J. Glazer, "Current Developments in Electronic Packaging Materials," *JOM*, p. 7, (June, 1991).
- [91HAD] A.M. Hadian, J.R. McDermid, R.A.L. Drew, "Joining of Si<sub>3</sub>N<sub>4</sub> to Molybdenum for High Temperature Applications," *Ceramic Transactions*, 19, The American Ceramic Society, Inc., Westerville, OH, pp. 221-27, (1991).

- [91HAN] T. Handa, S. Iida, M. Yamada, J. Utsunomiya, "Development of a High Speed, High Density Multi-chip Module for B-ISDN," Proceedings of the 24th International Symposium on Microelectronics, Orlando, FL, ISHM, Reston, VA, pp. 196-200, (1991).
- [91HAY] H. Hayashi, T. Ikeda, S. Nishigaki, "Newly Developed Multilayered Small Size LC Chip-Elements for EMC Noise Filters Made By Low Temperature Fireable Ceramics," Proceedings of the 24th International Symposium on Microelectronics, Orlando, FL, ISHM, Reston, VA, pp. 508-12, (1991).
- [91HEN] N.H. Hendricks, L.C. Hsu, C. Taran, M.L. Marrocco, "Thermoplastic Polyquinolines: New Organic Dielectrics for Highly Demanding Packaging Applications," Proceedings of the 24th International Symposium on Microelectronics, Orlando, FL, ISHM, Reston, VA, pp. 105-9, (1991).
- [91HOF] R.L. Hoffman, "Interrelationships of Particle Structure and Flow in Concentrated Suspensions," MRS Bulletin, pp. 32-37, (August, 1991).
- [91HOR] D.A. Horsma, F.W. Mercer, "Multichip Module Made from FLARE<sup>TM</sup>: A New Low Dielectric Constant, Moisture Insensitive Polymeric Thin Film Dielectric," Proceedings of the 24th International Symposium on Microelectronics, Orlando, FL, ISHM, Reston, VA, pp. 101-04, (1991).
- [91JES] C.A. Jessop, S.M. Riddiford, N.A. Seaton, J.P.R.B. Walton, N. Quirke, "The Determination of the Pore Size Distribution of Porous Solids Using a Molecular Model to Interpret Nitrogen Adsorption Measurements," Characterization of Porous Solids II, Edited by F. Rodriguez-Reinoso J. Roquerol, K.S.W. Sing, K.K. Ungar, Elsevier Science, Amsterdam, pp. 123-32, (1991).
- [91JOR] T.C. Jordon, M.T. Shaw, "Electrorheology," MRS Bulletin, pp. 38-43, (August, 1991).
- [91KAD] O. Kadlec, "The Differences in the Adsorption Processes in Micro and Supermicropores," Characterization of Porous Solids II, Edited by F. Rodriguez-Reinoso, J. Roquerol, K.S.W. Sing, K.K. Ungar, Elsevier Science, Amsterdam, pp. 759-70, (1991).
- [91KAR] A.P. Karnaukhov, "The Main Principles of Modelling of Porous Solids; Models of Systems with Needle-Like Particles," Characterization of Porous Solids II, Edited by F. Rodriguez-Reinoso, J. Roquerol, K.S.W. Sing, K.K. Ungar, Elsevier Science, Amsterdam, pp. 105-13, (1991).
- [91KAT] Z. Kato, J.Y. Kim, K. Saito, K. Uematsu, "Development of a New Direct Method for Determination of Granule Density by Micron-Order Array Technique," Ceramic Bulletin, 70, [1], pp. 129-31, (1991).

- [91KEU] R.L. Keusseyan, P.T. Goeller, J.L. Dilday, L.L. Waterman, L.E. Dellis, J.R. Thrash, M.S. Critzer, "Thermal Cycling Reliability of Interconnections to Low Temperature Fire/Cofired Ceramics," Proceedings of the 24th International Symposium on Microelectronics, Orlando, FL, ISHM, Reston, VA, pp. 493-97, (1991).
- [91KIM] K.H. Kim, M.K. Song, G.L. Park, H.J. Yoon, S.C. Park, "A New Low Impedance Package for the Simultaneous Switching Noise Reduction of a Plastic Package," Proceedings of the 24th International Symposium on Microelectronics, Orlando, FL, ISHM, Reston, VA, pp. 282-86, (1991).
- [91KOV] A.L. Kovacs, P.H. Reaves, "Thermal Performance of Multichip Modules," Proceedings of the 24th International Symposium on Microelectronics, Orlando, FL, ISHM, Reston, VA, pp. 17-21, (1991).
- [91KUM1] A.H. Kumar, R.R. Tummala, "Glass-Ceramic/Copper Multilayer Substrates for High Performance Computers-Materials and Process Challenges," Proceedings of the 24th International Symposium on Microelectronics, Orlando, FL, ISHM, Reston, VA, pp. 1-5, (1991).
- [91KUM2] A.H. Kumar, R.R. Tummala, "State-of-the-Art, Glass-Ceramic/Copper, Multilayer Substrate for High Performance Computers," The International Journal for Hybrid Microelectronics, 14, [4], pp. 137-50, (1991).
- [91KUR] S.J. Kurtz, "Materials Rheology: An Overview," MRS Bulletin, pp. 15-18, (August, 1991).
- [91LYN] S.Y. Lynn, D. Garg, D.S. Hoover, Diamond Thin Films: Applications in Electronic Packaging, Chap. 7, Electronics Packaging Forum, 2, Edited by J.E. Morris, Van Nostrand Reinhold, New York, NY, pp. 229-45, (1991).
- [91MAR] N. Martys, M. Cieplak, M.O. Robbins, "Critical Phenomena in Fluid Invasion of Porous Media," Physical Review Letters, 66, [8], pp. 1058-61, (1991).
- [91MAS1] M. Massiot, "Low Temperature Co-Fired Ceramic: An Emerging Technology in Europe," Proceedings of the 24th International Symposium on Microelectronics, Orlando, FL, ISHM, Reston, VA, pp. 517-22, (1991).
- [91MAS2] G. Mason, D.W. Mellor, "Analysis of the Percolation Properties of a Real Porous Material," Characterization of Porous Solids II, Edited by F. Rodriguez-Reinoso et. al, Elsevier Science, Amsterdam, pp. 41-50, (1991).
- [91MAT1] D.M. Mattox, "Glassy Phase-Limited Thermal Conductivity in Alumina Ceramics," Proceedings of the 24th International Symposium on Microelectronics, Orlando, FL, ISHM, Reston, VA, pp. 451-54, (1991).
- [91MAT2] E. Matjevic, "Interactions of Solutes and Solids with Monodispersed Colloids," Ceramic Transactions, 19, The American Ceramic Society, Inc., Westerville, OH, pp. 155-66, (1991).

- [91MAY] V. Mayagoitia, "The Five Types of Porous Structures and Their Hysteresis Loops," Characterization of Porous Solids II, Edited by F. Rodriguez-Reinoso, J. Roquerol, K.S.W. Sing, K.K. Ungar, Elsevier Science, Amsterdam, pp. 51-60, (1991).
- [91MCG] J. McGroarty, R. Subrahmanyam, C.Y. Li, "Damage Integral Analysis of Solder Joint Fatigue," JOM, pp. 16-20, (June, 1991).
- [91MEC] D.M. Mechtel, H.K. Charles, Jr., C.R. Westgate, "Electro-Optic Probing: A New Tool for the Electronic Packaging Engineer," Proceedings of the 24th International Symposium on Microelectronics, Orlando, FL, ISHM, Reston, VA, pp. 271-76, (1991).
- [91MIK] B. Mikiel, J. A. Varela, O.J. Wittemore, "Equivalence of Surface Areas Determined by Nitrogen Adsorption and by Mercury Porosimetry," Ceramic Bulletin, 70, [5], pp. 829-31, (1991).
- [91MIL] D.R. Milburn, B.D. Adkins, B.H. Davis, "Porosity of Silicas: Comparison of Nitrogen Adsorption and Mercury Penetration," Characterization of Porous Solids II, Edited by F. Rodriguez-Reinoso, J. Roquerol, K.S.W. Sing, K.K. Ungar, Elsevier Science, Amsterdam, pp. 543-51, (1991).
- [91MUS] D. Muscat, M.D. Pugh, R.A.L. Drew, "Pressureless Sintering of an Extruded Si<sub>3</sub>N<sub>4</sub> Whisker Reinforced Composite," Ceramic Transactions, 19, The American Ceramic Society, Inc., Westerville, OH, pp. 137-43, (1991).
- [91NAI] S.V. Nair, M.L. Shaio, "Initiation Toughness VS. Propagation Toughness of a Rubber Modified Glass Fiber Reinforced Thermoplastic Composite," Ceramic Transactions, 19, The American Ceramic Society, Inc., Westerville, OH, pp. 565-71, (1991).
- [91NEI] A.V. Neimark, "Percolation Theory of Capillary Hysteresis Phenomena and its Application for Characterization of Porous Solids," Characterization of Porous Solids II, Edited by F. Rodriguez-Reinoso, J. Roquerol, K.S.W. Sing, K.K. Ungar, Elsevier Science, Amsterdam, pp. 67-74, (1991).
- [91NOV] "Novel Processing for Electronic Packaging," Ceramic Bulletin, 70, [9], p. 1469, (1991).
- [91OTA] T. Ota, I. Yamai, J. Takahashi, "Effects of Filler Particle Size on the Electrical Resistance of Conductor-Polymer Composites," Ceramic Transactions, 19, The American Ceramic Society, Inc., Westerville, OH, pp. 381-87, (1991).
- [91ROB1] K. Robinson, W.K. Jones, "Thermal Management Using Cofired Grooved Substrates," Proceedings of the 24th International Symposium on Microelectronics, Orlando, FL, ISHM, Reston, VA, pp. 383-86, (1991).
- [91ROB2] E. Robens, K.F. Krebs, "Standardization, Reference Materials and Comparative Measurements for Surface Area and Pore Characterization," Characterization of Porous Solids II, Edited by F. Rodriguez-Reinoso, J. Roquerol, K.S.W. Sing, K.K. Ungar, Elsevier Science, Amsterdam, pp. 133-40, (1991).



- [91RUS] W.B. Russel, "Concentrated Colloidal Dispersions," MRS Bulletin, pp. 27-31, (August, 1991).
- [91SAC1] M.D. Sacks, M.S. Randall, G.W. Scheiffele, R. Raghunathan, J.H. Simmons, "Processing of Silicate Glass/Silicon Nitride Composites with Controlled Microporosity," Ceramic Transactions, 19, The American Ceramic Society, Inc., Westerville, OH, pp. 407-420, (1991).
- [91SAC2] M.D. Sacks, N. Bozkurt, G.W. Scheiffele, "Transient Viscous Sintering of Mullite and Mullite-Matrix Composites," Ceramic Transactions, 19, The American Ceramic Society, Inc., Westerville, OH, pp. 111-23, (1991).
- [91SAV] J.G. Saven, J.L. Skinner, J.R. Wright, "Classical and Quantum Continuum Percolation with Hard Core Interactions," J. Chem. Phys., 94, [9], pp. 6153-59, (1991).
- [91SCH1] J.M. Shoenung, "Analysis of the Economics of Silicon Nitride Powder Production," Ceramic Bulletin, 70, [1], pp. 112-16, (1991).
- [91SCH2] G.W. Scherer, "Viscous Sintering of Particle-Filled Composites," Ceramic Bulletin, 70, [6], pp. 1059-63, (1991).
- [91SCH3] G.W. Scherer, "Cell Models for Viscous Sintering," J. Am. Cer. Soc., 74, [7], pp. 1523-31, (1991).
- [91SCH4] G.W. Scherer, A. Jagota, "Effect of Inclusions on Viscous Sintering," Ceramic Transactions, 19, The American Ceramic Society, Inc., Westerville, OH, pp. 99-109, (1991).
- [91SEA] N.A. Seaton, "Determination of the Connectivity of Porous Solids From Nitrogen Sorption Measurements," Chemical Engineering Science, 46, [8], pp. 1895-1909, (1991).
- [91SHE1] G.S. Sheffield, J.R. Schorr, "Comparison of Thermal Diffusivity and Thermal Conductivity Methods," Ceramic Bulletin, 70, [1], pp. 102-06, (1991).
- [91SHE2] L.M. Sheppard, "Surge in Electronic Materials Continues," Ceramic Bulletin, 70, [9], pp. 1467-77, (1991).
- [91SHI1] H. Shibuya, M. Yamada, J. Utsunomiya, S. Iida, T. Handa, "Development of a Low Temperature Co-Fired Multilayer Substrate for High-Speed Signals," Proceedings of the 24th International Symposium on Microelectronics, Orlando, FL, ISHM, Reston, VA, pp. 91-95, (1991).
- [91SHI2] Y. Shimada, A. Dohya, K. Kata, J. Inasaki, "High Speed Computer Packaging with Multilayer Glass-Ceramic Substrate," Proceedings of the 24th International Symposium on Microelectronics, Orlando, FL, ISHM, Reston, VA, pp. 176-82, (1991).
- [91SHI3] M.L. Shively, "Analysis of Mercury Porosimetry for the Evaluation of Pore Shape and Intrusion-Extrusion Hysteresis," Journal of Pharmaceutical Sciences, 80, [4], pp. 376-79, (1991).



- [91SHO] G.P. Shorthouse, A. Berzins, S. Gee, K. Wardell, "A Hermetic Very Low K High Resolution Thick Film Dielectric for High Speed High Density Interconnections," Proceedings of the 24th International Symposium on Microelectronics, Orlando, FL, ISHM, Reston, VA, pp. 528-32, (1991).
- [91SIN] K.S.W. Sing, "Characterization of Porous Solids: An Introductory Survey," Characterization of Porous Solids II, Edited by F. Rodriguez-Reinoso, J. Roquerol, K.S.W. Sing, K.K. Ungar, Elsevier Science, Amsterdam, pp. 1-9, (1991).
- [91STE] S.J. Stein, R.L. Wahlers, C.Y.D. Huang, M.A. Stein, "Interconnection and Packaging of Advanced Electronic Circuitry," Proceedings of the 24th International Symposium on Microelectronics, Orlando, FL, ISHM, Reston, VA, pp. 130-34, (1991).
- [91STO] M.R. Stoudt, E. Escalante, R.E. Ricker, "The Influence of Water on the Mechanical Properties of a Glass-Epoxy Matrix Composite," Ceramic Transactions, 19, The American Ceramic Society, Inc., Westerville, OH, pp. 993-1000, (1991).
- [91SU1] W. Su, S.M. Riad, A. Elshabini-Riad, "Microwave Material Characterization Using Stripline Resonators," The International Journal for Hybrid Microelectronics, 14, [2], pp. 48-54, (1991).
- [91SU2] W. Su, S.M. Riad, T. Poulin, D. Fett, Z.Y. Shen, "Wideband Characterization and Modelling of TAB Packages Using Time Domain Techniques," The International Journal for Hybrid Microelectronics, 14, [2], pp. 55-61, (1991).
- [91SUN] A.J. Sunwoo, H. Hayashigatami, J.W. Morris, Jr., "The Effect of Pretinning on the Solderability of Copper," JOM, pp. 21-24, (June, 1991).
- [91TAN] Z. Tan, K.E. Gubbins, "Theory of Adsorption in Micropores," Characterization of Porous Solids II, Edited by F. Rodriguez-Reinoso, J. Roquerol, K.S.W. Sing, K.K. Ungar, Elsevier Science, Amsterdam, pp. 21-30, (1991).
- [91TSA] C.D. Tsakiroglou, A.C. Payatakes, "Effects of Pore-Size Correlations on Mercury Porosimetry Curves," Journal of Colloid and Interface Science, 146, [2], pp. 479-94, (1991).
- [91TUM] R.R. Tummala, "Ceramic and Glass-Ceramic Packaging in the 1990s," J. Am. Cer. Soc., 74, [5], pp. 895-908, (1991).
- [91UTS] K. Utsumi, "Development of Multilayer Ceramic Components Using Green-Sheet Technology," Ceramic Bulletin, 70, [6], pp. 1050-55, (1991).
- [91VEN] K.R. Venkatachari, B.C. Mutsuddy, "Dispersion of Silicon Nitride Powders in Aqueous Media with Coupling Agents," Ceramic Transactions, 19, The American Ceramic Society, Inc., Westerville, OH, pp. 75-82, (1991).
- [91VES] R.W. Vest, "A Loading Curve Model for RuO<sub>2</sub> Thick Film Resistors as a Function of Glass Viscosity," Proceedings of the 24th International Symposium on Microelectronics, Orlando, FL, ISHM, Reston, VA, pp. 418-25, (1991).

- [91VOL] V.R. Voller, "The Symposium on Materials Processing in the Computer Age," JOM, p. 6, (June, 1991).
- [91WAK] M. Wakamatsu, S. Ishida, N. Takeuchi, M. Ishekawa, K. Watanabe, "Study of the Mechanism of the Oxidation of Sintered  $\text{Si}_3\text{N}_4$  Under Wet Atmosphere by Mass Spectrometric Gas Analysis," Ceramic Transactions, 19, The American Ceramic Society, Inc., Westerville, OH, pp. 953-59, (1991).
- [91WAL] S. Wallace, Porous Silica Gel Monoliths: Structural Evolution and Interactions with Water, Ph. D. Dissertation, University of Florida, 1991.
- [91WES] A.D. Westwood, M.R. Notis, "An Issue in Thermal Management: Metallizing High Thermal Conductivity Ceramic Substrates in Microelectronics," JOM, pp. 10-15, (June, 1991).
- [91WIL1] C. Williams, "Design Considerations for Microwave Packages," Ceramic Bulletin, 70, [4], pp. 714-21, (1991).
- [91WIL2] J. Williams, K. Smith, E. Godshalk, "Improved Techniques for Characterization of High-Speed Packaging," Proceedings of the 24th International Symposium on Microelectronics, Orlando, FL, ISHM, Reston, VA, pp. 262-66, (1991).
- [91WIN1] W.L. Winterbottom, S.K. Kang, "Interconnection Technologies and Materials Science," JOM, pp. 8-9, (June, 1991).
- [91WIN2] A. Wineman, "Mechanical Response of Linear Viscoelastic Solids," MRS Bulletin, pp. 19-23, (August, 1991).
- [91WIN3] H.H. Winter, "Polymer Gels, Materials that Combine Liquid and Solid Properties," MRS Bulletin, pp. 44-48, (August, 1991).
- [91WIN4] A. Winter, "Wetting Phenomena in Porous Solids: Mechanisms and Models," Characterization of Porous Solids II, Edited by F. Rodriguez-Reinoso, J. Roquerol, K.S.W. Sing, K.K. Ungar, Elsevier Science, Amsterdam, pp. 85-96, (1991).
- [91YOK] K. Yokouchi, N. Kamehara, K. Niwa, "Packaging Technology for High-Speed Computers-Multilayer Glass/Ceramic Circuit Board," Proceedings of the 24th International Symposium on Microelectronics, Orlando, FL, ISHM, Reston, VA, pp. 183-86, (1991).
- [91ZGR] G. Zgrablich, S. Mendioroz, L. Daza, J. Pajares, V. Mayagoitia, F. Rojas, W.C. Conner, "Effect of Porous Structure on the Determination of Pore Size Distribution by Mercury Porosimetry and Nitrogen Sorption," Langmuir, 7, pp. 779-85, (1991).
- [91ZIE] J.F. Zievers, P. Eggerstedt, "Porous Ceramics for Gas Filtration," Ceramic Bulletin, 70, [1], pp. 108-11, (1991).
- [91ZUS] M.P. Zussman, Low Dielectric Constant Materials for Packaging High Speed Electronics, Chap. 8, Electronics Packaging Forum, 2, Edited by J.E. Morris, Van Nostrand Reinhold, New York, NY, pp. 247-80, (1991).

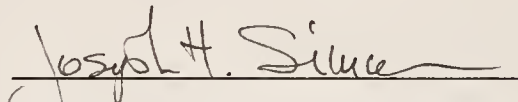
- [92ALL] D.T. Allen, "An Overview of Industrial Waste Generation and Management Practices," MRS Bulletin, pp. 30-33, March, (1992).
- [92AUL] N.N. Ault, R.L. Yeckley, "Silicon Nitride," Ceramic Bulletin, 71, [5], p. 816, (1992).
- [92BAL] J.W. Balde, "Crisis in Technology: The Questionable Ability to Make Thin Film Multichip Modules," Inside ISHM, pp. 13-16, (May/June, 1992).
- [92CAD] R.L. Cadenhead, "SMT: Its Roots and Evolution Through Technical Societies," Inside ISHM, pp. 37-39, January/February (1992).
- [92COX] M.R. Cox, L.H. Ng, "An Economic Comparison of High and Low-Temperature Cofired Ceramics," Inside ISHM, pp. 31-33, (1992).
- [92DEL] J.A. del Alamo, "GaAs Integrated Circuit Manufacturing," MRS Bulletin, pp. 42-44, April, (1992).
- [92ISH1] "Hybrid Technology: 1967-1972," Inside ISHM, p. 18, January/February, (1992).
- [92ISH2] "MCMs: What the Experts Say," Inside ISHM, pp. 5-10, (March/April, 1992).
- [92MAX] C. Maxwell, D.R. Dinger, "Ball Clay: Effects of Processing on Suspension Rheology," Ceramic Bulletin, 71, [8], pp. 1225-33, (1992).
- [92PFA] R.C. Pfahl, Jr., "Materials in Electronic Manufacturing: Electronic Packaging," MRS Bulletin, pp. 38-41, April, (1992).
- [92RIC] R.W. Rice, J.H. Enloe, J.W. Lau, E.Y. Luh, L.E. Dolhert, "Hot-Pressing--A New Route to High-Performance Ceramic Multilayer Electronic Packages," Ceramic Bulletin, 71, [5], pp. 751-55, (1992).
- [92SAS] A. Sasaki, Y. Shimada, "Electrical Design Technology for Low Dielectric Constant Multilayer Ceramic Substrate," IEEE Transactions on Components, Hybrids and Manufacturing Technology, 15, [1], pp. 56-63, (1992).
- [92SHE] L.M. Sheppard, "Particle Analysis Equipment: Capabilities Expand," Ceramic Bulletin, 71, [5], pp. 715-27, (1992).
- [92SKE] P.J. Skerrett, "The TeraFLOPS Race: Computing at One Trillion Operations Per Second," Popular Science, pp. 50-56, (March, 1992).
- [92WAT] R.D. Watkins, B. Granoff, "Introduction to Environmentally Concious Manufacturing," MRS Bulletin, pp. 34-38, March, (1992).

#### BIOGRAPHICAL INFORMATION


Michael Steven Randall was born June 25, 1963, in Hornell, New York. He attended Arkport Central School from kindergarten through 12th grade where he received a Regents Scientific Diploma, with honors, in 1981. He then attended the New York State College of Ceramics, at Alfred University in Alfred, New York where he graduated, magna cum laude, in 1985 with a Bachelor of Science degree in ceramic engineering (minoring in business administration and chemistry).

Michael Randall next attended the University of Florida, in Gainesville, Florida where he received a Master of Science degree in materials science and engineering, in 1987. He is currently working toward obtaining his Doctor of Philosophy in materials science and engineering, at the University of Florida, and is employed as a Principal Engineer at AVX Corporation in Myrtle Beach, South Carolina.

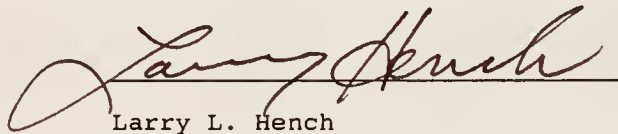
I certify that I have read this study and that in my opinion it conforms to acceptable standards of scholarly presentation and is fully adequate, in scope and quality, as a dissertation for the degree of Doctor of Philosophy.

  
Joseph H. Simmons, Chairperson  
Professor of Materials  
Science and Engineering

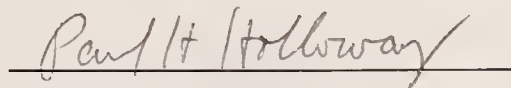
I certify that I have read this study and that in my opinion it conforms to acceptable standards of scholarly presentation and is fully adequate, in scope and quality, as a dissertation for the degree of Doctor of Philosophy.

  
Michael D. Sacks, Cochairperson  
Professor of Materials  
Science and Engineering

I certify that I have read this study and that in my opinion it conforms to acceptable standards of scholarly presentation and is fully adequate, in scope and quality, as a dissertation for the degree of Doctor of Philosophy.

  
Larry L. Hench  
Graduate Research  
Professor of Materials  
Science and Engineering

I certify that I have read this study and that in my opinion it conforms to acceptable standards of scholarly presentation and is fully adequate, in scope and quality, as a dissertation for the degree of Doctor of Philosophy.

  
Paul H. Holloway  
Professor of Materials  
Science and Engineering



I certify that I have read this study and that in my opinion it conforms to acceptable standards of scholarly presentation and is fully adequate, in scope and quality, as a dissertation for the degree of Doctor of Philosophy.

Dorothea E. Burk

Dorothea E. Burk  
Professor of Electrical  
Engineering

This dissertation was submitted to the Graduate Faculty of the College of Engineering and to the Graduate School and was accepted as partial fulfillment of the requirements for the degree of Doctor of Philosophy.

August 1993

Winfred M. Phillips

Winfred M. Phillips  
Dean, College of Engineering

Dean, Graduate School

UNIVERSITY OF FLORIDA



3 1262 08556 8631